



European
Commission

Horizon 2020
European Union funding
for Research & Innovation

IDENTIFYING EXTRACELLULAR VESICLE REGULATORS IN PROSTATE CANCER CELLS

DOCTOR OF PHILOSOPHY

2024

MARIAMA M'BENGUE

Abstract

Prostate cancer (PCa) cells secrete extracellular vesicles (EVs) that exhibit many disease promoting functions. The mechanisms involved in EV generation, however, remain to be fully elucidated. We aimed to identify mechanistic factors responsible for the regulation of EV secretion in PCa cells.

Candidates with a putative role in EV generation were selected based on a comprehensive database and literature interrogation. Identified candidates included Rab6a, Rab7a, Rab11b, Rab27b, Rab35, Rab37, CHMP4C, VPS28, CD81, CD9, SCAMP3, SIMPLE, Syntaxin-6, SNAP23, VAMP3, Piccolo and Synaptogyrin-2; all had some previous association with vesicle regulation but have not been comparatively tested in a single PCa model. A shRNA-based approach was successfully utilised to attenuate gene expression of most (14/17) candidates. Nanoparticle tracking analysis revealed that the target attenuations did not induce major changes in EV size nor number secreted. Immuno-affinity analysis showed that knockdown of CD9, CD81, CHMP4C and Synaptogyrin-2 had the biggest impact on vesicle-tetraspanin expression. RNA-sequencing analysis revealed a candidate specific impact on various transcripts with implications on stem cell-like status (CD9), RNA processing (CD81), cell division (CHMP4C) and virus processing (Synaptogyrin-2). Furthermore, most manipulations induced changes in the endolysosomal pathway, consistent with our expectation in regulation of endosomally-derived EVs.

We explored the impact of modification of EV secretory processes on EV function and demonstrated that EVs from knockdown cells exhibited a reduced capacity to modulate the secretome of recipient fibroblasts. We also observed differences in knockdown EV-mediated phosphorylation of several cellular targets, indicating a knockdown dependent qualitatively distinctive fibroblast response to the EVs.

The study has demonstrated some of the challenges in targeting global EV production pathways and hence this is also likely to be difficult in a therapeutic setting. Nonetheless, introducing subtle changes to the EV phenotype, rather than attenuating total EV secretion, confer downstream functional impacts that may be therapeutically exploited.

Table of contents

Abstract.....	ii
List of figures.....	vii
List of tables.....	ix
Abbreviations.....	xi
Acknowledgments.....	xvi
Scientific contributions.....	xviii
Chapter 1: Introduction.....	1
1.1 Prostate cancer.....	2
1.2 PCa diagnostics.....	4
1.2.1 Multiparametric magnetic resonance imaging as a PCa diagnostic tool.....	5
1.3 Biopsy of suspected PCa samples.....	6
1.3.1 Current guidelines in the UK.....	9
1.4 Treatment.....	10
1.4.1 Radiotherapy.....	11
1.4.2 Androgen deprivation therapy.....	13
1.4.3 Docetaxel.....	13
1.5 The tumour microenvironment.....	14
1.5.1 Cancer-associated fibroblasts.....	15
1.5.2 Markers for CAFs.....	16
1.5.3 CAFs in PCa.....	16
1.5.4 Functional diversity of CAFs.....	17
1.5.5 Origins of CAFs.....	20
1.5.6 Transforming growth factor β signalling in CAFs.....	22
1.6 Extracellular vesicles.....	24
1.6.1 Biogenesis of EVs.....	25
1.6.2 Intracellular transport.....	30
1.6.3 Release of EVs out of the cell.....	31
1.6.4 Considerations about EV-secretion in PCa.....	32
1.6.5 EV Cargo.....	33
1.6.6 Functional role of EVs.....	35
1.6.7 EVs as drug delivery vehicles.....	37
1.6.8 Methods to study EVs.....	38
1.6.9 Characterisation of EVs.....	42

1.7 Hypothesis and aims	45
Chapter 2: Materials and Methods	46
2.1 Bioinformatic tools	47
2.1.1 Candidate interaction network	47
2.1.2 Artificial neural networks (ANN)	47
2.1.3 CancerTool	49
2.2 Cell culture	49
2.2.1 Monolayer cell culture	49
2.2.2 shRNA-mediated knockdown of candidates within PC3 cells	50
2.3 Cell characterisation	56
2.3.1 Bicinchoninic acid (BCA) protein assay	56
2.3.2 Western blotting	56
2.3.3 RNA isolation and reverse transcription	57
2.3.4 Quantitative polymerase chain reaction (qPCR)	59
2.3.5 Detecting surface antigens by flow cytometry	60
2.3.6 Assessment of cell proliferation	63
2.4 EV characterisation	63
2.4.1 Conditioned media collection and EV isolation	63
2.4.2 Ultracentrifugation	64
2.4.3 Nanoparticle tracking analysis	65
2.4.4 Immunophenotyping of EVs	65
2.4.5 EVQuant	66
2.5 Functional analysis of EVs	68
2.5.1 Fibroblast to myofibroblast differentiation assay	68
2.5.2 Assessment of EV induced α -SMA expression in fibroblasts	68
2.5.3 Microscopy	69
2.5.4 Assessment of EV-mediated signalling and cytokine production in recipient fibroblasts	70
2.5.5 Proteome Profiler Human Phospho-Kinase Array Kit (R&D Systems)	71
2.6 RNA Sequencing (RNA-Seq)	71
2.6.1 Pre RNA-seq quality control	72
2.6.2 Library preparation and sequencing	72
2.6.3 Downstream analysis of differentially expressed genes	73
2.7 Statistical analysis	74
Chapter 3: Identification of potential EV regulators in PCa cells	75
3.1 Introduction	76

3.2	Aims and objectives	78
3.3	Results	79
3.3.1	Selection of candidate factors involved in EV secretion.....	79
3.3.2	Interaction network of the selected candidates	87
3.3.3	Involvement of the candidates in EV regulating pathways	90
3.3.4	Clinical relevance of the selected candidates	95
3.4	Discussion	102
Chapter 4: Attenuation of potential EV regulators in PC3 cells		106
4.1	Introduction	107
4.1.1	Characterisation of EVs.....	108
4.1.2	Aims and objectives	108
4.2	Results	110
4.2.1	Puromycin kill curve for PC3 cells	110
4.2.2	Targeted attenuation of EV regulators	112
4.2.3	The Impact of candidate attenuation on cell proliferation.....	117
4.2.4	The impact of putative EV regulators on EV secretion.....	121
4.2.5	The impact of putative EV regulators on the molecular features of EVs.....	127
4.2.6	The stability of the target attenuation in the KD cell lines	135
4.2.7	The impact of candidate attenuation on proliferation	140
4.2.8	Characterisation of purified vesicles derived from CD9KD, CD81KD, CHMP4CKD and SYNGR2KD PC3 cells.....	141
4.2.9	TGF- β 1 levels is altered in the KD EVs.....	143
4.3	Discussion	146
Chapter 5: Impact of knockdown of CD9, CD81, CHMP4C or SYNGR2 on fibroblast function		151
5.1	Introduction	152
5.1.1	Tumour microenvironment.....	152
5.1.2	Markers for cancer associated fibroblasts	152
5.1.3	Secretome of CAFs	153
5.1.4	Precursor cells of CAFs.....	154
5.1.5	Aim and objectives.....	155
5.2	Results	157
5.2.1	PC3 CM does not impact cell proliferation in recipient fibroblasts.....	157
5.2.2	The PC3 secretome induces fibroblast differentiation	159
5.2.3	PC3 CM induce changes in α -SMA transcript expression in fibroblasts	163
5.2.4	PC3 CM induces changes in α -SMA protein expression in fibroblasts	166

5.2.5	PC3 CM modulates the secretion of various growth factors by fibroblasts	169
5.2.6	PC3 EVs alter the phosphorylation profile of fibroblasts	177
5.3	Summary	194
5.4	Discussion	195
Chapter 6: Understanding the impact of candidate attenuation by analysis of cellular and vesicular RNA.....		200
6.1	Introduction	201
6.1.1	RNA encapsulated in EVs	201
6.1.2	RNA-sequencing techniques for transcriptome analysis.....	204
6.1.3	Aims and objectives	208
6.2	Results	209
6.2.1	Isolation of vesicular RNA	209
6.2.2	Isolation of cellular RNA	219
6.2.3	Transcriptomic differences between the KDs.....	225
6.2.4	Gene set variation analysis (GSVA)	230
6.2.5	Attenuation of CD9 impacts various biological processes	234
6.2.6	Attenuation of CD81 impacts various EV regulating processes.....	242
6.2.7	Attenuation of CHMP4C impacts the cellular transcriptome in PC3 cells	250
6.2.8	Attenuation of SYNGR2 has a significant impact on the gene expression	254
6.2.9	Impact of knockdown on the transcripts of our other candidates	262
6.2.10	Summary.....	265
6.3	Discussion	267
Chapter 7: General Discussion.....		270
7.1	Summary of results	271
7.1.1	The rationale for a candidate-based approach	271
7.1.2	shRNA based attenuation	272
7.1.3	Impact on EVs.....	273
7.1.4	Functional impact.....	274
7.1.5	KD of candidates.....	275
7.2	Limitations	276
7.3	Future directions	277
7.3.1	Defining the molecular composition of EVs	277
7.3.2	Functional explorations	279
7.4	Conclusion	281
Annexes		282
References.....		293

List of figures

Figure 1.1: PCa is a major global health burden.	3
Figure 1.2: Histological features of Gleason pattern (grades) 3, 4 and 5.	7
Figure 1.3: Cancer associated fibroblasts in the TME support the tumour.	21
Figure 1.4: Simplified TGF- β signalling.	23
Figure 1.5: The generation of EVs involves a range of regulators.	26
Figure 1.6: Overview of different commonly used EV isolation methods.	39
Figure 2.1: Gating strategy used for the analysis of surface proteins by flow cytometry.	62
Figure 3.1: Search strategy for our candidate list.	81
Figure 3.2: Interaction network of the selected candidates.	89
Figure 3.3: The majority of the selected candidates overlap with an EV related pathway.	91
Figure 3.4: Functional enrichment analysis of the 1 st neighbours of SYNGR2.	93
Figure 3.5: Functional enrichment analysis of the 1 st neighbours of PCLO.	94
Figure 3.6: SNAP23 and Rab7a mRNA expression is altered in PCa patients.	98
Figure 4.1: Puromycin kill curve for PC3 cells.	111
Figure 4.2: Validation of candidate mRNA attenuation by TaqMan Gene Expression assays.	113
Figure 4.3: Validating the attenuation of candidates likely involved in intracellular vesicle transport by TaqMan Gene Expression assays.	115
Figure 4.4: Validating the attenuation of candidates likely involved in vesicle release by TaqMan Gene Expression assays.	116
Figure 4.5: Impact of shRNA transductions on cell proliferation in PC3 cells.	118
Figure 4.6: Characterising vesicles from lentiviral transduced PC3 cell CM by NTA.	125
Figure 4.7: Characterising vesicles form lentiviral transduced PC3 CM by EVQuant.	128
Figure 4.8: Characterising tetraspanin positive vesicle populations using an immunofluorescence plate-based assay.	131
Figure 4.9: Validation of CD9 and CD81 attenuation in the generated PC3 variants.	138
Figure 4.10: Stability of CHMP4C and SYNGR2 attenuation over time.	139
Figure 4.11: Growth curves of the NMC, CD9KD, CD81KD, CHMP4CKD and SYNGR2KD cell lines.	140
Figure 4.12: Characterising purified vesicles from lentiviral transduced PC3 cells by NTA. .	142
Figure 4.13: CD9, CD81 and SYNGR2 influence vesicular TGF- β 1 levels.	144
Figure 5.1: Strategy to explore the functional impact of CD9, CD81, CHMP4C and SYNGR2 dependent PCa factors on recipient fibroblasts.	156
Figure 5.2: PC3 cell-derived CM does not stimulate the proliferation of AG02262 fibroblasts.	158
Figure 5.3: PC3 CM triggers fibroblast differentiation to a myofibroblastic phenotype.	162
Figure 5.4: PC3 CM downregulates α -SMA mRNA in fibroblasts.	165
Figure 5.5: PC3 KD cCM dependant modulation of α -SMA protein expression in fibroblasts.	167
Figure 5.6: CD9KD, CD81KD, CHMP4CKD and SYNGR2KD derived EVs lose their potency to induce IL-6 secretion in recipient fibroblasts.	172
Figure 5.7: CD9, CD81, CHMP4C, and SYNGR2 dependant EVs induce HGF secretion in fibroblasts.	175
Figure 5.8: PC3 EVs increase HGF secretion in fibroblasts independent of HGF mRNA upregulation.	176

Figure 5.9: PC3 EVs alter target phosphorylation in recipient fibroblasts.....	180
Figure 5.10: PC3 EVs alter target phosphorylation in recipient fibroblasts.....	189
Figure 6.1: Locally performed vesicular RNA quality control.....	210
Figure 6.2 Quality control of vesicular RNA performed at Genomescan.....	214
Figure 6.3: RNA traces of vesicular samples isolated by an ExoRNeasy kit (Qiagen).	217
Figure 6.4: Integrity and size distribution of cellular RNA isolated from NMC cells and CMP4CKD cells.....	222
Figure 6.5: Quality control of the sequencing library and the sequencing results.....	224
Figure 6.6: The transcriptome of NMC cells, CD9KD, CD81KD, CHMP4CKD, and SYNGR2KD cells have a distinct transcriptome.....	226
Figure 6.7: RNA-seq data features.....	229
Figure 6.8: CD9KD, CD81KD, CHMP4CKD, SYNGR2KD and NMC cells have a KD specific distinct gene set enrichment pattern.....	231
Figure 6.9: Distribution of differential expressed genes comparing CD9KD and NMC cells.....	235
Figure 6.10: Top ranking biological function hits enriched in CD9KD cells.....	238
Figure 6.11: Top ranking cellular compartment hits enriched in CD9KD cells.....	240
Figure 6.12: Distribution of differential expressed genes comparing CD81KD and NMC cells.	243
Figure 6.13: Top ranking biological function hits enriched in CD81KD cells.....	246
Figure 6.14: Top ranking cellular compartment hits enriched in CD81KD cells.....	248
Figure 6.15: Distribution of differential expressed genes comparing CHMP4CKD and NMC cells.....	251
Figure 6.16: Top ranking biological function hits enriched in CHMP4CKD cells.....	252
Figure 6.17: Top ranking cellular compartment hits enriched in CHMP4CKD cells.....	253
Figure 6.18: Distribution of differential expressed genes comparing SYNGR2KD and NMC cells.....	255
Figure 6.19: Top ranking biological function hits enriched in SYNGR2KD cells.....	258
Figure 6.20: SYNGR2KD is associated with changes in the expression of endosomal genes.	260

List of tables

Table 1.1: PCa Grade groups and their clinical features.	8
Table 1.2: TNM staging system for PCa. Table based on the guidelines provided by the European association of urology (https://uroweb.org/guidelines/prostate-cancer/chapter/classification-and-staging-systems#note_103).	9
Table 1.3: CPGs table from (Gnanapragasam et al., 2018).	10
Table 2.1: Gene lists for the functional hierarchical clustering analysis.	48
Table 2.2: Table of MISSION® lentiviral particles (Sigma-Aldrich) used to transduce PC3 cells.	52
Table 2.3: Antibodies tested for Western Blotting.	57
Table 2.4: Reverse transcription reaction mix Kit with RNase inhibitor (applied biosystems by Thermo Fisher Scientific).	59
Table 2.5: TaqMan assays used for this work.	60
Table 2.6: Overview of samples included in flowcytometry experiments.	60
Table 2.7: Antibodies used for flow cytometry.	61
Table 2.8: Calculations for the normalisation of CM.	64
Table 2.9: Antibodies used for the microplate based immunophenotyping of EVs.	66
Table 2.10: TMED and APS mix for immobilising EVs.	67
Table 3.1: Candidates selected for this study.	82
Table 3.2: Potential clinical relevance of the selected candidates.	100
Table 4.1: Impact of candidate attenuation in PC3 cells on cell proliferation.	120
Table 4.2: Summary of the immunophenotyping of EVs derived from CM.	134
Table 5.1: Summary of the impact of PC3 cCM on fibroblasts in regard to α -SMA expression in stress fibres, at mRNA level and at protein.	169
Table 5.2: Summary of the impact of PC3 EVs on recipient fibroblasts.	177
Table 5.3: Most prominent alterations in the phosphorylation pattern in fibroblasts upon EV stimulation.	182
Table 5.4: Top NMC EV hits compared to KD EV stimulation.	191
Table 6.1: Calculation of the ribosomal, globins and mitochondrial in the sequencing library based on the indicate vesicular RNA samples which were extracted using a phenol-based method.	215
Table 6.2: Vesicular RNA concentrations of the indicated vesicular RNA samples, which were extracted using the exoRNeasy kit (Qiagen), were determined utilising a Quant-it™ RiboGreen RNA assay.	216
Table 6.3: Calculation of the ribosomal, globins and mitochondrial in the sequencing library based on the indicate vesicular RNA samples which were extracted using a exoRNeasy kit (Qiagen).	219
Table 6.4: Cellular RNA was isolated from NM control cells, CD9KD cells, CD81KD cells, CHMP4CKD and SYNGR2KD cells. RNA concentrations were determined using a Quant-it™ RiboGreen RNA assay.	219
Table 6.5: The top 5 up and top 5 down regulated genes identified in the DEG list from the CD9KD cell line.	236
Table 6.6: Impact of CD9 attenuation on cellular compartments.	241
Table 6.7: The top 5 up and top 5 down regulated genes identified in the DEG list from the CD81KD cell line.	244

Table 6.8: extended list of DEGs identified in the CD81KD DEG list limited to ESCRT components, tetraspanins and previously described EV regulators.	245
Table 6.9: Impact of CD81 attenuation on cellular compartments.	249
Table 6.10: The top 5 up and top 5 down regulated genes identified in the DEG list from the CHMP4CKD cell line.....	250
Table 6.11: The top 5 up and top 5 down regulated genes identified in the DEG list from the SYNGR2KD cells.	254
Table 6.12: List of DEGs identified in the SYNGR2KD DEG list focused on members of the synaptogyrin family and integrins.....	256
Table 6.13: Impact of SYNGR2 attenuation on cellular compartments.....	261
Table 6.14: Influence of the candidate attenuation (CD9, CD81, CHMP4C and SYNGR2) on each other.	264

Abbreviations

°	Degree
μ	Micro
3D	3 dimensions
3D-CRT	Three-dimensional conformal radio therapy
A	
ADT	Androgen Deprivation Therapy
AF4	Asymmetrical-flow field-flow fractionation
AGO2	Argonaute-2
ALIX	Apoptosis-linked gene 2-interacting Protein X
ANN	Artificial Neural Networks
ANOVA	Analysis of Variance
APS	Ammonium persulfate
ARF1	ADP-ribosylation factor 1
ARF6	ADP ribosylation factor 6
ASR	Age standardised rates
B	
BCA	Bicinchoninic acid
BED	Biological Effector Database
Bp	Base pair
BSA	Bovine serum albumin
C	
C	Celsius
CAF	Cancer-associated fibroblast
CAS9	CRISPR-associated protein 9
CCL2	C-C motif ligand 2
cCM	Cell number corrected conditioned media
CD105	Endoglin
CD81	Cluster of differentiation 81
CD9	Cluster of differentiation 9
cDNA	Complementary DNA
CHMP4C	charged multivesicular body protein 4C
CM	Conditioned media
CO ₂	Carbon dioxide
CPG	Cambridge Prognostic Group
CPM	Counts per million
Cre-loxP	Cre-locus of crossing (X) over, P1
CRISPR	Clustered regularly interspaced short palindromic repeats
Cryo-EM	Cryogenic
ct	Cycle threshold
CXCL12	C motif chemokine ligand 12
CXCL8	C-X-C motif ligand 8

D

DAPI	4',6-diamidino-2-phenylindole
DEGs	Differentially expressed genes
DFS	Disease free survival
DHEA	Dehydroepiandrosterone
DMEM	Dulbecco's modified eagle's media
DNA	Deoxyribonucleic acid
dNTPs	Deoxynucleoside triphosphate
DOI	Digital Object Identifier
DPBS	Dulbecco's Phosphate-Buffered Saline
DRE	Digital rectal examination
DTT	Dithiothreitol
dUTP	Deoxy uridine triphosphate

E

e.g.,	Exempli gratia
ECM	Extracellular matrix
ELISA	Enzyme-linked immunosorbent assay
EMT	Epithelial mesenchymal transition
ERK	Extracellular signal-regulated kinase
ESUR	European Society of Urogenital Radiology
et al.	et alia

F

FAP	Fibroblast activating protein
FBS	Foetal bovine serum
FGF2	Fibroblast growth factor 2
FGFR	Fibroblast growth factor receptor
FSC-A	Forward scatter area
FSC-H	Forward scatter height
F.U.	Fluorescent unit

G

GAPDH	Glyceraldehyde-3-Phosphate Dehydrogenase
GMO	Genetically modified organism
GO	Gene ontology
GS	Gleason score
GSVA	Gene Set Variation Analysis
GEA	Gene Set Enrichment Analysis

H

H	Hour(s)
H ₂ O	Water
HDR	High dose rate
HeLa	Henrietta Lacks
HGF	Hepatocyte growth factor
hnRNP	Heterogenous nuclear ribonucleoprotein
HRP	Horseradish peroxidase

Hsp	Heat shock protein
HSPA	Heat-shock 70kda protein 1A
HUVEC	Human umbilical vein endothelial cells
I	
IgG	Immunoglobulin
IHC	Immunohistochemistry
IL-6	Interleukin-6
ILVs	Intraluminal vesicles
IMRT	intensity modulated radiotherapy
J	
JAK	Janus kinases
K	
KD	Knockdown
KO	Knockout
L	
LAMP	Lysosomal-associated membrane protein
LAP	Latency associated peptide
LBPA	Lysobisphosphatidic acid
LDR	Low dose rate
LDS	Lithium dodecyl sulphate
LITAF	Lipopolysaccharide Induced TNF Factor
LM	Loading marker
LNCaP	Lymph Node Carcinoma of the Prostate
lncRNA	Long non-coding RNA
LOD	Limit of detection
LOXL2	Lysl oxidase like 2
M	
M	Metastatic side
MS	Mass spectrometry
MFI	Median fluorescent intensity
MHC	Major histocompatibility complex
min	minute(s)
miRNA	Microribonucleic acid
MISEV	Minimal Information for Studies of Extracellular Vesicles
MMP	Matrix metalloproteinase
MOI	Multiplicity of infection
MOP	3-Morpholinopropane-1-sulfonic acid
MRI	Magnetic resonance imaging
mRNA	Messenger ribonucleic acid
MRP1	Multidrug Resistance Protein 1
MSC	Mesenchymal stem cell
MSigDB	Molecular Signatures Database
MV	Microvesicle vesicle
MVB	Multivesicular bodies

MVE	Multivesicular endosome
N	
N	Normal tissue
NA	Non applicable
NaOH	Sodium hydroxide
NHS	National Health Service
NICE	National Institute for Health and Care Excellence
NMC	Non-mammalian control
nSMase	Neutral sphingomyelinase
nt	Nucleotide
NTA	Nanoparticle tracking analysis
NVEP	Non vesicular extracellular particles
P	
PBS	Phosphate buffered saline
PCa	Prostate cancer
PCLO	Piccolo
PCR	Polymerase chain reaction
PDGF	Platelet derived growth factor
PDGF R β	Platelet-derived growth factor receptor beta
PDL-1	Programmed Death-Ligand 1
PEG	Polyethylene glycol
PI-RAD	Prostate Imaging Reporting and Data System
PMSF	Phenyl methane sulfonyl fluoride
PRAS40	Proline rich Akt substrate 40
PSA	Prostate specific antigen
PSMA	Prostate specific membrane antigen
PT	Primary tumour
PVDF	Polyvinylidene fluoride
Q	
QC	Quality control
qPCR	Quantitative polymerase chain reaction
R	
Rab	RAS-related protein
RISC	Ribonucleic acid inducing silencing complex
RNA	Ribonucleic acid
RNAi	Ribonucleic acid interference
RNA-seq	RNA sequencing
RPMI	Roswell Park Memorial Institute
RQ	Relative quantification
rRNA	Ribosomal RNA
S	
SCAMP3	Secretory carrier membrane proteins 3
SD	Standard deviation
SDS	Sodium dodecyl sulphate

SEC	Size-exclusion chromatography
SEC	Size-exclusion chromatography
SEM	Standard error of mean
SFPR1	Secreted frizzled related protein 1
shRNA	Short hairpin ribonucleic acid
SIMPLE	Lipopolysaccharide Induced TNF Factor
siRNA	Short-interfering ribonucleic acid
SMAD	Suppressor of Mothers against Decapentaplegic
SNAP	Synaptosomal-Associated Protein
SNARE	Soluble N-ethylmaleimide-sensitive fusion attachment protein
SSC-A	Side scatter area
STAT	Signal transducer and activator of transcription
STX6	Syntaxin 6
SYNCRIP	Synaptotagmin Binding Cytoplasmic RNA Interacting Protein
SYNGR2	Synaptogyrin-2

T

TCGA	The Cancer Genome Atlas
TES	Transposable element
TF	Transcription factor
TGFBR1	TGF- β receptor 1
TGF- β	Transforming growth factor beta
TIMP-1	Tissue inhibitor of metalloproteinase-1
TIMP-2	Tissue inhibitor of metalloproteinase-2
TME	Tumour microenvironment
TNM	Tumour node metastasis
TRF	Time resolved fluorescence
TRUS	Trans-rectal ultrasound
TSS	Transcription start site
t-SNE	T-distributed stochastic neighbour embedding
TU	Transduction units

U

UC	Ultracentrifugation
UF	Ultrafiltration
UK	United Kingdom
UV	Ultraviolet

V

V/V	Volume per volume
VAMP	Vesicle-associated membrane protein
VEGF	Vascular Endothelial Growth Factor
VPS	Vacuolar protein sorting

W

Wnt	Wingless/integrated
WWP1	W domain containing E3 ubiquitin protein ligase 1

Acknowledgments

Firstly, I would like to thank the European Union's Horizon 2020 research and innovation programme for funding this research under the Marie Skłodowska-Curie grant agreement proEVLiFeCycle. I am very grateful for the exceptional opportunities I had through participating in this network.

I would also like to express my gratitude to my supervisors Dr Jason Webber and Prof Dr Aled Clayton for introducing me to the extracellular vesicle field. Their guidance and support throughout my journey as a PhD student helped me grow both personally and as a scientist.

During my PhD studies, I had the privilege of being part of the ProEVLiFeCycle network. I would like to thank the coordinators Guido Jenster, Katie Wright and Diana Brusik - van Houten for their outstanding efforts to organise excellent network meetings and training sessions. I also owe a huge thank you to our collaborators in the proEVLiFeCycle network: Pedro M. Filipe and Judith Farrés from Anaxomics for working together on the bioinformatic analysis of the candidates. To Ingrid Tomljanovic, Sander Tuit and Magda Grudniewska-Lawton thank you for collaborating on the RNA-sequencing part of the project and the many discussions about the technical challenges. To Martin van Royen and Ardalan Mansouri thank you for hosting me in the lab at Erasmus medical centre and teaching me how to conduct EVQuant.

A special thank you goes to the members of the tumour microenvironment group at the division of cancer and genetics (Cardiff University). I would especially like to thank Marie Wiltshire for her tremendous efforts during the COVID-19 pandemic to ensure that all lab members gained access to the lab as soon as possible and ensuring that health and safety procedures were put in place. Kate Milward thank you for all the flow cytometry training. Thank you to Amr; it was great to have another new starter to find our way around the lab. I also would like to thank Haiyan An (Swansea University) for guiding me with RNA-seq quality control. Thank you to Muireann and Thea, for the nice chats in the lab and Esma for the fun science conversations

about EVs outside of the lab. I also would like to thank Emily Bullen for helping with sending multiple parcels to the EU.

I would also like to thank my friends back home; the numerous video calls during the pandemic tremendously helped during this time. Luke, thank you for your continuous encouragement especially in the writing-up period. As a first-generation university graduate, I want to say a huge thank you to my family - especially my mother - this was only possible with her unwavering support.

Scientific contributions

PUBLICATIONS

Shephard, A. P., Giles, P., Mbengue, M., Alraies, A., Spary, L. K., Kynaston, H., Gurney, M. J., Falcón-Pérez, J. M., Royo, F., Tabi, Z., Parthimos, D., Errington, R. J., Clayton, A., & Webber, J. P. (2021). Stroma-derived extracellular vesicle mRNA signatures inform histological nature of prostate cancer. *Journal of extracellular vesicles*, *10*(12), e12150. <https://doi.org/10.1002/jev2.12150>

Welsh, J. A., Goberdhan, D. C. I., O'Driscoll, L., Buzas, E. I., Blenkiron, C., Bussolati, B., Cai, H., Di Vizio, D., Driedonks, T. A. P., Erdbrügger, U., Falcon-Perez, J. M., Fu, Q. L., Hill, A. F., Lenassi, M., Lim, S. K., Mahoney, M. G., Mohanty, S., Möller, A., Nieuwland, R., Ochiya, T., ... Witwer, K. W. (2024). Minimal information for studies of extracellular vesicles (MISEV2023): From basic to advanced approaches. *Journal of extracellular vesicles*, *13*(2), e12404. <https://doi.org/10.1002/jev2.12404>

ORAL PRESENTATIONS

Exploring the mechanisms of extracellular vesicle secretion by prostate cancer cells, 1st proEVLifeCycle Network meeting, virtual, March 2020

Exploring potential regulators of extracellular vesicle secretion in prostate cancer cells, 2nd proEVLifeCycle Network meeting, virtual, October 2020

Characterizing EV sub-population manufacture/secretion by prostate cancer cells, 3rd proEVLifeCycle Network meeting, virtual, May 2021

Characterizing EV sub-population manufacture/secretion by prostate cancer cells, 4th proEVLifeCycle Network meeting, Cardiff, November 2021

Characterizing EV sub-population manufacture/secretion by prostate cancer cells, 5th proEVLifeCycle Network meeting, Paris, May 2022

Characterizing EV sub-population manufacture/secretion by prostate cancer cells, 6th proEVLifeCycle Network meeting, Barcelona, November 2022

Exploring the mechanisms of extracellular vesicle secretion by prostate cancer cells, Division of Cancer and Genetics postgraduate research symposium (Cardiff university) 2021

Elucidating potential regulators of extracellular vesicle secretion in prostate cancer cells, Invited speaker at the Division of Cancer and Genetics postgraduate research symposium (Cardiff university), October 2022

AWARDS

Best Presentation at the Division of Cancer and Genetics postgraduate research symposium (Cardiff university) 2021

Chapter 1:

Introduction

1.1 Prostate cancer

The healthy prostate is a walnut sized gland that is located below the bladder surrounding the urethra. Malignant growth of the prostate poses a global burden on patients, families, healthcare systems and economies (Figure 1.1). In 2022, 14.2 % of the 10.3 million cancer cases in men are estimated to be attributed to Prostate cancer (PCa), making it the second most common diagnosed malignancy (<https://gco.iarc.fr>, 2024). PCa is also associated with the 5th highest death rate (6.7%) (<https://gco.iarc.fr>, 2024). In the United Kingdom (UK), more than 50,000 newly diagnosed cases occur each year (cancerresearchuk.org), consequently 1 in 8 men will get PCa within their lifetime. The underlying mechanisms that promote the development of the disease are still unclear and a combination of microbiome, socioeconomic, lifestyle and environmental factors could contribute to establishment of the malignancy (Rebello et al., 2021). In particular, the risk of PCa increases sharply with progressing age (Rawla, 2019). Furthermore, genetic factors also appear as a major contributor to an increased risk of PCa suggested by an elevated incidence in men with a family history of PCa (Mucci et al., 2016, Johns and Houlston, 2003). In addition to this, 1 in 4 Black men will be diagnosed with PCa (cancerresearchuk.org), underscoring the increased risk of men of African descent (Uzamere et al., 2022).

In England, the life expectancy of men with localised PCa with organ confined malignant growth is high with up to 89% surviving 5 years after the initial diagnosis (crukcanerintelligence.shinyapps.io/CancerStatsDataHub/). However, men that present with metastatic disease have a sharply reduced life expectancy and only 53% survive 5 years after the disease diagnosis (crukcanerintelligence.shinyapps.io/EarlyDiagnosis/). This points to an urgent clinical need to improve early identification of those patients who are at risk of progressing to the metastatic stage. This will hopefully allow targeted clinical intervention for these patients, therefore preventing disease progression, whilst also avoiding unnecessary treatment of patients who will not benefit from therapy.

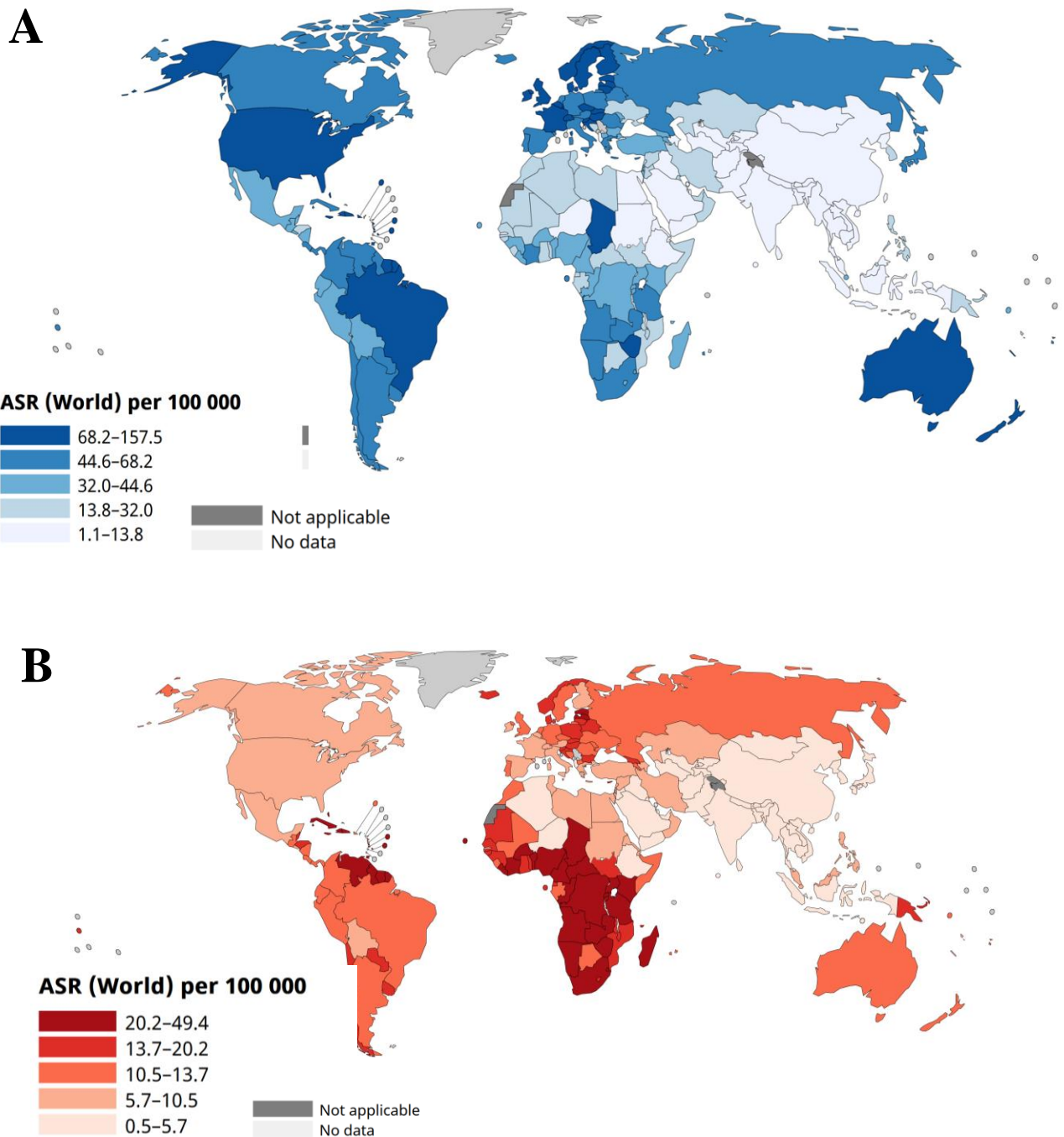


Figure 1.1: PCa is a major global health burden.

Numbers were adjusted to world standard population (age standardised rates=ASR), to accommodate the differences in age distribution in different regions. A) Age standardised incidence of PCa per 100,000 in 2022. Dark blue indicates regions with a high PCa mortality. B) Age standardised mortality rate per 100,000 in 2022. Dark red indicates regions with a high mortality rate. Grey indicates regions for which no data was obtained. Graphs retrieved from the Global Cancer Observatory (<https://gco.iarc.fr>, 2024).

1.2 PCa diagnostics

PCa can cause a range of symptoms, e.g., erectile dysfunction, blood in urine (haematuria), changes in the urination (frequency, urgency, retention) (Merriel et al., 2018), or indeed there may be no urinary-related symptomatic presentation at all, and cases are identified by incidental prostate specific antigen (PSA) checks at primary care for example after reporting bony pain. In the event of symptoms, primary care practitioners may investigate potential PCa by running the PSA levels and a digital rectal examination (DRE), both of which can be inconclusive for a variety of reasons.

The luminal cells of the prostate produce and release various factors e.g., PSA that contribute to the composition of the seminal fluid (Ittmann, 2018). In patients with suspected PCa, PSA levels are clinically assessed and compared to an age dependant reference value, set by the National Institute for Health and Care Excellence (NICE), to guide further clinical decisions. For instance, in the age group 40-45 PSA level of $>2.5 \mu\text{g/l}$ warrant additional clinical assessment, whereas this is only required at higher levels $> 6.5 \mu\text{g/l}$ in the age group 70-79. However, relying solely on the PSA measurement is insufficient to provide a clear PCa diagnosis because other pathological conditions e.g., prostatitis and benign prostatic hyperplasia also induce high PSA levels. Furthermore, in some severe PCa cases PSA levels may remain below the age specific threshold, although the underlying mechanisms for PSA-low PCa are currently unknown (Thompson et al., 2004, Fankhauser et al., 2023).

Another clinical diagnostic tool is DRE, which is used to determine changes of the prostate by palpation. This method has lower sensitivity compared to the assessment of PSA levels. A combination of the assessment of PSA level and DRE has a higher value for indicating suspicion of cancer compared to either technique alone. Nevertheless, the detection of false positives with these methods leads to over intervention revealing an unmet clinical need for more precise diagnostic tools (Catalona et al., 2017).

Based on suspicious results from the DRE and PSA test, and under consideration of other risk factors for increased incidence of PCa (Black African-Caribbean family background, older age,

comorbidities, family history of PCa or history of other cancers), the doctor and the patient might decide to proceed to an multiparametric magnetic resonance imaging (MRI). Although there continue to be advances in these imaging modalities and their subsequent clinical assessment, the MRI is again often inconclusive.

1.2.1 Multiparametric magnetic resonance imaging as a PCa diagnostic tool

An expert panel formed by members of the American College of Radiology, European Society of Urogenital Radiology (ESUR), and AdMeTech Foundation developed the Prostate Imaging Reporting and Data System (PI-RADS) which aids in stratifying PCa patients (Turkbey et al., 2019, Greer et al., 2017). A specific MRI imaging sequence is used to reveal suspicious radiographic appearances in the tissue. Subsequently, the radiologist inspects the images for cancer indicating features e.g., heterogenous appearance of nodules and signal intensity, and assigns a risk score, which predicts the probability of the occurrence of clinically significant cancer, between PI-RAD 1 (unlikely) and PI-RAD5 (highly likely).

MRI images contain critical information about the tumour localisation and extent of tissue infiltration (restriction to the prostate gland or expansion beyond the gland) and thus this information can be exploited for image guided interventions e.g., tissue biopsy. MRI imaging can also play a vital role in reducing overtreating patients with suspected PCa. The PRECISION study (patient cohort:500) showed that an MRI scan reduces the number of unnecessary biopsies performed on clinically insignificant PCa (Kasivisvanathan et al., 2018). This is an important finding considering that obtaining tissue specimen via e.g., transrectal ultrasound-guided (TRUS) biopsy (Allen and Embry, 1991) is accompanied by potential risks e.g., infection (Nam et al., 2010). Hence, it is of interest to reduce the number of biopsies especially in vulnerable patients.

Currently (2024), there is no national (UK) screening for PCa as the available tools, outlined above, do not provide a clear benefit for the patient when used in a population wide approach. A recently announced trial, the TRANSFORM trial, aims to assess screening tools for a population wide testing including MRI and other not yet announced tools ([gov.uk/government/news/biggest-prostate-cancer-screening-trial-in-decades-to-start-in-uk](https://www.gov.uk/government/news/biggest-prostate-cancer-screening-trial-in-decades-to-start-in-uk))

1.3 Biopsy of suspected PCa samples

In cases where a biopsy is required for a definitive diagnosis, the obtained samples are subject to histopathological examination by a pathologist. The Gleason Score (GS) is used to classify the disease grade, and hence the severity of cancer abnormality based on tissue growth patterns (Figure 1.2). To calculate the GS, the pathologist inspects the tissue and assigns Gleason patterns based on the detected morphology features. Briefly, Gleason pattern 1 and 2 are currently not in use because in low grade disease it is difficult to differentiate PCa from other benign proliferations due to similar histopathological features, e.g., small glands in benign proliferations (Egevad et al., 2020). Gleason pattern 3 is assigned to tissue sections with well-formed glands. Gleason pattern 4 is used to characterise tissue with irregular masses with ill-defined glands, which can present in the cribriform and/or fused glands. The cribriform morphology is identified as a sieve-like epithelial sheet morphology and a lack of intervening vasculature or stroma or mucin, yet often exhibiting a boundary of abnormal stroma. Samples with a Gleason pattern 5 show a disrupted tissue architecture, that is characterised by the absence of clearly defined gland structures (Epstein, 2018).

There is ongoing interest in assigning a more detailed assessment of structural features, as some of these so-called sub-pathologies of PCa are significant for risk prediction and hence the likelihood for development of metastatic disease. Of specific interest is the cribriform morphology, a type of grade 4 morphology. Some forms of Gleason pattern 4 lesions, lacking this morphology may carry a similar risk as Gleason pattern 3 tissue, whilst large cribriform lesions may be equivalent to Gleason pattern 5, in terms of overall survival. However, more studies assessing the occurrence of cribriform and other sub-pathologies in large patient cohorts are required before this could be potentially exploited for diagnostic or prognostic purposes (Gordetsky et al., 2022). Nonetheless, pathology reports in the UK are beginning to be annotated with this added information to help in clinical decision making, although there can be discordance amongst pathologists in both recognising some of these sub-pathologies, and their true value in risk prediction (Iczkowski et al., 2021).

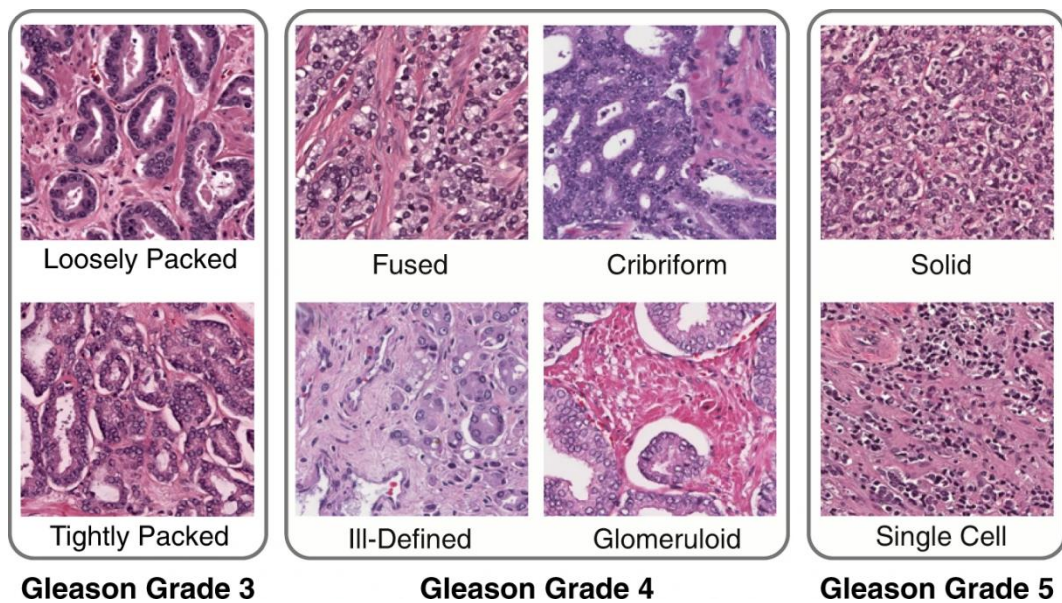


Figure 1.2: Histological features of Gleason pattern (grades) 3, 4 and 5.

Based on histopathological features of the primary prostate tumour the severity of the disease is assessed using the Gleason scoring system. For this purpose, Gleason patterns are identified and the addition of the two most common patterns provides the final Gleason Score. Gleason pattern 3 is characterised by glands of varying size in 1 section. Gleason pattern 4 is indicated by increased heterogeneity of the gland architecture with poorly defined glands and the occurrence of the cribriform, fused glands, sheets, glomeruloid (renal glomerulus like morphology with intraluminal cribriform outgrowth). Gleason pattern 5 shows a severely disrupted, poorly differentiated tissue architecture. The glands are ill defined, and cells form solid nests or occur as single cells. Figure shows haematoxylin and eosin staining. Figure taken from (Lawson et al., 2019).

For the calculation of the GS, numerically adding the two most common patterns in the tissue samples provides the GS (Ong et al., 2020). For instance, the predominant observation of the most common growth pattern 3 and the second most common pattern 4 provides a final GS of 7 ($3 + 4 = 7$). Another example where the principal pattern is 4 and the second most common grade is 3, provides a score of 7 ($4+3$). This latter case, however, exhibits a higher proportion of the tissue of high-grade lesions, and consequently it would be considered more likely to be cancerous than the GS 7 ($3+4$) comparator. In addition, tissue which is principally of pattern 3,

and hence GS 6 (3+3) is currently considered as not clinically significant and would be unlikely in itself to warrant active treatment.

Because of the oddities of these scores, and the confusion it creates for patients, the grade group system (Grade 1-5) was developed by Pierorazio et al. to depict histological severity in a simplified and clearer fashion (Pierorazio et al., 2013) (table 1.1). The grade groups divide GS 6 and higher into 5 Grade groups: Grade 1 (GS3+3=6), Grade 2 (GS 3+4=7), Grade 3 (GS4+3=7), Grade 4 (GS4+4=8), Grade 5 (GS4+5, GS5+4, GS5+5). The proposed system was validated in a study cohort with more than 20,000 men (Epstein et al., 2016, Pierorazio et al., 2013).

Table 1.1: PCa Grade groups and their clinical features.

<u>Grade (GS)</u>	<u>Glands</u>	<u>Differentiation</u>	<u>Benign or malignant</u>
Grade 1 (GS <6)	Small	Good	Benign
Grade 2 (GS 3+4)	Increased stroma	Good/moderate	Benign
Grade 3 (GS 4+3)	Poorly defined	Moderate	Malignant
Grade 4 (GS 4+4)	Poorly defined	Poor	Malignant
Grade 5 (GS 4+5, GS 5+4 or GS 5+5)	Disrupted tissue architecture	Poor	Malignant

Another important standardised assessment tool is the tumour node metastasis (TNM) staging system, which is used to assess the severity of the disease based on anatomical criteria. T describes the degree of tissue infiltration and the extent of the dissemination of the cancer (table 1.2). N denotes whether the malignancy has spread to nearby lymph nodes and M characterises metastatic spread to distant organs (Saoud et al., 2020).

Table 1.2: TNM staging system for PCa. Table based on the guidelines provided by the European association of urology (https://uroweb.org/guidelines/prostate-cancer/chapter/classification-and-staging-systems#note_103).

Group	Characterised by
T1a	Clinically not suspicious, not palpable during DRE, cancerous cells are found in less than 5% in a tissue sample obtained by biopsy
T1b	Clinically not suspicious, not palpable during DRE, cancerous cells are found in more than 5% in a tissue sample obtained by biopsy
T1c	Clinically not suspicious, not palpable during DRE, cancerous cells are found by biopsy
T2	Cancerous tissue completely enclosed by the prostate gland and palpable during DRE
T3a	Cancerous cells have spread beyond the capsule of the prostate gland
T3b	Cancerous cells have invaded into the seminal tubes
T4	Metastatic spreading of the disease
N0	Lymph nodes in close proximity to the tumour are free of metastasis
N1	Lymph nodes in close proximity to the tumour have metastasis
M0	No metastatic spread of the neoplastic cells to distant sides
M1	Metastatic spread of the neoplastic cells to distant sides

1.3.1 Current guidelines in the UK

The above-mentioned tools (staging, PSA levels, GS/Grade groups) have been used as individual parameters to stratify patients. Gnanapragasam et al. combined this information in one novel grading system, the Cambridge Prognostic Group (CPG), which is based on the clinical data of 12,000 men (Gnanapragasam et al., 2018) (Table 1.3). The grading system aids in predicting the mortality rates and provides a simplified categorising compared to utilising each parameter separately and is currently the standard practice recommended by NICE to aid patient stratification (NICE, 2021).

Table 1.3: CPGs table from (Gnanapragasam et al., 2018).

CPGs	Features
1	GS 6 and PSA < 10 ng/ml <u>and</u> stages T1-2
2	GS 3+4=7 Or PSA 10-20 ng/ml <u>and</u> stages T1-T2
3	GS 3+4=7 <u>and</u> PSA 10-20 ng/ml <u>and</u> stages T1-T2 Or GS 4+3=7 <u>and</u> stages T1-T2
4	One of GS8 <u>or</u> PSA > 20 ng/ml <u>or</u> stage T3
5	Any combination of GS8, PSA >20 ng/ml or stage T3 Or GS 9-10 Or Stage T4

Alternate diagnostic tools

Recently, there have also been a number of other diagnostic tools developed that are used for risk stratification (reviewed in Fujita and Nonomura, 2018). For instance, the ExoDx Prostate detects three genes (PCA3, ERG and SPDEF) in urinary extracellular vesicles (EVs), small lipid encapsulated vesicles, in urinary samples. There are also genomic tests such as Decipher, Genomic Prostate Score and Prolaris with limited benefits in directing patient management as reviewed (Boyer et al., 2023). Certainly, these tests hold potential to aid situations of uncertainty in patients of intermediate histological risk (Grade group 2 and 3), however they are not used within the UK NHS system, as their added value, in terms of cost:benefit ratio, has not yet been universally accepted.

1.4 Treatment

The individual treatment plan for the patient depends on the severity of the disease, which is judged by the above-mentioned methods, the estimated life expectancy, and comorbidities.

Potential side effects of each treatment option also play a vital role in the clinical decision-making process.

In the UK, NICE recommends using the CPGs to consider treatment options (NICE, 2021). The guidelines suggest for patients with CPG1-3 active surveillance, which means the status of the disease is regularly assessed but no interventions are taken at this stage, that is no radical prostatectomy or radical radiotherapy. For patients with CPG4 and 5 active surveillance is not recommended, and patient should be offered radical treatment. In addition to this, the NICE guidelines recommend for the patients in risk groups CPG2-5 to combine radical radiotherapy with androgen deprivation therapy (ADT), when the patients are undergoing long term treatment. The different therapies are outlined in more detail below.

Surgical removal of the prostate (prostatectomy) is standard of care for a subset of patients in good health with locally confined, non-metastatic PCa, where there is evidence of worsening symptoms or from clinical imaging indicating a greater likelihood of extra-prostatic spread. Surgery leads to a sharp decrease in PSA levels, and is hopefully curative in most cases, also resulting in some significant improvement in quality-of-life issues such as incontinence and/or impotence. After surgery, the progression of the disease can be monitored by measuring PSA and in this setting, PSA is indeed considered as a valuable cancer monitoring marker, as it is rare to see recurrence without what is referred to often as “biochemical relapse”. In the event of this, treatments, such as ADT or chemotherapy, are administered (Sekhoacha et al., 2022).

1.4.1 Radiotherapy

Radiotherapy is a treatment option that should be considered for patients with a low metastatic burden at risk of pelvic lymph node metastasis (NICE, 2021). High energy X-rays induce DNA damage in the cancerous cells which ultimately lead to cell death and the shrinkage of the tumour. There are three methods available that exploit the cancer cell destroying function of radiation: external beam, brachytherapy, and radionuclide therapy.

Traditional radiotherapy utilises external beam photons. A radiation plan is prepared, and image guided radiotherapy include, three-dimensional conformal radio therapy (3D-CRT) and

intensity modulated radiotherapy (IMRT). Software assisted, a precise beam is directed at the PCa, with the highest dose directed at the malignant tissue and a lower dose at the margins resulting in a limited damaging impact of the radiation of the surrounding tissue (Ling et al., 1996).

Another radiotherapy option is internal brachytherapy, which involves the placement of a radioactive seed in the tumour or at the metastatic site. The seeds can be a low dose rate (LDR) and are permanently placed at the targeted site or can be a high dose rate (HDR), which requires repeated temporary treatment (Kamran and Zietman, 2021).

Administration of radionucleotides is a recent technique that is gaining more attention. Target specific radioactive nucleotides are administered to the patient. Currently, Lutetium-177 Prostate Specific Membrane Antigen (PSMA), a radionucleotide, is used for treatment of PCa. This is however, only recommended for end-of-life care according to NICE guidelines. Another example is Radium-223 which can be administered in cases of PCa with bone metastasis (Czerwinska et al., 2020). All of the radiotherapeutic treatments can be accompanied by severe side effects including, but not limited to urogenital and bowel problems (Valle et al., 2021). Therefore, it is crucial to only select this option when required and the side effects are tolerable by the patient (NICE, 2021).

Active surveillance, radical prostatectomy and radiotherapy have been the first line of treatment for decades. The ProtecT trial aimed to compare the clinical benefits of these strategies in a patient cohort of 1,643 and found a less than 1% PCa associated death rate 10 years after an initial diagnosis (Hamdy et al., 2016). However, increased occurrence of metastasis in patients under active surveillance (8%) compared to radiotherapy and radical prostatectomy (both 3%) occurred. These findings support the use of active surveillance and points to the requirement of better diagnostic tools to identify the patients that will inadvertently develop metastasis if left untreated, or rather tests that are more sensitive to detect micro-metastasis are needed during diagnostic investigations.

1.4.2 Androgen deprivation therapy

Androgen receptors play an important role, for instance, in the development of the prostate gland under physiological conditions and are considered a major driver of the progression of PCa. The binding of this cytosolic receptor to its ligand e.g., testosterone, triggers the translocation of the receptor to the nucleus, where it exerts its main function as a transcription factor (reviewed in Desai et al., 2021, Rebello et al., 2021, Chan and Dehm, 2014). Given the critical role of the androgen receptor and its signalling pathways in the pathogenesis and progression of PCa, several drugs have been developed to target androgens termed ADT by targeting the androgen receptor directly, e.g., with Enzalutamide, or by targeting an enzyme, e.g., CYP17A1, that converts the androgen precursor pregnenolone to Dehydroepiandrosterone (DHEA) (Desai et al., 2021). An alternative to this biochemical castration is surgical castration, but this has long since been discontinued due to the unacceptable nature of the surgery for patients. Unfortunately, all patients that are initially castration sensitive develop resistance to the treatment over an 18–24-month period, and hence a change in the treatment plan is required.

Previously, it was thought that therapy resistance was due to a developed resistance to androgen. However, recent research indicates that androgen dependant pathways are reactivated in the tissue by increased expression of the androgen receptors (reviewed in Rebello et al., 2021, Chan and Dehm, 2014) and consequently leading to metastatic diseases in a subset of patients.

1.4.3 Docetaxel

The PCa treatment landscape is dynamic and continually evolving. There is a range of chemotherapeutic treatment for PCa patients available which are selected on the patient's clinical parameters (age, health, genetics) and disease status (e.g., localisation) (Gillesen et al., 2020). Docetaxel, an apoptosis inducing antineoplastic agent (Pienta, 2001), is considered for patients (without major comorbidities) with locally confined, high risk PCa. A clinical trial showed Docetaxel slows the progression of the disease in this subset of PCa patients (James et al., 2016). Furthermore, Docetaxel in combination with Prednisone has been the most widely

used therapy shown to increase survival rates and improve quality of life (Tannock et al., 2004).

If the disease progresses to the metastatic state only limited treatment options are available. Current NICE recommendations recommend considering surgical removal of the testis in combination with Docetaxel treatment (NICE, 2021). Furthermore, the CHAARTED trial showed that compared to ADT monotherapy, treatment with Docetaxel when administered in combination with ADT in PCa with metastatic disease increased the overall survival rate by 13.6 months and the progression free survival by 8.5 months (Sweeney et al., 2015).

Despite these available treatment options, PCa at the metastatic stage is currently not curable, and the lifespan is difficult to predict. New therapies are urgently needed, perhaps targeting pathways that are independent of the androgen axis could offer novel routes to help address the current intractability of castrate resistant PCa.

1.5 The tumour microenvironment

The occurrence of PCa is accompanied by dramatic changes in the tissue architecture of the prostate and these are associated with the severity / aggressiveness of the disease. The tumour microenvironment (TME) has been shown to play a role in this process by promoting the growth of the malignant tissue (Hanahan and Weinberg, 2011). The TME contains acellular components such as the extracellular matrix (ECM) and various cell types e.g., endothelial cells and fibroblasts (reviewed in Chen et al., 2021b).

The stroma, which forms part of the TME, and includes non-immune cells, structural components and other cells, is increasingly considered to be a major contributor to the development and progression of PCa. A small study in 50 PCa patients who underwent radical prostatectomy, indicated that increased ratios of stroma to epithelia tissue, judged by immunohistochemistry (IHC) staining of Vimentin, was correlated with reduced disease free survival rates (Tomas et al., 2010). In a larger study, evaluating biospecimens of 845

participants, increased percentage of stromal tissue in the resected tumour sections was correlated with increased occurrence of a relapse of the disease (Ayala et al., 2011). Furthermore, the frequency of smooth muscle cells in the stroma is reduced in malignant prostate tissue and replaced by fibroblasts (Taboga et al., 2008, Yang et al., 2017, Tuxhorn et al., 2002). This indicates an important role of fibroblasts, or rather cancer-associated fibroblasts (CAFs), in supporting neoplastic cells.

1.5.1 Cancer-associated fibroblasts

Indeed, CAFs found in the TME play a critical role in reorganising the stroma by matrix turnover/deposition and release of a range of bioactive factors. In PCa the pivotal roles of CAFs have been described by several studies (Davies et al., 2003, Olumi et al., 1999, Ishii et al., 2018, Cheteh et al., 2020, Gong et al., 2013). Co-culturing CAFs with normal prostate epithelial cells that underwent the initial steps of epithelial mesenchymal transition (EMT) initiated tumorigenesis both *in vitro* and in a mouse model. CAFs assisted in the generation of very large and well vascularised xenografts. Importantly, fibroblasts isolated from benign hyperplastic prostates, failed to do so, where the tumour mass was barely palpable (Olumi et al., 1999). Despite indications of the importance of the reciprocal communication between cancer cells and CAFs for decades (Olumi et al., 1999), the underlying mechanisms are only beginning to be uncovered, perhaps, due the intra-and inter-tissue complexity of CAF heterogeneity.

There is mounting evidence that CAFs play a significant role in PCa treatment resistance. Cioni et al. suggested androgen deprivation induces tumour promoting paracrine signalling in CAFs and thus might contribute to the development of ADT resistance (Cioni et al., 2018). Suppression of androgen receptor signalling in these CAFs elicited elevated secretion of C-C motif ligand 2 (CCL2) and CXCL8, which in turn promoted the migration of PCa cells *in vitro*. The research was conducted with CAFs from a small number of PCa patients and thus requires validation in a larger patient cohort. It was also suggested that CAFs confer resistance to Enzalutamide in PCa cells when co cultured mediated by the activation of the Akt signalling pathway. The study, however, did not delineate the molecular mechanisms in more detail (Eder et al., 2016). Kato et al. explored the underlying causes of Enzalutamide resistance in more depth (Kato et al., 2019). The study proposed that combining ADT with targeting stromal cells

is superior to either treatment alone. The authors showed that ADT treatment upregulated Endoglin (CD105) expression in CAFs, which lead to secretion of secreted frizzled related protein 1 (SFPR1). This signalling molecule induced the neuroendocrine differentiation in PCa cells via paracrine signalling and was shown in a 3D CWR22Rv1-mouse fibroblast co culture model and subsequently validated in a mouse model, where the treatment combination of Enzalutamide and a CD105 inhibitor reduced the tumour burden (Kato et al., 2019).

1.5.2 Markers for CAFs

Various markers for CAFs have been proposed such as fibroblast activating protein (FAP), alpha smooth muscle actin (α -SMA) and Vimentin (Tuxhorn et al., 2002). However, these proteins are only expressed in a subset of CAFs and consequently, fail to identify all CAF subpopulations in a tissue (Chen et al., 2021b). A consensus statement from 2020 compiled by CAF experts (Sahai et al., 2020) described the difficulty in defining a nomenclature for CAFs and suggests using a combination of a functional description and cell surface markers to describe the complexities of CAF subpopulations.

1.5.3 CAFs in PCa

Different studies have aimed to delineate the CAF subpopulations in PCa. Utilising flow cytometry Zhao et al. identified CD90 high and CD90 low expressing CAF subpopulations in samples isolated from PCa patients (no clinical parameters provided). The researchers found high CD90 expression was correlated with increased expression of the chemokines IL-6, Vascular Endothelial Growth Factor A (VEGFA), fibroblast growth factor 2 (FGF2), and C-X-C motif chemokine ligand 12 (CXCL12) (Zhao and Peehl, 2009). A CD90 high expressing CAF subpopulation in the context of PCa was later also confirmed by others (Orr et al., 2012). Since these discoveries were made, the advances in single sequencing techniques shed more light on the diversity of the CAF populations in PCa.

Noteworthy are studies by Vickman et al. and Chen et al. (Vickman et al., 2020, Chen et al., 2021a) that inspected PCa patient derived CAFs. Both studies found a homogenous high expression of Vimentin in the CAFs with a majority of cells also expressing α -SMA. Despite

these overlapping findings, the two studies identified distinct CAF subpopulations. Vickman et al. utilised single-cell messenger ribonucleic acid (mRNA) sequencing analysis to define 6 CAF clusters (0 to 5). Interestingly, the differential expression of a panel of 5 genes (BIRC5, CD63, GLRX, PHKG1, PKM, and MALAT1) was sufficient to distinguish the different clusters. The authors also suggested that there were at least two functionally distinct subpopulations, one that promotes the attraction of macrophages (CCL2 positive, low CXCL12 expressing) and another one that promotes inflammatory cells (low CCL2 expressing, CXCL12 positive) (Vickman et al., 2020).

In contrast, Chen et al. identified 5 CAF clusters separated by their unique gene expression profile, which were further summarised in three CAF subtypes (S1-S3): S1 (enriched gene expression of PDGFR β , CAV1, SPARC activation of transcription factor (TF) ETS1) with a predicted function in cell adhesion, S2 (enriched gene expression of PDGFR β activation of TF CREB3L1 and PLAGL1) with a predicted function in ECM regulation and S3 (enriched gene expression of FAP, TNC, CAV1, activation of TF HOXB2 and MAFB) with a predicted a predicted contractile phenotype (Chen et al., 2021a).

These studies clearly show that the intra- and inter patient heterogeneity of CAF subpopulations remain a challenge in defining specific CAF subpopulations that can be validated across different studies. Perhaps, to achieve to this, a disease stage specific analysis might be required which would also require consideration to clinical parameters (e.g., GS, PSA-value).

1.5.4 Functional diversity of CAFs

Not only is there complexity in defining the transcriptome of distinct CAF subpopulations but there is also a functional diversity in CAFs and assigning specific functions to genetic phenotypes remains difficult. Many reviews tried to simplify the categorising of CAFs into at least three most obviously apparent and distinct subpopulation based on their function: antigen presenting, myofibroblastic phenotype and inflammatory phenotype (examples of reviews: (Yang et al., 2023, Ping et al., 2021, Lavie et al., 2022)). However, this appears to be an oversimplified view on CAFs as many different subpopulations within, for instance, the α -SMA positive subpopulations exist (Chen et al., 2021a). In addition to this, there is evidence

that CAFs maintain the ability to convert from one subtype to another as reported for the conversion between CAFs with a low α -SMA and high IL-6 expression to a myofibroblast like subtype with high α -SMA expression (Öhlund et al., 2017). Hence, categories used to characterise CAF subpopulations should be considered carefully.

At least one subpopulation of CAFs modulate ECM structure organisation through enhanced deposition of ECM molecules, ECM modifying matrix metalloproteinases (MMPs) and alterations in the ECM fibres, which lead to increased tissue stiffness. Elevated ECM secretion by CAFs results in a higher stromal density, which protects neoplastic cells from elimination by immune cells (Salmon et al., 2012). In addition to this, Gaggioli et al. suggested that the deposited ECM components form tracks that promotes tumour migratory capabilities and invasiveness (Gaggioli et al., 2007).

There is growing evidence that this CAF subtype plays an important role in PCa. For instance, increased density of the ECM component hyaluronan in the tumour stroma has been observed at the advanced stages of the disease (e.g., high GS) (Lipponen et al., 2001). Furthermore, single cell sequencing showed that fibroblasts adjacent to the primary tumour have an ECM remodelling genetic signature (Hirz et al., 2023). However, the study did not focus on delineating CAF subpopulations and functional properties in more detail. Another recent single cell sequencing study performed in a mouse model suggested that ACTA2 and MYL9 positive fibroblasts contribute to TME remodelling in the early stages of the disease by increased secretion of ECM components (Pakula et al., 2024). Important bioactive molecules, that are released by CAFs are MMPs, which aid in weakening the ECM barrier surrounding the tumour and thus facilitate the dissemination of the cancer cells. Various MMPs have been reported to be released by PCa related CAFs. For instance, it was shown that in PCa, stromal cells isolated from patients that underwent radical prostatectomy secrete MMP2 (Wilson et al., 2002). Furthermore, in tissue sections from high grade prostate tumours (GS8-10) elevated expression of both MMP2 and MMP9 was found and this was accompanied by a reduced expression of tissue inhibitor of metalloproteinase-1 (TIMP-1) and tissue inhibitor of metalloproteinase-2 (TIMP-2) (Wood et al., 1997). More recently, Eiro et al. found in 37 CAF samples isolated from patients with a castration resistant tumour, elevated mRNA expression of AR, Matrix

metalloprotease 11 (MMP11, involved in invasion) and Heat–shock 70kda protein 1A (HSPA) (Eiro et al., 2017).

The molecular mechanism that contributes to the functional role of CAFs in ECM remodelling are also beginning to be uncovered. A proteomic analysis of CAFs isolated from four PCa patients that underwent radical prostatectomy, showed an enrichment of ECM modulators and validated lysyl oxidase like 2 (LOXL2) as a CAF derived regulator of ECM architecture (Nguyen et al., 2019). Furthermore, Erdogan et al. demonstrated that CAFs induce linearisation of fibronectin fibres which promote PCa cell dissemination (Erdogan et al., 2017).

The existence of CAFs with a proinflammatory secretion profile has been proposed by a few studies (e.g., (Erez et al., 2010, Öhlund et al., 2017) and has also been described in PCa patient derived CAFs (Eiro et al., 2022). A critical function of CAFs is the secretion of a range of pro-angiogenic chemokines which stimulate the formation of a neo-vasculature providing the growing tumour with oxygen and essential nutrients to maintain growth and serving as waste disposal route (reviewed in Biffi and Tuveson, 2021).

IL-6 is a pro-angiogenic (Motro et al., 1990) and pro inflammatory chemokine (Raskova et al., 2022). There is mounting evidence for a pivotal role of CAF derived IL-6 in modulating a favourable TME (Shintani et al., 2016, Vicent et al., 2012, Öhlund et al., 2017, Elyada et al., 2019). The role of IL-6 derived from CAFs to induce angiogenesis was recently validated with an *in vitro* model with Human Umbilical Vein Endothelial Cells (HUVEC). In the context of PCa, IL-6 secreted by fibroblasts has been shown to stimulate the secretion of VEGF in PCa cells (Ishii et al., 2018) and to elicit endothelial cell migration (Paland et al., 2009).

Furthermore, IL-6 released from CAFs suppresses Doxorubicin (chemotherapeutic drug) mediated cell death by inhibiting p53 accumulation in PCa cells *in vitro* (Cheteh et al., 2020).

Another example of a paracrine signalling molecule released by CAFs is hepatocyte growth factor (HGF), which has been confirmed in various tumours including for instance head and neck cancer (Kumar et al., 2018), squamous cell carcinoma (Eikesdal et al., 2018) and PCa (Qin et al., 2021). In PCa, it was shown CAF derived HGF enhances migratory capacity of PC3

cell *in vitro* and tumour growth *in vivo* when PC3 cells and fibroblasts were co-injected into mice (Davies et al., 2003).

1.5.5 Origins of CAFs

Various cell types have been proposed as precursors of CAFs, however, given the complexity of heterogeneous CAF populations and the lack of CAF specific markers, tracking of CAF origins is challenging and it might be possible that multiple cell origins contribute to formation of the diversity, and dynamics of CAFs (Figure 1.3). These include epithelial cells that underwent EMT leading to the acquiring of mesenchymal (fibroblast-like) features (Zeisberg et al., 2007). Other possible source cells include mesenchymal stem cells, which may emanate from bone or adipose tissue origins, as part of a population of tissue infiltrating cells (Karnoub et al., 2007), pericytes (Hosaka et al., 2016) and endothelial cells (Radisky et al., 2007).

Furthermore, Arina et al. reported that tissue resident fibroblasts in the peritumour milieu can be the progenitors of CAFs in a mouse model (Arina et al., 2016), and perhaps this is the likeliest principal source of CAFs. Tissue resident fibroblasts comprise a diverse population of mesenchymal cells, that are characterised by producing components of the connective tissue and are considered to maintain tissue homeostasis. Upon a stimulus, for instance tissue injury, fibroblasts have well documented capabilities to adapt and react, and may undergo differentiation into myofibroblastic cells. This is defined by the *de novo* onset of α -SMA monomers, which are polymerised into stress fibres providing muscle-like capacity to undergo cellular contraction, and exert mechanical force on the surrounding ECM (Hinz et al., 2001, Welch et al., 1990, Chrzanowska-Wodnicka and Burridge, 1996). Myofibroblasts also become highly secretory in terms of their growth factor profiles, and are an important source of one of the most important tissue-modulating factors, transforming growth factor-beta (TGF- β) (Sahai et al., 2020, Plikus et al., 2021), and a host of others, which collectively contribute to alteration of the tissue architecture and cellular composition in cancer.

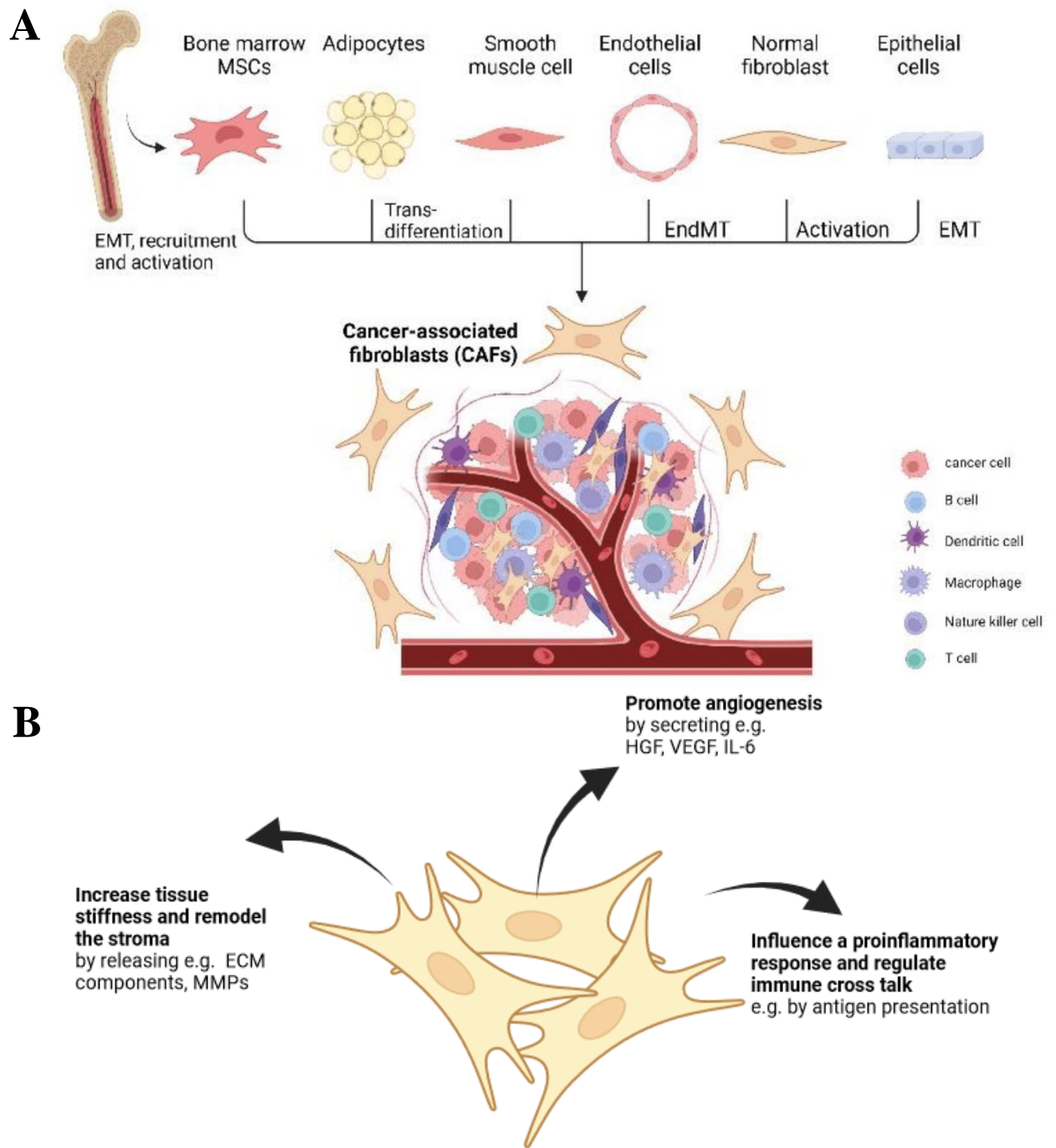


Figure 1.3: Cancer associated fibroblasts in the TME support the tumour.

CAFs can derive from multiple cell sources including bone marrow mesenchymal stem cells (MSCs), adipocytes, smooth muscle cells, epithelial cells, fibroblasts and epithelial cells. CAFs are located in the peritumour space and secrete various tumour promoting factors. CAFs attributed functions that were described in the text are summarised in (B). A) taken from (Zhang et al., 2022), (B) created in BioRender.

1.5.6 Transforming growth factor β signalling in CAFs

Transforming growth factor-beta 1 (TGF- β 1) is a pleiotropic regulator of homeostasis across various tissues with immune suppressive functions in adaptive and innate immunity (Massague and Sheppard, 2023). This cytokine is also an important regulator of fibroblast activation by inducing differentiation to myofibroblasts (Desmoulière et al., 1993) and thus stimulating the production and release of collagens into to the extracellular space and consequently tissue remodelling (as reviewed Massague and Sheppard, 2023, Chen et al., 2021a).

Cytosolic TGF- β , in an inactive form in complex with latency associated peptide (LAP), is released from the producing cells into the extracellular space. There, the TGF- β -LAP complex is subsequently bound to the LAP binding protein complex. The mechanism releasing TGF- β from the complex is currently unclear; while proteolytic cleavage has been proposed to mediate this process but has not been confirmed *in vivo*. The released activated homodimer TGF- β binds to TGF- β receptor 2 (TGF- β R2) on the cell surface and thereby recruits TGF- β receptor 1 (TGF- β R1) (Figure 1.4). Then, TGF- β R1 binds the TFs Suppressor of Mothers against Decapentaplegic 2 (SMAD2) and Suppressor of Mothers against Decapentaplegic 3 (SMAD3) and subsequently phosphorylates both. The SMAD2/SMAD3 complex translocates into the nucleus and upregulates the transcription of its target genes including, α -SMA and genes regulating ECM production. This functional impact of TGF- β is not exclusively mediated via the above SMAD-dependent route as other signalling pathways in the target cells are also activated, producing a different set of responses such as hyaluronan coat formation (Webber et al., 2010, Webber et al., 2009).

Interestingly, TGF- β is also found bound to EVs and delivery in this form promotes fibroblast to myofibroblast differentiation in fibroblasts (Webber et al., 2010) and in addition to this, also elicits an elevation in the release of pro-angiogenic factors such as HGF and VEGF (Webber et al., 2016, Webber et al., 2015). Importantly, utilising mouse models studies demonstrated a key finding: co-administering fibroblasts and PCa cells with reduced EV output, reduces the tumour growth when compared to co-administering fibroblasts with wild type PCa cells (Webber et al., 2015, Yeung et al., 2018). These latter studies highlight that the communicative networks that occur in cancer environments can involve EVs, with ample evidence that they can promote tumour progression by modulating varied components of the TME.

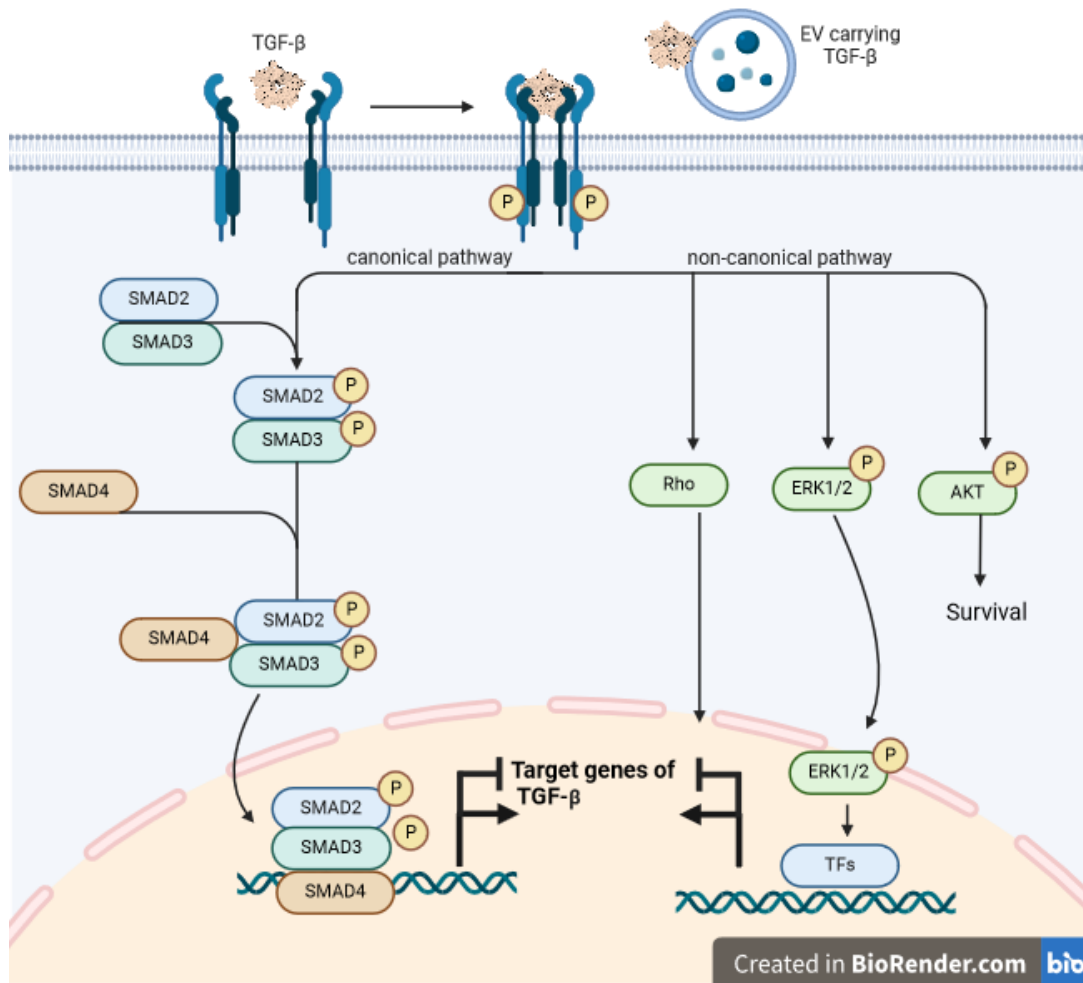


Figure 1.4: Simplified TGF-β signalling.

TGF-β binds to TGF-βR2, which induces the formation of a heterocomplex of TGF-βR2 and TGF-βR1 and transphosphorylation. The activated receptor complex phosphorylates SMAD2 and SMAD3 (canonical pathway). Subsequently, SMAD4 binds to the phosphorylated SMAD2:SMAD3 and the complex is translocated into the nucleus where the transcription factors bind to the DNA and induce the suppression/expression of target genes. EVs have been shown to activate the canonical SMAD dependant pathway (Webber et al., 2010).

Alternatively, TGF-β can also activate the non-canonical, SMAD independent pathway, which activates several downstream signalling pathways including e.g., the AKT pathway, which suppresses apoptosis (Huang et al., 2020), Rho GTPases, which regulate myofibroblasts activation and ECM secretion (Ni et al., 2013) and the ERK1/2 pathway, which modulate myofibroblast activation (Carthy et al., 2015). Figure created in BioRender based on (Gungor et al., 2022, Shi et al., 2020, Massague and Sheppard, 2023). ERK=Extracellular signal-regulated kinase, TF= transcription factor, TGF-β=Transforming growth factor β, EVs= extracellular vesicles.

1.6 Extracellular vesicles

Historically, different forms of EVs have been classified by their distinct subcellular origins which includes two main routes of either endosomally derived small vesicles (exosomes) or small and large plasma membrane derived (e.g., ectosomes or microvesicles). However, it is experimentally difficult to determine the cellular origin of EVs, present within the secretome, or isolated, due to a lack of definitively discriminating markers for either route. Additionally, there is inconsistency in terminology used to describe EVs in the past literature, although some guidance on these issues has been published within the *Journal of Extracellular Vesicles* where a combination of biophysical descriptors (e.g., protein markers, size and/or density) are potentially more valuable than attempting to define a vesicle based on its subcellular origin (They et al., 2018, Lötvald et al., 2014, Welsh et al., 2024).

The biogenesis of microvesicles (100 – 1000 nm and sometimes larger and potentially smaller) occurs by an outward budding of the plasma membrane. Several factors have been implicated in the biogenesis of microvesicles (Tricarico et al., 2017). For instance, the GTPase ADP-ribosylation factor 1 (ARF1) has been described to regulate the contractile machinery at the cell surface that controls the pinching off of microvesicles (Schlienger et al., 2014) and Rab22a has been proposed as regulator of microvesicles in breast cancer cells (Wang et al., 2014). Furthermore, Stachowiak et al reported that the mere accumulation of proteins at the plasma membrane was sufficient to induce membrane curvature and eventually leading to the release of microvesicles (Stachowiak et al., 2012). However, the mechanistic details of vesicle formation and budding remain to be fully defined.

The Endosomal Sorting Complex Required for Transport (ESCRT), a vital machinery for the remodeling of the endosomal membrane, as a set of molecular features was previously considered to specifically define endosomally derived EVs. More recently these components have also been found adjacent to the plasma membrane and thought to also play a role in the biogenesis of microvesicles (Tricarico et al., 2017, Cocucci et al., 2009). Interestingly, the small GTP binding protein ADP ribosylation factor 6 (ARF6) was discovered as a regulator of selective cargo recruitment into microvesicles (Clancy et al., 2019) and for microvesicle shedding (Muralidharan-Chari et al., 2009), and this may offer us a means of discriminating

EVs from microvesicles. However, whether this is definitive across varied cellular systems, or indeed if its role varies by cell activation states, remains to be clarified.

The major focus of our group is on the small EVs historically referred to as exosomes. These vesicles (30-130 nm) are endosomally derived vesicles, albeit defining these as such remains a constant challenge. This subset of EVs is manufactured within late endosomal compartments, in structures known as multi-vesicular endosomes (MVE often referred to as multivesicular bodies (MVB)). Whilst it is known that such MVE can deliver material to lysosomal compartments, presumably for degradation, MVE can also alternatively traffic to the plasma membrane and undergo an exocytic fusion event. At the plasma membrane the pre-formed small vesicles are thereafter released, into the pericellular space, as EVs (reviewed in van Niel et al., 2018).

1.6.1 Biogenesis of EVs

The first step of the biogenesis of EVs takes place at the limiting-membrane of the late endosome (Figure 1.5, reviewed in van Niel et al., 2018). There, intraluminal vesicles are formed by the invagination of the endosomal membrane, and the eventual pinching off, of these to become free-floating nanovesicles within the endosome lumen. Multiple intraluminal vesicles arise and remain enclosed by the limiting membrane of the MVE. Current models of the biogenesis of intraluminal vesicles categorise at least two processes that are either ESCRT dependent or ESCRT independent, however there is no established standard model system for studies of this nature, and hence cell type specific differences across these diverse systems must be considered, where findings in one model cell type may not be relevant in a different system.

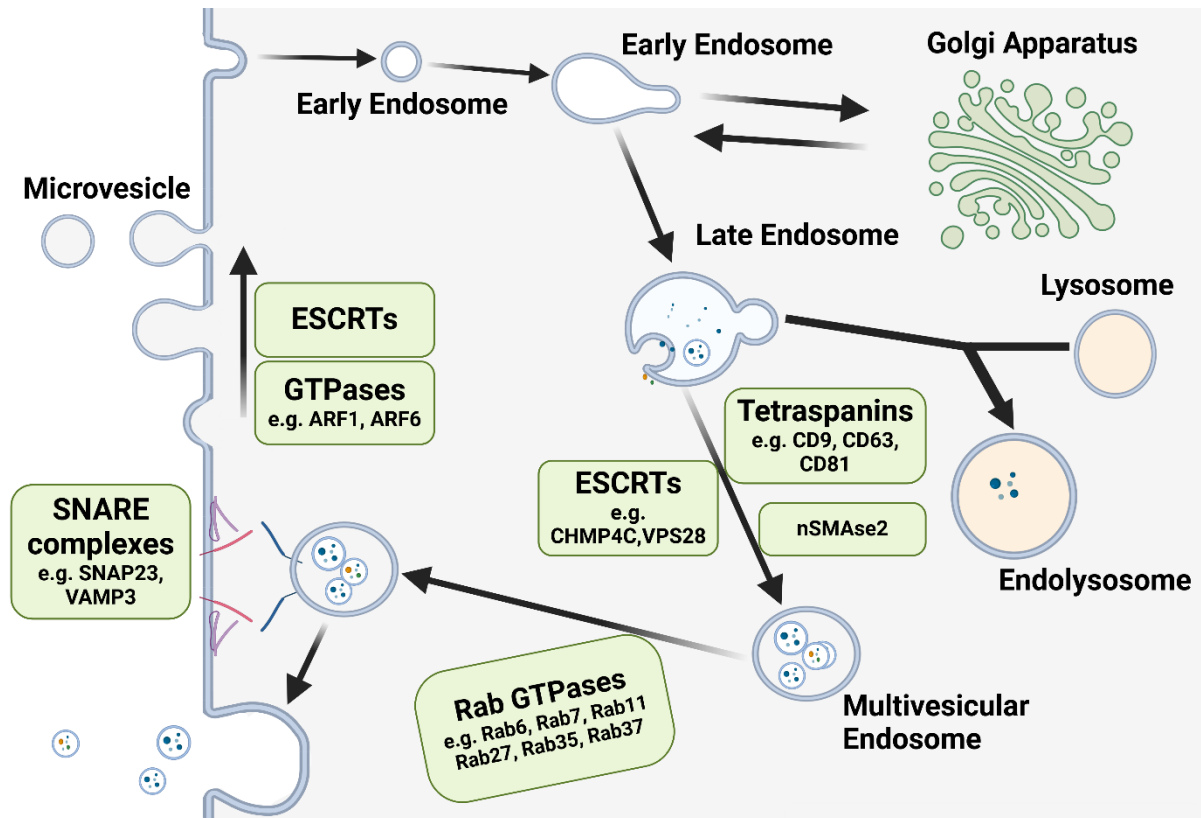


Figure 1.5: The generation of EVs involves a range of regulators.

The cellular machinery and molecular modulators leading to the formation, budding and release of EVs are depicted with a focus on key compartments involved in the generation of endosomally derived EVs. Inward budding of the endosomal membrane forms intraluminal vesicles that pinch off into the lumen of the late endosome to form multivesicular endosomes. This process is regulated by ESCRTs, tetraspanins and neutral sphingomyelinase-2 (nSMase2). The multivesicular endosomes are transported to and fuse with the plasma membrane. This step is facilitated by SNARE complexes. In contrast, microvesicles are directly formed at plasma membrane. There is an overlap of the machineries used for the biogenesis of endosomally derived EVs and microvesicles (e.g., ESCRT complexes). Green boxes detail machineries involved at the indicated step and provided examples of constituents of these machineries.

The ESCRT machinery (ESCRTs 0 - III and associated factors) modulates membrane remodelling at endosomes in a stepwise process resulting in the formation of intraluminal vesicles, loaded with ubiquitinated proteins. First, the ESCRT-0 (e.g., HRS, STAM1,2) recruits selective vesicle cargo and ESCRT-I to endosomes. Next, ESCRT-I (e.g., TSG101, VPS28) initiates vesicle budding into the endosomal lumen and recruits ESCRT-II. ESCRT-II mediates the polymerization of ESCRT-III fibres. For instance, Apoptosis-linked gene 2-interacting Protein X (ALIX), an ESCRT-accessory factor involved in EV biogenesis (Baietti et al., 2012), binds to charged multivesicular body protein 4C (CHMP4C) monomers (McCullough et al., 2008). This interaction leads to the polymerisation of the ESCRTIII components and is an essential step required for the final pinching off and the release of the intraluminal vesicles (ILVs) into the endosomal lumen (Tang et al., 2016). ESCRT-III recruits the VPS4 complex, which triggers the deconstruction of the ESCRT complex (Juan and Furthauer, 2018).

Tamai et al. revealed that the attenuation of HRS (ESCRT-0) in dendritic cells causes a decrease in the secretion of EVs and thus demonstrated that the ESCRT machinery is involved in the regulation of EV biogenesis (Tamai et al., 2010). Furthermore, depletion of TSG101 (ESCRT-I), VPS22 (ESCRT-II) and CHMP4 (ESCRT-III) has been shown to diminish the release of CD63-positive EVs in epithelial cells (Baietti et al., 2012).

Later, Colombo et al. elegantly demonstrated that different ESCRT-components have distinct influences on size and/or protein composition of released EVs in Henrietta Lacks (HeLa) cells (Colombo et al., 2013). Attenuation of the ESCRT 0 and I components HRS/HGS, STAM1/STAM and TSG101 diminished EV secretion. In contrast to this, knockdown (KD) of the ESCRT-III component and accessory protein ALIX caused enhanced EV expulsion. Interestingly, none of the KDs caused a complete inhibition of EV release suggesting that distinct vesicle populations are regulated by different factors, hence the known diversity of small vesicles that are produced is likely to involve a variety of distinctive regulating factors, and importantly suggest the existence of several vesicle-generating pathways operating in parallel and/or reacting in a compensatory fashion to such manipulations. Furthermore, in contrast to HeLa cells, attenuation of ALIX in dendritic cells did not impact the level of EV secretion hence these vesicle-generating systems are likely to show cell-type specific differences in their biogenesis and regulators.

This makes comparisons across cellular and model systems to understand the general rules surrounding vesicle regulators very challenging. Nevertheless, these studies suggest that

ESCRT components regulate the recruitment of distinct cargo and the likely existence of molecularly distinct MVE compartments (Colombo et al., 2013).

More recently, several studies in *Drosophila* have validated the important role of ESCRT-dependent EV biogenesis. For instance, depletion of VPS28 (ESCRT-I) in this model organism causes an altered MVB morphology (Firkowska et al., 2019) and impairs the number of ILVs (Fan et al., 2023). Furthermore, another study in *Drosophila* demonstrated that attenuation of multiple components of the ESCRT machinery, including components of ESCRT-0 (HRS and STAM), ESCRT-I (VPS28 and TSG101), ESCRT-II (VPS25 and VPS36) and ESCRT-III (SHRUB) reduces the number of ILVs and secreted vesicles (Marie et al., 2023).

In addition to the ESCRT-dependent pathway, there is also evidence for an ESCRT-independent, ceramide-dependant pathway involved in the formation of MVE. Upon activation of this pathway sphingomyelin is cleaved into ceramide, through the catalytic activity of nSMase2 (Trajkovic et al., 2008). This spontaneously causes a physical fold in the membrane structure. In acellular vitro models, artificial MVE were created with sphingomyelin and mixtures of other lipids upon the addition of active nSMase2, demonstrating the importance of this ceramide generation for membrane folding and spontaneous scission processes. Chemical inhibition of nSMase2 appears to attenuate EV secretion in some, but not all, cell systems (Kajimoto et al., 2013) again pointing to an important, yet poorly defined, cell-specificity in the mechanisms involved. The impact of nSMase2 inhibition on EV secretion has been confirmed in a wide range of model systems and these include for instance, neuroblasts (Iguchi et al., 2016), muscle cells (Tavakoli Dargani et al., 2018), colorectal cancer cells (Huang et al., 2018) and neurone-like cells (Sackmann et al., 2019).

In addition to these generally accepted systems for EV biogenesis, other processes are also likely involved in these mechanisms in particular tetraspanins, which are transmembrane proteins that transverse through the membrane four times, and thereby possibly inducing a curvature of the membrane that aids in the formation of ILVs (reviewed in Toribio and Yanez-Mo, 2022). For instance, Cluster of differentiation 63 (CD63) has been implicated in regulating the molecular composition of small EVs and their release. CD63 knockout (KO) in

HEK293 causes a drastic reduction in the number of released EVs and the loading of LMP1, an Epstein Barr virus encoded protein, into EVs (Hurwitz et al., 2016a, Hurwitz et al., 2017).

Cluster of differentiation 9 (CD9) is another tetraspanin and induces membrane curvature in its closed confirmation and thus is considered to be involved at the endosomal membrane to regulate EV biogenesis (reviewed in Toribio and Yanez-Mo, 2022). The impact of CD9 attenuation has been explored in various model systems indicating CD9 as a potential EV regulator across different cell systems. Interestingly, CD9 KO in melanoma cells causes an increase of EVs in the conditioned media (CM) (Suarez et al., 2021) The authors suggest that this was caused by compensatory mechanisms in the cells with an increased expression of other tetraspanins. The same study investigated the impact of CD9 KO in a melanoma cell line in regard to changes in cell organelles and reported CD9 KO induces a downregulation of the number of early endosomes accompanied by an increase in CD63 positive EVs. The tetraspanin CD9 has also been indicated as a regulator of EV cargo recruitment. Overexpressing CD9 in HEK 293T cells promotes the incorporation and export of β -catenin in EVs and thus regulates the Wnt/Integrated (Wnt) signalling pathway in these cells (Chairoungdua et al., 2010). Furthermore, CD9 modulates the incorporation of metalloproteinase CD10 in EVs (Mazurov et al., 2013).

The role of CD9 in EVs in the context of PCa has also been explored in a few studies. In a recent report, EVs derived from a PCa cell lines (WPE1-NB26), a prostate derived wildtype cell line (RWPE1) and a newly generated RWPE1 cell line with decreased CD9 expression were compared. Interestingly, the CD9 low expressing cells indicated similar concentrations of EVs in the CM compared to both the unmodified wildtype prostate cells and the PCa cell line. Furthermore, the results suggested that EVs from the PCa cell line and the prostate cell line with attenuated CD9 expression were enriched in proteins targeting protein degradation (proteasome subunit beta type-5, Proteasome subunit beta type-6, Proteasome subunit beta type-7 and proteasome activator complex subunit 2) compared to the EVs from unmodified prostate cell line (Brzozowski et al., 2018). CD9 was also previously attenuated in our lab in DU145 cells and had a minor impact on the molecular features of the released EVs (Yeung et al., 2018).

Despite these multiple lines of evidence that CD9 is a regulator of EV composition, a recent paper suggested that CD9 and Cluster of differentiation 81 (CD81) only play a minor role in modulating the composition of EVs in breast cancer cells as determined by a proteomic comparison of EVs derived from a CD9 and CD81 double and single KO cell line (Fan et al., 2023). However, this might be a cell line specific observation and clearly showing that further work is required to elucidate roles for tetraspanins in the biogenesis of EV.

1.6.2 Intracellular transport

The second step of the generation of endosome derived EVs is the intracellular traffic of MVE towards the plasma membrane. MVE are transported along microtubules and released following a plasma-membrane fusion event (reviewed in van Niel et al., 2018). Key factors involved in this traffic are molecular motors and molecular switches and parallels can be drawn with other endosome-trafficking factors. In particular, there is considerable interest in some of the Rab GTPases (e.g., Rab6a, Rab7a, Rab37) for their roles as switches in regulating MVE trafficking. Most noteworthy is the study by Ostrowski et al., who conducted a screen in HeLa cells to elucidate the function of Rab GTPases in EV secretion. The screen identified Rab2b, Rab5a, Rab9a, Rab27a and Rab27b whose inhibition by short-interfering RNA (siRNA) negatively regulated exocytic expulsion of vesicles. More precisely, the study indicated that Rab27a regulates the size of MVE and the fusion of MVE with the plasma membrane. It was also revealed that Rab27b regulates the transfer of MVE to the cell cortex (Ostrowski et al., 2010). These Rab proteins were thought to be specific for controlling vesicle secretion, because their KD impaired EV release but did not inhibit secretion of a model protein, ovalbumin. However, subsequent studies involving the same authors admitted the absolute specificity of these factors in exclusive EV secretion was not the case, and a range of classically soluble cytokines and growth factors seemed also to be perturbed by Rab27 attenuation (Bobrie et al., 2012a). Also, in contrast to Rab27b's role in HeLa cells, the study showed that attenuation of Rab27b in both the metastatic mammary carcinoma cell line 4T1 and the non-metastatic cell line TS/A does not impact the amount of the released EVs or the levels of ALIX, TSG101, HSC70 and CD63 present on isolated EVs. This again points towards a highly cell type specific role of EV regulators and inhibition of EV expulsion whilst minimally impacting other constituents of the secretome might be impossible.

In the absence of a comprehensive global-inhibition of EV release when targeting putative EV regulators, the idea was proposed that effects of such perturbations may be more subtle and there might be distinct pathways inside cells responsible for generating distinct EV-subpopulations i.e. some of these were inhibited whilst other pathways remained functional.

In our lab, it was shown previously that Rab35 and Rab11b are important regulators of EV release. KD of either resulted in a modest (20%) attenuation of vesicle output from DU145 PCa cells, suggesting initially that these molecular switches controlled the same pathway. However, molecular profiling revealed the remaining 80% of expelled EVs were molecularly distinct. This study also revealed that EV secreted in a Rab35-dependent fashion were functionally distinctive also, in terms of their capacity to activate fibroblastic cells (Yeung et al., 2018). Thus, Yeung et al. revealed a functional relevance of distinct EV subpopulations in communicating to the tumour microenvironment and highlighted importance of Rab35 for generating tumour promoting EVs by the DU145 PCa cell line.

There is further evidence that different Rab GTPases are essential regulators for distinct EV subsets. In HeLa cells, in the presence of glutamine, late endosomal Rab7a dependent CD63 enriched EVs are predominantly released. In contrast, under glutamine depleted conditions, a switch from the Rab7a dependent pathway to Rab11a recycling pathway takes place. This “EV switch” is accompanied by phenotypic changes in the release of EVs to an increased Rab11a positive Cav-1 enriched EV population (Fan et al., 2020). Hence the regulators of traffic can have significant effects on the repertoire of EVs being secreted, and these are highly dynamic systems and can be affected by microenvironmental conditions.

1.6.3 Release of EVs out of the cell

The final step of the generation of EVs takes place at the plasma membrane, where MVE fuse with the plasma membrane and the vesicles are released into the extracellular space. The helical Soluble N-ethylmaleimide-sensitive fusion attachment protein receptor (SNARE) proteins regulate the expulsion of the vesicles at the plasma membrane. SNAREs located on vesicles are termed v-SNAREs (e.g., SNAP23, Syntaxin6), SNAREs located on the target membrane are termed t-SNARE (e.g., VAMP3). The fusion of the MVE membrane with the plasma membrane is mediated by a SNARE complex formed by the helices of v- and t-

SNAREs (Tang, 2020). The formation of the SNARE complex brings the two membranes in close proximity and thus allows the fusion of the membranes. A recent study showed the important role of SNAP23 in EV release. A non-functional truncated version of SNAP23 which attenuates the function of the SNARE complex showed a drastic reduction of released EVs from HeLa cells (Verweij et al., 2018). It is important to note, that SNARE complexes are involved in the release of various vesicular classes, including lysosomal and autophagosomal vesicles and hence the specificity of a SNARE complex to specifically only regulate endosomally derived EVs is difficult to establish (Vats and Galli, 2022).

1.6.4 Considerations about EV-secretion in PCa

Accumulating evidence suggests that the secretion of EVs is modulated in PCa and this observation is influenced by antineoplastic treatment. For instance, in plasma samples, CD9 positive EVs are found at increased levels in patients with PCa when compared to samples of patients with benign prostatic growth (Soekmadji et al., 2017a). Notably, an elevation in CD9 and AR double positive EVs in patients with aggressive PCa has also been reported (Mizutani et al., 2014). Furthermore, research by Martens-Uzunova et al. suggested that EVs in blood plasma samples from a PCa patient exhibit a distinct disease stage specific signature. The study showed that organ confined PCa was associated with elevated levels of CD9 CD63 double positive EVs in the blood stream, whereas elevated CD9 PSMA positive EVs were increased in advanced PCa (Martens-Uzunova et al., 2021).

Treatment of PCa cells with androgen-axis targeting drugs (e.g., Enzalutamide) induces changes in the EV cargo (Soekmadji et al., 2017b). Specifically, dihydrotestosterone administration in Lymph Node Carcinoma of the Prostate (LNCaP) cells elicited an increased secretion of CD9 positive EVs (Soekmadji et al., 2017a). Urabe et al. showed that, in PC3 cells, targeting an EV miRNA regulator reduces EV secretion *in vitro* and diminishes the tumour burden *in vivo* in a mouse model (Urabe et al., 2020).

These studies point to an important role of EVs in PCa and understanding the nuanced modulation of the EV cargo and functional role, outlined in more detail in section 1.6.6, will

be critical to unravel the underlying disease mechanisms and in the development of novel targeted therapies.

Taken together, there is considerable complexity in the endogenous, cell intrinsic machineries that produce EVs, and these may be highly cell-type specific. The context of EV production such as cell starvation, hypoxic stress and other environmental influencers are presumed to drive changes from constitutive EV manufacture, and hence these pathways are likely to be highly dynamic and responsive to external factors. Additionally, there is a possible overlap in some of the machineries used for the generation of endosome derived EVs and the generation of plasma membrane derived microvesicles. This potential confounder renders the experimental distinction of the two major EV classes difficult. Yet, given the manifold roles of EVs in driving pathological processes such as cancer, it remains of interest to devise modalities for inhibiting their secretion, and to identify EV subsets that are most relevant for tumour-promoting biological activities. Targeting such EV sub-populations, if possible, might be useful in therapeutic settings to constrain specific EV-mediated effects whilst limiting undesirable consequences of global EV attenuation.

1.6.5 EV Cargo

EVs encapsulate highly complex cargo including a range of RNA species, DNA and proteins. Importantly, in addition to internal EV cargo, EVs also carry functional external cargo, which has been described as a protein corona. (Toth et al., 2021, Palviainen et al., 2020).

The composition of the internal EV load, depends on the cell status with cancer cells carrying cargo that is distinct from wildtype cells, as reported for example by Hosseini-Beheshti et al. who described the proteome of PC3 EVs compared to normal prostate EVs (Hosseini-Beheshti et al., 2012). Another example of cell status driven EV cargo was described for mutant KRAS, that promotes the incorporation of signalling molecules and metabolic enzymes into EVs (Demory Beckler et al., 2013). External stimuli, such as hypoxia, ultraviolet (UV) radiation, TGF- β treatment have also been reported to modulate the cargo loading in cells (Dixon et al., 2023). Furthermore, external stimuli can also regulate the release of distinct subsets of EVs to be released. For instance, fibroblast growth factor modulates the release VAMP3 positive EVs (Kumar et al., 2020).

The underlying mechanisms of EV content recruitment are not yet fully elucidated. EV cargo loading could be a passive process directed by the mere proximity of the substrates at the location of EV biogenesis. However, there is increasing evidence the EV cargo sorting is a selective process during which cargo is incorporated into nascent EVs. Perhaps, a combination of passive and active loading drives the molecular diversity of EVs.

Recently, proteins containing the KFERQ motif were found to be enriched in a subset of EVs supporting the notion of selective EV cargo sorting (Ferreira et al., 2022). Furthermore, various posttranslational modifications have been reported to promote the loading of proteins into EVs for instance phosphorylation induced by the activation of oncogenic signalling (Imjeti et al., 2017) or glycosylation (Wehman et al., 2011). In addition to this, the ESCRT machinery binds to ubiquitinated epidermal growth factor receptor resulting in locally cargo enriched regions on the endosomal membrane (Eden et al., 2012).

Various mechanisms responsible for the specific incorporation of RNA into EVs have also been proposed. Janas et al. reported that the affinity of selective RNA species to lipids leads to an accumulation of these species at the MVEs and consequently enhanced loading in EVs (Janas et al., 2015). Oncogenic signalling has also been suggested to influence the EV content as described for example for KRAS signalling, which modulates the incorporation of miRNAs into EVs and mediates target suppression in recipient cells (Cha et al., 2015). In colon cancer cells KRAS signalling promotes Argonaute-2 (AGO2) localisation to endosomes mediating AGO2 dependent miRNA loading into EVs (McKenzie et al., 2016).

Furthermore, specific RNA binding motifs have been found that drive the selective enrichment of RNA in EVs. An example of this are factors associated with the heterogenous nuclear ribonucleoprotein (hnRNP) family such as hnRNPA2B (Villarroya-Beltri et al., 2013). In this study, the sequence motif GAGG was identified in a subset of miRNAs enriched in EVs that bind to hnRNPA2B. Another example of RNA binding protein driving specific RNA loading into EVs, is the RNA binding protein synaptotagmin binding

cytoplasmic RNA interacting protein (SYNCRIP), which binds to the hEXO motif on microRNA (Santangelo et al., 2016).

1.6.6 Functional role of EVs

EVs fulfil a plethora of functions by transferring signalling cues ranging from modulating the metabolism of recipient cells, conferring resistance to chemotherapeutic treatment (reviewed in Zhang et al., 2021) to activating CAFs in the TME as described earlier. In the context of cancer, EVs have been shown to promote the progression of the disease at all stages from the beginning of tumorigenesis to metastatic spread and resistance to treatment.

Evidence is accumulating that EVs play a significant role in the transformation of normal and neoplastic cells to a more aggressive phenotype. *In vitro*, patient derived PCa EVs have been shown to drive phenotypic changes in recipient non-malignant cells that increase their migratory and proliferative capacity (Souza et al., 2018). Furthermore, Brzozowski et al. reported that PCa EVs derived from reduced CD9 expressing cells elicit increased motility and invasion in a recipient prostate cell line suggesting that these cells possibly acquired a neoplastic like cell status (Brzozowski et al., 2018). In addition to this, PCa EVs have been demonstrated to play a role in intra tumour communication and to drive malignant transformation of adjacent neoplastic cells as shown by El-Sayed et al. who demonstrated that EVs from a mesenchymal like PCa cell line confer EMT transition in recipient epithelial-cell like PCa cells (El-Sayed et al., 2017). EVs also promote the tumour growth by influencing energy generating pathways, glycolysis and oxidative phosphorylation (Zhang et al., 2018c). A metabolic shift in cancer cells conferred by EVs has also been reported by Zhao et al. on EVs isolated from PCa patient CAFs. The study suggested that these EVs encapsulate nutrients that induce a shift from aerobic to anaerobic energy to satisfy the increased energy demand of the tumour tissue (Zhao et al., 2016).

Escape from the immune surveillance is a critical step in the establishment of neoplastic tissue to prevent the clearance of abnormal cells by the immune system and thus considered a hallmark of cancer (Hanahan and Weinberg, 2011). In PCa, EVs appear to contribute to the suppression of the immune system and confer antitumour immunity. EVs from the LNCaP cell line suppress T-cell activation and induce apoptosis (Abusamra et al., 2005). PCa EVs

have also been reported to inhibit natural killer cells (Liu et al., 2006) and the differentiation of dendritic cells (Yu et al., 2007). In a study by Poggio et al. it was shown that Programmed Death-Ligand 1 (PD-L1), a molecule that suppresses T-cell activation, on PCa EVs inhibited T-cell activation. Importantly, diminished PD-L1 expression on EVs by targeted attenuation, caused a reduced tumour growth which was rescued by injecting PD-L1 positive EVs (Poggio et al., 2019).

There is mounting evidence that EVs are a significant contributor to the formation of the pre-metastatic niche thus supporting the spreading of the disease to distant sites as reported for melanoma (Peinado et al., 2012) and breast cancer (Li et al., 2022b). EVs from non-tumour cells also appear to play a role in this process. Research by Hsu et al indicates that bone marrow derived EVs are involved in creating the pre-metastatic niche in the liver for the arrival of lung cancer cells (Hsu et al., 2020). Regarding PCa, it has been shown that PC3 cell derived EVs contribute to osteolysis and thereby to the establishment of the bone as an environment for tumour progression (Ma et al., 2021). The EV composition likely plays a major role in these processes. For instance, integrins on EVs were described to drive the organotropism in metastasis (Hoshino et al., 2015). Furthermore, in melanoma, EVs promote metastasis mediated by transporting receptors to distant sites where they bind to target cells, induce the expression of various signalling molecules and subsequently promote lymph angiogenesis (Garcia-Silva et al., 2021).

At later stages of a cancerous growth, EVs also appear to play a crucial role in the development of resistance to therapies. For instance, in breast cancer cells treatment with the chemotherapeutic drug Doxorubicin increases the release of EVs that prime the premetastatic niche (Wills et al., 2021). In PCa, Enzalutamide-resistant PCa cells have an elevated secretion of EVs, mediated by STX-6, as suggested by reduced EV release and increased cell death upon STX-6 attenuation (Peak et al., 2020). However, the authors of the study did not elucidate the detailed mechanisms. In a different study, GW4869 treatment of Paclitaxel resistant PC3 cells leads to shift to larger EVs (>150 nm) and in a xenograft model, GW4869 treatment reduced the tumour burden (Kumar et al., 2022). The authors speculated that the smaller EVs were required for the cancer cell survival. Furthermore, Docetaxel resistant PCa cancer cell variants (derived from DU145 and 22Rv1) export multidrug-resistant proteins

(including P-glycoprotein and Multidrug Resistance Protein 1 (MRP1)), which promote the efflux of drugs from cells, packaged in EVs (Corcoran et al., 2012). Interestingly, these EVs were able to confer drug resistance to recipient Docetaxel sensitive PCa cells suggesting an important role of EVs in the establishment of therapy resistance.

Taken together, there is strong evidence that EVs contribute to the establishment and maintenance of cancer and at the later stages of the disease also the failure of therapeutic treatment. Understanding the mechanisms that drive these observations will aid in the development of new therapeutic targets. For this purpose, it is essential to isolate and characterise EVs with robust methods outlined in 1.6.8-1.6.9.

1.6.7 EVs as drug delivery vehicles

EVs have gained attention as promising possible drug delivery systems due to their biophysical properties and capabilities to transport bioactive molecules such as proteins and nucleic acids (reviewed in Kim et al., 2024, Elsharkasy et al., 2020). The vesicular bilipid layer provides a protective environment for the cargo and thus serves as a shield for the cargo against degradation, e.g., proteolysis, when the content is transported through the body. Furthermore, injecting EVs in mice has been shown to be accompanied by a low immunogenicity (Sun et al., 2023b, Lu et al., 2023), which represents an advantage of this route of drug delivery compared to, e.g., lipid nanoparticles (reviewed in Lee et al., 2023). Another important characteristic of EVs is their capability to traverse across biological barriers including the blood brain barrier (Ridder et al., 2014, Alvarez-Erviti et al., 2011) and thus EVs provide a potential delivery route for traditionally hard to reach target sites. In addition to this, the molecular features of the EVs drive the biodistribution *in vivo*, which was shown e.g., by Hoshino et al., who demonstrated that the type of integrins expressed on EVs dictates, whether the vesicles accumulate in the brain, the lung or the liver (Hoshino et al., 2015). The organotropism of EVs could be exploited to engineer EVs for a target cell-specific delivery of the content and thus also lower the required dose of the administered drug when compared to injecting a drug in solution.

However, it is important to acknowledge the challenges and concerns regarding exploiting EVs as a drug delivery vehicle (reviewed in Wang et al., 2023, Durmaz et al., 2024). The

industrial scale-up of the EV production and reproducibility across different batches remains a major challenge due to the cell derived nature of the product and its inherent variability. Furthermore, the uptake mechanisms of EVs at the target cell are currently not fully understood. These could include a direct fusion of the EV with the membrane and subsequently the release of the cargo into the cytosol. However, endocytosis is thought to be the main entry route of EVs, which destines the cargo for degradation (Joshi et al., 2020, Ghoshal et al., 2021). Hence, for a therapeutic application of EVs, the EVs must either exert their function via a different route, e.g., direct membrane fusion and release of the cargo into the cytosol, or the cargo must escape from the endosome (Pham et al., 2023). Another concern is the possible delivery of pro-neoplastic signals on the EVs and thus the triggering of neoplastic effects in recipient patients. Despite these challenges, several pre-clinical and clinical stage trials have been or are currently conducted with promising results (reviewed in Elsharkasy et al., 2020, Wang et al., 2023).

1.6.8 Methods to study EVs

There is a plethora of techniques that can be utilised to concentrate, isolate and enrich EVs from biofluids and CM based on their biophysical properties (e.g., size, density) (reviewed in Zhang et al., 2018b, Chiriaco et al., 2018, Hendrix et al., 2023). It is important to note, that there is no gold standard method that is suitable for the general usage and the selection of an appropriate method depends on the source material and downstream application. In addition to this, important considerations for the decision on the best techniques are the initial sample volume, efficiency and specificity to retain EVs, protocol durations and complexity, requirement of specialised equipment and associated costs (Figure 1.6) (Hendrix et al., 2023). In general methods that yield a highly purified EV preparation have a low efficiency to retain EVs and the inverse.

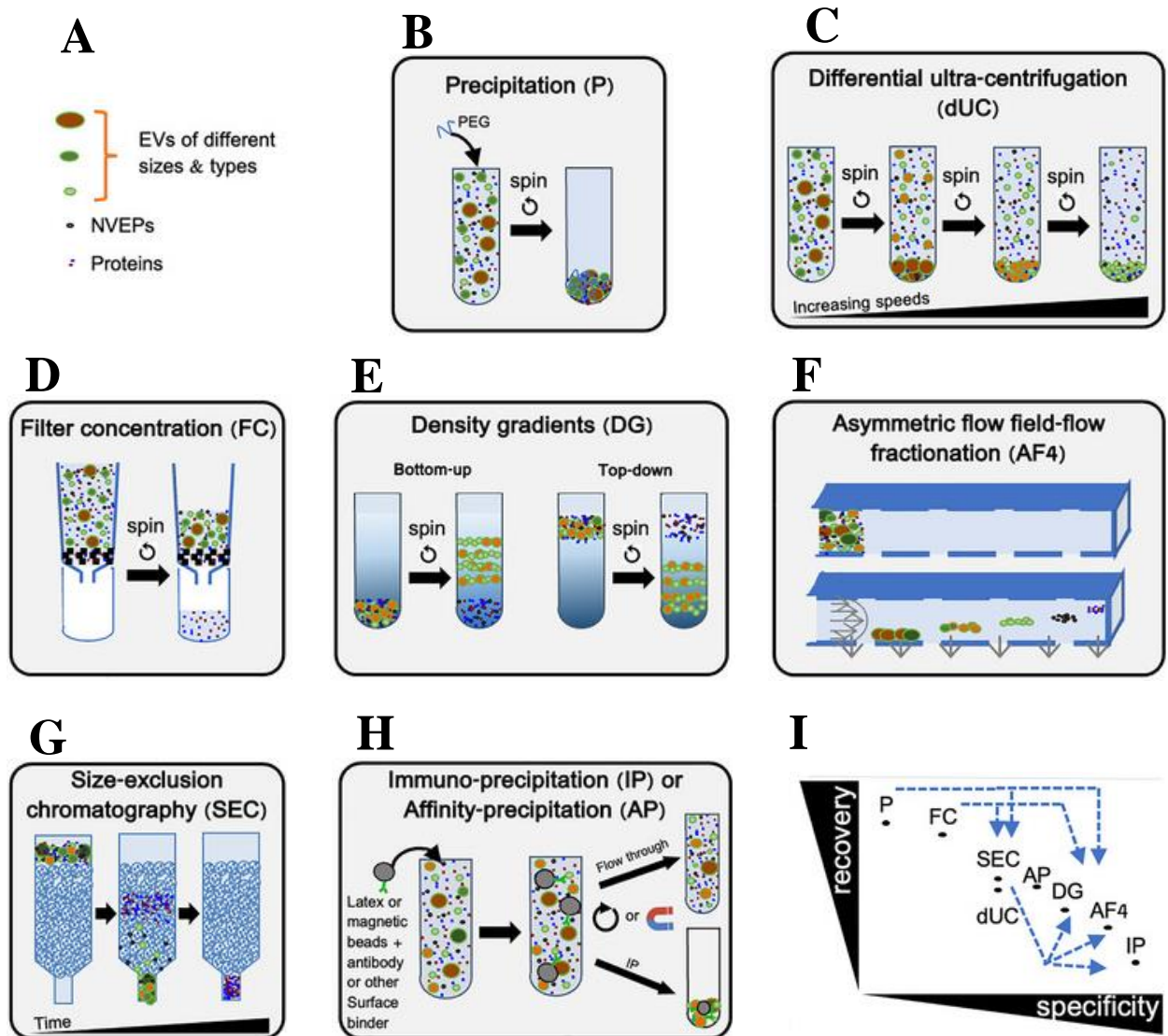


Figure 1.6: Overview of different commonly used EV isolation methods.

A) shows a graphical depiction of different EVs and co-isolated contaminants. EVs can be isolated based on biophysical parameters such as solubility (precipitation (P) (B)), size (differential ultra centrifugation (dUC) and filtration (C and D)), density (density gradients (DG) (E)), hydrodynamic size (asymmetrical-flow field-flow fractionation (AF4) (F)), size (gravity dependant, Size-exclusion chromatography (SEC) (G)), or EV surface markers (immuno- precipitation (IP) or affinity-precipitation (AP) (H)). I) shows that each method has a distinct efficiency to retain EVs (recovery, y-axis) and fidelity to only retain EV (specificity, x-axis). Dashed blue lines signify combinations of techniques that result in a superior purification. NVEPs=non vesicular extracellular particles, FC=Filter concentration. Figure adapted from (Welsh et al., 2024).

A commonly used technique to purify the EVs from the source material uses serial centrifugation: low speed centrifugation at 400 g to pellet cells and 2,000 g to pellet very large EVs, followed by 10,000 x g to pellet microvesicles and 100,000 x g-200,000 x g to pellet small EVs (Raposo et al., 1996). Using this protocol, bulk EV isolation can be conducted to obtain EV preparations which contain an unbiased spectrum of EVs from smaller (less dense) to larger (dense) EVs and including larger ectosomes. However, capturing a wide variety of different EV populations, could also cause challenges in the downstream applications and interpretation of results. In addition to this, non-vesicular extracellular particles, e.g., proteins, are co-sedimented and hence contaminate the sample. To circumvent this problem, the isolated EVs can subsequently be further purified, for example, by passing the sample through a 0.2 µm filter (Théry et al., 2006). Alternatively, combining ultracentrifugation (UC) and a density gradient, which retains the EVs at a density of 1.1-1.2 g/ml (Raposo et al., 1996) or a discontinuous sucrose/deuterium oxide gradient, which retains EVs of density <1.2g/ml in an isotonic cushion (Lamparski et al., 2002), can be applied to isolate the EVs based on their buoyant density. A disadvantage of these purification methods is that they are time consuming and are accompanied by a lower yield of EVs compared to a simple UC step. Furthermore, the EV containing preparations can be contaminated by the gradient material which can complicate the usage of the sample.

Ultrafiltration (UF) (Lamparski et al., 2002) and tangential flow filtration (Busatto et al., 2018) are commonly used alternative techniques, which are membrane based isolation methods that result in the enrichment of EVs based on weight or size. The protocol is suitable for large sample volumes of liquid, fast to conduct, and the obtained EV preparations have a high sample purity. However, other non-vesicular extracellular particles can be co-enriched and thus contaminate the EV preparation.

Size-exclusion chromatography (SEC) is a technique used to isolate EVs based on size (gravity dependent). The protocol distinguishes itself by its simplicity, high reproducibility, and high purity of the obtained EV sample. In addition to this, this technique causes minimal disruption of the EV structures, maintains the structural integrity, and there is no risk of contamination from the column. Nevertheless, it is a time-consuming technique, which bears the risk of a low yield. In addition to this protein aggregates and complexes of equal size can

be co-purified and thus contaminate the sample. There are also commercially available SEC based isolation kits such as qEV (iZON) and Exo-spin™ (Cell Guidance Systems). However, the consensus guidelines Minimal Information for Studies of Extracellular Vesicles (MISEV) 2023 warrant caution due to the limited EV specificity of the kits. It is also important to note, that the details (chemicals, components) of the kits are often not specified and hence kit-introduced contaminations can be difficult to determine and evaluate.

Rapid protocols based on the solubility or aggregation of EVs have also been developed and include polymer precipitation e.g., polyethylene glycol (PEG). EVs purified by this method maintain their integrity, however, there is a risk of contamination with the polymer and inevitable proteins are co-precipitated. Several commercially available kits have been established based on precipitation and these include e.g., miRCURY Exosome Kits (QIAGEN) and Total Exosome Isolation Kit (Invitrogen), ExoQuick (System Biosciences). Again, due to limited EV specificity, these kits should be used with caution.

Proteins expressed on the EV surface can also be used to enrich EVs in a sample of interest. This is implemented by selecting a marker on the EV surface for an immune-affinity based capture e.g., utilising antibody coated beads (Clayton et al., 2001) or latex beads (Lamparski et al., 2002). A clear advantage of these techniques are the ease and speed of the handling of the samples. Furthermore, only a small volume is required and a specific subpopulation of interest (e.g., CD81 positive EVs) can be selected. However, this can also be a drawback, as the true diversity of the EV populations of the initial sample source is not represented in the final purified sample. It is challenging to elute EVs from the beads and thus, there is limited downstream applications suitable for instance characterisation by flow cytometry is applicable, while functional experiments not.

Recently, AF4, has been introduced as a novel high resolution isolation method, which can be used to simultaneously fractionate and characterise EVs based on hydrodynamic size (Zhang et al., 2018a). The sample of interested is injected into a flow chamber and then subject to both, a parabolic channel flow and, perpendicular to that, a cross flow. EVs are subsequently detected and eluted (Zhang and Lyden, 2019). AF4 isolations have advantages which include the low impact on the EVs, maintaining integrity of the EVs, reproducibility of the results,

and global EV collections (small and large EVs). Limitations of AF4 comprise that only small sample quantity can be used, and it might require additional downstream concentrations. Furthermore, the specialised equipment is expensive, and thus might not be easily available.

As outlined above all methods have advantages and disadvantages that should guide the selection of a suitable method for the specific research question. For instance, if a researcher is interested in evaluating the RNA content of bulk EVs in a large sample volume only UC, UF or SEC, Density gradient, or PEG are suitable techniques. If additionally, a high EV yield is required, the choice is further limited to only UC, UF, PEG, density gradient. Furthermore, to avoid contamination introduced by the isolation method the researcher might opt for UC or UF for the isolation of EVs.

1.6.9 Characterisation of EVs

There are many challenges associated with quantifying and characterising EVs in a given sample. The Inter-laboratory comparison is complicated by confounding factors such as preanalytical variables that also influence EV quantity and quality including cell status, available nutrients and oxygen. In addition to this, there is a remarkable heterogeneity of EVs (molecular composition and size). Despite ever evolving techniques and increased accuracy, there is currently no single method alone that can characterise all EV populations in a sample of interest, while also being able to discriminate between a true EV and other extracellular particulate material.

Given these challenges, best practices to characterise EVs in CM, body fluids or isolated EVs is under constantly evolving debate. The MISEV guidelines, recently in the updated third version (Welsh et al., 2024), is an effort to provide guidance in this regard without proposing to adhere to strict rules. Welsh et al. stipulate that EVs should be characterised by utilising various and orthogonal techniques to assess the quantity/quality of the EVs to ascertain molecular characteristics and prior to defining functional properties of the EV sample of interest. To achieve this, the guidelines suggest including key steps:

- Quantification of the source material, this can include for instance cell number/ CM volume
- Quantification of the EV preparation, for instance particle and protein concentrations
- Determining the physical features of the EVs such as diameter or density
- Analysing the biochemical composition, for instance tetraspanin expression (CD9, CD63, CD81)

Furthermore, the limit of detections of an instrument can result in biased quantification of one EV population. Hence, it is important to consider the respective limitations of each instrument used prior to the analysis and later when analysing the results.

There are several different EV quantification techniques based on distinct biophysical features and with instrument specific advantages and disadvantages. For instance, cryo-electron microscopy (cryo-EM) is an important microscopy-based technique used to qualitatively analyse EVs and characterise native structural features of EV populations in a sample. The EV preparation is immobilised by vitrification and vesicular structures appear as round shapes confined by a lipid bilayer (Yuana et al., 2013). Limitations of this technique are the low sample throughput and the laborious processing of the samples, which makes this method incompatible with routine assessment of all EV preparations obtained in a lab.

Another microscopy-based technique utilised for the quantification of the size and distribution of EVs, is nanoparticle tracking analysis (NTA). This method exploits the light scattering and Brownian motion of particles in a solution to calculate their hydrodynamic diameter (Dragovic et al., 2011). Advantages of NTA measurements compared to cryo-EM are the simple sample preparation and high quantification of particles. However, there is also a drawback of this method that it is not possible to distinguish genuine EVs and other extracellular particulate material in the sample. In addition to this, NTA inadvertently, induces biases by overestimates the proportion of particles that scatter more light (large particles) compared to particles that scatter less light (smaller particles).

The results of EV quantification are often complemented by utilising other techniques that assess the vesicular molecular content. A major challenge in this regard is that currently, no

universal EV marker is available. To tackle this issue, the MISEV guidelines 2023 established a five-component framework (section 5.7) that aids to show the enrichment of EV markers, while also demonstrating the absence of co-isolated contaminants. 5 categories were defined, that recommend to:

- Validate the presence EV associated markers that represent transmembrane proteins such as CD9, CD63
- Validate the presence of EV associated markers that represent cytosolic protein such as ALIX
- Demonstrate the lack of contamination such as lipoproteins

Category 4 (showing the cellular origin of the EVs e.g., detecting endosomal proteins) and category 5 (showing co-isolates that are secreted by the cells) serve as optional additional assessments.

A practical example for the assessment of tetraspanin levels is for example, a plate-based assay akin a classical Sandwich Enzyme-linked immunosorbent assay (ELISA) which uses one tetraspanin antibody, e.g., anti CD63, to capture the EVs in a sample and another antibody e.g., a biotinylated anti CD9 antibody to detect the EVs. Tetraspanins can also be explored microscopically, for instance by EVQuant which immobilizes EVs in a gel, followed by staining of the EVs with Rhodamine and fluorescently labelled antibodies (mouse CD9 Monoclonal–Alexa Fluor® 647 antibody, mouse CD63–Alexa Fluor®488) allowing to detect changes in the expression of tetraspanin on individual EVs (Hartjes et al., 2020).

It is important to note, that there is a plethora of other methods which include for instance western blotting and flow cytometry that can be utilised to explore the molecular composition of an EV sample and the MISEV 2023 guidelines provide excellent guidance in the initial considerations prior to the utilisation of these techniques (Welsh et al., 2024).

In recent years, several EV specific markers to delineated EV origin have been proposed that include for ectosomes SLC3A2 and BSG (Mathieu et al., 2019) and Annexin A1 (Jeppesen et al., 2019), LAMP1 (Mathieu et al., 2021) and for endosome-derived EVs Syntenin-1 (Kugeratski et al., 2021). However, these markers are not yet universally accepted and require further validation across multiple EV sources before they can be used as a definite EV

marker. Again, this highlights the complexity of characterising EV specific features in a sample of interest.

1.7 Hypothesis and aims

There is mounting evidence that EVs released from cancer cells promote the development and growth of the tumour, in a variety of different ways. One aspect of focus to our group has been that EVs drive changes in the TME by activating fibroblasts to a CAF like phenotype.

In this thesis, I hypothesise that inside PCa cells, distinct machineries regulate the biogenesis, transport and release of molecularly and functionally distinct EV subpopulations, and that attenuating some of these may highlight an association between distinct subsets of EVs and specific PCa promoting functions.

The overarching goal of the work presented in this thesis is to provide insights into endogenous factors that regulate EV-secretion which thereafter contribute to PCa-relevant processes. The study will centre around 3 principle aims that will be explored with a range methods:

- 1) Identification of potential regulators (candidates) involved in EV biogenesis, intracellular transport and release based on a literature review and aided by bioinformatic tools.
- 2) Generation of PCa cell line variants with attenuated expression of the selected candidates, and subsequent characterisation of the released EVs to understand their impact on vesicle-production.
- 3) Exploration of the functional impact of EVs derived from the PCa cell variants, with particular emphasis on the fibroblast response.

Chapter 2:

Materials and Methods

The materials and methods described in this chapter were carefully selected with the goal to identify and evaluate potential EV regulators. Candidates, which were defined here as elements that were targeted in the scope of this thesis, were selected based on extensive literature search and evaluated with bioinformatic tools (2.1). In addition to this, various approaches were used and these ranged from cell culture (2.2), genetic manipulations of PCa cells (2.2), and also included both standard and novel methodology to measure the effect of these perturbations on the parent cells (2.3,2.6), corresponding EVs (2.4), as well as EV recipient cells (2.5).

2.1 Bioinformatic tools

2.1.1 Candidate interaction network

To explore relationships of the selected candidates, the Biological Effector Database (BED) (<https://anaxomics.com/biological-effectors-database.php>, (Iborra-Egea et al., 2017) created by our ProEVLifecycle consortium partner Anaxomics was used to analyse the general interaction network of the selected candidate genes. The BED is a proprietary database containing information from publicly available datasets and is also manually curated from published literature including network information. The network analysis was subsequently visualised in Cytoscape. The interaction network was created by our collaborators Pedro Matos Filipe and Dr. Judith Farrés at Anaxomics.

2.1.2 Artificial neural networks (ANN)

A machine learning model developed by Anaxomics (Loging et al., 2011) was used to investigate if the set of candidate genes overlap with various known pathways. By this, we mean that the candidate list in its entirety will encompass genes that are involved in a number of biologically well-defined pathways, and the algorithm will identify these overlaps. The algorithm is based on ANN, that were trained in a cross-validation protocol using the BED as described recently (Segu-Verges et al., 2022). The output of the model is a relationship score that ranges from 0% to 100%. A higher score corresponds to a higher likelihood of interaction between the protein of interest and the investigated pathway. The significance of the ANN scores were evaluated in a Monte Carlo simulation and the method was validated in a recent study (Artigas et al., 2020).

The pathways explored here are those that are relevant for EV biogenesis, transport, or release. For this purpose, relevant gene sets (table 2.1) were selected from various sources:

Gene ontology (GO) terms associated with EV biogenesis, transport or release were selected from https://www.informatics.jax.org/vocab/gene_ontology. The GO terms for the ESCRTI and II (GO: 0000813 and GO:0000815) did not provide a comprehensive list of all ESCRT components that have been described to be involved in EV biogenesis. Hence, I combined the aforementioned GO terms and additionally included those genes that were described by (McGough and Vincent, 2016, van Niel et al., 2018) to be involved in EV biogenesis. The functional hierarchical clustering analysis was performed by our collaborators Pedro Matos Filipe and Dr. Judith Farrés, at Anaxomics.

Table 2.1: Gene lists for the functional hierarchical clustering analysis.

For the functional hierarchical clustering analysis of the 17 selected candidates, several gene lists were compiled using the following sources outlined below. Some additional genes (specified) are included to provide fuller coverage of ESCRT-related machineries. Selected candidates that were also included in the specified gene list are found in the column on the right.

<u>Gene list/origin</u>	<u>Named</u>	<u>Includes the following candidates</u>
GO: 1903543	Exosomal secretion	Rab7a
GO: 1905668	Endosomal localisation	-
GO: 0051047	Upregulation of secretion	Rab7a, Rab27b
GO: 0060627	Vesicle mediated transport	PCLO, Rab7a, Rab11b
GO: 0031340	Vesicle fusion	-
GO: 0000813	ESCRT I	VPS28
GO: 0000815	ESCRTIII	CHMP4C
GO: 0000149	SNARE binding	STX6, VAMP3
GO: 0099023	Vesicle tethering	-
GO: 0000813 and 0000815 and adding the following genes: HRS, STAM1, STAM2, CEP25, ALG-2, ARRDC1, VPS37A, VPS37C, VPS37D, MVB12A, UBAP1, EAP1, EAP20, EAP30, EAP45, CHMP1A, CHMP7, IST1, VPS4.	ESCRT	VPS28, CHMP4C

Extracted from reactome.org	Vesicle mediated transport	Rab6a, STX6, VAMP3, CHMP4C
Created by Anaxomics (see Annex A)	Apoptosis	-

2.1.3 CancerTool

The potential clinical relevance of the candidates was examined utilising CancerTool (<http://genomics.cicbiogune.es/CANCERTOOL/index.html>) a web based bioinformatic tool to exploits publicly available transcriptomic data sets (Cortazar et al., 2018). Two data sets were included in this analysis. The TCGA dataset (patient cohort size (n=497)) (Cancer Genome Atlas Research et al., 2013, Cancer Genome Atlas Research, 2015) was used to explore the differences in mRNA levels between the identified candidates and PCa status by both Gleason Score (GS) and disease-free survival (DFS). The latter is defined as the recurrence of the disease after the treatment has finished and the patient was deemed disease free. The DFS dataset in concertool is retrieved from <https://portal.gdc.cancer.gov/>. It needs to be noted that the DFS calculated here represents a crude overview of the DFS irrespective of the perceived treatment and how the DFS was assessed. While this analysis provides an excellent general overview, the authors of the paper admit that this warrants caution when interpreting the data and to gain a deeper understanding an extensive analysis of the primary data set would be required e.g., by separate the patients into subgroups based on the received treatment.

To gain a more comprehensive overview of the respective candidate transcript levels in normal tissue (N), the primary tumour (PT) and the metastatic side (M) hence revealing possible correlation with disease stage, the Taylor data set (patient cohort size n=185) was additionally included in the analysis (Taylor et al., 2010).

2.2 Cell culture

2.2.1 Monolayer cell culture

The highly metastatic PC3 cell line is a patient derived bone metastatic PCa cell line. The cell line was a kind gift of Dr Hector Peinado (Centro Nacional de Investigaciones Oncológicas (CNIO), Spain) who received them fresh from the biobank, and immediately performed a

series of validation experiments to certify their specification. This involved using short tandem repeat profiling. The consortium partners received cell stocks following this from Dr Peinado, in the interest of harmonising materials throughout the ProEVLifecycle consortium. The cells were maintained at 37 Degree (°) Celsius (C) with 5% Carbon dioxide (CO₂) in Dulbecco's Modified Eagle's Medium (DMEM) GlutaMAX™. The media was supplemented with 100 U/ml penicillin (Sigma-Aldrich, UK), 100 µg/ml streptomycin (Sigma-Aldrich, Dorset, UK), 2 mM L-glutamine (Sigma-Aldrich) and 10% foetal bovine serum (FBS). When the cell monolayer reached 90% confluency, the cells were washed with Dulbecco's Phosphate-Buffered Saline (DPBS) and proteolytically detached from their substrate with Trypsin-EDTA at 37°C/5% CO₂ for up to 5 min. The dissociation process was stopped by adding FBS and after a DPBS wash cells were then passaged to a new cell culture flask containing fresh medium supplemented with 10% FBS. This split was performed twice a week.

The lung fibroblast cell line AG02262, obtained from the National Institute of Aging Cell Repository, at the Coriell Institute for Medical Research, is a primary diploid normal fibroblast cell of lung origin, isolated from a healthy male donor with no evidence of lung disease. It has been used by the group extensively as a model to investigate aspects of stromal differentiation and in terms of the response to cancer derived vesicles (Webber et al., 2010, Webber et al., 2016, Yeung et al., 2018, Webber et al., 2015). These fibroblasts were grown in DMEM:F12 (Gibco - Thermo Fisher Scientific) containing 100 U/ml penicillin (Sigma-Aldrich, UK), 100 µg/ml streptomycin (Sigma-Aldrich, Dorset, UK), 2 mM L-glutamine (Sigma-Aldrich) and 10% FBS.

2.2.2 shRNA-mediated knockdown of candidates within PC3 cells

Lentiviral vector systems allow the exploitation of the endogenous RNA interference system of cells to generate stable attenuation of a target mRNA. Here, we used MISSION® short hairpin (sh) RNA lentiviral transduction particles (Sigma-Aldrich) for establishing KD of our candidate genes. Additionally, the usage of a pLKO.1-puro cassette allows the selection of successfully transduced cells by puromycin resistance. A shRNA sequence targeting a non-mammalian target was also included and the transduced cells are hereafter termed NMC. An amended risk assessment was approved by the Cardiff University Genetic Modified

Organisms safety committee for the new candidates identified for this project (Local project reference: GM130/634).

For transductions, PC3 cells were plated at 4,000 cells/well in a 96-well plate (Greiner) in DMEM GlutaMAX™ supplemented with 10% FBS, at a confluency of approximately 50-60%. After 24 h, PC3 cells were transduced with lentiviral particles (table 2.2) at a multiplicity of infection (MOI) of 20, in the presence of hexadimethrine (8 µg/ml) (Sigma-Aldrich), a cationic polymer which can increase transduction efficiencies. The MOI was calculated as following:

$$\begin{aligned} & (\text{total number of cells per well}) \times (\text{Desired MOI}) \\ & = \text{total transducing units needed (TU) (total TU needed)} / (\text{TU/ml reported on vial}) \\ & = \text{total ml of lentiviral particles required} \end{aligned}$$

The transduction unit (virus titre) was provided by the supplier. For each target, five different shRNA sequences were used, as the performance of KD can be variable. In the past, exploring five distinct shRNA sequences per target has resulted in at least one of these downregulating the specific mRNA by 80% or more. 24 h after the transduction, the media was replaced with fresh pre-warmed DMEMGlutaMAX™ supplemented with 10% FBS containing 1 µg/ml puromycin. This puromycin dose had been predetermined to kill >90% of non-transduced cells, within the first 24 h. The transduced cells were passaged twice a week, aiming to achieve 6 passages fairly rapidly, in order to fully eliminate infectious virus particles from the system, in accordance with the formal safety requirements. After a total of 6-passages, and not before this stage, the transduced cultures were considered as virus free, and amenable to evaluations and including the explorations of vesicle expulsion. The containment requirements prevented significant handling of the cells up until this point.

Table 2.2: Table of MISSION® lentiviral particles (Sigma-Aldrich) used to transduce PC3 cells.

Target	Clone ID	Oligo Sequence	Clone Name
CD9	TRCN0000291711	CCGGGCTGTTCCGATTAACTTCATCTCGAGATGAAGTTAAATCCGAACAGCTTTTTG	NM_001769.2-150s21c1
	TRCN0000057609	CCGGCCTGCTCTTCGTCCTCAATTTCTCGAGAAATTGAAGACGAAGAGCAGGTTTTTG	NM_004356.2-76s1c1
CD81	TRCN0000381171	GTACCGGCACATGTAGGTGGCGTGTATGCTCGAGCATAACGCCACCTACATGTGTTTTTTG	NM_004356.3-1128s21c1
	TRCN0000382433	GTACCGGACATCCTGACTCCGTCATTTACTCGAGTAAATGACGGAGTCAGGATGTTTTTTTG	NM_004356.3-1429s21c1
	TRCN0000300291	CCGGCCTGCTCTTCGTCCTCAATTTCTCGAGAAATTGAAGACGAAGAGCAGGTTTTTG	NM_004356.3-269s21c1
	TRCN0000300293	CCGGGATCATGATCTTCGAGATGATCTCGAGATCATCTCGAAGATCATGATCTTTTTG	NM_004356.3-875s21c1
	TRCN0000179569	CCGGGATGGCACACTTTCTACCATTCTCGAGAATGGTAGAAAGTGTGCCATCTTTTTTG	NM_152284.2-425s1c1
CHMP4C	TRCN0000147799	CCGGGCGATGAAATCTGTTTCATGAACTCGAGTTCATGAACAGATTTTCATCGCTTTTTTG	NM_152284.2-521s1c1
	TRCN0000146312	CCGGCCAAGAAATCTCAGAAGCATTCTCGAGAATGCTTCTGAGATTTCTTGGTTTTTTG	NM_152284.2-604s1c1
	TRCN0000179242	CCGGGACAAATATCCGCCTTCCAAACTCGAGTTTGGAAAGCGGATATTTGTCTTTTTTG	NM_152284.2-718s1c1
	TRCN0000297971	CCGGCCAAGAAATCTCAGAAGCATTCTCGAGAATGCTTCTGAGATTTCTTGGTTTTTTG	NM_152284.3-600s21c1
	TRCN0000013458	CCGGGCACACAGATTCACCTTAATTCTCGAGAATTAAGTGAATCTGTGTGCTTTTT	NM_004862.1-1266s1c1
LITAF	TRCN0000013459	CCGGGCATGAATCCTCCTTCGTATTCTCGAGAATACGAAGGAGGATTCATGCTTTTT	NM_004862.1-397s1c1
	TRCN0000013460	CCGGGCCACCTTCATGTCTTCTTTCTCGAGAAAGAAGACATGAAGGTGGGCTTTTT	NM_004862.1-831s1c1
	TRCN0000297834	CCGGGCACACAGATTCACCTTAATTCTCGAGAATTAAGTGAATCTGTGTGCTTTTTG	NM_004862.3-1265s21c1
	TRCN0000280440	CCGGGCCACCTTCATGTCTTCTTTCTCGAGAAAGAAGACATGAAGGTGGGCTTTTTG	NM_004862.3-830s21c1
	TRCN0000056483	CCGGGCCCTATTAAGGAGAGAGAAGTCTCTCTCTCTTAAATAGGGCTTTTTG	NM_033026.2-1077s1c1
PCLO	TRCN0000056484	CCGGCCACGAAATTATGTCTAATTCTCGAGAATTAGGACATAATTCGTGGTTTTTG	NM_033026.2-1773s1c1
	TRCN0000056485	CCGGCCTCTGTCTATGGGCTTGATTCTCGAGAATCAAGCCATAGACAGAGTTTTTG	NM_033026.2-2533s1c1

	TRCN0000448162	CCGGACCGAGGGCTATACGACTAAACTCGAGTTTAGTCGTATAGCCCTCGGTTTTTTTTG	NM_033026.5-11387s21c1
	TRCN0000441676	CCGGGGATGCTAATAGAGGATTATACTCGAGTATAATCCTCTATTAGCATCCTTTTTTG	NM_033026.5-6135s21c1
RAB27B	TRCN0000293979	CCGGGACGCCATGGGCTTCTTATTACTCGAGTAATAAGAAGCCCATGGCGTCTTTTTG	NM_004163.3-382s21c1
	TRCN0000293978	CCGGCCAGTCAACAGAGCTTCTTAACTCGAGTTAAGAAGCTCTGTTGACTGGTTTTTG	NM_004163.3-416s21c1
	TRCN0000047691	CCGGGCCAACTGCAAGCAAATGCTTCTCGAGAAGCATTGCTTGCAGTTGGCTTTTTG	NM_004163.3-455s1c1
	TRCN0000286658	CCGGGCCAACTGCAAGCAAATGCTTCTCGAGAAGCATTGCTTGCAGTTGGCTTTTTG	NM_004163.3-455s21c1
	TRCN0000294016	CCGGCATCATCATGGATACTCAATTCTCGAGAATTGAGTATCCATGATGATGTTTTTG	NM_004163.3-995s21c1
RAB35	TRCN0000380335	GTACCGGTGATGATGTGTGCCGAATATTCTCGAGAATATTCGGCACACATCATCATTTTTTG	NM_006861.4-475s21c1
	TRCN0000380080	GTACCGGTTACGAAATCAACCAGAACTCTCGAGAGTTCTGGTTGATTTTCGTGAATTTTTTG	NM_006861.4-453s21c1
	TRCN0000380003	GTACCGGGGAGAATGTCAACGTGGAAGACTCGAGTCTTCCACGTTGACATTCTCCTTTTTTG	NM_006861.4-601s21c1
RAB37	TRCN0000047906	CCGGAGCTTCCAGATCCGAGACTATCTCGAGATAGTCTCGGATCTGGAAGCTTTTTTG	NM_175738.2-1042s1c1
	TRCN0000047905	CCGGCTATGTAGAGTCCCAGAAGAACTCGAGTTCTTCTGGGACTCTACATAGTTTTTG	NM_175738.2-1059s1c1
	TRCN0000047907	CCGGCCGAAGCGTCACCCATGCTTACTCGAGTAAGCATGGGTGACGCTTCGGTTTTTG	NM_175738.2-711s1c1
	TRCN0000047904	CCGGGCAGCGAAAGAGTGATCCGTTCTCGAGAACGGATCACTCTTTCGCTGCTTTTTG	NM_175738.2-878s1c1
	TRCN0000381942	GTACCGGGCTAGGCAACAAGGCGGATATCTCGAGATATCCGCCTTGTTGCCTAGCTTTTTTG	NM_175738.4-869s21c1
RAB6A	TRCN0000047983	CCGGCGTTGGAAAGACATCTTTGATCTCGAGATCAAAGATGTCTTTCCAACGTTTTTG	NM_002869.4-590s1c1
	TRCN0000379592	GTACCGGACACCTATCAGGCAACAATTGCTCGAGCAATTGTTGCCTGATAGGTGTTTTTTTTG	NM_002869.4-640s21c1
	TRCN0000379494	GTACCGGCATCATGCTAGTAGGAAATAACTCGAGTTATTTCCCTACTAGCATGATGTTTTTTTTG	NM_002869.4-881s21c1
	TRCN0000382500	GTACCGGGACAAGAGGCAAGTGTCAATTCTCGAGAATTGACACTTGCTCTTGTCTTTTTTG	NM_002869.4-915s21c1
	TRCN0000379588	GTACCGGGAGCTGAATGTTATGTTTATTCTCGAGAATAAACATAACATTGAGCTCTTTTTTG	NM_002869.4-960s21c1

RAB7A	TRCN0000380577	GTACCGGGGTTATCATCCTGGGAGATTCTCGAGGAATCTCCCAGGATGATAACCTTTTTTG	NM_004637.5-262s21c1
	TRCN0000379950	GTACCGGACCAGTATGTGAATAAGAAATCTCGAGATTTCTTATTCACATACTGGTTTTTTTG	NM_004637.5-309s21c1
	TRCN0000229641	CCGGGGCTAGTCACAATGCAGATATCTCGAGATATCTGCATTGTGACTAGCCTTTTTG	NM_004637.5-396s21c1
	TRCN0000229642	CCGGACTGCTGCGTTCCTGGTATTTGCTCGAGCAAATACCAGAACGCAGCAGTTTTTTTG	NM_004637.5-477s21c1
	TRCN0000381534	GTACCGGACGTAGGCCTTCAACACAATTCTCGAGAATTGTGTTGAAGGCCTACGTTTTTTTG	NM_004637.5-904s21c1
SCAMP3	TRCN0000416861	CCGGACAGCAGTATCCGTGCTCATGCTCGAGCATGAGCACGGATACTGCTGTTTTTTTG	NM_005698.2-1070s21c1
	TRCN0000146864	CCGGCTAGGAATTGTCATGCTGAAACTCGAGTTTCAGCATGACAATTCCTAGTTTTTTTG	NM_005698.2-1127s1c1
	TRCN0000436488	CCGGTGACTTAGCTCCCGTCCCTAACTCGAGTTAGGGACGGGAGCTAAGTCATTTTTTG	NM_005698.2-1338s21c1
	TRCN0000148974	CCGGGACTTGGAGAGACATCACTAACTCGAGTTAGTGATGTCTCTCCAAGTCTTTTTTG	NM_005698.2-1368s1c1
	TRCN0000148522	CCGGCGGAGTGACAGTTCATTCAATCTCGAGATTGAATGAACTGTCACTCCGTTTTTTTG	NM_005698.2-929s1c1
SNAP23	TRCN0000229795	CCGGGAGTCTGGCAAGGCTTATAAGCTCGAGCTTATAAGCCTTGCCAGACTCTTTTTG	NM_003825.2-371s21c1
	TRCN0000218039	GTACCGGGTGGATACATTA AACGCATAACTCGAGTTATGCGTTTAATGTATCCACTTTTTTG	NM_003825.2-501s21c1
	TRCN0000144789	CCGGGCAATGAGATTGATGCTCAA ACTCGAGTTTGAGCATCAATCTCATTGCTTTTTTG	NM_003825.2-612s1c1
	TRCN0000142094	CCGGGCCAGAGCAAAGAAACTCATTCTCGAGAATGAGTTTCTTTGCTCTGGCTTTTTTG	NM_003825.2-698s1c1
	TRCN0000218715	GTACCGGGAAACTCATTGACAGCTAAAGCTCGAGCTTAGCTGTCAATGAGTTTCTTTTTTG	NM_003825.2-709s21c1
STX6	TRCN0000059467	CCGGCACAGCAACAAGGGAAGAAATCTCGAGATTTCTTCCCTTGTTGCTGTGTTTTTG	NM_005819.3-279s1c1
	TRCN0000059464	CCGGGCATAGTTGAAGCAAATCCTACTCGAGTAGGATTTGCTTCAACTATGCTTTTTTG	NM_005819.3-377s1c1
	TRCN0000059466	CCGGGACAATGTGATGAAGAACTTCTCGAGAAGTTTCTTCATCACATTGTCTTTTTTG	NM_005819.3-817s1c1
	TRCN0000291946	CCGGGCATAGTTGAAGCAAATCCTACTCGAGTAGGATTTGCTTCAACTATGCTTTTTTG	NM_005819.4-443s21c1
	TRCN0000379555	GTACCGGATGCAACTGAATTGAGTATAACTCGAGTTATACTCAATTCAGTTGCATTTTTTTG	NM_005819.4-479s21c1

SYNGR2	TRCN0000158365	CCGGCTAAGCAGATGTACTGCGTGTCTCGAGACACGCAGTACATCTGCTTAGTTTTTTG	NM_004710.2-190s1c1
	TRCN0000178877	CCGGCTTCCTGTGGTTTTGTTGGTTTTCTCGAGAAACCAACAAACCACAGGAAGTTTTTTG	NM_004710.2-377s1c1
	TRCN0000420094	CCGGCCCATGTGCTACTGACAAGTGCTCGAGCACTTGTCAGTAGCACATGGGTTTTTTG	NM_004710.3-1008s21c1
	TRCN0000427952	CCGGGCCGCTATTATCTGCGTTCTCCTCGAGGAGAACGCAGATAAATAGCGGCTTTTTTG	NM_004710.3-1065s21c1
	TRCN0000414151	CCGGCATCTGTGGACAACTACCAACCTCGAGGTTGGTAGTTGTCCACAGATGTTTTTTG	NM_004710.3-620s21c1
VAMP3	TRCN0000380472	GTACCGGACCAGAAGCTCTCTGAGTTAGCTCGAGCTAACTCAGAGAGCTTCTGGTTTTTTTG	NM_004781.3-234s21c1
	TRCN0000029817	CCGGCAGGCGCTTCTCAATTTGAAACTCGAGTTTCAAATTGAGAAGCGCCTGTTTTT	NM_004781.3-279s1c1
	TRCN0000330914	CCGGGCAGCCAAGTTGAAGAGGAAACTCGAGTTTCCTCTTCAACTTGGCTGCTTTTTG	NM_004781.3-305s21c1
	TRCN0000330915	CCGGGACTTAGAACCTGCTATATTACTCGAGTAATATAGCAGGTTCTAAGTCTTTTTG	NM_004781.3-470s21c1
	TRCN0000380088	GTACCGGTAAGTTCCAGAGTGCTATAATCTCGAGATTATAGCACTCTGGAACCTATTTTTTG	NM_004781.3-663s21c1
VPS28	TRCN0000293241	CCGGGAGGGAGAAGTACGACAACATCTCGAGATGTTGTCGTACTTCTCCCTCTTTTTG	NM_016208.2-186s21c1
	TRCN0000298464	CCGGGCGGTGGTGAAGACAATGCAACTCGAGTTGCATTGTCTTCACCACCGCTTTTTG	NM_016208.2-220s21c1
	TRCN0000298465	CCGGGTCAGCCTACAACGCCTTCAACTCGAGTTGAAGGCGTTGTAGGCTGACTTTTTG	NM_016208.2-717s21c1
	TRCN0000004149	CCGGGAGGGAGAAGTACGACAACATCTCGAGATGTTGTCGTACTTCTCCCTCTTTTT	NM_016208.x-186s1c1
	TRCN0000004151	CCGGGTCAGCCTACAACGCCTTCAACTCGAGTTGAAGGCGTTGTAGGCTGACTTTTT	NM_016208.x-717s1c1

2.3 Cell characterisation

2.3.1 Bicinchoninic acid (BCA) protein assay

The MicroBCA Protein Assay kit (Thermo Fisher Scientific) was used to determine protein concentrations of cell lysates and EVs. For this purpose, a 12-point serial dilution of a certified standard bovine serum albumin solution (BSA) ranging from 0 µg/ml BSA to 2,000 µg/ml was performed to generate a standard curve. To determine EV protein concentrations, 10 µl of EVs was added to 70 µl DPBS and mixed with the provided Working Reagent (25 parts Micro BCA Reagent MA, 24 parts Micro BCA reagent MB and 1 part Micro BCA reagent MC). The mixture was incubated at 37°C for 35 min. Then, the absorbance was read at 562 nm using a BMG Pherastar plate reader. For the assessment of cellular protein concentrations, the manufacturers protocol (number 23235) was followed. Briefly, 150 µl of sample or BSA standard was added to 150 µl Working Reagent (25 parts Micro BCA Reagent MA, 24 parts Micro BCA reagent MB and 1 part Micro BCA reagent MC) and incubated at 37°C for 2 h. The absorbance was read at 562 nm using a BMG Pherastar plate reader.

2.3.2 Western blotting

Cells were grown in 6-well plates until confluent and subsequently washed with DPBS. The cells were then lysed with RIPA lysis buffer (Santa Cruz, Texas, USA) containing 1X protease inhibitor cocktail, 200 mM phenylmethane sulfonyl fluoride (PMSF), 100 mM sodium orthovanadate and 1X lysis buffer on ice for 5 min. The lysate was centrifuged at 10,000 x g for 10 min at 4°C and the supernatant transferred to new tube and stored at -80°C until further use. Protein concentrations were determined using a Micro BCA™ protein assay kit (Thermo scientific). For reducing conditions, 20 µg of cell lysate was mixed with fresh 20 mM dithiothreitol (DTT; Santa Cruz) in lithium dodecyl sulphate (LDS) sample buffer (Invitrogen, USA), and boiled at 70°C for 10 min. For samples analysed under non-reducing conditions the addition of DTT was omitted. Then the samples and a molecular weight marker (SeeBlue® Plus 2 Precision Stain; Life Technologies, USA) were loaded on NuPAGE™ precast 4-12% Bis-Tris gradient gels (Life Technologies) mounted in 1x NuPAGE™ MOPS sodium dodecyl sulphate (SDS) running buffer (Life Technologies). The proteins were separated by electrophoresis using an Invitrogen™ PowerEase® 500 (ThermoFisher Scientific) power supply and running the gel at 90 V for 12 min, followed by 120 V for 90

min. Proteins were blotted onto methanol activated polyvinylidene fluoride (PVDF) membranes (GE Life Sciences, UK) at 80 V for 90 min. The protein transfer was done in a BioRad Mini Trans-Blot Electrophoretic Transfer Cell (BioRad) filled with 25 mM Tris, 192 mM glycine (both Sigma-Aldrich, St Louis, USA) transfer buffer. The membranes were blocked overnight in 5% (w/v) non-fat powdered milk (Marvel, London, UK) in DPBS containing 0.5% Tween®20 (Sigma-Aldrich). The membranes were incubated with primary antibodies (table 2.3) for 2 h at room temperature (RT) or overnight at 4°C. After the incubation, the membranes were washed 3 times for 5 min in 0.5% Tween®20 in DPBS before a 1 h incubation with the secondary goat anti-mouse-horseradish peroxidase (HRP) conjugate or goat anti rabbit conjugate (Santa Cruz) at RT. The membranes were subject to another 3 times 5 min washes with 0.5% Tween®20 in DPBS. Enhanced chemiluminescent substrate (Li-Cor) was added to the membranes prior to the detection of the bands with a C-Digit blot scanner (Li-Cor, Lincoln, USA).

Table 2.3: Antibodies tested for Western Blotting.

Target (Host/Isotype)	Stock concentration	Dilutions tested	Catalogue# (company)
CHMP4C (rabbit/IgG)	1 mg/ml	1:250 1:500 1:1000	#TA890004 (ThermoFisher Scientific)
SYNGR2 (rabbit/IgG)	1 mg/ml	1:250 1:500 1:1000	# PA5-20877 (Thermo Scientific)
SYNGR2 (mouse/IgG₃)	100 µg/ml	1:200	# sc517053 (Santa Cruz)

2.3.3 RNA isolation and reverse transcription

Cellular and EV RNA was isolated using a phenol-based extraction method to assess transcriptomic changes upon candidate attenuation, using TaqMan gene expression assays (2.3.4) and RNA-sequencing (2.6). For the extraction of cellular RNA, cells were grown in 6-well plates (Greiner) until the monolayer reached confluency. Then, the cells were washed with DPBS (Life Technologies Limited), lysed by the addition of TRI Reagent® (Sigma-Aldrich) and transferred into 1.5 ml Eppendorf tubes. Samples were stored at -80°C. For the extraction of vesicular RNA, EVs were isolated from cells grown in 9 flasks per replicate

(described in detail in 2.4.1-2.4.2). The isolated EVs were lysed by adding 1 ml of TRI Reagent® (Sigma-Aldrich) for 5 min at RT. The EV lysates were then stored at -80°C.

The cellular lysates and corresponding vesicular lysates were subsequently processed the same way by adding 200 µl of Chloroform (Sigma Aldrich). The solution was vigorously shaken for 15 s. Then, the aqueous and the phenol phase were separated by incubating the samples on ice for 5 min prior to centrifugation at 16,000 x g for 20 min at 4°C.

Subsequently, the aqueous phase was transferred to a new Eppendorf tube containing ice cold isopropanol. RNA was precipitated overnight at -20°C. On the next day, the RNA was pelleted by centrifugation at 16,000 x g for 20 min, at 4°C and the isopropanol discarded. The RNA pellet was washed in 70% ethanol and centrifuge at 16,000 x g for 20 min, at 4°C. This step was repeated once and the RNA pellet air dried. 12 µl DNase- and RNase-free H₂O was used to resuspend the RNA pellet.

RNA concentrations were determined by measuring the absorbance of the sample at 260 nm and 280 nm with a NanoDrop™ 2000 Spectrometer (ThermoFisher Scientific). Nucleic acid and protein peak absorbance occurs at 260 nm and 280 nm respectively. A 260: 280 ratio ~2 is considered pure RNA and was used as threshold for the work presented in this thesis. A lower ratio is indicative of contamination with e.g., proteins and phenol or could be due to a low sample concentration.

2.3.3.1 Reverse transcription

1 µg RNA was reverse transcribed utilising the random primer method in a final volume of 20 µl per reaction (table 2.4). As a negative control, RNA was replaced with molecular biology grade H₂O. Samples were loaded onto the S1000 Thermal Cycler (BioRad) and complementary DNA (cDNA) generated, which included an initial primer annealing step at 25°C for 10 min, followed by deoxynucleoside triphosphate (dNTP) and reverse transcriptase dependent primer extension at 37°C for 2 h. The enzyme was deactivated by heating the samples to 85°C for 5 min. The samples were stored at -80°C.

Table 2.4: Reverse transcription reaction mix Kit with RNase inhibitor (applied biosystems by Thermo Fisher Scientific).

Reagent	Volume (µl)
10X Reverse transcriptase buffer	2
25X dNTP Mix (100 mM)	0.8
10X Reverse transcriptase random primers	2
Multiscribe™ Reverse transcriptase	1
RNase inhibitor	1
Nuclease-free H ₂ O	3.2
Diluted RNA (1 µg) or nuclease-free H ₂ O	10

2.3.4 Quantitative polymerase chain reaction (qPCR)

In order to assess the level of mRNA, TaqMan gene expression assays were used. The method is described in detail in a previous laboratory publication (Yeung et al., 2018). For the PCR amplifications, 20 µl reactions were prepared containing 10 µl of TaqMan® Universal Master Mix (20X), 8 µl of H₂O, 1 µl of a TaqMan® gene expression assay containing the forward and reverse primer and a TaqMan reporter probe, (all from ThermoFisher Scientific) (table 2.5) and either 1 µl of sample cDNA or H₂O as a negative control. The samples were loaded on a StepOnePlus™ Real-Time PCR System Thermocycler (ThermoFisher Scientific). The cDNA was amplified in step wise process by heating the samples to 50°C for 2 min, then 95°C for 15 s, followed by 60°C for 1 min. The cycles were repeated 40 times.

The cycle threshold (CT) value marks the amplification cycle where the target gene amplification is in the linear range and crosses a set threshold. The comparative CT method was utilised to determine changes in the relative gene expression of a target of interest across samples. Glyceraldehyde 3-phosphate dehydrogenase (GAPDH) was used as a reference gene, as this has been demonstrated to be stable in these cells by previous members of the group, and the relative gene expression calculated as follows:

$$\Delta\Delta Ct = (Ct_{\text{target Gene}} - Ct_{\text{GAPDH}})_{\text{treatment cell line}} - (Ct_{\text{target Gene}} - Ct_{\text{GAPDH}})_{\text{control cell line}}$$

$$\text{Relative expression} = 2^{-\Delta\Delta Ct}$$

Table 2.5: TaqMan assays used for this work.

TaqMan assay for	Assay ID	Catalogue number
CD9	Hs00233521_m1	4331182
CD81	Hs00174717_m1	4453320
CHMP4C	Hs00298926_m1	4448892
GAPDH	Hs99999905_m1	4351370
LITAF	Hs01556090_m1	4448892
PCLO	Hs00382694_m1	4448892
Rab6a	Hs00818388_m1	4448892
Rab7a	Hs01115139_m1	4453320
Rab11b	Hs00188448_m1	4331182
Rab27b	Hs00188156_m1	4448892
Rab35	Hs00199284_m1	4331182
Rab37	Hs01005170_m1	4448892
STX6	Hs00274072_m1	4448892
SYNGR2	Hs00855143_g1	4448892
SNAP23	Hs01047496_m1	4448892
VPS28	Hs01598026_m1	4448892
VAMP3	Hs00922164_m1	4448892
SCAMP3	Hs00903114_m1	4448892
IL-6	Hs00174131_m1	4453320
HGF	Hs00300159_m1	4453320
ACTA2	Hs00426835_g1	4453320

2.3.5 Detecting surface antigens by flow cytometry

The generated PC3 cell variants were grown as described (2.2.1). Once, 80% confluent, cells were harvested using trypsin (Lonza) and transferred to 96-well v-bottom plates (Greiner) at 100,000 cells/well. Cells were washed with 150 µl DPBS and centrifuged at 600 x g for 5 min. The experiments were set-up to include the conditions summarised in table 2.6.

Table 2.6: Overview of samples included in flowcytometry experiments.

Cell type/ treatment	Purpose
Mix of PC3NMC cells and PC3 KD cells (permeabilised)	Mixed with not permeabilised cells used for gating (positive signal for the viability dye, representing dead cells, see table 2.7 for details about the dye).
Mix of all PC3 NMC cells and PC3 KD cells (not permeabilised)	Mixed with permeabilised cells used for gating (negative signal for the viability dye, representing viable cells).
Mix of all PC3 NMC cells and PC3 KD cells (isotype controls)	Assess non-specific binding
PC3 KD cells (antibody treatment)	Assess KD efficiency at protein levels
PC3 NMC cells (antibody treatment)	Used to compare constitutive expression levels of the target

As a control, one treatment condition included cells that were permeabilised with 50 μ l 1x permeabilization buffer for 10 min. All cells were labelled, by incubating the samples with 20 μ l antibody mix or isotype control (table 2.7) for 30 min at 4°C in the dark. Subsequently, cells were washed with DPBS and fixed with 100 μ L 25% fixation buffer (1 part IC Fix buffer: 3 parts DPBS).

For multicolour compensation on the flow cytometer oneComp beads (Thermo Fischer Scientific) were used. For this purpose, one drop of OneComp beads was added to one 1 μ l antibody and mixed by vortexing. Subsequently the mix was incubated for 15 min at RT in the dark. Beads were washed with 1 ml DPBS prior to centrifugation at 600 g for 5 min. The supernatant was discarded, and the beads resuspended in 250 μ l DPBS.

All samples were analysed with the of BD FACSVerser cytometer (BD Biosciences) using the FACSuite v1.2.1 software (BD Biosciences).

Table 2.7: Antibodies used for flow cytometry

Antigen/dye (Flouochrome)	Stock concentration	Final concentration/Dilution	Catalogue # (company)
Anti-CD81 (Alexa647)	200 μ g/ml	20 μ g/ml	#FAB1880R-100UG (R&D)
Anti- CD9 (PE)	12 ug/ml	1.2 ug/ml	#12-0098-42 (eBioscience)
Isotype mIgG ₁ (PE)	-not specified,	5 μ l/10 ⁶ cells	#12-4714-42 (eBioscience)
Isotype mIgG _{2b} (Alexa647)	-not specified,	5 μ l/10 ⁶ cells	# IC0041R (R&D)
Viability dye (AlexaFlour780)	1,000 x	1: 1,000	Thermo Fisher Scientific # 65-0865-14

The gating strategy is visualised in Figure 2.1. First, the forward scatter height (FSC-H) and forward scatter area (FSC-A) channels were utilised to gate singlet cells which cluster around a diagonal axis. Doublets cells which appear as larger cells off the diagonal axis were excluded. Next, the side scatter area (SSC-A) and FSC-A channels were used to eliminate cell debris based on their granularity from further analysis. As a final step FSC-A combined with

the viability dye channel was utilised to exclude dead cells (positive staining). The viability dye binds to intracellular amines that are only accessible for the dye following permeabilization of the cell membrane. Data were analysed using FlowJo_v10.8.1_CLFlowJo_v10.8.1. Marker expression was analysed focusing on percentage/proportion of cells expressing the marker compared to the NMC cells.

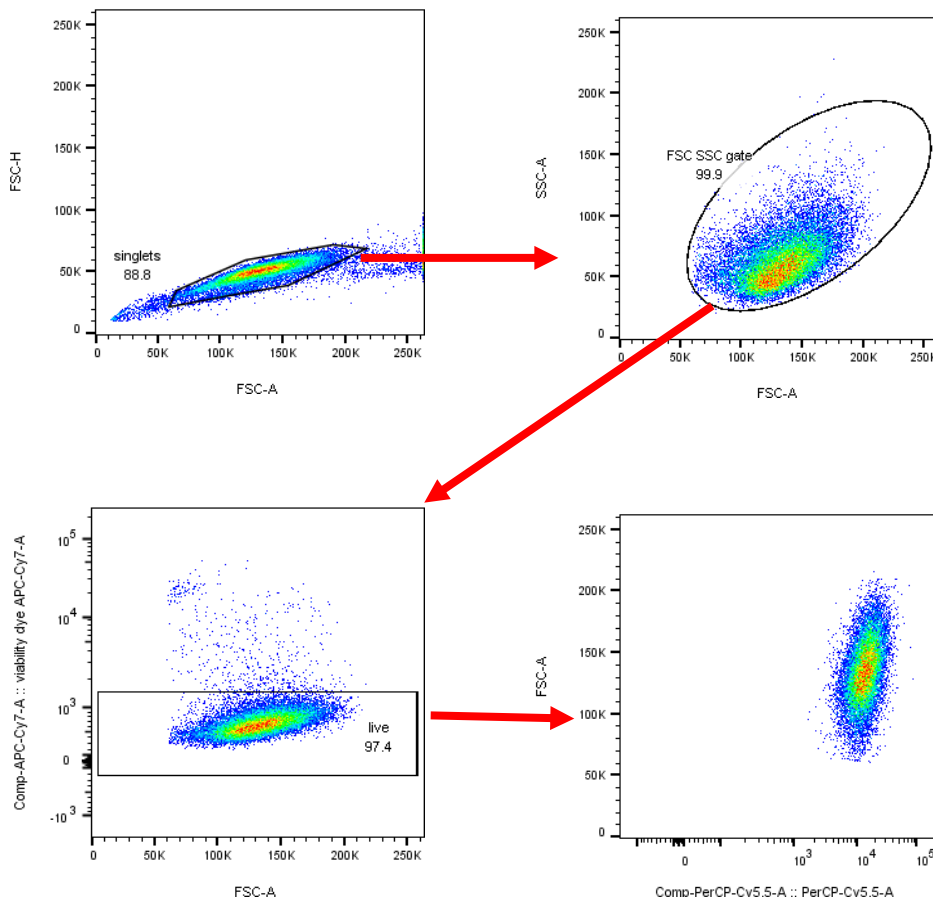


Figure 2.1: Gating strategy used for the analysis of surface proteins by flow cytometry. Representative stepwise gating strategy and associated dot plots for the flow cytometry analysis. First, single cells were gated based on size (FSC-H and FSC-A). Doublets localised outside the diagonal axis were excluded at this step. Then cell debris were excluded from further analysis using the SSC-A and FSC-A channels. As final step FSC-A combined with the viability dye channel was utilised to exclude dead cells (positive staining).

2.3.6 Assessment of cell proliferation

Cell proliferation was determined using water-soluble tetrazolium WST-8 (OrangU™ CellGS). In the presence of mitochondrial NAD(P)H, WST is cleaved to formazan, a dye. Hence, the concentration of formazan correlates with the number of active mitochondria and provides a surrogate measure of live, proliferating cells when performed longitudinally. To assess cell proliferation upon puromycin treatment, PC3 cells were counted in a Neubaur chamber and plated at 2,000, 5 000 or 10,000 cells/ well in a 96-well plate (Greiner) in DMEM GlutaMAX™ supplemented with 10% FBS. The cells were treated with puromycin (up to 10 µg/ml). Cell proliferation was assessed every 24 h up to 96 h by adding 10 µl WST-8 /well for 1 h or 1.5 h at 37°C. The absorbance was measured at 450 nm and 650 nm using a PHERAstar FS Microplate Reader.

2.4 EV characterisation

2.4.1 Conditioned media collection and EV isolation

2.4.1.1 Media preparation

For experiments requiring a media with a low particle concentration, media was prepared as following. First, EVs and other particulate matter were removed from the FBS by a centrifugation at 100,000 x g for 18 h. Then, the FBS was filtered using consecutively, a 0.22 µm filter and a 0.1 µm filter (Milipore), to both ensure sterility and eliminate possible aggregates formed due to centrifugation. DMEM GlutaMAX™ was supplemented with 5% EV depleted FBS. Afterwards the DMEM GlutaMAX™ supplemented with EV-free FBS was filtered again with a 0.1 µm filter.

2.4.1.2 Conditioned media collection

FBS is composed of a poorly defined mixture of cell growth promoting components, which also include EVs, lipoproteins and protein complexes that are difficult to distinguish in size and density from the cultured cell derived EVs. To minimise FBS derived contaminations, the PC3 cells were starved as outlined below. PC3 cell variants were seeded at 8.75×10^6 cells per T25 flask (Greiner Bio-One) in filtered, EV-free media (2.4.1.1) until the cell monolayer

reached 80% confluency. Then, the cells were washed with DPBS and fresh 0.1 μm filtered DMEM GlutaMAX™ without FBS was added to the cells for 48 h or 72 h prior to CM collection. Reaching a sufficient EV yield to perform extensive characterisations and functional experiments is a challenge of the EV field. Here, to increase the EV yield, a 72 h conditioning time point was included. The extended time point could possibly impact the cells and lead to e.g., a reduced cell viability and the induction of autophagy. Therefore, the cells were microscopically inspected at each collection timepoint, which showed a lack of any gross differences for both time points. To assess possible changes in the EV type, a comparison of the EV size distribution by Nanoparticle tracking analysis (NTA) and the expression of tetraspanins by EVQuant was performed on isolated EVs from the 48 h and 72 h conditioning time points and showed a high overlap in these vesicular features for both time points (data not shown). A cell count was performed at the collection points to allow assays of vesicles to be normalised for potential differences in cell number across flasks/conditions at the media harvest point. To pellet any floating cells and cell debris, the CM was subject to differential centrifugation including the following steps: 400 x g for 6 min at 4°C, another centrifugation at 400 x g for 6 min at 4°C followed by 2,000 x g at 4°C for 20 min. The pre-cleared CM was filtered through a 0.22 μm pore filter to remove larger particles. The purified CM was stored at -80°C. Where indicated the CM was corrected for cell numbers and termed Cell number corrected conditioned media (cCM) (table 2.8).

Table 2.8: Calculations for the normalisation of CM.

		NMC	KD 1
Collected CM	Collected CM	5 ml	5 ml
	Cell number	50,000	100,000
	Correction factor	1	2
CM normalised to 50,000 cells (cCM)	Final volume	10 ml	10 ml
	CM sample	10 ml (10 ml / 1)	5 ml (10 ml / 2)
	Filtered media	0 ml (10 ml - 10 ml)	5 ml (10 ml - 5 ml)

2.4.2 Ultracentrifugation

To isolate EVs from the pre-cleared CM, the CM was subject to ultracentrifugation at 100,000 x g (R_{max}) in a fixed angle 70Ti rotor (Beckman Coulter) for 2 h at 4°C. The supernatant was

removed and the visible pellet of EVs was then resuspended in DPBS and aliquoted before storage at -80°C.

For the functional experiments, the CM, EV depleted media and isolated EVs were investigated. To achieve this, CM was pre-cleared as described above and normalised to cell number (table 2.8). One aliquot of the sample was kept representing the whole secretome of the PC3 cells. Another aliquot of the pre-cleared media was subject to ultracentrifugation at 110, 000 x g (TLA-110 fixed angle rotor, Beckman Coulter) for 2 h at 4°C. The supernatant was transferred into a new tube and used to investigate EV depleted media, the pelleted EVs were used to investigate isolated EVs.

2.4.3 Nanoparticle tracking analysis

To determine the size distribution and concentrations of particles in CM, nano particle tracking analysis (NTA) was used. The measurements were done using a NanoSight™ NS300 additionally equipped with a temperature controlled 488 nm laser module and a high-sensitivity sCMOS Camera System (OrcaFlash 2.8, Hamamatsu C11440, Hamamatsu City, Japan) and a syringe-pump system (Malvern Instruments). 100 nm standard latex beads (Malvern Instruments) were used to assess the accuracy of the NTA measurements and run on each occasion. Samples were injected with a constant syringe pump speed set to 50 and the temperature set to 25°C. Triplicate videos of 30 to 60 s were taken and analysed using NTA3.1 software (version 3.1 build 3.1.54).

2.4.4 Immunophenotyping of EVs

There is a consensus in the EV research community, that the assessment of tetraspanins is deemed a useful possible approach to characterise EVs in a given sample (Welsh et al., 2024). To evaluate EVs in cCM in the scope of this thesis, a microplate-based immunophenotyping assay was performed. This assay was developed in-house, and is similar to commercial ELISA kits, which involve coating microtiter plates with antibody, capturing EV to the plate through this affinity interaction, and thereafter detecting EV-related surface proteins by biotin-conjugated detection antibody. The in-house nature of the assay allows us to modify the capture and detection antibodies readily, to explore possible effects of KDs on tetraspanin expression of EVs.

Antibodies against CD9, CD81, CD63 or an isotype control (table 2.9) at 1 µg/ml in 0.1% BSA was added to the wells of a high binding 96-well strip plate (cat # 756071 Greiner Bio one) and incubated at 4°C. After washing the wells with 1x Delfia wash buffer (Perkin Elmer), remainder protein binding sites were blocked with 1% (wt/vol) BSA in PBS for 2 h at RT. Following 3 wash steps with 1x Delfia wash buffer (Perkin Elmer), cCM was added to the precoated wells in triplicates and incubated at RT for 2 h. This was followed by 3 washing steps with 1X Delfia wash buffer (Perkin Elmer). For the detection of vesicle-specific surface molecules, biotinylated CD9 or CD81 antibodies (monoclonal antibodies from CellGS) to a working concentration of 1µg/ml in 0.1% (wt/vol) BSA in PBS was added overnight at 4°C. After 3 wash steps with Delfia wash buffer (Perkin Elmer), streptavidin:europium conjugate diluted 1:1,000 in red assay buffer (Kaivogen) was added for 45 min at RT. The red assay buffer is validated to be free of interfering substances, allowing the optimal measurement of fluorescence by europium. Next, the plates were washed 6x with Delfia wash buffer (Perkin Elmer) and enhancement solution was added for 5 min at RT. Time resolved fluorescence (TRF) of europium was measured on a BMG Pherastar plate reader.

Table 2.9: Antibodies used for the microplate based immunophenotyping of EVs.

Antigen (Host)	Isotype	Stock concentration (mg/ml)	Dilution (final concentration) (1 µg/ml)	Catalogue # (company)
Anti-CD9 (mouse)	IgG _{2b}	0.5	1:500	#MAB1880 (R&D)
Anti-CD63 (mouse)	IgG ₁	1	1:1,000	#MCA2141 (Bio-Rad)
Anti-CD81 (mouse)	IgG ₁	1	1:1,000	#MCA1847EL (Bio-Rad)
IgG ₁ (mouse)	-	0.5	1: 500	# 14471482 (ThermoFischer Scientific)
IgG _{2b} (mouse)	-	0.5	1:500	#14473285 (ThermoFisher Scientific)

2.4.5 EVQuant

The EVQuant (Hartjes et al., 2020) is not yet a generally accepted method in the EV-field, but it is an assay platform that has been developed as a commercial tool, by colleagues' from

Erasmus MC, Rotterdam, Netherlands and has been utilised in various studies (Blijdorp et al., 2022, Blijdorp et al., 2021, Erozenski et al., 2021). It is a confocal imaging-based method, involving the labelling of vesicles with fluorescent dyes and antibodies, followed by their immobilisation in an optically compatible gel. The data shown herein, were collected at Erasmus MC, under the supervision of Dr Martin van Royen, inventor of the technique.

The proportion of CD9 and CD63 positive EV subpopulations in CM were assessed using EVQuant as described in (Hartjes et al., 2020). Briefly, fluorescently labelled mouse CD9 Monoclonal–Alexa Fluor® 647 antibody (cat# MA5-18154 ThermoFisher) and/or mouse CD63-Alexa Fluor®488 cat# sc-5275 AF488 Santa Cruz) was added to the wells of a deep well plate, followed by the addition of the 40 µl of cCM samples. The plates were sealed, briefly vortexed and incubated for 2 h at RT protected from the light. 100 µl of Octadecyl Rhodamine B Chloride R18 (cat# O246, Life Technologies, final staining concentration of 0.33 ng/µl) was added to each sample and incubated for 10 min at RT. The EVs were immobilised by adding first 90 µl of an Ammonium persulfate (APS) Bis-Acrylamide mix and then 90 µl of a TMED Bis-Acrylamide mix (table 2.10).

Table 2.10: TMED and APS mix for immobilising EVs.

Mixture	Component	cat# (company)	Per sample (µl)
TMED mix	Acrylamide/Bis Solution (37,5:1 30% w/v)	10688.01 (SERVA)	89.5
	Ultra pure TMED (100%)	15524-010 (Life Technologies)	0.5
APS mix	Acrylamide/Bis solution (37,5:1 30% w/v)	10688.01 (SERVA)	85
	APS (10% in water)	7727-54-0 (Life Technologies)	5

250 µl of each sample mixture was transferred to 96-well imaging plates (cellvis). The plate was imaged with an opera Phenix system with the following settings: 25 fields were scanned, the exposure time set to 500 ms at 40 µm above the bottom of the plate. The Harmony software was used to determine Rhodamine positive spots which were considered to be EVs

and fluorescent spots. The data was exported, and a R-script was run, which analysed the fluorescent intensity data of each detected spot across all channels simultaneously, ultimately determining the concentrations and the composition of the EV population (CD9+CD63-, CD9-CD63+, CD9+CD63+ & CD9-CD63-). The script is available on request by the inventors of the assay.

2.5 Functional analysis of EVs

2.5.1 Fibroblast to myfibroblast differentiation assay

Fibroblasts were seeded in 6-well, 24-well plates, 96-well plates (all Greiner Bio-One) or Nunc™ Lab-Tek™ 8-Well Chamber Glass Slides (ThermoFisher) and grown until they reached 80% confluency. Fibroblasts in culture release a range of growth factors which could potentially induce the expression of α -SMA mediated by autocrine signalling. There is also TGF- β 1 within bovine FBS which may also contribute to a non-resting endogenous level of α -SMA expression. To prevent this, fibroblasts were growth arrested by washing the cells with prewarmed serum-free DMEM/F12 (Lonza) to remove residual FBS and then grown in serum-free DMEM/F12 (Lonza) for 72 h as previously described by our lab (Webber et al., 2015). Next, fibroblasts were incubated for 72 h with either TGF- β 1 (0.75 or 1.5 ng/ml), only media (negative control), cCM from the NMC and KD cell variants or isolated EVs from the NMC and KD cells. A 72 h stimulation was selected because this time point was shown in a previous study to exhibit peak α -SMA polymerisation upon stimulation (Webber et al., 2010). Subsequently, the CM was collected and analysed with ELISAs (section 2.5.4). The fibroblasts seeded in the 8-well chambers were prepared for microscopy as described below (section 2.5.3). The fibroblasts seeded in 96-well plates were assessed for α -SMA protein expression (section 2.5.2).

2.5.2 Assessment of EV induced α -SMA expression in fibroblasts

After 72h of treatment (2.5.1), the fibroblasts seeded in 96-wells were fixed with 4% Paraformaldehyde (diluted in DPBS) for 10 min. Subsequently the paraformaldehyde solution was removed, and the cells gently washed twice with DPBS, before adding DPBS. The plates

were stored at 4°C until further use. After removing the DPBS, cells were permeabilised with 0.1% Triton X-100 (diluted in DPBS) for 10 min at RT. Subsequently, the cells were gently washed twice with DPBS. The cells were then incubated with either the primary antibody targeting α -SMA (Santa Cruz) diluted in 1% BSA in DPBS to 1 μ g/ml or the IgG_{2a} isotype control (eBioscience) at 4°C overnight. Following 3 wash step with 1x Delfia wash buffer (Perkin Elmer), the cells were incubated with the secondary antibody anti mouse IgG_{2a} goat biotin in 1% BSA diluted in DPBS to 1 μ g/ml for 1h at RT. Next, the cells were washed three times with 1x Delfia wash buffer (Perkin Elmer) and subsequently a streptavidin: europium conjugate (Perkin Elmer) diluted 1:1,000 in red assay buffer (Kaivogen) was added for 45 min at RT. Next, the plates were gently washed 6x with Delfia wash buffer (Perkin Elmer) and enhancement solution (Kaivogen) was added for 5 min at RT. TRF of europium was then measured on a BMG Pherastar plate reader.

2.5.3 Microscopy

After 72 h of treatment (2.5.1), the fibroblasts were washed with DPBS and fixed with cold acetone/methanol (1:1) for 5 min. Subsequent to decanting of the solvent, the cell-layer was allowed to air dry in a Class II cabinet, to fully remove any remaining traces. Slides were stored dry at 4°C. To prepare the samples for imaging, the cells were rehydrated with DPBS for 10 min, washed with DPBS and blocked with 5% goat serum in DPBS at 4°C overnight. Then, cells were washed with 0.1 % BSA in DPBS and incubated with either 1 μ g/ml primary antibody targeting α -SMA (Santa Cruz) diluted in 0.1 % BSA/DPBS (1 μ g/ml) or 1 μ g/ml IgG_{2a} isotype control (eBioscience) overnight at 4°C. The next day, an Alexa488 conjugated goat anti mouse secondary antibody (Thermo Fisher Scientific) at 10 μ g/ml in 0.1% BSA/DPBS was added for 1 h protected from the light, at RT. Nuclei were stained with 4',6-diamidino-2-phenylindole (DAPI) (Thermo Fisher Scientific) from 1 mg/ml stock solution, diluted 1:1,000 times in DPBS for 1 min in the dark at RT. Images were taken on the Axio Observer Z1 (Zeiss) configured with structural illumination capability using an apotome 2.0 module and using the Zen Pro Software. A Plan Apochromat 63x/ 1.4 Oil lens was used in combination with Alexa488/594 and DAPI filters. The exposure time and intensity was kept constant across all samples. Images were exported in TIF format and figures compiled in PowerPoint.

2.5.4 Assessment of EV-mediated signalling and cytokine production in recipient fibroblasts

2.5.4.1 Enzyme-Linked Immunosorbent Assay (ELISA)

HGF and IL-6 present in the CM from PC3 cells or treated fibroblasts was quantified using the DuoSet ELISA systems (R&D Systems) according to the manufacturer's protocol except for the last step where HRP-streptavidin was replaced with europium streptavidin for a TRF readout. The wells of a high protein binding ELISA strip 96-well plate (GreinerBio-One) were covered with 100 μ l of IL-6 or HGF capture antibody at a dose of 1 μ g/ml and incubated overnight at RT. On the next day, the antibody solution was discarded, and the wells washed three times with Delfia® Wash Buffer (1X in water) (Perkin Elmer) prior to adding blocking buffer (1% BSA in DPBS) for 2 h at RT. Subsequently, wells were washed three times with Delfia® Wash Buffer. An 8-point serial dilution of HGF standard (starting at 8,000 pg/ml) and IL-6 standard (starting at 600 pg/ml) was performed and added to the wells in duplicate. cCM from the PC3 cell variants or CM from the treated fibroblasts was added to the wells for 2 h at RT. Next, the solutions were aspirated, and wells washed with Delfia® Wash Buffer. Then, the wells were incubated with a biotinylated goat anti mouse detection antibody raised against the respective target at the following concentrations: 50 ng/ml (IL-6), or 200 ng/ml (HGF). After 2 h at RT, wells were washed 3 times with Delfia® Wash Buffer prior to the addition of europium-streptavidin conjugate (Perkin Elmer) diluted in a red buffer solution (Kaivogen) for 45 min at RT. Following, the wells were washed 6 times with Delfia® Wash Buffer and incubated with enhancement solution (Kaivogen) for 5 min at RT. The absorbance was measured by TRF on a PHERAstar FS Microplate Reader. The TRF values of the standard curve (IL-6, HGF) were used to extrapolate the protein concentrations in the samples.

TGF- β 1 ELISA

TGF- β 1 was also quantified using the DuoSet ELISA systems (R&D Systems) according to the manufacturer's protocol, which followed the same steps as outlined above. However, to detect TGF- β 1 by the DuoSet ELISA kit requires the activation of the latent TGF- β 1. For this purpose, prior to adding the samples to the microtiter plates, the samples were acid activated by mixing the samples with 20 μ l of 1N hydrochloric acid (HCL) and incubating them for 10 min at RT. Subsequently, the solutions were neutralised by the addition of 20 μ l of 1.2N sodium hydroxide (NaOH)/0.5 M HEPES and 100 μ l added to the wells. The 8-point serial

dilution of the TGF- β 1 standard (starting at 2,000 pg/ml) was performed and added to the wells in duplicate. The absorbance was measured by TRF on a PHERAstar FS Microplate Reader. The absorbance values of the standard curve were used to extrapolate the TGF- β 1 protein concentrations in the samples.

2.5.5 Proteome Profiler Human Phospho-Kinase Array Kit (R&D Systems)

The Proteome profiler Phospho-kinase array kit is an antibody-based technique that allows the simultaneous detection of the phosphorylation of 37 analytes. Briefly, cellular lysates or CM are added to the provided membranes, which contain duplicate antibody spots for each analyte. Subsequently, a biotinylated detection antibody is added. This is followed by the addition of a horseradish peroxidase-conjugated detection antibody, which allows the chemiluminescent detection of the targets.

In the scope of this thesis, fibroblasts were grown in 24-well cell culture plates (BioGreiner) and once they reached 80% confluency serum starved for 72 h. Following this, the fibroblasts were treated with 200 μ g/ml EVs or DMEM/F12 for 2 h and then lysed with RIPA lysis buffer. Protein concentrations were quantified using a BCA as described in 2.3.1. The proteome profiler protocol was run according to the manufacturer's instructions except of the use of Chemi Reagent which was replaced with WesternSure PREMIUM Chemiluminescent Substrate (Li-Cor), which provides brighter/longer light emission and is hence a better choice when using the C-Digit instrument. Phosphorylated proteins were then detected using the C-Digit blot scanner (Li-Cor). Densitometry of the dots on the membranes was performed using ImageJ.

2.6 RNA Sequencing (RNA-Seq)

RNA samples derived from EVs, and corresponding parent cells were prepared to explore transcriptomic differences induced by the candidate KD. To be more precise, RNA from

isolated EVs and cells was extracted using a phenol-based method described in 2.3.3 in initial experiments. A second method, aimed at delivering highly purified vesicular RNA involved using the exoRNeasy kit (Qiagen) according to the manufacturer's instructions.

The RNA concentrations of both cellular RNA and EV RNA were determined using the RNA-specific fluorescent dye based-kit, Quant-iT™ RiboGreen® RNA assay (ThermoFischer Scientific) according to the manufacturer's instructions, optimised for low quantity RNA. The fluorescence was measured with a BMG Pherastar plate reader (excitation ~480 nm, emission ~520 nm). The fluorescence values of the RNA standard curve were used to extrapolate the RNA concentrations of the vesicular RNA samples.

2.6.1 Pre RNA-seq quality control

The isolated RNA was subject to stringent quality controls both locally at Cardiff University and at our consortium partner Genomescan. Prior to submitting the RNA samples to Genomescan, the EV RNA samples were investigated for traces of ribosomal RNA (rRNA). For this purpose, the EV RNA samples were prepared according to RNA 6000 Pico Kit (Agilent) instructions. The microchips were mounted on the automated electrophoresis system 2100 Bioanalyzer Systems (Agilent).

The traces of the ladder were used to identify 7 peaks (1 marker peak and 6 RNA peaks) and subsequently assign nt sizes (25 nt, 200 nt, 500 nt, 1000 nt, 2000 nt, 4 000 nt and 6 000 nt) to the measured run times. The nt size ladder was then used to assign nt sizes to the traces of the tested EV RNA samples. This analysis was done in Excel and the results visualised in GraphPad Prism. Samples that lacked rRNA peaks were sent to Genomescan for another quality control using the Agilent DNF-472 HS RNA (15 nt) Kit on a Fragment Analyzer (Agilent).

2.6.2 Library preparation and sequencing

The SMARTer® Stranded Total RNA-Seq Kit v3 - Pico Input Mammalian (Takara) with an integrated rRNA depletion step was used by our collaborators at Genomescan for library

construction. The libraries were then sequenced using the NovaSeq6000 sequencing system (Illumina®) obtaining 150 base pair (bp) paired-end reads. The library preparation was checked by calculating ribosomal, globin, and mitochondrial content in each sample.

The subsequent workflow standardised by Genomescan included a raw data quality control, unique molecular identity processing, adapter trimming, alignment of short reads, feature counting. The quality control (QC) of the results included several steps which will be outlined below.

A raw data quality control was performed to detect sample and barcode contamination by utilising a set of standard quality metrics QC tools by a third-party (FastQC v0.11.9) and in-house (Genomescan) (FastQA v3.1.27) QC tools. The quality of raw sequence reads was examined for adapter-pollution, and large number of undefined base reads. Reads with adapter-pollution were identified by an overlap with bases from the adapter sequence set (TruSeq) and excluded from further analysis. Furthermore, reads were excluded when there was a high probability of an incorrect base (>40% of the bases average Phred score below Q15) or > 5 unknown bases were detected. In addition to this, reads shorter than 15 bp were also discarded. The trimmed reads were mapped to the human GRCh38.p13 (Homo_sapiens.GRCh38.dna.primary_assembly.fa) reference genome using a short read aligner based on Burrows-Wheeler Transform (STAR2 v2.7.10) with default settings. The frequency of successful mapping of reads was assessed with HTSeq v2.0.2.

2.6.3 Downstream analysis of differentially expressed genes

The processing of the RNA-seq data sets was done in collaboration with Ingrid Tomljanovic (Genomescan, Netherlands). For purposes of clustering and visualisation, the raw counts were transformed by applying the variance stabilizing transformation using the DESeq2 R package. Using this as the input data, t-distributed stochastic neighbour embedding (t-SNE) plots were generated with the Rtsne package (v0.16) and principal component analysis (PCA) plots were generated using DESeq2. To determine differences in the transcript levels upon candidate KD compared to the NMC cells, DESeq2 was also utilised to perform differential gene expression analysis. To increase the accuracy of detecting differentially expressed genes, LFC shrinkage

was applied using the 'apeglm' method. The hallmark gene sets retrieved from the Molecular Signatures Database v2023.2. Hs (MSigDB) (Liberzon et al., 2015) was used to perform a gene set variation analysis (GSVA). This was done by applying the GSVA package (v1.48.3) to the dataset. Furthermore, the biological pathway and cell compartment gene sets from MSigDB were utilised for gene enrichment analysis (GSEA) by applying the clusterProfiler package (v4.8.21) (Yu et al., 2012). In addition to this, the pheatmap package (v1.0.12) was used to create hierarchically clustered gene expression heatmaps. The results were compiled in tables and graphs. A P-value cut off was set to <0.05 after Benjamini-Hochberg correction for all analyses, unless stated otherwise.

2.7 Statistical analysis

Statistical analyses were performed using GraphPad Prism (version 10). Statistical tests that were performed are specified in figures legends. p values less than 0.05 were considered statistically significant. Statistical significance was annotated using the following symbols: ns = non-statistical significance, * = $P < 0.05$; ** = $P < 0.01$; *** = $P < 0.001$; **** = $P < 0.0001$.

Chapter 3:

Identification of potential EV regulators in PCa cells

3.1 Introduction

The biogenesis of endosomally derived EVs is controlled by multiple intracellular regulators (reviewed in van Niel et al., 2018). Key processes in the formation of this type of vesicles take place at the endosomal compartment, where the inward budding of the membrane gives rise to ILVs, that encapsulate the vesicular cargo including for instance, nucleic acids and proteins. The generation of multiple ILVs eventually leads to the formation of the then termed MVE. Multiple cellular machineries have been reported to be involved in this process including an ESCRT-dependant and an ESCRT-independent mechanisms and will be outlined below.

The ESCRT-dependent biogenesis of endosomal EVs involves the membrane remodelling ESCRT-machinery (ESCRT 0- III and associated factors) and components of this machinery can be incorporated into the nascent EVs (reviewed in D'Souza-Schorey and Schorey, 2018, Juan and Furthauer, 2018). Briefly, ESCRT-0 regulates the binding of biotinylated cargo at the late endosomal membrane and recruitment of ESCRT-I. Then, ESCRT-I mediates the initial invagination of the endosomal membrane and the recruitment of ESCRT-II. ESCRT-III assembles around the budding neck of the forming ILV and mediates the budding of the ILVs. To complete the process, VPS4 is recruited and mediates disassemble of the complexes.

Several studies have explored the role of ESCRT components in the regulation of the secretion of EVs. For instance, Colombo et al., demonstrated in HeLa cells that KD of distinct ESCRT-components has a distinct impact on EVs; KD of HRS, STAM1 (both ESCRT-0 members) and TSG101 (ESCRT-I) reduce secretion of CD63 positive EVs, while depletion of VPS4b has the opposite effect (Colombo et al., 2013). Importantly, none of the targeted attenuations caused a complete elimination of EV secretion and thus these results suggest that multiple EV-biogenesis pathways exist. Another study conducted by Stuffers et al. reported that targeting all four ESCRT complexes simultaneously in the HeLa derived Hep-2 cell line failed to eliminate EV release completely, further validating the involvement of ESCRT-independent mechanisms in the generation of EVs (Stuffers et al., 2009).

An ESCRT-independent mechanism of ILV formation involves the nSMASE mediated generation of ceramide. The cone-shape structure of ceramide then induces inward projections of the membranes resulting in the creation of MVEs (Trajkovic et al., 2008). Chemically targeting nSMASE with GW4869 has been shown to reduce EV secretion for instance in enteroendocrine cells (Menck et al., 2017) and PCa cells (Peng et al., 2022). Furthermore, proteins of the tetraspanin family have also been implicated to regulate EV biogenesis in an ESCRT-independent process (Chairoungdua et al., 2010, van Niel et al., 2011), which is likely mediated by tetraspanin induced curvature of the membrane (Umeda et al., 2020). For instance, diminishing the expression of the tetraspanin CD81 in enteroendocrine cells causes changes of the vesicular phenotype (Luga et al., 2012).

Rab GTPases are key regulators of intracellular trafficking, which are involved in regulating the transport of the fully matured MVE containing the ILVs to the periphery of the cell. A study by Ostrowski et al. suggested that specific RabGTPase regulate distinct steps of the intracellular transport of MVEs (Ostrowski et al., 2010). To be more precise, the study proposed that Rab27b regulates the trafficking of MVE, while Rab27a controls the docking of the MVE at the cell periphery. It has also been proposed that different Rabs control distinct EV subpopulations. For instance, our lab found that while KD of Rab35 and Rab11b in DU145 PCa cells had a similar impact on the number of released EVs, the molecular phenotype of the released EVs showed a clear KD dependant impact and thus these results point to EV type specific transport mechanisms.

Upon arrival and docking of the MVEs at the plasma, the MVE fuses with the membrane and subsequently the vesicles are secreted as exosomes. This fusion event at the plasma membrane is regulated by the binding of SNAREs on the vesicles (v-SNARES) to SNAREs on the target membrane (t-SNARES) (Tang, 2020). Various SNAREs have been implicated in regulating endosomally derived EV expulsion and these include for instance SNAP23 (Verweij et al., 2018), SNAP29 (Hessvik et al., 2023) and VAMP3 (Zhu et al., 2015).

Taken together, the generation and expulsion of EVs is a highly complex process, that is regulated by a repertoire of intracellular machineries and exhibit cell-type specificities and there is wide range of model systems used. Most of the above described studies explored only

one pathway, for instance the ESCRT pathway (Colombo et al., 2013), Rab GTPases (Ostrowski et al., 2010, Hsu et al., 2010) or factors potentially involved in EV release (Hessvik et al., 2023). However, a comprehensive investigation of EV regulators in PCa cells covering EV biogenesis, transport and release has not been done yet. This could be achieved by for instance, a shRNA screening targeting all candidates potentially involved in these EV regulating pathways and could provide major insights into these processes. However, this approach would encompass potentially thousands of targets and thus pose feasibility questions in terms of handling the generated cell line variants.

An alternative option to this strategy is a candidate approach, aiming to identify targets based on previous studies in other model systems and explore their relevance in PCa cells. This would provide comprehensive insights in the regulation of EVs in PCa and perhaps reveal EV subpopulations that are most relevant for tumour-promoting biological activities. Targeting such sub-populations of EVs, if possible, might be useful in therapeutic settings to constrain specific EV-mediated effects whilst limiting undesirable consequences of global EV attenuation.

3.2 Aims and objectives

The aim of the work described in this chapter is to identify potential EV regulators in PCa cells. The objectives to achieve this aim are:

- 1.) Perform a detailed literature search in order to establish a set of candidate regulators implicated in EV secretion.

- 2.) Validate the appropriateness of the candidates with bioinformatic tools.

3.3 Results

3.3.1 Selection of candidate factors involved in EV secretion

Our aim is to describe factors regulating biogenesis, transport, and release of EVs in PCa, and thereafter to inhibit these in a PCa cell line and test the effect of perturbations on EV secretion. For this purpose, an extensive literature search was conducted to identify promising candidates that may be involved in these complex processes.

Often factors involved in the biogenesis of EVs are also found as an integral part of the released EV cargo, for instance ESCRT components, ubiquitin and tetraspanins, and a host of others. To narrow down the literature search, I focused on cargo from endosome derived EVs that was previously described for PCa cell lines and annotated in Exocarta. Exocarta is an openly available database providing a comprehensive summary of tissue specific exosome cargo.

The 1,053 potential candidates identified in Exocarta were then included in a manual search in PubMed®, specifically to identify any factors implicated in EV biogenesis, transport or release. This aspect was intentionally broad however, and included cases that were unrelated to prostate or PCa. The rationale was to identify factors that were likely to be general regulators of EVs, and hence potentially applicable beyond this study. This led to identification of 29 factors of potential interest.

From a practical perspective, creating 29 cell-line variants, reflecting attenuated expression of these candidates was unlikely to be feasible. Hence it was important to narrow this list further and prioritise some of these based on two criteria. Firstly, it was important to have candidates for which our confidence in their impact on EV output was high (such as tetraspanins, ESCRT components and Rab GTPases (e.g., Rab7a). This was based on the presence of more than one study, across varied cell model systems depicting EV-modulating effects. Second, we also wanted to allow for identification of less well-established candidates, where the opposite was true (e.g., SYNGR2, PCLO). It was intended that this approach would provide opportunities to identify some novel regulators for these EV-production processes, and to confirm the

impact of the established factors in a PCa model system. The final candidate list included 17 putative EV regulators (Figure 3.1 and table 3.1).

Furthermore, protein atlas was used to confirm that the 17 candidates are expressed in PCa tissue. Albeit far from giving us a definite confirmation that the candidates are also expressed in our selected PCa cell line, these gives us somewhat assurance that the candidates will be expressed. Additionally, the expression of the candidates was also investigated in EVs from PCa patient derived biofluids (table 3.1).

Although the search strategy was focused on endosomal EVs and thus the exosome specific Exocarta database was queried, many of the studies inputting into the database will rely on a host of diverse methods- and hence the dataset may incorporate exosomes and other secreted vesicle types. Furthermore, there is a known overlap in some machineries regulating exosomes and microvesicles. Consequently, the candidates included here might induce changes in either or both exosomes and microvesicles of PCa cells, and it is important to note these limitations.

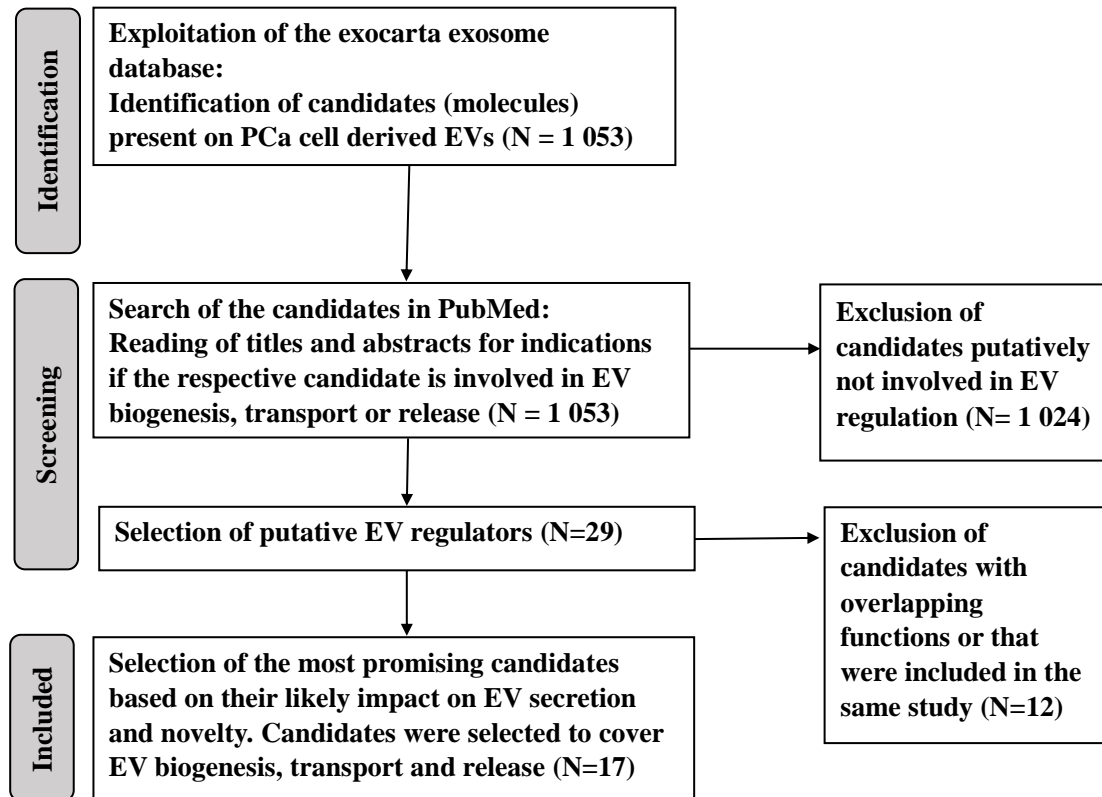


Figure 3.1: Search strategy for our candidate list.

The boxes describe the search strategy used to identify putative regulators of EV biogenesis, intracellular transport and release. The grey boxes on the left describe the different steps in the process: identification of possible candidates, screening of the found candidates and finally the selection of the candidates for this work.

Table 3.1: Candidates selected for this study.

Overview of the 17 candidates identified for this study including a short description of the candidates previously identified role in EV biology and expected impact of candidate attenuation on EV output and cargo. Furthermore, the overview includes in which cell lines the respective candidate was explored and evidence of the candidate expression in EV samples from biopsies. The overall confidence in candidates was based on all the aforementioned factors. + denotes yes, - denotes no.

Group	Candidate	Previously described role in EV biology (+/-) Regulates	Expected result of KD	Explored in PCa cells (+/-) (Cell line(s) used)	Explored in other cell lines (+/-) (Cell line(s) used)	Expressed in samples from biopsy	Overall confidence in candidate	References
EV biogenesis: ESCRT components	CHMP4C	+ MVE biogenesis	Altered EV cargo, enhanced EV secretion	-	+ HeLa (ovarian cancer cell line), MCF-7 (Breast cancer cell line)	+ (Urinary EVs)	+++	(Colombo et al., 2013, Baietti et al., 2012, Fujita et al., 2017)
	VPS28	+ MVE biogenesis	Altered EV cargo, reduced EV secretion	-	+ 293T cell embryonic (Kidney cells) Zebrafish	+ (<i>In vivo</i> Tissue samples)	+++	(Duijvesz et al., 2019, Firkowska et al., 2019, Dong et al., 2022)
EV biogenesis:	CD9	+ EV cargo	Altered EV cargo	+ PC3 cells	+ SW620 (metastatic lymph nod cell line)	+ (Urinary EVs)	++++	(Chairoungdua et al., 2010, Brzozowski et al.,

				The RWPE1 (CRL-11609) and WPE1-NB26 (CRL-2852)	Expi293F (Human embryonic kidney cell line)			2018, Fujita et al., 2017, Duijvesz et al., 2019, Yeung et al., 2018, Santos et al., 2022, Osteikoetxea et al., 2022)
	CD81	+ EV cargo	Altered EV cargo, reduced EV secretion	-	+ MDA-MB-231 (breast cancer cell line)	+ (Urinary EVs)	+++	(Luga et al., 2012, Fujita et al., 2017)
	SCAMP3	+ MVE biogenesis	Altered EV cargo, reduced exosome secretion	-	+ BHK-21 (fibroblasts) and HeLa (ovarian cancer cell line)	+ (Urinary EVs)	++	(Falguieres et al., 2012, Fujita et al., 2017)
	SIMPLE /LITAF	+ MVE biogenesis	Altered EV cargo, reduced EV secretion	-	+ Primary mouse embryonic fibroblasts and primary mouse Schwann cells	?	++	(Zhu et al., 2013)
Intracellular traffic and/or docking:	Rab6a	+ Intracellular transport to the plasma membrane	Reduced EV secretion	-	+ HeLa	+ (Urinary EVs)	+++	(Grigoriev et al., 2007, Grigoriev et al., 2011, Øverbye et al., 2015)

Rab7a	+ EV cargo	Altered EV cargo and	-	+ HUVEC (Human umbilical vein endothelial cells)	+ (Urinary EVs)	+++	(Jae et al., 2015, Øverbye et al., 2015)
Rab35 and Rab11	+ EV cargo and quantity	Altered EV cargo	+ (PCa cell line DU145)	+ Oli-ne (oligodendroglial precursor cell line)	+ (Urinary EVs)	++++	(Fan et al., 2020, Yeung et al., 2018, Hsu et al., 2010, Øverbye et al., 2015)
Rab27b	+ EV cargo	Altered vesicle cargo and reduced EV secretion	-	+ HeLa, HUVEC	+ (Urinary EVs)	+++	(Ostrowski et al., 2010, Jae et al., 2015, Øverbye et al., 2015)
Rab37	+ Secretion of EVs	Altered EV cargo	-	+ CL1-0 and CL1-5 (Human lung cancer cell lines), PC-14 (human lung adenocarcinoma cell line), H1299 (metastatic lung adenocarcinoma cell line) and H460 (large cell carcinoma cell line)	+ (Urinary EVs)	+++	(Tsai et al., 2014, Wang et al., 2018, Fujita et al., 2017)

EV release	Syntaxin 6 (STX6)	+ Fusion of EVs with the plasma membrane	Reduced EV secretion	+ PCa cell lines C4-2B, CWR-R1, and LNCaP	+ PC12 cells (neuronal precursor cell line)	?	+++	(Peak et al., 2020, Bock et al., 1997)
	SNAP23	+ Fusion of EVs with the plasma membrane	Reduced EV secretion	-	+ HeLa, HCT116 (colorectal cancer cell line), and SW480 (adenocarcinoma of the colon cell line) HUVEC	+	+++	(Zhu et al., 2015, Verweij et al., 2018, Fujita et al., 2017)
	VAMP3	+ Fusion of EVs with the plasma membrane	Reduced EV secretion (of Rab35 positive EVs)	-	+ HUVEC (Human umbilical vein endothelial cells), HepG2	+	++	(Zhu et al., 2015, Hsu et al., 2010, Yang et al., 2019, Fujita et al., 2017, Sneegeen et al., 2019)

EV release: limited described factors	Piccolo (PCLO)	<p>Role in EV biology unknown EV biogenesis and release?</p> <p>Reported Role: Regulates synaptic vesicle release and uptake</p>	Altered vesicle cargo, reduced EV secretion	-	+ KYSE30, KYSE180, KYSE410, KYSE450 and KYSE510 (esophageal squamous cell carcinoma cell lines)	?	+	(Zhang et al., 2017, Ackermann et al., 2019, Fenster et al., 2003)
	Synaptogyrin -2 (SYNGR2)	<p>Role in EV Biology unknown EV release?</p> <p>Reported Role: Regulates synaptic vesicle biogenesis, involved in GLUT4 membrane trafficking, modulates viral replication</p>	Reduced EV secretion	-	+ Drosophila	+ Urinary EV	++	(Raja et al., 2019, Boesze-Battaglia et al., 2017, Stevens et al., 2012, Øverbye et al., 2015, Sun et al., 2016, Kioumourtoglou et al., 2015)

3.3.2 Interaction network of the selected candidates

Only few of the candidates selected for this work have been well established as EV regulators (e.g., CD9 and CD81) (table 3.2). Candidates, such as SYNGR2 have not been studied as extensively, yet there is emerging evidence that they might play a role in the modulation of EV production. As described in the introduction regulation of EV biogenesis is a complex process, with multiple regulators working in concert via direct and indirect interactions. Consequently, direct interaction of a less well described candidate, e.g., SYNGR2, with a well described candidate could potentially indicate that both regulate the same EV biogenesis, transport, or release pathway and therefore the same EV subset.

To explore potential pathway inter-relationships of the selected candidates, the biological effector database (BED) by Anaxomics was used. This database includes publicly available datasets in addition to manually selected datasets which can then be utilised to extract information about the interaction and/or influence of proteins on each other and to create an interaction network. Thus so, the BED can be used to provide insights into the potential involvement of proteins in molecular pathways.

For the analysis of the 17 candidates, the BED (<https://anaxomics.com/biological-effectors-database.php>, (Iborra-Egea et al., 2017) was queried by our collaborator Pedro Matos Filipe for first level effectors, also termed first neighbours, of the 17 selected candidates and revealed that there is a known, previously published direct connection to another candidate for 12 of the 17 candidates (SYNGR2, Rab7a, Rabb11b, Rab6a, STX6, SNAP23, VAMP3, CHMP4C, VPS28, CD81, SCAMP3 and CD9). 5 candidates (PCLO, LITAF, Rab37, Rab27b and Rab35) could not be connected to the interaction network as first neighbours (Figure 3.2.)

As expected, the candidates that were previously described to be involved in defined pathways or complexes were indicated to directly interact with each other as 1st degree neighbours. For instance, CD81 was a 1st degree neighbour of the tetraspanins SCAMP3 and CD9, whereas no connection between CD9 and SCAMP3 was found. Looking into the experimental proofs of these connections, revealed that CD9 and CD81 have been previously co-immunoprecipitated in CM (Park et al., 2010) and cell lysates (Park et al., 2010, Mazurov

et al., 2013) and there is evidence that the two tetraspanins form a complex (Charrin et al., 2002). Furthermore, a mass spectrometry (MS) based approach showed that CD81 precipitated with SCAMP3 (Palor et al., 2020). The network analysis also indicated a connection between CD81 and SNAP23. This is based on the observation that CD81 co-immunoprecipitated with SNAP23 (Palor et al., 2020). However, this study did not focus on this interaction in more detail.

Interestingly, CHMP4C, an ESCRT protein, was indicated to influence/interact with SNAP23, a protein previously described to specifically regulate endosomally derived EVs (Verweij et al., 2018). This connection was identified in a MS analysis focusing on telophase (Capalbo et al., 2019). However, the authors did not study this interaction in more detail. Therefore, it remains to be seen whether the observed interaction between the proteins are the result of the mere proximity of the proteins or if they have indeed a functional relationship.

The interaction network also suggested connections between Rab GTPases and other EV regulators. An example of this is the proposed interaction of Rab6a and STX6, which was experimentally shown (Laufman et al., 2011). Interestingly, SYNGR2 was indicated as a first neighbour to Rab7a, which points to the possibility that they regulate the same EV subset. The possible interaction was identified in an MS experiment where SYNGR2 co-immunoprecipitated with Rab7a (Yamano et al., 2018) and clearly requires validation.

Taking non-direct connections, which are connections via another protein, another three candidates (LITAF, PCLO and Rab35) were connected to the initial 12. The network analysis including both first and second neighbours showed that SIMPLE/LITAF and SCAMP3 share a common connection: W domain containing E3 ubiquitin protein ligase 1 (WWP1). SCAMP3 was indicated as potential interacting partner by SILAC-MS (Nielsen et al., 2019) and WWP1 was found to co-immunoprecipitated with SIMPLE/LITAF (Li et al., 2015b). Interestingly, WWP1 was also found in EVs (Hurwitz et al., 2016b).

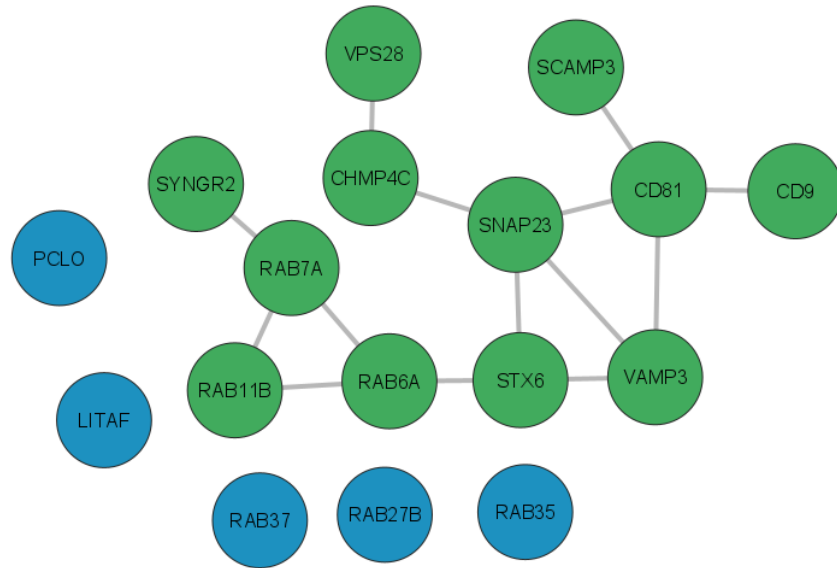
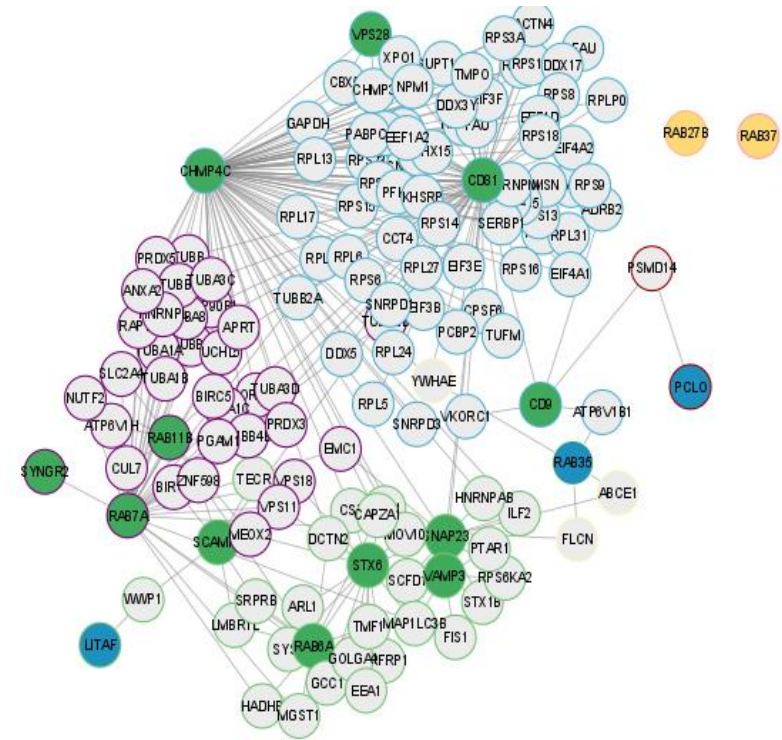
A**B**

Figure 3.2: Interaction network of the selected candidates.

The BED from Anaxomics was queried by our collaborator Pedro Matos Filipe for the effectors of the 17 selected candidates. The interaction network in (A) shows the interaction of the candidates with each other. The lines represent a connection (influence/interaction). The candidates highlighted in green could be directly connected to another candidate. The candidates highlighted in blue could not be connected to another candidate as a 1st degree neighbour. The interaction network in (B) shows the candidates and their 2nd degree neighbours which subsequently connect to another candidate

PCLO, a less well described candidate, and CD9 shared a common first neighbour: PSMD14, a subunit of the proteasome (Figure 3.2B). This interaction was found via MS (Wang et al., 2019). Interestingly, evidence is starting to emerge that EVs carry functional proteasome subunits (Ben-Nissan et al., 2022). Furthermore, PSMD14 was also found in EVs from osteosarcoma cells (Luu et al., 2022). Thus, it would be interesting to explore a potential role of CD9 and PCLO and the extracellular proteasome.

Overall, the interaction network supports our selection of candidates as it indicates that the candidates are potentially involved in EV regulating pathways, e.g., the SNARE complex, via 1st- or 2nd-degree neighbours.

3.3.3 Involvement of the candidates in EV regulating pathways

Using the BED from Anaxomics gave first indications of the candidate involvement in EV regulating pathways. To explore this in more depth, we also investigated whether the selected candidates could be mapped onto selected, already described pathways involved in EV biogenesis, transport and release. For this purpose, gene lists of EV relevant pathways were selected (chapter 2.1 and table 2.1). To be more precise, GO terms with relevance to EV generation were chosen from https://www.informatics.jax.org/vocab/gene_ontology. The GO terms for the ESCRTI and II (GO: 0000813 and GO:0000815) did not provide a comprehensive list of all ESCRT components that have been described to be involved in EV biogenesis. Hence, I combined the aforementioned GO terms and additionally included those genes that were previously described (McGough and Vincent, 2016, van Niel et al., 2018) to be involved in EV biogenesis. The ANN tool developed by Anaxomics (Loging et al., 2011) (chapter 2.1) was then used by our collaborators to explore the likelihood of interaction between the respective candidate and the investigated pathway.

As expected, most candidates could be mapped onto EV regulating pathways indicating that the majority of the 17 candidates are potentially involved in EV modulating pathways. The functional enrichment analysis indicated a tight relationship of the ESCRT proteins CHMP4C and VPS28 with the ESCRT pathways (Figure 3.3). Furthermore, the analysis indicated CD9 and Rab11b to be associated with the ESCRTIII, vesicle transport, and upregulation of

secretion. ESCRT III was also associated with VAMP3, Rab35 and Rab7a. Furthermore, Rab27b and SNAP23 were associated with vesicle transport.

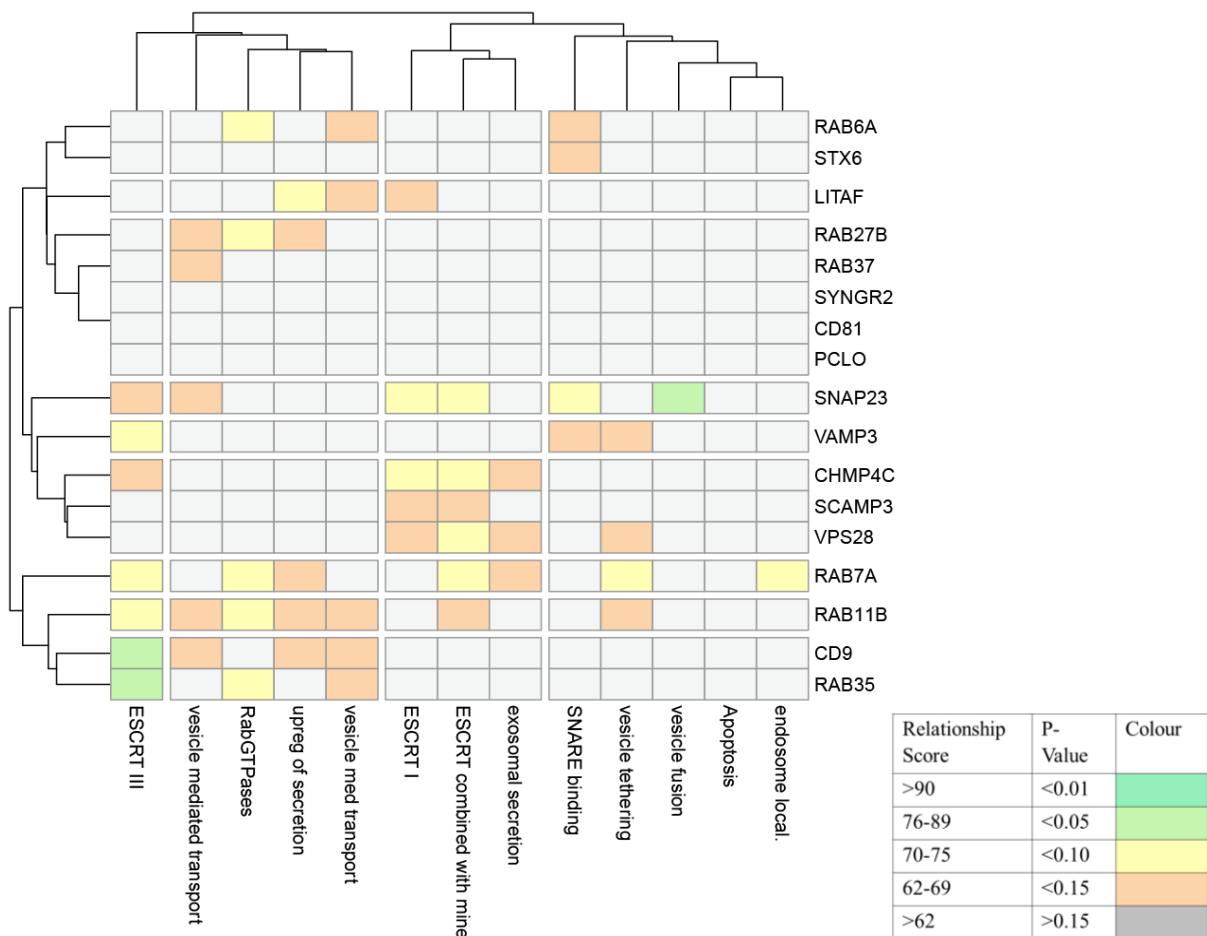


Figure 3.3: The majority of the selected candidates overlap with an EV related pathway.

The ANN tool trained on the BED from Anaxomics was used to create the functional hierarchical cluster plot for all 17 candidates. The pathways were selected by Anaxomics (apoptosis) and me (the rest of the indicated pathways). The colour represents a relationship score: grey values (muted) indicate a low relationship score below 62% and a P-value > 0.15. Orange indicates a relationship score between 62-69% and a P-value < 0.15. Yellow represents a relationship score 70-75% and a P-value < 0.10. Light green represents a relationship score 76-86% and a P-value < 0.05. Dark green represents a high relationship score > 90% and a P-value < 0.01. Analysis provided by Pedro Matos Felipe. Figure created in R. For three candidates, CD81, SYNGR2 and PLCO there was no association with these pathways.

For those candidates for which there was no connection (CD81, PCLO, SYNGR2), first neighbours were included as a proxy (Figure 3.4, 3.5). For example, examining SYNGR2, the protein failed to overlap with any of the analysed pathways. Taking the 1st neighbours of SYNGR2 as proxy for the candidate, indicated a relationship of SYNGR2 and vesicle mediated secretion and ESCRTIII (Figure 3.4). Similar, PCLO did not show any overlaps with the selected pathways. However, using PCLO's 1st neighbours as a proxy, there was an overlap with the vesicle mediated transport for some of interaction partners of PCLO (Figure 3.5).

We aim to attenuate the expression of the selected candidates as a tool to explore their function. However, KD of the selected candidates could cause a perturbation of apoptosis in the target cell. Increased apoptosis induces the increased release of small apoptotic bodies, which can be difficult to distinguish from small EVs. This would pose a major challenge for this work. Therefore, we were interested if the selected candidates are involved in or influence apoptosis. Using the ANN tool, we found no indications of a relationship between all selected candidates and apoptosis (Figure 3.3). Nevertheless, it must be noted, that the lack of a connection could mean that there is no connection, the connection is poorly described due to lack of evidence, or the gene set (pathway) was poorly defined.

In conclusion, promising candidates were selected for an exploration of their role in EV regulation. These findings support the notion that most of the selected candidates influence/impact each other. Most candidates could be mapped onto EV relevant pathways, such as the ESCRT dependant pathway, using the ANN tool trained on the BED by Anaxomics.

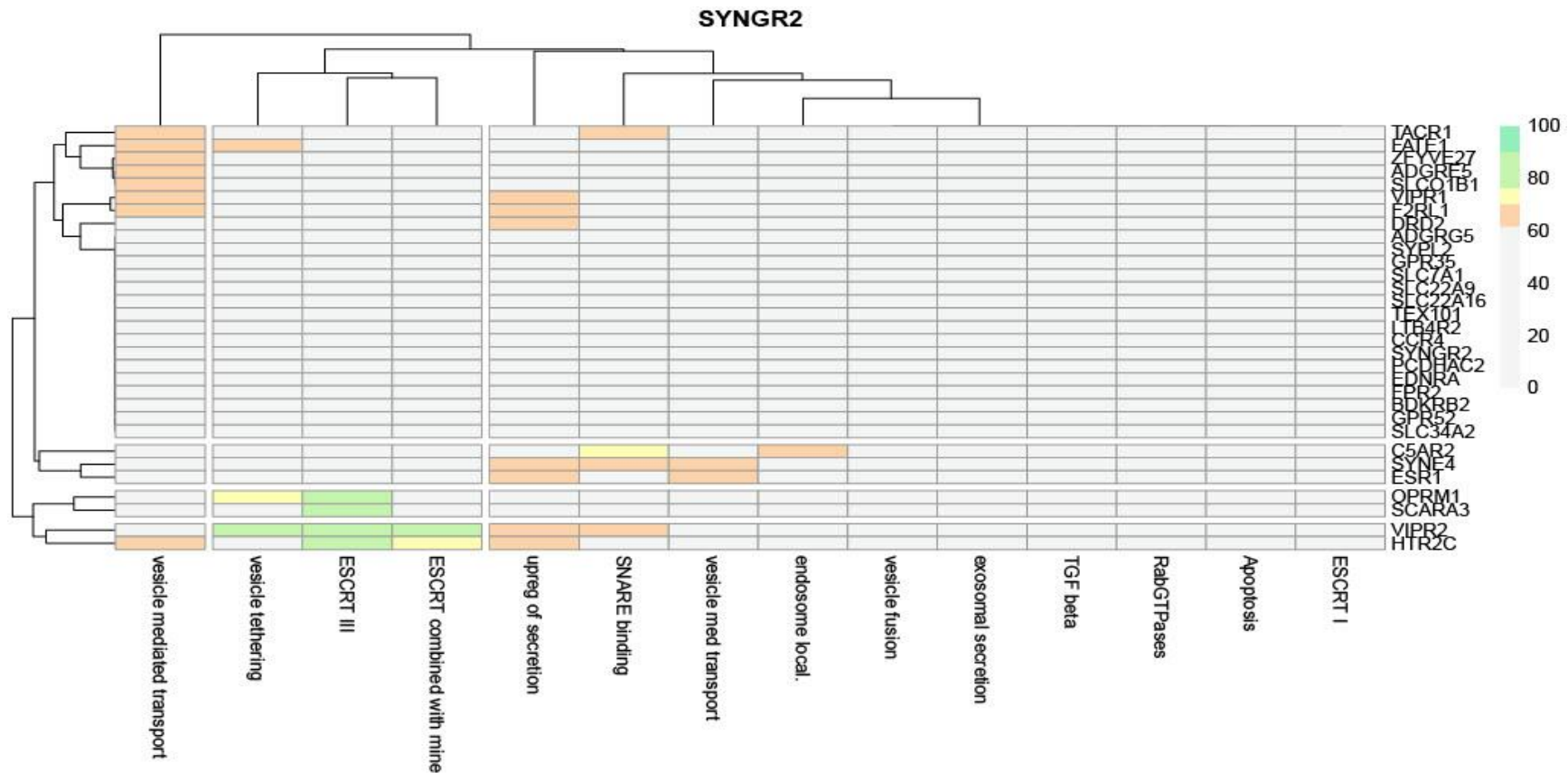


Figure 3.4: Functional enrichment analysis of the 1st neighbours of SYNGR2.

The ANN tool trained on the BED from Anaxomics was used to create the functional hierarchical cluster plot for the 1st neighbours of SYNGR2. The pathways were selected by Anaxomics (apoptosis) and me (the rest of the indicated pathways). The colour represents a relationship score: grey values (muted) indicate a low relationship score below 62% and a P-value > 0.15. Orange indicates a relationship score between 62-69% and a P-value < 0.15. Yellow represents a relationship score 70-75% and a P-value < 0.10. Light green represents a relationship score 76-86% and a P-value < 0.05. Dark green represents a relationship score > 90% and a P-value < 0.01. Analysis and image done by Pedro Matos Felipe.

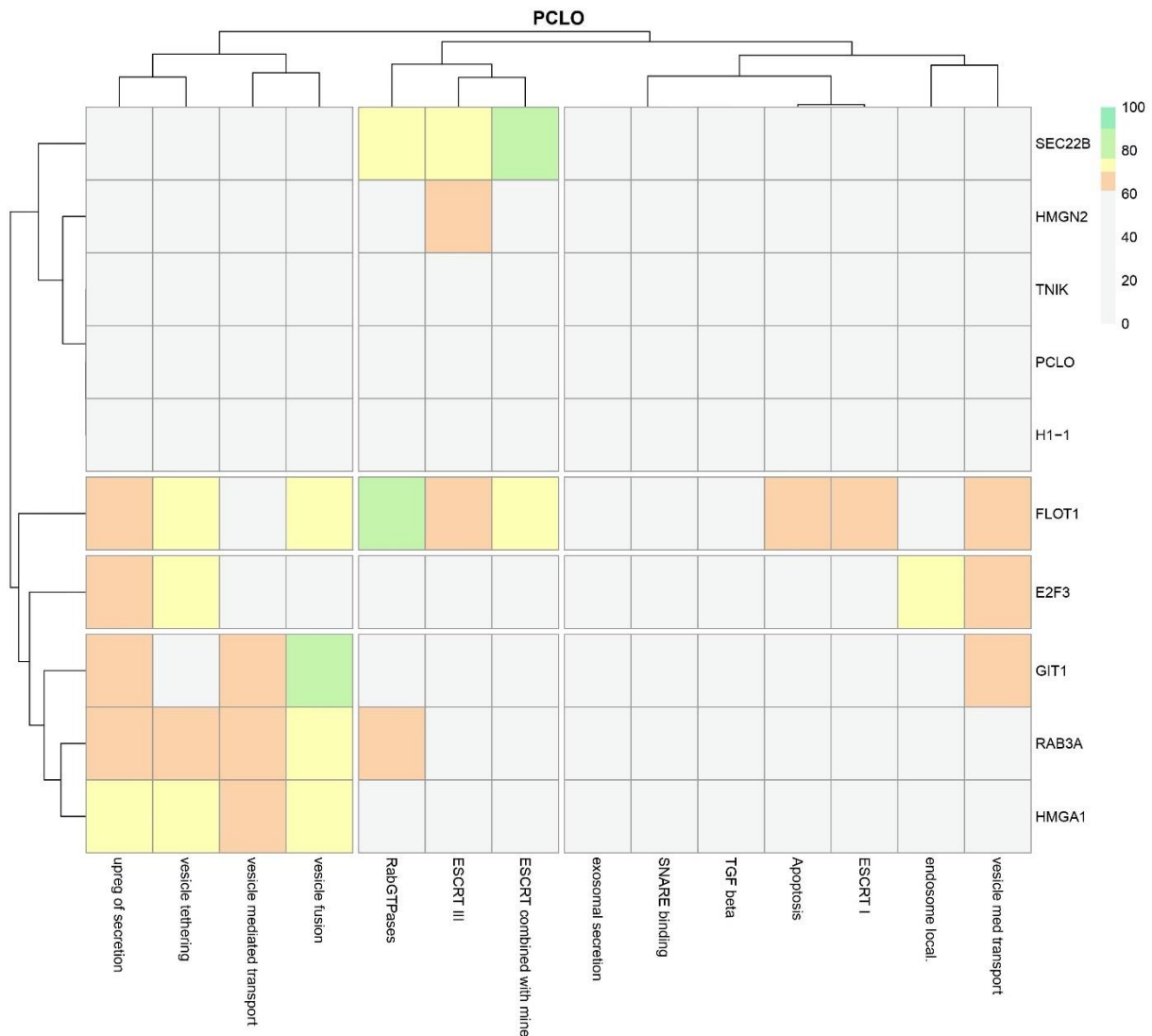


Figure 3.5: Functional enrichment analysis of the 1st neighbours of PCLO.

The ANN tool trained on the BED from Anaxomics was used to create the functional hierarchical cluster plot for the 1st neighbours of PCLO. The pathways were selected by Anaxomics (apoptosis) and me (the rest of the indicated pathways). The colour represents a relationship score: grey values (muted) indicate a low relationship score below 62% and a P-value > 0.15. Orange indicates a relationship score between 62-69% and a P-value < 0.15. Yellow represents a relationship score 70-75% and a P-value < 0.10. Light green represents a relationship score 76-86% and a P-value < 0.05. Dark green represents a relationship score > 90% and a P-value < 0.01. Analysis and image done by Pedro Matos Felipe.

3.3.4 Clinical relevance of the selected candidates

This study specifically focuses on the role of PCa derived EVs and accompanied tumour promoting properties of the EVs. Hence, it was considered potentially useful to explore the possible clinical relevance of the candidates, in terms of what is known about the relationship between mRNA transcript-levels and disease correlates.

I exploited public repositories using CancerTool, a web based bioinformatic tool, to analyse publicly available transcriptomic data sets (Cortazar et al., 2018). The cancer genome atlas (TCGA) dataset is characterised by a large patient cohort size (n=497) (Cancer Genome Atlas Research et al., 2013, Cancer Genome Atlas Research, 2015) who underwent prostatectomy and was used to reveal some significant differences in mRNA levels between the identified candidates and PCa status by both GS and disease free survival (DFS), depicting the recurrence of the disease in PCa patients after the treatment finished.

The TCGA dataset lacked information on transcript levels in relation to normal tissue (N), the primary tumour (PT) and metastatic (M) side. Therefore, the Taylor set was included in this analysis albeit reflecting a smaller cohort (n=185) (Taylor et al., 2010).

As an example of such exploration, SNAP23 mRNA expression levels across different stages of the disease were investigated. The analysis showed that in the Taylor sample cohort, significantly increased mRNA levels of SNAP23 were detected in the PT compared to N tissue. In contrast, SNAP23 mRNA levels in N tissue and in the M tissue were at comparable levels, suggesting there is a role for SNAP23 in earlier as opposed to late/metastatic stages of the disease (Figure 3.6A). I also evaluated differences between varied histological severities, ranging from low grade Gleason 6 (GS6) to high grade GS10, using the TCGA cohort.

Overall, there were significant differences in the SNAP23 mRNA expression across the different GSs. Interestingly, SNAP23 mRNA expression was decreased in GS9 compared to GS6-8 (Figure 3.6B). The DFS data in the TCGA patient cohort with respect to SNAP23 mRNA expression was also of particular interest. The Kaplan-Meier curve, representing the recurrence of the disease, in Figure 3.6.C indicates that there is a highly significant difference in DFS when segregating groups by the mean expression of SNAP23, with a 2.23-fold increased risk of disease recurrence in the low SNAP23 expressing group (Figure 3.6C). This could indicate that SNAP23 regulates a cancer suppressive EV population at the later stages

of the disease. However, the TCGA datasets lacks important clinical information about the specific treatment combinations the patients received, which can be diverse, thus these results require further confirmation (Cortazar et al., 2018, Cancer Genome Atlas Research et al., 2013).

Another example of such exploration is Rab7a. In contrast to the results of SNAP23, however, no significant differences could be detected in the mRNA expression of Rab7a in terms of PCa progression, comparing N tissue, the PT and M site. Nevertheless, a significant difference in the expression of Rab7a across different GS was found, indicating a potential role in the primary tissue disorganisation but less impact in the systemic disease. The potential clinical correlates for all 17 candidates were analysed in this fashion and is summarised in table 3.2.

Overall, most of the candidates exhibited some correlates in terms of these clinical parameters, however, this was not true for all. PCLO and Rab11b showed no significant differences with any of these clinical parameters- suggesting that they do not fluctuate during the course of PCa development and progression. For the remainder, the exploratory data shown may be interpreted as preliminary evidence supporting the view that these selected EV-constituents are relevant in the complex processes driving PCa.

Cancer critical regulators often play a role across different cancers. Thus, a regulator contributing to the disease in PCa might also be critical in other cancers. To further explore the role of the candidates in cancer, the literature was searched for additional evidence of the relevance of the candidates in cancer. This analysis is summarised in table 3.2. and showed that most candidates were previously reported to be over or under expressed in various cancer types further supporting the selection of the candidates and potentially providing additional cancer types for future investigations.

To sum up, in this chapter 17 promising candidates were identified that likely play a role in EV regulation by an extensive literature search. This notion was supported by an interaction network analysis and that most of the candidates overlapped with EV focused pathways.

Importantly, for the majority of the candidates an exploration of their clinical relevance indicated a role of the candidates in DFS, GS and tumour progression in PCa.

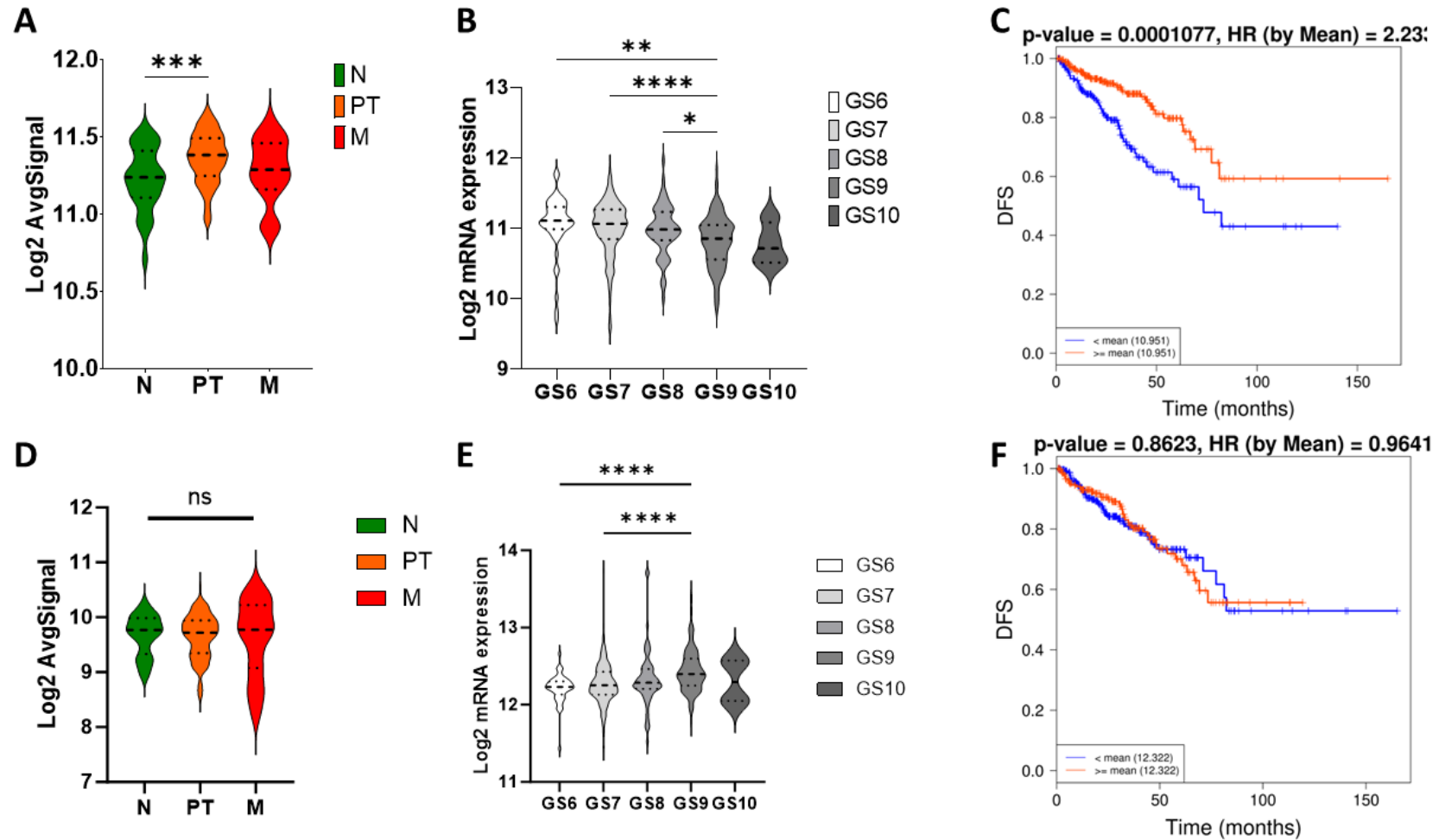


Figure 3.6: SNAP23 and Rab7a mRNA expression is altered in PCa patients.

Cancer tool was used to explore the potential clinical relevance of SNAP23 and Rab7a mRNA expression. The mRNA expression of SNAP23 comparing normal tissue (N), the primary tumour (PT) and metastatic prostate tissue (M) based on the Taylor dataset is shown in (A). SNAP23

mRNA expression across GS6-10 is depicted in (B). The DFS curves depicted in Kaplan Meier plots for SNAP23 are shown in (C). The patient cohort was divided by the mean mRNA expression of SNAP23, and a Cox proportional regression model was performed to determine the Hazard ratio. The curves represent the recurrence of the disease in the patient cohort. A Mantel-cox test was applied to determine the significance of the differences between the curves. Similarly, data are shown for Rab7a mRNA (D), (E), (F). A, (B), (D) and (F) were created in GraphPad and a one-way Analysis of Variance (ANOVA) with Tukey as a post-hoc test was applied, ns= non-significant, *= P< 0.05, ** = P< 0.01, *** = P<0.001, **** = P<0.0001.

Table 3.2: Potential clinical relevance of the selected candidates.

The 17 candidates were analysed using Cancertool to reveal their potential clinical relevance. Cancertool was queried for differences in candidate mRNA expression in the progression of the disease comparing N, PT and M. Cancertool was also queried for differences of candidate mRNA expression across GS 6-10. A one-way ANOVA with Tukey as a post-hoc test was applied for both. The DFS were also explored. The patient cohort was divided by the mean mRNA expression of the indicated candidate and a Cox proportional regression model was performed to determine the Hazard ratio. A Mantel-Cox test was applied to determine the statistical significance. ns= non-significant, * = P< 0.05, ** = P< 0.01, *** = P<0.001, **** = P<0.0001. ^A=based on the Taylor study, ^B=based on the TCGA study.

Candidate/ Clinical factor investigated	^AProgression (Differences in the mRNA expression comparing normal tissue, the primary tumour and the metastatic site)	^BGS (Differences in the mRNA expression comparing GS 6-10)	^BDFS (Differences in the DFS rates, samples divided by the mean)	Expression in PCa and other cancers, examples	References
CD9	***	ns	ns	Downregulated in PCa High expression in various cancers	(Wang et al., 2007, Folkmanis et al., 2022) (Koh et al., 2021)
CD81	***	ns	ns	Overexpressed in PCa	(Zhang et al., 2020)
CHMP4C	***	***	ns	Overexpressed in lung tumour tissue and cervical cancer	(Liu et al., 2021) (Lin et al., 2020)
LITAF	***	***	ns	Decreased in pancreatic cancer	(Zhou et al., 2018)
PCLO	ns	ns	ns	Increased in oesophagus cancer	(Zhang et al., 2017)

Rab6a	*	***	ns	Negatively correlated with patient survival in lung adenocarcinoma	(Xiao et al., 2023)
Rab7a	ns	****	ns	Increased expression in pancreatic cancer	(Liu et al., 2022)
Rab11b	ns	ns	ns	Overexpression associated with better overall survival in colorectal cancer	(Kottorou et al., 2023)
Rab27b	***	*	**	Overexpressed in Esophageal Squamous Cell Cancer	(Yu et al., 2020)
Rab35	***	ns	*	Overexpressed in ovarian cancer cells upon androgen treatment	(Sheach, Adeney et al. 2009)
Rab37	ns	**	ns	Decreased expression in oesophageal cancer	(Tzeng et al., 2017)
SCAMP3	***	ns	ns	Overexpressed in glioma	(Li et al., 2020).
SNAP23	***	***	***	Upregulated in ovarian cancer and pancreatic cancer, Downregulated in cervical cancer	(Sun et al., 2016) (Mitani et al., 2022)
STX6	*	***	*	Overexpressed in pancreatic and liver cancer	(Li et al., 2022b).
SYNGR2	***	**	ns	Proposed as a potential cross cancer marker	(Li et al., 2022a)
VAMP3	***	ns	*	Negatively correlated with patient survival with colon adenocarcinoma	(Hou, Ma et al. 2022)
VPS28	**	ns	ns	Overexpressed in breast cancer	(Shi et al., 2021)

3.4 Discussion

Our goal is to identify novel regulators of EV biogenesis, transport and release in PCa cells which contribute to disease process by the fact they generate bioactive EVs. In this chapter, I described an extensive literature search combined with a database search to identify potential candidates that would satisfy this aim. Often regulators of EV biogenesis are incorporated as cargo into the released EVs. Hence, I searched for candidates previously described to be present on PCa cell derived EVs using exocarta.org and selected those with a putative function in regulating EV diversity (Figure 3.1). However, this approach has some limitations. Here we make an assumption that cell-endogenous regulatory elements become incorporated into the secreted vesicle. Whilst there are several examples of this e.g., the ESCRT component CHMP4C (Colombo et al., 2013), it is not a certainty for all cases, and hence the strategy would fail to identify genuine EV-regulating factors which are retained in or associated with the endosome-tethered machinery, and excluded from incorporation into the secreted structure. In addition, the quality EV isolations which provide data into this and other (e.g., Vesiclepedia) databases is heterogeneous, and hence the information contained may reflect exosome-type vesicles, ectosomes and a host of vesicular contaminants. There will therefore always remain some element of imperfection within these curated datasets.

When reflecting on a candidate approach, other studies exploring regulators of EVs have mainly focused on one pathway, for instance on the ESCRT pathway (Colombo et al., 2013), RabGTPases (Ostrowski et al., 2010, Hsu et al., 2010) or factors potentially involved in EV release (Hessvik et al., 2023). One study by Yeung et al focused on an array of 6 different factors involved in EV biogenesis, transport and release and found Rab35 to be a regulator of an EV subpopulation in DU145 PCa cells. An alternative to a candidate approach like this might utilise a screening strategy to attenuate random, or semi-random elements, perhaps targeting hundreds or more elements and to subsequently assess their consequences in terms of vesicle impact. A noteworthy example of this approach was a recent study that aimed to identify EV secretion regulators in a shRNA screen targeting more than 21,000 proteins in microglia (Ruan et al., 2022). Others have used large scale Clustered regularly interspaced short palindromic repeats (CRISPR) associated protein 9 (CRISPR-Cas9) based screens to identify EV regulators (Lu et al., 2018).

In this chapter 17 most promising candidates were selected from different pathways possibly involved in the regulation of EVs as described above to maximise the chances of identifying novel EV regulators that have a dramatic impact on the released EVs. This to my knowledge would reflect the most extensive repertoire of candidates to target across different pathways ever investigated in PCa cells in one study. There was also a pragmatic element here in that the future aim is to attenuate the expression of the selected candidates in a PCa cell line by using lentiviral variants, and ultimately compare the relative potencies in terms of EV output, and ultimately EV cargo and functions. Escalating this from 17 or so to 30 candidates or more would present feasibility challenges in scale and capacity to assess potential hits. Thus, the candidate approach described in this chapter, which is partly informed by a priori studies, is more likely to deliver verifiable hits and leading to subsequent functional explorations more quickly.

Pathways that regulate EV biogenesis are dependent on the coordinated interaction of various molecules. For instance, VAP-A interacts with CERT at membrane contact sites and drives the biogenesis of RNA enriched EVs. Depletion of the proteins leads to similar changes in vesicle output (Barman et al., 2022). Another example is the sequential interaction of Rab7a/Arl8b/Rab27a for the release of CD63 positive endosomally derived EVs (Verweij et al., 2022). Hence, we wondered if by revealing the interaction of the selected candidates could be used to extrapolate potential functions. Especially, we aimed to gain insights into the connections of less well described candidates such as SYNGR2 and PCLO. A direct or indirect interaction of a barley described candidate with a well described candidate would suggest that both regulate the same EV biogenesis, transport, or release pathway and as a consequence the same EV subset. Manually searching for all interactions of the selected candidates is extremely labour and time intensive and thus, was deemed not suitable. However, there are databases for the exploration of interaction networks such as reactome.org (Jassal et al., 2020) which is manually curated, and other online bioinformatic tools (reviewed in Garcia-Campos et al., 2015).

For the analysis of the 17 candidates the BED of Anaxomics (Iborra-Egea et al., 2017) was used. A key advantage of this database is that it is based on a vast variety of information sources, e.g., other pathway analysis tools such as reactome.org, and combines them with selected publications (<https://anaxomics.com/biological-effectors-database.php>). Thus, giving a more comprehensive overview of potential interactions than a single database tool alone.

The BED was queried for the 17 candidates by our collaborator Pedro Matos Filipe for first level effectors of the 17 selected candidates. As expected, the candidates that were previously described to be involved in defined pathways or complexes were shown to interact with each other. For instance, candidates that were associated with ESCRT components (CHMP4C and VPS28), or SNARE proteins (STX6, SNAP23 and VAMP3) were shown to interact in their respective group. Interestingly, Rab7a, a previously described EV regulator and SYNGR2, a putative EV regulator, were indicated to have a direct connection, which points to the possibility that they regulate the same EV subset.

Only 2 candidates (Rab27b and Rab37) could not be connected based on the BED. However, the database relies on previously described interaction. Hence, this might simply reflect our current lack of knowledge of these interactions or indeed there is no interaction.

The next step was to embed the candidates in EV regulating pathways. Again, online bioinformatic tools such as string.db or reactome.org can be used for this purpose. However, analysing multiple proteins and gaining a comprehensive overview using multiple pathway analysis tools is labour and time intensive. Here, a machine learning model based on Artificial Neural Networks (ANN), trained on the BED developed by Anaxomics was used to investigate if the set of candidate genes overlap with various known pathways. The functional hierarchical clustering analysis was performed by our collaborators Pedro Matos Filipe and Judith Farrés, at Anaxomics. The analysis indicated that the majority of candidates or their 1st neighbours overlap with EV regulating pathways. Thus, supporting the selection of the candidates as potential EV regulators.

The association of EV regulator pathways and several disease have been described in a systems biology approach (Gézi et al., 2019) demonstrating that EVs contribute to the development of various disease. As this project is focused on PCa, Cancertool was used to explore the potential clinical relevance of the selected candidates in PCa. Although far from definitive, the majority of these selected candidates appear to have changes in mRNA transcript levels during the development and progression of PCa. For example, high SYNGR2 mRNA expression is associated with a progression of the disease. At the disease status, with overall high SYNGR2 mRNA expression compared to normal tissue, SYNGR2 mRNA becomes reduced with histological severity. Whilst of course SYNGR2 and many of the other

candidates are involved in cellular processes that are not exclusively EV related, taken together it is intriguing that most of these vesicle-elements are dynamic in disease, suggesting EV changes occur alongside or perhaps contributing towards worsening disease status.

Interestingly, most of the selected candidates have also been previously described to have altered expression levels in various cancers (table 3.3). Thus so, potentially indicating a cross cancer role, and adding to credibility of the findings, in that these are not a peculiarity to PCa. Notably, a recent paper explored the expression of SYNGR2 across several cancers. A low SYNGR2 expression was favourable for DFS for most cancers and the authors strongly suggested SYNGR2 as a potential cross cancer marker (Li et al., 2022a).

All in all, 17 promising candidates have now been selected for an experimental exploration of their role in EV regulation. The findings presented in this chapter support the notion that the majority of the selected candidates are part of a broader network of interacting elements regulating endosome dynamics. Most candidates could be mapped onto known EV relevant pathways, such as the ESCRT dependant pathway, using the ANN tool by Anaxomics. In the next chapters, the impact of the selected candidates on EV output will be explored experimentally.

Chapter 4:

Attenuation of potential EV regulators in PC3 cells

4.1 Introduction

EVs transport a myriad of signalling molecules thereby modulating the behaviour of recipient cells both in close proximity (El-Sayed et al., 2017, Zhang et al., 2018c) and at more distant sides (Peinado et al., 2012, Garcia-Silva et al., 2021). This is especially critical in regard to all stages of tumour development for which EVs have been reported to be a significant contributor to the establishment and progression of the diseases. For instance, Souza et al. reported that EVs isolated from PCa patients confer phenotypic changes in recipient non-neoplastic cells that are characterised by an enhanced migratory and proliferative ability (Souza et al., 2018). Consequently, altering EV production can possibly have a big impact on a number of diverse recipient cells, locally and distant and hence contribute to a positive benefit in slowing the disease's progress.

Our lab has a long-standing interest and experience in EVs from PCa cells. In particular EVs derived from the metastatic PCa cell line DU145 have been well described by our group (Yeung et al., 2018, Webber et al., 2016). To explore the potential EV regulating role of the candidates selected for the work presented here, we reverted to the highly metastatic and poorly differentiated adenocarcinoma PCa cell line PC3 to expand our knowledge about EVs in PCa. This cell line is of bone metastatic origin and homes to lymph nodes when injected into mice (Wu et al., 2013). The cell line was a kind gift of prof Hector Penado (CNIO, Spain) and was subject to short tandem repeat profiling to validate the cell origin. A proteomic description of the EVs has also been performed in his lab (Annex B). Interestingly, the majority of the candidates used in this work have been identified to be present in the PC3 cell line derived EVs used for this study, except Rab37 and SIMPLE (LITAF). This is noteworthy because it indicates that majority of our candidates are expressed in this cell line and thus can be targeted for attenuation.

Using Mission® lentiviral particles to generate modified PCa cell variants with attenuated candidate gene expression is a previously successfully established tool in our lab (Yeung et al., 2018). Integration of a reverse transcribed RNA sequence into the genome of the cell, allows a stable KD over multiple passages (Shearer and Saunders, 2015). A complete KO of target might render the cells non-viable and hence not suitable for further investigation in the

scope of this study. Importantly, partial KD of a candidate induced by target specific shRNA, might be sufficient to induce measurable changes in the EV quantity and quality whilst marginally impacting cell viability or other general cell properties, and hence this method was considered a pragmatic route to explore these putative EV regulators.

4.1.1 Characterisation of EVs

EVs present in CM, and purified EVs can be characterised by a plethora of methods. Currently, there is still an ongoing debate how to best characterise EVs. In an effort to provide guidance on the best practices the MISEV 2023 guidelines were published and suggest for the characterisation of EVs various techniques should be used including methods to quantify the EVs and characterisation of EV related proteins (Welsh et al., 2024). However, it needs to be noted that these are guidelines and should not be considered as strict rules.

A commonly used technique to quantify EVs in a sample is NTA which is a light scatter - based technique utilised to evaluate nanosized particles (<1 μm) in a solution. This method uses the Brownian motion of particles in a solution to calculate their particle diameter and concentration. Thousands of particles can be analysed in a sample; however, it is not possible to distinguish between a genuine EV and other particulate material in the solution. Hence, NTA is often used in combination with other techniques that assess the tetraspanins CD9, CD63 and CD81 which are enriched in EVs. For instance, immunophenotyping of EV samples can be achieved by using a plate-based assay akin a classical Sandwich ELISA which uses one tetraspanin antibody, e.g., anti CD63, to catch vesicles in a solution and another antibody e.g., a biotinylated anti CD9 antibody to detect the vesicles.

4.1.2 Aims and objectives

Despite the important tumour promoting role of EVs, a lot remains to be uncovered about the specific machineries involved in the generation of EVs. Key questions in this regard are firstly which factors are involved in the regulation of EVs and secondly do these regulators control distinct EV population or do these machineries operate in a general fashion to regulate all such vesicles. In the last chapter, 17 potential regulators of EV biogenesis, intracellular

transport and release were identified based on an extensive literature search and utilising bioinformatic tools. In this chapter, we aim to contribute to filling the knowledge gaps described above by investigating the potential contribution of these 17 candidates *in vitro* in the context of PCa. The following objectives were set to reach this goal:

- 1.) Silence candidate expression in PC3 cells with target specific shRNA and validate the target attenuation by qPCR and flow cytometry.
- 2.) Evaluate the impact of candidate KD on cell proliferation, to assess whether the cell can withstand the perturbation.
- 3.) Determine changes in the quantity and molecular phenotype of the released EVs using molecular biological techniques.

4.2 Results

4.2.1 Puromycin kill curve for PC3 cells

To explore the role of the selected candidates on EV biogenesis, transport and release, a range of PC3-cell variants with attenuated candidate gene expression were generated. For this purpose, MISSION® shRNA lentiviral particles (Sigma-Aldrich) containing a puromycin resistance gene for selection, were commissioned, and transduction conditions previously optimised in earlier studies handling other MISSION® lentiviral particles were used.

To determine the optimal puromycin concentration in PC3 cells, a WST-8 based (Orangu™) cell proliferation assay, was performed, in the presence of escalating puromycin doses up to 10 µg/ml. PC3 cells were seeded at different densities (2,000 cells/well, 5,000 cells/ well and 10,000 cells/well) to ascertain the optimal cell densities (Figure 4.1).

The number of proliferating PC3 cells was sharply reduced at a puromycin concentration of 0.5 µg/ml and higher. At intermediate or high seeding densities, the cells were hyperconfluent by 72 h, and this had attenuated the general proliferation independent of puromycin dose, giving a comparatively reduced absorbance value at 0 ug/ml. Nevertheless, seeding at low density provided a clear and unambiguous effect of puromycin, with a complete kill achieved at 0.5 ug/ml. Based on these results, we decided to use a puromycin concentration of 1 µg/ml for the transductions. This allowed us to be confident in the survival of transduced cells despite variation between experiments, e.g., differences in cell distribution.

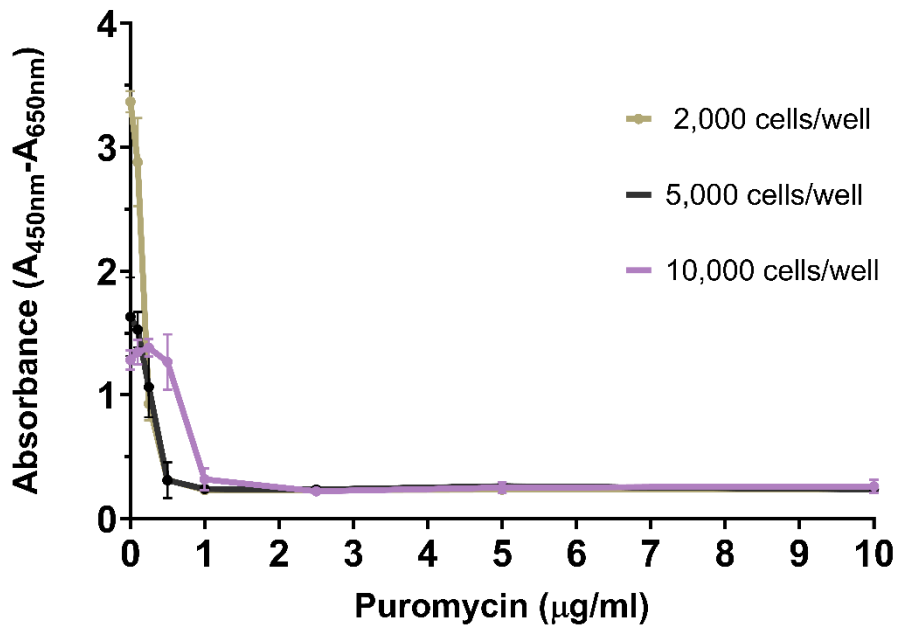


Figure 4.1: Puromycin kill curve for PC3 cells.

PC3 cells were seeded at the indicated densities and treated with puromycin concentrations (0 µg/ml – 10 µg/ml). After 72 h. the cells were incubated for 1.5 h with WST-8. The formation of formazan was detected with a PHERAstar FS Microplate Reader measuring the absorbance at 450 nm. The background was measured at 655 nm and subtracted. Symbols represent mean +/- SD, based on 5 replicate wells

4.2.2 Targeted attenuation of EV regulators

Next, PC3 cells were transduced with Mission® lentiviral particles with shRNA sequences listed in table 2.2 at a MOI of 20. For each target, 5 different shRNA sequences were used, to maximise the chances of a successful attenuation. The exceptions to this were for CD9 and Rab35, in which an shRNA sequences had been previously validated as effective in our lab (Yeung et al., 2018). A shRNA sequence targeting a non-mammalian target was also included as a control (NMC), under identical conditions. This cell variant would be the benchmark comparator for the specific shRNA targets. In total, the number of transductions performed was 79. The newly generated cell variants were handled in line with safety guidelines (local project reference: GM130/634) stipulated by the Cardiff University genetically modified organism (GMO) committee until passage 6 at which stage the cell variants were considered lentiviral free and deemed suitable for further analysis without strict containment.

The magnitude of mRNA attenuation was assessed by qPCR using TaqMan Gene expression assays. The Delta Delta Ct method was used to quantify the difference in expression between candidate mRNA and the NMC. The housekeeping gene GAPDH served as a control because this was previously evaluated in our lab and confirmed as unaltered by MISSION® lentiviral transductions.

In the candidates likely representing EV biogenesis, the shRNA sequence targeting CD9 showed a mRNA KD of 80%, which was pleasing as we had only one shRNA sequence for this target. The magnitude of effect was similar to a past study with the same lentiviral particles but utilised on DU145 cells (Yeung et al., 2018) (Figure 4.2A). Targeting CD81 was also highly successful with mRNA attenuation ranging from 82%-91% for 4 (of 5) sequences (Figure 4.2B). Disappointingly, when targeting CHMP4C we achieved a significant yet modest reduction of mRNA expression of 53% with only one sequence (Figure 4.2C). For SCAMP3, a highly variable KD between 32%-70% for 3 (of 5) sequences was achieved (Figure 4.2D). For VPS28 the magnitude of KD ranged between 69% and 57% for 2 (of 5) shRNA sequences (Figure 4.2E). However, the 3 other shRNA sequences resulted in poor attachment and poor cell proliferation, indicating potential presence of some off target effects, or highlighting the sensitivity of the cells to VPS28 deficiency leading to some toxic effects. These data are summarised in Figure 4.2.

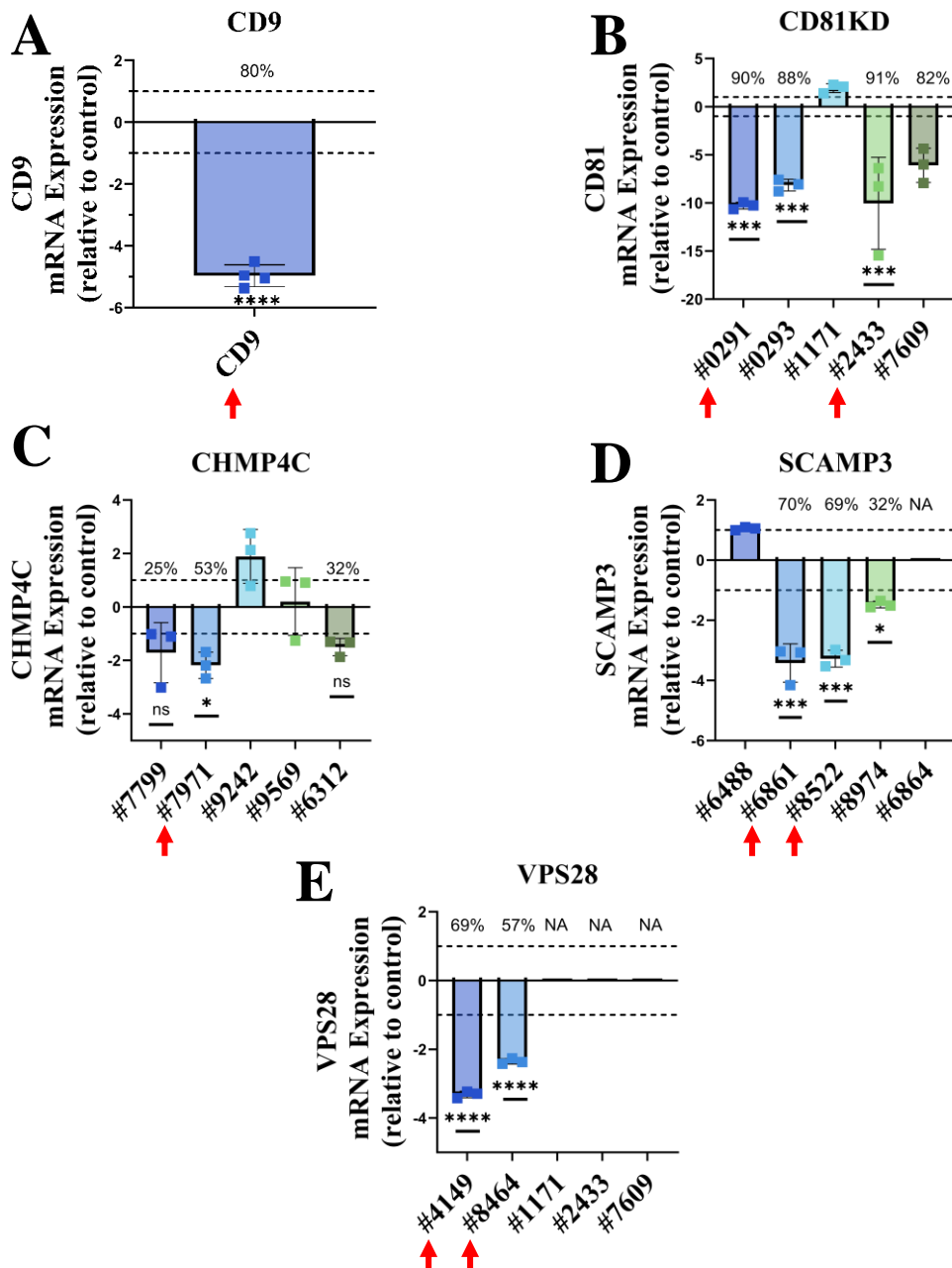


Figure 4.2: Validation of candidate mRNA attenuation by TaqMan Gene Expression assays.

PC3 cells were transduced with MISSION® shRNA lentiviral particles targeting the indicated candidates. Relative mRNA expression levels of the candidates were assessed by TaqMan gene expression assays (qPCR). The ct-values were normalized to GAPDH and compared to the mRNA levels in PC3 cells transduced with NMC viral particles. Candidates likely involved in EV biogenesis were assessed: CD9 (A), CD81 (B), CHMP4C (C), SCAMP3 (D) and VPS28 (E). The bar chart shows the mean +/- SD of 3 technical replicates. NA= non applicable. % downregulation is indicated above the bars. Red arrows indicate selected KDs for further analysis. One-way ANOVA with Dunnett's multiple comparison post-hoc test was performed. ns = non-significant, * = $P < 0.05$, ** = $P < 0.01$, *** = $P < 0.001$, **** = $P < 0.0001$.

In the RabGTPase group, likely representing intracellular membrane trafficking, the shRNA sequence targeting these were broadly very successful, with at least one shRNA sequence providing confident statistically significant attenuation of >75% KD (Figure 4.3). For example, Rab6A showed a mRNA KD between 37% and 82% (Figure 4.3A), and similarly for the other candidates: Rab7a (60%-91%), Rab11b (51%-82%), Rab27b (23%- 75%) and Rab35 (15%-77%) (Figure 4.3B-E).

For candidates likely representing the fusion of MVE to the plasma membrane the shRNA sequences also showed some variability in the magnitude of KD such as PCLO, for which only a modest reduction of mRNA expression between 31%- 47% with 4 shRNA sequences was achieved (Figure 4.4A). Further target attenuation was achieved for SNAP23 (63% and 84%), SYNGR2 (24%-78%) and VAMP3 (44%-93%) (Figure 4.4B and D-E). The attenuation of the target was not successful for all tested sequences as shown for 5 different sequences targeting STX6, which did not achieve a significant KD (Figure 4.4C). The mRNA levels for Rab37 and LITAF were also not detectable, even in the control cells (data not shown), and hence demonstrating attenuation was not possible.

Taken together, these data reveal some heterogeneity in the efficacy of KD with good success for several factors regulating EV biogenesis (CD9, CD81, VPS28, CHMP4C, SCAMP3) (Figure 4.2) and release (SNAP23, VAMP3, PCLO, SYNGR2) (Figure 4.4) and transport (Rab6a, Rab7a, Rab11b, Rab27b, Rab35) (Figure 4.3) was achieved. Attenuation of LITAF and Rab37 could not be confirmed by the TaqMan assays used here. Additionally, significant downregulation of STX6 mRNA was not successful (Figure 4.4C). At this stage, it was important to narrow down the large number of cell variants for further analysis to allow a detailed exploration of the impact of target attenuation. Hence, based on these results it was reasonable at this point to exclude STX6, LITAF and Rab37 from further exploration. CD9KD, CD81KD (#0291 and #2433), CHMP4CKD (#7971), Rab6aKD (#9588 and #7983), Rab7aKD (#0577 and #9642), Rab11bKD (#0618 and #1919), Rab27bKD (#4016 and #3978), Rab35KD (#0003 and #0335), PCLOKD (#6484 and #6485), SCAMP3KD (#6861 and #8522), VAMP3KD (#0472 and #0915), VPS28 (#4149 and #8464) were chosen for future experiments, based on the strong downregulation of mRNA and no obvious issues with the general attachment/viability of the transduced cells was observed.

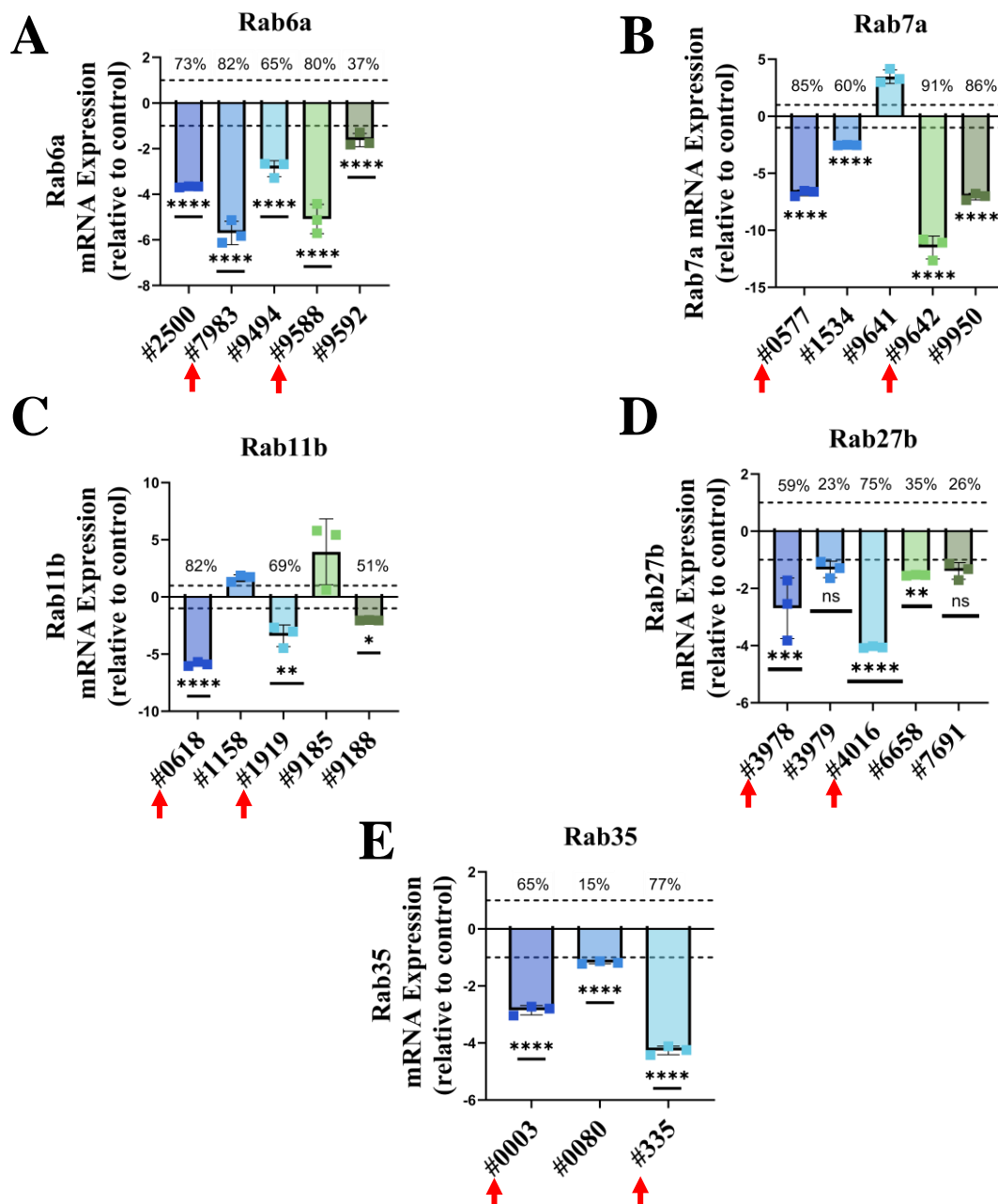


Figure 4.3: Validating the attenuation of candidates likely involved in intracellular vesicle transport by TaqMan Gene Expression assays.

PC3 cells were transduced with MISSION® shRNA lentiviral particles targeting the indicated candidates. Relative mRNA expression levels of the candidates were assessed by TaqMan gene expression assays (qPCR). The ct-values were normalized to GAPDH and compared to the mRNA levels in PC3 cells transduced with NMC viral particles. Candidates likely involved in intracellular EV transport were assessed: Rab6a (A), Rab7a (B), Rab11b (C), Rab27b (D) and Rab35 (E). The bar chart shows the mean \pm SD of 3 technical replicates. % downregulation is indicated above the bars. Red arrows point out clones that were selected for further analysis. One-way ANOVA with Dunnett's multiple comparison post-hoc test was performed and ns= non-significant, * = $P < 0.05$, ** = $P < 0.01$, *** = $P < 0.001$, **** = $P < 0.0001$.

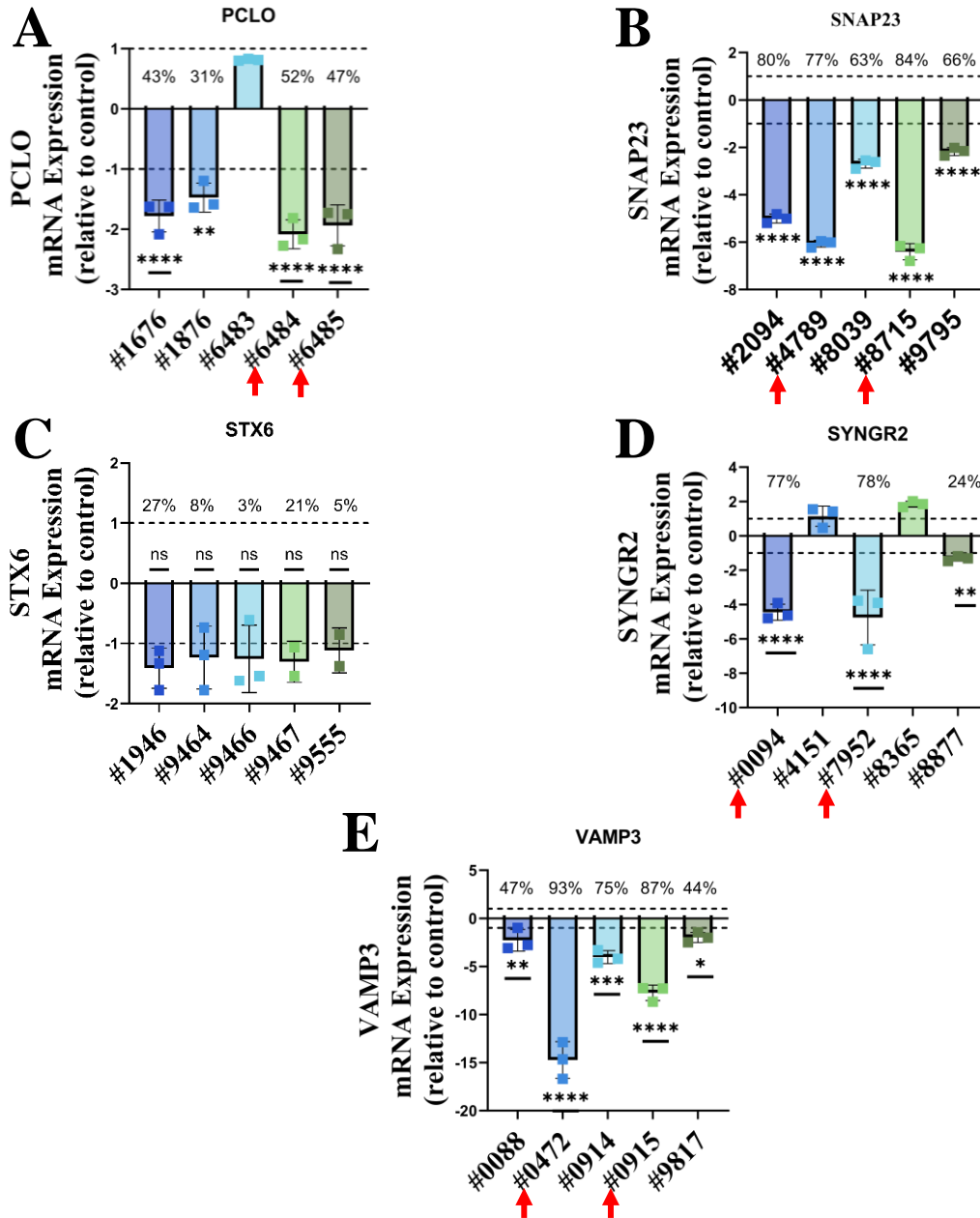


Figure 4.4: Validating the attenuation of candidates likely involved in vesicle release by TaqMan Gene Expression assays.

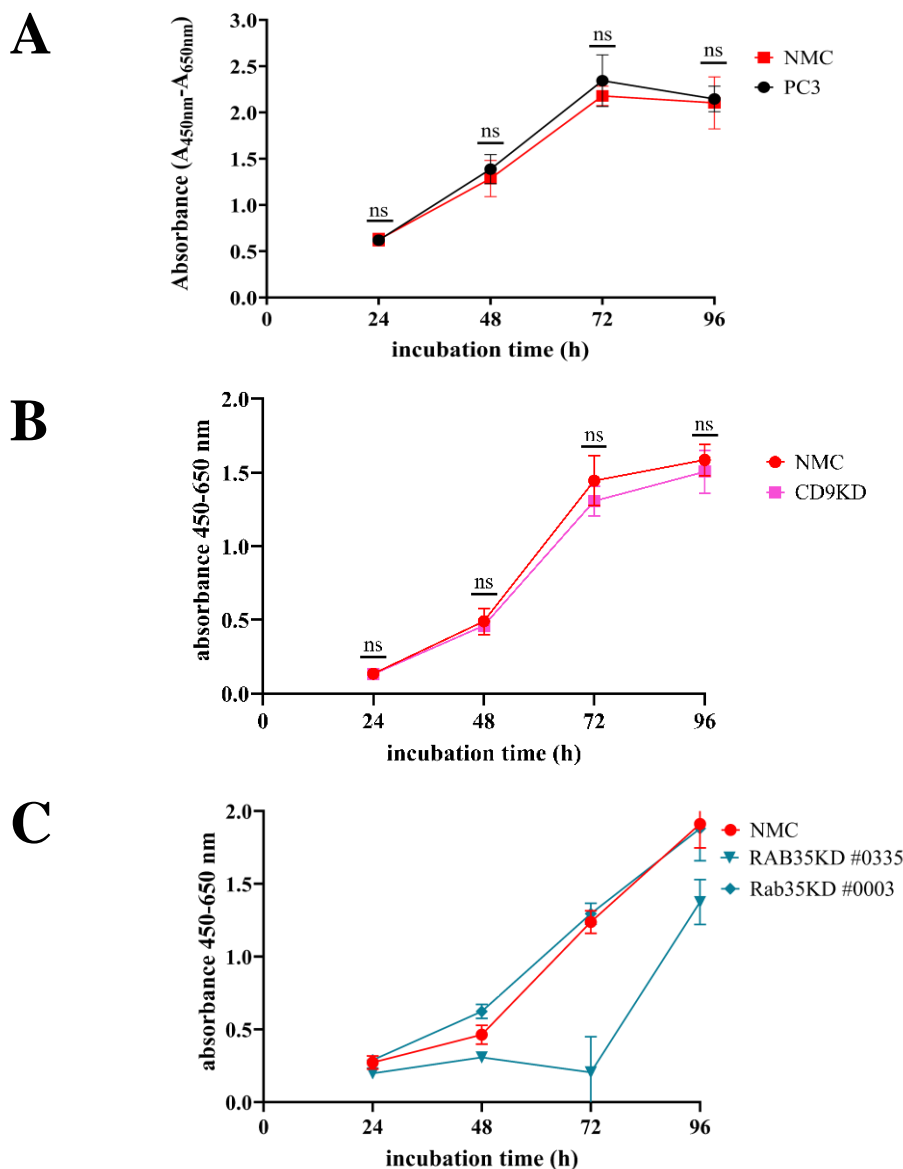
PC3 cells were transduced with MISSION® shRNA lentiviral particles targeting the indicated candidates. Relative mRNA expression levels of the candidates were assessed by TaqMan gene expression assays (qPCR). The ct-values were normalized to GAPDH and compared to the mRNA levels in PC3 cells transduced with NMC viral particles. Candidates likely involved in EV biogenesis were assessed: PCLO (A), SNAP23 (B), STX6 (C), SYNGR2 (D) and VAMP3 (E). The bar chart shows the mean +/-SD of 3 technical replicates. % downregulation is indicated above the bars. Red arrows point out clones that were selected for further analysis. One-way ANOVA with Dunnett's multiple comparison post-hoc test was performed. ns= non-significant, * = P<0.05, ** = P< 0.01, *** = P<0.001, **** = P<0.0001.

4.2.3 The Impact of candidate attenuation on cell proliferation

On occasion, interfering with a particular transcript may cause significant perturbation to the cells in their capacity to operate major biological processes, causing attenuation of attachment and proliferation, or leading to a promotion of cell death. Because the roles of the targeted transcripts are not fully understood, these arguably unwanted effects may indeed be due to the activities of the loss of target expression. Alternatively, such effects may instead be associated with unknown off target impacts of the transduction. Before moving ahead to evaluate the effect of KDs on EVs, it was important to consider the KD from a general cell-health perspective. Given the repertoire of cell variants, we considered cell proliferation as a good measurement of this, where any significant deviation from the non-transduced wild-type cells would raise concerns.

This was assessed by performing a colorimetric WST-8 assay, in a similar fashion to the puromycin kill curve, in order to ascertain the potential toxicities associated with the KD. First, to compare the wildtype PC3 cells and the NMC cells both cell variants were seeded at identical densities on the same plate. At specified time points up to 96 h, the WST-8 assay was performed, and absorbance values (proportional to the number of living cells per well) were compared (Figure 4.5A). Across all time points measured here, the formation of formazan, and hence the cell number, were similar for wildtype PC3 cells and NMC cells. Therefore, the NMC cells were considered as a suitable control, because viability was not impacted by transduction using an irrelevant shRNA-sequence.

As an example of such investigation for a KD cell variant, the impact of CD9 attenuation on cell viability was explored (Figure 4.5B). In this cell line CD9 mRNA levels were downregulated by 80% and this was very well tolerated as we did not see significantly reduced cell numbers compared to the NMC over the time span tested here. Consequently, we did not have any toxicity concerns for this cell variant.



NMC vs	24 h	48 h	72 h	96 h
Rab35KD (#0335)	*	**	***	***
Rab35KD (#0003)	ns	**	ns	ns

Figure 4.5: Impact of shRNA transductions on cell proliferation in PC3 cells.

A) NMC cells and PC3 cells, (B) NMC cells and CD9KD cells and (C) NMC cells and Rab35KD cells (clones #0335 and #0003) were seeded at 4,000 cells/well in a 96-well plate. Cells were incubated with WST-8 at specified time points up to 96 h after seeding. The formation of formazan was detected with a PHERAstar FS Microplate Reader measuring the absorbance at 450 nm. The background was measured at 650 nm and subtracted. Symbols represent mean +/- SD, based on cells in 6 wells. A 2-Way-ANOVA with Tukey's as post-hoc test was performed and ns= non-significant, * = $P < 0.05$, ** = $P < 0.01$, *** = $P < 0.001$, **** = $P < 0.0001$.

Another example for such exploration is shown for Rab35 in figure 4.5C. It was previously validated in our lab that the attenuation of Rab35 does not have a detrimental impact on cell proliferation in a PCa cell line (DU145). Using the same shRNA sequences for the attenuation of Rab35 in PC3 cells, we found KD of Rab35 had either a severe (clone# 0335) or no (clone #0003) impact on cell proliferation. These results prompted us to exclude clone #0335 from our study.

The impact of target attenuation was investigated for all selected candidates in this fashion and is summarised in table 4.1. Clones with significantly downregulated cell proliferation on more than two timepoints compared to the NMC cells posed serious toxicity concerns and hence were excluded from further evaluation (Rab7aKD (clone #0577), Rab11bKD (clone #1919, clone #0618), Rab35KD (clone #0335), SCAMP3KD (clone #8522), SYNGR2 (clone #7952) and VPS28KD (clone #8464)). Clones which showed reduced cell proliferation at one time point but recovered to normal levels afterwards were not considered a major concern in regard to their cell toxicity and considered for further evaluation. In cases, where both clones did not raise toxicity concerns, the clone with the lower expression of the candidate gene was selected for further evaluation.

Applying these criteria, for the majority of candidates, we were able to select one clone that had significant target attenuation and lacked a detrimental impact on cell proliferation: CD9KD, CD81KD clone #2433, CHMP4CKD clone #7971, Rab6aKD clone #9488, Rab7aKD clone #9642, Rab27bKD clone #4016, Rab35KD clone #0003, PCLOKD clone #6484, SCAMP3KD clone #6861, SYNGR2KD clone #0094, SNAP23KD clone #8715, VAMP3KD clone #0472 and VPS28KD clone#4149. The selection of clones covered candidates in groups likely representing EV biogenesis, Rab GTPases and EV release representing various molecular machineries and thus we expected to observe a range of EV impact in regard to quantity and molecular composition. Importantly, narrowing down the candidate list allowed a first exploration of the potential role of the selected candidates on EV secretion and molecular composition.

Table 4.1: Impact of candidate attenuation in PC3 cells on cell proliferation.

Cells were seeded at 4,000 cells/well in a 96-well plate and incubated with WST-8 at specified time points up to 96 h after seeding. The formation of formazan was detected with a PHERAstar FS Microplate Reader measuring the absorbance at 450 nm. The background was measured at 650 nm and subtracted. Cell proliferation for the indicated KD was compared to the NMC cells based on cells in 6 wells. 2-Way-ANOVA with Tukey's as post-hoc test was performed. ns= non-significant, * = P< 0.05, ** = P< 0.01, *** = P<0.001, **** = P<0.0001.

NMC compared to	24 h	48 h	72 h	96 h	Toxicity concern	Included in further analysis
CD9KD	ns	ns	ns	ns	No	Yes
CD81KD (#0291)	ns	**	ns	ns	No	No
CD8KD (#2433)	ns	ns	*	ns	No	Yes
CHMP4CKD (#7971)	ns	ns	*	ns	No	Yes
Rab6aKD (#9488)	ns	ns	ns	ns	No	Yes
Rab6aKD (#7984)	ns	*	ns	ns	No	No
Rab7aKD (#0577)	ns	**	ns	**	Yes	No
Rab7aKD (#9642)	ns	ns	ns	ns	No	Yes
Rab11bKD (#0618)	**	***	ns	ns	Yes	No
Rab11bKD (#1919)	*	ns	*	***	Yes	No
Rab27bKD (#3978)	ns	ns	**	ns	No	No
Rab27bKD (#4016)	ns	ns	*	ns	Yes	Yes
Rab35KD (#0335)	*	**	***	***	Yes	No
Rab35KD (#0003)	ns	**	ns	ns	No	Yes
PCLOKD (#6484)	ns	ns	ns	ns	No	Yes
PCLOKD (#6485)	ns	ns	ns	ns	No	No
SCAMP3KD (#6861)	ns	ns	ns	*	No	Yes
SCAMP3KD (#8522)	ns	**	***	ns	Yes	No
SYNGR2KD (#7952)	**	*	ns	ns	Yes	No
SYNGR2KD (#0094)	**	ns	ns	ns	No	Yes
SNAP23KD (#4789)	ns	**	ns	ns	No	No
SNAP23KD (#8715)	ns	**	ns	ns	No	Yes
VAMP3KD (#0472)	ns	ns	***	ns	No	Yes
VAMP3KD (#0915)	ns	ns	***	ns	No	No
VPS28KD (#4149)	ns	**	ns	ns	No	Yes
VPS28KD (#8464)	ns	***	**	*	Yes	No

4.2.4 The impact of putative EV regulators on EV secretion

We next wanted to explore whether or not there was an attenuation of EV release in the KD cells. This represented a first-pass exploration, given the large number of candidates to be evaluated. It was later intended that there would be some further attrition and a simplification of the repertoire of candidates, which would allow for confirmatory analysis to be undertaken on a fewer number of cell line variants.

For the first pass, we evaluated a single (strongest KD) shRNA sequence for CD9, CD81, CHMP4C, Rab6a, Rab7a, Rab27b, Rab35, PCLO, SCAMP3, SYNGR2, SNAP23, VAMP3 and VPS28. Cells were seeded at equal cell densities and grown in media containing EV-depleted FBS until the cell monolayer reached 80%. Subsequently, the media was replaced with FBS free media and following 72 h of incubation cell CM was harvested for EV analysis. Cell counts were performed at CM harvesting time-points and this data was used to correct for small differences in cell numbers, which may otherwise explain differences in EV quantities. Hence, data presented here are articulated as particles per cell. The number and size distribution of nanosized particles in the CM was determined using the Nanosight™ NTA platform.

Comparing biological replicates of two different CM collections from the NMC cells, the difference in the number of particles per cell (data not shown) (17,366 vs 9,343 particles/cell) was very high, although experimental conditions were kept as identical as possible. One explanation for the observed differences is slightly different seeding densities. Another more likely issue, however, is the day-to-day variation which we often encounter when making measurements on the NTA platform. This may be an issue with the platform itself or related to pipetting errors when making large dilutions.

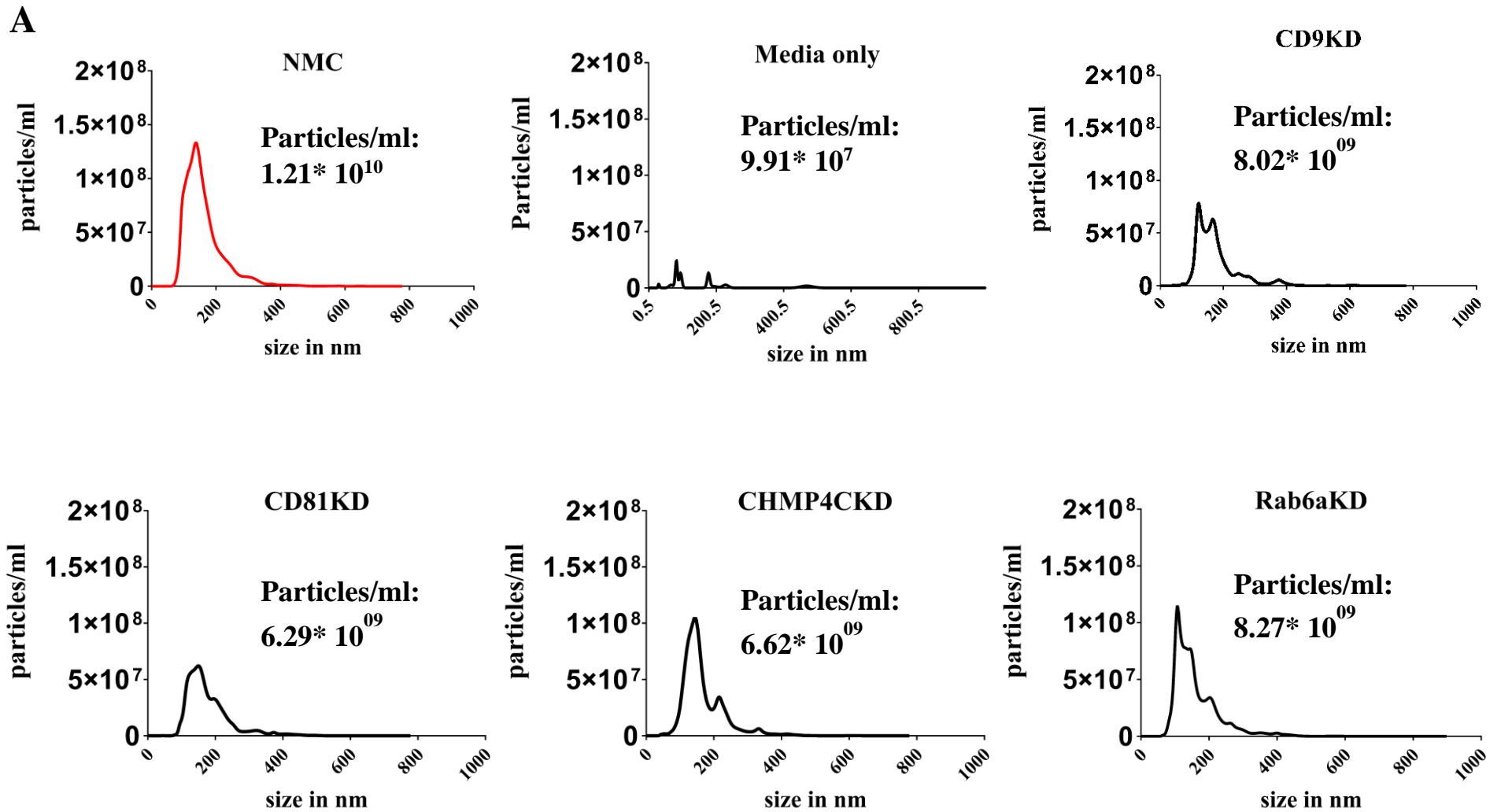
The size distribution histograms were broadly similar, irrespective of the KD, revealing a polydisperse population of nano-particulates with a mode between 100 and 200 nm, together with a typical shoulder of 250-400 nm which may reflect large vesicles, or some aggregated material (Figure 4.6A). Importantly, the media only control, lacking exposure to cells, showed

more than 100-fold fewer particles/ml than the NMC CM, thus most particles in the CM are cell derived (Figure 4.6A).

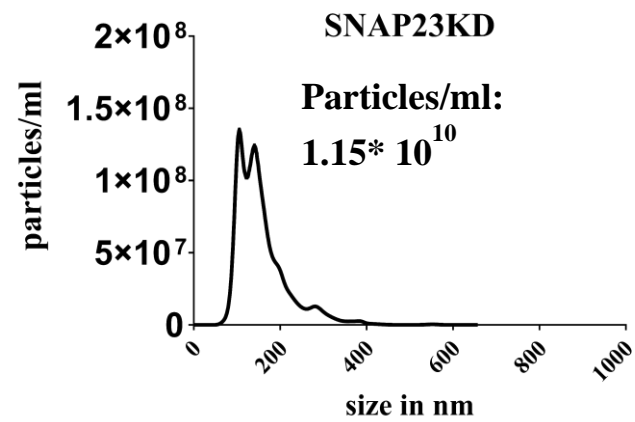
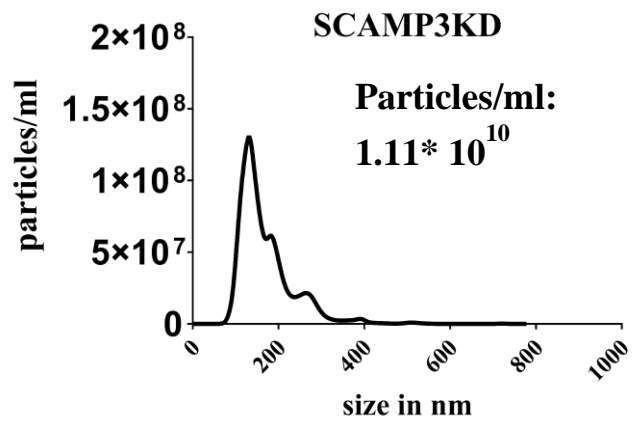
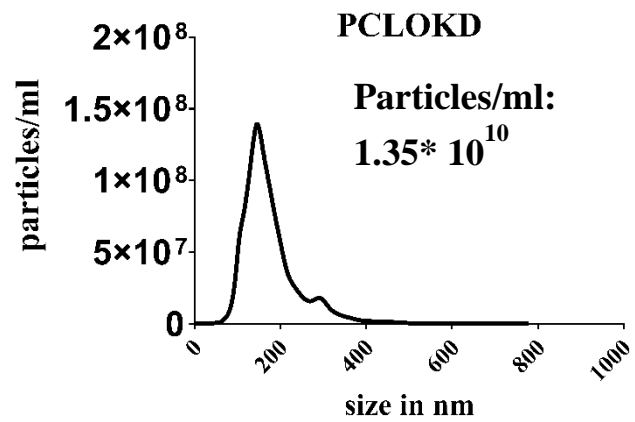
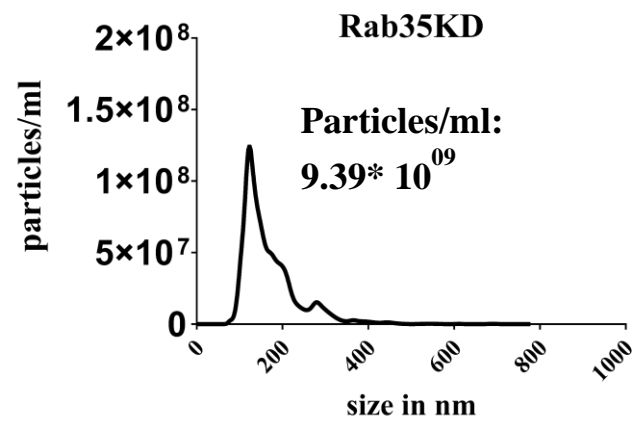
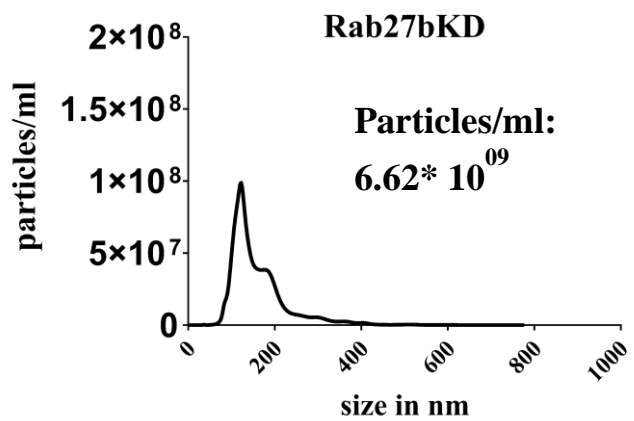
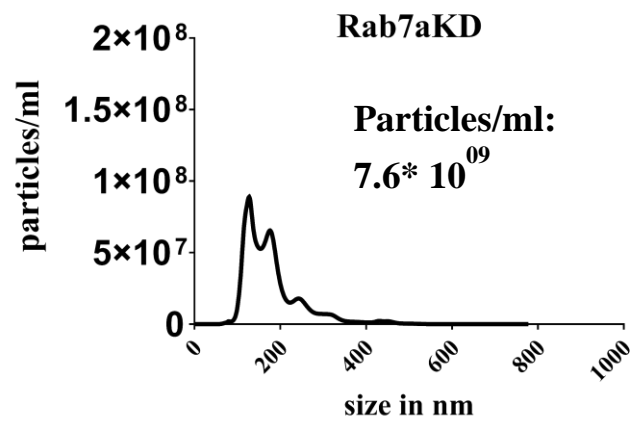
Across the repertoire of PC3-variants, there were no significant differences in the particles/cell ratio. The measurements were largely within the variation of repeat measures of the NMC sample (Figure 4.6B, dotted line), suggesting little to no impact on the capacity of the cells to generate and secrete EVs. There was a modest impact for the VPS28KD cells although our confidence that this is a real finding is low as the replicates were highly variable (Figure.4.6B).

The mean particle size in the CM from the NMC cell variant ranged from 159 nm to 179 nm across two biological replicates (Figure 4.6C). The mean particle size in the CM collected from all of the cell line variants was similar (Figure 4.6C), and within this range of variance. Again, indicating that there was no measurable change in the proportion of small versus large particles in the system following target attenuation.

Overall, these data were very surprising, and not at all what was expected based on our groups past experience using the DU145 cell line (Yeung et al., 2018). It is striking that even with a significant target attenuation of >80% no major impact on the number of released EVs was detected. In particular, for Rab35 attenuation in the DU145 caused a reduction in the number of EVs by 20% (Yeung et al., 2018) which was not observed in the PC3 cells tested here. This points to a highly cell line specific impact of the candidates and could perhaps be due to aggressive nature of the PC3 cell line compared to the DU145 cell line.



continued on the next page



continued on the next page

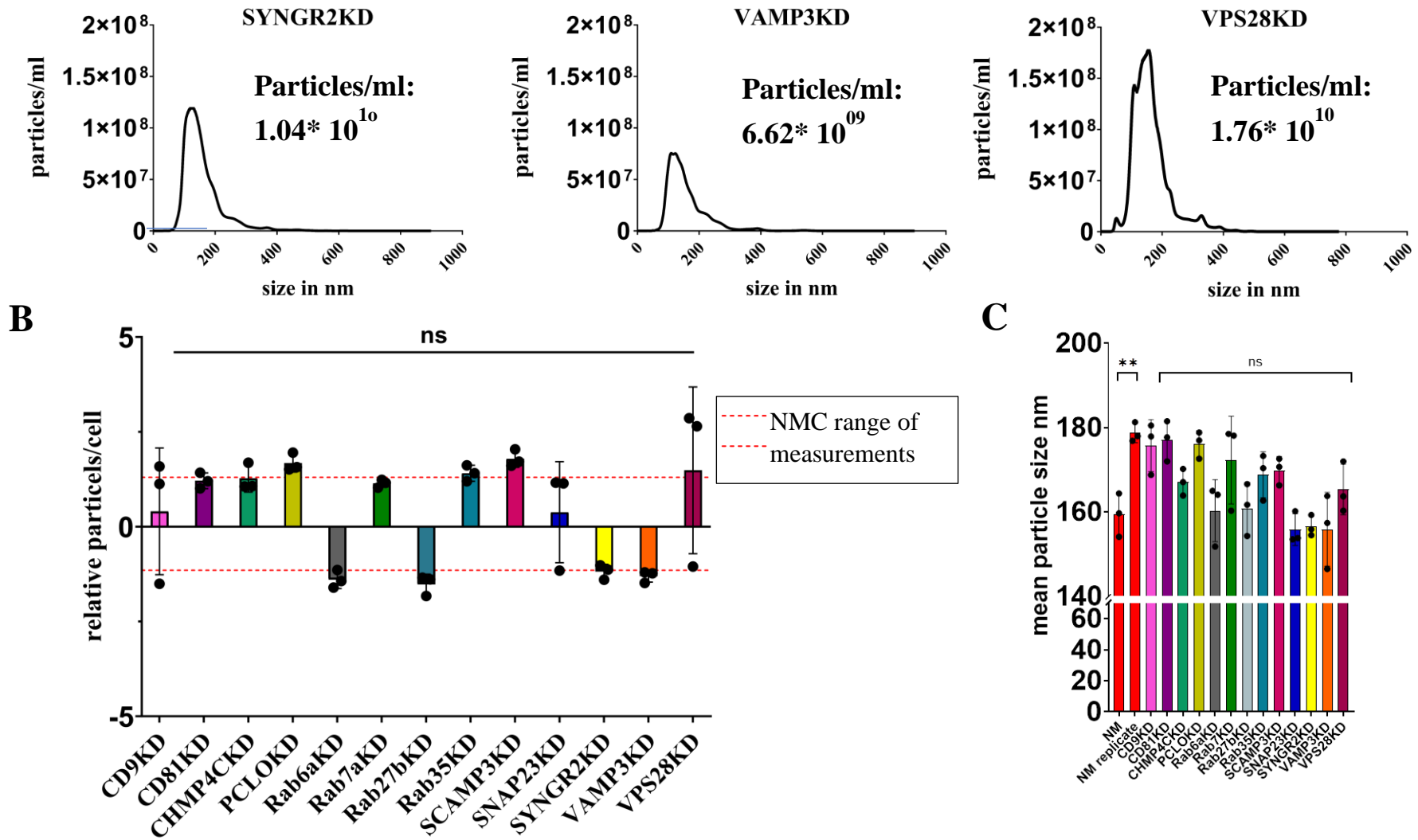


Figure 4.6: Characterising vesicles from lentiviral transduced PC3 cell CM by NTA.

The particles in the cell CM of the indicated KD cell lines were analysed using NTA revealing the overall size distribution of the CM samples. A) Measurements for NMC are highlighted in red. Graphs show the mean of 9 videos obtained from 3-measurments for each of 3 technical replicates. The particle number was normalised to the cell number and the number of background particles in filtered media was subtracted from the measurements. The relative vesicles/cell compared to the NMC was calculated B). Graph C) shows mean size +/- SD, One-way ANOVA with Dunnett's multiple comparison post-hoc test was performed was performed. ns = non-significant.

4.2.5 The impact of putative EV regulators on the molecular features of EVs

4.2.5.1 Quantifying and Immunophenotyping of EV populations by EVQuant

The issues surrounding the reliability of NTA as a measure of vesicles, prompted us to validate the findings using an independent orthogonal method. EVQuant is a microscopy-based technique, developed by consortium partner Dr Martin van Royan, Erasmus Medical Centre, Rotterdam. Using this method, EVs are fluorescently labelled with a lipid-incorporating dye (Rhodamine) prior to being immobilised in an acrylamide gel in specialist 96-well imaging plates. The EVs are thereafter visualised by confocal microscopy, and fluorescence-events present in a single optical plane are counted. In addition, using different tetraspanin specific antibodies, that are directly conjugated with compatible fluorophores allows to quantify the distribution of EV subpopulations based on their tetraspanin expression in one sample (Figure 4.7) (Hartjes et al., 2020). This approach therefore has the capability of nanoparticle counting combined with immuno-labelling detection for EV phenotyping.

To minimise the impact of sample-to-sample variation, the same samples as used for the NTA analysis were also used for the EVQuant analysis. All CM samples (CD9KD, CD81KD, CHMP4CKD, Rab6aKD, Rab7aKD, Rab27bKD, Rab35KD, PCLOKD, SCAMP3KD, SYNGR2KD, SNAP23KD, VAMP3KD and VPS28KD) were processed on the same imaging plate and indicated that the overall number of detected particles in the EVQuant assay was lower (5,800- 8,000 detected particles/ml) compared to the detected particles by NTA (1,800- 12,000 particles/ml). This is likely because of the increased specificity of the EVQuant to detect lipid-containing nanoparticles, when compared to the NTA which cannot discriminate a true vesicle from a solid-aggregate of protein.

As previously done for the assessment of particles/cell by NTA, the particles measured by EVQuant were corrected for cell numbers. The results revealed no major changes in the number of EVs/cell upon attenuation of the candidate RNA compared to the NMC and thus so confirming the NTA results in terms of the lack of change in secreted EVs (Figure 4.7B).

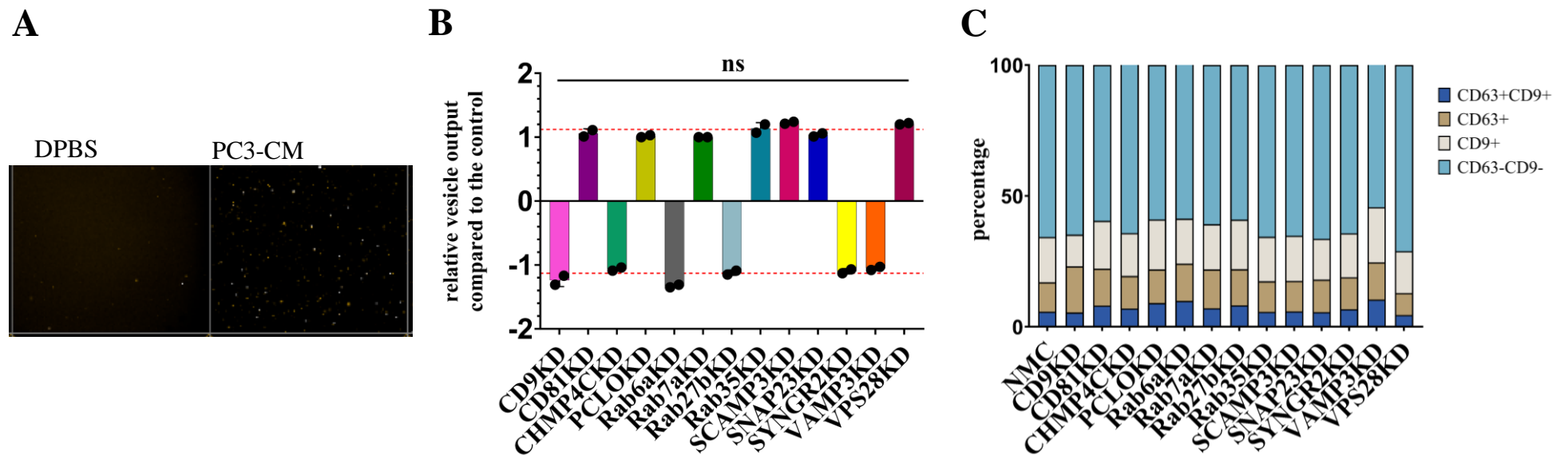


Figure 4.7: Characterising vesicles from lentiviral transduced PC3 CM by EVQuant.

Representative images of the EVQuant assay showing background particles in DPBS (left) and in PC3 CM (right) stained with the membrane dye Rhodamine (A). CM of the KD cell lines were analysed by EVQuant in duplicate. The concentration of EVs was normalized to the cell number. Red dotted lines represent the range of vesicle output compared to the NMC cells (B). The composition of the EV populations (CD9+, CD63+, CD63-CD9- and CD63+CD9 positive EVs) were determined by an overlap of the Rhodamine staining and the indicated tetraspanin staining (anti-CD9 Alexa Fluor® 647C and anti-CD63 Alexa Fluor® 488 antibody). Images were captured using the Opera Phenix, Perkin Elmer. Mean of the duplicates \pm SD is shown. One-way ANOVA with Dunnett's multiple comparison post-hoc test was performed. ns= non-significant.

These findings in which independent methods have been performed on the same samples, suggest that the efforts to attenuate EV secretion have largely failed in terms of impacting the gross quantity of vesicles. It remains possible however, that there may be some minor changes in vesicle expulsion which are below the detection sensitivities of these methods, and hence not detectable.

Simultaneously to providing a quantification of the number of particles, the EVQuant assay also provides insights into the relative proportions of different tetraspanin positive EV subpopulations. Initially, we planned to include CD81 in the exploration of tetraspanins. Unfortunately, the suitable antibody was not available due to severe delivery delays caused by the COVID-19 pandemic and hence, we opted for the pre-established antibody combination of CD9 and CD63. For this purpose, fluorescently labelled anti-CD9 and anti-CD63 antibodies were added to the CM samples and the distribution of CD9, CD63 single positive, double positive, and double negative EVs microscopically determined.

Compared to the CM from the NMC cells, there were no dramatic differences in the distribution of CD63CD9 double negative, CD63CD9 double positive, CD9 positive and CD63 positive population arising from any of the new PC3 cell variants generated (Fig 4.7C). Since one of the chosen targets for attenuation was CD9, we had expected to see a sizeable reduction in detectable levels of CD9 positive EVs from these cells. Rather surprisingly the analysis by EVQuant failed to show any major difference in the proportion of CD9 positive EVs secreted from the CD9-deficient PC3 cells. However, EVQuant only differentiates between positive and negative expression of a specific tetraspanin, based on carefully considered thresholds as discussed in the manuscript detailing these matters (Hartjes et al., 2020). This is a binary positive/negative readout therefore we can't currently assess the ligand density per vesicle. Despite this limitation, we can state that the overall proportion of the tetraspanins CD9 and CD63 across the population of EVs are generally static, irrespective of the candidate KD.

4.2.5.1 Immunophenotyping EVs using a microplate assay

To further explore relative changes of tetraspanin expression on EVs from the PC3 cell variants we used an immuno-affinity plate-based assay for bulk EV detection previously established within our group (Welton et al. 2016, Webber et al. 2016). Different configurations of the assay were used to detect CD81 and CD9 in CM derived from the cell variants (Figure 4.8). With this assay system we note that the output reflects an average bulk-population metric rather than a proportional measure reflecting vesicle subsets.

To assess levels of tetraspanin-positive vesicles across the repertoire of cell variants the collected CM of these cells was normalised to 700,000 cells/ml (cCM), prior to immuno-affinity-based analysis. This was to allow relative comparisons to be made, by correcting for possible differences in overall cell number.

CD81 levels in the cCM samples were assessed using a CD81 antibody to catch the vesicles and a biotinylated CD81 antibody to detect the vesicles (Figure 4.8A). cCM collected from the SYNGR2KD cells showed a significant ($P < 0.001$) decrease in the signal for CD81 compared to NMC, suggesting a decrease in the number of CD81 positive vesicles in the population, or a decrease in the levels of CD81 present on vesicles within the population. Within this assay, we expected to see a dramatic reduction of CD81 signal when examining the CD81KD sample. Indeed, there was a drastically reduced signal for CD81 here, which indicates that this mRNA attenuation led to a negative impact on cellular and thereafter vesicular CD81 protein. It also validates the assay system as suitable to detect changes in CD81 positive vesicles.

Next, a variation of the assay was used, combining a CD9 antibody to catch the vesicles and a biotinylated CD9 antibody to detect the vesicles (Figure 4.8B). The detected fluorescent intensity was lower compared to the fluorescent intensity detected for CD81. This could be due a lower affinity of the CD9 antibody compared to the CD81 antibody used in this assay, or lower general levels of CD9 in the vesicle population. Nevertheless, there was a clear indication of reduced signal for CD9 when testing the CD9KD sample as we would expect. Most candidates tested here did not appear to have an impact on the CD9 signal.

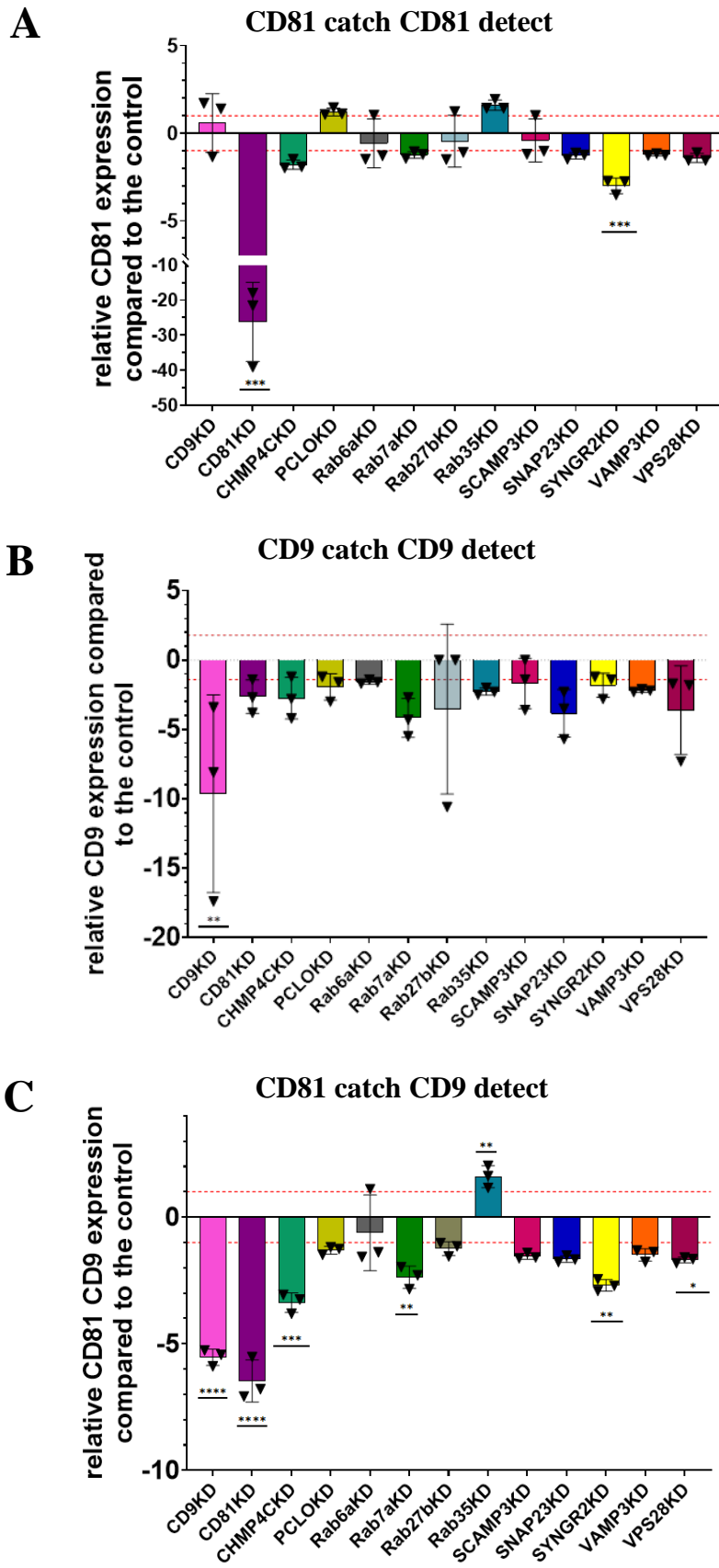


Figure 4.8: Characterising tetraspanin positive vesicle populations using an immunofluorescence plate-based assay.

Cell CM was collected from the indicated KD cell variants. The cell CM was normalised to 700,000 cells/ml before addition to the wells of an ELISA strip plate. A CD81 antibody was used to catch the vesicles and a biotinylated CD81 antibody was used to detect the vesicles (A). A CD9 antibody was used to catch the vesicles and a biotinylated CD9 antibody was used to detect the vesicles (B). A CD81 antibody was used to catch the vesicles and a biotinylated CD9 antibody was used to detect the vesicles (C). Europium:streptavidin conjugate was used as a fluorescent reporter. Graph shows mean of triplicate wells. Red dotted lines represent the range of detection for the NMC cell variant. 1-way ANOVA with Dunnett's multiple comparison post-hoc test was performed. ns= non-significant, * = $P < 0.05$, ** = $P < 0.01$, *** = $P < 0.001$, **** = $P < 0.0001$.

Another configuration of the assay was used, exploring a CD81 antibody to catch the vesicles, followed by detection using a CD9 biotinylated antibody (Figure 4.8C). In this arrangement several KDs showed changes in the signal. Again, regarding SYNGR2KD, there was a significant decrease in the signal ($P < 0.001$). There was also a significant reduction in the signal for VPS28KD, CHMP4CKD, and Rab7aKD. The biggest signal loss was seen with either the CD9KD or CD81KD cells respectively, again consistent with the assay specificity being as expected. Unexpectedly, CM from Rab35KD cells appeared to give an increased signal for this configuration (CD81 catch/CD9 detect). This contrasts with previous observations of the consequences of Rab35 attenuation in PCa cells (Yeung et al., 2018), albeit on a different cell line.

The results of the various catch detect assay performed (CD9CD9, CD81CD81, CD81CD9 and CD81CD63) are summarised in table 4.2. An important point to consider when interpreting these combined results is that in the previous section (4.2.4) the quantity of EVs was similar across all cell variants. Taken, the EVQuant results into consideration as well, no changes in the distribution of CD63 CD9 single and double positive subpopulations were observed. Hence, changes in the relative expression of CD9 detected by immunophenotyping is likely a reflection of changes in the composition of EVs and not due to a decreased EV quantity. Clearly, variations in the expression levels of tetraspanins on single EVs requires further validation for instance by utilising super resolution microscopy.

The goal of the characterisations performed (NTA, EVQuant, immunophenotyping) was to identify the most promising candidates in regard to potential impact on modulating EV quantities and molecular features and to subsequently use these results as an attrition step to narrow down the candidate list and allowing a detailed characterisation of the selected candidates. Given that we did not observe any changes in the EV output, the rather complex immunophenotyping assays were used to narrow down the candidate list.

The CM from the CD9KD, CD81KD and SYNGR2KD cells were the only samples that appeared to have changes in two EV populations (table 4.2) and hence were included in further experiments. The CHMP4CKD cell variant was also selected because this variant

appeared to have (together with the CD9KD and CD81KD variant) the biggest impact on CD81 CD9 positive EV subpopulations.

Table 4.2: Summary of the immunophenotyping of EVs derived from CM.

Arrows indicate an increased or decreased detection of the indicated tetraspanins relative to the cCM of the control cells (NMC). Highlighted in green are those candidates taken forward for the following experiments. NA= non applicable. 1-way ANOVA with Dunnett's multiple comparison post-hoc test was performed. ns= non-significant, * = P< 0.05, ** = P< 0.01, *** = P<0.001, **** = P<0.0001.

Sample/ Assay	CD81-catch CD81 detect	CD9 catch CD9 detect	CD81 catch CD9 detect	CD81catch CD63 detect	Included in further analysis
NMC	NA	NA	NA	NA	Yes
CD9KD	==	** ↓	**** ↓	* ↑	Yes
CD81KD	*** ↓	==	**** ↓	** ↓	Yes
CHMP4CKD	==	==	*** ↓	==	Yes
Rab6aKD	==	==	==	NA	No
Rab7aKD	==	==	** ↓	NA	No
Rab27bKD	==	==	==	NA	No
Rab35KD	==	==	** ↑	NA	No
PCLOKD	==	==	==	NA	No
SCAMP3KD	==	==	==	NA	No
SNAP23KD	==	==	==	NA	No
SYNGR2KD	*** ↓	==	** ↓	** ↓	Yes
VAMP3KD	==	==	==	NA	No
VPS28KD	==	==	* ↓	NA	No

To gain more insights in the effect of the target attenuation of the four candidates, a final plate configuration was used, combining a CD81 antibody to catch the vesicles and a biotinylated CD63 antibody to detect the vesicles (summarised in table 4.2). The CD81 CD63 levels

appeared constant in the cCM derived from the CHMP4CKD cells. Furthermore, there was a clear indication of reduced signal for CD81 CD63 when testing the CD81KD and SYNGR2KD sample. In contrast an increase in CD81 CD63 was observed for the cCM from the CD9KD cell variant. Importantly, together with the other immunophenotyping results, CD9KD, CD81KD and CHMP4C appeared to have a unique impact on the tetraspanin levels suggested by various combinations of tetraspanin up- and downregulations and the magnitude of the impact. Interestingly, the CD81KD and SYNGR2KD appeared to have a similar impact on the tetraspanin levels. Thus, these results are the first indications that the selected candidates control distinct EV subpopulations and support the selection of the four candidates.

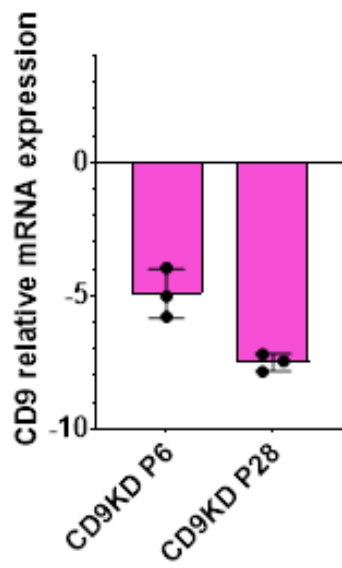
4.2.6 The stability of the target attenuation in the KD cell lines

The attenuation of all targets at mRNA level was previously validated by qPCR. Due the large number of cell variants, confirmation of attenuation of all the candidates at a protein level and the stability of the KDs was not attainable at an earlier stage of the project. Reducing the number of candidates, the attenuation of the targets at a protein level and the stability of the candidate KD was confirmed (Figure 4.9 and Figure 4.10).

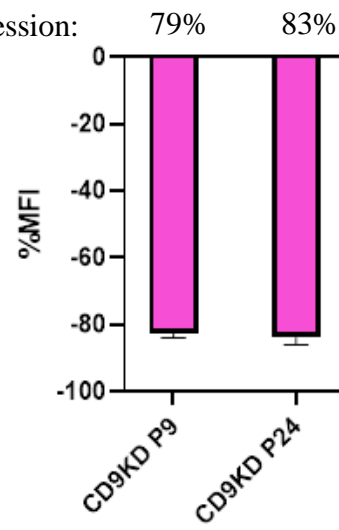
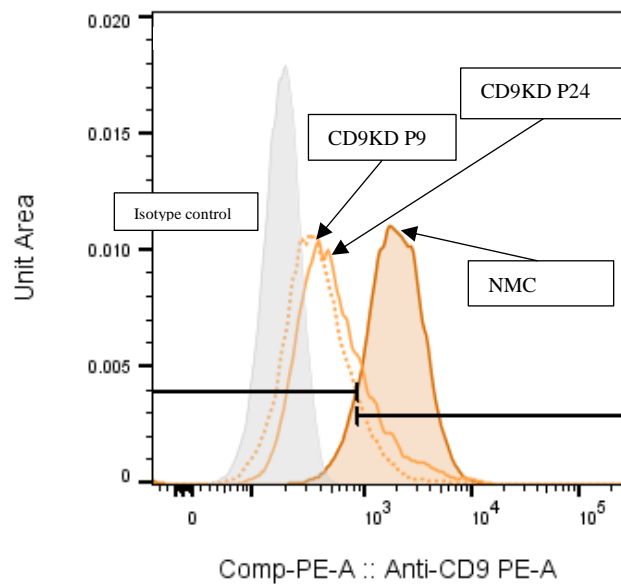
In the CD9KD cell variant, KD at a mRNA-level was stable over serial passage, as determined by qPCR comparing the RNA levels at P6 (4.3-fold decrease compared to the NMC cells), and much later with continuous growth at P26 (7.5-fold decrease compared to the NMC cells) (Figure 4. 9A). Determining the protein expression of CD9 by flow cytometry revealed that the stable attenuation of CD9 was reflected also at a protein level as detected by a CD9 antibody coupled to PerCP-Cyanine5.5 (Figure 4.9B and C). Compared to the NMC, the mean fluorescent intensity (MFI) in the CD9KD was 79% reduced at passage (P6) and 83% reduced at P24 (Figure 4.9B). Importantly, the fluorescent intensities were homogenously distributed across the cell population, revealing that the percentage of cells expressing low CD9 levels at both passage numbers was more than 78% (Figure. 4.9B and C).

In the CD81KD cell variant, mRNA levels of CD81 were 2.4-fold lower than in the NMC cell variant at an early passage number (P6) (Figure 4.9D). However, the CD81 mRNA levels

increased above NMC levels at a later passage number (P26). The CD81 protein levels were also determined using flow cytometry with a CD81 antibody coupled to AlexaFlour 647 (Figure 4.9E and F). At an early passage number (P6), the MFI of the CD81KD cell variant was 85% reduced compared to the NMC cells. Importantly, the majority of cells showed low CD81 expression and only a small proportion of cells (10%) expressed high CD81 levels confirming that this cell variant can be used at early passage numbers. At a much later passage number (P24), the MFI in the CD81KD slightly increased but was still 77% lower compared to the NMC. However, we detected a drift in the population towards a high CD81 expression (around 50% of the population). This prompted us to use this cell variant only at an early passage number and confirm the attenuation remained in place regularly.

A**B**

Cells with low
CD9 expression:

**C**

continued on the next page

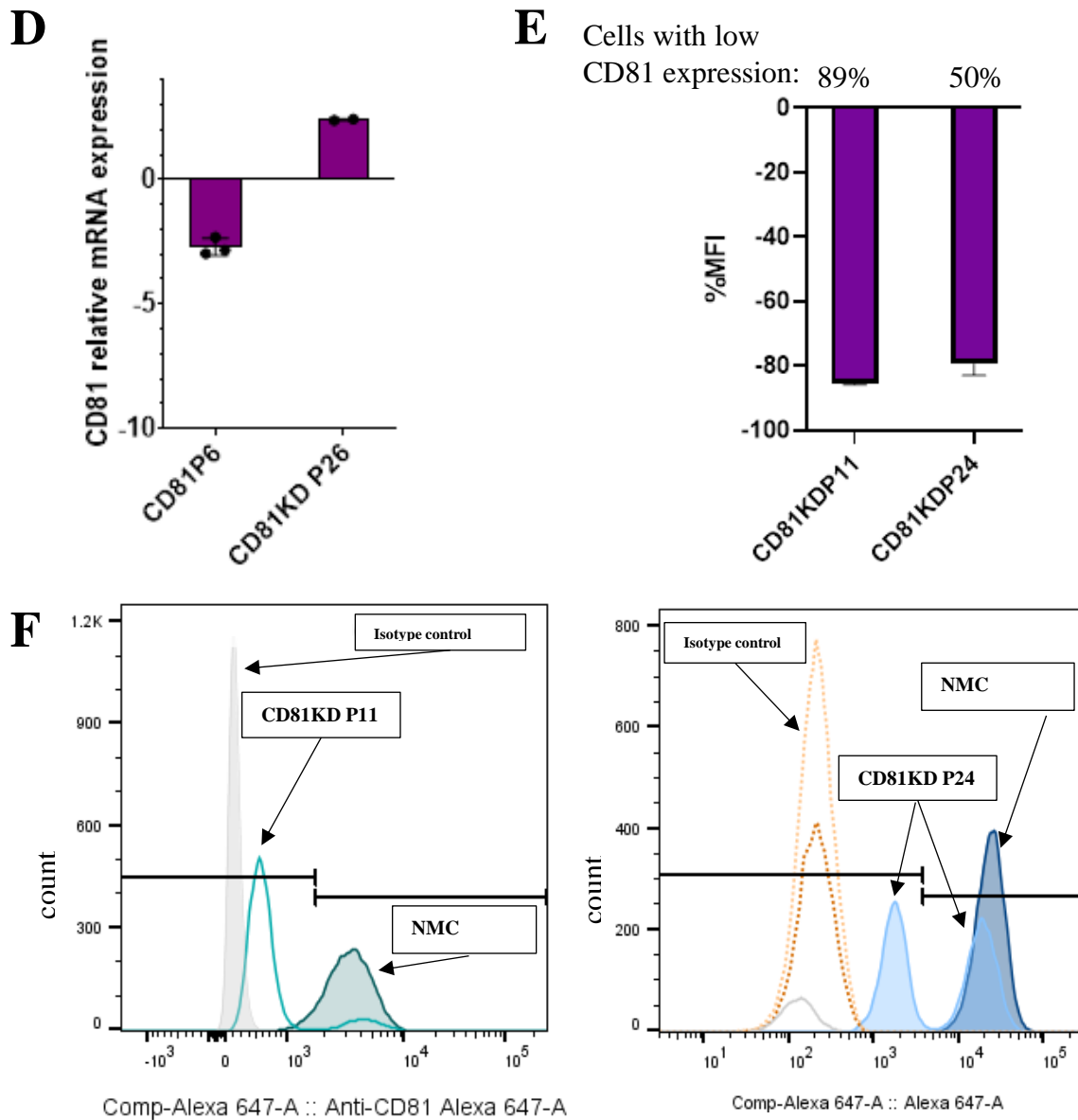


Figure 4.9: Validation of CD9 and CD81 attenuation in the generated PC3 variants.

Stability of the indicated target attenuation at mRNA level in the previously generated PC3 cell variants: CD9KD and CD81KD. Symbols indicate technical replicates. Relative cellular CD9 mRNA expression levels in the CD9KD cell variant was assessed by qPCR at P6 and P28 (A). The ct-values were normalized to GAPDH and compared to the mRNA levels in PC3 cells transduced with NMC viral particles. B) and (C) The CD9KD cell line and the NMC cell line were stained with an anti CD9 antibody coupled with PerCP-Cyanine5.5. The CD9 protein levels were assessed using flow cytometry. Relative cellular CD81 mRNA levels in the CD81KD cell line compared to the NMC cells was determined by qPCR at P6 and P26 (D). The CD81KD cell line and the NMC cells were stained with an anti CD81 antibody coupled with AlexaFlour 647. CD81 protein levels were then assessed using flow cytometry (E) and (F). The bar chart shows the mean +/-SD of 3 technical replicates. A student's test was performed * = $P < 0.05$.

The stability of target attenuation was also assessed for the CHMP4CKD cell variant and the SYNGR2KD cell variant (Figure 4.10). In the CHMP4CKD cells, there was a slight decrease in the magnitude of CHMP4CKD attenuation over time at mRNA level (P6 compared to P26) (Figure 4.10A). In contrast to this, downregulation of SYNGR2 was stable (2.7-fold reduction at P6, 4.4-fold reduction at P26 of SYNGR2 mRNA (Figure 4.10B). Both proteins, CHMP4C and SYNGR2 are barely described in the literature (2023) and therefore only a limited number of antibodies are available against each target. For both targets, a polyclonal antibody under different conditions (denaturing, non-denaturing, various incubation times and antibody concentrations, cell lysate concentrations) were tested by Western blotting. Despite our efforts to optimise the detection of SYNGR2 and CHMP4C this was unsuccessful. For SYNGR2 an additional monoclonal antibody was sourced and tested using Western blotting, again to no avail. We were therefore unable to determine protein expression at baseline nor under influence of shRNA for these targets.

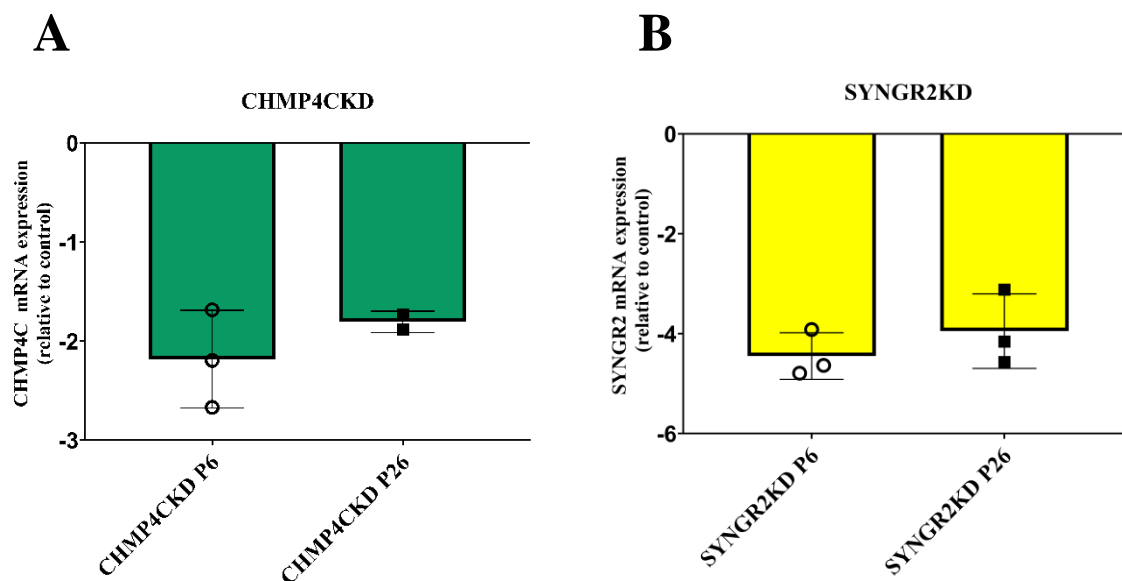


Figure 4.10: Stability of CHMP4C and SYNGR2 attenuation over time.

Stability of the target attenuation in the CHMP4CKD (A) and SYNGR2KD (B) cell variants was determined. Relative cellular mRNA expression levels were assessed by qPCR at P6 and P28. The ct-values were normalized to GAPDH and compared to the mRNA levels in PC3 cells transduced with NMC viral particles. Symbols indicate technical replicates. The bar chart shows the mean +/-SD of 3 technical replicates.

4.2.7 The impact of candidate attenuation on proliferation

As discussed, manipulating the secretory or intracellular transport pathway may be toxic for cells. For instance, attenuation of the ESCRT component VPS25 has been shown to have an impact on cell proliferation in DU145 cells (Yeung et al., 2018). Consequently, alterations in EV secretion upon the attenuation of candidates, could rather reflect the impact on the cell health instead of target specific impacts. Previously we have shown that attenuation of CD9, CD81, CHMP4C and SYNGR2 did not impact cell viability in our first pass analysis. Here, we complemented these results with a growth curve of the selected KD cell variants (CD9KD, CD81KD, CHMP4C, SYNGR2KD) over a 96-h period to re-confirm that the impact of the candidate attenuation on cell proliferation is indeed negligible (Figure 4.11).

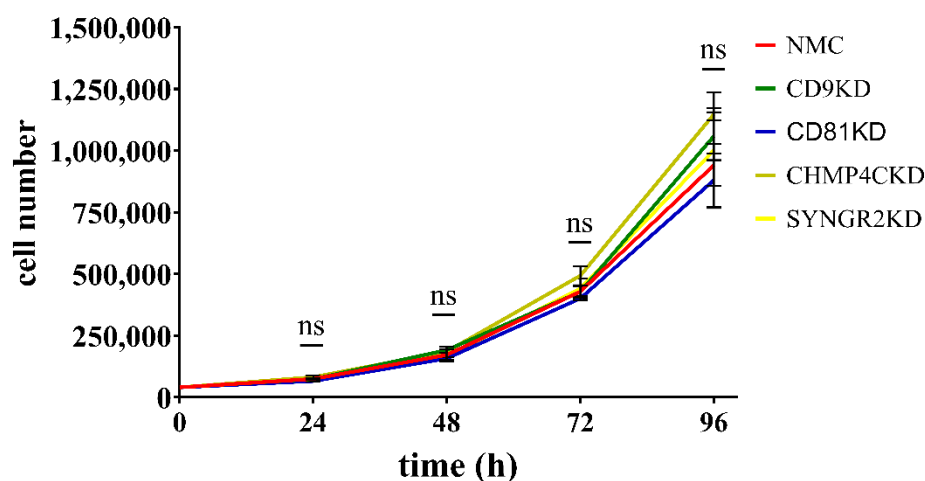


Figure 4.11: Growth curves of the NMC, CD9KD, CD81KD, CHMP4CKD and SYNGR2KD cell lines.

The impact of the KDs on cell proliferation was determined by seeding the cells at equal numbers in triplicate and quantifying the cell numbers over 96 h. Each replicate was counted three times at the indicated time points and is represented as the mean. A one-way ANOVA for each time point with Dunnett's multiple comparison post-hoc test was performed. ns = non-significant.

4.2.8 Characterisation of purified vesicles derived from CD9KD, CD81KD, CHMP4CKD and SYNGR2KD PC3 cells

Reducing the number of candidates from 17 to only four allowed a more in-depth exploration of the potential role of the selected candidates. However, before embarking on the functional exploration (Chapter 5), the impact of target attenuation on vesicle output was again validated. Despite the limitations of the Nanosight™ platform described earlier, NTA is currently one of the most routinely performed analysis in the EV field. To improve chances of accurate EV counting, CM was subject to ultracentrifugation to separate EVs from other factors, including non-EV particulates, and the NTA conducted on this concentrated material.

The reduced sample number allowed extensive measurements on three biological replicates per KD capturing >10,000 tracks in total. As observed previously the size distribution across the tested samples was broadly similar with a peak around 100 nm (Figure 4.12A- F). Importantly, no peaks at larger sizes were detected suggesting a reduction in protein aggregations in the sample for example. Furthermore, the number of particles per cell was similar across the control cell variant and the KD cell variants (CD9KD, CD81KD, CHMP4CKD, SYNGR2KD) validating that these candidates did not have a major impact on EV quantities (Figure 4.12I).

Interestingly, investigating the mean size and mode size in more detail, indicated slight differences across the samples may be apparent. All of the particles derived from the KD cells were below both the mode size of particles from the NMC samples which was 132 nm and the mean 149 nm (Figure 4.13G and H): CD9KD (mean:124 nm and mode: 107 nm), CD81KD (mean:131nm and mode:119 nm) CHMP4CKD (mean:118 nm and mode:95 nm) SYNGR2KD (mean:128 nm and mode: 119 nm) (Figure. 4.12G and H). This could potentially indicate differences in the biophysical nature of the released EVs, but would need confirmation e.g., by Cryo-EM to be certain.

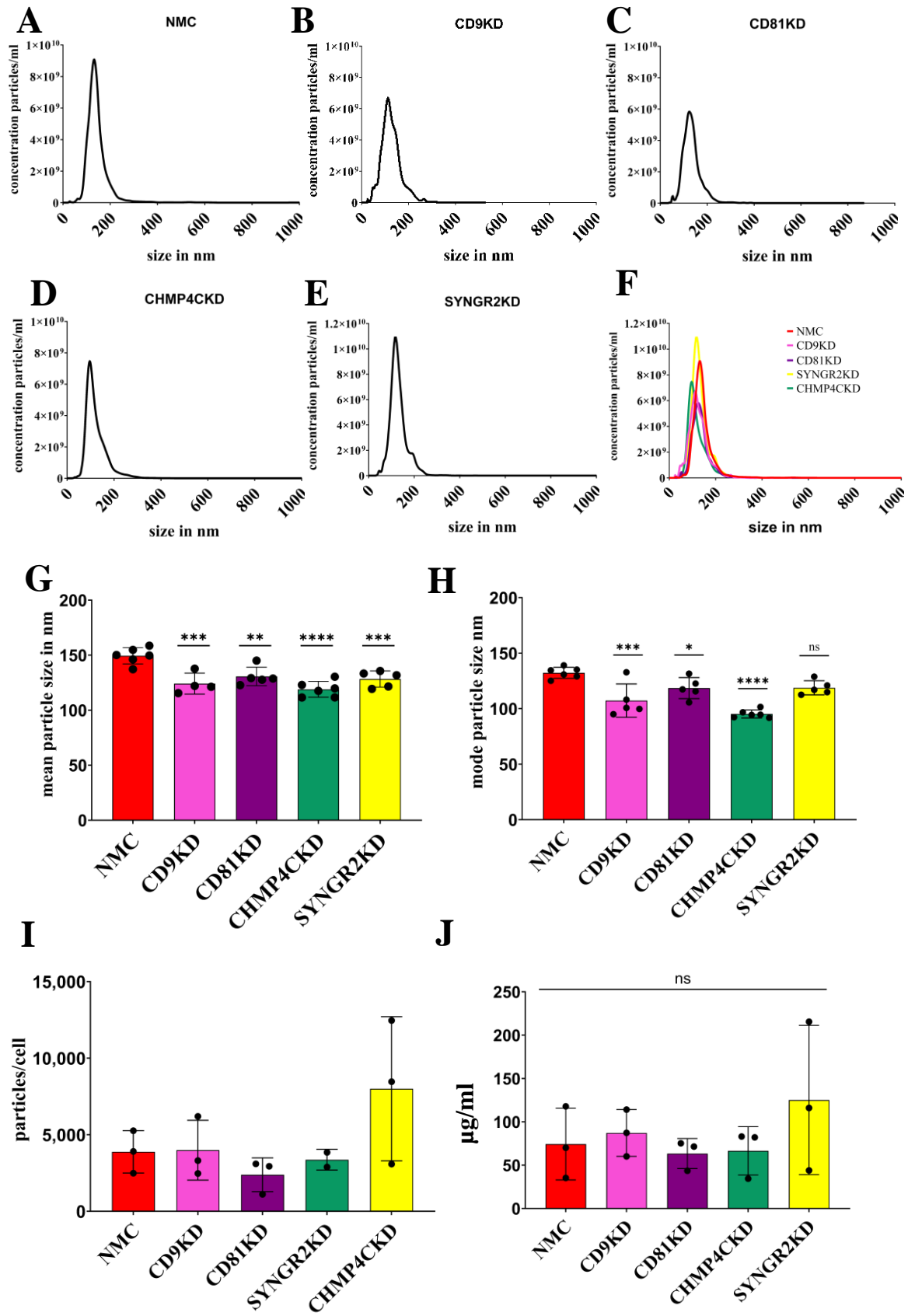


Figure 4.12: Characterising purified vesicles from lentiviral transduced PC3 cells by NTA.

Purified EVs of the indicated KD cell variants were analysed using NTA to determine the overall size distribution and particle concentrations of the isolated EV samples. For each cell line, 3 technical replicates of three biological replicates were measured (A)-(H). Mean and mode particle size of the purified EVs from the indicated KD cell lines is shown in (G) and (F) respectively. The particle number was normalized to the cell number and the number of background particles in filtered media was subtracted from the measurements (I). The protein concentrations of the analysed samples are shown in (E). Graph shows mean \pm SD. 1-way ANOVA with Dunnett's multiple comparison post-hoc test was performed. ns= non-significant, * = $P < 0.05$, ** = $P < 0.01$, *** = $P < 0.001$, **** = $P < 0.0001$.

Furthermore, using a BCA assay protein, concentrations were determined and revealed that the mean NMC EV protein concentration was 74 $\mu\text{g/ml}$ (Figure 4.12J). The protein concentrations varied across the triplicates of the NMC ranging from 35 $\mu\text{g/ml}$ to 117 $\mu\text{g/ml}$. Compared to the NMC EVs, the mean protein concentrations of the KD EV samples did not show major differences in the overall protein cargo of the EVs.

4.2.9 TGF- β 1 levels is altered in the KD EVs

We were interested in evaluating the impact of the candidates on other EV cargo components (other than tetraspanins) and elected to assess levels of TGF- β 1. This signalling molecule is a pleiotropic regulator of homeostasis across various tissues with immune suppressive functions in adaptive and innate immunity (Massague and Sheppard, 2023). Importantly, research by our groups and others has shown that EVs are carriers of functional TGF- β 1 (Webber et al., 2010), which is relevant for stromal cell responses. Hence, TGF- β 1 on EVs was assessed (Figure 4.13).

CM from the NMC, CD9KD, CD81KD, CHMP4CKD and SYNGR2KD cells were collected, normalised according to cell numbers and subjected to an ultracentrifugation step, to concentrate EVs. The supernatants were discarded and TGF- β 1 concentrations in the total pelleted material was assessed. TGF- β 1 concentrations in the pelleted material from NMC and CHMP4CKD were detected at comparable levels (725 pg/ml and 648 pg/ml respectively).

Surprisingly, both the CD9KD EVs and CD81KD EVs showed significantly elevated concentrations of TGF- β 1 (1,060 pg/ml and 1,321 pg/ml). Furthermore, SYNGR2KD EVs appeared to have a lower concentration of TGF- β 1 (490 pg/ml) compared to the NMC EVs. This could suggest changes in the TGF- β 1 vesicular TGF- β 1 cargo upon CD9, CD81 and SYNGR2 attenuation. However, it needs to be noted that this was a crude ultracentrifugation step and hence other soluble material might have co-pelleted.

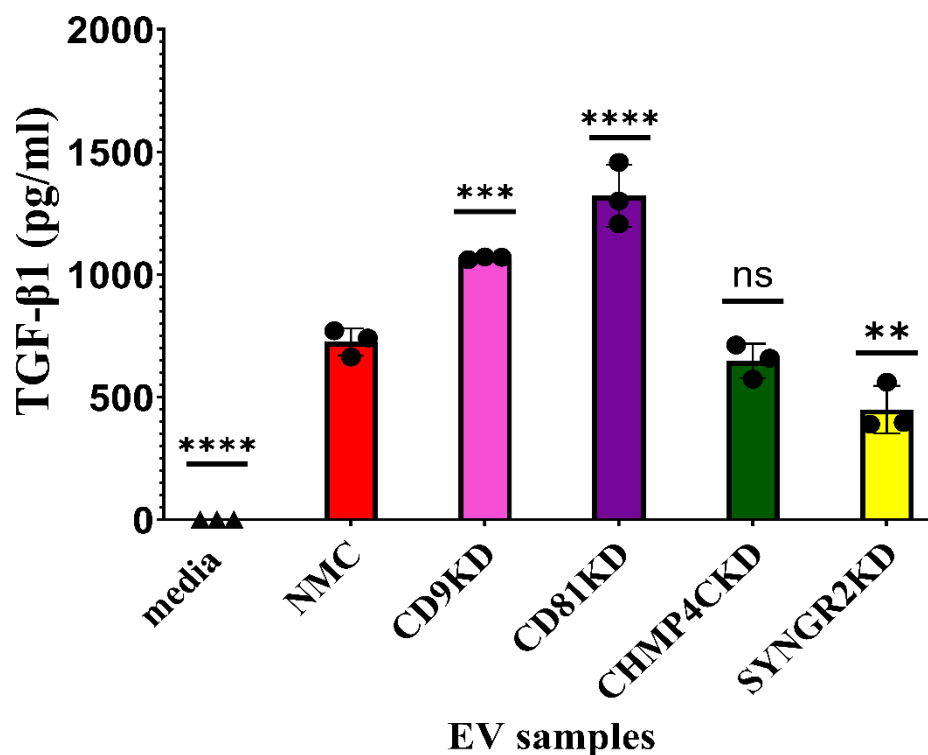


Figure 4.13: CD9, CD81 and SYNGR2 influence vesicular TGF- β 1 levels.

TGF- β 1 levels on isolated EVs from the NMC cell line, CD9KD, CD81KD, CHMP4CKD and SYNGR2KD cell line were assessed with a TGF- β 1 ELISA. Symbols indicate technical replicates of the same cell population. One-way ANOVA with Dunnett's multiple comparison post-hoc test was performed, and ns= non-significant, * = $P < 0.05$, ** = $P < 0.01$, *** = $P < 0.001$, **** = $P < 0.0001$.

Summarising the results in this chapter, we did not observe major differences in size and total EV output as a consequence of any of the KDs. A microplate immunophenotyping assay indicated CD9, CD81, CHMP4C and SYNGR2 as potential regulators of the tetraspanin-related phenotype of EVs. Analysing directly isolated EVs from this select set of KDs, again revealed no differences in EV output per cell. However, a slight decrease in the EV size was observed together with some differences in TGF- β 1-load. Taken together the impact of KDs on the PC3 cells have been very disappointing, resulting in some very subtle changes in the EV which display non-uniformity across the four KDs tested.

4.3 Discussion

The work presented in this chapter falls in line with previous successful attempts by our lab and others to attenuate potential EV regulators by an shRNA-based approach to explore and define the roles of potential EV regulators (Colombo et al., 2013, Yeung et al., 2018), and thereafter act as a basis to explore the functional consequences of such attenuation in a number of experimental settings.

Targeting 17 candidates selected for this work showed heterogeneity in the efficacy of KD as we expected, with strong attenuation of >80% for many and at least 52% attenuation for several factors that putatively control EV biogenesis (CD9, CD81, VPS28, CHMP4C, SCAMP3) and release (SNAP23, VAMP3, PCLO, SYNGR2) in PC3 cells. Furthermore, we significantly attenuated the mRNA for several Rab GTPases (Rab6a, Rab7a, Rab11b, Rab27b, Rab35), associated with endocytic traffic functions. Perhaps, attenuation of LITAF and Rab37 could not be confirmed by the TaqMan assays used here because these mRNA transcripts may be at such low levels or absent in the PC3 cell line and consequently unlikely to be hugely important for the investigation at hand. Additionally, significant attenuation of STX6 was not apparent, even though we had five attempts at this. Based on these results it was reasonable at this point to exclude these three latter targets from further exploration.

Attenuating genes can cause a perturbation of a variety of cellular systems such as cell proliferation or apoptosis. As a consequence, increased cell death might occur which renders the analysis of the secreted vesicles difficult. This can lead for instance to an increase in the release of necrotic vesicles, cellular organelles and fragments which have a distinct molecular make up (Shlomovitz et al., 2021) and renders the analysis of EVs in a noisy background of structures very difficult. Therefore, the impact of the KDs on cell proliferation was investigated. Indeed, a range of KD cell variants raised toxicity concerns and were thus excluded from the following experiments (table 4.1). However, it is important to note that EVs also play a role in wide range of biological functions including cell proliferation and export of cellular waste. Thus, perturbation of cell proliferation might also be a consequence of EV dysregulation and hence serve as a potential readout of EV regulation. It would, however, be challenging to explore this in more detail given the increased cellular complexity comparing different cellular states. Another aspect to consider is, that the KD might also have

off target effects eliciting an endogenous stress response to viral infection and thus ultimately leading to cell death (Olejniczak et al., 2010).

We proceeded to investigate whether the attenuation of our selected candidates modulates the quantity and phenotype of released EVs. Using NTA, we only detected a slight impact on the number of particles/cell for one candidate, VPS28. The Nanosight™, like all current NTA instruments, measures all particles in a sample and is therefore not EV specific. Additionally, our system is increasingly insensitive to small particles, we think due to laser power being reduced as the laser ages. Hence background particles are an issue with these measurements, and subtle changes in EV concentrations might be masked by measures of background particulate matter. Furthermore, there are a plethora of factors that influence the sample and consequently the measurement. For instance, it has been shown that the storage container of the samples influences the detected particle concentrations (Griffiths et al., 2020). Hence, for polydisperse samples it is crucial to keep the sample storage conditions and measurement settings identical to reduce variations between measurements and we have tried to ensure these considerations are in place.

To validate the NTA results, we used EVQuant, a microscopy-based high-throughput EV specific technique to determine the number of EVs per cell in CM (Hartjes et al., 2020). Like the NTA data, detection of vesicles was readily possible yet revealed little compelling data in terms of a KD-mediated alteration in vesicle output. We only detected a slight increase in the number of particles per cell for the VPS28KD cell line by NTA. Interestingly, in a previous screen by Colombo et al., targeting a different ESCRT component CHMP4C in HeLa cells enhanced exosome secretion (Colombo et al., 2014), and hence perhaps this small elevation may be real. In other systems, SNAP23, LITAF (SIMPLE) and Rab27b have well documented and dramatic effects in regulating vesicle output. A point mutation of SIMPLE in primary mouse fibroblasts caused a decrease in exosome release by ~70% (Zhu et al., 2013). A truncated version of SNAP23 which forms a non-functional SNARE complex showed a drastic reduction of released exosomes in HeLa cells (Verweij et al., 2018). Rab27b KD in HeLa-CIITA cells causes a slight but significant reduction in the concentration of EVs. (Bobrie, A., et al., 2012). In contrast however, we did not observe changes in the EV output in the PC3 cell line, following SNAP23KD, SIMPLEKD or Rab27bKD, yet we know that the

attenuation of mRNA for these was successful. Rab35 and CD9 have previously been attenuated in the PCa cells DU145. However, only KD of Rab35 in DU145 cells resulted in a significant reduction (23 %) of the detected particles, whereas KD of CD9 failed to do so (Yeung et al., 2018). Here, we did not see any changes in the EV concentration upon attenuation of either CD9 or Rab35 in PC3 cells. Interestingly, CD9 KO in melanoma cells causes an increase of EVs in the CM (Suárez et al., 2021). The authors claim that this was caused by compensatory mechanisms in the cells with an increased expression of other tetraspanins.

The cross-platform (Nanosight™ and EVQuant) validation of the results described in this chapter supports the finding that there were no dramatic changes in the number of EVs secreted by the manipulated PC3 cells, and for the overarching aims of the study this is an extremely disappointing finding. The reasons for this failure to even partially attenuate vesicle production in these cells, are currently unclear. The PC3 cells were selected with the view of performing *in vivo* studies, and to induce a deficiency in metastasis upon EV-attenuation. PC3 cells are reported to be highly aggressive, and highly metastatic in immune-deficient mice (reviewed in Wu et al., 2013). This apparent ability of PC3 cells to be resistant to manipulations targeting endogenous EV production machineries might suggest unusual processes in PC3 cells in terms of vesicle regulation that are beyond what is currently known about vesicle biogenesis, traffic and exocytosis, and that perhaps resistance to vesicle-modulation in this specific cell line may underpin the aggressive growth and spread of this cell line *in vivo*. Alternatively, it may be that this cell line predominantly produces vesicles from a plasma membrane (ectosomal) route, and that our attempts of targeting endosomal manufactured vesicles (exosomes) are negligible in PC3 cells. Some advanced imaging tools may be helpful to explore the secretory rate in live cells, using for example the well documented pHluorin-fusion protein system (Verweij et al., 2018).

Another aspect that influences the amount of detected EVs in CM is the re-uptake of EVs after their expulsion. Importantly, the molecular features of the EVs appear to influence the uptake rate e.g., platelet-derived EVs are up taken at a higher rate compared to EVs from red blood cells (Koponen et al., 2020). Furthermore, PC3 cell derived EVs show a high uptake rate by PC3 cells and benign epithelial cells compared to primary malignant prostate epithelial

cells RC92a/hTERT (Lázaro-Ibáñez et al., 2017). In addition to this, the expression of dynamin, a regulator of endocytosis is increased in advanced PCa, indicating increased endocytosis (Xu et al., 2014). This might be the case for the PC3 cells where rapid re-acquisition and processing in an autocrine fashion may be a confounding element that constrains our capacity to show definitive changes in the production pathways. Hence, considering the extensive range of PC3 variants generated here, an increased EV release might be not detected by NTA and EVQuant because of concomitantly increased uptake of EVs as a consequence of high endocytosis rates.

Analysing purified KD EVs by NTA indicated that these EVs were slightly smaller than the EVs from the NMC cells. Interestingly, there are regulators that specifically modify the size of EVs. It was previously shown that oncogenes in endothelial cells can modulate the size of EVs by altering the lipid metabolism and the lipid composition of the released EVs (Kilinc et al., 2021). Furthermore, KO of SYNGR2 in neuronal cells from drosophila results in a shift to a heterogenous population of synaptic vesicles, indicating SYNGR2 as a regulator of synaptic vesicle size (Stevens et al., 2012). If SYNGR2 performs a similar function in PC3 cells needs to be confirmed by transmission electron microscope and additionally using lipidomics to determine the abundance of lipid species in the released EVs would potentially provide major insights into EV biogenesis.

As well as quantity changes detailed by Yeung et al., the authors also reported alterations in the vesicle protein composition following shRNA attenuation of certain Rab proteins. This raises the possibility that the KD of certain candidates might impart a subtle impact on the molecular composition of the vesicles and be more subtle than effects such as vesicle quantity inhibition. To scope this among our candidates, we explored whether the attenuation of the candidates had an impact on tetraspanins with a focus on CD9, CD81 and CD63. These tetraspanins are of particular interest for the work presented here as for instance, Kaur et al. reported that CD81 positive EVs form the main subpopulation of EVs derived from PC3 cells (Kaur et al., 2022). Interestingly, attenuation of CD9 in epithelial cells was shown to not impact the expression CD81 on EVs (Brzozowski et al., 2018). This was also reported in PCa cells, where levels of CD81 positive EVs remained stable in a CD9KD DU145 cells compared

to control DU145 cells (Yeung et al., 2018). The results obtained here are in line with these reports as we detected no impact on CD81 in cCM from the CD9KD cell line.

CD9 has been reported to regulate the quantity of released EVs in different model cell systems. In CD9KO dendritic cells, exosome secretion is attenuated compared to the wild type cells (Chairoungdua et al., 2010). In B-cells, KD of CD9 results in a decrease in secreted microvesicles. In plasma samples from PCa patients, CD9 positive EVs are enriched compared to those of men with benign prostate hyperplasia (Soekmadji et al., 2017a); indicating a potential role of CD9 positive EVs in PCa. Hence, there was a particular interest for this tetraspanin. For the CD9KD cells, we achieved a stable attenuation of CD9 at the cellular level of more than 90% over a period of 24 passages. The tetraspanin expression on EVs is regulated by the expression of the tetraspanin of the parent cell. Hence, we expected to see drastically reduced detection of CD9 positive EVs by EVQuant. However, measuring CM from the CD9-attenuated PC3 cells, we did not detect major changes in the secretion of CD9 positive vesicle populations. This indicates that there was not a 90% depletion of CD9 positive EVs. EVQuant only differentiates between positive and negative expression of a specific tetraspanin. Perhaps, the number of CD9 molecules on individual EVs is reduced, but the overall number of CD9 positive EVs is stable, this would be also in line with the plate based immunophenotyping where we saw a reduction in the overall CD9 levels in CM.

To summarise, after generating an extensive set of PC3 variants we have demonstrated that vesicle secretion from them remains robust, with little impact irrespective of often strong mRNA attenuation. This surprising finding was validated with orthogonal methods, and several rounds of confirmation. Instead, the attenuation of the EV regulators appeared to elicit very subtle modifications in the repertoire of EVs being produced, indicated by changes in the tetraspanin levels but also likely encompasses a range of other molecular alterations, impacting vesicle size. The collated data suggests that the attenuation of CD9, CD81, CHMP4C and SYNGR2 have the biggest impact on the molecular composition of EVs, hence we decided to focus only on these candidates in the following experiments. Excitingly, we showed for the first time to my knowledge a potential role of SYNGR2 on the molecular composition of EVs. Whether or not these subtle effects exert a functional consequence is the next question, to be detailed in the following chapter.

Chapter 5:

Impact of knockdown of CD9, CD81, CHMP4C or SYNGR2 on fibroblast function

5.1 Introduction

5.1.1 Tumour microenvironment

Solid cancers reside within a specialised niche termed the tumour microenvironment (TME) which is comprised of cancer cells, various immune cells e.g., macrophages and the tumour stroma (Gocheva et al., 2010, Wyckoff et al., 2007). Constituents of the stroma include non-cancerous cells (for instance, but not limited to, mesenchymal stromal cells, endothelial cells) and acellular components such as the ECM and the tumour adjacent vascular system (Hanahan and Weinberg, 2011, Baghban et al., 2020).

The reciprocal communication between the non-tumour components of the TME with the neoplastic cells promote the growth and altered architecture of the malignant tissue through a variety of well documented processes which ultimately lead to metastatic dissemination and disease lethality (Hanahan and Weinberg, 2011). CAFs, present within the stroma of the TME, play a critical role in remodelling and reorganisation of the acellular matrix, thereby facilitating various processes that support disease progression (Baghban et al., 2020, Chen et al., 2021b).

5.1.2 Markers for cancer associated fibroblasts

There are various markers of CAFs, such as fibroblast activating protein (FAP) and α -SMA. However, due to the functional and phenotypic heterogeneity of the CAF cell population within one tissue and across various tissues, these marker proteins are not expressed in the whole cell population and a universal CAF-specific marker remains to be found (Chen et al., 2021b). Despite this, α -SMA positive CAF populations have been found across various cancers, thus many studies focus on this cell population (Elyada et al., 2019, Costa et al., 2018).

α -SMA monomers, arranged in filamentous stress fibres, provide a muscle-like capacity enabling the cell to undergo cellular contraction and exert mechanical force on the surrounding ECM. Focal adhesion complexes at the cell membrane link the intracellular

polymerised α -SMA fibres to the extracellular fibronectin fibrils and thus mediate the propagation of the contractile force to the local ECM (Hinz et al., 2001, Welch et al., 1990, Chrzanowska-Wodnicka and Burridge, 1996). Interestingly, single cell sequencing studies on samples derived from PCa patients showed that α -SMA positive CAFs represent a major CAF subpopulation in this malignancy and thus this CAF subpopulation might contribute to the aggressiveness of the disease (Tuxhorn et al., 2002). Furthermore, a recent single cell RNA-seq study identified at least two distinct α -SMA positive populations in the context of PCa showing the heterogeneity of CAFs within one tissue (Chen et al., 2021a).

5.1.3 Secretome of CAFs

CAFs release a wide range of factors such as ECM components and growth factors (including cytokines and chemokines) that orchestrate infiltration, cell activation and changes in cellular behaviours like motility that act to foster tumour growth and invasion and will be outlined in more detail below. It is important to note, that despite the recent advances in describing genetic phenotypes, uncertainty remains in assigning these genetic phenotypes to a distinct functional phenotype.

Increased ECM secretion by CAFs leads to a higher stromal density, which protects neoplastic cells from the elimination by immune cells (Salmon et al., 2012). In addition to this, Gaggioli suggested that the deposited ECM components form tracks that boost tumour migratory capabilities and invasiveness (Gaggioli et al., 2007).

CAFs have been reported to secrete a range of pro-angiogenic chemokines which stimulate the formation of a neo vasculature providing the growing tumour with oxygen and essential nutrients to maintain growth. One example is the paracrine signalling molecule HGF which has been reported to be secreted by CAFs and promote migration of PC3 cells *in vitro* and tumour growth *in vivo* when PC3 cells and fibroblasts are co injected into mice (Davies et al., 2003). The important role of fibroblast derived HGF has also been confirmed in various other tumours including for instance, head and neck cancer (Kumar et al., 2018), squamous cell carcinoma (Eikesdal et al., 2018) and PCa (Webber et al., 2010, Qin et al., 2021).

IL-6 is another pro-angiogenic chemokine, which also contributes to a pro inflammatory response (Raskova et al., 2022, Motro et al., 1990). Accumulating evidence points to an important functional role of IL-6 released by CAFs to support the tumour (Shintani et al., 2016, Vicent et al., 2012, Öhlund et al., 2017, Elyada et al., 2019). In the context of PCa, IL-6 secreted by fibroblasts has been shown to stimulate the secretion of VEGF in PCa cells (Ishii et al., 2018) and to elicit endothelial cell migration (Paland et al., 2009).

5.1.4 Precursor cells of CAFs

The originating cells responsible for the emergence of CAFs remain debated, and the complexities of cellular plasticity where several different cell types may trans-differentiate to acquire features of CAFs add to the difficulties of pin-pointing pathways contributing to CAF-development. Classical examples where epithelial cells become altered towards mesenchymal (fibroblast-like) cells through EMT are well documented as components of the TME (Zeisberg et al., 2007). A range of other possible CAF source cells have also been proposed. For instance, Karnoub et al. showed that mesenchymal stem cells co-injected with tumour cells in mice lead to the conversion of the mesenchymal stem cells into CAFs (Karnoub et al., 2007). Other cell types that might be the origin of CAFs include pericytes (Hosaka et al., 2016), endothelial cells (Radisky et al., 2007) and of course, resident fibroblasts.

Fibroblasts are however, also present constitutively in prostate interstitial stromal. The activation of resident fibroblasts to become CAFs accompanies cancer formation, and, in the prostate, such changes can be seen almost immediately in response to carcinogenesis. Specifically, myofibroblasts adjacent to pre-cancerous lesions of the prostate, termed prostatic intraepithelial neoplasia, have been documented (Tuxhorn et al., 2002), and their numbers and ratio relative to glandular epithelial cells often increases with disease stage (Sahai et al., 2020). Furthermore, in a mouse model it was shown that CAFs can arise from tissue resident fibroblasts located adjacent to neoplastic tissue as opposed to circulating fibroblasts being recruited to the tissue and thereafter becoming CAFs (Arina et al., 2016).

Since there are populations of fibroblastic cells, as well as bundles of smooth muscle cells, present in the healthy prostate interstitium it is reasonable to explore potential for such

resident cells to become altered toward a CAF-like phenotype in response to tumour derived factors including EVs. Indeed, cancer cell derived EVs have been shown to induce a cancer promoting CAF phenotype in fibroblasts isolated from normal regions of the human prostate. For instance, EVs carrying TGF- β 1 induce the onset of α -SMA, and release of HGF by fibroblasts, and in other words elicit myofibroblastic differentiation (Webber et al., 2010, Webber et al., 2015). Fibroblasts that are activated by EV associated TGF- β 1 exhibit pro-angiogenic properties (Webber et al., 2016). In contrast, recombinant human TGF- β 1 induces α -SMA positive fibroblasts that fail to secrete HGF and fail to promote angiogenesis *in vitro*. Importantly, the CAF-generating functions of PCa derived EVs was also indicated in murine xenografts by a reduced tumour growth when co-injecting EV deficient PCa cells with fibroblasts (Webber et al., 2015).

5.1.5 Aim and objectives

In the previous chapter, I demonstrated evidence showing CD9, CD81, CHMP4C and SYNGR2 have a distinct influence on the composition of the released EVs. Here, we aimed to explore whether these observed changes had functional consequences with a focus on the impact on the stromal response. The objectives to meet this aim were:

- 1.) Assess the onset of α -SMA polymerisation in response to PC3 CM (from the KD cell variants) by microscopy.
- 2.) Determine the impact of purified EVs isolated from the KD cell variants on the secretome and mRNA in the recipient fibroblasts using modified ELISAs and qPCR.
- 3.) Gain insights into possible differences in the activation of signalling pathways upon KD EV stimulation using a phosphokinase array.

An overview of the strategy to achieve these aims is described in Figure 5.1.

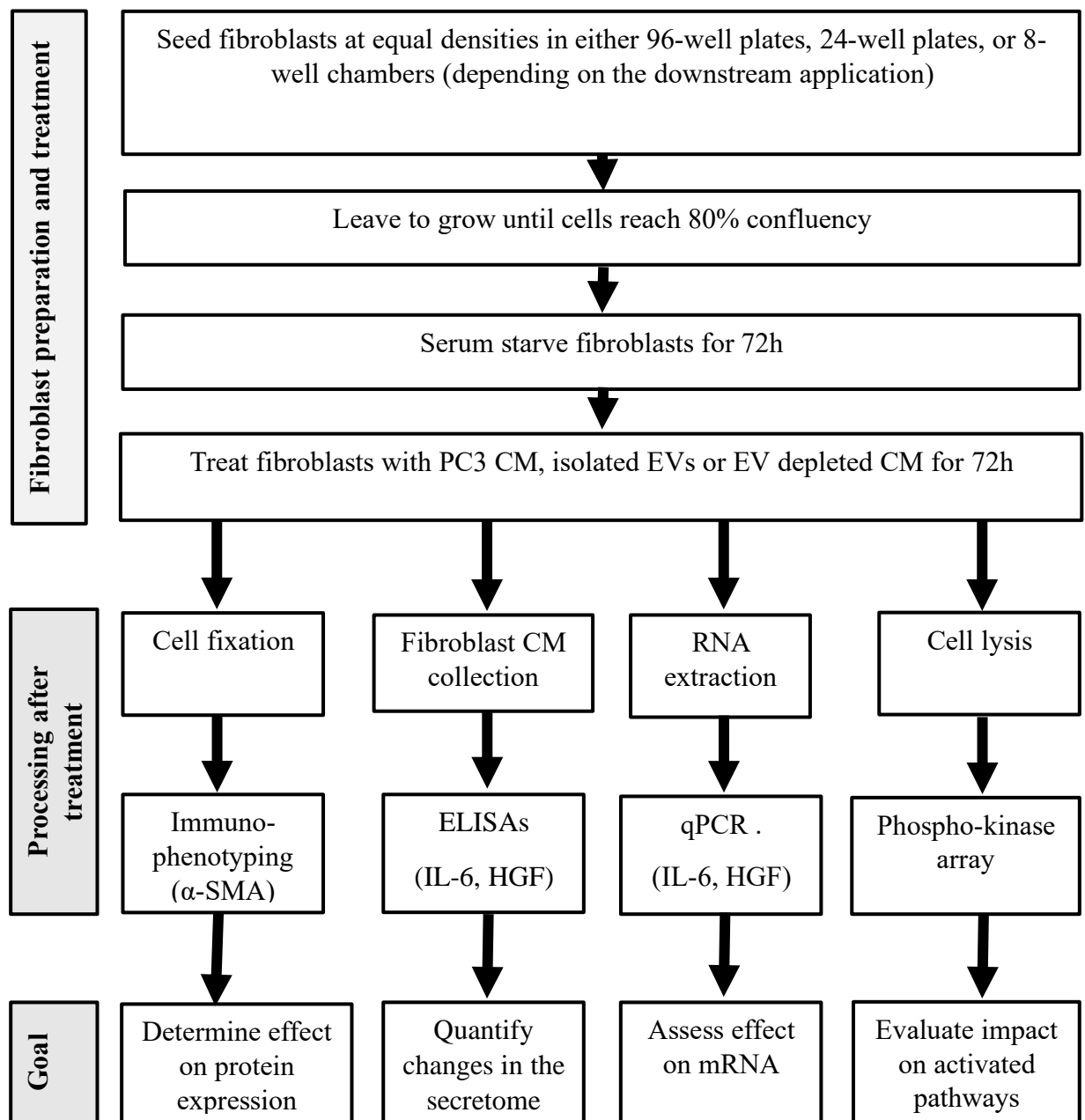


Figure 5.1: Strategy to explore the functional impact of CD9, CD81, CHMP4C and SYNGR2 dependent PCa factors on recipient fibroblasts.

The boxes describe the experimental set-up to investigate the fibroblast response to CM, EV depleted CM and isolated EVs from the KD cell lines (CD9KD, CD81KD, CHMP4CKD and SYNGR2KD). CM was volume corrected based on PC3 cell number at harvest time (cCM).

5.2 Results

5.2.1 PC3 CM does not impact cell proliferation in recipient fibroblasts

We are interested in exploring possible roles of the candidates in modulating the functional properties of PC3 cell derived EVs from a stromal fibroblast perspective. Before exploring a range of such impacts, it was important to establish whether or not the vesicles had similar or different effects on the general health and proliferative properties of the recipient fibroblasts. For some of our experiments, exposure of fibroblasts to EVs for 72 h was essential- as typically this is when peak expression of the newly polymerised α -SMA is seen during fibroblast to myofibroblast differentiation (Webber et al 2010). Hence determining differences in proliferative capacity during this timeframe was important in terms of interpretation of results, such as when quantifying cytokine secretion.

The effect of PC3 cell-derived CM on the cell numbers of fibroblasts was assessed by a WST-8 based Orangu assay. To achieve this, fibroblasts were seeded at equal densities and grown until 80% confluency. Subsequently, the cells were serum starved for 72 h, which was followed by treatment with TGF- β 1 (1.5 ng/ml) or only media. The results were compared to fibroblasts treated with PC3 CM (NMC, CD9KD, CD81KD, CHMP4CKD, SYNGR2KD), which was volume corrected based on PC3 cell number at harvest time (72 h) and is hereafter termed cCM. The fibroblasts were stimulated for 72 h and subsequently, an Orangu assay was performed to determine differences in fibroblast cell number (Figure 5.2).

Treatment with TGF- β 1 (1.5 ng/ml) had a similar impact on the cell numbers as untreated cells, consistent with expectations of TGF- β 1 not being a mitogen for fibroblasts. Stimulating fibroblasts with cCM from PC3 cells also had no apparent impact on stimulating cell proliferation. Microscopic observations confirmed the cells remained attached, and as viable cells (not shown). Hence, PC3 cCM did not stimulate a proliferative response in fibroblasts, and hence cell numbers at experimental end points would be equivalent throughout.

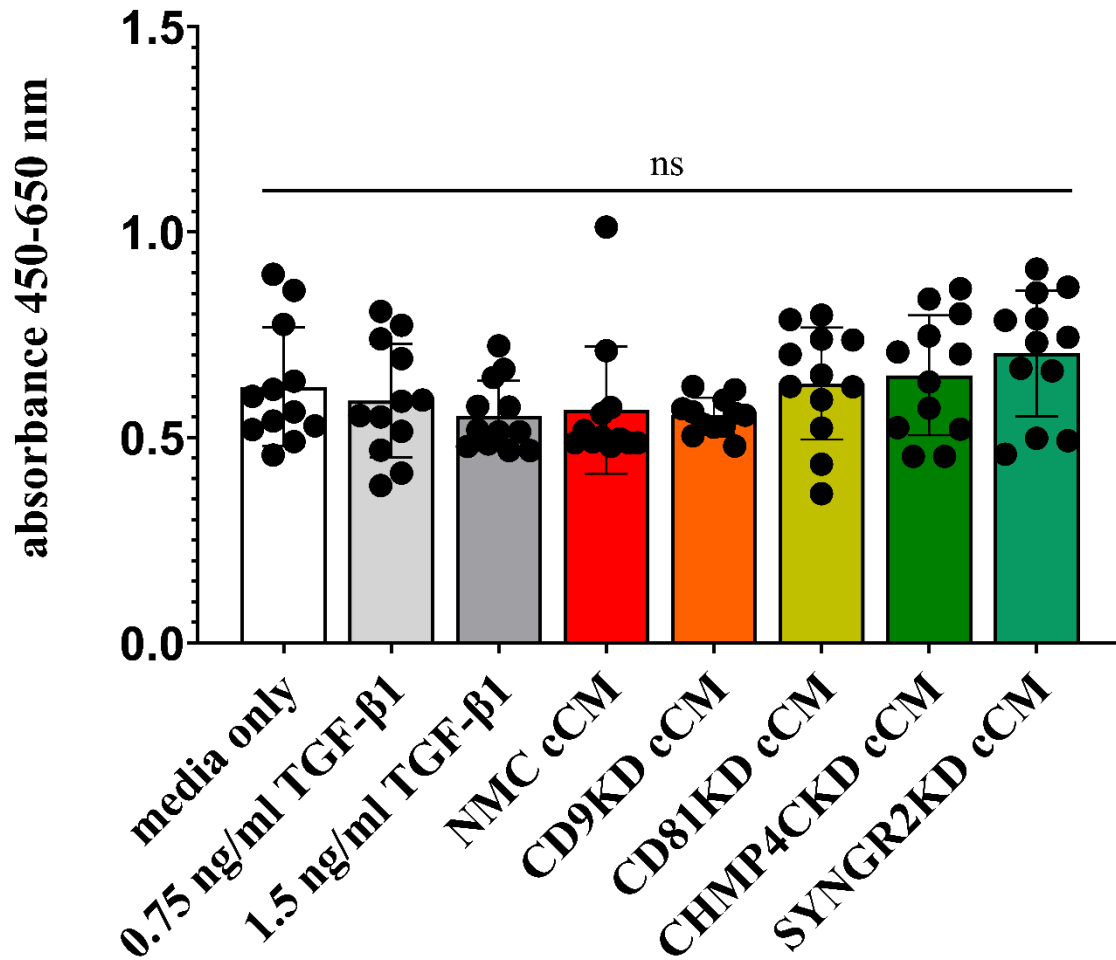


Figure 5.2: PC3 cell-derived CM does not stimulate the proliferation of AG02262 fibroblasts.

AG02262 fibroblasts were seeded at a density of 1,760 cells per well in a 96-well plate. Fibroblasts were treated for 72 h with cCM isolated from the PC3 cell variants NMC, CD9KD, CD81KD, CHMP4CKD, and SYG NR2KD after 72 h of conditioning. Fibroblasts were incubated with OrangU for 1 h and thereafter absorbance was measured with a PHERAstar FS Microplate Reader. Graph shows mean +/-SD, based on 12 wells per condition. The experiment was repeated twice with similar results. One-way ANOVA with Dunnett's multiple comparison post-hoc test was performed. ns= non-significant.

5.2.2 The PC3 secretome induces fibroblast differentiation

Our lab has previously shown that CM derived from DU145 cells, a PCa cell line with a lower metastatic potential than PC3 cells, is sufficient to induce a weak differentiation of fibroblasts to express α -SMA positive stress fibres and therefore acquire a myofibroblast phenotype. Importantly a Rab35 dependant vesicle population was identified as strongly contributing to this mechanism, whilst a Rab11b dependent EV subset was not potent in this process (Yeung et al., 2018). This past evidence highlights that distinct EV subpopulations exert distinct functions on stromal cell recipients.

This provided a precedent therefore to investigate whether there was a CD9, CD81, CHMP4C or SYNGR2 dependent effect on the tumour cell induced polymerisation of α -SMA into stress fibres in fibroblasts. To investigate this, fibroblasts were seeded at equal densities in 8-well chambers and serum starved for 72 h once the fibroblast confluency reached 80%. The starved fibroblasts were treated for 72 h with TGF- β 1 (1.5 ng/ml) as a positive control or media only as a baseline condition. The response was compared to stimulation with cCM from the KD cell variants (CD9KD, CD81KD, CHMP4CKD, SYNGR2KD and the NMC). We used PC3 CM harvesting time points at 48 h and 72 h to detect potential functional consequences of the target attention during early (cCM48h) and later (cCM72h) EV secretion where an accumulation of more EVs at the later timepoint was predicted to give a stronger response. Following the stimulation, the fibroblasts were fixed, and the cells were immunolabelled for α -SMA and microscopically assessed (Figure 5.3).

Stimulating fibroblasts with TGF- β 1 (1.5 ng/ml) induced robust and homogenous α -SMA polymerisation in most fibroblasts. The staining was clearly and unambiguously focussed to stress fibres that were mostly positioned at the longitudinal axis of the cell body. There was the appearance of an alteration in cell shape in addition, with shorter more triangular morphology apparent, compared to other treatments, and this is consistent with past observations of the TGF- β response. As expected, treatment with media only failed to trigger the expression of α -SMA positive stress fibres.

NMC cCM (cCM48h and cCM72h) both caused α -SMA polymerisation, although this was more heterogeneous in its distribution amongst the cell population compared to the positive control. Some individual fibroblasts strongly expressed α -SMA, again as stress fibres in a stellate shape (Figure 5.3, indicated by yellow arrows), whereas others stained weakly and notable stress fibres were not clearly evident (Figure 5.3). The heterogeneity in the expression of α -SMA, with some cells clearly expressing stress fibres while others show a lack thereof, was previously observed in our lab when treating fibroblast with CM or isolated EVs from the DU145 PCa cell line (Yeung et al., 2018, Webber et al., 2015). However, the mechanisms driving this observation are not yet uncovered. Overall, the expression of α -SMA positive structures appeared slightly more obvious in fibroblasts treated with cCM72h compared to a treatment with cCM48h. This indicates that factors released later by PC3 into the CM had accumulated during this period to have stronger potency in modulating the morphology of fibroblasts, as we had expected.

Interestingly, however focusing on the cCM48h treatment conditions (NMC cCM48h, CD9KD cCM48h, CD81KD cCM48h, CHMP4CKD cCM48h and SYNGR2KD cCM48h) differences in the magnitude of the fibroblast response occurred. NMC cCM48h caused a weak expression of α -SMA accompanied by a stellate shape (Figure 5.3, indicated by yellow arrows) of the fibroblasts which was similar to the impact of SYNGR2KD cCM48h. In contrast to this, treatment with CD9KD cCM48h and CD81KD cCM48h appeared to trigger a slightly weaker expression of α -SMA predominantly expressed in fibroblasts with an elongated shape (Figure 5.3, indicated by green arrows). Furthermore, CHPM4CKD cCM48h promoted a strong fibroblast differentiation response characterised by a strong α -SMA expression and a stellate shape of the cells (Figure 5.3).

cCM72h from NMC, CD81KD, CHMP4CKD and SYNGR2KD cells all induced a heterogeneous expression of α -SMA in stress fibres that was accompanied by a mix of stellate and elongated shapes. However, the signal of α -SMA in the fibroblasts generally appeared weaker across the KD cCM stimulations (CD9KD, CD81KD, CHMP4CKD and SYNGR2KD) compared to the NMC stimulation, suggesting all the KDs were functionally perturbed in some fashion. Interestingly, the predominant shape of fibroblasts treated with CD9KD cCM72h appeared to be elongated which indicates that this CM has a reduced

capacity to promote the triangular morphology which was observed upon treatment with NMC cCM72h. Furthermore, fibroblasts subject to CHMP4CKD cCM72h showed a flattened morphology but a reduced α -SMA signal strength compared to both NMC cCM72h and CHMP4CKD cCM48h. This suggests that CHMP4C dependant factors released late by PC3 cells contribute to the potency of the PCa secretome in terms of modulation of fibroblast differentiation, whereas CHMP4C dependant factors released earlier appear to have an independent role.

Taken together, the soluble secretome of PC3 cells was sufficient to elicit weak fibroblast differentiation. All the KD cell lines (CD9KD, CD81KD, CHMP4CKD and SYNGR2KD) cCM72h appeared to have a diminished potency in inducing fibroblast differentiation. However, importantly, some differences in the response depending on the source of the KD cCM were observed. This suggests that the factors released by the PC3 KD cell variants were not only molecular but also functionally distinct with respect to myofibroblast differentiation potency.

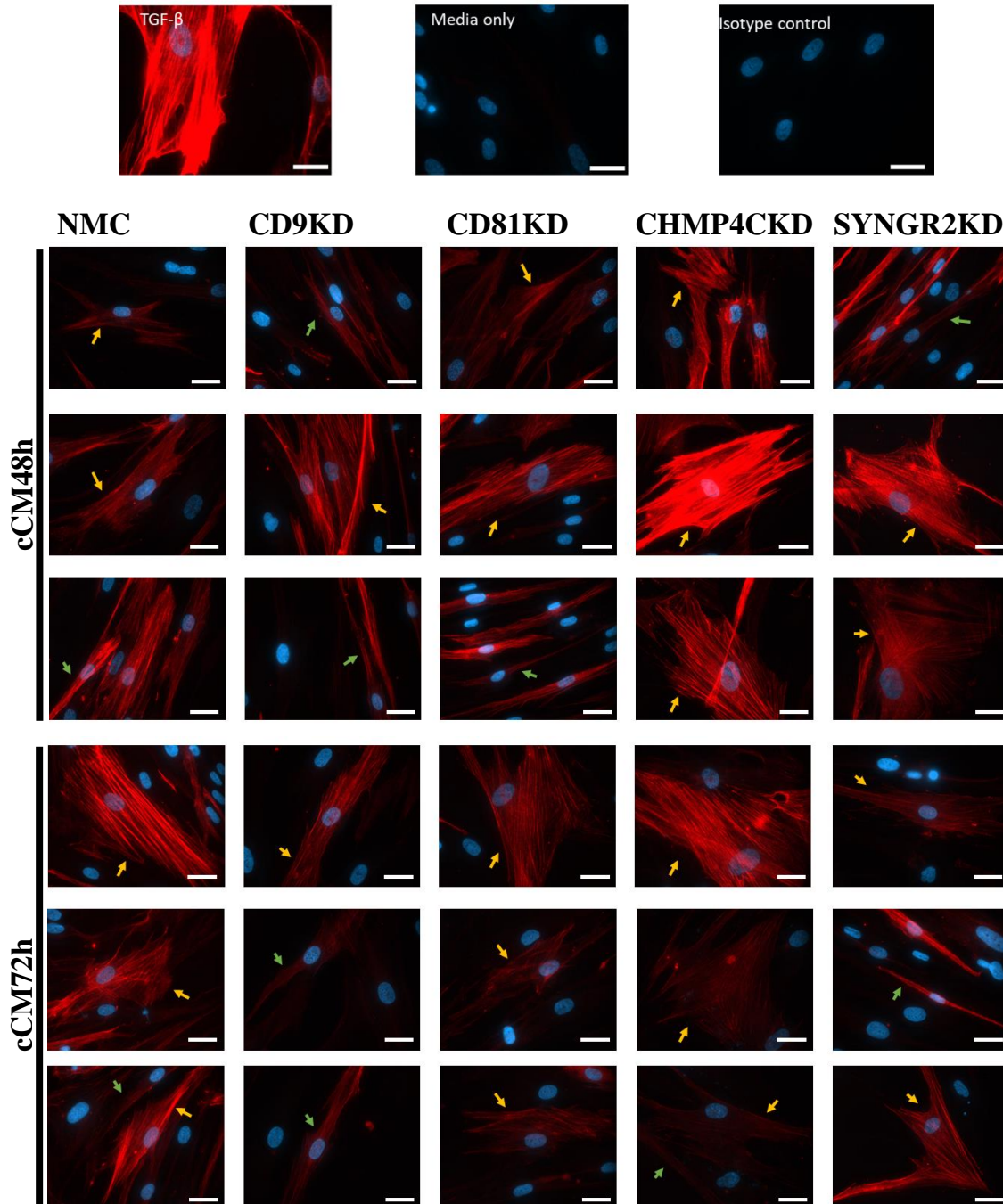


Figure 5.3: PC3 CM triggers fibroblast differentiation to a myofibroblastic phenotype.

Starved fibroblasts were either treated for 72 h with TGF-β1 (1.5 ng/ml), media only, or cCM48h and cCM72h from the PC3 NMC, CD9KD, CD81KD, CHMP4CKD and SYNGR2KD cell variants. The polymerisation of α-SMA in stress fibres was examined by immunofluorescent microscopy visualising the expression of α-SMA (red) and DAPI (blue). Yellow arrows indicate stellate fibroblast shape. Green arrows indicate elongated fibroblast shape. Images were captured in duplicate wells per treatment. 6 microscopic fields were examined per treatment. Representative fields are shown. scale bar = 100 μm.

5.2.3 PC3 CM induce changes in α -SMA transcript expression in fibroblasts

The mechanisms underlying the onset of polymerisation of α -SMA into stress fibres in PC3 CM treated fibroblasts are unclear and perhaps involve a transcriptional upregulation of α -SMA mRNA, increased α -SMA protein translation or increased polymerisation of cytosolic α -SMA monomers into stress fibres, independently of the former two processes. Hence, we briefly explored this and assessed changes in the α -SMA mRNA by qPCR and α -SMA protein levels by immunophenotyping.

Fibroblasts were subject to the same treatment conditions as described above (Figure 5.3). Subsequently RNA was extracted and α -SMA mRNA expression determined by qPCR. α -SMA mRNA expression in fibroblasts remained stable upon TGF- β 1 stimulation, and there was clearly a lack of strong induction of mRNA compared to the media only control (Figure 5.4A and B).

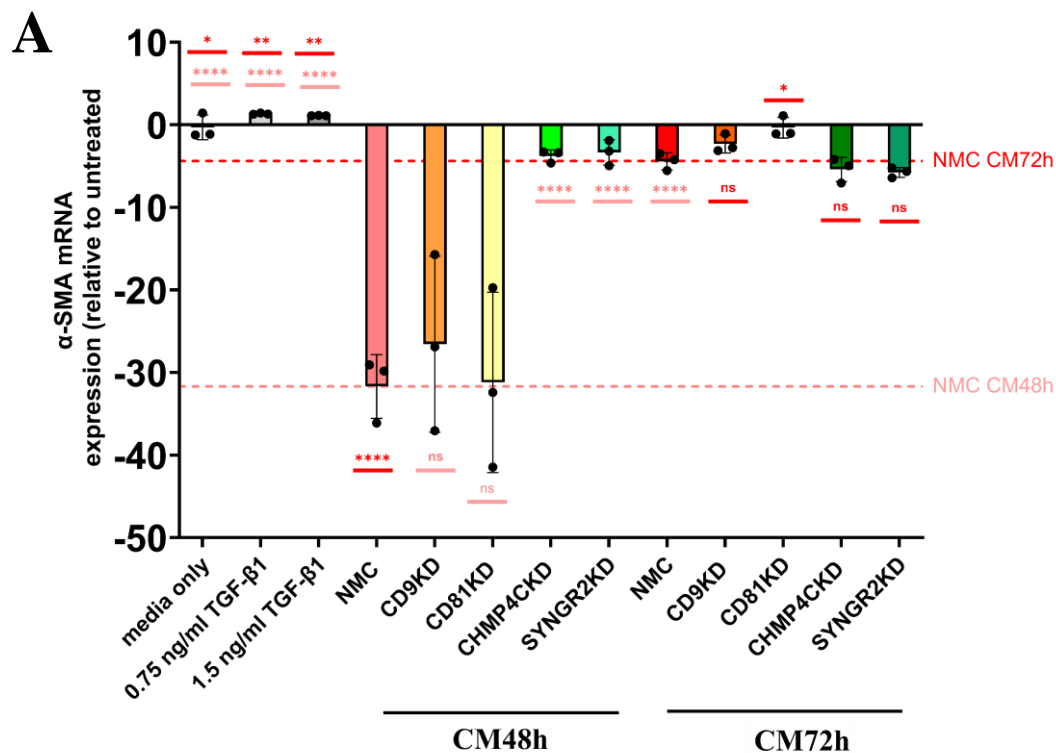
Perhaps unexpectedly, following treatment by CM, we saw a drastic decrease in mRNA for α -SMA in almost all cases. Compared to the media only control, treating fibroblasts with NMC cCM induced downregulation of α -SMA transcripts which was more pronounced under cCM48h (-32-fold change, $P < 0.0001$) than cCM72h treatment (-3.5-fold change, $P < 0.05$) (Figure 5.4). This stronger response to cCM48h was surprising as we predicted a stronger response to cCM72h, where an accumulation of EVs in the CM is present. Hence, these results suggest that cCM72h does not contain a mere accumulation of cellular factors, and perhaps indicates a unique molecular composition compared to cCM48h.

Importantly, the magnitude of α -SMA mRNA downregulation in cCM treated fibroblasts was dependent on the source of cCM (Figure 5.4). Compared to the media only, stimulation with cCM48h from the PC3 cell variants α -SMA mRNA expression was most prominently reduced in the fibroblasts treated with cCM from the NMC cells (-32-fold change), the CD9KD cells (-27-fold change) and the CD81KD cells (-31-fold change), all at comparable levels ($P < 0.0001$). Perhaps, pointing to a rapid RNA utilisation and then degradation caused by this stimulus.

cCM48h from the CHMP4CKD (-4.6-fold compared to the media only treatment) and SYNGR2KD (-3.1-fold compared to the media only treatment) failed to elicit such a strong response and this was consequently also accompanied by a highly significant difference compared to the NMC cCM48h stimulation ($P < 0.0001$). This indicates that both candidates regulate PC3 derived factors that promote the downregulation of α -SMA transcripts in PC3 cCM (Figure 5.4A and B).

At the extended timepoint of 72 h for cCM-conditioning, the dramatic differences became less apparent, and α -SMA mRNA became broadly comparable across the cCM-types (ranging between a -2.3 and -5.4-fold change compared to media only treatment). An exception to this observation was CD81KD cCM72h, which appeared to have a reduced potency indicated by a less prominent downregulation of α -SMA transcripts in the fibroblasts treated with this cCM compared to NMC ($P < 0.05$).

The observed differences in the fibroblast response upon cCM treatment further indicate that the functional potency of the cCM across the KD cell lines is distinct from each other. Furthermore, these results suggests that the onset of α -SMA-stress fibres in cCM treated fibroblasts is not principally regulated by a sustained upregulation of the transcript.



B

Dunnett's multiple comparisons test					
media only vs.	Summary	NMC cCM48h vs.	Summary	NMC cCM72h vs.	Summary
0.75 ng/ml TGF-β1	ns	media only	****	media only	*
1.5 ng/ml TGF-β1	ns	0.75 ng/ml TGF-β1	****	0.75 ng/ml TGF-β1	**
NMC cCM48h	****	1.5 ng/ml TGF-β1	****	1.5 ng/ml TGF-β1	**
CD9KD cCM48h	****	NMC cCM72h	****	NMC cCM48h	****
CD81KD cCM48h	****	CD9KD cCM48h	ns	CD9KD cCM72h	ns
CHMP4CKD cCM48h	ns	CD81KD cCM48h	ns	CD81KD cCM72h	*
SYNGR2KD cCM48h	ns	CHMP4CKD cCM48h	****	CHMP4CKD cCM72h	ns
NMC cCM72h	*	SYNGR2KD cCM48h	****	SYNGR2KD cCM72h	ns
CD9KD cCM72h	ns				
CD81KD cCM72h	ns				
CHMP4CKD cCM72h	ns				
SYNGR2KD cCM72h	ns				

Figure 5.4: PC3 CM downregulates α -SMA mRNA in fibroblasts.

31,500 fibroblasts were seeded in 24-well plates and grown until 80% confluence. The fibroblasts were serum starved for 72 h and subsequently treated for 72 h with media-only, TGF- β 1 or cCM48h or cCM72h from the PC3 NMC, CD9KD, CD81KD, CHMP4CKD and SYNGR2KD cell variants. RNA was extracted and the relative mRNA expression of α -SMA mRNA was determined by qPCR. The ct-values were normalised to GAPDH and compared to the mRNA levels in media only treated fibroblast (A). One-way ANOVA with Dunnett's multiple comparison post-hoc test was performed. ns= non-significant, * = $P < 0.05$, ** = $P < 0.01$, *** = $P < 0.001$, **** = $P < 0.0001$. Light pink stars indicate a comparison to NMC cCM48h, red stars indicate a comparison to NMC cCM72h. A summary of the comparisons is shown in (B).

5.2.4 PC3 CM induces changes in α -SMA protein expression in fibroblasts

Next, we explored whether the induction of stress fibres was caused by an upregulation of α -SMA at a protein level. For this reason, an immunophenotyping plate-based assay was performed. It is important to note, that the immunophenotyping used here gives an overall measurement of the α -SMA content in fibroblasts, in contrast, the microscopy-based approach described above, which is useful to indicate the incorporation of α -SMA into structural stress fibres.

Fibroblasts were seeded at equal densities in 96-well plates. Once the cells reached 80% confluency, the cells were serum-starved, and subsequently treated with TGF- β 1 (0.75 ng/ml or 1.5 ng/ml) or cCM72h from the KD cell variants and the NMC. Given that the microscopy images indicated a bigger impact on α -SMA incorporation in stress fibres when the fibroblasts were stimulated with NM cCM72h, only the impact of cCM72h was assessed in these readouts and all following experiments. The fibroblasts were fixed and incubated with a mouse anti α -SMA antibody. This was followed by the addition of a biotinylated anti mouse antibody. A streptavidin: europium conjugate was added, and the absorbance measured (Figure 5.5).

TGF- β 1 (1.5 ng/ml) treatment induced the formation of α -SMA positive stress fibres (Figure 5.3) independent of an upregulated α -SMA mRNA expression (Figure 5.4). TGF- β 1 treatment (0.75 ng/ml and 1.5 ng/ml) was accompanied by a significant upregulation of α -SMA protein expression compared to the media only control ($P < 0.01$ and $P < 0.0001$ respectively, Figure 5.5). In contrast, NMC cCM72h caused a significant downregulation of the α -SMA protein by 32% compared to the media only treated fibroblasts (Figure 5.5). This indicates that TGF- β 1 and PC3 cCM regulate the expression of α -SMA in fibroblasts through distinct mechanisms, and possibly points to a minor role of soluble TGF- β 1 present in PC3 CM compared to other more prominent factors, perhaps EVs, that contribute to the differentiation of fibroblasts to a myofibroblast phenotype.

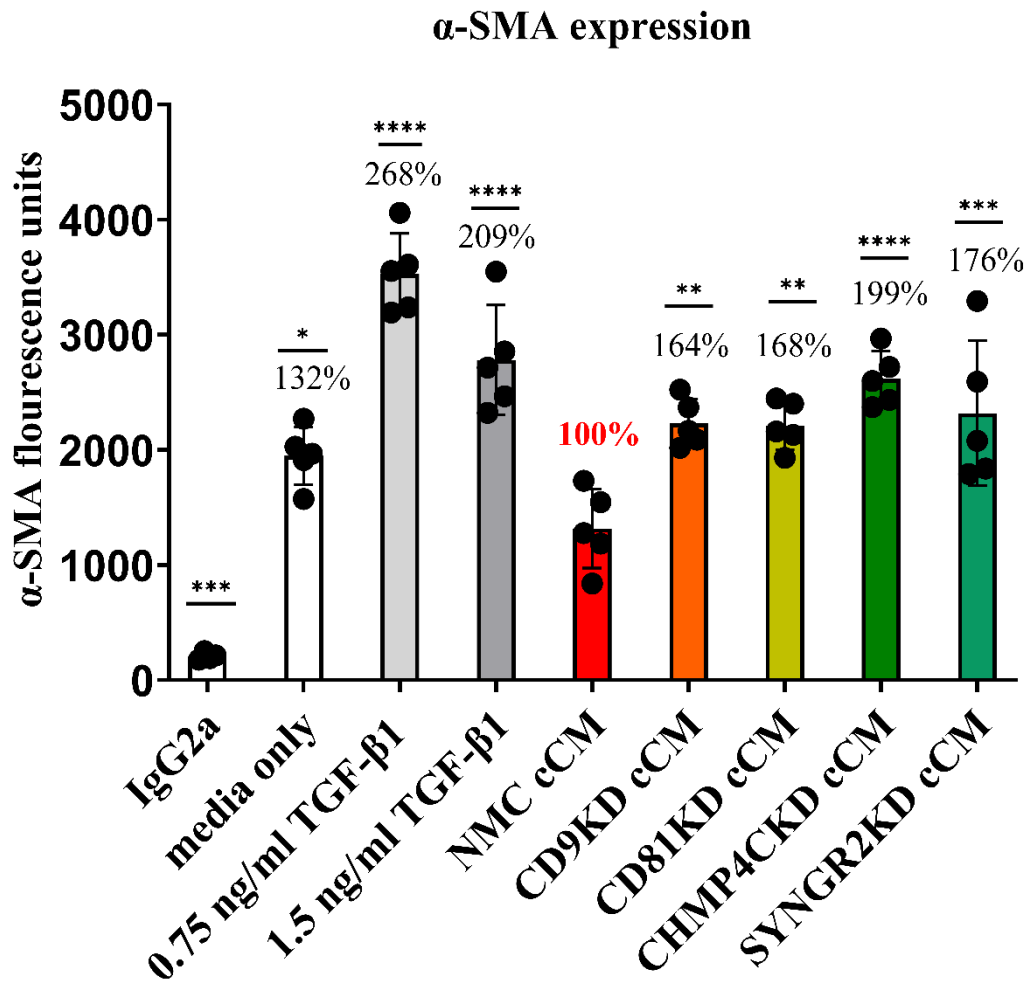


Figure 5.5: PC3 KD cCM dependant modulation of α -SMA protein expression in fibroblasts.

Fibroblasts were seeded at a density of 1,760 cells per well in a 96-well plate and grown until 80% confluent. Subsequently, the cells were treated for 72 h with media only, TGF- β 1 (1.5 ng/ml) or cCM72h obtained from the PC3 cell variants NMC, CD9KD, CD81KD, CHMP4CKD, SYG NR2KD. Fibroblasts were fixed, and a mouse anti α -SMA antibody was added. This was followed by the addition of a biotinylated anti mouse antibody. A streptavidin: europium conjugate was added, and the absorbance measured. Graph shows mean of 5 wells. Percentage above bars indicate percentage upregulation compared to NMC cCM72h treated fibroblasts set at 100%. One-way ANOVA with Dunnett's multiple comparison post-hoc test was performed to compare NMC cCM to the indicated treatment conditions. ns= non-significant, * = P< 0.05, ** = P< 0.01, *** = P<0.001, **** = P<0.0001.

Furthermore, compared to the NMC cCM72h treatment all of the KD cCM72h induced a significant increase in α -SMA protein expression that varied in the magnitude of the impact (Figure 5.5). In comparison to the NMC cCM72h, cCM72h from the CHMP4CKD and SYNGR2KD cell variants both caused the biggest increase in α -SMA protein expression by 99% ($P < 0.0001$) and 76% ($P < 0.001$) respectively. Treatment with the cCM72h derived from the CD9KD cell variant showed the smallest increase compared to the other KDs (64%, $P < 0.01$). Interestingly, CD81KD cCM72h showed increased α -SMA mRNA compared to the NMC cCM72h and this was also accompanied by an increase in the protein by 68% ($P < 0.01$) compared to the NMC cCM72h.

To summarise, these results show that the expression of stress fibres in TGF- β 1 stimulated fibroblasts is induced by an upregulation of protein expression leading to elevated α -SMA protein polymerisation (summarised in table 5.1). In contrast, a different mechanism independent of α -SMA protein and mRNA expression appears to underly the expression of stress fibres in PC3 cCM treated fibroblasts (summarised in table 5.1). Thus, supporting a unique regulatory role of PC3 cell derived factors in modulating fibroblasts.

Importantly for our study, there was considerable variety in the response of the fibroblasts depending on the source of KD cCM treatment with regard to α -SMA expression (in stress fibres, mRNA and protein) (summarised in table 5.1). From all KD cCM72h tested, only CD81KD cCM72h appeared to have a reduced strength in downregulating the α -SMA expression at both mRNA and protein level. In contrast, cCM72h from the CD9KD, CHMP4CKD and SYNGR2KD cell variants all showed only a reduced capacity to suppress the expression of α -SMA protein and not the transcripts. Importantly, these different CM conditions had a distinct impact on the expression α -SMA in stress fibres and the cell shape. cCM72h from the CD9KD cell variant induced a triangular fibroblast morphology, whereas fibroblasts treated with cCM72h CHMP4CKD showed a flattened morphology. SYNGR2KD cCM72h treatment elicited a mix of elongated and triangular α -SMA positive fibroblasts.

This points to a distinct molecular composition dependent on the KD cell variant (CD9KD, or CD81KD, or CHMP4CKD or SYNGR2KD) of the PC3 secretome, which was associated with a perturbed functionality on stromal cells.

Table 5.1: Summary of the impact of PC3 cCM on fibroblasts in regard to α -SMA expression in stress fibres, at mRNA level and at protein.

^ denotes comparison to NMC cCM48h, ^^ denotes comparison to NMC cCM72h. The controls (TGF- β 1 and media only treatment) were also included. \uparrow Indicates upregulation, number of arrows indicate the magnitude of the response, \downarrow indicates downregulation. NA=not applicable.

Treatment		α -SMA expression		
		stress fibres	mRNA	protein
cCM48h	NMC	\uparrow	$\downarrow\downarrow$	NA
	CD9KD [^]	\downarrow	=	NA
	CD81KD [^]	\downarrow	=	NA
	CHMP4CKD [^]	\uparrow	\uparrow	NA
	SYNGR2KD [^]	=	\uparrow	NA
cCM 72h	NMC	$\uparrow\uparrow$	\downarrow	\downarrow
	CD9KD ^{^^}	\downarrow	=	\uparrow
	CD81KD ^{^^}	\downarrow	\uparrow	\uparrow
	CHMP4CKD ^{^^}	\downarrow	=	\uparrow
	SYNGR2KD ^{^^}	\downarrow	=	\uparrow
Controls	TGF- β 1 (1.5 ng/ml)	$\uparrow\uparrow\uparrow$	=	\uparrow
	media only	=	=	=

5.2.5 PC3 CM modulates the secretion of various growth factors by fibroblasts

As described, acquisition of α -SMA stress fibres is indicative of myofibroblast differentiation, but the nuanced phenotype(s) arising from CM as opposed to soluble TGF- β 1 stimulation cannot solely be revealed by this marker alone. Hence, we have investigated the impact of the PC3 CM on the fibroblast secretome with a particular interest in IL-6 and HGF as both have been described to play a critical role in creating a tumour promoting environment (Paland et al., 2009, Davies et al., 2003, Ishii et al., 2018). CM is a complex solution containing soluble factors and EVs, which might work in concert to elicit a robust response in the treated fibroblasts. Therefore, we were interested in investigating the contribution of each PC3

derived fraction (EVs, soluble factors and a combination of both) on the secretome of recipient fibroblasts by utilising modified ELISAs.

To investigate this, serum-starved fibroblasts were treated with full cCM72h as discussed before where a host of various cell derived factors are released from cancer cells. Or, to assess the contribution of EVs, the cCM72h was subject to ultracentrifugation to pellet EVs and subsequently the isolated EVs and the corresponding EV depleted cCM were used for the following experiments. It must be noted that the efficacy of depletion in these experiments was not confirmed but studies previously done by colleagues in the lab clearly showed a depletion of >80% by these methods, and a concomitant loss of potency with depletion, and a restoration of potency upon adding the EV-rich pellet. The levels of the chemokines IL-6 and HGF secreted by the treated fibroblasts was then quantified by a modified ELISA. Importantly, the concentrations of both chemokines present in the PC3 CM were below the detection threshold of the modified ELISAs, and thus, the measured IL-6 and HGF levels in the system are largely or entirely secreted by fibroblasts.

5.2.5.1 PC3 EVs modulate the secretion of IL-6 in recipient fibroblasts

In baseline conditions, media only treated fibroblasts secreted 108 pg/ml IL-6 which became increased to 1,081-1,375 pg/ml IL-6 upon stimulation with TGF- β 1 (0.75 ng/ml and 1.5 ng/ml) (Figure 5.6A). All NMC treatment conditions caused a significant increase of IL-6 that ranged between 711 pg/ml (NMC EVs) - 2,017 pg/ml (NMC cCM). EV depletion was only partially successful in reducing the maximum level to 1,778 pg/ml (NMC cCM-EV) (Figure 5.6A and B). This highlights that most of the IL-6 inducing potency herein resides within the non-EV fraction of the cCM. Of note, this seems to be case for all of the KD CM tested here (Figure 5.6A and B).

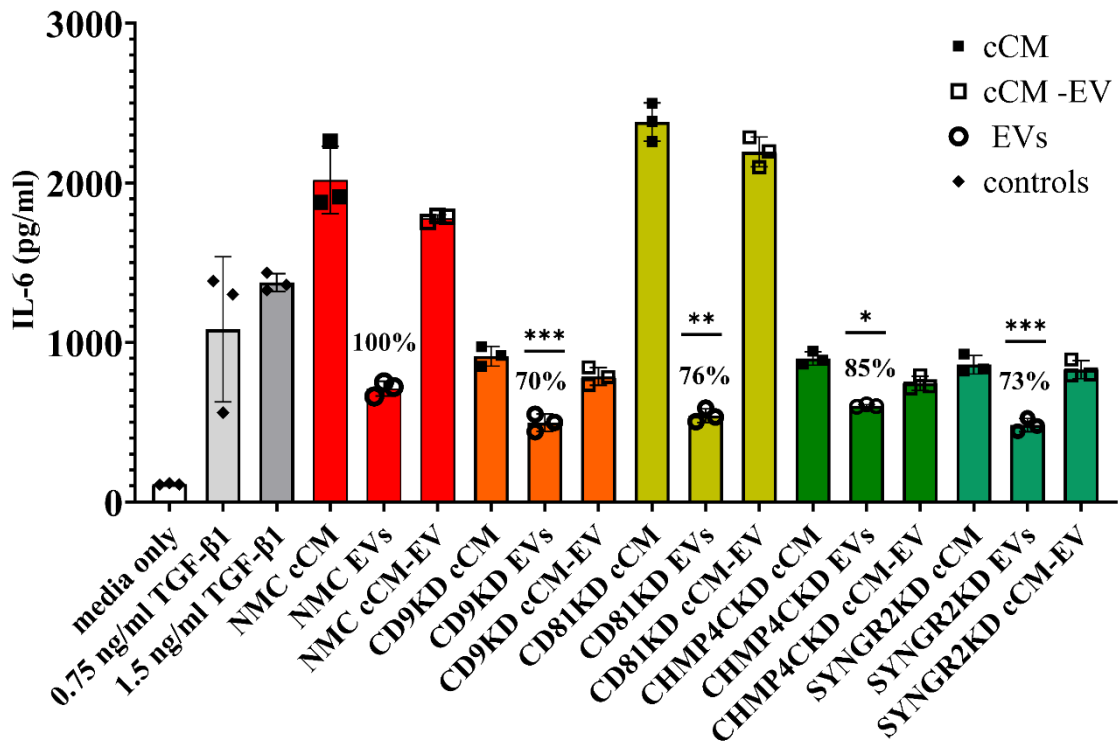
Direct stimulation of fibroblasts with the pelleted NMC EVs was, however, were sufficient to elevate the IL-6 concentration to 711 pg/ml which is 35% of the NMC cCM treatment (2,017 pg/ml). When comparing across the various EV treatments, all KD EVs appeared to elicit a significantly reduced secretion of IL-6 compared to the NMC EVs (711 pg/ml, 100%). The most dramatic reduction was observed for CD9KD EVs (497 pg/ml, 70%, $P < 0.001$) and

SYNGR2KD EVs (522 pg/ml, 73%, $P < 0.001$), followed by CD81KD (541 pg/ml, 76%, $P < 0.01$) and CHMP4CKD EVs, which also induced a slightly reduced IL-6 secretion (603 pg/ml, 85%, $P < 0.05$).

An increase in the detection of IL-6 in the fibroblast secretome can be caused by an upregulation of IL-6 transcription, increased release, inhibited uptake or a combination of the aforementioned. To briefly explore this, fibroblasts were cultured as previously described and treated with the repertoire of isolated EVs from cCM72h, media only or TGF- β 1 (0.75 ng/ml or 1.5 ng/ml). We investigated only the impact of EVs, as this is the major focus of the work. Fibroblast RNA was extracted, and IL-6 mRNA levels determined by qPCR. This showed no significant differences at the IL6 mRNA level under these conditions (Figure 5.6C).

To summarise, PC3 CM modulates the secretion of IL-6 in treated stromal fibroblasts. cCM derived EV pellets alone were sufficient to trigger a partial increase in this release. Importantly, compared to NMC EVs, EVs from all the KD cells (CD9KD, CD81KD, CHMP4CKD, SYNGR2KD) showed a significant reduction in their ability to promote increased IL-6 secretion. Hence, the KDs have perturbed the pro-inflammatory functionality of the EVs.

A



B

fibroblast treatment	IL-6 concentrations in pg/ml		
	cCM	EVs	cCM-EVs
NMC	2,017	711	1,778
CD9KD	914	497	787
CD81KD	2,380	541	2,193
CHMP4CKD	899	603	744
SYNGR2KD	860	522	829

C

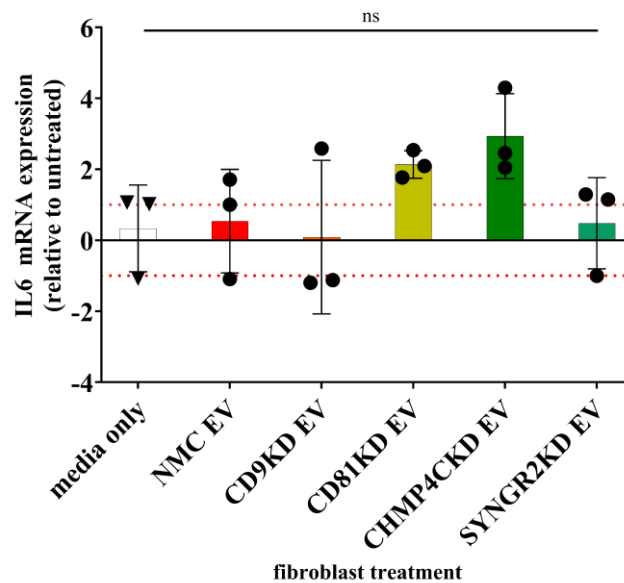


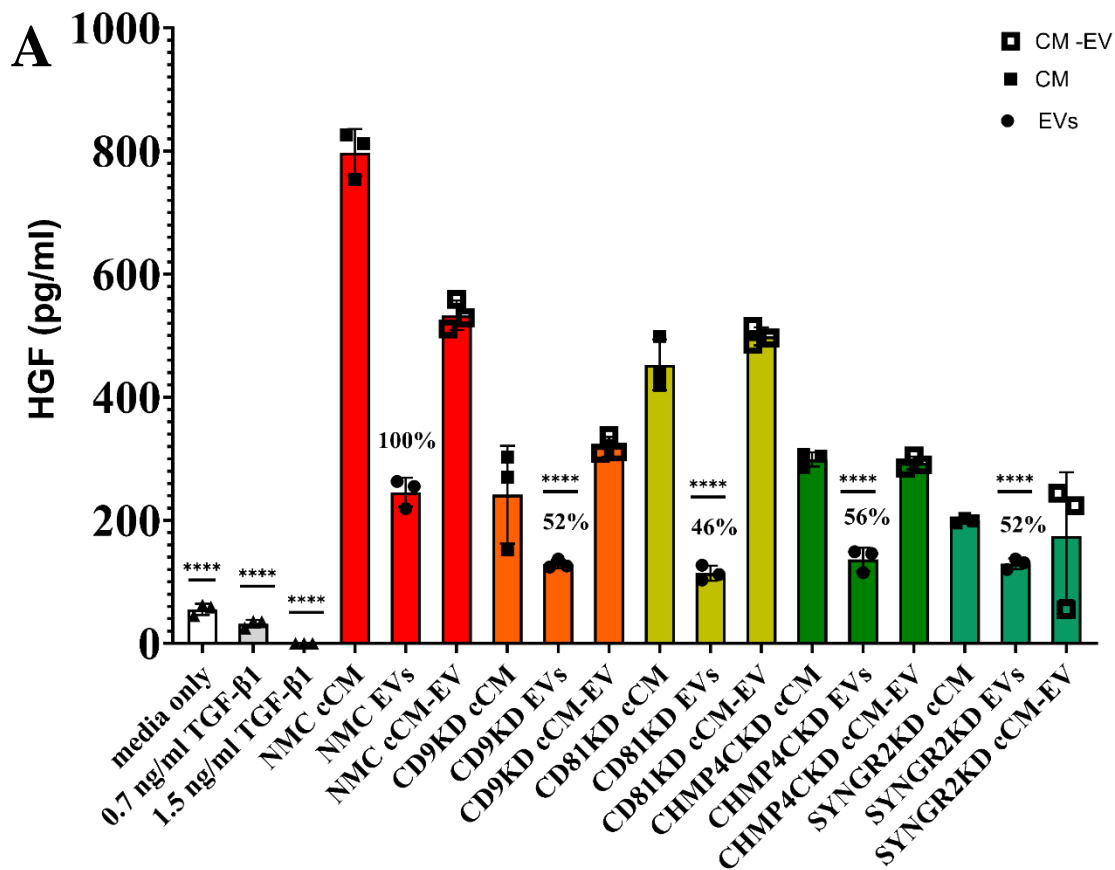
Figure 5.6: CD9KD, CD81KD, CHMP4CKD and SYNGR2KD derived EVs lose their potency to induce IL-6 secretion in recipient fibroblasts.

CM from NMC, CD9KD, CD81KD, CHMP4CKD and SYNGR2KD cells was collected, normalised to cell number and subject to an ultracentrifugation step. The cCM, the EV pellet (EVs) and EV depleted fraction (cCM-EV) were used for the experiments. Fibroblasts were starved and treated with media only, TGF- β 1 (0.75 or 1.5 ng/ml), EV depleted media (cCM-EV), EVs or full CM (cCM). CM from the treated fibroblasts was collected and IL-6 levels were determined with an ELISA for IL-6 (A and B). RNA was extracted from the stimulated fibroblasts and the relative mRNA expression of IL-6 was determined by qPCR (C). The ct-values were normalized to GAPDH and compared to the mRNA levels in media treated fibroblast. Symbols indicate technical replicates of the same cell population. One-way ANOVA with Dunnett's multiple comparison post-hoc test was performed, and ns= non-significant, * = $P < 0.05$, ** = $P < 0.01$, *** = $P < 0.001$, **** = $P < 0.0001$. Red lines indicate the IL-6 mRNA expression range of the fibroblasts (C). The symbols denote the treatment conditions: circles=EVs, filled squares=cCM., only square outlines=cCM-EV.

5.2.5.2 PC3 EVs modulate the secretion of HGF in fibroblasts

Media only treated fibroblasts, secreted 62 pg/ml HGF which was reduced by treatment with increasing TGF- β 1 concentration (47 pg/ml for treatment with 0.75 ng/ml TGF- β 1, and 14 pg/ml for treatment with 1.5 ng/ml TGF- β 1). This HGF reduction is well documented and is perhaps counter intuitive given the potent myofibroblast differentiation trigger of TGF- β 1 (Webber et al., 2015). Yet HGF is secreted by myofibroblasts that are generated through EV-stimulus as we previously reported (Webber et al., 2015). NMC cCM induced the biggest increase in HGF release in fibroblasts compared to all other full CM conditions tested here (Figure 5.7A and B). Importantly, compared to the NMC cCM, NMC EV depleted media failed to elicit the same concentration of HGF (797 pg/ml vs 533 pg/ml), which indicates that soluble factors alone are insufficient to trigger full HGF secretion, and that the potency is present in the pelleted EV rich material (Figure 5.7A and B). Interestingly HGF concentrations that were caused by NMC EVs (246 pg/ml) and NMC EV depleted media (533 pg/ml) together added up to 779 pg/ml, which is similar to the HGF concentration measured for fibroblasts treated with NMC full media (797 pg/ml). This indicates that NMC EVs are a critical constituent of NMC cCM working additively to elicit the elevated HGF secretion in fibroblasts, and account for ~30% of the total activity.

Noticeably, this seemed not to be the case for the fibroblasts stimulated with CM from the CD9KD, CD81KD, CHMP4CKD and SYNGR2KD cell variants (Figure 5.7). Compared to NMC EV pellets (246 pg/ml, 100%), EV concentrates derived from all the KD cell variants caused a relatively poor increase in the release of HGF in fibroblasts ($P < 0.0001$), giving only about 50% of the control EV-activity.



B

fibroblast treatment	HGF concentrations in pg/ml		
	cCM	EVs	cCM-EVs
NMC	797	246	533
CD9KD	242	129	319
CD81KD	453	114	499
CHMP4CKD	299	137	293
SYNGR2KD	200	129	174

Figure 5.7: CD9, CD81, CHMP4C, and SYNGR2 dependant EVs induce HGF secretion in fibroblasts.

CM from NMC, CD9KD, CD81KD, CHMP4CKD and SYNGR2KD cells was collected, normalised to cell number and subject to an ultracentrifugation step and all fractions used for the experiment. Fibroblasts were starved and treated with media only, TGF- β 1 (0.75 or 1.5 ng/ml), EV depleted media (cCM-EV), EVs or full CM (cCM). CM from the treated fibroblasts was collected and HGF levels were determined with an ELISA for HGF (A). The corresponding absolute HGF concentrations are shown in (B). One-way ANOVA with Dunnett's multiple comparison post-hoc test was performed, and ns= non-significant, * = $P < 0.05$, ** = $P < 0.01$, *** = $P < 0.001$, **** = $P < 0.0001$. A) displays the statistical analysis comparing NMC EV treatment to KD EV treatment. The symbols denote the treatment conditions: circles=EVs, filled squares=cCM., only square outlines= cCM-EV.

HGF production by fibroblasts can be modulated at the transcriptional level. This was explored by determining the HGF mRNA levels in treated fibroblasts by qPCR (Figure 5.8). Here, treating fibroblasts with TGF- β 1 (0.7 ng/ml and 1.5 ng/ml) caused a decrease in the detection of HGF in fibroblast CM. This was also reflected at a transcript level as a 4.4-fold downregulation in the expression of HGF mRNA upon treatment with TGF- β 1 (1.5 ng/ml) (Figure 5.8). The correlation of HGF secretion and HGF mRNA levels were also investigated for fibroblasts stimulated with EVs and revealed there were no changes in the HGF transcript level across all conditions tested (Figure 5.8). This shows that EVs and soluble TGF- β 1 elicit distinct cellular responses in recipient fibroblasts.

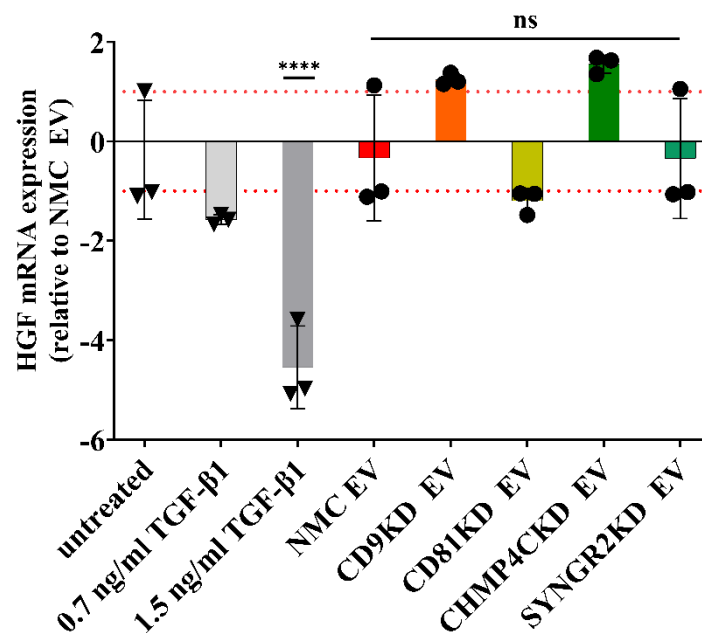


Figure 5.8: PC3 EVs increase HGF secretion in fibroblasts independent of HGF mRNA upregulation.

CM from NMC, CD9KD, CD81KD, CHMP4CKD and SYNGR2KD cells were collected, normalised to cell number and subject to an ultracentrifugation step to purify the EVs. Fibroblasts were starved and treated with media-only, TGF- β 1 (0.75 or 1.5 ng/ml) or EVs. RNA was extracted from the stimulated fibroblasts and the relative mRNA expression of HGF was determined by qPCR. The ct-values were normalized to GAPDH and compared to the mRNA levels in media only treated fibroblast. Symbols indicate technical replicates of the same cell population. Red lines indicate the range of the relative HGF mRNA levels of fibroblasts treated with NMC EVs. One-way ANOVA with Dunnett's multiple comparison post-hoc test was performed, and ns= non-significant, **** = $P < 0.0001$.

Taken together, the data presented here indicates that EVs are a critical component in the PC3 cell derived CM that modulate the secretome of fibroblasts. Importantly, the results suggest a critical role of CD9, CD81, CHMP4C and SYNGR2 in contributing to the functional properties of the EVs (summarised in table 5.2).

Table 5.2: Summary of the impact of PC3 EVs on recipient fibroblasts.

↓ indicates reduced levels, = indicates no changes observed, ↑ indicates elevated levels.

	Treatment	Impact on fibroblasts			
		IL-6		HGF	
		secretion	mRNA	secretion	mRNA
compared to NMC EV	NMC EV	↑	=	↑	=
	CD9KD EV	↓	=	↓	=
	CD81KD EV	↓	=	↓	=
	CHMP4CKD EV	↓	=	↓	=
	SYNGR2KD EV	↓	=	↓	=
controls	TGF-β1 (1.5 ng/ml)	↑	↑	↓	↓
	media only	=	=	=	=

5.2.6 PC3 EVs alter the phosphorylation profile of fibroblasts

After showing that EVs from the KD cells had diminished potency in triggering a cellular response in recipient fibroblasts, we aimed to explore the activated pathways that possibly regulate cytokine secretion and the cellular phenotype in more detail. For this purpose, a phosphokinase assay, detecting the phosphorylation of 37 human analytes in one sample, was utilised to explore possible changes in activated pathways upon EV stimulation.

Fibroblasts were grown as previously described and treated with 200 µg/ml of EVs (NMC, CD9KD, CD81KD, CHMP4CKD, SYNGR2KD) or media only. After 2 h, fibroblasts were

lysed, and the protein concentration determined. Thereafter, equal amounts of cell lysates were added to the array membranes, and phosphorylated proteins were detected.

The impact on protein phosphorylation, of media only treated fibroblasts was compared to fibroblasts stimulated with isolated NMC EVs first (Figure.5.9 and table 5.3). Interestingly a few analytes were phosphorylated even when the fibroblasts were treated with media only: PDGF, SRCp53, STAT3 and Akt, presumably reflecting baseline activation or constitutive autocrine stimulation of these pathways.

With, NMC EVs stimulation, some kinases were more strongly phosphorylated, indicated by a 1.5 stronger spot intensity compared to the control, and others interestingly were less phosphorylated, indicated by 0.5 less strong spot intensity compared to the control (7 and 3 respectively, Figure 5.9 and table 5.3). Thus, suggesting that EVs induce the activation of several kinases and whilst also suppressing the phosphorylation of others, or activating phosphatases.

Focusing on the analytes that were detected with at least a 1.5 higher spot intensity on the membranes subject to NMC EV treated fibroblasts compared to the control, revealed the activation of several constituents linked to differentiated fibroblasts. These included regulators of α -SMA expression (Akt1), immunomodulation (STAT3) and ECM remodelling (RSK1 and STAT3), suggesting a strong and multi-pathway activation of fibroblasts (described in detail in table 5.3). Given the important role of STAT3 in controlling cytokine secretion, this analyte was of particular interest. In the previous chapter, I described that NMC EVs carry TGF- β 1, interestingly TGF- β 1 has previously been described to induce the phosphorylation of STAT3 in human dermal fibroblasts, which in turn promotes the deposition of collagen (Chakraborty et al., 2017).

However, it is also important to note that both IL-6 and HGF, promote the phosphorylation of STAT3 (Wegenka et al., 1993, Zhang et al., 2002), thus the observed increase in STAT3 phosphorylation could be due autocrine stimulation and only reflect a secondary impact of EV stimulation.

A number of analytes (3) were also detected with lower spot intensity subject to NMC EV treated fibroblasts compared to the media only treated fibroblasts (0.5 or less, described in detail in table 5.3). Surprisingly, these targets included several potential positive regulators of CAF activation and hence the decreased phosphorylation of some of these analytes suggest this is not a general global fibroblast activation, but a specific response which reflects a balance of activated and regulated pathways. Of specific interest here, is the decreased phosphorylation of β -Catenin. Increased phosphorylation targets the protein for degradation where it cannot induce the expression of its target genes. On the other hand, unphosphorylated β -Catenin remains as a stable pool in the cytosol. Recently, low β -Catenin expressing fibroblasts were associated with an inflammatory CAF phenotype in colorectal cancer (Mosa et al., 2020). Hence, an increased cytosolic pool of β -Catenin, as suggested by the decreased phosphorylation, appears to contradict the observations described in this chapter that NMC cCM72h and NMC EVs modulate the secretome of fibroblasts. However, Mosa et al. investigated CAF β -Catenin expression in the context of colorectal cancer, and thus their findings may represent a distinct impact on stromal cells specific to this cancer type (Mosa et al., 2020). Furthermore, the phosphokinase assay performed here only provides indications of activated pathways and a subsequent confirmation with orthogonal methods is required to draw firm conclusions.

Taken together, stimulation of fibroblasts with NMC EVs induced the phosphorylation of several analytes that are associated with differentiated fibroblasts, that express and secrete ECM and chemokines. Nevertheless, several targets exhibited reductions in phosphorylated targets implying selectivity in the response.

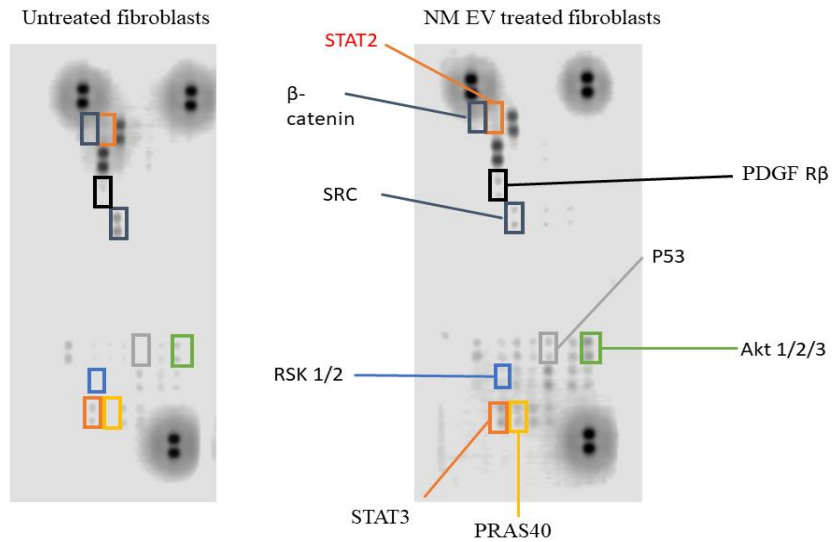
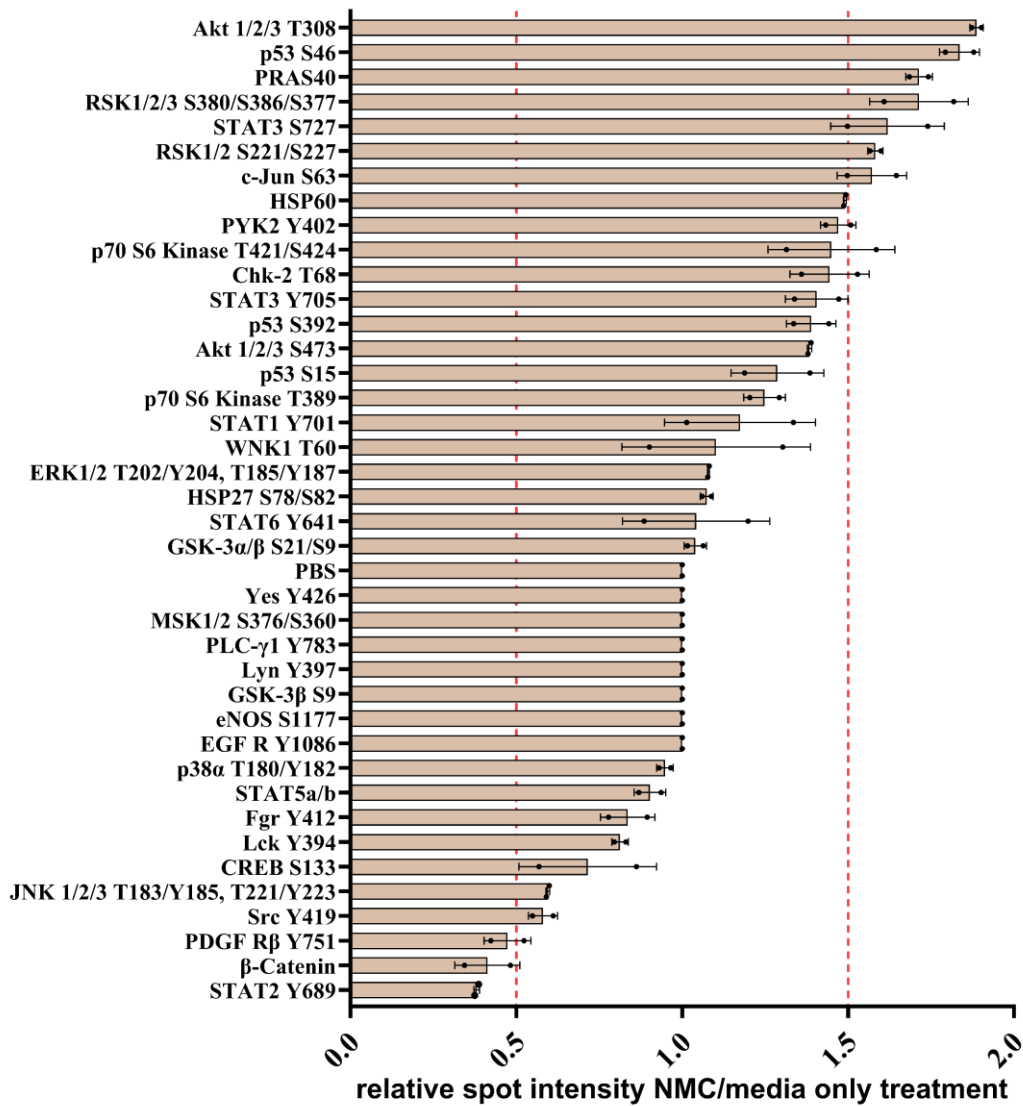
A**B**

Figure 5.9: PC3 EVs alter target phosphorylation in recipient fibroblasts.

Starved fibroblasts were either treated with media only or 200 $\mu\text{g/ml}$ NMC EVs. The fibroblasts were lysed, and the lysate analysed with a proteome profiler phosphokinase array. Membranes were scanned to measure spot intensity as a relative measure of analyte-phosphorylation (A). The mean intensity of the detected spots on the membrane treated with the lysate from the NMC EV treated fibroblasts was determined and compared to the mean intensity of the detected spots on the membrane treated with the lysate from media only treated fibroblasts (B). The dotted line indicates a relative 0.5 and 1.5-fold spot intensity comparing NMC EV treatment to the media only treatment. y-axis shows the respective analyte, x-axis shows relative spot intensity.

Table 5.3: Most prominent alterations in the phosphorylation pattern in fibroblasts upon EV stimulation.

The mean intensity of the detected spots on the membrane treated with the lysate from the NMC EV treated fibroblasts was determined and compared to the mean intensity of the detected spots on the membrane treated with the lysate from media only treated fibroblasts. Mean intensities >1.5 and <0.5 are summarised in the table. The reported function of the analyte, and the potential functional consequences of decreased or increased phosphorylation in the fibroblasts are also noted. + indicates positive result/activation, - indicates negative results/suppression.

Analyte	Proposed function in fibroblasts and other potentially relevant information	References	Phosphorylation increased (+) or decreased (-) compared to media only	Possible functional consequence here		
				Chemokine release	α SMA expression	ECM components deposition
STAT3 S727	<ul style="list-style-type: none"> -Is phosphorylated by IL-6, HGF and TGF-β1 -Target gene is IL-6 -Regulates pro-inflammatory response -Regulates the deposition of collagen -Promotes ECM disposition in a mouse model of colitis (not yet confirmed in a cancer model) -Is activated in an inflammatory CAF phenotype 	(Wegenka et al., 1993) (Zhang et al., 2002) (Chakraborty et al., 2017, Biffi et al., 2019) (Li et al., 2015a). (Yang et al., 2016) (Allam et al., 2021)	+	+		

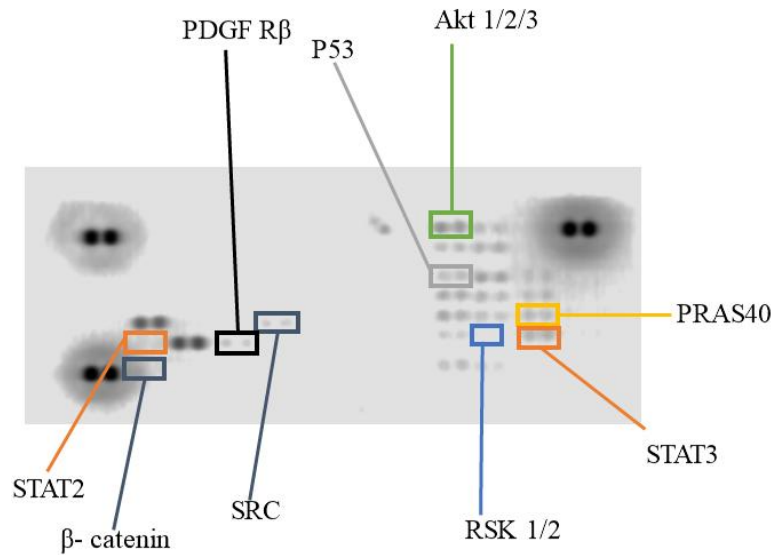
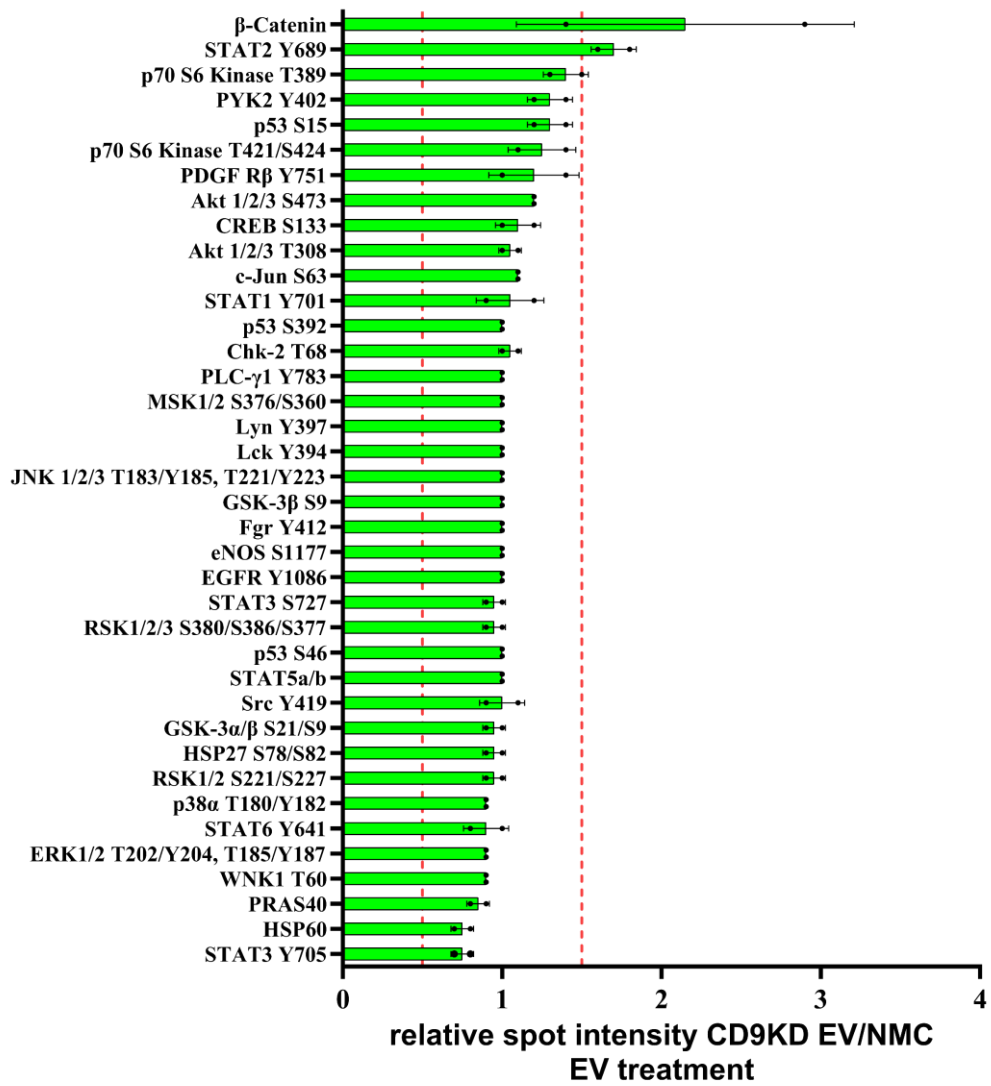
Akt 1/2/3 T308	-IL-6 induces Akt phosphorylation in skin fibroblasts -HGF induces Akt phosphorylation -Increases the expression of α -SMA in fibroblasts	(Abdalla et al., 2013) (Nishikai-Yan Shen et al., 2017) (Huang et al., 2012, Reyes-Gordillo et al., 2011)	+		+	
RSK1/2 S221/S227/ S380/S386/ S377	-Regulates cell motility and proliferation in PCa cells -Anti-apoptotic function -During hypoxia, RSK1 upregulates metalloproteinase 17 in lung fibroblasts	(Cronin et al., 2021) (Sun et al., 2023a) (Chen et al., 2017b)	+			+
PRAS40	-TGF- β induces phosphorylation of PRAS40 in kidney cells -Protection from apoptosis	(Dey et al., 2012, Lv et al., 2017b)	+	?	?	?
c-Jun S63	-Phosphorylates JNK/SAP -Anti-apoptotic function	(Wisdom et al., 1999)	+	?	?	?
p53 S46	-Regulates apoptosis (tested in different cell lines) -Activates RSK1	(Smeenck et al., 2011, Feng et al., 2006, Bohuslav et al., 2004)	+	?	?	+? (via RSK1)
STAT2 Y689	-Regulator of α -SMA negative FAP positive CAFs	(Pan et al., 2023).	-		-	

PDGF R β Y751	-Myofibroblast activation in renal fibrosis -Co-expressed with α -SMA in CAFs from PCa (CAF-S1 phenotype, PDGFR α , CREB3L1 and PLAGL1 positive (CAF-S2), α -SMA, HOXB2 and MAFB positive (CAF-S3)	(Chen et al., 2011, Chen et al., 2021a)	-		-	
β -Catenin	-Low β -Catenin expression in fibroblasts was associated with an immunomodulatory CAF phenotype	(Mosa et al., 2020).	-	+		

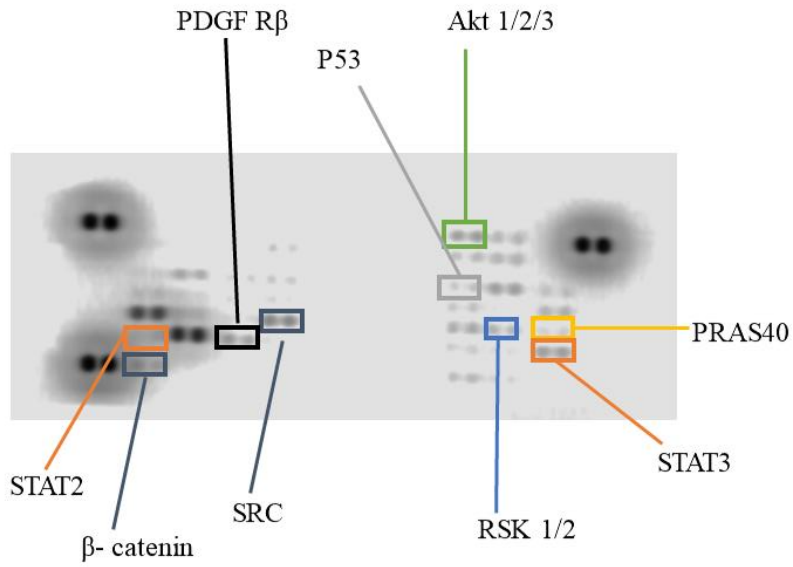
The cell variants generated for this work CD9KD, CD81KD, CHMP4CKD, SYG NR2KD all have attenuated expression of the respective target, but we expect also to have impacted a number of other constituents of the vesicles that may be related to the target's influence on vesicle biogenesis/molecular loading. As a consequence, an overlap in the functional properties of EVs from these cell variants with NMC EVs is expected, in terms of the phospho-protein alterations. Indeed, stimulating fibroblasts with these EVs from the KD cells showed a similar impact on the phosphorylation of targets in fibroblasts compared to the NMC EVs (Figure 5.10).

Inspecting the subtle changes in the phosphorylation patterns, it was clear that many of the top hits for NMC EV stimulation (1.5 spot intensity compared to media only treated) appeared to be less phosphorylated upon stimulation with the KD EVs (table 5.4). In addition, many of the top hits that showed reduced phosphorylation upon NMC EV treatment appeared to be more phosphorylated upon KD EV treatment. The magnitude of the impact depended on the source of the EVs with CHMP4CKD and SYNGR2KD showing the biggest impact (compared to the NMC EV stimulation, 9 analytes detected with at least 1.5 higher spot intensity, Figure 5.10F and H) and CD9KD EV the smallest (compared to the NMC EV stimulation, 2 analytes detected with at least 1.5 higher spot intensity, Figure 5.10A and B)). Strikingly, increased phosphorylation of 3 targets (β -catenin, PDGF R β and STAT2) was consistently found across all KD EV treatment conditions pointing to consistent changes across all KD conditions (table 5.4). This suggests at least a partial functional overlap of the KD EVs and consequently indicates that the target attenuations had a partial common impact on the PC3 cells.

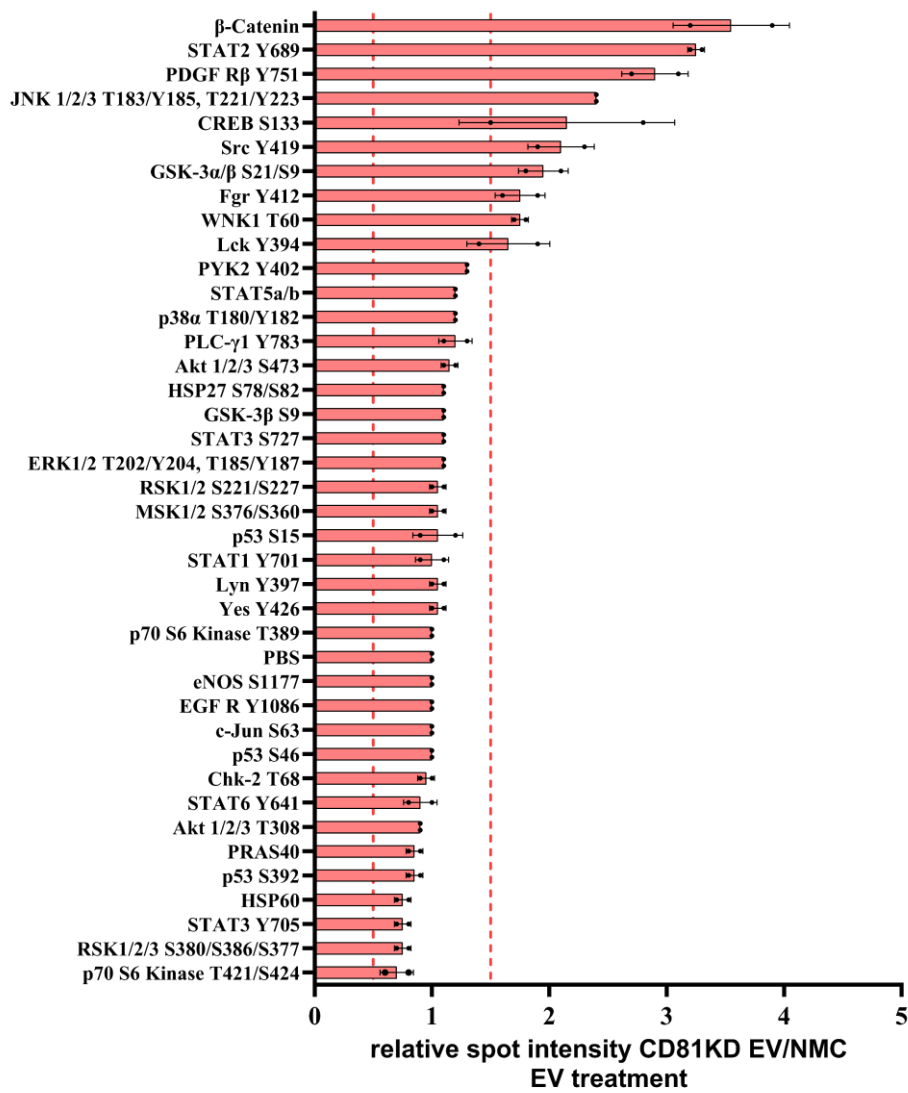
Of specific interest is the phosphorylation of STAT2, which has been recently proposed to regulate an α -SMA negative CAF population in PCa (Pan et al., 2023). This is in line with the observation that the KD PC3CM showed reduced potency for inducing the polymerisation of α -SMA. However, the potential role of EVs in regulating the described α -SMA negative CAF subtype is currently not known and highlights the importance for further investigations to unravel the functional significance of α -SMA-negative fibroblasts upon EV stimulation.

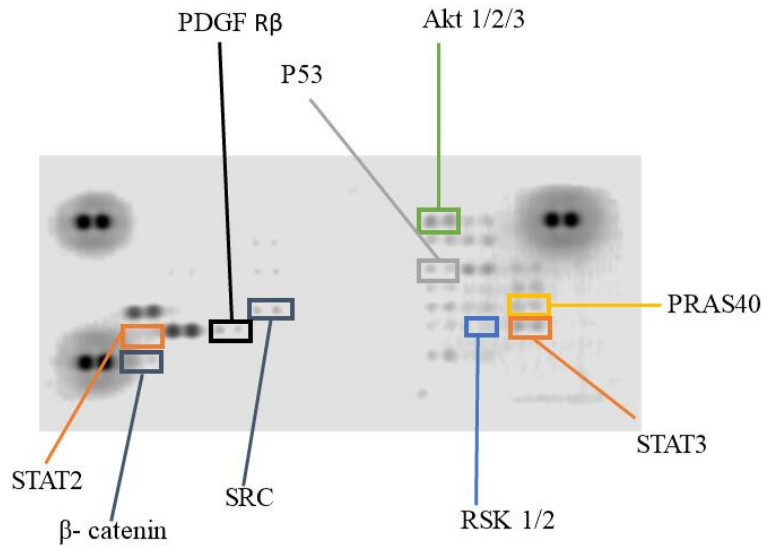
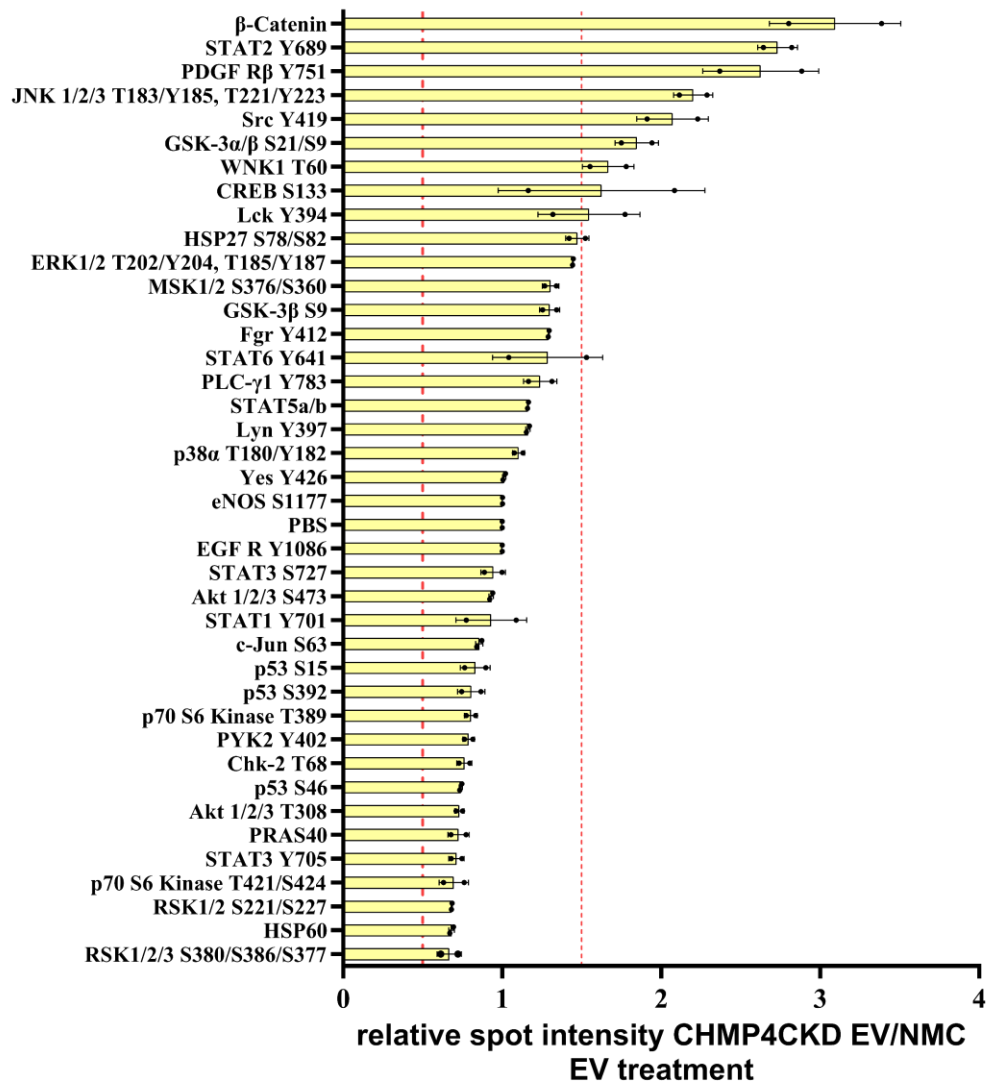
A**B**

C

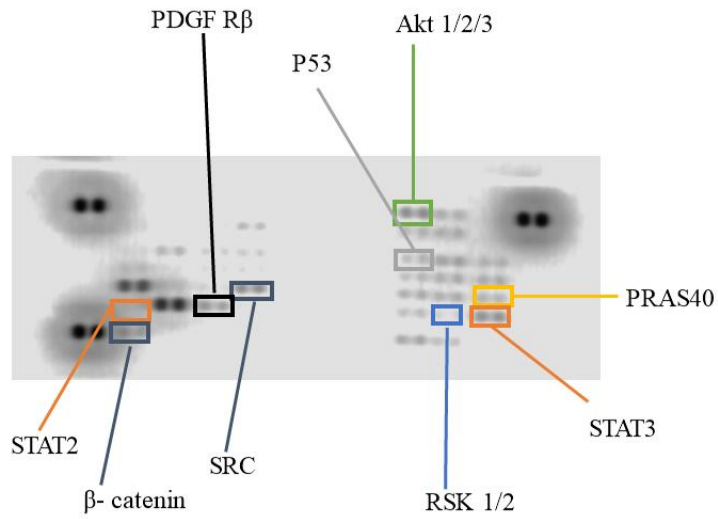


D



E**F**

G



H

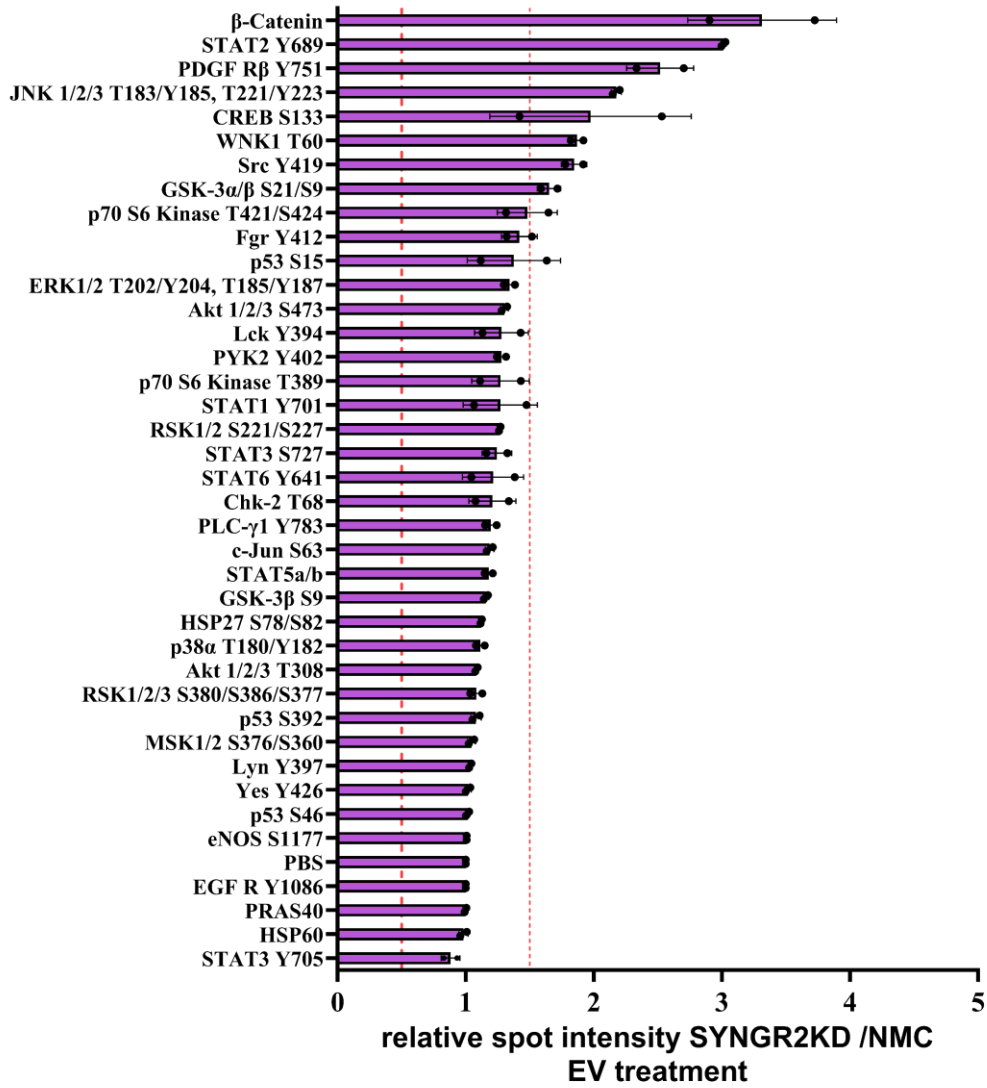































Figure 5.10: PC3 EVs alter target phosphorylation in recipient fibroblasts.

Starved fibroblasts were either treated with media, 200 ug/ml NMC EVs, CD9KD EVs, CD81KD EVs, CHMP4CKD EVs or SYNGR2KD EVs. The fibroblasts were lysed, and the lysate analysed with a proteome profiler phosphokinase array. Membranes were scanned to detect the phosphorylation of the analytes in fibroblasts treated with CD9KD EVs (A), CD81KD EVs (C), CHMP4CKD EVs (E), SYNGR2KD EVs (G). The mean intensity of the spots was measured and compared to fibroblasts treated with NMC EVs. CD9KD/NMC (A and B), CD81KD/NMC (C and D), CHMP4CKD/NMC (E and F), SYNGR2KD/NMC (G and H). The dotted line indicates a relative 0.5 or 1.5-fold spot intensity comparing the respective KD EV treatment to the NMC EV treatment. y-axis shows the respective analyte, x-axis shows relative spot intensity.

Table 5.4: Top NMC EV hits compared to KD EV stimulation.

The mean intensity of the detected spots on the membrane treated with the lysate from the NMC EV treated fibroblasts was determined and compared to the mean intensity of the detected spots on the membrane treated with the KD EV treated fibroblasts. The results are summarised in the table. Arrows down indicate decreased detection, with blue arrow representing the most prominent impact; arrows up indicate increased detection with red arrows indicating the most prominent impact.

	Hits with increased phosphorylation in NMC EV stimulated fibroblasts								Hits with decreased phosphorylation in NMC EV stimulated fibroblasts				
KD EV stimulation	Akt 1/2/3 T308	P53 S46	PRAS40	RSK 1/2/3 S380/S386/S377	STAT3 S727	STAT3 Y705	c-Jun S63	HSP60	STAT2 Y689	β -catenin	PDGF R β Y751	SRC Y419	JNK 1/2/3 T183/Y185 T221/Y223
CD9KD EV	=	=	=	=	=		=					=	=
CD81KD EV	=	=	=		=		=						
CHMP4CKD EV					=		=						
SYNGR2KD EV	=	=	=	=	=	=	=	=					

CD81KD EVs, CMP4CKD EVs and SYNGR2KD EVs all induced a stronger phosphorylation of several common targets compared to the NMC EVs. These included analytes associated with inducing α -SMA (WNK1 T60, GSK-3 α/β S21/S9, STAT2 Y689), ECM remodelling (SRC Y419, JNK 1/2/3 T183/Y185 and potentially CREB S133) immune-modulation (β -catenin and potentially CREB S133) in fibroblasts. All of these analytes are associated with an activated fibroblast. It is also noteworthy, that GSK-3 phosphorylates β -catenin. Hence, it is no surprise to find simultaneously increased phosphorylation of both targets compared to the NMC EV stimulation. However, it is critical to note that the magnitude of the impact, and downstream consequences in terms of a cellular impact are unclear. Nevertheless, these results give interesting hints for further explorations to determine the impact of KD EVs on fibroblasts.

Importantly, there were also KD specific differences in the phosphorylation of analytes. This suggests that the cell manipulation have modified the corresponding EVs in distinct ways as opposed to a general global perturbation of EVs and this was linked to a unique and specific response of the recipient fibroblasts.

Treating fibroblast with CD9KD EVs elicited a distinct response compared to NMC EVs (reduced polymerisation of α -SMA in stress fibres, reduced secretion of IL-6, HGF), hence a reduced activation of pathways in the fibroblasts was expected. Here, stimulating fibroblasts with NMC EVs and CD9KD EVs induced a similar phosphorylation pattern. Surprisingly, compared to the NMC EVs, only 3 analytes (STAT3, HSP60 and PRAS40) appeared slightly less phosphorylated and 2 analytes (β -catenin and STAT2) more phosphorylated (1.5 higher spot intensity compared to NMC EV treatment) (Figure 5.10A and B). This indicates that relatively small changes in the phosphorylation patterns cause dramatic differences in the cellular phenotype (chemokine release, α -SMA polymerisation) and importantly, that CD9 dependant EVs make an important contribution.

CD81KD EVs appeared to induce the phosphorylation of targets involved in chemokine release (Figure 5.10C and D). FGR Y412 and Lck Y394 were detected with greater spot intensity on the membranes (1.5 or higher spot intensity compared to NMC EV stimulation) in CD81KD EV treated fibroblasts. Fgr Y412 promotes the ECM and chemokine release in lung

fibroblasts, (Mukherjee et al., 2023) and cell migration (Continolo et al., 2005). Lck Y394 regulates the release of the chemokine CXCL12 in T-cells and NK1 cells (Inngjerdingen et al., 2002). All of this points to increased activation of the fibroblasts, which was not observed in the limited experiments performed here to assess the fibroblast secretome and thus might require a broader approach to establish the impact of CD81KD on EV-mediated fibroblast activation.

Stimulating fibroblasts with CHMP4CKD EVs promoted the phosphorylation of the targets described before (table 5.4) in addition two further targets were found to be specifically more phosphorylated upon CHMP4CKD EV treatment: HSP27 S78/S82 and STAT6 Y641, both of which have been implicated in regulating fibroblast phenotypes. HSP27 S78/S82 regulates the anti-inflammatory response (Zou et al., 2023) and lung fibrosis (Kim et al., 2019). The transcription factor STAT6 Y641 is involved in myofibroblast differentiation and ECM deposition myeloid fibroblasts to (Jiao et al., 2021) and is expressed in bone marrow fibroblasts (Yan et al., 2015).

The last treatment condition was EVs from the SYNGR2KD cell line (Figure 5.10G and H). A mix of regulators for chemokines (Fgr Y412) and ECM deposition (STAT1 Y701) were detected with a higher spot intensity compared to the NMC EV treatment. Of specific interest here is the p70 S6 phosphorylation which promotes Akt mediated ECM deposition (Goc et al., 2015) and downregulates IL-6 secretion in osteoblasts (Takai et al., 2008), which could point to reduced IL-6 secretion described earlier.

These results point to an overall trend in the KD EV induced phosphorylation pattern in recipient fibroblasts, which suggests that these EVs had a diminished functionality in regard to both suppression of the phosphorylation of certain targets and triggering the phosphorylation of others. Importantly, there were also some differences, supporting the notion that these altered EVs are not functionally identical.

5.3 Summary

In summary, PC3 CM stimulates fibroblasts to express α -SMA in stress fibres and this is accompanied by an increase in the secretion of HGF and IL-6 (Figures 5.3, 5.6 and 5.7). The effect appeared to be more pronounced in fibroblasts treated with NM cCM72h, indicating quantitative and/or qualitative differences in the factors later released by PC3 cells.

Remarkably, isolated NMC EVs alone were sufficient to stimulate a significant increase in the secretion of IL-6 and HGF in fibroblasts (Figures 5.6 and 5.7). Importantly, all of the KD cell derived EVs (CD9KD, CD81KD, CHMP4CKD, SYG NR2KD) showed a reduced potency to promote IL-6 and HGF secretion in fibroblasts. Furthermore, NMC EV stimulated phosphorylation of a set of targets, and KD EVs in comparison stimulated differential signalling pathways (Figure 5.10, table 5.4). Thus, these findings demonstrate that the target attenuation in the PC3 cells induced distinct EV modifications and importantly, the functional response of stromal cells upon stimulation was specific and unique depending on the EV source.

5.4 Discussion

In this chapter, I describe the functional relevance of PCa cell line derived CD9, CD81, CHMP4C and SYNGR2 dependant vesicle sub-populations in modulating the phenotype and secretome of fibroblasts within the tumour stroma.

Full cell CM was analysed initially as it mimicked aspects of the *in vivo* setting in which cells release EVs together with other soluble molecules and they likely work in concert to exert their overall combined functional influences. Furthermore, it has been previously shown that endogenous EV regulators not only control the release of EVs but also the release of other soluble secreted factors, which may share the machinery for exocytosis. For instance, KD of Rab27a also impacts the secretion of MMP-9 (Bobrie et al., 2012b) and the pro-angiogenic cytokines PDGF-AA and osteopontin (Peinado et al., 2012). This raises the question whether it is possible to specifically attenuate the expression of EVs without impacting the non-vesicular secreted factors. However, compounding these considerations is the realisation that the biomolecular corona of EV can accommodate numerous factors that are classically considered as soluble entities- and hence clearly defining a factor as EV-associated from not EV-associated is not always straightforward.

To explore the contribution of EVs in the CM, isolated EVs generated from ultracentrifugation pellets, and CM depleted of EV (the supernatant) was used. In the previous chapter, I described that the KDs did not impact the quantity of the released vesicles. Hence for the work described in this chapter the CM, and as a consequence the concentrated EVs, was normalised to the input PC3-cell numbers.

Interestingly, the fibroblast response depended on the PC3 conditioning time. cCM72h stimulated a stronger α -SMA polymerisation into stress fibres, whereas cCM48h induced a more prominent downregulation of the corresponding transcript. These results suggest that the factors released at the later time points by PC3 cells have unique functional properties and thus challenge the assumption of a mere accumulation of factors released by the cells. This

also underscores the complexity of the PC3 derived factors which mediate responses of fibroblasts and the dynamics of these.

There is growing evidence for various EV-associated factors being involved in the activation of fibroblasts. Such examples include various proteins, coding RNAs, non-coding of transposable RNAs (reviewed in Naito et al., 2022). EV derived TGF- β 1 has been well described by our lab (Chowdhury et al., 2015, Webber et al., 2010, Webber et al., 2015) and thereafter others (Huang et al., 2021, Ringuette Goulet et al., 2018) to induce the expression of α -SMA in recipient fibroblasts. TGF- β 1 positive EVs activate the TGF- β 1 / SMAD3 signalling pathway and promote an α -SMA positive myofibroblast phenotype (Webber et al., 2015, Webber et al., 2010). Betaglycan, at the vesicle surface was critical for tethering and the handover of TGF- β , to drive this signalling response (Webber et al., 2010). Incidentally, the SMAD-independent pathway is also activated by EV-stimulus in these cells. A recent study in head and neck cancer claimed that vesicular TGF- β 1 induces the formation of α -SMA independent of SMAD phosphorylation as judged by Western blotting and instead induces the expression of α -SMA positive stress fibres via the increased expression of fibronectin (Huang et al., 2021). This highlights the complexity of an EV driven cellular response in fibroblasts which perhaps depends on both the source of the EVs and the origin of the CAFs, and the broader microenvironmental context.

Phosphokinase assays with EV stimulated fibroblasts were conducted to gain insights into the EV-induced phosphorylation profile of the fibroblasts (Figure 5.9 and 5.10). Overall, the results suggested a trend that factors that were more phosphorylated in NMC EV stimulated fibroblasts were less phosphorylated upon KD EV treatment. The inverse was also apparent with analytes that were less phosphorylated with NMC EV stimulation, showed an increased phosphorylation upon KD EV stimulation. This suggested that all the KD EVs exhibited a reduced functionality and were less potent in altering phosphorylation of certain targets. Importantly, the PC3-cell manipulations we have generated, have modified the corresponding EVs in distinct ways as opposed to a general global perturbation of EVs and this was linked to a unique and specific response of the recipient fibroblasts, demonstrated by distinctive phosphorylation profiles. If we assume that the EV-dosing in these experiments was correct, and every effort was made to satisfy this aspect, the KD-derived EV must therefore be

phenotypically different from each other, and these differences are functionally relevant in terms of fibroblast signalling responses.

An interesting finding was that β -catenin phosphorylation was lower in fibroblasts treated with NMC EVs compared to media only treated fibroblasts. β -catenin is an important component of the Wnt signalling pathway and the unphosphorylated form induces the transcription of its target genes. Active Wnt molecules have been reported to be transported by EVs and activate the Wnt signalling cascade (Gross et al., 2012). Interestingly, across the fibroblasts treated with KD EVs, β -catenin phosphorylation was more readily detected. This might indicate that the KD EVs have a reduced amount of active Wnt cargo. However, this clearly needs validation by exploring for instance the proteome of the PC3 KD cell variants. Alternatively, assessment of the vesicular transcriptome could also provide further insights as Wnt signalling has been reported to be regulated by miRNAs (Lv et al., 2017a, Lu et al., 2017). Furthermore, in the phosphokinase array a strong signal for STAT3 phosphorylation was detected in fibroblasts stimulated with NMC EVs compared to media-only treated fibroblasts. This is typically indicative of an inflammatory CAF type (reviewed in Allam et al., 2021) and is in line with the observed increased release of IL-6 and HGF release by fibroblasts treated with NMC EVs. Interestingly, various mechanisms of EV induced STAT3 activation, and their functional relevance have recently been described. Zhang et al showed in a colorectal cancer cell line that EVs carry phosphorylated STAT3 that confers chemotherapeutic resistance (Zhang et al., 2019a). A different research group found that vesicular miR-193a-3p, miR-210-3p and miR-5100 activated STAT3 in lung cancer cells (Zhang et al., 2019b). STAT3 was less phosphorylated in the fibroblasts stimulated with KD EVs, which is in line with the decreased release of IL-6 and HGF in these fibroblasts.

Here, NMC cCM induced a heterogenous expression of α -SMA positive stress fibres in fibroblast, which was less prominent in KD cCM treated fibroblasts. The phosphorylation assay pointed to several pathways that might be involved in this observation.

In NMC EV treated fibroblasts increased phosphorylation of Akt1 was detected. This is important because Akt1 has been reported to increase the expression of α -SMA in fibroblasts (Abdalla et al., 2013, Kulkarni et al., 2011, Reyes-Gordillo et al., 2011). In addition to this, STAT2, which has been identified in a RNA-seq study as a potential regulator of an α -SMA

negative FAP positive CAF population in PCa (Pan et al., 2023), was found to be suppressed by NMC EV stimulation. This suggests PC3 EV mediated activation of signalling pathways in recipient fibroblasts that might be reflected in the phenotype.

There were also some discoveries that appeared to contradict the previous phenotyping (α -SMA polymerisation in stress fibres, HGF and IL-6 secretion). For instance, PDGFR β showed greater phosphorylation in the KD EV treated fibroblasts compared to the NMC EV stimulation. The activation of this receptor has been linked to promotion of α -SMA expression in mesenchymal stromal cells (Ball et al., 2014). Hence, a more pronounced α -SMA expression would have been expected upon KD treatment conditions. It is important to acknowledge in that regard the phosphokinase array is a snapshot of the phosphorylation of several targets. However, confirmation that the full activation of a specific pathway translates into a cellular response would require the assessment of additional downstream targets in the same pathway, as well as potential assessment of antagonistic signalling pathways, and a better appreciation of the kinetics and stabilities of the responses.

Another important consideration in the interpretation of these results, is the emergence of multiple CAF subpopulations, upon stimulation, when conducting bulk functional fibroblasts experiments, as this might cause apparently opposing results. It was shown that TGF- β 1 induces the matrix producing, strongly α -SMA positive, myofibroblast phenotype and simultaneously induces the reduction of IL-6 release. In contrast to the ECM modulating CAF phenotype, an immunomodulatory fibroblast phenotype shows increased secretion of IL-6 which is activated by the JAK/STAT pathway in pancreatic ductal adenocarcinoma (Biffi et al., 2019). This indicates that IL-6 secreting and α -SMA positive fibroblasts likely represent at least two distinct fibroblast phenotypes. Moreover, in CAFs from PCa, at least three CAF phenotypes have been recently proposed, based on the differential expression of α -SMA in combination with other genes: CAF-S1 (α -SMA and PDGFR β positive) CAF-S2 (PDGFR α , CREB3L1 and PLAGL1 positive) and CAF-S3 (α -SMA, HOXB2 and MAFB positive) (Chen et al., 2021a) showing the heterogeneity of CAFs within one tissue. While we did not attempt to delineate sub-types in this study and focused on the population as a whole and their response to the varied stimuli, this provides an interesting opportunity to assess possible differences in EV induced CAF subpopulations, or differences in how subpopulations respond

to EVs. This could be experimentally explored in more depth by tracking the uptake of PC3 EVs and subsequently phenotyping the fibroblast subpopulations for instance by using various combinations of α -SMA and other markers, and single cell sorting and sequencing technologies.

To summarise, I have described that CD9KD, CD81KD, CHMP4CKD and SYG NR2KD derived EVs appear to have a reduced potency to modulate the secretion of IL-6 and HGF in recipient fibroblasts. Importantly, the observed impact was unique and specific for each KD EV population. This strongly suggests that the cell manipulations did not induce a global perturbation of the EVs, but rather a candidate specific impact on the EV cargo and/or distinct EV subpopulations, which were functionally relevant changes in terms of the fibroblast response.

Chapter 6:

Understanding the impact of candidate attenuation by analysis of cellular and vesicular RNA

6.1 Introduction

The transcriptome of PCa cells undergoes dynamic changes with the progression of the disease (Bolis et al., 2021) and in response to treatment (Shah et al., 2020, Rajan et al., 2014). For instance, a study including 1,000 clinical PCa tissues from 13 different studies and covering all disease stages from the early onset to the metastatic stage revealed disease stage specific gene expression patterns and in particular genes regulating chromatin remodelling are upregulated at later stages of the disease (Bolis et al., 2021).

Various PCa cell line models have been developed to capture the clinical intra and inter patient transcriptomic heterogeneity of PCa tumours. A recent transcriptomic analysis of 20 commonly used PCa cell lines showed that the cell lines exhibit transcript profiles that cluster as androgen negative and androgen positive subgroups and can be further categorised by changes in response to Enzalutamide, an antagonist of the androgen receptor (AR), and Mifepristone, an antagonist to progesterone receptors (Smith et al., 2020). The study validated that the PC3 cell line has a low mRNA expression of the AR and the protein is not detectable by WB, and the cell line is resistant to Enzalutamide, while maintaining sensitivity to Mifepristone. Such profiles provide useful information that correspond to behavioural and other cellular properties and aid in embedding studies of cell populations in the broader context of PCa.

6.1.1 RNA encapsulated in EVs

Cells expel a repertoire of RNA species encapsulated in EVs. This possibly serves critical functions that regulate intracellular RNA homeostasis by exporting RNA as a disposal mechanism and/or as a means of intercellular communication by transporting RNA from an EV releasing cell to a recipient cell (reviewed in O'Brien et al., 2020). RNAs residing in EVs are manufactured by the parent cell, hence one might expect the overall transcriptome of EV to mirror that of the cell. However, this is not entirely true and the parent cell and the corresponding EVs are distinct in their composition of RNA species (Dong et al., 2021, Hessvik et al., 2012, Santangelo et al., 2016). The studies also showed that non-coding RNA is enriched in EVs relative to the parent cell, and classically it is generally accepted that

ribosomal RNA (rRNA) which is highly abundant in the cells is excluded from endosomally derived vesicle inclusion.

6.1.1.1 Vesicular Messenger RNA (mRNA)

The functional importance of mRNA encapsulated in EVs is controversial. Early studies suggested that functional mRNA encapsulated in EVs is translated into proteins in recipient cells (Valadi et al., 2007, Skog et al., 2008). In a recent paper Hung et al demonstrated that mRNA encapsulated in genetically modified EVs that contain vesicular stomatitis virus glycoprotein for increased RNA loading, were successfully taken up by recipient PCa cells. The engineered EVs, however failed to escape the endosome, a necessary step for the mRNA to reach the cytosol where it can be translated (Hung and Leonard, 2016). In contrast to this De la Cuesta et al. demonstrated that functional mRNA is indeed transferred from smooth muscle cells to endothelial cells, via vesicle transmission, using a Cre-locus of crossing over, P1 (Cre-loxP) reporting system (de la Cuesta et al., 2019). Furthermore, a different study showed in a murine model, that cre mRNA encapsulated in EVs mediated the deletion of the genetic sequence between the loxP sites in recipient tumour cells (Zomer et al., 2015). These results highlight our lack in understanding of the mechanisms in the recipient cells for handling acquired RNA-containing EVs and raises questions about the physiological relevance, and rules which govern vesicular RNA-transmission.

6.1.1.2 Non-coding vesicular RNA

There are several classes of RNAs with a regulatory function that do not encode a protein, termed non-coding RNAs, that have been extensively documented in EVs. Examples of this are miRNA and long noncoding RNA (lncRNA) both of which have been found to contribute to various diseases.

miRNAs are single stranded RNA molecules that modulate post-transcriptional gene expression. In breast cancer, various miRNAs have been described to be transported to adjacent tumour cells and other cells within tumour microenvironment. For instance, miR-9, which can alter the expression of motility genes in recipient fibroblasts (Baroni et al., 2016).

lncRNAs are longer than 200 bp and have multiple functions in regulating RNA activity, for instance by inducing conformational changes in chromatin, gene activation and gene suppression (reviewed in Statello et al., 2021). lncRNA is encapsulated in EVs and released into the extracellular space by the parent cell. Consequently, vesicular lncRNA can be found in various body fluids, for instance in urinary samples from PCa patients (Almeida et al., 2022). Vesicular lncRNAs have also been reported to induce transcriptional changes in recipient cells, such as lncRNA NEAT1 that drives changes in the expression of pro-fibrotic genes in recipient fibroblasts in cardiac tissues (Kenneweg et al., 2019). Another example is vesicular lncRNA AL139294.1 which mediates an aggressive cell phenotype in lung cancer cells (Ma et al., 2024). Transmission of such lncRNA by vesicles may contribute towards disease processes.

6.1.1.3 Diagnostic usage of vesicular RNA

There is also an increasing interest in utilising EV RNA samples from patient derived biofluids to serve as biomarkers for diagnosing and monitoring diseases. For instance, our lab found that the mRNA encapsulated in EVs from PCa stromal cells have a distinct signature compared to those from normal stromal cells and such EV-encapsulated mRNAs were found to correlate with histological assessment during diagnosis (Shephard et al., 2021).

Various vesicular miRNAs have been proposed as biomarkers for PCa to distinguish between disease status. As an example, miRNA-375 from EVs has been found in patient derived samples from urine (Foj et al., 2017) and blood (Huang et al., 2015, Bryant et al., 2012).

Furthermore, in 2020, the FDA approved the ExoDx™ prostate (IntelliScore) (EPI) test which is utilised to stratify patients with suspected high grade PCa for further biopsy based on a panel of three genes detected in urinary EV samples (Tutrone et al., 2020, Tutrone et al., 2023, McKiernan et al., 2020). These examples highlight the utility of measuring various vesicular RNA species and the potential for further exploitations for clinical usage. To achieve this, a better understanding of the mechanisms regulating RNA loading into EVs is urgently needed.

6.1.1.4 Loading of RNA into EVs

The underlying mechanisms contributing to the sorting of specific RNAs into EVs are still unclear. RNA enrichment in EVs could be a result of passive loading as a consequence of mere proximity of RNA to the place of EV biogenesis. It has also been proposed that the affinity of selective RNA species to lipids causes an enrichment of these species at MVEs and thus increased loading in EVs (Janas et al., 2015).

EVs compared to their parent cell carry a distinct composition of RNA molecules. This points to a selective and regulated active loading of RNA into nascent EVs. Indeed, there is mounting evidence that incorporation of RNA species is an active process and not purely by random occurrence. Various RNA binding proteins (RBPs) have been described to regulate RNA loading in EVs. For instance, localisation of the RBP argonaut RISC catalytic component 2 (AGO2) to endosomes increases AGO2 dependent microRNA encapsulation into EVs in colon cancer cells (McKenzie et al., 2016). Furthermore, factors associated with the heterogenous nuclear ribonucleoprotein (hnRNP) family have been suggested to drive miRNA enrichment into nascent EVs as reported for hnRNPA2B which binds to the GAGG sequence motif found in a subset of miRNAs enriched in EVs (Villarroya-Beltri et al., 2013). Another example of a RBP is synaptogamin binding cytoplasmic RNA interacting protein (SYNCRIP), which has been described to regulate the loading of microRNAs with a GGCU sequence (hEXO motif) into small EVs (Santangelo et al., 2016). Again, several mechanisms are identified therefore, but do not fully explain the complexity of vesicular RNA-loading, and relating these strictly to specific classes of EVs and vesicle biogenesis processes remains a challenge.

6.1.2 RNA-sequencing techniques for transcriptome analysis

To gain insights into the composition of the transcriptome, low throughput analysis techniques such as qPCR can be used, when addressing questions around known RNAs of interest. In contrast RNA-sequencing is a high throughput technique to assess the presence and quantity of RNA in biological samples derived from e.g., different treatment conditions or various disease status. To achieve this, next generation-sequencing (NGS) platforms are utilised to define the transcript repertoires in depth.

Distinct RNA-seq protocols involve several common steps, however the specific protocol used depends on the research question and source material. As a first step, RNA is isolated from the investigated sample and subsequently rRNA is removed. This step is critical for the processing of the samples because up to 90% of the cellular transcriptome comprises rRNA (Wilhelm and Landry, 2009). Hence, analysing all cellular rRNA in addition to other transcripts would involve an extensive time-consuming sequencing process and might interfere with revealing the diversity of other transcripts. Removal of rRNA can be achieved by rRNA depletion or polyadenylated (poly-A) mRNA tail enrichment. The remaining RNA is fragmented to allow simultaneously sequencing in the following steps (reviewed in Eaves et al., 2020). In the next steps RNA is reverse transcribed to cDNA and adapters added for the sequencing. To be more precise, random primers are added to the RNA template and the RNA is subsequently reverse transcribed into cDNA. Another round of amplification is started by the addition of DNA polymerase and nucleotides to generate the second strand of the DNA. Information about strand direction can be maintained at this stage by utilising the deoxy-UTP (dUTP) method, which uses UTP nucleotides for the synthesis of the second cDNA strand (Parkhomchuk et al., 2009). The dUTP is incorporated in the second cDNA is later digested by enzymes. The last step of the library preparation includes the ligation of oligonucleotide adapters to the cDNA. Adapters can serve as a barcode in multiplexed experiments to allow sample identification. Furthermore, adapters have a primer binding site for amplification and a capture sequence to allow binding of the cDNA to the flow cell for the subsequent sequencing step (Mohideen et al., 2020).

Specific steps of the sequencing depend on the sequencing platform. As an example, the NovaSeq 600 platform from Illumina includes the following steps:

The cDNA library is loaded onto a flow cell which is covered with DNA, allowing the binding of the cDNA via the adapter to the complementary sequence on the flow cell. The cDNA sequences are then amplified by bridge amplification generating clusters of identical sequences and thus aiding amplification of the signal during the sequencing (Bentley et al., 2008). Next, each nucleotide is read by a method termed sequencing by synthesis (Bentley et al., 2008) which is continuously optimised (Rodriguez and Krishnan, 2023). During this process, one fluorescently labelled oligonucleotide is incorporated into growing strands in each sequencing cycle (Fuller et al., 2009). After each sequencing cycle is finished the incorporated base is recorded. The obtained reads are aligned to an annotated reference

genome (Modi et al., 2021) and the results saved in FASTQ files for subsequent bioinformatic processing.

6.1.2.1 Bioinformatic analysis of RNA-seq data

Normalisation is a critical step in the data analysis to account for unwanted technical and artificial variations and different methods have been developed for this purpose.

Variations in the sequencing depth can lead to inter sample variations. To address this issue, samples can be normalised by dividing the individual genes in a sample by the number of total genes. The data can then be transformed to counts per million (CPM) for further analysis. However, few highly expressed genes can introduce a bias in the normalisation because the total counts are significantly influenced by these genes and consequently other genes appear as lowly expressed. In addition to this, CPM is calculated without considering the gene length, hence this method could potentially introduce bias by over or underestimating (Eaves et al., 2020).

DESeq2 is an R package developed to identify differentially expressed genes. The algorithm is used to normalise the raw counts and perform gene ranking based on a negative binomial distribution (Love et al., 2014). Variance stabilising transformation is applied to render the normalised counts variance independent of the mean. The algorithm provides an option to visualise the data, for instance plotting the results of a Principal Component Analysis (PCA) to assess variations between samples.

Changes in gene expression at an individual level might not reach statistical significance but may nevertheless exert a biologically relevant alteration at the pathway level when in concert with other changes in the transcriptome. To scope this from RNA-seq data, pathway analysis is performed, which uses a priori knowledge of gene sets involved in a common pathway and consequently also reduces the complexity of the RNA-seq data set. Commonly used analyses to explore the transcriptomic profiles of investigated samples include Over Representation Analysis (ORA), Gene Set Enrichment Analysis (GSEA) and Gene Set Variation Analysis (GSVA).

ORA applies a Fisher's hypergeometric test to compare a differentially expressed gene (DEG) list to a predefined reference gene list and identify significant overlaps, thus revealing changes in pathway activity (Tavazoie et al., 1999). The input gene list for ORA comprises significant DEGs, however the additional (layer of) information coming from their associated P-values and/or fold changes is discarded for use of this method. Hence this results in limitations in the interpretability of the results. For instance, the gene input list might exclude important differently expressed genes and consequently subtle changes in pathways might not be detected. On the other hand, the gene list might include genes that are not relevant and hence introduce false positive results. The analysis of a large number of gene sets involves multiple hypothesis testing, which also bears the risk of increasing false positive results and requires statistical correction.

An important advance in the analysis of large RNA data sets was the GSEA method proposed by Subramanian (Subramanian et al., 2005) which is applied to determine whether the genes of a predefined gene set of interest (list A, e.g., a signalling pathway) overlap at the bottom or top of a gene list ranked by statistical significance or fold change estimates arising from differential expression analysis (list B). Importantly, in contrast to ORA, this analysis does not apply artificial cut off values for the gene list and includes all detected genes. A random walk, a statistical method which assesses whether each gene from list B is present on the gene set of interest (list A), is applied and an enrichment score is determined, which reflects the enrichment of genes on list A at the top or bottom of list B (Subramanian et al., 2005).

Gene set variation analysis (GSVA) is a gene set enrichment method performed on a per sample basis (individual replicates), ideally on a dataset of at least 10 samples. The input data is the gene expression matrix of the investigated samples, which gets transformed into a pathway activity matrix of the investigated samples (Hänzelmann et al., 2013).

In the scope of this thesis, we elected to perform first a GSVA to gain an overview of the differences between the samples and then conducted a GSEA to focus on the comparison between the KD cell variants and the NMC.

6.1.3 Aims and objectives

We aim to gain a holistic understanding of the transcriptomic changes caused by imposing the KD of the candidates (CD9, CD81, CHMP4C, SYNGR2) in both the parent cell and the corresponding EVs. This might provide a modality to link candidates with discrete repertoires of RNAs, and hence be an indication of the existence and regulation of distinct EV-subpopulations secreted by PC3 cells. To achieve this, we aim to explore the transcriptomic changes in the KD cells (CD9KD, CD81KD, CHMP4CKD and SYNGR2KD) and the NMC cells and the corresponding EVs by setting the following objectives:

- 1.) Isolate RNA from the parent cell and the corresponding EVs from all KD cell variants and the NMC to assess the transcriptomic features of the samples by RNA-sequencing.
- 2.) Conduct a comprehensive analysis of the RNA-seq datasets by analysing DEGs and conducting GSVA and GSEA to evaluate the potential impact of candidate KD on intracellular pathways, including but not limited to EV biogenesis, transport and release.

6.2 Results

6.2.1 Isolation of vesicular RNA

6.2.1.1 Vesicular RNA isolation using a phenol based method

First, we aimed to obtain purified vesicular RNA for the assessment of the vesicular transcriptome by RNA-sequencing. For this purpose, vesicular RNA from the KD cells (CD9KD, CD81, CHMP4C, SYNGR2KD) and the NMC variant was extracted from EVs by utilising a phenol/chloroform-based method, which is a well-established and reliable method in our lab (Shephard et al., 2021). Of note, per biological replicate CM from 9 T75 flasks was collected, and subsequently EVs were purified and RNA isolated and this was done for each biological replicate separately. The vesicular RNA concentrations were determined using a Quant-it™ RiboGreen RNA Assay (Thermo Fisher Scientific) (Figure 6.1A). This RNA quantification kit utilises the properties of the fluorescent dye Ribogreen, which specifically binds to RNA. Other colleagues in the lab had compared the performance of this approach with other solutions such as the Qbit platform, concluding the performance was overall superior for the limited input material available (data not shown). The total RNA concentrations per sample was determined and ranged from 6.1 -101.5 ng/μl in a total of 12 μl across the repertoire of EV-samples (Figure 6.1A).

An initial quality control, using the RNA 6000 Pico Kit in a Bioanalyzer (Agilent), was performed to assess the size distribution of isolated RNA and to detect potential rRNA present which is not a usual feature of purified EVs (Figure 6.1B-F). The RNA profile from the NMC EV sample showed an enrichment of small RNA with a peak below 200 nt (Figure 6.1B). The presence of some larger RNA was also indicated by two smaller peaks, one close to 200 nt and a second peak between 500 - 1,000 nt, hence a polydisperse population of RNA was present in the vesicles. Furthermore, the traces reassuringly lacked major rRNA peaks (28s at 4,700 nt and 18s at 1,900 nt). This size distribution profile was similar to previously reported RNA size distributions from vesicular RNA derived from PC3 cells (Lazaro-Ibanez et al., 2017), and consistent with other studies in our laboratory when assessing EV-RNA from other cellular sources.

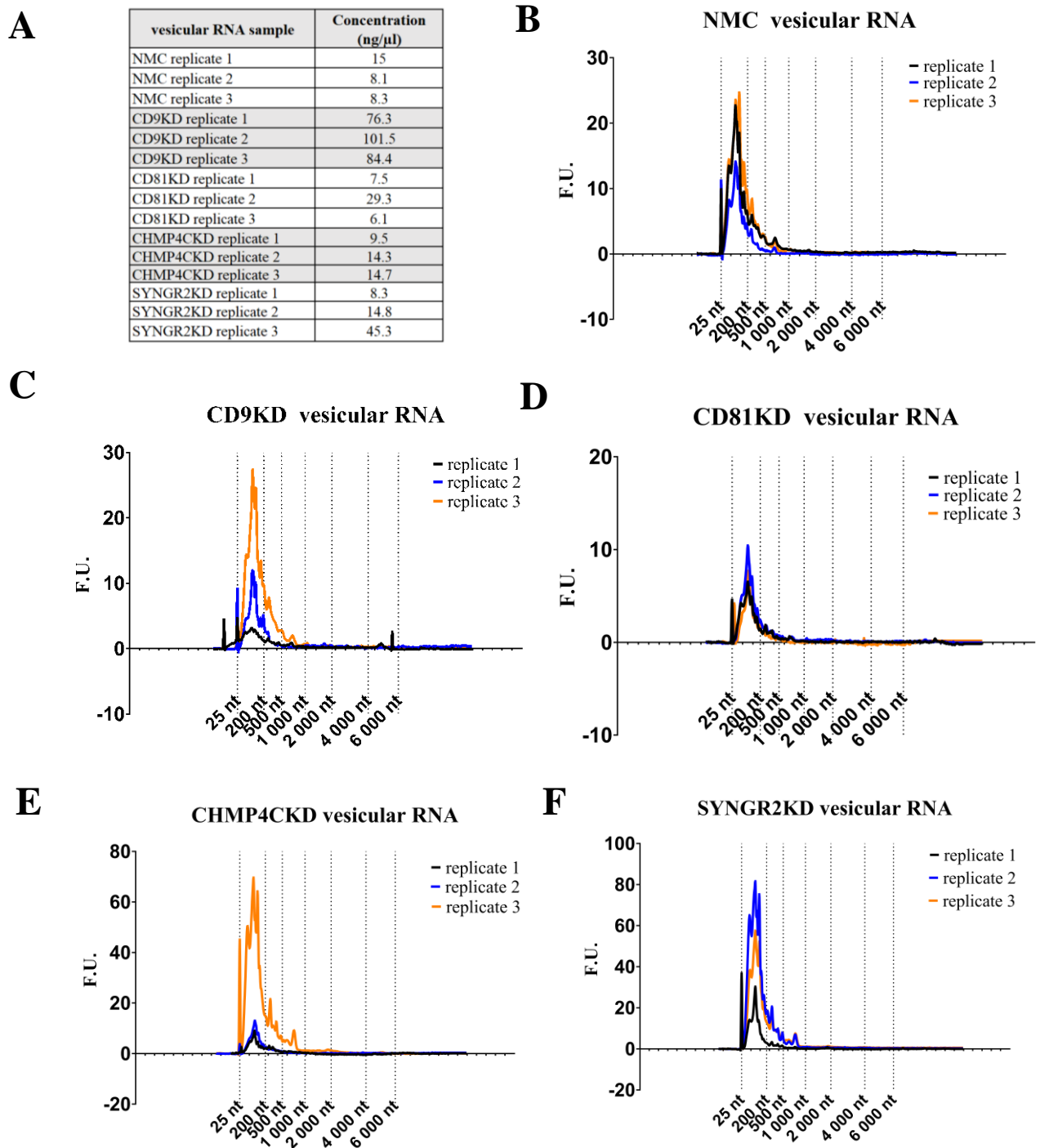


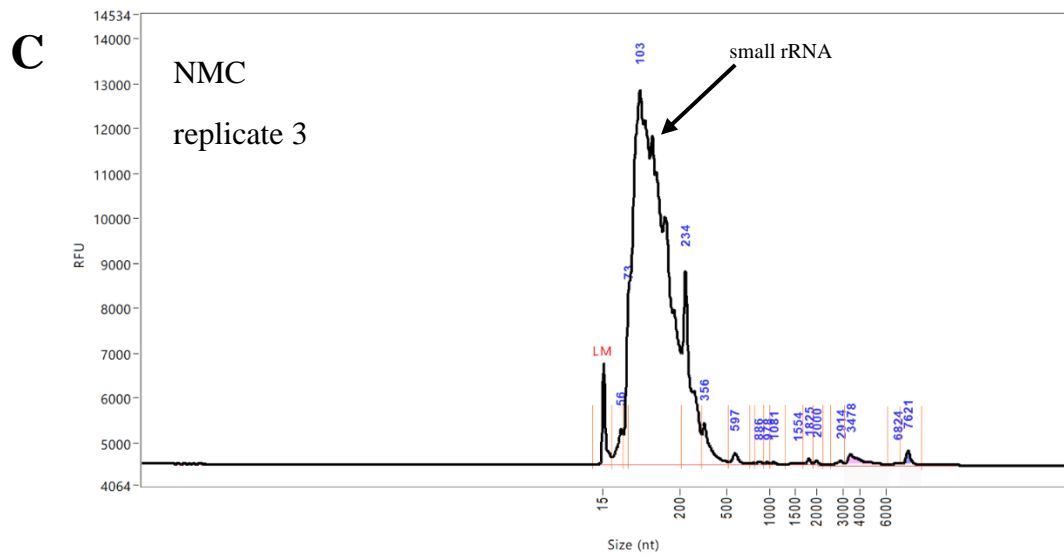
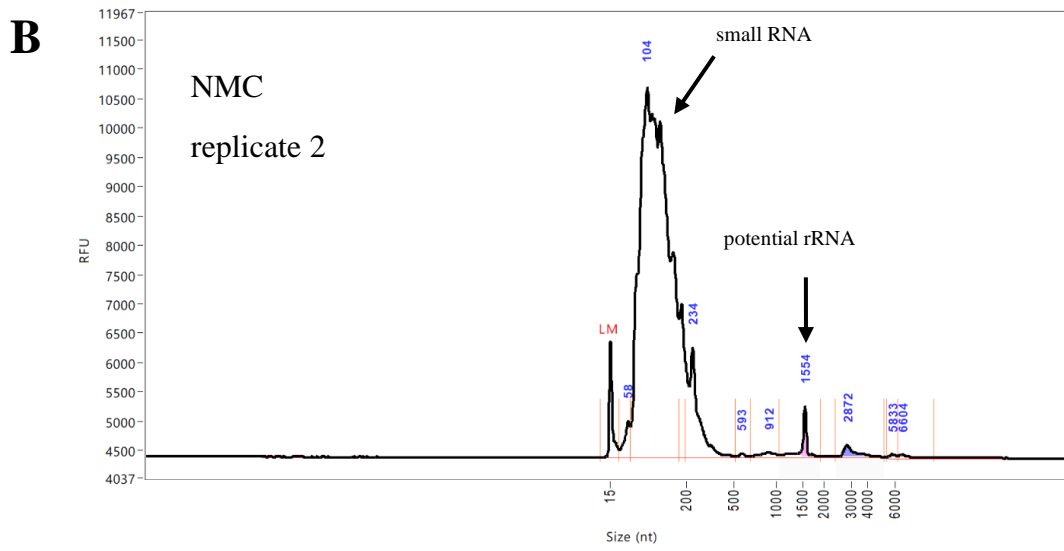
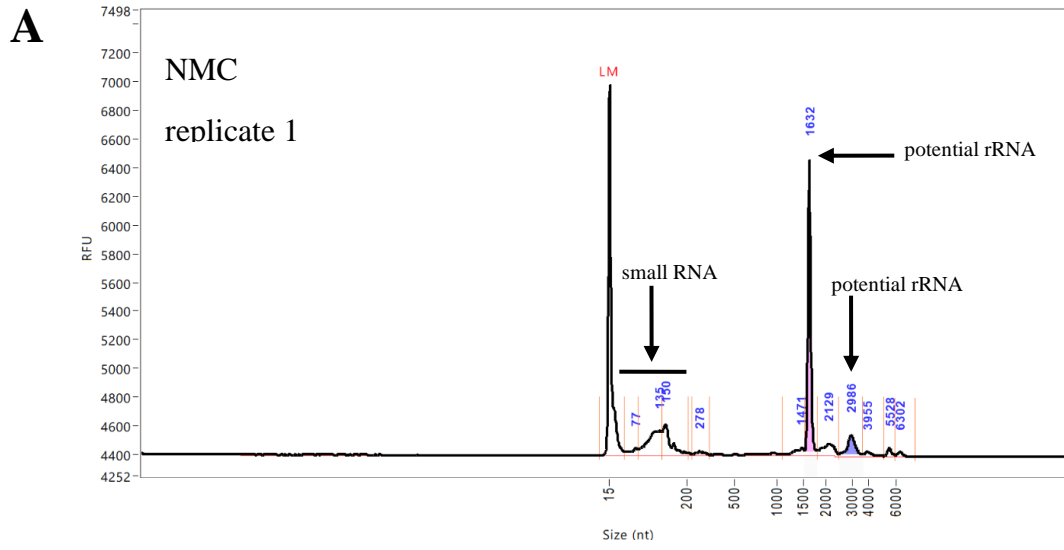
Figure 6.1: Locally performed vesicular RNA quality control.

EVs were isolated from the CD9KD, CD81KD, CHMP4CKD, SYNGR2KD and NMC cells. Vesicular RNA was extracted using a phenol/chloroform-based method. Total RNA quantities were determined with a Quant-it™ RiboGreen RNA Assay (A). The quality of all isolated vesicular RNA samples was assessed using a RNA 6000 Pico Kit in a Bioanalyzer for vesicular RNA derived from NMC cells (B), CD9KD cells (C), CD81KD cells (D), CHMP4CKD cells (E) and SYNGR2KD cells (F).

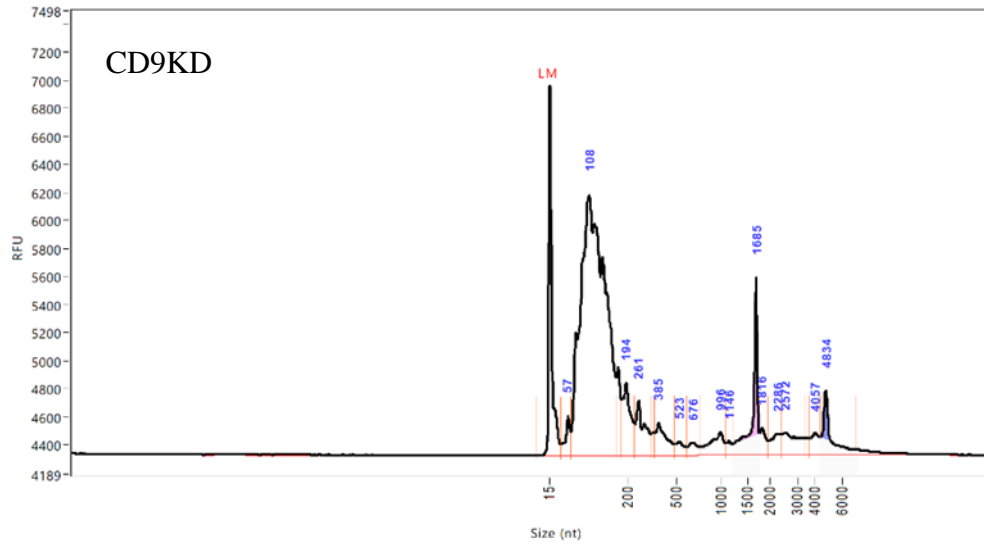
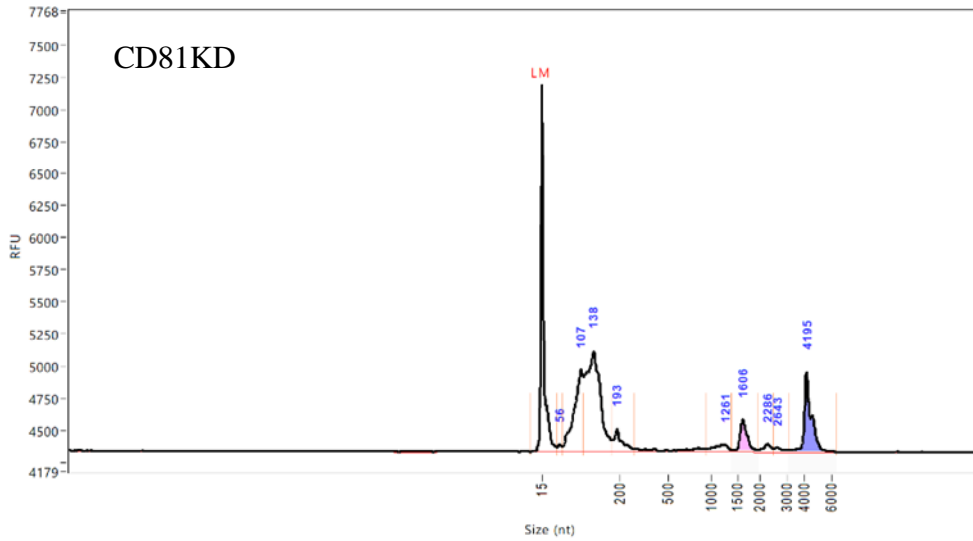
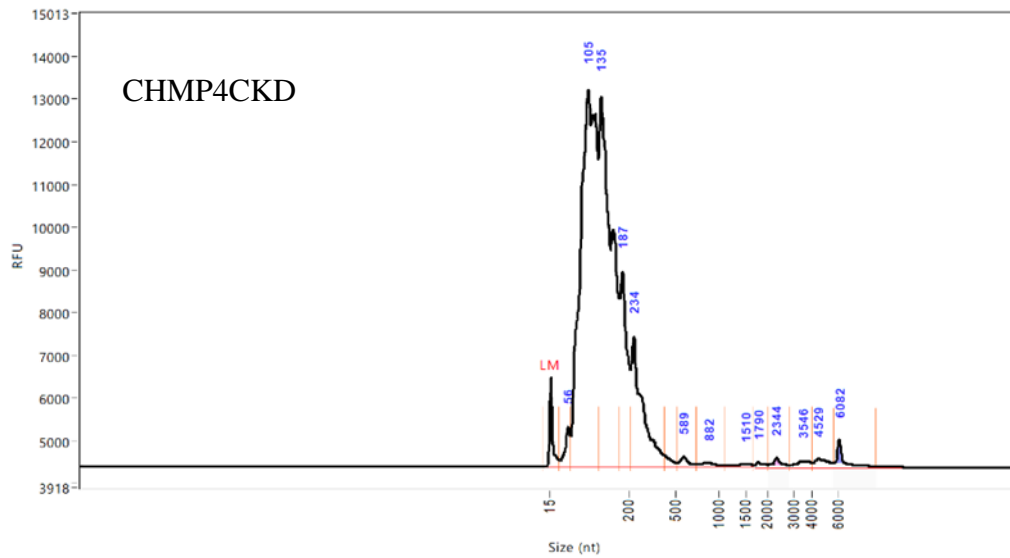
The size distribution profile across the vesicular RNA samples from the KD cells was similar to the NMC with the majority being of smaller RNAs detected below 200 nt (Figure 6.1B-F). In addition, two small peaks, one after 200 nt and a second one between 500 and 1,000 nt was detected suggesting the presence of larger RNA species. Importantly, the traces lacked major rRNA peaks (28s at 4,700 nt and 18s at 1,900 nt). As described above biological replicates were distinct CM collections and subsequent processing and thus inadvertently, induced some variations in the obtained RNA concentrations across the replicates. In addition to this, the Bioanalyzer was performed on three chips, which likely introduced variations in the magnitude of the detection of RNA. However, importantly, the goal of this analysis was to examine the overall RNA size distribution and hence the differences in the magnitude of detection were not a concern here.

Since the RNA traces from all the vesicular samples showed a similar size distribution and lacked major rRNA peaks, the samples were considered of sufficient quality by us for RNA-sequencing. Next, the specimens were shipped to the Netherlands and the quality of the RNA upon arrival was further assessed by our collaborator Genomescan, in order to qualify for subsequent RNA-seq and ensure they had withstood transportation successfully.

The samples were subject to gel electrophoretic separation with a fragment analyzer (Agilent), a similar method to the Bioanalyzer with slightly updated hardware, to confirm RNA size distribution. In contrast to the Bioanalyzer results, the traces for the NMC EV RNA obtained by the fragment analyzer indicated some differences in the size among the replicates (Figure 6.2A-C). Two of the three samples showed presence of some ribosomal RNA small indicated by a major peak between 1,554 nt-1,632 nt and a minor peak between 2,872 nt- 2,986 nt. The remainder replicate lacked these peaks in the same size range. The reason for the discrepancy between the Bioanalyzer and Fragment analyser is unclear, as both techniques have a comparable sensitivity according to the manufacturer, however the fragment analyser at the commercial site is subject to consistent use and throughput and is likely to provide greater confidence in the data arising. The Bioanalyzer traces also indicated a minor peak ~200 nt. This was confirmed with the fragment analyzer for two of three samples (Figure 6.2B and C), indicated by a peak at ~230 nt.



Continued on the next page

D**E****F**

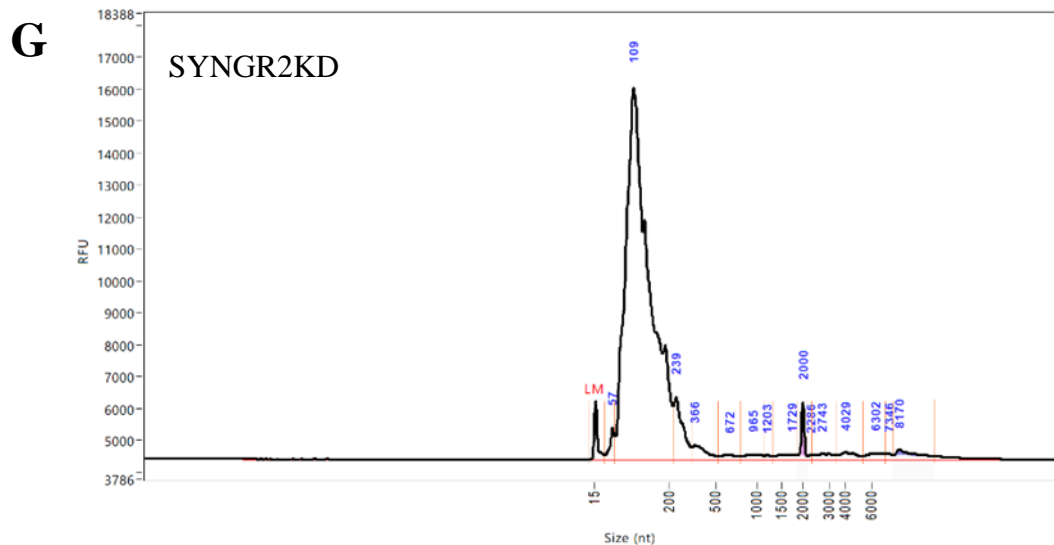


Figure 6.2 Quality control of vesicular RNA performed at Genomescan.

The quality of the vesicular RNA samples, which were extracted using a phenol/chloroform-based method, was determined using the fragment analyzer Agilent DNF-472 HS RNA (15 nt) kit on a Fragment Analyzer (Agilent). A)-(C) show the traces of the vesicular RNA isolated from NM control EVs. Traces of 1 replicate of isolated vesicular RNA purified from CD9KD cells (D), the CD81KD cells (E), CHMP4CKD cells (F) and SYNGR2KD cells (G) are shown. Red bars indicate detected peaks. Images on the right of each trace show the corresponding lane in the electrophoresis gel. Light pink small rRNA subunit, purple large rRNA subunit, LM= loading marker, RFU= relative fluorescent units.

The traces of the vesicular RNA derived from the KD cells (CD9KD, CD81KD, CHMP4CKD and SYNGR2KD) were also analysed and an example of each KD is depicted in Figure 6.2D-G). The size distribution traces of these vesicular RNA samples also showed some inconsistencies amongst replicates with some showing presence of rRNA subunits (CD9KD (Figure 6.2D), CD81KD (Figure 6.2E)), or one peak in the size range of the small subunit (CHMP4CKD, SYNGR2KD Figure 6.2F-G). The complete set of traces is found in annex C.

The SMARTer Stranded Total RNA-Seq Kit v3 - Pico Input Mammalian used here, includes an rRNA depletion step for the preparation of the sequencing library. Hence, we decided to check if this step was sufficient to deplete the samples of rRNA on a few vesicular RNA samples, isolated from the NMC cells, and CD9KD cells. The library preparation was

subsequently checked by calculating ribosomal, globin, and mitochondrial content in each sample. Surprisingly, despite the rRNA depletion step, rRNA was clearly found in the samples ranging between 0.2136-0.3074 (table 6.1). Because rRNA can mask the true diversity of the transcripts in a RNA-seq analysis, we aimed to reduce the amount of rRNA in our samples further by repeating the entire EV-isolation experiment aiming to optimise the RNA collection process via a different method, purpose designed for EV-RNA isolation.

Table 6.1: Calculation of the ribosomal, globins and mitochondrial in the sequencing library based on the indicate vesicular RNA samples which were extracted using a phenol-based method.

vesicular RNA sample	Ribosomal	Globins	Mitochondrial
NMC replicate 1	0.2572	0	0.0085
NMC replicate 2	0.3074	0	0.0081
NMC replicate 3	0.2759	0	0.0164
CD9KD replicate 1	0.2879	0	0.0156
CD9KD replicate 2	0.2662	0	0.015
CD9KD replicate 3	0.2136	0	0.0154

6.2.1.2 Vesicular RNA isolation using a exoRNEasy kit (Qiagen)

The phenol based vesicular RNA isolation approach was unsuccessful for these specimens, despite multiple efforts. The reasons for this have not been fully identified because a parallel study, involving stromal cells of prostate origin, and involving EV-isolation and RNA-extraction using a slightly different method was successful, in terms of isolating high-quality RNA with low rRNA-content. This method is the exoRNEasy kit (Qiagen), tailor made for EV RNA extraction. The kit includes a column-based EV isolation step, to entrap EVs, and consequently should reduce contamination by a-vesicular cell derived free RNA, followed by an in-column EV-lysis, and RNA clean-up steps thereafter. To help simplify the processes, we elected to focus on the two KD cell variants that were best described with regard to validation of the KD (CD9KD and CD81KD).

Freshly prepared EV samples (derived from the NMC, CD9KD and CD81KD cells) were prepared, and the vesicular RNA isolated according to the manufacturer's protocol. The vesicular RNA concentrations were determined using a Quant-it™ RiboGreen RNA Assay (Table 6.2) and ranged from 5.8- 22.6 ng/ µl in total volume of 12 µl.

Table 6.2: Vesicular RNA concentrations of the indicated vesicular RNA samples, which were extracted using the exoRNeasy kit (Qiagen), were determined utilising a Quant-it™ RiboGreen RNA assay.

Vesicular RNA sample	Concentration (ng/μl)
NMC replicate 1	13.7
NMC replicate 2	14.7
NMC replicate 3	15.3
CD9KD replicate 1	6.9
CD9KD replicate 2	9.6
CD9KD replicate 3	5.8
CD81KD replicate 1	22.6
CD81KD replicate 2	20.8
CD81KD replicate 3	20.8

As before we explored RNA-size distribution using the RNA 6000 Pico Kit in a Bioanalyzer (Figure 6.3). The replicates of the NMC EV RNA samples showed a similar size distribution with a small peak between 200 and 500 nt and a lack of gross rRNA peaks (Figure 6.3A). The traces of the vesicular RNA from both, the CD9KD cell variant and the CD81KD cell variant showed a similar size distribution pattern as the NMC samples with an enrichment of smaller size RNA below 200 nt (Figure 6.3B and C). In addition to this, the presence of larger RNA species was indicated by two small peaks between 500 -1,000 nt.

Taken together, all of the obtained EV RNA samples had a concentration of at least 5.8 ng/μl and a similar size distribution pattern characterised by an enrichment of small RNA (<200 nt) and a lack of major rRNA peaks.

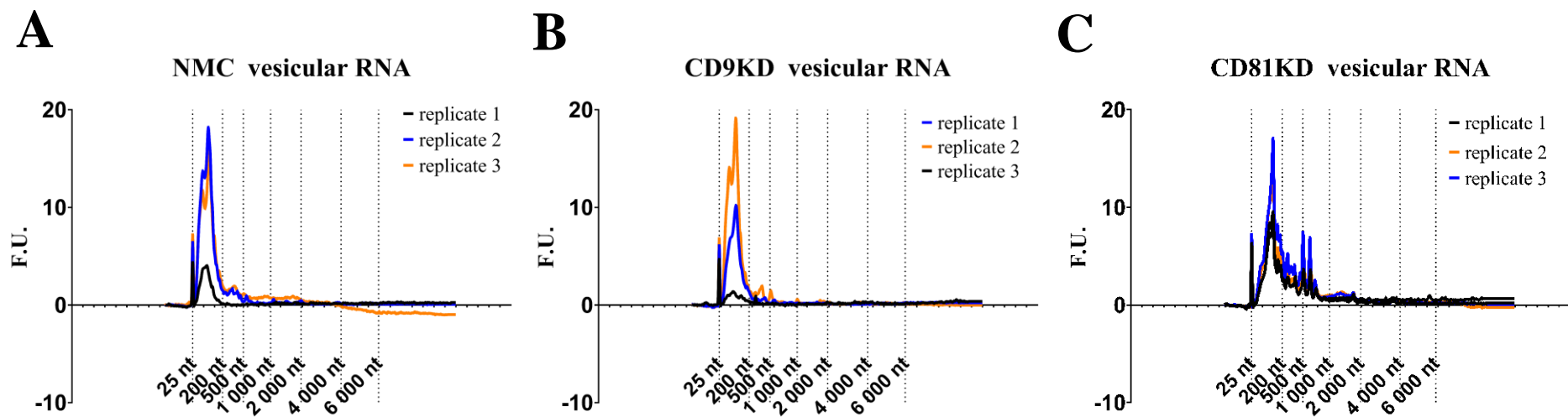


Figure 6.3: RNA traces of vesicular samples isolated by an ExoRNeasy kit (Qiagen).

EVs were isolated from the CD9KD, CD81KD and NMC cells. Vesicular RNA was extracted using an exoRneasy kit (Qiagen). The quality of all isolated vesicular RNA samples was assessed using a RNA 6000 Pico Kit in a Bioanalyzer. Samples analysed included vesicular RNA isolated from NM control cells (A), CD9KD cells (B) and CD81KD cells (C). F.U.=fluorescent units. Dotted lines show the indicated sizes.

Next, the RNA samples were processed for RNA-sequencing by our collaborator Genomescan. Libraries of the samples were prepared using the SMARTer® Stranded Total RNA-Seq Kit v3 - Pico Input Mammalian (Takara) with an integrated rRNA depletion step and subsequently the ribosomal proportion in the samples was assessed (table 6.3).

The ribosomal fraction in all samples tested at this step, ranged from 0.043-0.625 with the majority of samples showing a high ribosomal fraction of > 0.43 and thus higher than in the samples obtained by the phenol-based RNA extraction. This was a surprising observation considering that the ExoRneasy kit was previously successfully used in our lab to isolate vesicular RNA from fibroblasts, which was in turn sequenced by Genomescan successfully. The increased rRNA could be due a contamination of the EV preparations or reflect the biology of the samples. To ascertain this, would require including another, previously successfully sequenced sample (fibroblasts), and performing all the steps from EV isolation to RNA isolation in parallel. However, this was impossible with the limited time frame remaining on this project.

Few studies have focused on the sequencing of PC3 cell derived vesicular RNA, and none of these studies report a high proportion of rRNA e.g., (Probert et al., 2018, Almeida et al., 2022). Hence, we took advice from the collaborator, based on their extensive experience not to proceed to sequence these samples, as this was unlikely to deliver clear interpretable data that would add important information to the thesis. Despite these disappointing results, we proceeded to sequence the cellular RNA as this might provide some insights into the changes in the general cellular transcriptome arising in response to the KD of these select targets.

Table 6.3: Calculation of the ribosomal, globins and mitochondrial in the sequencing library based on the indicate vesicular RNA samples which were extracted using a exoRNeasy kit (Qiagen).

Vesicular RNA sample	Ribosomal	Globins	Mitochondrial
NMC replicate 1	0.625	0	0.0012
NMC replicate 2	0.6545	0	0.0052
NMC replicate 3	0.347	0	0.0045
CD9KD replicate 1	0.6807	0	0.0002
CD9KD replicate 2	0.0432	0	0.0003
CD9KD replicate 3	0.1156	0	0.0003
CD81KD replicate 1	0.5013	0	0.0017
CD81KD replicate 2	0.4359	0	0.0014
CD81KD replicate 3	0.55	0	0.0004

6.2.2 Isolation of cellular RNA

Cellular RNA from the cell variants (NMC, CD9KD, CD81KD, CHMP4CKD and SYNGR2KD) was extracted using the phenol-based extraction. Subsequently the concentrations were determined utilising the Ribogreen assay (table 6.4) showing that the cellular RNA concentrations ranged from 698 – 4565 ng/ μ l.

Table 6.4: Cellular RNA was isolated from NM control cells, CD9KD cells, CD81KD cells, CHMP4CKD and SYNGR2KD cells. RNA concentrations were determined using a Quant-it™ RiboGreen RNA assay.

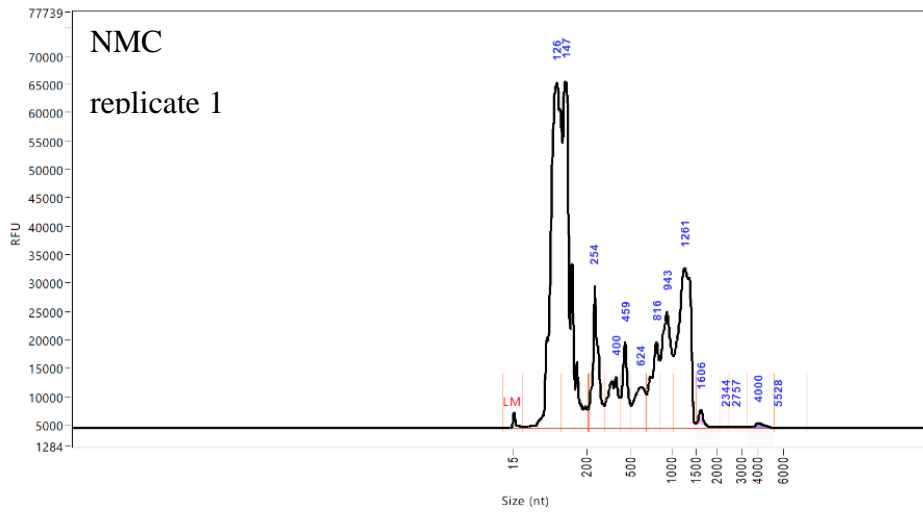
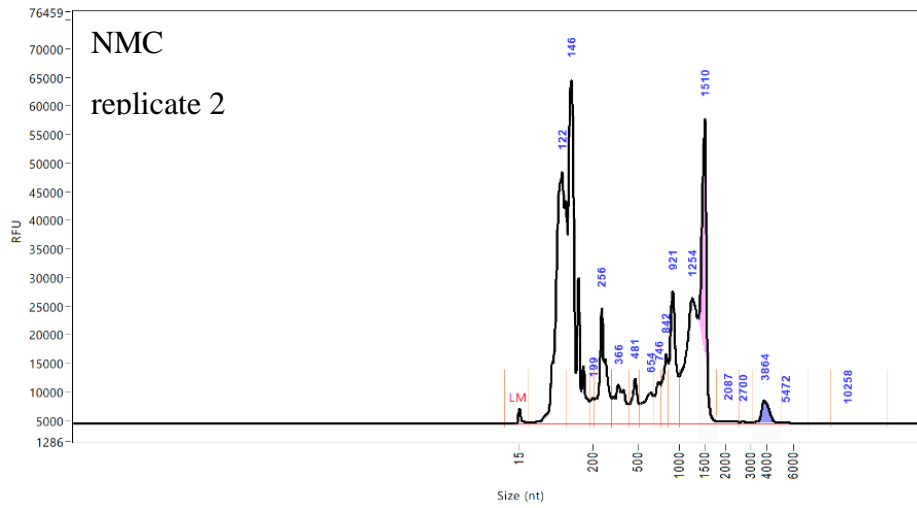
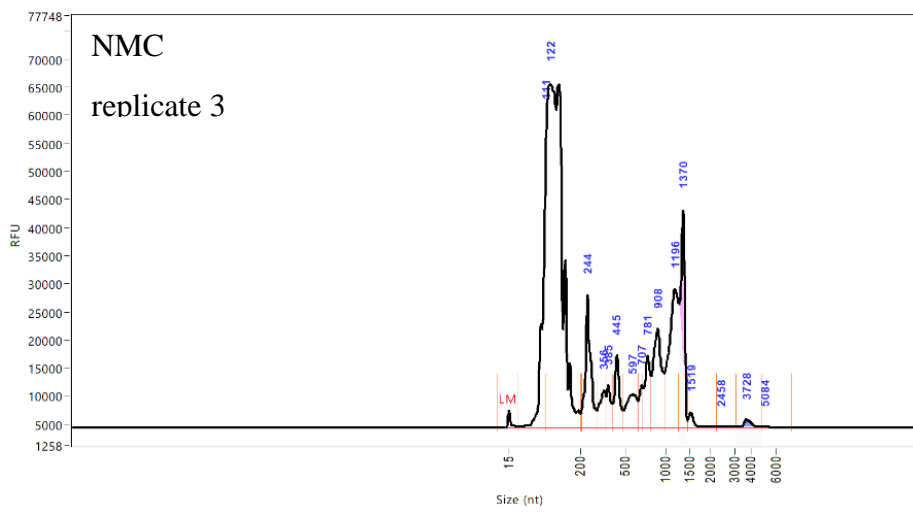
cellular RNA sample	Concentration (ng/ μ l)
NMC replicate 1	1,500.4
NMC replicate 2	2,071
NMC replicate 3	1,641.1
CD9KD replicate 1	698.8
CD9KD replicate 2	1,247.2
CD9KD replicate 3	768.1
CD81KD replicate 1	3,729
CD81KD replicate 2	4,812.1
CD81KD replicate 3	4,044

CHMP4CKD replicate 1	1,831.6
CHMP4CKD replicate 2	4,565.3
CHMP4CKD replicate 3	2,570
SYNGR2KD replicate 1	1,710.4
SYNGR2KD replicate 2	2,974.1
SYNGR2KD replicate 3	2,366.4

The cellular RNA samples were subject to the entry QC at Genomescan to assess RNA integrity and size distribution by using a fragment analyser (Figure 6.4 and annex C). The cellular samples showed varying quality of RNA indicated by some degradation and not always clear peaks for rRNA. Some of this degradation might have occurred during transportation, although a temperature monitoring probe throughout the journey confirmed the stability of the dry ice, with temperature remaining consistently below -80 °C.

The cellular RNA samples derived from the NMC cells showed a similar size distribution profile across the replicates with peaks at 240 nt and around 1,400 nt (Figure 6.4A-C). However, the samples showed some RNA degradation indicated by a peak below 200 nt. The SMARTer Stranded Total RNA-Seq Kit v2 - Pico Input Mammalian kit is specifically designed for partially degraded samples hence, we decided to proceed with these samples.

An example of a high-quality RNA sample (RNA from CHMP4CKD cells) is shown in Figure 6.4D). The small (18s at 1,737 nt) and large ribosomal subunits (28s at 4,806 nt) are detected as sharp peaks on the traces. Furthermore, only a small peak is detected in the size range below 200 nt indicating that RNA is largely intact. Traces of the complete sample set can be found in annex D.

A**B****C**

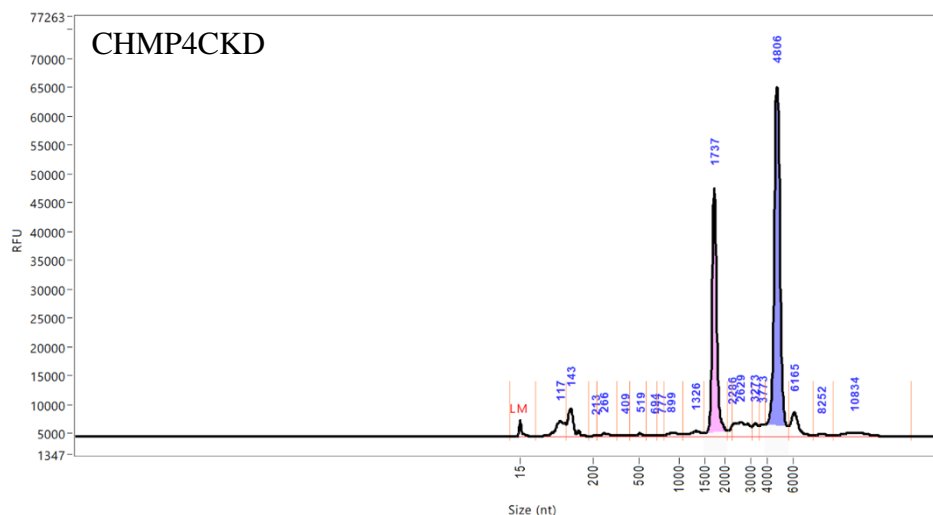
D

Figure 6.4: Integrity and size distribution of cellular RNA isolated from NMC cells and CHMP4CKD cells.

Purified RNA from the NM control cells and CHMP4CKD cells was separated by electrophoresis using the fragment analyzer Agilent DNF-472 HS RNA (15 nt) kit on a fragment Analyzer (Agilent). A)-(C) show the traces of the cellular RNA isolated from NMC cells. D) show the trace of cellular RNA isolated from CHMP4CKD cells. Light pink indicates small rRNA subunit peak, purple indicates large rRNA subunit, LM= loading marker, RFU= relative fluorescent units. Red bars indicate peaks. RFU= relative fluorescent units. Right, the image of the gel. Light pink small rRNA subunit peak, purple large rRNA subunit.

6.2.2.1 Quality control of the sequencing library and the RNA-sequencing reads

The library for sequencing was prepared using the The SMARTer Stranded Total RNA-Seq Kit v2 - Pico Input Mammalian kit. The quality of the library was assessed by determining the contribution of ribosomal, globins and mitochondrial fractions as before, and showed that across all samples the ribosomal contribution was less than 0.01 (Figure 6.5A). Thus, the generated library was of good quality to detect the transcriptional diversity within the cells. Then, the cellular RNA samples were subject to next-generation sequencing on a NovaSeq 6000 sequencer. The trimmed reads were mapped to the human GRCh38.p13

(Homo_sapiens.GRCh38.dna.primary_assembly.fa) reference genome using a short read aligner based on Burrows-Wheeler Transform (STAR2 v2.7.10) with default settings.

Between 23,608,633 (SYNGR2KD cells)– 43,069,068 (NMC cells) reads with an average read length between 149.5-150.7 were obtained for the samples (Figure 6.5B and C). The frequency of successful mapping of reads was assessed with HTSeq v2.0.2 and used for further analysis. The frequency of successful mapping of reads was assessed with HTSeq v2.0.2. Overall, a good map read distribution was achieved for all samples ranging from 97.6% (SYNGR2KD) to 98.7% (NMC) (Figure 6.5C).

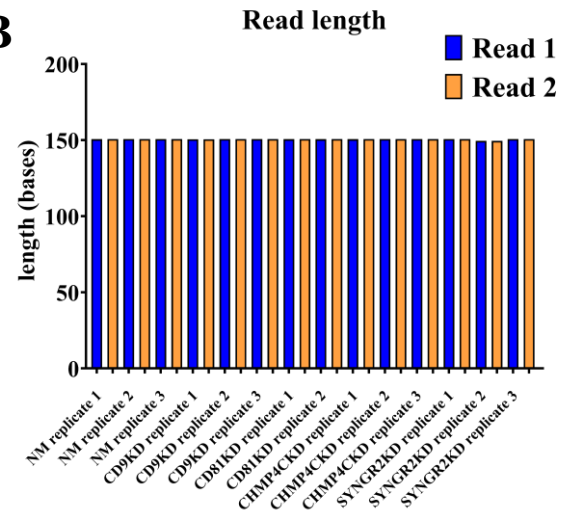
Highly degraded RNA can cause shifts in the genomic feature distribution (Gallego Romero et al., 2014). Hence, the genomic features were also examined (Figure 6.5D) and indicated homogeneity of the feature distribution across the samples. 64-73% were exonic sequences with 69-70% in NMC RNA samples. The intronic sequences comprised 5-17%, with 8-9% in the NMC samples. The NMC feature distribution did not deviate from the KD samples in the feature distribution.

The data was processed for the subsequent analysis in collaboration with our consortium partners Ingrid Tomljanovic and Sanders Tuit. The RNA-seq data set was analysed in R using DESeq2 in combination with various other packages. For an overall inspection of the transcriptomic data, a t-distributed Stochastic Neighbor Embedding (t-SNE) plot and Principal Component Analysis (PCA) plot were generated. GSEA was performed using the clusterProfiler package, while the GSVA was done with the GSVA package and will be described in more detail below.

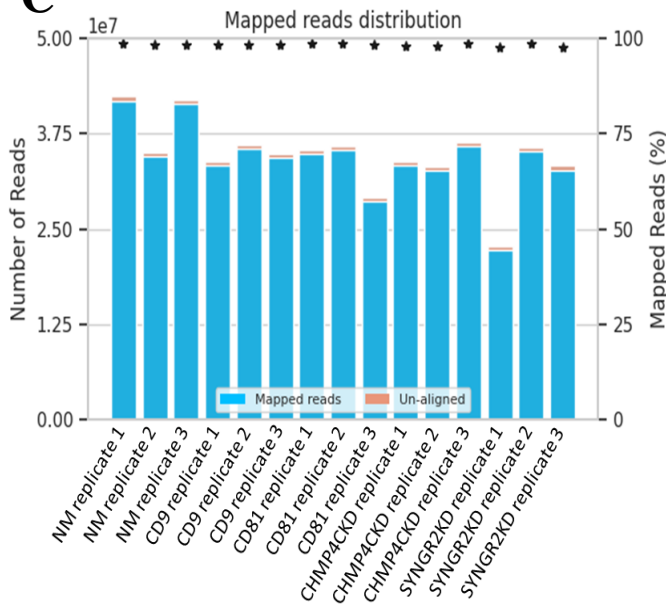
A

Cellular RNA sample	Ribosomal	Globins	Mitochondrial
NM control replicate 1	0.0005	0.0	0.0833
NM control replicate 2	0.0	0.0	0.0905
NM control replicate 3	0.0008	0.0	0.0916
CD9KD replicate 1	0.0013	0.0	0.0268
CD9KD replicate 2	0.0011	0.0	0.035
CD9KD replicate 3	0.001	0.0	0.0338
CD81KD replicate 1	0.0011	0.0	0.1554
CD81KD replicate 2	0.001	0.0	0.1497
CD81KD replicate 3	0.0007	0.0	0.1497
CHMP4CKD replicate 1	0.0015	0.0	0.1485
CHMP4CKD replicate 2	0.0012	0.0	0.0862
CHMP4CKD replicate 3	0.0005	0.0	0.0782
SYNGR2KD replicate 1	0.0018	0.0	0.043
SYNGR2KD replicate 2	0.009	0.0	0.0147
SYNGR2KD replicate 3	0.0016	0.0	0.0523

B



C



D

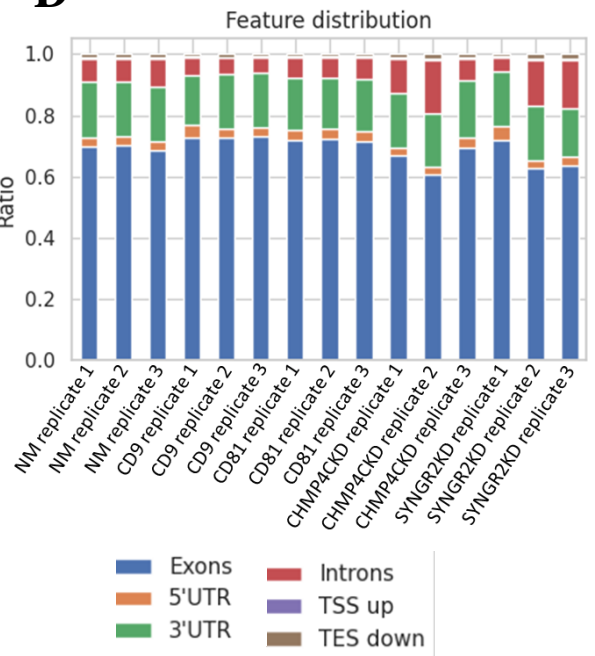


Figure 6.5: Quality control of the sequencing library and the sequencing results.

A sequencing library was prepared based on the indicated cellular RNA samples and was sequenced. The ribosomal, globin and mitochondrial fraction was calculated (A). The average read length is shown in (B). C) shows the number of reads per sample (indicated by blue bars) and the percentage of mapped reads (indicate by black stars). D) depicts the genomic feature distribution across the indicated samples. TSS=transcription start site, TES= transposable element, 3'UTR=3' untranslated regions of mRNA, 5'UTR=5' untranslated regions of mRNA.

6.2.3 Transcriptomic differences between the KDs

6.2.3.1 Initial RNA-seq data exploration and identification of potential outliers

We aimed to explore the overall transcriptomic similarities and differences across the samples and to identify potential outliers. For this purpose, using DESeq2, the RNA data was regularized log (rlog) transformed, the Euclidean distance between the samples calculated and the sample-sample distances visualised in a heatmap (Figure 6.6).

The clustering of the replicates from the majority of cell variants (NMC, CD9KD, CD81KD and CHMP4CKD cells) indicated a high, cell variant specific, similarity with regard to their gene expression profile. In contrast only two of the three replicates for SYNGR2KD showed high similarity with one replicate failing to cluster with the other two replicates. This indicates transcriptomic differences in the expression profile of the third SYNGR2KD replicate compared to the other two. Furthermore, there were varying degrees of transcriptomic similarity of the KD cells to the NMC cells with the CHMP4CKD cell variant showing the biggest similarities and the CD81KD cells showing the least similarities.

Hence, these findings are the first evidence that the genetic manipulations performed to attenuate the expression of the candidates had an impact on the general cellular transcriptome of the cell and importantly induced KD specific differences in the gene expression.

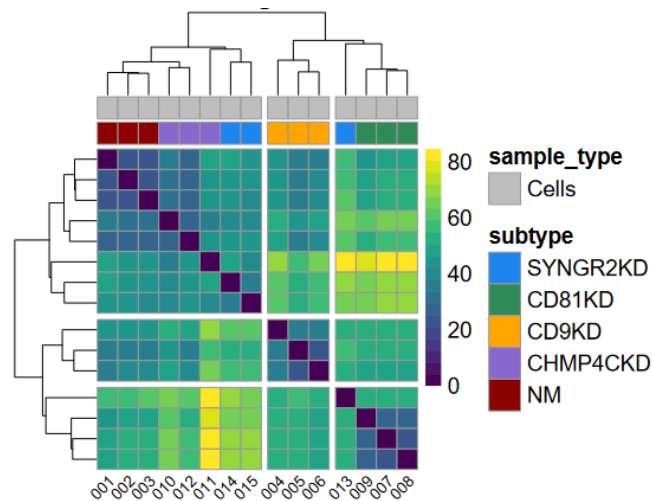


Figure 6.6: The transcriptome of NMC cells, CD9KD, CD81KD, CHMP4CKD, and SYNGR2KD cells have a distinct transcriptome.

RNA from NMC, CD9KD, CD81KD, CHMP4CKD and SYNGR2 cells was sequenced. The reads were rlog transformed and the Euclidean distances between all samples calculated and visualised in a heatmap. Yellow indicates highly different samples (80). Dark purple indicates identical samples (0). The analysis and data visualisation were performed in R using DESeq2.

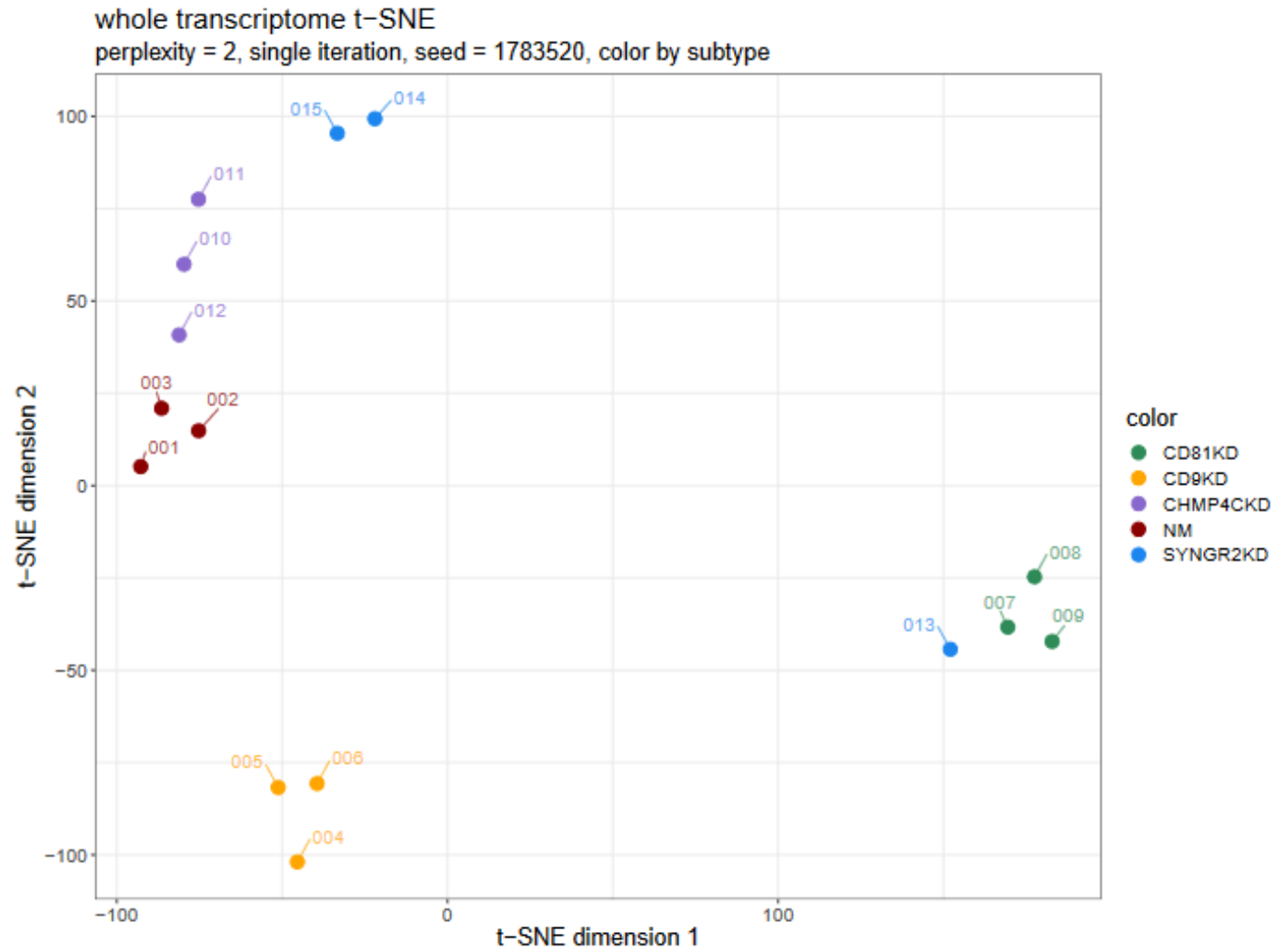
Next, we aimed to gain an overview of the data structure and important features by condensing the information of the multi-dimensional RNA-seq data set. This was achieved by projecting the data points in 2D with a focus on local features visualised in a t-SNE plot (Figure 6.7A) and global features visualised in a PCA plot (Figure 6.7B).

In both, the t-SNE plot and the PCA plot, the replicates of each cell variant showed limited variability and separated in distinct clusters from the other cell variants (Figure 6.7). The replicates of the CHMP4CKD cell variant appeared similar to the NMC cluster, yet these still formed two distinct clusters indicating differences in the overall gene expression. The sample-sample distance representing the biggest gene expression differences were between NMC cells and CD81KD cells (Figure 6.6). Across the KD cell lines, the t-SNE and PCA plot both indicated the biggest gene expression variance of the CD81KD cells from the NMC cells (Figure 6.7). The CD9KD cluster was found between NMC and CD81KD and thus less distinct from the NMC cell cluster.

Two replicates of SYNGR2 formed a cluster in the sample -sample distance heatmap (Figure 6.6). Here, both, the t-SNE and PCA plot also showed that two of the three replicates of SYNGR2 clustered together, whereas the third replicate was not in close proximity to the expected cluster (Figure 6.7A and B), and instead appeared closer to CD81 datapoints. This indicates that this third replicate of SYNGR2 was for reasons unknown an anomaly, and hence, this outlier was consequently excluded from the following analysis.

Taken together, the sample-sample distance, t-SNE and PCA indicate that candidate attenuation (by KD) induced multiple, distinct changes in the transcriptome creating cell variants with a unique gene expression pattern. The most extreme difference in pattern was most prominent in the CD81KD cells. Next, we explored, whether these unique changes in the transcriptome translated to distinct changes in gene networks and consequently predict the generation of distinct cellular phenotypes.

A



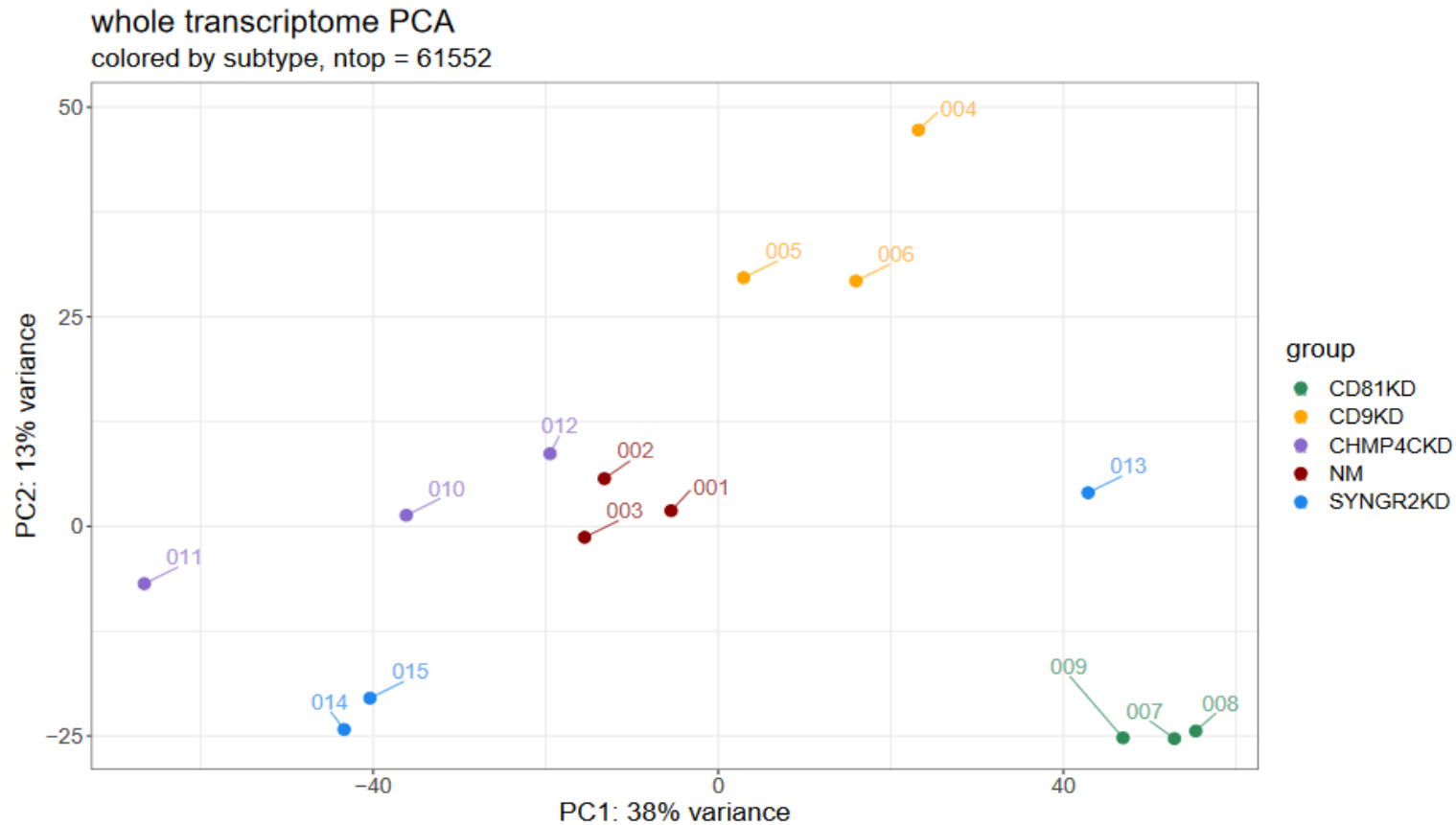
B

Figure 6.7: RNA-seq data features.

T-SNE plots and PCA plots were generated in R using the DESeq2. Examples for a t-SNE plot is shown in (A), an example for PCA plot is shown in (B). Dots of the same colour represent RNA samples derived from the same cell variant. Green represents the transcriptome from the CD81KD cell variant, pink represents the transcriptome from the CD9KD cell variant, light purple represents the transcriptome from the CHMP4CKD cell variant, red represents the transcriptome of the NMC cell variant and blue represents the transcriptome of the SYNGR2KD cell variant.

6.2.4 Gene set variation analysis (GSVA)

We aimed to get an overview of differences in enriched pathways across all samples (CD9KD cells, CD81KD cells, CHMP4CKD cells, SYNGR2KD cells and the NMC cells) to explore the distinct impact of candidate KD on the respective cell transcriptome. For this purpose, gene set variation analysis (GSVA) (Hänzelmann et al., 2013) was selected with the hallmark gene set from the human Molecular Signature Database (MSigDB) (Liberzon et al., 2015) as a reference gene list. The manually curated MSigDB is one of the most commonly used databases for gene set enrichment studies which grew from > 10 000 in 2011 to > 34 000 in 2024. Based on this database a comprehensive list of 50 gene sets was created by removing redundant and overlapping gene sets and thereby creating a list of “hallmark” gene sets describing a biological state (e.g., angiogenesis), process (e.g., DNA repair upon DNA damage) or location (e.g., peroxisome) (Liberzon et al., 2011).

The t-SNE and PCa analysis indicated distinct transcriptomes across the KD cell variants (Figure 6.7). Overall, this also translated into a distinct enrichment pattern of the hall marks across the cell variants (Figure 6.8). Importantly, the biological replicates showed a similar enrichment pattern.

CHMP4CKD cells and to a lesser extend SYNGR2KD cells had a similar enrichment pattern to NMC cells. CD9 and CD81 are both tetraspanins and hence a similar enrichment pattern was expected in these cell variants. Indeed, the CD9KD cells and the CD81KD cells showed an overlap in the enrichment pattern (Figure 6.8).

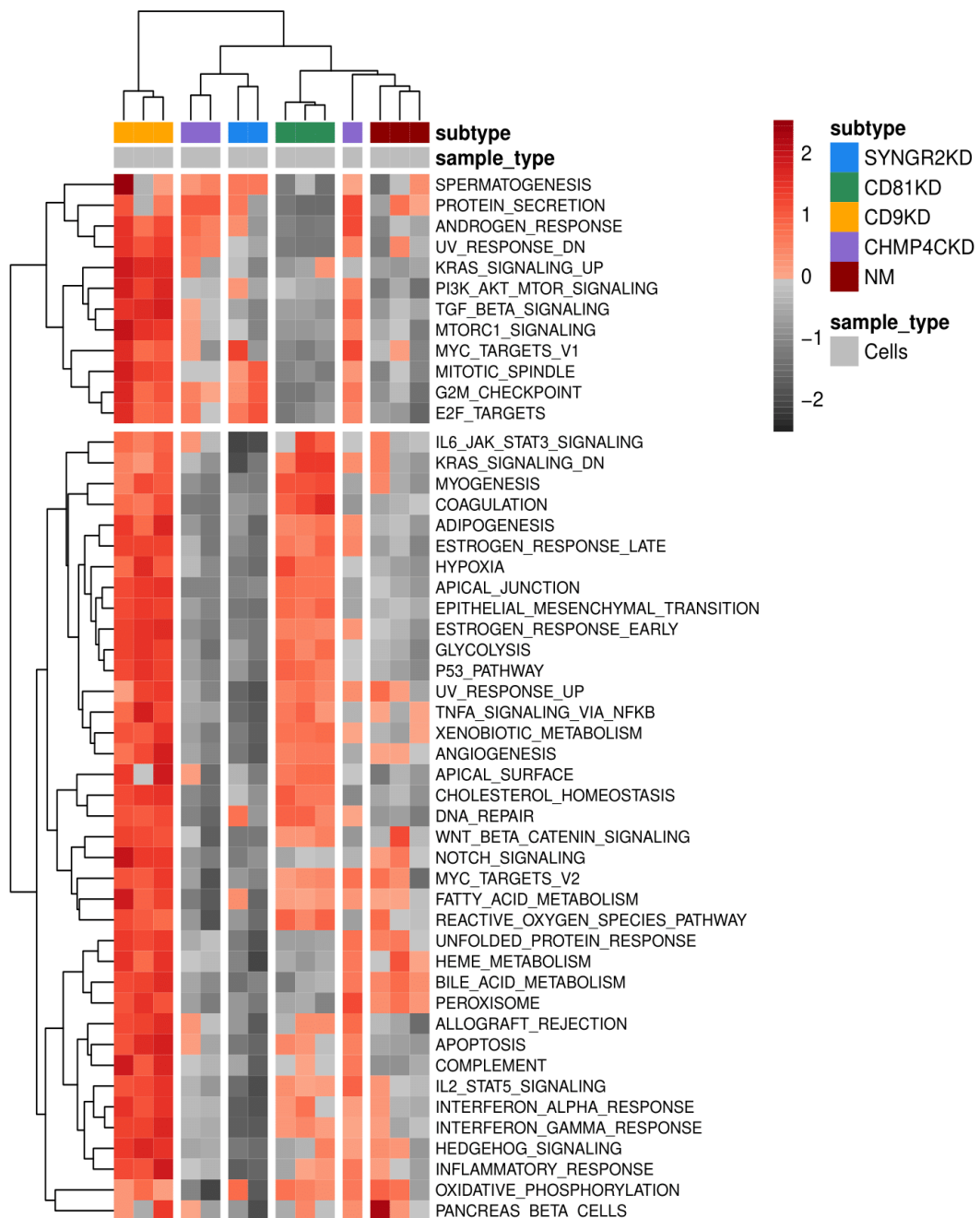


Figure 6.8: CD9KD, CD81KD, CHMP4CKD, SYNGR2KD and NMC cells have a KD specific distinct gene set enrichment pattern.

GSEA was utilised to examine the complete RNA-seq data (CD9KD, CD81KD, CHMP4CKD, SYNGR2KD and NMC cell) on a per replicate basis. The analysis was performed in R using the hallmark gene set described in MSigDB as a reference gene list. Red indicates a positive enrichment; dark grey indicates negative enrichment. The colours at the top indicate the sample shown where green represents the transcriptome from the CD81KD cell variant, pink is CD9KD, light purple is the CHMP4CKD and red is the transcriptome of the NMC cell and blue represents the transcriptome of the SYNGR2KD cell variant.

In CD81KD and CD9KD cells, genes were enriched in relation to response to tissue status (e.g., metabolism, hypoxia, cell differentiation, EMT), inflammation and activation of the immune system (e.g., allograft rejection, coagulation, complement cascade, Interferon alpha and gamma response, IL-6 Jak stat3 signalling, inflammation), DNA damage response (e.g., DNA repair, UV response), metabolic pathways (cholesterol homeostasis, glycolysis, oxidative phosphorylation, xenobiotic metabolism, metabolism). Enrichment of these pathways is indicative of increased cellular stress, and response through pro-inflammatory mediation. This complex set of changes, perhaps not entirely expected from KD of a single tetraspanin, is challenging to fully explain but clearly identifies these target molecules as relevant components in these stress responses, and indeed the cell variants here whilst perfectly viable are nonetheless clearly perturbed in their general phenotype.

Specifically for the CD9KD cells, unique gene sets also included signalling pathways that contribute to a stem cell like phenotype (reviewed in Matsui, 2016) were enriched in this cell variant: TGF- β signalling, JAK/SAT signalling, Hedghog signalling, Wnt signalling, PI3K AKT MTOR signalling and epithelial mesenchymal transition. Furthermore, gene sets associated with proliferation were enriched (E2F targets, G2M checkpoint, myc targets v1, myc targets v2, p53 pathway, mitotic spindle). These gene changes in the gene set enrichment indicate that the CD9KD cell variant has acquired stem cell like properties, potentially suggesting a highly aggressive cellular phenotype.

Interestingly, in the CD81KD cells cholesterol homeostasis was indicated as enriched. Cholesterol is an important component of EVs and essential for the fusion of MVEs with the plasma membrane (reviewed in Pfrieder and Vitale, 2018). An excess of cholesterol at the late endosome has been described to impair the endosomal trafficking (Sobo et al., 2007) and thus as a consequence likely influences EV secretion in some manner. Furthermore, another tetraspanin, CD63, has been described to regulate cholesterol deposition in endosomes and EVs (Palmulli et al., 2022). Thus, exploring a potential similar role of CD81 in PCa cells would be interesting. In contrast to the CD9KD cells, some gene sets appeared up regulated and other gene sets downregulated that include genes associated with cell proliferation (myc target V1, mitotic spindle, G2M checkpoint, E2F targets). This suggests that the two tetraspanins have both overlapping and some non-overlapping specific functions.

Compared to the NMC, CHMP4CKD cells also showed an enrichment of some gene sets associated with cell proliferation (MYC targets V1, G2M checkpoint, E2F targets) which is in line with a recent publication that suggested a role of CHMP4C in regulating the cell cycle in PCa cells (Zhang et al., 2023). Interestingly, CHMP4CKD also showed enrichment in protein secretion and downregulation of the angiogenesis pathway which are both likely to contribute to tumour growth.

In SYNGR2KD cells, most gene sets appeared less enriched compared to the NMC cells and this included signalling pathways (IL6 JAK STAT3 signalling, wnt beta catenin signalling), EMT transition and interferon α response. Furthermore, some of the gene sets associated with cell proliferation were downregulated in the SYNGR2KD (Myc targets V2, p53 pathway), whereas others appeared as enriched (G2M checkpoint, E2F). However, the functional consequences are not readily predictable. It is important to note that we have seen no impact on cell proliferation in this cell variant (Chapter 4). This SYNGR2KD specific enrichment pattern could point to a less aggressive cancer cell phenotype compared to the NMC cells, which could also be reflected in the released EVs. Interestingly, in chapter 5, we found that EVs derived from the SYNGR2KD had a diminished potency to modulate the secretome of recipient fibroblasts

Taken together, the GSVA indicated that the candidate attenuation induced changes in the enrichment of gene sets and importantly these changes were different, depending on the specific KD. Hence, the KD cell variants represent distinct cellular phenotypes, and this was most prominent in the CD9KD and CD81KD cells. The next goal was, to gain a detailed insight in the KD specific impact at both the single gene level and at a pathway level, which could aid in understanding the functional relevance of the candidates. DEGs comparing the gene expression of each KD cell variant to the NMC cells were determined from the raw counts using DESeq2. Subsequently gene set enrichment analysis (GSEA) was conducted to reveal functionally relevant gene networks. The analysis for the KD cell variants is outlined below on a sample-by-sample basis.

6.2.5 Attenuation of CD9 impacts various biological processes

6.2.5.1 Differential gene expression in the CD9KD cell variant

The DEGs in the CD9KD cells compared to the NMC cells was graphically represented in a volcano plot (Figure 6.9). The DEG list comprised 13,341 genes in total, with 871 genes found to be significantly ($P < 0.05$) differentially expressed with a log₂ fold change ± 0.5 (fold change smaller than 0.7 and bigger than 1.4). To narrow down this extensive gene list, stringent criteria were applied with a cut off value for the log₂fold change set to ± 2 and the P-value to < 0.001 . Applying these strict criteria, 31 genes were found to be upregulated and 9 genes downregulated. The top 5 up and top 5 down regulated genes are summarised in table 6.5. Importantly, the expression of the CD9 transcript showed a sharp decrease (-8.1-fold change) in the CD9KD cells compared to the NMC confirming successful and expected attenuation of the target. Some genes exhibited a greater fold change than this, suggesting quite a dramatic impact therefore on these elements that were not directly targeted by shRNA. The GSVA indicated the TGF- β signalling pathway as upregulated, consistent with this observation perhaps, *INHBB*, a gene that encodes a member of TGF β superfamily proteins, showed a significantly increased expression (25.4-fold change, table 6.5) in the CD9KD cells.

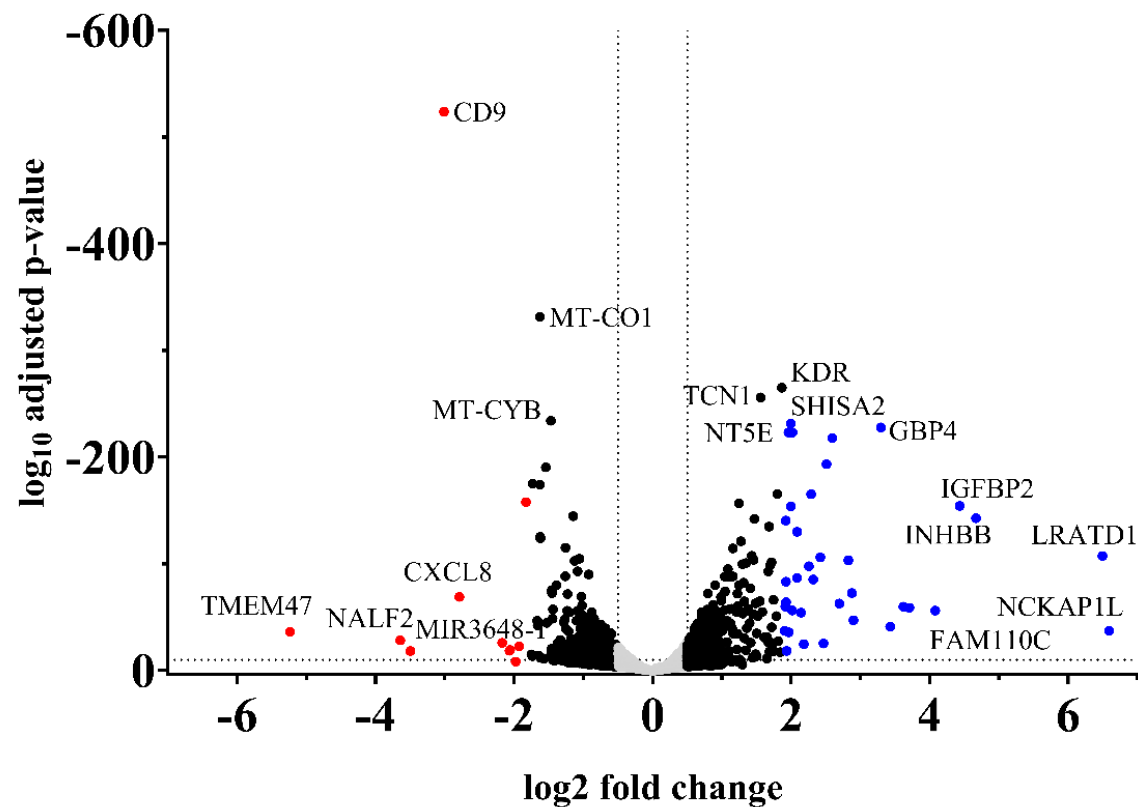


Figure 6.9: Distribution of differential expressed genes comparing CD9KD and NMC cells.

DEGs with a log₂ fold change <0.5 or >-0.5 are represented as grey dots, while DEGs with a log₂ fold change >0.5 or <-0.5 are visualised in black. Red dots denote DEGs that were found with log₂ fold change >2 or <-2. Dotted vertical line indicates log₂ fold change of +/-0.5 and the dotted horizontal line indicates p-value <0.001. Top ranking genes with highest log₂ fold change and most significance are labelled. The graph was generated in GraphPad Prism.

Table 6.5: The top 5 up and top 5 down regulated genes identified in the DEG list from the CD9KD cell line.

	Gene	Fold change	Adjusted p-value
UPREGULATED	NCKAP1L	96.3	5.58E-12
	LRATD1	90.2	4.88E-33
	INHBB	25.4	9.58E-44
	IGFBP2	21.6	3.34E-47
	FAM110C	16.9	1.15E-17
DOWNREGULATED	CXCL8	-6.9	1.58E-21
	CD9	-8.1	2.2E-158
	MIR3648-1	-11.3	3.09E-06
	NALF2	-12.5	2.66E-09
	TMEM47	-37.7	1.23E-11

6.2.5.2 Gene set enrichment analysis of the CD9KD cells

We aimed to explore whether the gene expression differences between CD9KD cells and NMC cell variant are reflected in changes in the functional gene networks. For this purpose, a GSEA with a focus on molecular functions, signalling pathways, cellular compartments, and biological processes was performed utilising the gene sets curated in the MsigDB. The following results are focused on the biological process and cellular compartment in an effort to A) simplify the results and focus on surprising/unexpected findings and B) reveal possible EV regulator relevant changes.

GSEA was performed utilising the biological process gene set retrieved from the MSigDB as a reference set to reveal enriched pathways in the CD9KD compared to the NMC cell variant and the top hits are shown in Figure 6.10. This GSEA showed that CD9 attenuation dramatically changed the cellular phenotype and strikingly all top hits appeared as enriched in this cell variant.

Decreased adhesion has been associated with a highly metastatic cancer phenotype. Tetraspanins form tetraspanin webs and play crucial roles in cell attachment by interacting with a range of cellular molecules (Matsushita et al., 2016, Zilber et al., 2005), consequently a negative impact on cell attachment upon CD9KD was expected. Surprisingly, CD9KD lead to enrichment of pathways related to cell attachment (positive regulation of cell adhesion, regulation of cell adhesion, amebodial type cell migration (locomotion), cell substrate adhesion). In addition to this, several biological pathways related to wound healing were found to be upregulated (response to wound healing, wound healing) and could point to a more aggressive phenotype since cancers are often likened to chronic wounds (Ganesh et al., 2020).

Other commonly observed top-ranking hits were related to response to stimuli (kinase cell signalling, cytokine production) and developmental processes (Skin, vasculature, axon, morphogenesis).

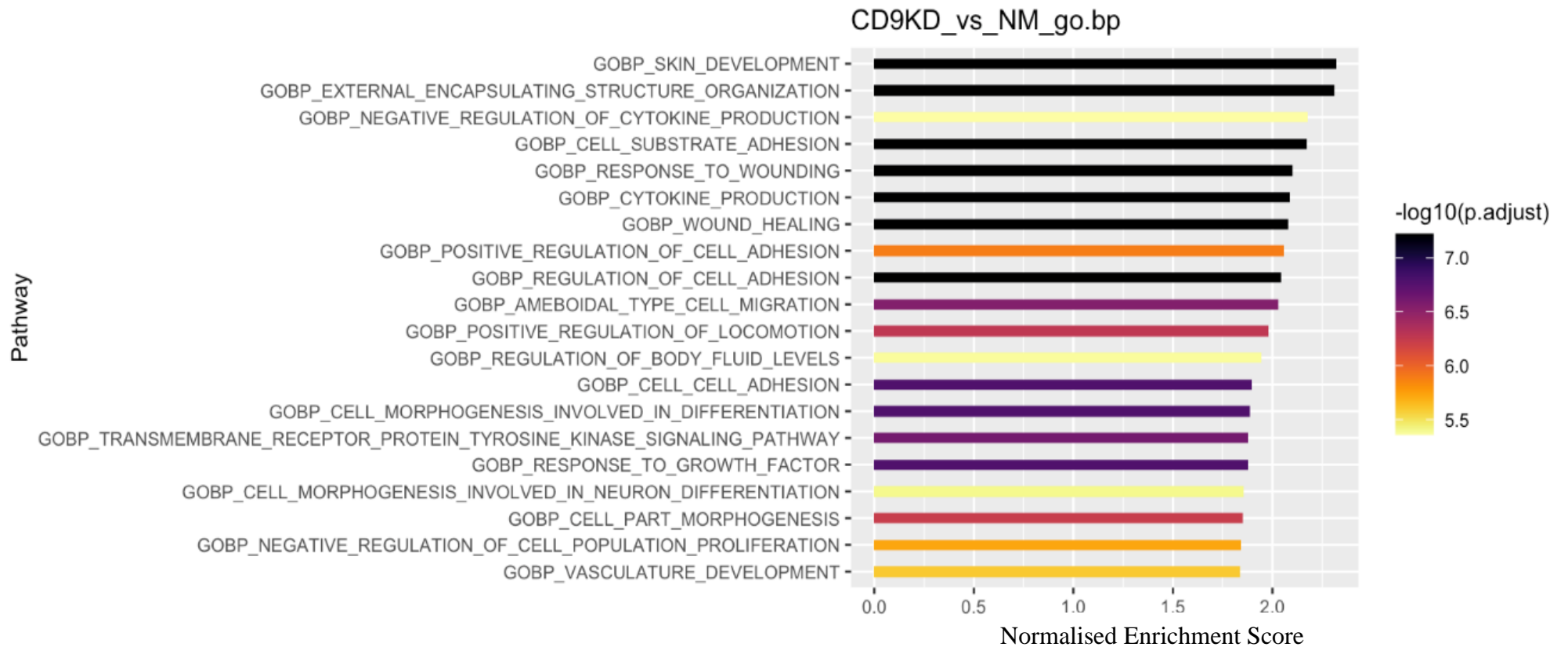


Figure 6.10: Top ranking biological function hits enriched in CD9KD cells.

Gene set enrichment analysis of the CD9KD cells was performed using R and the biological pathway gene set compiled in the MSigDB as reference gene sets. Top 20 most significant biological process hits were selected and then listed according to their normalised enrichment score.

Tetraspanin are transmembrane proteins and hence decreased expression of the proteins might impact cellular compartments that are bound by a membrane. To investigate this, GSEA was performed with a focus on cellular compartments based on the cellular compartment gene set retrieved from MSigDB. The top 20 significant (Figure 6.11) hits included several cellular membrane compartments e.g., endoplasmic reticulum lumen, plasma membrane, cell projection membrane. Another interesting observation was the downregulation of several hits associated with the mitochondrial compartment and cell respiration including e.g., NADH dehydrogenase complex. This is in line with a recent study by Suarez that reported that treating melanoma cells with a CD9 peptide reduced mitochondrial activity and induced an adaptation of the endolysosomal compartment in response to the intracellular redox state (Suarez et al., 2021). Unexpectedly, the GO analysis also indicated an enrichment of DNA related compartments (DNA packing complex and protein DNA complex) with an unknown functional relationship to CD9.

Interestingly one of the top hits also indicated transcriptional changes in the recycling endosome membrane (Figure 6.11). This could indicate a switch from increased formation of late endosomes to recycling endosomes. To investigate this idea and the general impact further, I explored the complete cellular compartment GSEA dataset in more detail (table 6.6). Intriguingly, several membrane compartments appeared enriched in the CD9KD cells, especially granules and synaptic vesicles. This could indicate a general perturbation of the secretome of the CD9KD cells. This is in line with the results in the previous chapter (chapter 5) that attenuation of CD9 in PC3 cells had a general impact on the secretome and thus suggesting that attenuation of an EV regulator without disturbing the general cellular secretome might not be possible. Importantly, several membranes associated with EV biogenesis appeared enriched: recycling endosomes, endocytic vesicles, vesicle lumen and early endosome indicating a possible switch to recycling endosomes. Interestingly, the late endosome compared appeared not enriched. These results indicate an involvement of CD9 in endosomal pathway and thus possibly EV biogenesis.

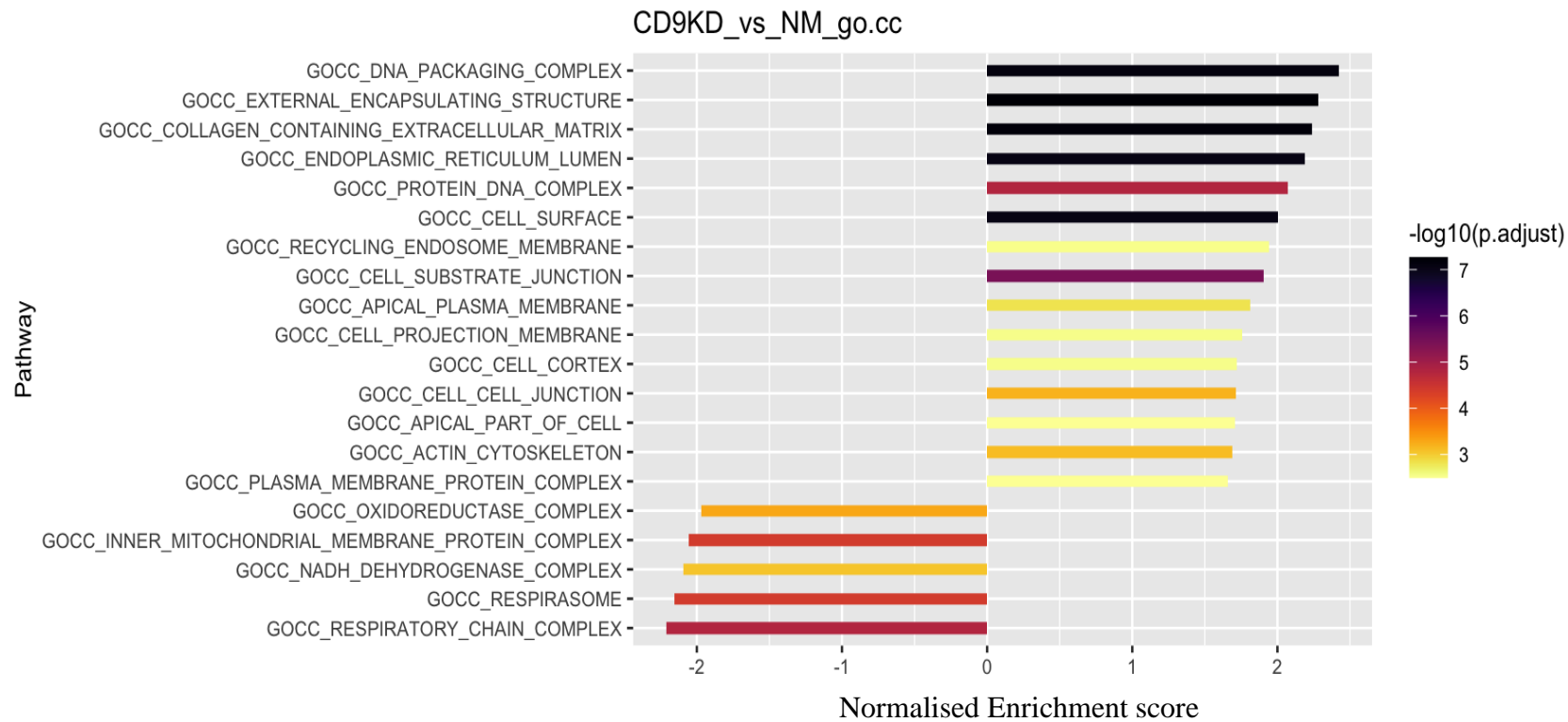


Figure 6.11: Top ranking cellular compartment hits enriched in CD9KD cells.

Gene set enrichment analysis of the CD9KD cells was performed using R and the cellular compartment gene set compiled in the MSigDB as reference gene sets. Top 20 most significant biological process hits were selected and then listed according to their normalised enrichment score.

Table 6.6: Impact of CD9 attenuation on cellular compartments.

Table shows the complete GSEA on cellular compartments comparing the CD9KD to NMC cells. Left column shows possible broader categories summarising the hits. Only hits with $P < 0.5$ are included. NES= normalised enrichment score.

	ID	NES	p.adjust
endosomal membranes	GOCC_RECYCLING_ENDOSOME_MEMBRANE	1.9	0.00288679
	GOCC_RECYCLING_ENDOSOME	1.7	0.01209992
	GOCC_ENDOCYTIC_VESICLE	1.6	0.01446397
	GOCC_EARLY_ENDOSOME	1.5	0.01446397
synaptic vesicle	GOCC_POSTSYNAPTIC_SPECIALIZATION_MEMBRANE	1.8	0.02296846
	GOCC_INTRINSIC_COMPONENT_OF_POSTSYNAPTIC_DENSITY_ME	1.8	0.03255835
	GOCC_POSTSYNAPTIC_MEMBRANE	1.7	0.02188438
	GOCC_INTRINSIC_COMPONENT_OF_SYNAPTIC_MEMBRANE	1.7	0.04718901
	GOCC_SYNAPTIC_MEMBRANE	1.6	0.02848781
	GOCC_PRESYNAPSE	1.4	0.04722543
	GOCC_VESICLE_LUMEN	1.6	0.01446397
cytoskeleton	GOCC_INTERMEDIATE_FILAMENT	1.9	0.0058568
	GOCC_INTERMEDIATE_FILAMENT_CYTOSKELETON	1.8	0.01837508
	GOCC_CELL_CORTEX	1.7	0.00284111
	GOCC_ACTIN_CYTOSKELETON	1.7	0.00073561
	GOCC_ACTIN_FILAMENT_BUNDLE	1.7	0.04796669
	GOCC_ACTIN_BASED_CELL_PROJECTION	1.6	0.02148233
	GOCC_CLUSTER_OF_ACTIN_BASED_CELL_PROJECTIONS	1.6	0.04718901
	GOCC_POLYMERIC_CYTOSKELETAL_FIBER	1.5	0.00608276
DNA	GOCC_DNA_PACKAGING_COMPLEX	2.4	7.3638E-08
	GOCC_PROTEIN_DNA_COMPLEX	2.1	1.5928E-05
plasma membrane	GOCC_POSTSYNAPTIC_DENSITY_MEMBRANE	2.0	0.01446397
	GOCC_CELL_SURFACE	2.0	8.6334E-08
	GOCC_ANCHORED_COMPONENT_OF_MEMBRANE	1.9	0.01643023
	GOCC_APICAL_PLASMA_MEMBRANE	1.8	0.00153764
	GOCC_BASAL_PART_OF_CELL	1.8	0.008565
	GOCC_CELL_PROJECTION_MEMBRANE	1.8	0.00284111
	GOCC_EXTERNAL_SIDE_OF_PLASMA_MEMBRANE	1.8	0.00856506
	GOCC_PLASMA_MEMBRANE_PROTEIN_COMPLEX	1.7	0.00318269
	GOCC_BASOLATERAL_PLASMA_MEMBRANE	1.7	0.01927318
	GOCC_APICAL_PART_OF_CELL	1.7	0.00318269
	GOCC_BASEMENT_MEMBRANE	1.7	0.04718901
	GOCC_MEMBRANE_MICRODOMAIN	1.5	0.04718901
	GOCC_CELL_LEADING_EDGE	1.5	0.0179315
	GOCC_ADHERENS_JUNCTION	1.5	0.04464138
		GOCC_SIDE_OF_MEMBRANE	1.5
protrusions	GOCC_STEREOCILUM_BUNDLE	1.8	0.02735985
	GOCC_FILOPODIUM_MEMBRANE	1.8	0.03198407
	GOCC_SCAR_COMPLEX	1.8	0.04865911
mitochondria	GOCC_RESPIRATORY_CHAIN_COMPLEX	-2.2	1.5727E-05
	GOCC_RESPIRASOME	-2.2	3.8958E-05
	GOCC_NADH_DEHYDROGENASE_COMPLEX	-2.1	0.00087722
	GOCC_INNER_MITOCHONDRIAL_MEMBRANE_PROTEIN_COMPLEX	-2.1	3.8958E-05
	GOCC_OXIDOREDUCTASE_COMPLEX	-2.0	0.00051332
	GOCC_CYTOCHROME_COMPLEX	-1.9	0.0185987
	GOCC_RESPIRATORY_CHAIN_COMPLEX_IV	-1.8	0.04682521
	GOCC_MITOCHONDRIAL_PROTEIN_CONTAINING_COMPLEX	-1.6	0.008565
	GOCC_ENDOPLASMIC_RETICULUM_LUMEN	2.2	8.6334E-08
	GOCC_LUMENAL_SIDE_OF_ENDOPLASMIC_RETICULUM_MEMBRAN	1.8	0.02148233
	GOCC_GOLGI_LUMEN	1.7	0.04822315
granules	GOCC_TERTIARY_GRANULE	1.8	0.00848712
	GOCC_FICOLIN_1_RICH_GRANULE_MEMBRANE	1.8	0.03218453
	GOCC_SECRETORY_GRANULE_MEMBRANE	1.7	0.00526925
	GOCC_FICOLIN_1_RICH_GRANULE	1.7	0.01293746
Junc-tions	GOCC_CELL_SUBSTRATE_JUNCTION	1.9	3.6555E-06
	GOCC_CELL_CELL_JUNCTION	1.7	0.0006242
Myo-sin	GOCC_MYOSIN_COMPLEX	1.8	0.02359444
	GOCC_ACTOMYOSIN	1.8	0.02614766
	GOCC_CELL_BODY	1.5	0.02134025
	GOCC_KERATIN_FILAMENT	1.8	0.04865911
	GOCC_GLYCOPROTEIN_COMPLEX	2.0	0.00418254
external structures	GOCC_EXTERNAL_ENCAPSULATING_STRUCTURE	2.3	5.44E-08
	GOCC_COLLAGEN_CONTAINING_EXTRACELLULAR_MATRIX	2.2	6.4231E-08
	GOCC_COLLAGEN_TRIMER	1.9	0.01174306
	GOCC_COMPLEX_OF_COLLAGEN_TRIMERS	1.7	0.04722543

Taken together, KD of CD9 caused an upregulation of several biological processes indicating that this cell variant acquired a stem cell like cellular phenotype with more aggressive properties compared to the control cells. Hence, EVs derived from this cell variant are expected to reflect the phenotype of the parental cell and promote the tumour growth. Intriguingly, despite these findings, the corresponding EVs appeared to lose their tumour promoting properties judged by the decreased potency in modulating the secretome of fibroblasts (chapter 5). This results clearly show that more research is required to understand the impact of an acquired stem cell like phenotype on the molecular and functional features of EVs. Analysing the proteome and transcriptome of both parental cell and corresponding EVs could provide further insights and perhaps reveal the target cells for the EVs.

6.2.6 Attenuation of CD81 impacts various EV regulating processes.

6.2.6.1 Differential gene expression in the CD81KD cell variant

The impact of CD81 attenuation in PC3 on the cellular transcriptome was analysed following the same approach as done for the CD9KD cells. The comparative analysis between CD81KD and NMC cells revealed 13,449 DEGs which were visualised in a volcano plot (Figure 6.12). Out of these, 4,891 genes were significantly (P -value < 0.05 , \log_2 -fold change ± 0.5) differentially expressed. Applying strict criteria (\log_2 fold change ± 2 and P -value < 0.001) 20 genes were found to be upregulated and 7 genes downregulated. Importantly, CD81 mRNA was found to be successfully attenuated (-4.2 -fold change, Figure 6.12). The top 5 up and top 5 downregulated hits are summarised in table 6.7.

The t-SNE, PCA and sample-sample distance indicated that the CD81KD cells and the CD9KD cells have a distinct gene expression profiles. This was also reflected in the DEGs with the top hits lacking an overlap.

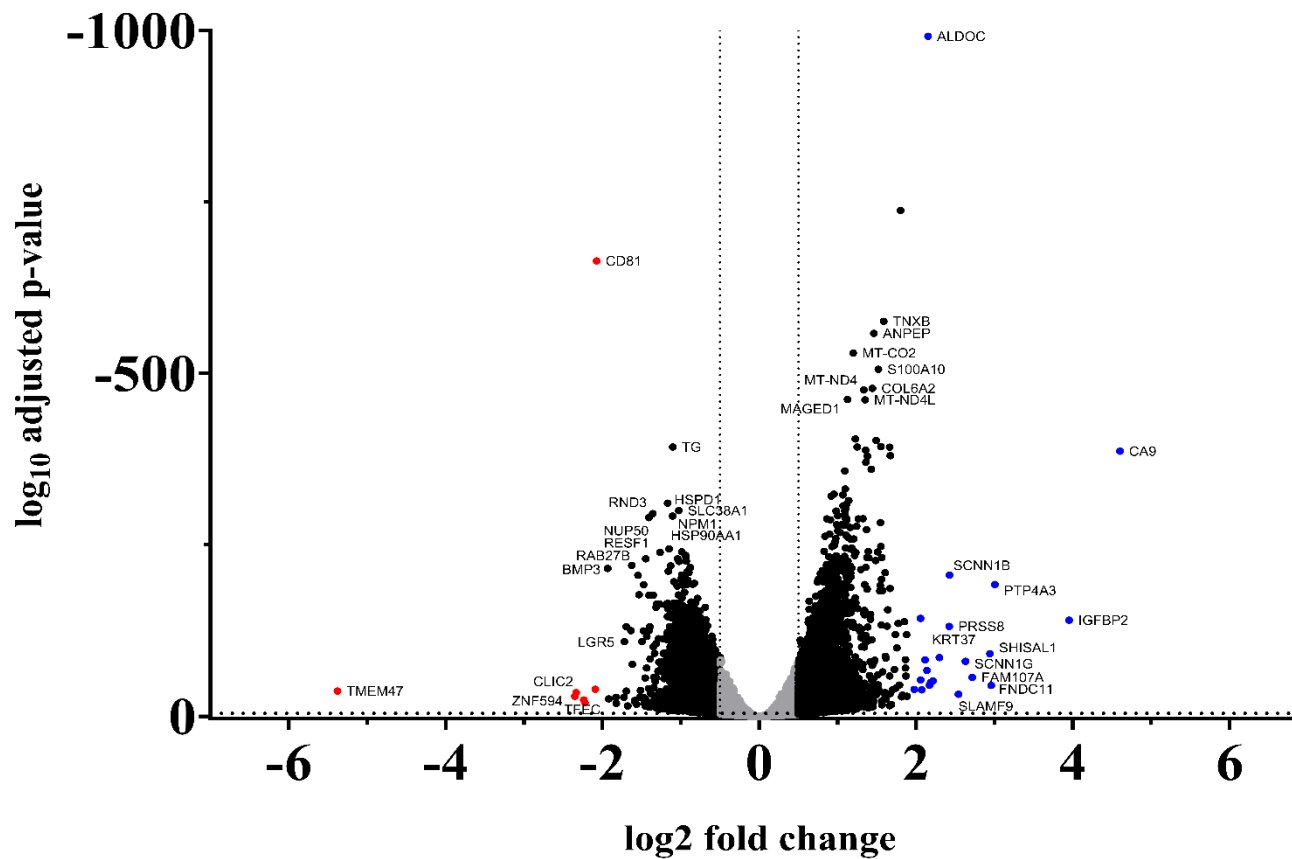


Figure 6.12: Distribution of differential expressed genes comparing CD81KD and NMC cells.

DEGs with a log₂fold change <0.5 or >-0.5 are represented as grey dots, while DEGs with a log₂ fold change >0.5 or <-0.5 are visualised in black. Red dots denote DEGs that were found with log₂fold change >2 or <-2. Dotted vertical line indicates log 2-fold change of +/-0.5 and the dotted horizontal line indicates p-value <0.001. Top ranking genes with highest log₂fold change and most significance are labelled. The graph was generated in GraphPad Prism.

Table 6.7: The top 5 up and top 5 down regulated genes identified in the DEG list from the CD81KD cell line.

	Gene	Fold change	Adjusted p-value
DOWNREGULATED	TMEM47	-41.6	6.4782E-12
	ZNF594	-5.1	1.3648E-09
	CLIC2	-5.0	3.2029E-11
	TRPM8	-4.7	5.3167E-08
	TFEC	-4.7	7.612E-07
UPREGULATED	CA9	24.3	4.066E-117
	IGFBP2	15.5	5.2796E-43
	PTP4A3	8.0	1.1866E-58
	FNDC11	7.8	2.5387E-14
	SHISAL1	7.7	2.8745E-28

Interestingly, previously described EV cargo regulators were also identified to be differentially expressed: SYNCRIP, which regulates microRNA sorting into small EVs (Santangelo et al., 2016) showed a 2-fold downregulation. Remarkably, an interaction/influence of SYNCRIP and CD81 was predicted in the interaction network (Chapter 3). Besides, CERT1 (-1.8-fold change) appears to regulate RNA loading in the same pathway (Barman et al., 2022). These findings suggest that CD81 is involved in EV biogenesis.

In addition to this, several other genes associated with EV secretion were differentially expressed in the CD81KD cells (table 6.8). SDC1 and SDC4 appeared enriched (1.9- fold change and 1.7-fold change respectively), whereas SDCBP was downregulated (-2.1-fold change). All of these components are involved in the same syndecan-syntenin-ALIX pathway. Hence a downregulation of one component and upregulation of the other two is surprising. In addition to this, CD81 involvement in the regulation of EVs is thought to be independent of this pathway (Roucourt et al., 2015) and no interaction has been previously described between

CD81 and the Syntenin-Syndecan ALIX pathway to my knowledge. Perhaps, the CD81KD caused a downregulation of SDCBP and then as a response caused an upregulation of SDC to compensate. Alternatively, CD81KD could have caused an upregulation of SDC1 and SDC4, which in turn could have caused a downregulation of SDCBP. This indicates a possible interconnection between the different pathways and thus provides an interesting opportunity for further explorations.

Table 6.8: extended list of DEGs identified in the CD81KD DEG list limited to ESCRT components, tetraspanins and previously described EV regulators.

	Gene	Fold change	Adjusted p-value
EV RNA regulator	CERT1	-1.8	3.1109E-22
	SYNCRIP	-2.0	2.5211E-40
	SDC1	1.9	6.9045E-76
	SDCBP	-2.1	6.76063E-33
	SDC4	1.7	1.21682E-19

GSEA was also utilised to explore the potential biological processes regulated by CD81 (Figure 6.13). There were only four biological processes in the top 20 most significant hits that were upregulated in the CD81KD cell line (glycolytic process through fructose-6-phosphate, response to wound healing, external encapsulating structure organization, keratinization). Interestingly, various terms associated with RNA biology were downregulated, including RNA trafficking (establishment of RNA localisation and export from nucleus), modifications of RNA (processing of ncRNA and mRNA, splicing of RNA), and ribosome biogenesis regulation of mRNA metabolic process. These finding suggest that CD81 is involved in RNA regulation. It would be interesting to explore if this is also reflected in changes in the RNA cargo of EVs.

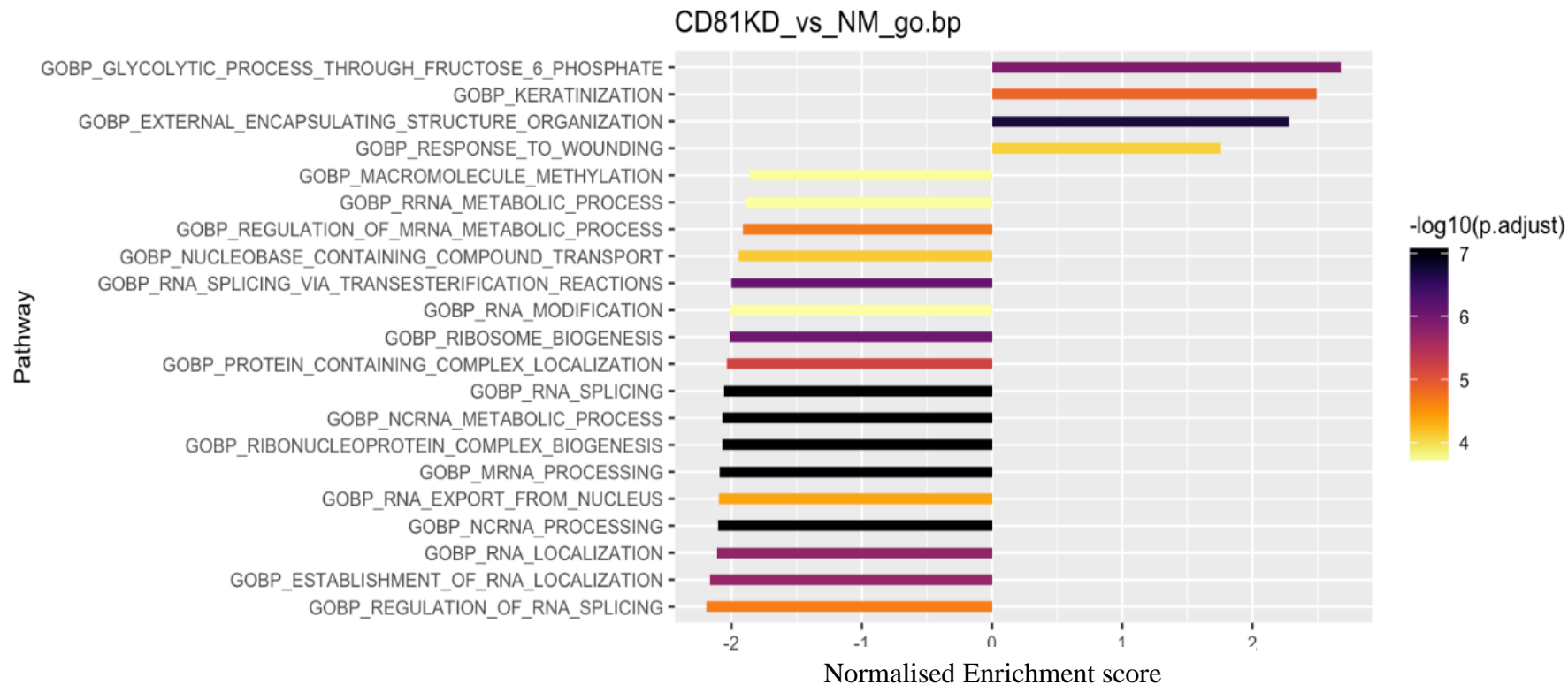


Figure 6.13: Top ranking biological function hits enriched in CD81KD cells.

Gene set enrichment analysis of the CD81KD cells was performed using R and the biological pathway gene set compiled in the MSigDB as reference gene sets. Top 20 most significant biological process hits were selected and then listed according to their normalised enrichment score.

Next, transcriptomic changes in the cellular compartment in the CD81KD cells were explored (Figure 6.14, table 6.9). It is striking that CD81 attenuation appeared to induce an upregulation of cellular compartments that are enclosed by a membrane, such as for instance the Golgi lumen, Endoplasmic reticulum lumen, lysosomal and vesicle lumen. These membranes are all places of cargo sorting or loading of molecules destined for export or degradation. Furthermore, the results indicate changes in overall cellular structure suggested by an enrichment of hits associated with the cytoskeleton (e.g., actin cytoskeleton).

Several terms also appeared as downregulated, and these included hits related to DNA (e.g., replication fork), the nuclear compartment (e.g., nuclear pore) and RNA processing units (e.g., spliceosome), which might indicate perturbate homeostasis. Surprisingly, the analysis did not show an enrichment of the endosomal compartments. In addition to this, an enrichment of mitochondrial hits was evident perhaps suggesting an increased energy demand for this cell variant (table 6.9). This is in contrast to the results obtained from the sequencing of the CD9KD cells and thus supports that CD81 and CD9 control different processes.

Taking the results for CD81 together, the GSEA of cellular compartments indicated that CD81 attenuation in PC3 cells induced changes in membrane compartments associated with molecular cargo transport. In addition to this, several gene sets associated with RNA processing were downregulated. Furthermore, the DEGS and GSEA indicated a clear and unique enrichment pattern of biological pathways that was distinct from the CD9KD cells and thus confirming a KD specific impact on the cellular transcriptome and specific gene networks.

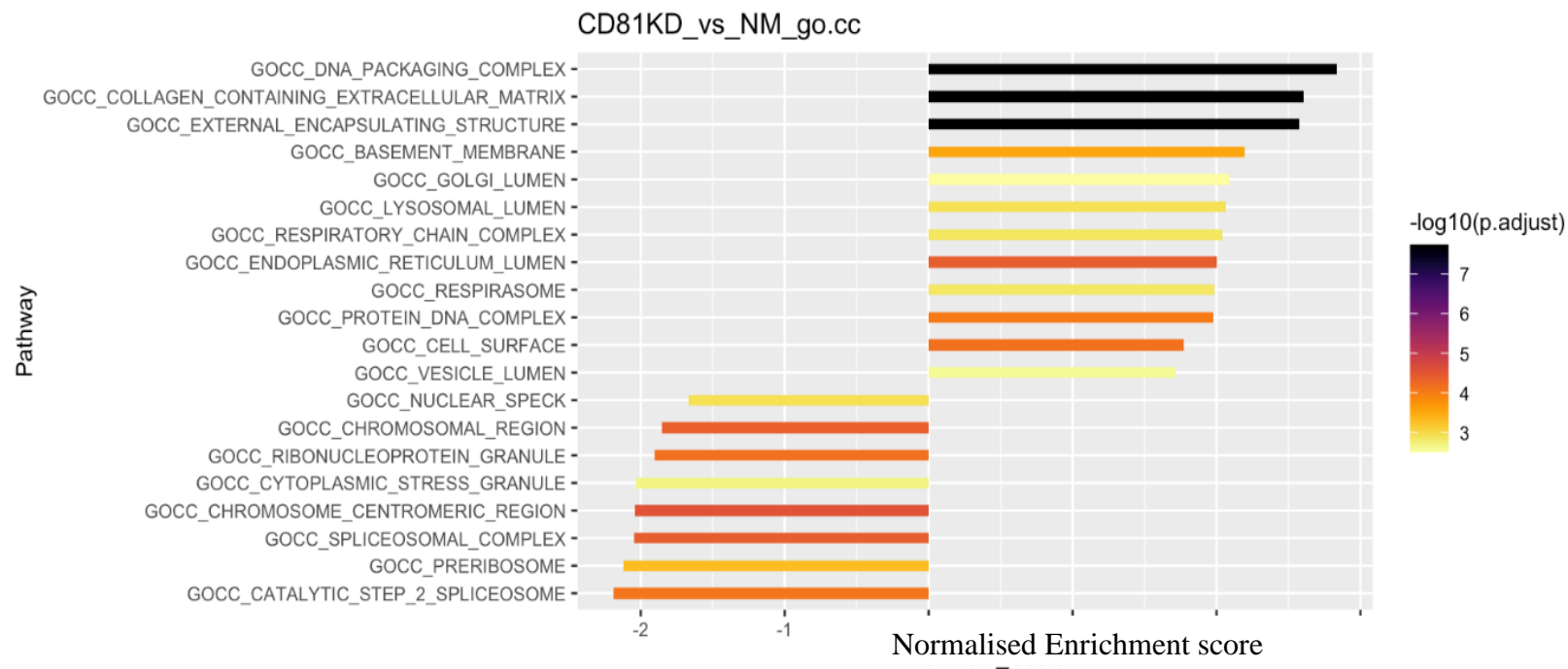


Figure 6.14: Top ranking cellular compartment hits enriched in CD81KD cells.

Gene set enrichment analysis of the CD81KD cells was performed using R and the cellular compartment gene set compiled in the MSigDB as reference gene sets. Top 20 most significant biological process hits were selected and then listed according to their normalised enrichment score.

Table 6.9: Impact of CD81 attenuation on cellular compartments.

Table shows the complete GSEA on cellular compartments comparing the CD81KD to NMC cells. Left column shows possible broader categories summarising the hits. Only hits with P<0.5 are included. NES= normalised enrichment score.

	ID	NES	p.adjust
DNA	GOCC_DNA_PACKAGING_COMPLEX	2.8	1.81333E-08
	GOCC_CHROMOSOMAL_REGION	-1.9	4.34438E-05
	GOCC_PROTEIN_DNA_COMPLEX	2.0	9.48747E-05
	GOCC_REPLICATION_FORK	-1.7	0.047979999
	GOCC_CHROMOSOME_TELOMERIC_REGION	-1.5	0.047979999
	GOCC_KINETOCHORE	-1.6	0.02703062
	GOCC_CHROMOSOME_CENTROMERIC_REGION	-2.0	2.77959E-05
	GOCC_CONDENSED_CHROMOSOME	-1.7	0.003433473
Lumen of organelles	GOCC_ENDOPLASMIC_RETICULUM_LUMEN	2.0	4.08644E-05
	GOCC_LYSOSOMAL_LUMEN	2.1	0.001165356
	GOCC_VESICLE_LUMEN	1.7	0.002582197
	GOCC_GOLGI_LUMEN	2.1	0.003106264
	GOCC_VACUOLAR_LUMEN	1.6	0.032195779
	GOCC_INTRINSIC_COMPONENT_OF_ORGANELLE_MEMBRANE	1.5	0.039138811
	GOCC_ORGANELLE_INNER_MEMBRANE	1.4	0.016573351
	GOCC_PLATELET_ALPHA_GRANULE_LUMEN	1.9	0.04045917
mitochondria	GOCC_RESPIRATORY_CHAIN_COMPLEX	2.0	0.00138192
	GOCC_RESPIRASOME	2.0	0.001422316
	GOCC_INNER_MITOCHONDRIAL_MEMBRANE_PROTEIN_COMPLEX	1.6	0.047979999
	GOCC_NADH_DEHYDROGENASE_COMPLEX	1.8	0.032195779
Granule	GOCC_RIBONUCLEOPROTEIN_GRANULE	-1.9	7.16701E-05
	GOCC_CYTOPLASMIC_STRESS_GRANULE	-2.0	0.002051108
	GOCC_SECRETORY_GRANULE	1.5	0.006616102
	GOCC_FICOLIN_1_RICH_GRANULE_LUMEN	1.8	0.013885373
	GOCC_FICOLIN_1_RICH_GRANULE	1.7	0.025746977
RNA processing units	GOCC_CATALYTIC_STEP_2_SPLICEOSOME	-2.2	8.39705E-05
	GOCC_SPLICEOSOMAL_COMPLEX	-2.0	4.08644E-05
	GOCC_PRERIBOSOME	-2.1	0.000515537
	GOCC_SMALL_SUBUNIT_PROCESSOME	-1.9	0.019648629
Membrane bound organelles	GOCC_BASEMENT_MEMBRANE	2.2	0.000289086
	GOCC_SIDE_OF_MEMBRANE	1.5	0.02492669
	GOCC_INTRINSIC_COMPONENT_OF_ENDOPLASMIC_RETICULUM_MEMBRANE	1.6	0.025746977
	GOCC_ANCHORED_COMPONENT_OF_MEMBRANE	1.7	0.042288762
	GOCC_PLASMA_MEMBRANE_PROTEIN_COMPLEX	1.5	0.042557896
	GOCC_INTERMEDIATE_FILAMENT	2.0	0.009983622
cyto-skeleton	GOCC_ACTIN_CYTOSKELETON	1.5	0.016573351
	GOCC_ACTIN_FILAMENT_BUNDLE	1.8	0.042557896
	GOCC_COLLAGEN_CONTAINING_EXTRACELLULAR	2.6	1.81333E-08
cell extensions	GOCC_MICROVILLUS	2.0	0.007235966
	GOCC_CILIARY_BASAL_BODY	-1.6	0.032195779
	GOCC_INTRACILIARY_TRANSPORT_PARTICLE	-1.9	0.040079747
	GOCC_CAJAL_BODY	-1.8	0.044851934
Nucleus	GOCC_NUCLEAR_PORE	-1.6	0.046730471
	GOCC_NUCLEAR_SPECK	-1.7	0.001165356
	GOCC_FIBRILLAR_CENTER	-1.6	0.02703062
	GOCC_EXTERNAL_ENCAPSULATING_STRUCTURE	2.6	1.81333E-08
	GOCC_CATION_CHANNEL_COMPLEX	1.8	0.02678778
	GOCC_CELL_SURFACE	1.8	7.16701E-05

6.2.7 Attenuation of CHMP4C impacts the cellular transcriptome in PC3 cells

6.2.7.1 Differential gene expression in CHMP4CKD cells

The CHMP4CKD cell variant showed a similar yet distinct gene expression pattern to the NMC (Figures 6.6 and 6.7). CHMP4C attenuation on the transcripts in PC3 cells was explored in more depth by compiling a DEG list comparing the CHMP4CKD cell variant to the NMC including 13,596 genes. The results were visualised in a volcano plot (Figure 6.15) and show that 362 genes were significantly differentially expressed (P-value < 0.05, log2fold change \pm 0.5 or fold change smaller than 0.7 and bigger than 1.4). Out of these, the majority of genes were downregulated (201), while 161 genes were found to be upregulated.

Applying strict criteria (log2 fold change of 2, P<0.001) only six genes were identified as downregulated and only one gene as upregulated. Importantly, CHMP4C attenuation was modest, yet significant (-2.9-fold change) (Figure 6.12, table 6.10) and sufficient to induce a significant impact on the gene expression profile. The top-ranking genes are summarised in table 6.10. Overall, less DEGs were identified here compared to the other KD cell variants.

Table 6.10: The top 5 up and top 5 down regulated genes identified in the DEG list from the CHMP4CKD cell line.

	Gene	Fold change	Adjusted p-value
DOWN-REGULATED	C3orf70	-9.2	4.46E-10
	SLC16A2	-5.9	3.71E-53
	ENSG00000287059	-5.8	7.58E-15
	CLIC2	-4.7	3.57E-09
	BEX2	-4.3	4.62E-05
UP-REGULATED	FERMT3	7.1	1.43E-13
	CNTN1	3.7	3.31E-05
	HTR2B	3.4	1.95E-08
	SCUBE1	3.1	2.22E-17
	LGR5	2.9	8.59E-29

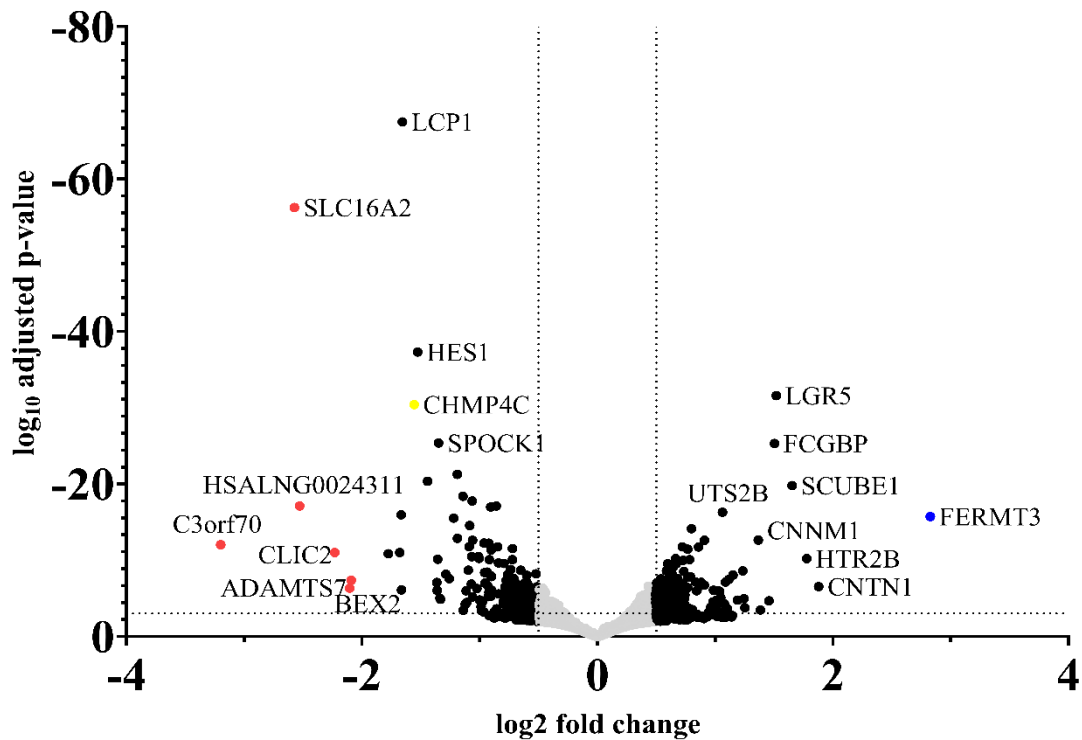


Figure 6.15: Distribution of differential expressed genes comparing CHMP4CKD and NMC cells.

DEGs with a log₂fold change <0.5 or >-0.5 are represented as grey dots, while DEGs with a log₂ fold change >0.5 or <-0.5 are visualised in black. Red dots denote DEGs that were found with log₂fold change >2 or <-2. Dotted vertical line indicates log₂-fold change of +/-0.5 and the dotted horizontal line indicates p-value <0.001. Top ranking genes with highest log₂fold change and most significance are labelled. CHMP4C is marked in yellow. The graph was generated in GraphPad Prism.

CHMP4C is an ESCRT component and consequently working in concert with other ESCRT components at the endosomal membrane. The perturbation of one component of the complex (CHMP4C) could therefore perhaps lead to a disruption of the complex as a whole which might be reflected at the gene level. To explore this, I searched the DEG list for other ESCRT components (chapter 2, table 2.1) to no avail.

A limited impact on the diversity of differential gene expression can still impact multiple pathways if the changes in the gene expression are in coordinated gene sets. To investigate this, GSEA with a focus on biological pathways was performed. Overall, CHMP4CKD appeared to only have minor impact across various biological pathways (Figure 6.16). There was only one top hit in the biological process that was enriched (regulation of centriole replication). Three biological processes appeared downregulated (rhythmic behaviour, negative regulation of DNA binding transcription factor activity, regulation of DNA binding transcription factor activity).

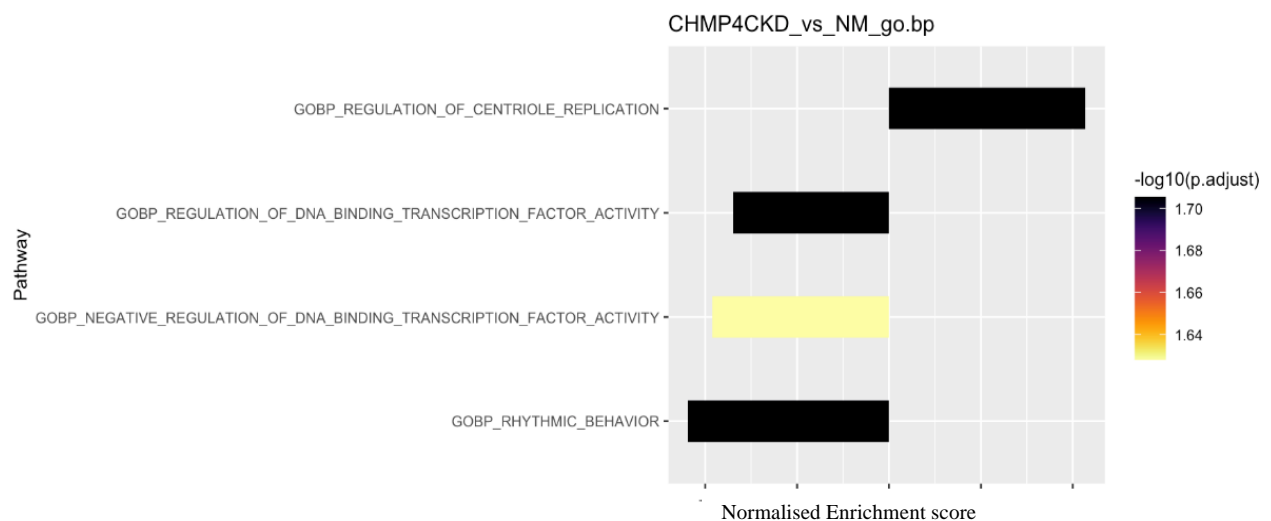


Figure 6.16: Top ranking biological function hits enriched in CHMP4CKD cells.

Gene set enrichment analysis of the CD9KD cells was performed using R and the biological pathway gene set compiled in the MSigDB as reference gene sets. The most significant biological process hits were selected and then listed according to their normalised enrichment score.

Performing GSEA with a focus on cellular compartments indicated that only few significant hits were enriched (Figure 6.17). Several GO terms that are associated with DNA related gene sets (e.g., upregulation of chromosome centric region) were found enriched, while terms describing ribosomal gene sets were downregulated (e.g., ribosomal subunit, cytosolic

ribosome). No major impact on other cellular compartment or biological pathways was observed implying a highly specialised function of CHMP4C in PC3 cells.

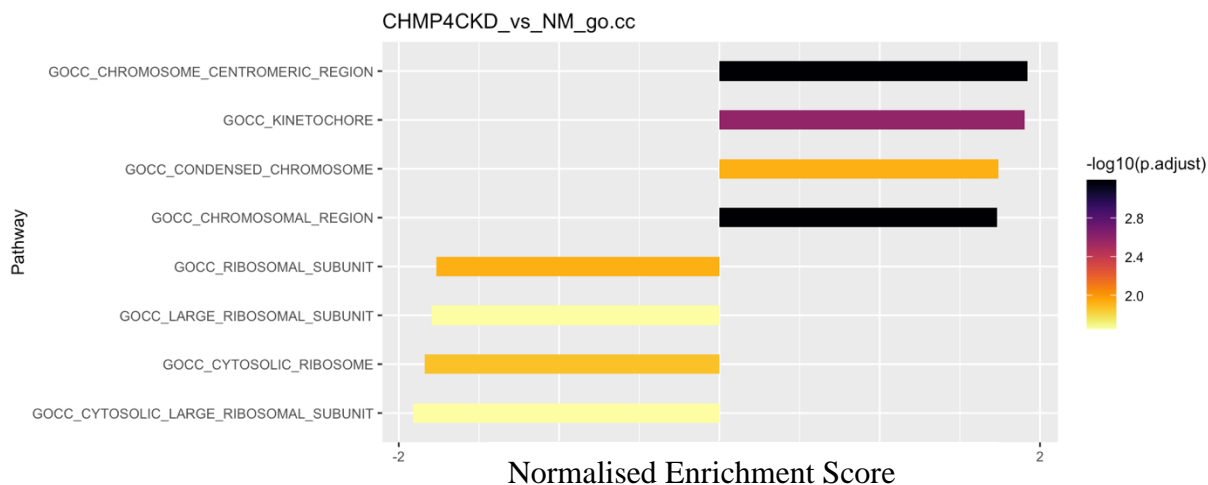


Figure 6.17: Top ranking cellular compartment hits enriched in CHMP4CKD cells.

Gene set enrichment analysis of the CHMP4CKD cells was performed using R and the cellular compartment gene set compiled in the MSigDB as reference gene sets. The top most significant biological process hits were selected and then listed according to their normalised enrichment score.

Collectively, these results suggest that CHMP4C attenuation induced a minor change in the cellular transcriptome compared to CD81KD and CD9KD, which was also reflected in a limited impact on biological processes and cellular compartments. Most hits were associated with chromosomes in line with the reported role of CHMP4C as a regulator of cell division (Carlton et al., 2012). Attenuation of a target gene can have significant impact on different cellular pathways, which can influence EV biogenesis indirectly. Hence, the limited confounding effects of CHMP4C attenuation render this cell variant potentially especially useful for further explorations.

6.2.8 Attenuation of SYNGR2 has a significant impact on the gene expression

6.2.8.1 Differential gene expression in SYNGR2KD cells

Next, the impact of SYNGR2 attenuation on the transcripts in PC3 cells was explored in more depth. The DEG set comparing the expression of transcripts in the SYNGR2KD to the NMC variant was graphically visualised in a volcano plot (Figure 6.18) showing the 13,4441 DEGs of SYNGR2KD vs NMC. 1,363 genes were significantly differentially expressed (P-value <0.05, log2fold change+/-0.5 or fold change smaller than 0.7 and bigger than 1.4) with 645 upregulated and 718 genes downregulated. Using strict criteria (P-value<0.001 and log2 fold change +/-2) only 21 genes were found to be upregulated, while 40 were found to be downregulated. The top 5 up and down regulated hits are summarised in table 6.11.

Importantly, downregulation of SYNGR2 in the SYNGR2KD cells could be confirmed (-7.4-fold change) (table 6.12).

Table 6.11: The top 5 up and top 5 down regulated genes identified in the DEG list from the SYNGR2KD cells.

	Gene	Fold change	Adjusted p-value
DOWNREGULATED	SLC16A2	-24.1	2.29558E-51
	KCNB1	-18.6	1.04086E-06
	CPNE2	-12.5	4.32485E-15
	PDLIM3	-11.3	5.55608E-07
	CLIC2	-9.7	1.38373E-08
UPREGULATED	CALB1	104.5	5.14865E-90
	MUC2	30.1	5.88197E-56
	SHISAL1	7.3	2.11934E-14
	SLC35F4	7.	2.49668E-20
	ZNF33BP1	6.4	3.06736E-08

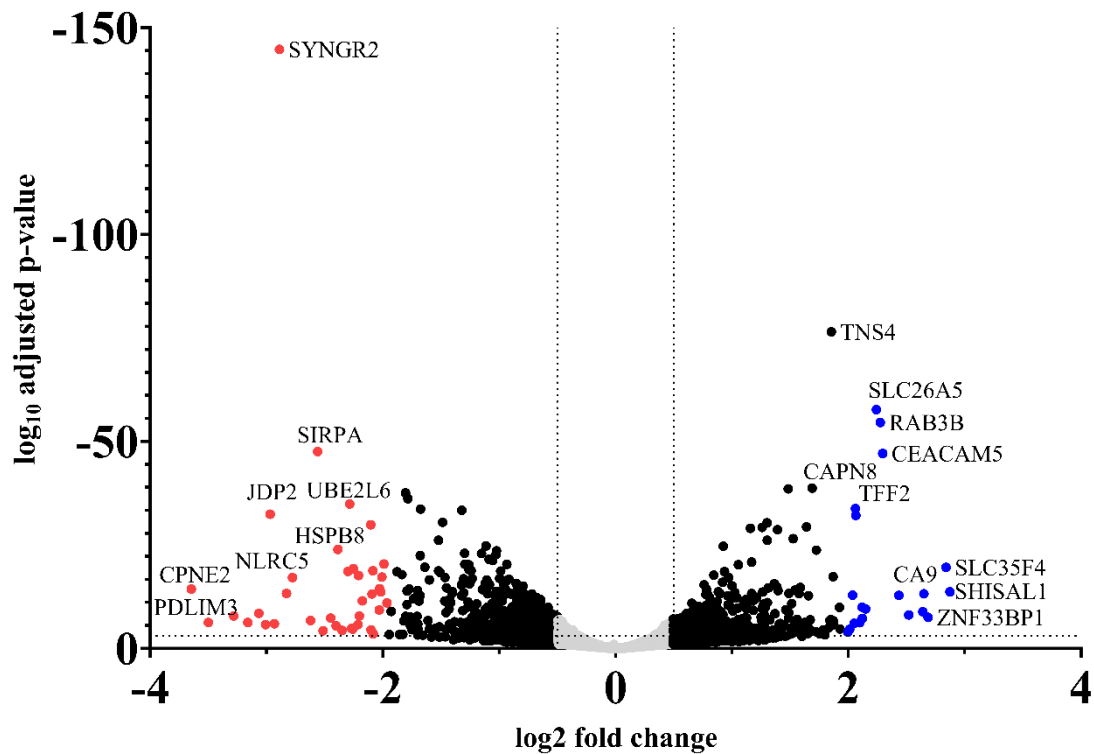


Figure 6.18: Distribution of differentially expressed genes comparing SYNGR2KD and NMC cells.

DEGs with a log₂ fold change <0.5 or >-0.5 are represented as grey dots, while DEGs with a log₂ fold change >0.5 or <-0.5 are visualised in black. Red dots denote DEGs that were found with log₂ fold change >2 or <-2. Dotted vertical line indicates log₂ fold change of +/-0.5 and the dotted horizontal line indicates p-value <0.001. Top ranking genes with highest log₂ fold change and most significance are labelled. The graph was generated in GraphPad Prism.

SYNGR2 belongs to the synaptogyrin family which are all characterised by 4 transmembrane domains and have been suggested to modulate membrane trafficking. Interestingly, additional synaptogyrins, SYNGR1 (-1.5-fold change) and SYNGR4 (-1.7-fold change) were identified and to my knowledge showing for the first time the impact of SYNGR2 on other members of the synaptogyrin family in a PCa cell line (table 6.12).

Of further interest in the DEG list are differentially expressed integrins which have been attribute a role in determining the EV localisation *in vivo* (reviewed in Lin et al., 2023). Thus, loading or the lack thereof of these molecules might have important functional consequences.

A number of integrins were enriched (ITGA2 (1.7-fold change), ITGB3 (2.6-fold change), ITGB4 (2.2-fold change) (table 6.12). Interestingly, the expression of another candidate selected for this work PCLO was found 1.5-fold enriched. PCLO was found to change the molecular features prompted me to explore the interactions of the different candidates in more detail which will be described later (6.2.9).

Table 6.12: List of DEGs identified in the SYNGR2KD DEG list focused on members of the synaptogyrin family and integrins.

	Gene	Fold change	Adjusted p-value
DOWN-REGULATED	SYNGR2	-7.4	1.7429E-145
	SYNGR1	-1.5	0.001264644
	SYNGR4	-1.7	0.012060184
UP-REGULATED	PCLO	1.5	9.42438E-08
	ITGA2	1.7	4.19236E-15
	ITGB4	2.2	1.33498E-21
	ITGB3	2.6	0.002340615

GSEA with a focus on biological processes was performed to gain better insights into biological pathways that are possibly regulated by SYNGR2 (Figure 6.19). The analysis revealed that many top enriched hits are related to chromosome segregation (e.g., sister chromatid segregation, nuclear chromosome segregation). The majority of the top GO terms appeared as downregulated for instance several virus-related terms appeared negatively enriched (negative regulation of viral process, regulation of viral life cycle) (Figure 6.19). This is interesting because viruses have been described to exploit EV generating processes such as the ESCRT machinery, RabGTPases and SNARE proteins (Nolte-t Hoen et al., 2016, Moulin et al., 2023). Furthermore, several of the top hits that were downregulated were associated with signalling pathways (e.g., response to type 1 interferon, cytokine mediated signalling pathway, negative regulation of phosphorylation). Cargo sorting of EVs is regulated by intracellular signalling molecules and modifications such as phosphorylation (Imjeti et al., 2017). Thus, these results could indicate that the phenotypic changes in the EVs upon SYNGR2 KD (described in Chapter 4 and 5) are partially due to changes in the

signalling rather than direct regulation of the EV cargo through SYNGR2. To explore this more, the impact on the cell compartment with a focus on compartments important for EV biogenesis was explored.

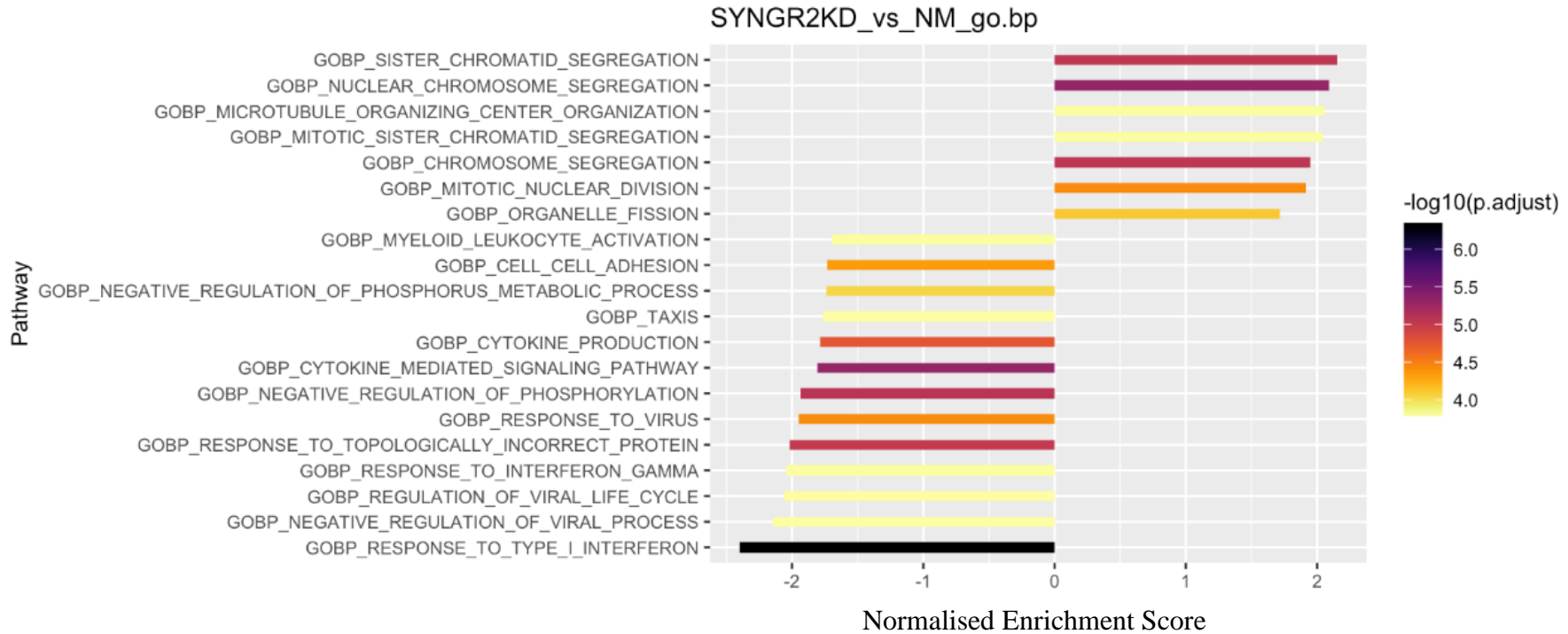


Figure 6.19: Top ranking biological function hits enriched in SYNGR2KD cells.

Gene set enrichment analysis of the SYNGR2KD cells was performed using R and the biological pathway gene set compiled in the MSigDB as reference gene sets. Top 20 most significant biological process hits were selected and then listed according to their normalised enrichment score.

GSEA with a focus on cellular compartments supported the finding that SYNGR2 might be involved in chromosome segregation since many of the top enriched hits were associated with chromosomes (e.g., condensed chromosome, kinetochore). SYNGR2 KD also appeared to be accompanied by downregulation of gene sets associated with various membrane compartments such as late endosomes, lysosomal lumen synaptic membrane, lysosomal lumen (Figure 6.20). Examining the complete GSEA cellular compartment results (table 6.13) indicated the downregulation of several membrane compartments associated with various vesicles and granules e.g., Ficolin_1_ Rich granule, secretory granule, secretory granule membrane, postsynaptic membrane synaptic membrane, pigment granule and COP9 signalosome which has been implicated in modulating autophagosomes (Su et al., 2011) (table 6.13). Intriguingly, several components of the endosomal trafficking pathways were also downregulated: early and late endosome, recycling endosome, endocytic vesicle, endocytic vesicle membrane and lysosomal lumen. Thus, providing evidence that SYNGR2 might be involved in EV regulating pathways.

Despite, the indicted disruption in the endosomal trafficking pathway, we did not observe a major impact on the quantity of released EVs (chapter 3). Interestingly, various routes for endosomal cargo appeared to be impacted (early and late endosome, recycling endosome and lysosomal lumen), while the trans GOLGI network was not enriched. This raises the questions whether SYNGR2 is an unspecific regulator of various endosomal routes.

Taken together, SYNGR2KD caused a downregulation of several biological functions compared to the NMC cell variant. This could indicate that the SYNGR2KD is less aggressive compared to NMC cells. Interestingly, this is also reflected in the potency of the EVs that lose their function to modulate the secretome of fibroblast (chapter 5). Importantly, the results indicated that SYNGR2 attenuation has significant impact on endosomal membranes (early, late, recycling) and thus provides the first evidence that SYNGR2 is potentially involved in the regulation of EV biogenesis in PCa cells.

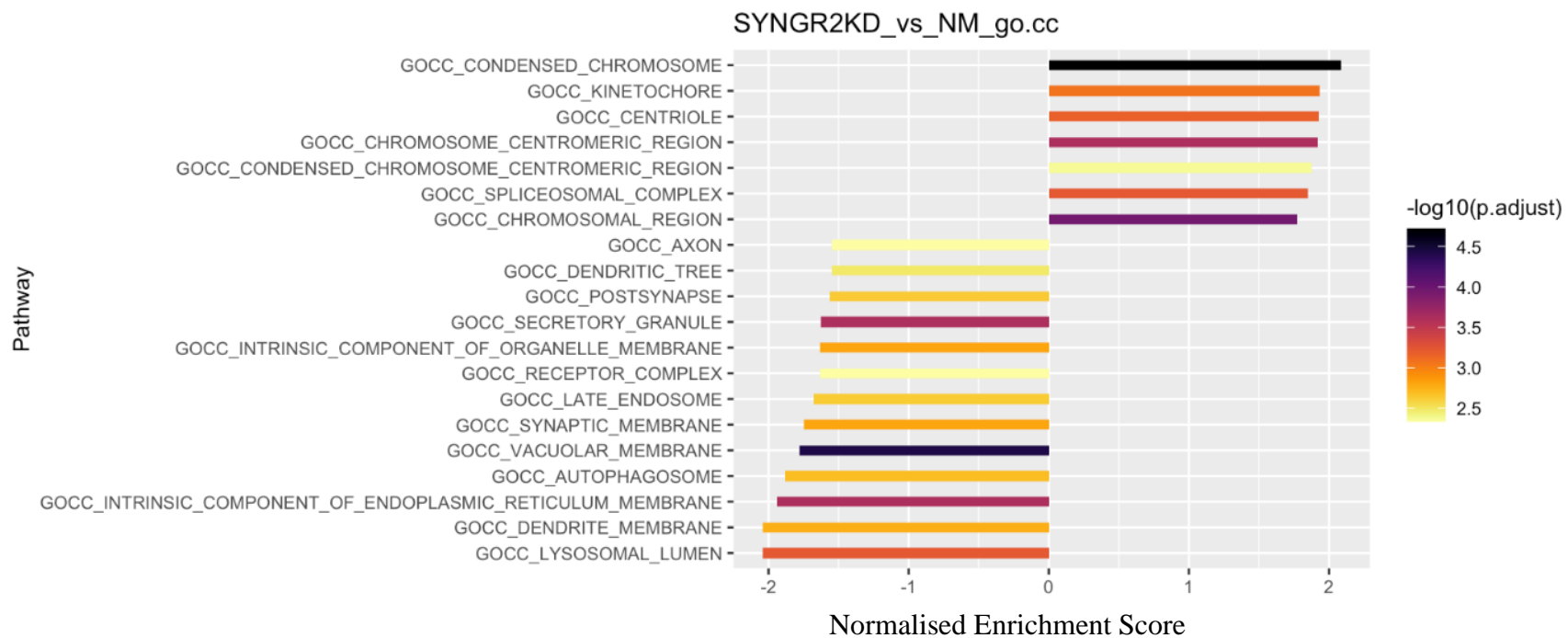


Figure 6.20: SYNGR2KD is associated with changes in the expression of endosomal genes.

Gene set enrichment analysis of the SYNGR2KD cells was performed using R and the cellular compartment gene set compiled in the MSigDB as reference gene sets. Top 20 most significant biological process hits were selected and then listed according to their normalised enrichment score.

Table 6.13: Impact of SYNGR2 attenuation on cellular compartments.

Table shows the complete GSEA on cellular compartments comparing the CD81KD to NMC cells. Left column shows possible broader categories summarising the hits. Only hits with $P < 0.5$ are included. NES= normalised enrichment score.

	ID	NES	p.adjust
endosome	GOCC_EARLY_ENDOSOME	-1.4	0.03850581
	GOCC_ENDOSOME_MEMBRANE	-1.4	0.01507085
	GOCC_RECYCLING_ENDOSOME	-1.5	0.04779124
	GOCC_LATE_ENDOSOME	-1.7	0.00237403
	GOCC_ENDOCYTIC_VESICLE	-1.6	0.01512949
	GOCC_ENDOCYTIC_VESICLE_MEMBRANE	-1.6	0.0378222
cell division	GOCC_CONDENSED_CHROMOSOME	2.1	1.9081E-05
	GOCC_KINETOCHORE	1.9	0.00084957
	GOCC_CENTRIOLE	1.9	0.00066547
	GOCC_CHROMOSOME_CENTROMERIC_REGION	1.9	0.00024178
	GOCC_CONDENSED_CHROMOSOME_CENTROMERIC_REGION	1.9	0.00425195
	GOCC_CHROMOSOMAL_REGION	1.8	0.00011059
	GOCC_NUCLEAR_CHROMOSOME	1.5	0.01862221
	GOCC_SPINDLE	1.4	0.03096103
Endoplasmic reticulum	GOCC_INTRINSIC_COMPONENT_OF_ENDOPLASMIC_RETICULUM_MEMBRANE	-1.9	0.00024178
	GOCC_ENDOPLASMIC_RETICULUM_GOLGI_INTERMEDIATE_COMPARTMENT	-1.6	0.03155415
	GOCC_ENDOPLASMIC_RETICULUM_PROTEIN_CONTAINING_COMPLEX	-1.6	0.01010571
	GOCC_ENDOPLASMIC_RETICULUM_LUMEN	-1.6	0.01010571
Granule	GOCC_FICOLIN_1_RICH_GRANULE_MEMBRANE	-2.0	0.00551282
	GOCC_PIGMENT_GRANULE	-1.7	0.01115553
	GOCC_FICOLIN_1_RICH_GRANULE	-1.6	0.01244633
	GOCC_SECRETORY_GRANULE	-1.6	0.00024178
	GOCC_SECRETORY_GRANULE_MEMBRANE	-1.7	0.00482495
neural signaling	GOCC_AXON	-1.5	0.00461214
	GOCC_DENDRITIC_TREE	-1.6	0.00332032
	GOCC_NEURON_TO_NEURON_SYNAPSE	-1.6	0.01252596
	GOCC_POSTSYNAPSE	-1.6	0.00234574
	GOCC_POSTSYNAPTIC_MEMBRANE	-1.7	0.01249049
	GOCC_SYNAPTIC_MEMBRANE	-1.7	0.00157268
	GOCC_MAIN_AXON	-1.9	0.02119273
	GOCC_NEURON_PROJECTION_MEMBRANE	-1.9	0.01249049
membrane bound organelles	GOCC_PLASMA_MEMBRANE_PROTEIN_COMPLEX	-1.4	0.03850581
	GOCC_MEMBRANE_MICRODOMAIN	-1.5	0.0364178
	GOCC_SIDE_OF_MEMBRANE	-1.5	0.03155415
	GOCC_CELL_SURFACE	-1.5	0.00551282
	GOCC_INTRINSIC_COMPONENT_OF_ORGANELLE_MEMBRANE	-1.6	0.00154551
	GOCC_VACUOLAR_LUMEN	-1.7	0.00932305
	GOCC_LUMENAL_SIDE_OF_MEMBRANE	-1.8	0.04779124
	GOCC_VACUOLAR_MEMBRANE	-1.8	3.6854E-05
	GOCC_AUTOPHAGOSOME	-1.9	0.00202814
	GOCC_DENDRITE_MEMBRANE	-2.0	0.00173083
	GOCC_LYSOSOMAL_LUMEN	-2.0	0.00058539
complexes	GOCC_RECEPTOR_COMPLEX	-1.6	0.00461214
	GOCC_COP9_SIGNALOSOME	-1.8	0.02222461
	GOCC_SPLICEOSOMAL_COMPLEX	1.8	0.00058539
	GOCC_CELL_BODY	-1.5	0.01507085
	GOCC_EXTERNAL_ENCAPSULATING_STRUCTURE	-1.5	0.01512949
	GOCC_TRANSPORT_VESICLE	-1.5	0.01512949

6.2.9 Impact of knockdown on the transcripts of our other candidates

In Chapter 3, an analysis indicated that several of the candidates interact with/influence each other in a complex interaction network (Figure 3.2 inserted again here on the next page). The ANN is based on diverse sets of input data that is not specific to PC3 cells hence there is uncertainty if these interactions are true in PC3 cells. I was interested therefore to briefly explore if some of these connections could be confirmed with the RNA-seq datasets and thus provide corroborating evidence supporting the predicted interactions (table 6.14).

Most of the network interactions could not be confirmed using the new transcriptional information herein. The ANN indicated CD9 and CD81 as 1st neighbours, which might have translated into compensatory mechanisms upon the KD of either CD81 or CD9 as reported for tetraspanins and thus potentially a reduced impact on the biogenesis of EVs. However, a mutual impact of CD81 and CD9 on the transcript levels was not observed and hence compensation, at least on the transcript level was not detected. Interestingly, the ANN predicted SYNCRIP as a 1st degree neighbour CD81. Indeed, in 6.2.6, I described that in the CD81KD cell variant the EV microRNA regulator SYNCRIP was found to be 2-fold downregulated.

Overall, the lack of a huge overlap is perhaps not entirely unexpected because the interaction network reflects non cell line specific previously reported interactions/influences.

As a next step, 2nd degree neighbours that connect one candidate to another candidate were also searched in the DEGs. Transcripts of the most of these candidate specific 2nd degree neighbours were identified in the DEG list, yet the changes in the transcript level did not reach statistical significance. Of note, the downregulation of CHMP4C in the CHMP4CKD cells was significant, but minor (-2.9-fold change) and hence only a minor impact on other transcripts was expected. Furthermore, CD81 and CD9 share two common first neighbours ADRB2 and VKORC1. Interestingly, in the CD9KD there was an increase in ADRB2 transcript (1.9-fold change), whereas in the CD81KD there was an increase in VKORC1 transcript (1.8-fold change).

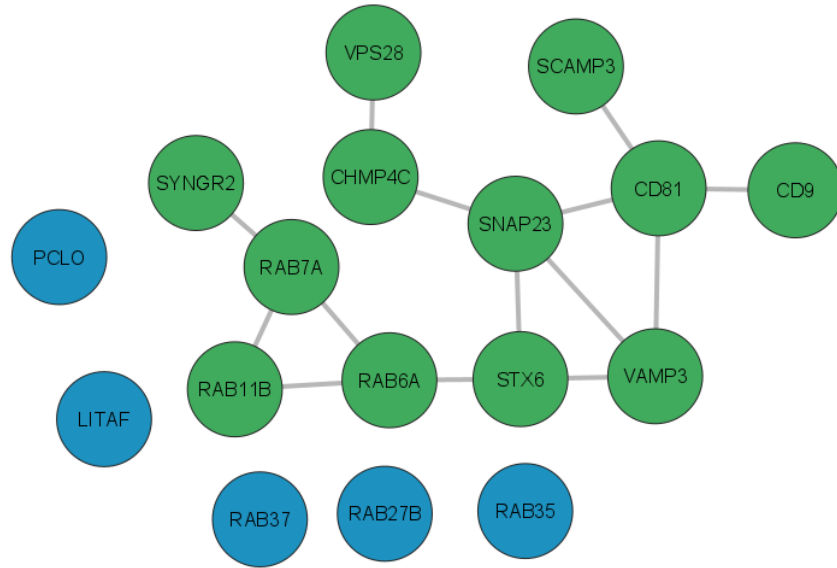
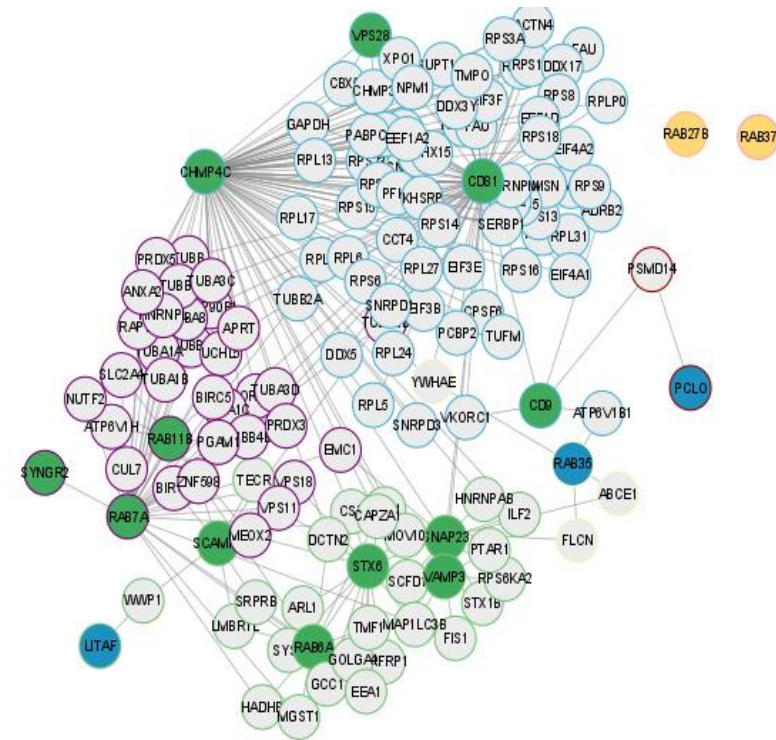
A**B**

Figure 3.2: Interaction network of the selected candidates.

The BED from Anaxomics was queried by our collaborator Pedro Matos Filipe for the effectors of the 17 selected candidates. The interaction network in (A) shows the interaction of the candidates with each other. The lines represent a connection (influence/interaction). The candidates highlighted in green could be directly connected to another candidate. The candidates highlighted in blue could not be connected to another candidate as a 1st degree neighbour. The interaction network in (B) shows the candidates and their 2nd degree neighbours which subsequently connect to another candidate

Table 6.14: Influence of the candidate attenuation (CD9, CD81, CHMP4C and SYNGR2) on each other.

The candidate interaction network (chapter 3) was used to retrieve information about the prediction of candidate – candidate interactions (1st degree neighbours). 2nd degree neighbours that connect two candidates were also retrieved. The identified 1st degree neighbours and 2nd degree neighbours were searched in the relevant DEG lists. Additionally, candidate interactions that were not predicted but reached statistical significance were also included. Not found indicated that the neighbour was not found in the specified DEG list. Not significant indicates that the respective neighbour was identified in the DEG lists, however the transcriptional changes did not reach statistical significance.

Candidate	Interaction network predicted interaction			Transcriptomic evidence of influence	
	1st degree neighbour	2nd degree neighbour (connects to)	Not predicted	RNA-seq data set (compared to NMC)	changes in 1st degree neighbour gene expression
CD9	PSMD14	PCLO		CD9KD	not significant
	ATP6V1B1	Rab35		CD9KD	not found
	ADRB2	CD81		CD9KD	1.9-fold change
	VKORC1	CD81		CD9KD	not significant
	CD81			CD9KD	not significant
SYNGR2	Rab7			SYNGR2KD	not significant
CHMP4C	CHMP3	VPS28		CHMP4CKD	not significant
	CBX5	VPS28		CHMP4CKD	not significant
	XPO1	VPS28		CHMP4CKD	not significant
	VSP28			CHMP4CKD	not significant
	HNRNPAB	SNAP23		CHMP4CKD	not significant
	ILF2	SNAP23		CHMP4CKD	not significant
	SNAP23			CHMP4CKD	not significant

CD81	ADRB2	CD9		CD81KD	not significant
	VKORC1	CD9		CD81KD	1.8- fold change
	CD9			CD81KD	not significant
			SYNGR2	CD81KD	2-fold change
			Rab11b		1.7-fold change
			VPS28		1.8-fold change
			Rab27b		-3-fold change

Though not captured in the ANN, CD81 attenuation impacted expression of the following genes: Rab11b (1.7-fold-change), VPS28 (1.8-fold change) and Rab27b (-3-fold change), Interestingly, SYNGR2 appeared upregulated (2-fold change) in the CD81KD cells providing an interesting opportunity to explore this relationship in more detail.

Taken together, albeit not fully overlapping, both the ANN analysis and the DEG analysis indicated complex interaction networks among the candidates. Nevertheless, the preceding protein interaction analysis proved useful for the exploration of RNA-sequencing dataset and revealed connections that might would be missed by the other tools used in this chapter (top DEGs, GSEA). Hence, some parts of the theoretical network (ANN) appear to be true in these PC3 cells, meaning the candidates selected at the beginning of the project were reasonable ones to choose, and should have (given these interactomes) delivered an impact on the EV-production systems of the cell.

6.2.10 Summary

EV isolations from the KD cell lines and the NMC harboured high rRNA concentrations which prompted us to not pursue sequencing of the samples. In contrast, RNA from the KD cells was successfully sequenced and the attenuation of the respective candidate was confirmed in the respective cell variant. All KD cell variants had a distinct transcriptome both

at single gene level and at the pathway level and therefore represent phenotypically distinct PC3 cell variants with KD specific features. The gene set enrichment analysis indicated that CD9KD cells were enriched in pathways that are associated with a stem cell-like phenotype. This may indicate a role of CD9 in the regulation of stem cell like features whose consequences for EV production is not obvious. In addition to this, gene sets associated with endosomal trafficking were indicated as enriched as well.

The transcript expression in the CD81KD cells was distinct and suggests that CD81 is involved in EV biogenesis. Several genes involved in EV regulation were identified as differentially expressed (ESCRT components, tetraspanins). In addition, CD81 KD appeared to induce significant changes in expression of gene sets describing membranes associated with molecular cargo transport.

In the CHMP4CKD cells a small impact on the cellular transcripts was detected compared to the other cell variants. Surprisingly, CHMP4C attenuation investigated here appeared to have a minor impact on biological pathways yet appeared to be sufficient to induce the release of molecular distinct EVs. This could potentially indicate a highly specialised function of CHMP4C.

KD of SYNGR2 appeared to induce a transcriptional downregulation of the majority of pathways analysed in this chapter (e.g., MSigDB hallmarks, biological processes, cellular compartment) perhaps indicating a reduced aggressiveness of this cell variant compared to the control cells. Importantly, SYNGR2 attenuation appeared to induce downregulation of transcripts associated with endosomal membranes (early, late, recycling) pointing to a possible role of SYNGR2 in maintaining these compartments and thus, pointing to a possible role of SYNGR2 in the regulation of EV biogenesis in PCa cells.

6.3 Discussion

In this chapter, I described the successful sequencing of the CD9KD, CD81KD, CHMP4CKD SYNGR2KD and NMC cells. All KD cell variants showed significant differences in their transcriptome compared to the NMC cells, indicating the intervention by shRNA had indeed a cellular impact, creating cell variants that were distinct from the control cells. The data presented here provide the first ever insights, to my knowledge, into the impact of a downregulation of SYNGR2 and CHMP4C on the cellular transcriptome in PC3 cells. Furthermore, several novel interactions between the candidates were discovered. For instance, in the CD81KD, an increase Rab11b (1.7-fold change), VPS28 (1.8-fold change) and SYNGR2 (2-fold change) was shown. Of specific interest here is also the downregulation of Rab27b (-3-fold change) which has not been described before. Interestingly, AuroraB kinase negatively regulates the expression of Rab27b (Liu et al., 2022) and was found to be enriched in the CD81KD cell line (1.7-fold change). There has been no previous description of how CD81 influences AuroraB therefore regulating the transcription of Rab27b. This clearly requires further validation. These results highlight the value of bioinformatic tools to predict biological interactions and usefulness to select which components to explore more. However, it also highlights some limitations in relying solely on these tools as novel interactions might be missed; rather a combination of exploring predicted and novel targets yields the best results.

Interestingly, across the CD9KD, CD81KD and the SYNGR2KD to a varying degree an impact on the transcripts related to the endosomal pathway and/or lysosomes were detected. As EVs are intrinsically linked to the endosomal pathway it would be interesting to explore the impact of these candidates in more depth. For instance, labelling various molecules of the endosomal compartment such as early endosome antigen 1, lysosomal associated membrane proteins, and CD63 would reveal changes in the organisation of the endosome, and potentially changes in their kinetics.

In chapter 4, the impact of the KDs on the molecular features of the released EVs was determined. In this chapter, it was confirmed that these changes in EV-functional potency coincided with changes in the cellular transcriptome. The changes in the cellular

transcriptome could solely be attributed to direct impact of the KD of the candidates. Another interesting factor that could have contributed to these observations could have been the alterations in the release of EVs. This was previously described by O'Grady et al who found treating the parental cell with EV inhibitors changed the cellular transcriptome. To be more precise long RNA species that were enriched in the EVs were downregulated at cellular levels and the inverse was observed as well (O'Grady et al., 2022). Thus, demonstrating that packing of RNA into vesicles is important for RNA homeostasis.

The vesicular RNA content derived from PC3 cells has been investigated in a few studies. In a microarray analysis, the majority of miRNA (333) found in PC3 cells overlapped with their vesicular counterpart with 31 miRNAs specific to EVs (Hessvik et al., 2012). In contrast, a recent study, which used a NanoString low RNA input nCounter assay to determine vesicular mRNA content of PC3 variants, found that the mRNA from the parent cell and the corresponding EVs showed significant differences (Dong et al., 2021). Another study focused on the differences in the EV population and found that distinct EV subpopulations carry distinct mRNA, and that the cargo reflects the parental cell line (Lazaro-Ibanez et al., 2017). We aimed to sequence the RNA content of EVs derived from the KD cell variants (CD9KD, CD81KD, CHMP4CKD, SYNGR2KD) and the NMC cells. EVs were isolated and RNA extracted by various methods (phenol based, kit based). Despite the efforts undertaken large amounts of rRNA were found in the samples. The source of rRNA was not explored in more detail here. Sources of rRNA could have been traces of rRNA in the serum deprived media that was culturing the cell. However, the cells were washed with DPBS and incubated with serum free media before the CM was collected, thus the chances of non-PC3 cell derived rRNA are low. Despite a high cell viability when the CM was collected, we cannot exclude that apoptotic bodies were co-isolated. However, an increase in apoptosis would have been expected to be accompanied by an up-regulation of the apoptosis relevant transcripts across all the cell variants tested here, which was not the case.

The presence of rRNA in EVs is controversial with some research proposing the presence of rRNA in EVs (Mateescu et al., 2017). For instance, in glioma cells, the majority of vesicular RNA represents rRNA and even after a rRNA depletion step 10-37% of the reads were classified as rRNA (Wei et al., 2017). Another example is a study that focused on five different cell lines that are commonly used to study neurodegenerative disease and showed

that all contained a high proportion of rRNA fragments in the vesicular RNA content (Sork et al., 2018), although it is important to acknowledge that laboratory isolation methods can be highly variable across different groups, and is an issue notoriously difficult to standardise in the field- impacting interoperability of EV-quality/purity. Nevertheless, these point to the possibility that the high rRNA content detected in our samples might be rRNA that is genuinely encapsulated in EVs. We did not undertake an RNase digestion of intact EVs to experimentally determine this, given the time constraints faced, and hence this needs to be validated formally. This raises the question of the functional relevance of encapsulating rRNA in EVs. Perhaps, exporting fragmented rRNA is mechanism to maintain cellular homeostasis. Interestingly, Koeppen et al proposed a functional property of vesicular rRNA delivered to the bacteria *Pseudomonas aeruginosa* (Koeppen et al., 2023). The authors claim that human airway epithelial cells release EVs that carry rRNA fragments that in turn modulate the activity of an efflux pump that is associated with antibiotic sensitivity. However, the authors admit that more research to elucidate the mechanisms behind this observation is required.

Taken together, the technical aspects of generating PC3 cell variants, which are impacted regarding some of the known machineries involved in EV biogenesis, traffic and secretion, appear to have been successful, and has both revealed and confirmed the existence of interdependencies perhaps but certainly relationships between the candidates of interest and a range of other transcripts related to these machineries. Nevertheless, the measured impacts on EV output from these manipulated cells has been unexpectedly subtle, and not fully consistent with the data presented in this chapter. In conclusion this might show that the PC3 cells are robust against manipulations and perhaps represents an essential characteristic of cancer cell survival.

Chapter 7:

General Discussion

7.1 Summary of results

The overarching aim of this study was to identify novel regulators of EV biogenesis, to perturb these, and demonstrate the value of targeted attenuation of specific EV-regulating elements/pathways in reducing disease-promoting processes, such as stromal cell activation. To achieve this, a range of bioinformatic tools, cell biology and molecular biology techniques were exploited.

7.1.1 The rationale for a candidate-based approach

Large scale studies that aim to identify factors involved in EV biogenesis, intracellular transport and/or release often involve hundreds and sometimes even up to thousands of targets (Urabe et al., 2020, Lu et al., 2018, Ruan et al., 2022). The power of these comprehensive studies undoubtedly lies in the unbiased selection of targetable candidates combined with the vast number of screened candidates. Nevertheless, it needs to be noted that these studies usually involve highly technically challenging methods that require expertise knowledge, e.g., Ruan et al. utilised for a shRNA-based screen targeting more than 21,000 protein coding genes a combination of fluorescent activated cell sorting, high throughput sequencing and subsequent bioinformatic analysis of a large number of transduced cells (Ruan et al., 2022). Furthermore, the researchers might rely on previously in the specific lab established techniques as done for instance by Urabe et al. who screened the impact of more than 1,500 miRNAs by exploiting the high throughput ExoScreen assay, which determines tetraspanin levels in CM (Urabe et al., 2020). In addition to this, the focus of these high throughput studies was on the identification of regulators, while the functional impact of EVs on recipient cells was either not explored (Ruan et al., 2022, Lu et al., 2017) or played only a minor role (Urabe et al., 2020). In contrast, for the work executed here, it was important to identify a pragmatic number of putative candidates to allow a sufficient exploration of the impact of attenuating the candidate genes on features and functions of vesicle output. Given that the focus of this project was to also conduct a functional exploration, we wanted to be able to expand the newly generated cell variants enough to conduct functional experiments. Establishment of a new, large-scale, screening technique was therefore deemed unsuitable for the current study, both in terms of time required and also utility in achieving the goal of our study. Hence, we employed a candidate-based approach, as an immediately tractable route to

achieve these aims. To start, I identified more than 1,000 candidates previously described to be present on PCa EVs using exocarta.org. A repertoire of additional filtering methods were applied to trim the list to the 17 of the most promising candidates out of which the attenuation of 14 candidates caused changes in the molecular features of the EVs (**Chapter 4**), whereas only three (Rab27b, PCLO, VPS28) appeared to not influence the tetraspanin composition of EVs. Thus, clearly demonstrating the effectiveness of utilising a candidate-based search strategy to obtain verifiable hits. The counter side to this is a priori knowledge of the nature/function of the candidates in endolysosome/vesicle related processes is required and biases around this has limited the opportunity to discover entirely novel factors which might be picked up in a broad screening approach.

7.1.2 shRNA based attenuation

The role of putative regulators of EV biogenesis can be explored with various molecular tools. For instance, a CRISPR-Cas based approach can be utilised to KO the respective candidate as previously done by Lu et al. to identify EV release regulators in lymphoblasts (Lu et al., 2018). However, a single sgRNA can induce distinct genetic alterations/mutations in different recipient cells and thus a phenotypic heterogenous population of cells emerges. Consequently, this might require the selection of single clones, which renders sufficient expansion of cells for CM collection time intensive. Furthermore, the extensive application of the CRISPR-Cas technology outpaced our understanding of the off target effects (Hunt et al., 2023). These unwanted genomic alterations are a major concern especially in cancer cells which are more susceptible to DNA damage. To prevent this, methods have been developed to detect clones with these unwanted side effects, e.g., sequencing (Pan et al., 2022) and various other *in silico*, *in vitro* and *in vivo* technologies, however there is currently no gold standard for their utilisation (Naeem et al., 2020). It needs to be noted that these off-target effects are currently also a concern for other RNA based tools including shRNAs, and it will be important to refine techniques to predict the cellular impact for the advancement of these technologies.

In most cases a successful CRISPR-Cas based approach appears to be more efficient in downregulating the expression of a target compared shRNAs, as shown in a study by Konermann et al. which demonstrated that targeting the same gene with CRISPR-Cas achieved a 96% attenuation whereas a shRNA based attenuation achieved a reduced downregulation of only 65% (Konermann et al., 2018). In this regard it is also worth

considering whether the targets are essential or non-essential genes and whether a negative impact on cell viability is a concern for the experimental question. A recent study by Deans et al. demonstrated that a shRNA based strategy was superior in identifying essential genes that require only a partial KD to exert a measurable phenotypic impact, whereas a CRISPR-Cas strategy excelled to uncover non-essential genes, whose complete KO was well tolerated by the cells (Deans et al., 2016). For some of the candidates selected for this work, the impact of downregulation was previously investigated in various model systems with some candidates reported to influence cell viability. For instance, in PC3 cells it was shown that CHMP4C KD impairs cell viability (Zhang et al., 2023). Furthermore, in breast cancer cells, when downregulation of the CHMP4C protein exceeded 50%, cell viability was reduced, and this cellular impact was more prominent with a stronger KD (Jin et al., 2024). This suggests that a complete KO or a strong KD of CHMP4C, typically achieved with CRISPR-Cas, likely has a more pronounced negative impact on the cell viability, and thus would represent a complicating factor in assessing the impact on EVs. Here, we used a shRNA-based approach to attenuate the expression of the respective candidate which proved to be an excellent strategy. Using five different sequences allowed us to select the cell variants with the highest KD and the least impact on cell viability.

7.1.3 Impact on EVs

The initial 17 candidates were always intended to be streamlined to a more manageable set of cell variants, and became narrowed down to four (CD9, CD81, CHMP4C and SYNGR2) because KD of these targets had a distinct impact on the detection of CD81, CD81CD9 and CD9 expression on vesicles, when analysed in bulk in a microplate assay (**Chapter 4**).

Intriguingly, these targetable factors did not appear to have a quantitative impact on EV secretion as assessed by both EVQuant and Nanosight (**Chapter 4**). This was a surprising finding, as some of these candidates were reported to influence EV quantity in other systems. For example, CD9 attenuation in DU145 PCa cell caused a downregulation of the EV output (Yeung et al., 2018), noting this was achieved using the exact same shRNA/lentivirus preparation. Hence, we were initially astounded and disappointed in the relatively stable vesicle output in the PC3-cell line model. However, other reports exist, where perturbations have elicited phenotypic alterations in EV-quality with minimal impacts in EV-quantity. For instance, Brzozowski et al. reported that whilst the EV numbers the prostate cell line RWPE1

remained stable following KD of CD9, while the vesicular proteome was altered (Brzozowski et al., 2018). The discrepancy underlying the observation are unclear but indicate a highly cell type specific role of EV regulators and possibly examples of resistance to perturbations of EV-production in some cases. This is perhaps a concern when considering therapeutic targeting of vesicle-generating pathways, should there be a host of compensatory processes which adapt allowing a continuation of maximal vesicle output. It is also important to note that EVs have been described as waste disposal units of the cell, and in fact some of the original studies by Rose Johnstone and others had articulated the principal purpose for vesicle secretion was to purge unwanted material from the cell (Johnstone et al., 1991). Also, Takahashi et al. demonstrated relatively recently that cells expel damaged DNA encapsulated in EVs to protect the cell from the cytotoxic impact of accumulating DNA (Takahashi et al., 2017). Perhaps, export of EVs as a waste disposal mechanism is essential for these highly aggressive PC3 cells, and thus compensatory mechanisms that ensure efficient EV secretion are induced. Furthermore, regulation of EV release is a highly dynamic process in response to stimuli. For instance, upon glutamine depletion cells shift their EV population from a late endosome derived Rab7 regulated population to a recycling endosome Rab11 regulated population (Fan et al., 2023), and importantly, the study detected this shift of pathway without a change in the number of released EVs. Hence there are precedents where measurable alterations in vesicle-producing pathways can occur, without a global and drastic change in the number of expelled vesicles.

7.1.4 Functional impact

NMC EVs stimulated myofibroblast differentiation (onset of α -SMA in stress fibres), elicited the secretion of IL-6 and HGF, and triggered changes in the fibroblast phosphoproteome consistent with the activation of multiple signalling pathways at once. Importantly, all of the KD CMs or isolated EVs showed a reduced potency to promote α -SMA polymerisation and reduced IL-6 and HGF secretion. A highlight of the thesis was that the KD EVs induced a source dependant phosphorylation pattern in the recipient fibroblasts, suggesting that the EVs are functionally distinct and impart a different signalling response in these fibroblast recipients (**Chapter 5**).

The altered tetraspanin expression and reduced ability to trigger fibroblast differentiation raises an interesting consideration about the functional relevance of tetraspanins on EVs. The functional role tetraspanins on the plasma membrane is getting increasingly better understood. CD9 tethers growth receptors (VEGFR binding VEGF) to integrins and thereby provides increased signalling (Kamisanuki et al., 2011). Furthermore, CD9 and CD81 bind to the extracellular region of the TGF- β R and stabilise the complex (Wang et al., 2015). Whether EV derived tetraspanins can also aid in this stabilisation is unclear, but a reasonable assumption perhaps. Interestingly, we have seen an increase in TGF- β 1 on CD9KD and CD81KD EVs, but decreased signalling as judged by α -SMA expression. This raises the question whether the tetraspanin expression is essential to elicit a robust TGF- β 1 response, perhaps by stabilising the TGF- β R hetero complex, in the recipient fibroblasts. Due to the interactions of TGF- β with many components present on EVs (the heparan sulphate proteoglycans, CD44 and others) (Webber et al., 2010, Nakamura et al., 2017), detailed experiments to understand the exact roles of tetraspanins on EV-TGF- β delivery will not be straightforward.

7.1.5 KD of candidates

The attenuation of the four candidate genes (CD9, CD81, CHMP4C and SYNGR2) was confirmed by qPCR (**Chapter 4**) and RNA-seq (**Chapter 6**). KD of the candidate genes also caused a range of transcriptomic changes in the cell which was most prominent in the CD9KD and CD81KD cells and to a lesser extent apparent in the CHMP4CKD and SYNGR2KD cell variants (**Chapter 6**). Importantly, all KDs had a clearly distinctive impact on the cellular compartments and biological pathways. Given these unambiguously different cellular transcriptomes, it is surprising that only a subtle change in bulk EV tetraspanins was detected and the impact across the KDs was similar in regard to their functional properties to modulate fibroblast response (reduced secretion, reduced onset of α -SMA). This suggests at least a partial functional overlap between the KD EVs and thus points to a highly interactive network of EV regulators that ensure a robust EV output, that is resistant to manipulations. This is also supported by the ANN analysis (**Chapter 3**), which indicated a high level of influence/interaction between the selected candidates. Consequently, using the RNA-seq data sets, identifying only common DEGs across the KDs could prove useful in identifying overlapping functional pathways. An interesting consideration in this regard is the possible

occurrence of compensatory mechanisms occurring in response to the downregulation of a target as it has been described for tetraspanins. For instance, Suarez et al. reported in melanoma cells that KO of CD9 elicits the upregulation of CD63, which was not observed when targeting with a peptide (Suarez et al., 2021).

In addition to this, all KDs showed a multitude of changes in their gene expression profile which could potentially impact EV secretion. This raises the questions whether the impact of on the EVs reflects a possible primary effect of the KDs or a possible secondary effect. By that I mean it is possible that the candidates are involved in multiple cellular processes that effect the cell status and consequently EV output indirectly. For instance, enhanced EV secretion is observed in response to the activation of cellular stress such as hypoxia (Panigrahi et al., 2018) or activation of the p53 pathway (Yu et al., 2012). Alternatively, a primary impact on the EV output could have a secondary impact on the general cell. This was recently, reported by O'Grady who demonstrated that blocking EV release with GW4869 alters the parental transcriptome; to be more precise long RNA species that were enriched in the EVs were downregulated in the parental cell (O'Grady et al., 2022). However, the researchers did not conduct a GEA to evaluate the impact on biological pathways.

7.2 Limitations

The work described in this thesis provides compelling evidence that the genetic manipulations in PC3 cells induced changes that altered the secretome of the cells, and vesicle quality, and this had some functional impact. However, it is crucial to note the limitations of the work described here. Due to high number of cell variants, we selected a simple ultracentrifugation step for the isolation of EVs. It is important to consider that this method co-pellets other secreted extracellular particles and consequently we cannot ascertain with absolute certainty, that the reported functional implications can be attributed solely to EVs of endosomal origins. The product may include plasma-membrane derived elements, and other particulate entities. Hence, a validation of the results with a highly purified, more refined sample, e.g., by adding an ultracentrifugation step with a density gradient would underscore the relevance of the findings.

In addition to this, we did not investigate the vesicular material in the other fractions obtained during the centrifugation steps, which include larger microvesicles, oncosomes and avascular nanoparticles like exomeres. To gain a holistic understanding of the impact of the candidate

attenuation, these fractions should be also analysed. The rationale of candidate selection however was entirely focussed on endosome generated EVs and hence this was our focus herein.

7.3 Future directions

There are two potential layers of possible future investigations that would increase our understanding focusing on the molecular features of EVs and their functional role in the TME.

7.3.1 Defining the molecular composition of EVs

While the EVQuant performed here (**Chapter 4**), shed some light on the distribution of CD9 and CD63 on single EVs in a binary format (present versus absent), utilising other complementary techniques would significantly increase our knowledge of the potential role of the candidates in regulating the EV composition. In particular, it would be of interest to improve the resolution of tetraspanin expression and explore the tetraspanin loading on single EVs in more detail, and consequently reveal if there are differences in the quantitative loading of these tetraspanins upon candidate KD. Several recently emerged techniques could be exploited for this goal, for instance the NanoImager super-resolution microscope by ONI (Oxford, UK). This imaging platform is a dSTORM based single molecule detection method and is used widely by the EV community for exploring single-vesicle distribution of CD9, CD81 and CD63. An alternative imaging-based technique to this is the Leprechaun platform, which allows the detection of up to five co-localised markers on individual EVs. In addition to this, it would be more interesting to assess the molecular cargo of the EVs to ascertain whether the selected candidates indeed impact the composition of EVs in a broad sense, and for the predication of potential functions. This could be achieved by assessing the proteome of EVs. For instance, by utilising SOMAscan®, an aptamer-based technology, that has been validated for the suitability for vesicular samples (Welton et al., 2016) could be used. A remarkable advantage of this massive protein array technique is that it is possible to evaluate whether a protein is not expressed in a sample. Consequently, this technique is of specific interest here to gain insights in the impact of KDs on the composition of the EV cargo.

Furthermore, pathway enrichment, e.g., KEGG pathway analysis, would also provide indications of potential pathways that might be affected by EVs in recipient cells.

An alternative to this would be using MS, which could not only be used for assessing the vesicular proteome, but also phosphoproteins. Recently, it was shown that EVs carry a disease stage specific phosphoprotein signature in samples from breast cancer patients (Chen et al., 2017a) and from diabetes patients (Nunez Lopez et al., 2022). We have detected a shift in the phosphorylation pattern of EV treated fibroblast that was dependant on the EV source (KD cells vs NMC cells) (**Chapter 4**). The increased phosphorylation of these hits in EV treated fibroblasts might have been elicited by an activation of signalling pathways, alternatively, the EVs might have transferred phosphorylated proteins directly to recipient cells, although this is less likely due to issues of sensitivity of our readout. Hence, an assessment of the vesicular phosphoproteome could be useful in this regard.

It needs to be noted, that mechanistic details of how EVs mediate a response in recipient cells is under intensive research and often the subject of dispute. The main mechanisms by which EVs transfer biological activity could include the activation of cell surface receptors and/or the uptake of the EVs coupled with the intracellular release of the cargo (e.g., RNA species, lipids, proteins).

Some studies provide evidence that EVs bind to cell surface receptors. For instance, in an excellent study by Stauffer et al. it was suggested that EVs confer an increased potency to elicit receptor activation because EVs carry signalling cues on a concentrated area compared to soluble proteins found in a solution (Stauffer et al., 2022). The hypothesis of EVs as integrated delivery platforms of signalling cues is also of particular interest with regard to the delivery of vesicular TGF- β . Interestingly, several mechanisms involving integrins have been proposed to mediate the activation of this signalling molecule. For instance, binding of $\alpha\nu\beta 6$ to TGF- β has been reported to induce conformational changes leading to the release of TGF- β from LAP and consequently allowing the binding of the active domain to the TGF- β R (Annes et al., 2004, Dong et al., 2017). Furthermore, a recent cryo-EM study by Cambell et al. demonstrated that the binding of integrin $\alpha\nu\beta 8$ activates TGF- β , however importantly this activation mechanism did not require the displacement of LAP (Campbell et al., 2020).

Strikingly, $\alpha v\beta 6$ has been recently described to be expressed on PC3 cell derived EVs and to drive angiogenesis in endothelial cells (Krishn et al., 2020) but the authors of this study did not assess vesicular TGF- β content. It is tempting to speculate that perhaps, EVs serve as a delivery platform of integrin activated TGF- β which allows binding of the molecule to a TGF- β R on a recipient cell and consequently mediates the induction of angiogenesis and/or profibrotic responses in recipient cells.

An alternative to this mechanism of action is that EVs are taken up by the recipient cells. However, to exert a functional intracellular activity, the EV cargo is thought to require escaping from the endosome. In a recent paper O'Brien et al. utilising a fluorescent reporter system suggested that majority of internalised vesicular content is stored in the endosomal compartment destined for degradation (O'Brien et al., 2022).

To investigate the binding / uptake dynamics of the EVs different approaches could be used. For instance, labelling of EVs with membrane dyes, or using fluorophore tagged sequence e.g., the previously investigated EV specific KFERQ-like sequence (Ferreira et al., 2022) and subsequent microscopically tracing of the EVs when added to cells could provide insights whether the EVs attach to the cell surface or are taken up by the cells. Uptake studies could also be performed with a split Nano-luc system as described by van Solinge et al. that can also be exploited for *in vivo* studies (van Solinge et al., 2023).

7.3.2 Functional explorations

CAFs play a crucial role in the establishment and maintenance of the primary tumour. Targeting CAFs in the past lead to an enrichment of a pro neoplastic subpopulation and promoted the growth of the tumour (Ozdemir et al., 2015). In PCa, nanoparticles loaded with siRNA that targets CXCL12 was successfully shown to suppress CAF activity *in vitro* and *in vivo* in a mouse model (Lang et al., 2019). Recently, a clinical trial combining androgen deprivation therapy (ADT) with targeting of CAFs via the Fibroblast Growth Factor Receptor (FGFR) yielded unsatisfactory results as the therapy was accompanied by intolerable side-effects (Liow et al., 2022).

These studies show that a knowledge gap about the mechanisms that drive the emergence and heterogeneity of CAF populations remains and it will be crucial to gain a better understanding of this process to develop novel drugs interrupting the tumour promoting activity of the TME.

It has been suggested that proximity to the primary tumour might play a role in determining the CAF phenotype with fibroblasts in closer proximity to the primary tumour acquire an ECM remodelling phenotype while those more distal acquire a chemokine secreting phenotype (Öhlund et al., 2017). It is expected that the highest concentration of EVs is found at the side of the release and gets diluted with increasing distance to the tumour. The emergence of this gradient could potentially contribute to the establishment of different CAF phenotypes. In **Chapter 5**, we showed that PC3 CM treatment caused a heterogeneous expression of α -SMA, however, we did not continue to define the possible emergence of various fibroblast subpopulation. In general, an interesting aspect that is currently not well investigated is whether EVs contribute to emergence of one or multiple phenotypes of CAFs. This could be investigated by staining of EVs and then microscopically assessing the expression of marker proteins such as α -SMA in recipient fibroblasts. Other markers that should be considered could be based on the profiling data of PCa patient CAFs and potentially include PDGFR β , CAV1, SPARC (Chen et al., 2021a).

Another avenue of potentially fruitful investigations could centre around the EV driven impact on the secretome of recipient fibroblasts. The results in **Chapter 5** suggested that EVs drove inflammatory changes within the fibroblast secretome. To further establish the relevance of the results, a comprehensive assessment of the fibroblast secretome is required. Furthermore, our lab has previously shown that EVs promote the formation of angiogenesis. Here it would be interesting to explore, whether the KDs lose this functional activity, which could be explored by co culturing PC3 cells and endothelial cells as done in previously described model to recapitulate *in vivo* conditions (Webber et al., 2015). Validating the KD dependant EV function could be a crucial step prior to embarking on validation in animal studies, where e.g., fibroblasts and KD PC3 cells could be injected, and the tumour growth monitored to establish if a loss in fibroblast-accelerated disease is seen.

7.4 Conclusion

Taken together, the results presented here showed that EVs from PC3 cells exhibited remarkable resistance to genetic manipulations of the parent cells, yet subtle changes in the EVs were detected. Importantly, the manipulated EV populations appeared to have a nuanced functional impact on eliciting a finetuned fibroblast response. As a consequence, while targeting EV secretion in PCa patients might disrupt cancer critical processes, there may be some cancer cell populations that will be resistant to such attempts to suppress EV secretion, and the therapeutic benefit may be rather small. Hence, targeting EV secretion in PCa and perhaps in cancer in general is very challenging and requires deeper understanding of these vesicle generating machineries, their adaptation in the face of challenge and the cell type dependencies of these.

Annexes

Annex A: Apoptosis gene list provided by Anaxomics

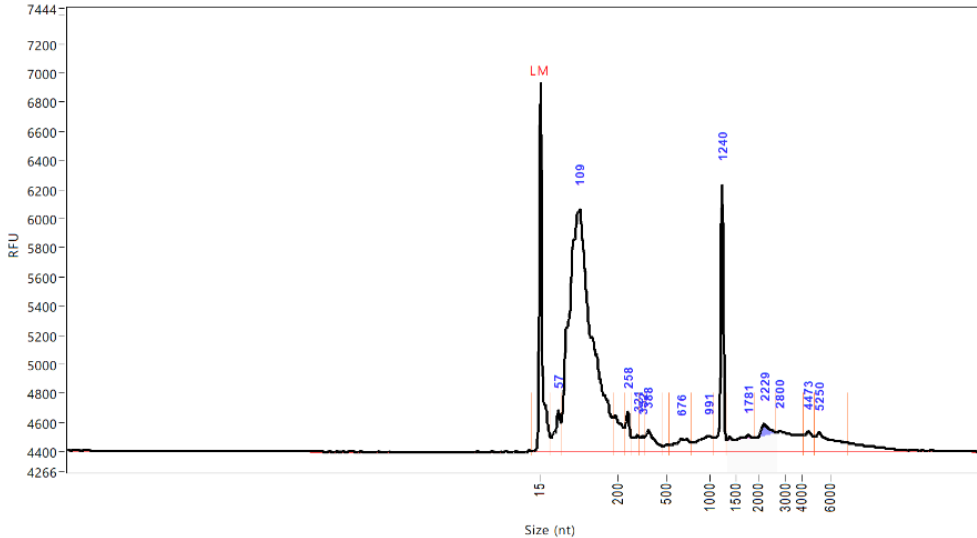
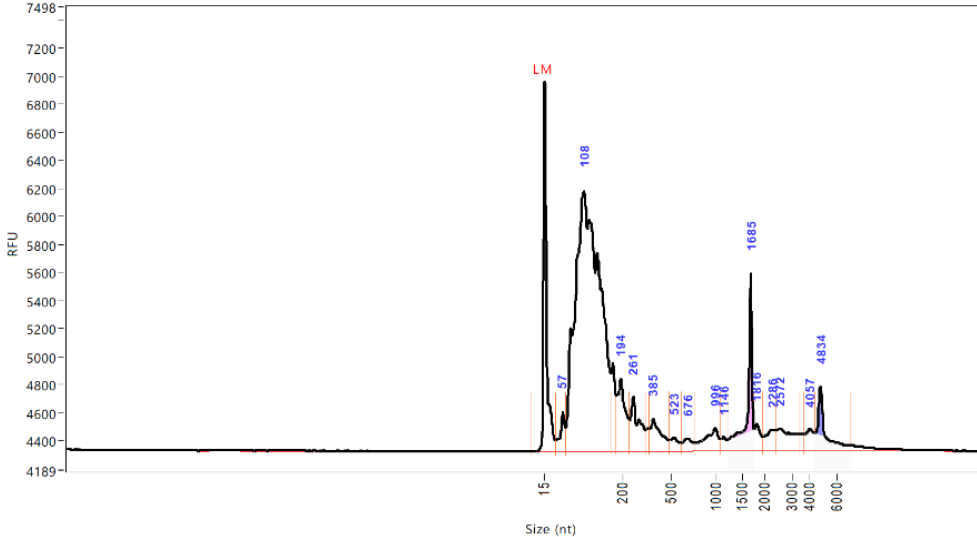
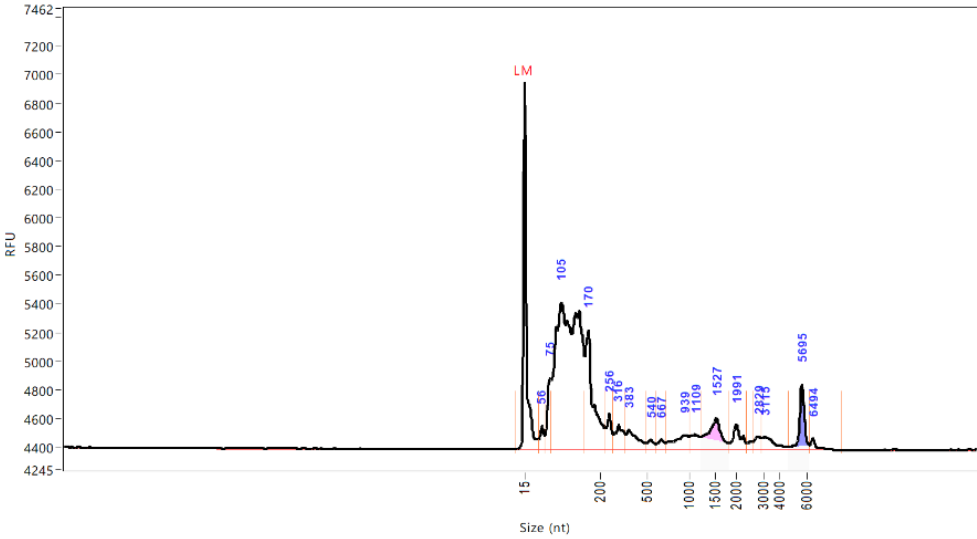
Uniprot ID	Uniprot ID	Uniprot ID	Uniprot ID	Uniprot ID	Uniprot ID	Uniprot ID	Uniprot ID	Uniprot ID	Uniprot ID	Uniprot ID	Uniprot ID	Uniprot ID	Uniprot ID	Uniprot ID	Uniprot ID	Uniprot ID
Q15118	Q9NWF9	Q69YI7	P36897	Q9HC96	O95343	Q9UBP9	O43623	O00571	Q99527	O75915	P36941	Q13618	O75197	P10124	O95185	
Q15119	Q969K3	P19838	P37173	P20807	Q8GZ02	Q9HAU6	Q92785	Q96QE3	P27469	Q9Y255	P25445	Q13619	Q9UIU2	O43464	Q6UXZ4	
P31947	Q8TEI3	Q14934	P30048	Q9Y2W7	Q9HZX6	Q15276	O75312	P54259	Q7L622	P49768	O95407	Q93034	Q9NRZ9	Q13315	O95631	
O75832	Q8IUQ4	Q13901	Q96FV9	Q9NPF2	Q9H422	P31749	Q96MX6	O14965	Q9LHV8	Q96LZ0	Q07011	P15336	P01374	Q9UEE5	P21359	
P51398	O43255	O60356	Q86W42	P06731	Q8IVG9	P31751	P63167	Q9HYI0	P09382	P09668	Q9UNE0	P18848	P04062	O94768	P07196	
P42765	Q9NS56	Q9Y466	P10828	P40199	POCJ72	P46695	O43734	O15169	Q05315	I0J062	Q15628	P06493	Q14728	Q9Y6E0	P46531	
O15530	Q6Q0C0	P22736	P55073	P49747	P42858	P04049	Q96J02	Q9BQE9	Q96D70	Q9UIV9	Q9H3D4	Q9UQ88	Q8WXG6	O00506	Q04721	
Q8IXM3	Q9BWF2	P43354	Q8IUC6	P68400	O00291	Q8WVW0	Q00987	Q8WUZ0	A8MUM7	Q9H0S4	Q96A56	P21127	Q9HBH9	Q9P289	Q9NPG2	
Q9NP92	Q9UPQ4	Q9Y2C4	Q9BX74	P19784	O75146	Q6ZTQ3	Q9H4P4	P20749	P47929	P17844	O15350	Q00535	Q8WU39	Q13188	Q15818	
Q71UM5	Q9HCM9	Q9Y3T9	Q13077	O15519	Q8TDS4	Q02833	Q8WZ73	Q95999	O95166	P35070	P50052	P38936	Q14680	Q13043	Q15465	
P23396	Q86WT6	O60936	Q12933	Q9UKL3	Q14526	Q7L523	Q86XS8	Q9C0K0	O75223	P07711	O43914	P46527	P14780	P15056	Q99523	
P62753	P98170	Q01085	Q13114	Q9HRG2	Q16665	Q9HB90	Q7Z419	Q9UHQ4	Q16666	Q8WUM4	P54577	Q86TLO	P78395	Q8IWQ3	Q96J17	
Q13702	Q8NEG5	Q13232	Q9BUZ4	Q9BXL6	Q9Y2N7	P11234	Q8N8N0	P51572	O95452	Q15116	P00519	P50238	Q9H213	O14757	O95470	
P10809	Q96CJ1	O75414	O00463	Q9BX69	Q6LXS9	Q96PV0	Q96D59	P30411	Q96QA5	Q9BUL8	Q06187	Q96S65	Q5TCQ9	O96017	Q9BX95	
P95510	Q14249	Q9Y239	Q8NFZ5	Q9Y2G2	Q07820	Q8TDY2	Q9NX16	Q13075	P06396	Q16342	O60674	Q9H175	Q658P3	Q15139	Q9BP22	
Q92667	Q9Y371	Q5TH74	O60603	P29466	Q9Y6Y0	P63244	P42857	Q13490	P19447	Q9BRP1	Q06418	Q8WYN3	P25713	P42345	Q14247	
Q9BZP6	P11021	Q8N573	O15455	Q92851	P08476	P21860	Q9NR71	Q13489	P18074	Q53EL6	P30530	P99999	Q96GX9	Q16512	O95630	
O00198	Q9UPY3	Q9BUP3	O15405	P31944	P09529	O00559	P14598	O15392	P04150	O14737	Q6R6M4	Q96L0	O75030	Q16513	Q9HDG2	
P36896	Q5D1E8	P51575	O43715	P42575	Q9UNL4	O00503	P80188	Q9NR09	Q13002	O75340	Q7RTZ2	P16678	Q66K74	Q9HC98	Q9H115	
Q8NER5	Q9HCU0	Q99571	Q92481	P42574	Q8WYH8	Q13546	Q9Y6K9	Q96CA5	P48507	Q8ND81	Q0WX57	Q96F07	Q9BR73	Q13153	Q6ZPB5	
Q9HZP0	Q19T08	Q99572	Q92858	P49662	Q14164	O43353	P25963	Q96P09	Q9NS18	O43272	A6NCW0	P51813	Q9NZJ7	Q13177	P00441	
Q5T1C6	P25101	Q96FX8	Q14186	P51878	Q14643	Q9Y572	O60934	Q99933	P07203	Q12884	A8MUK1	Q8WVK9	Q9Y3D6	O96013	P04179	
Q6UY14	Q92556	Q9HB75	Q01094	P55212	Q8IWB1	P08575	Q92542	O95817	Q9BUX1	Q9H6Z9	Q96RU2	P31483	Q9CZY8	Q9P286	Q9HBF5	
P49773	Q96J3	Q9HCN2	Q14209	P55210	P17936	Q9HD43	Q9Y2I1	Q9Y2J2	P04406	Q8NBP7	Q96K76	Q14154	Q9UDX5	O9NQUS	O75940	
Q9BX68	Q96BJ8	P23760	P41212	Q14790	Q86XT9	Q96TC7	Q8NC60	Q9BZE3	Q9HCL2	Q16647	Q92560	Q9UER7	Q3TCX8	P11309	A1L190	
P00813	P29317	Q969W1	P05412	P55211	P11215	Q8WUF5	Q9NPP4	P55061	P09466	P61289	Q9HM7	P78560	Q8X1Z2	Q9P1W9	Q9BX26	
P30542	Q15375	Q9NYG2	P17947	Q9BKF3	P06756	O95197	Q9H093	Q16611	P49840	Q13015	O95155	O75618	Q8X1I1	Q86V86	P61764	
P29274	P52803	P52045	P48436	P35221	P05107	Q9NQC3	Q13207	Q9NFY8	P49841	Q9BXY8	P63146	P51397	Q969V5	Q9H4B4	O43435	
P28907	P24390	P01270	Q12962	P35222	P01563	P06400	P06729	Q96PG8	Q99445	Q00994	P61077	P53355	O95140	O00141	Q6UX65	
P62330	Q538M3	Q86YC2	P49848	Q03135	Q96BMO	P10826	P07766	Q13323	O969N2	Q7L3V2	Q9HK32	Q9UIK4	P28482	P57059	Q03468	
Q15041	Q96HE7	Q9GZU2	P10071	Q86WG3	Q9HZX8	P13631	P06127	Q07817	Q6IC98	Q9NSK7	Q9NT62	O43293	Q16539	Q15831	O00273	
P12235	P15976	P62937	Q9NR00	Q99966	P40305	Q86TG7	P10747	Q9HD36	P12544	Q9UBY8	O15294	A0PJW8	P27361	Q7L7X3	O76075	
P12236	P01588	Q08752	P46937	P17676	P09912	Q96QBI	Q9ULW0	O43521	P10144	P30101	H3BRQ4	Q9BTC0	P45984	Q9UL54	P49917	
Q9HR70	O14681	P30405	Q2TAL8	O00622	P01579	O15052	P82094	Q9HB09	P20718	Q9HM9	MOQYV0	Q14185	Q02779	O75460	P40692	
P49588	P43005	Q14318	P01137	P26842	P10914	Q13464	Q86VP1	Q9BKK5	P51124	Q96A26	Q9J4A7	Q15392	Q99683	Q76M05	P43246	
P47895	O00471	Q9Y3E5	P61812	O43866	Q14653	P62745	POC1Z6	O75127	O60565	Q9Y421	K4DIB9	Q13609	O43318	O00005	P52701	
P35348	P41180	P14222	P61586	P32970	P20591	Q8TEB9	Q6NUS6	Q92843	P24522	P58499	K7ESF4	P24855	P80192	P30153	P06746	
P02511	Q8IWU6	P32119	Q8N9M5	Q96JB5	P09913	Q9BST9	Q8LZW8	Q96LC9	O75293	Q9UK73	U3KQA4	O00115	O43683	P30154	Q14814	
P00709	Q99502	P30044	Q9BVC6	Q9BY67	O14862	Q969G6	Q8IVF3	Q9UMX3	O95257	Q6IE81	Q5JPI3	Q8WZ79	O60566	P67775	Q90013	
P37840	O00167	Q03181	Q9HDC3	Q8N163	P01583	Q8IYM2	P49736	Q16548	O43903	Q9Y219	Q7Z4R8	Q9NR28	Q96BY2	P62714	P29966	
Q12904	Q9UK96	Q9UBK2	Q9Y6G1	Q99638	P01584	Q15418	P11388	Q7Z465	Q14393	O76095	P07911	P16444	P08571	P50453	Q9C000	
Q13155	Q9NVQ4	O60346	Q6NUQ4	Q96AQ7	P22301	Q15349	Q8WXP8	Q9H3K2	P17252	Q9BZF9	P53634	P84022	Q15464	P59046		
P51693	Q14296	Q13794	Q96RU7	O60543	P29459	P51812	P78527	Q12982	P43026	P05771	Q13488	Q6V1X1	Q07352	Q7M4L6	Q9NX02	
O00213	Q13158	Q9H2J4	Q9BT92	Q9UHD4	Q16552	P23443	Q96EY1	Q12983	Q6KF10	O05655	Q96QK1	P98082	Q96K67	Q96B97	Q96P20	
P05067	Q9UNN5	Q86VZ5	P49815	Q9NQS1	Q9UHD0	Q14684	Q8IXB1	O60238	Q9P0R6	Q02156	P01185	Q5VWQ8	Q9BQG0	Q9H0F6	Q96E86	
Q6EIF0	Q9NY88	P27986	P01375	Q9H305	P60568	O43159	Q9H3Z4	Q14457	P01112	Q9BWQ8	Q12981	Q13444	P01106	Q655L8	Q9P0J0	
Q6F81	Q9BRQ8	P60484	P21580	Q8IX12	P01589	Q8N488	P61803	Q8WYA6	P01116	Q9HC24	P09327	Q9Y6K1	P21145	Q9UL62	O75094	
Q15389	Q969F0	Q92835	Q95379	Q9BWT1	Q13007	Q9NYV6	Q9UBX2	P01138	P63211	Q6LX01	P11473	Q16531	Q99836	P51692	Q99835	
Q9BY76	O15520	P42336	P50591	P04637	Q95760	Q9HB65	O60216	Q16143	Q9LBP5	Q96Y0	P21796	Q8X1T1	Q969H8	P25063	Q13573	
P08133	Q9NSA1	P48736	O43508	Q13352	P05112	P98175	P55265	P55957	P61296	P61244	P45880	P35638	Q81ZQ8	Q9H719	Q99250	
Q9BZR8	P08620	Q86VP3	O43557	Q14432	P05231	P52756	P78563	Q8IZY5	P07900	Q5T4D3	Q9NZC7	Q9NX09	Q02078	P12757	Q8N695	
Q9BZZ5	P55075	O15162	O95150	Q9Y3E7	P08887	P35913	Q8N8B3	Q9NZS9	Q02577	O75807	P17861	Q8N682	Q06413	O94813	Q8WVX8	
Q07812	P21802	Q9NRY6	P48023	P36222	P13232	Q9HCK4	P45985	Q6QNY1	P09601	P49593	Q6GPH4	P61278	P32745	Q9NP59	Q9UM63	
P10415	P22607	Q8TCE9	O00220	PODNR6	Q9NWB7	Q92736	P52564	P49789	P35680	P29590	Q5GH76	Q9NXX7	P28360	O96014	Q9HA38	
O15304	Q8NFG4	Q96599	O14763	PODNR7	P10997	O43865	O14733	P50583	P52789	Q8WUY3	Q6UX68	Q13829	P35548	P56705	Q96PM9	
Q9ULZ3	Q8TF40	Q8TD55	O14798	P26992	Q8N9B5	Q9NWH9	Q92630	P62952	P04629	Q9HCY8	Q5GH73	P49682	P52952	P41221	Q569K4	
Q8WTP8	Q9P278	Q8WV24	Q9UBN6	O14578	P05783	O14983	O00429	P12644	P26583	P05109	Q5GH72	P61073	A6NCS4	O00755	Q9Y2A4	
O95831	Q12948	Q53GA4	O00300	Q96KAS	P35900	Q93084	O60313	P18075	Q92993	P06702	Q9H6D3	O75844	Q99801	Q5VZV1	Q969S3	
Q96NN9	Q99958	Q9Y515	Q9NP84	P10909	B2CW77	Q8N474	P28331	Q13873	Q09472	Q9H4B6	Q5GH70	Q99828	O75360	Q14289	Q92782	
O15033	P58012	P09874	P08138	P02458	Q92845	Q96HF1	Q9Y5S8	Q6PIG6	Q03164	Q14160	P16989	Q9LUQ7	Q15475	Q8IY19	QRIZ11	
Q96KQ4	Q12778	Q9UGN5	Q9Y5U5	Q01955	O60333	Q5T4F7	Q96PH1	Q9HCU9	Q03112	Q8N114	Q9H171	P25705	P34947	Q15319		
Q13625	O43524	Q9UHX1	Q9NS68	Q9BWP8	P21583	Q9Y6D0	P60323	P38398	P56177	Q8N9V7	Q05516	Q13617	Q969G2	Q13501		
Q9UKV3	P78423	P35226	Q969Z4	Q07021	Q63ZY3	Q14563	Q9Y2A7	P51587	P31271	Q9UBK9	Q8N5P1	P43146	Q6ZN44	Q9HAV5		
O14727	P51114	P35227	P19438	P31146	Q96MU8	Q9HZ66	Q13564	Q9NZ9N	O00144	Q01851	O75509	P46109	P46379	Q14674		
P35869	Q13467	O15296	P20333	Q9UEE9	O14901	Q9PU03	P48681	Q15121	Q9NQ88	Q12837	Q93038	Q13616	Q9UBR4	O43236		

Gene name	DU-145_vs_PC-3_logFC	p-value	Intensity DU145 replicate 1	Intensity DU145 replicate 2	Intensity DU145 replicate 3	Intensity DU145 replicate 4	Intensity PC3 replicate 1	Intensity PC3 replicate 2	Intensity PC3 replicate 3	Intensity PC3 replicate 4
CD9	1.25	5.8E-10	32.8761	32.8727	33.0453	33.0794	31.8065	31.7301	31.4672	31.8729
CD81	1.16	4.3E-09	32.3625	32.4896	32.5958	32.6828	31.3338	31.2928	31.44	31.4203
CHMP4C	2.72	2.9E-06	25.5007	25.6425	24.401	25.9922	21.9829	22.1699	23.5375	22.9619
LITAF	Not detected	-	-	-	-	-	-	-	-	-
RAB6A	0.06	5.5E-01	28.8561	28.7327	28.7076	28.7154	28.9096	28.6926	28.6088	28.5762
RAB7A	-0.42	3.4E-04	30.5977	30.6093	30.7447	30.712	31.0954	31.0384	31.1253	31.1021
RAB11B	0.82	2.8E-08	30.2045	30.1203	30.3004	30.192	29.2876	29.3008	29.4883	29.4429
RAB27B	-1.08	1.3E-04	26.1048	26.2255	25.4336	26.1092	27.1903	27.0922	26.8845	27.0367
RAB35	0.31	1.0E-02	28.5118	28.3474	28.3245	28.3549	28.0942	28.1006	28.163	27.9221
Rab37	Not detected	-	-	-	-	-	-	-	-	-
PCLO	Not detected	-	-	-	-	-	-	-	-	-
SCAMP3	-0.88	1.7E-07	28.6159	28.7245	28.6322	28.3992	29.3935	29.3574	29.7043	29.4498
SYNGR2	-1.47	4.1E-03	23.372	23.3958	23.3934	24.8423	25.1199	25.2754	25.2009	25.2799
SNAP23	0.43	9.7E-03	28.1491	28.2125	28.0615	28.2883	27.8065	27.7244	27.902	27.5785
VAMP3	-1.96	7.1E-04	27.21	27.1468	27.0748	27.1346	29.0413	28.9108	29.3175	29.138
VPS28	-0.26	1.5E-02	28.322	28.2228	28.4812	28.5673	28.7736	28.5213	28.7994	28.5473

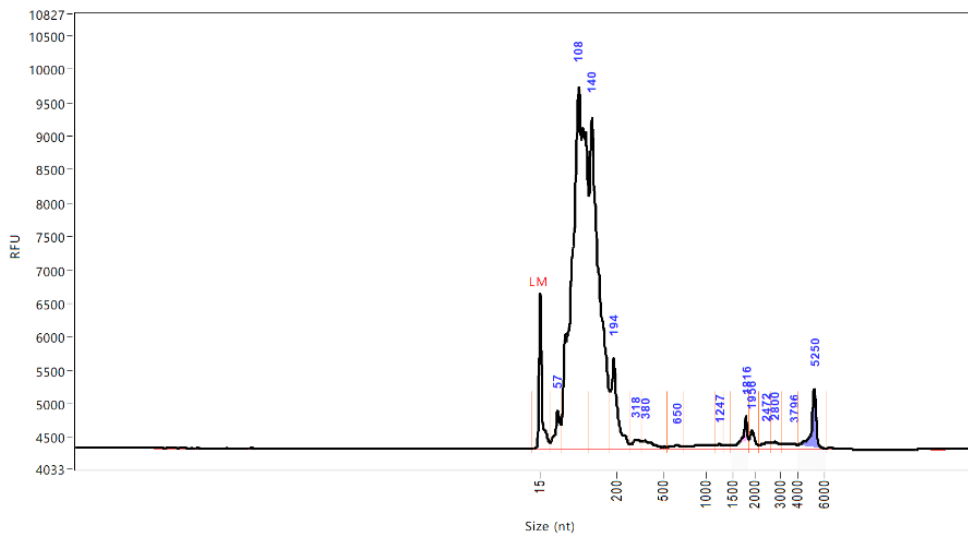
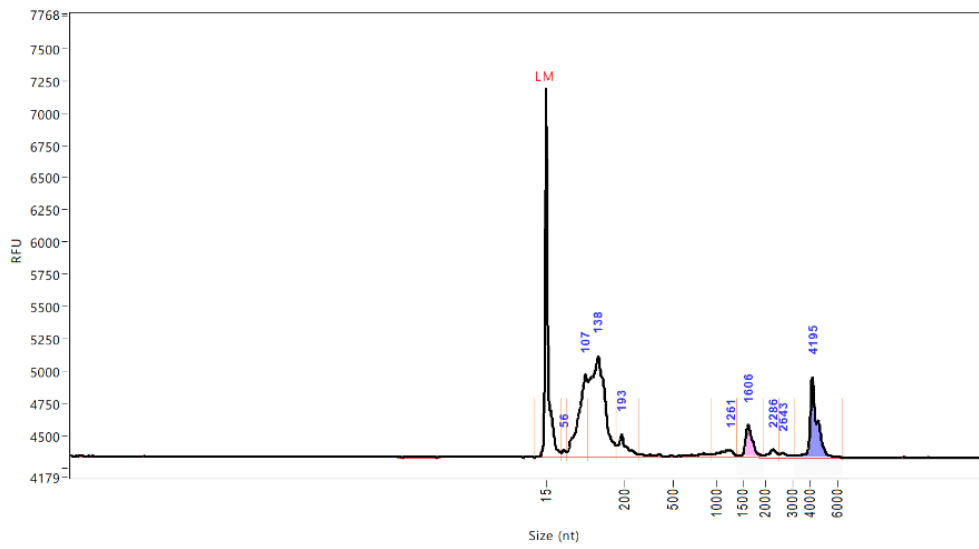
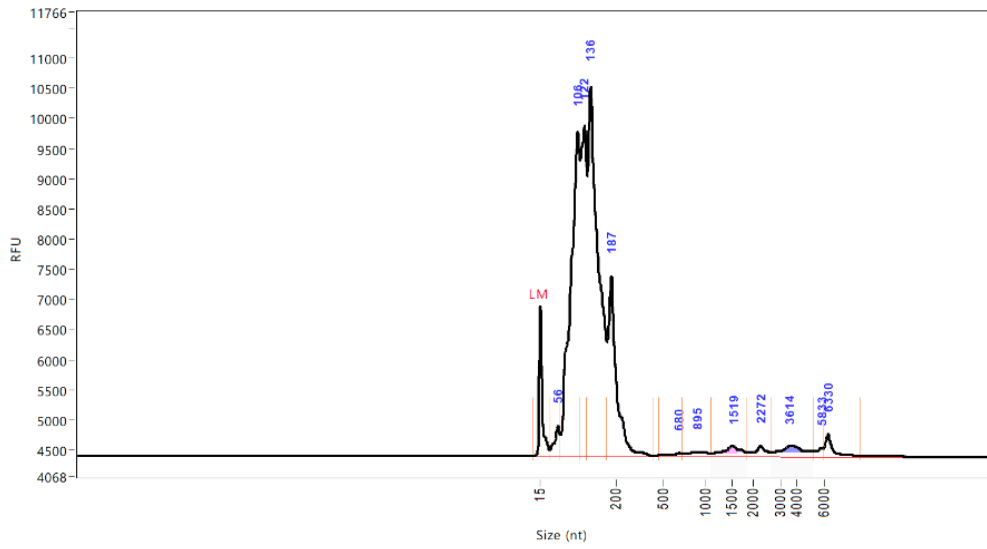
Annex B. protein expression of the selected candidates in isolate EVs from PC3 cells and DU145 cells. Data was kindly shared by consortium partners Elena Castellano and Hector Peinado.

Annex C

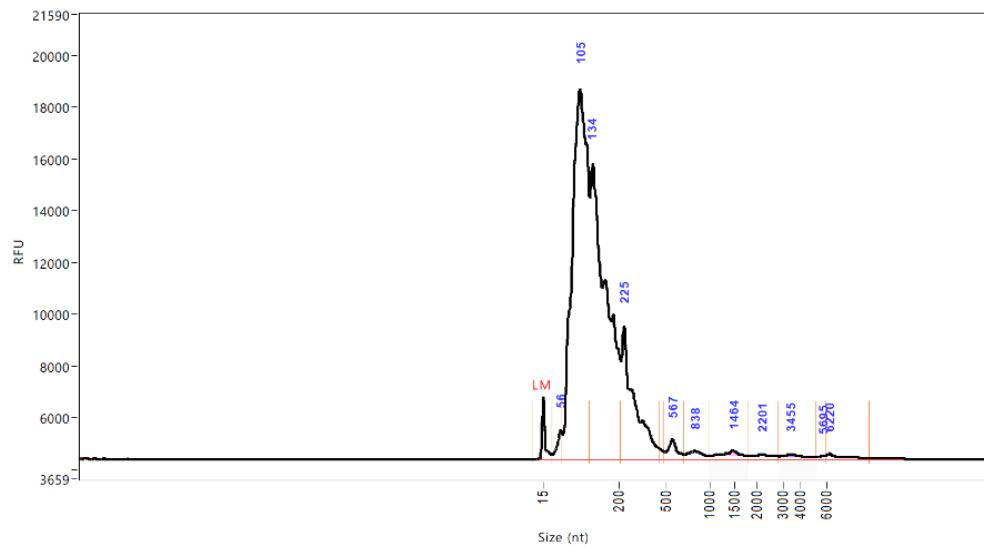
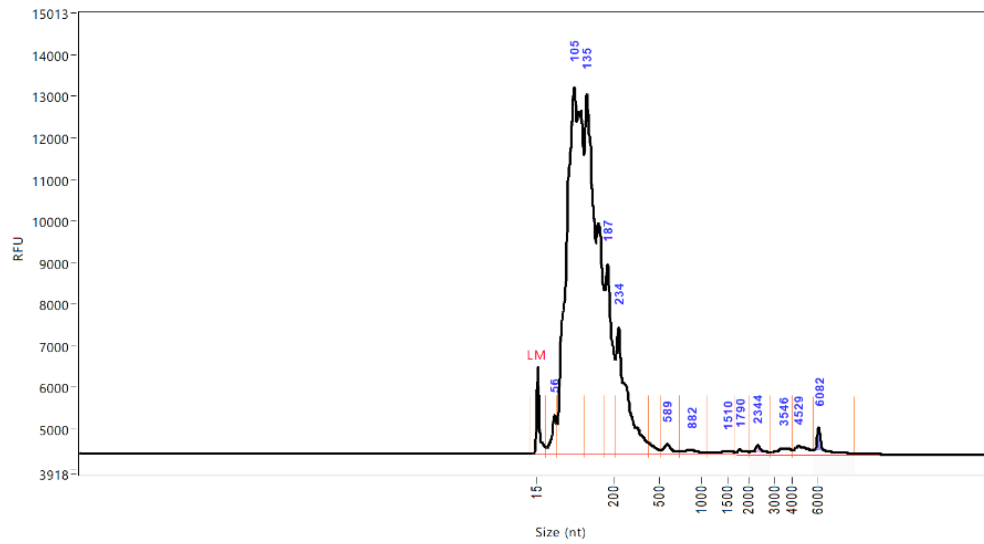
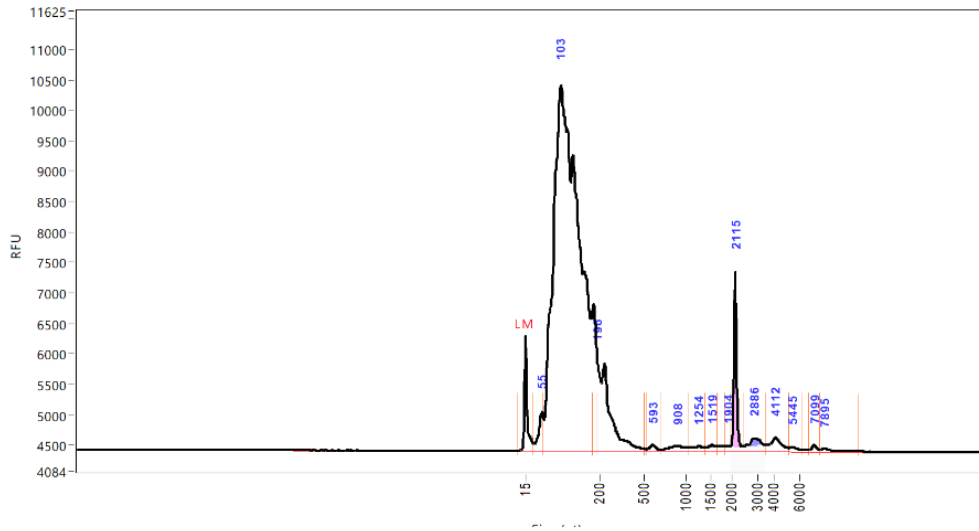
CD9KD



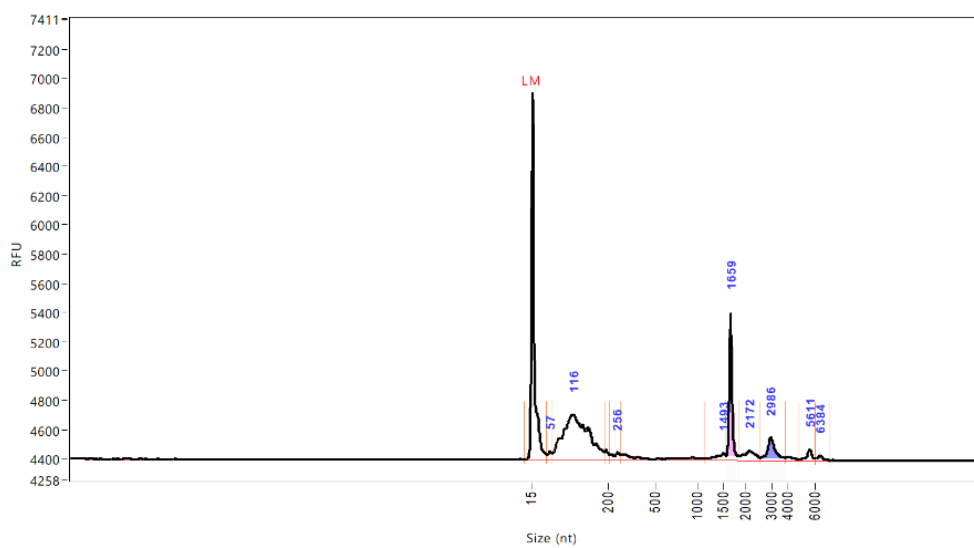
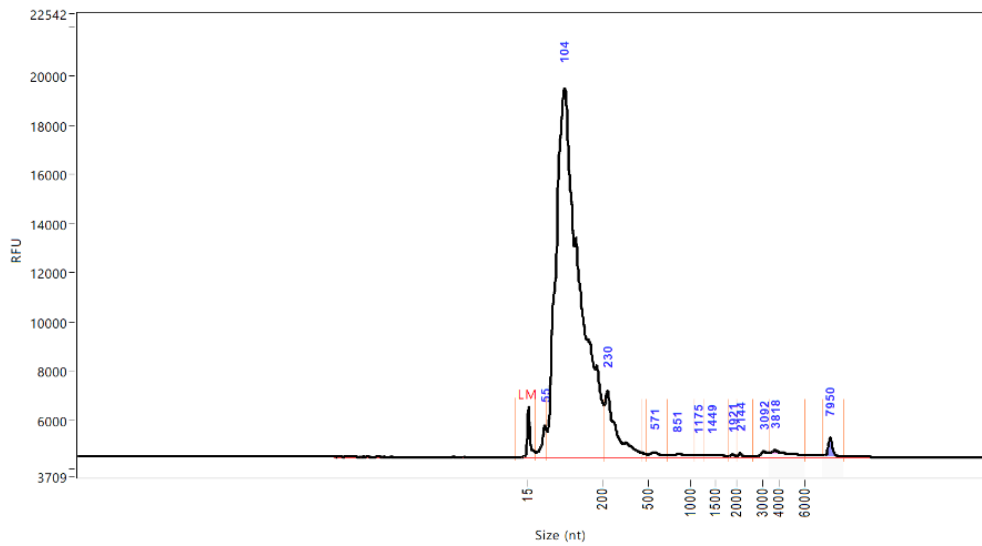
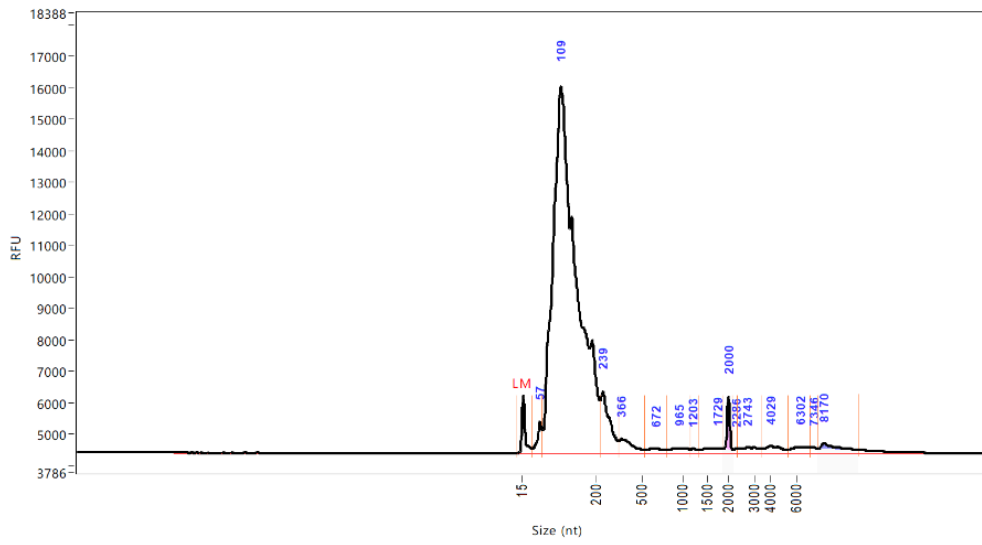
CD81KD



CHMP4CKD



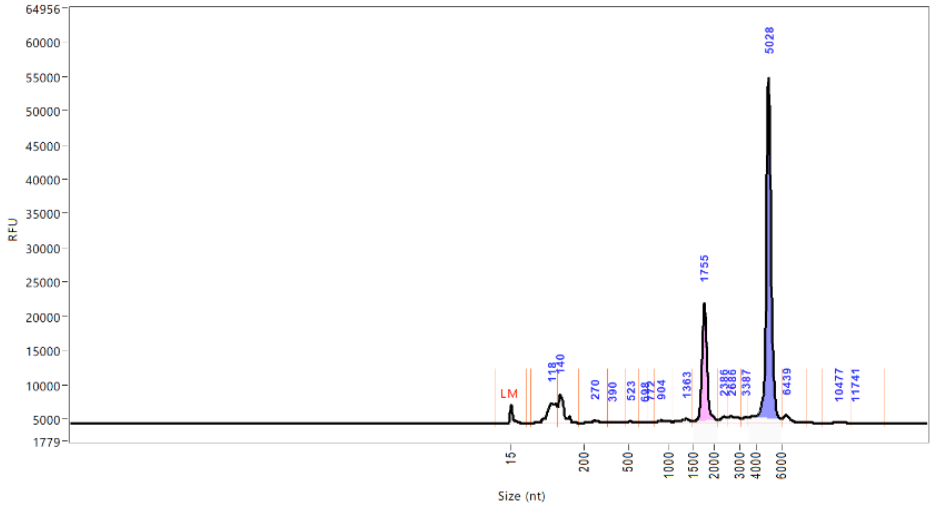
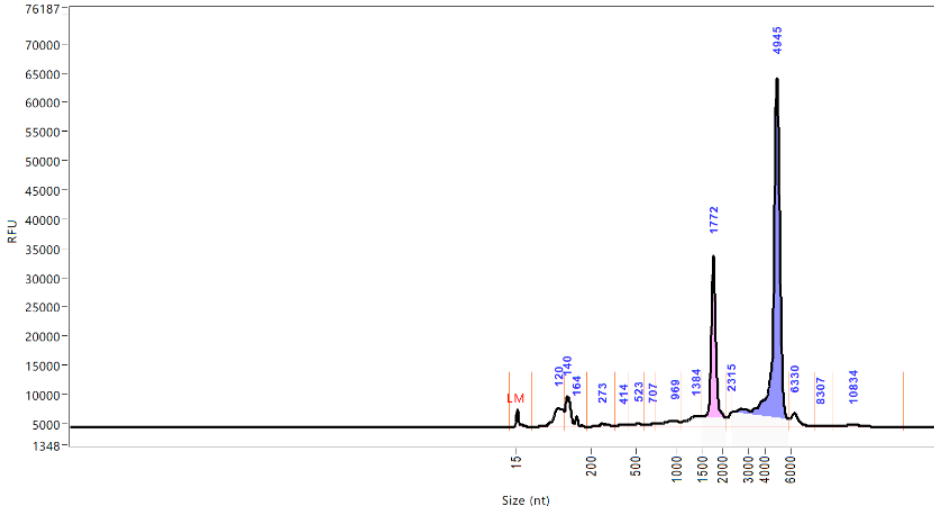
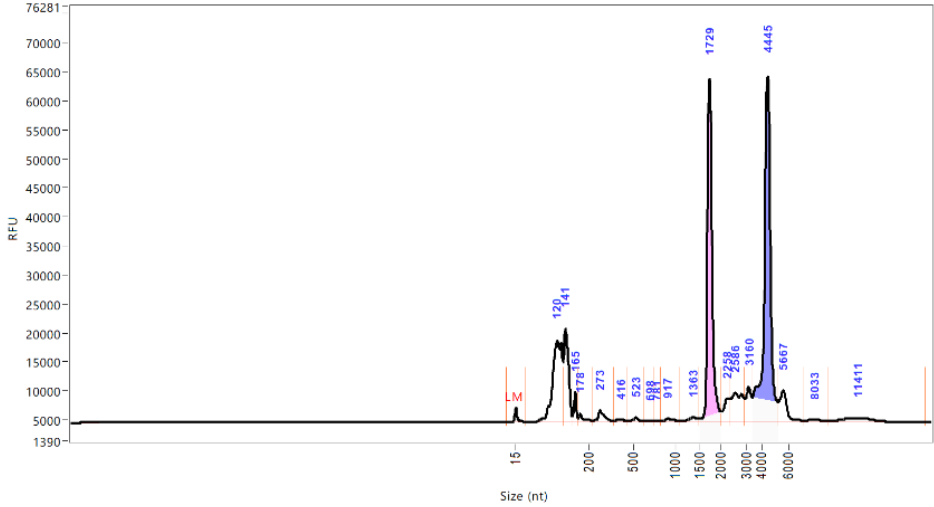
SYNGR2KD



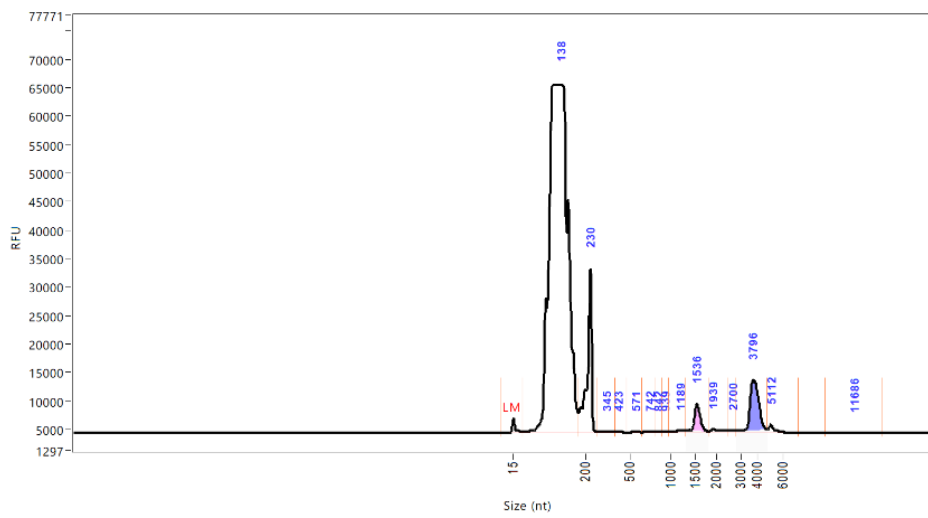
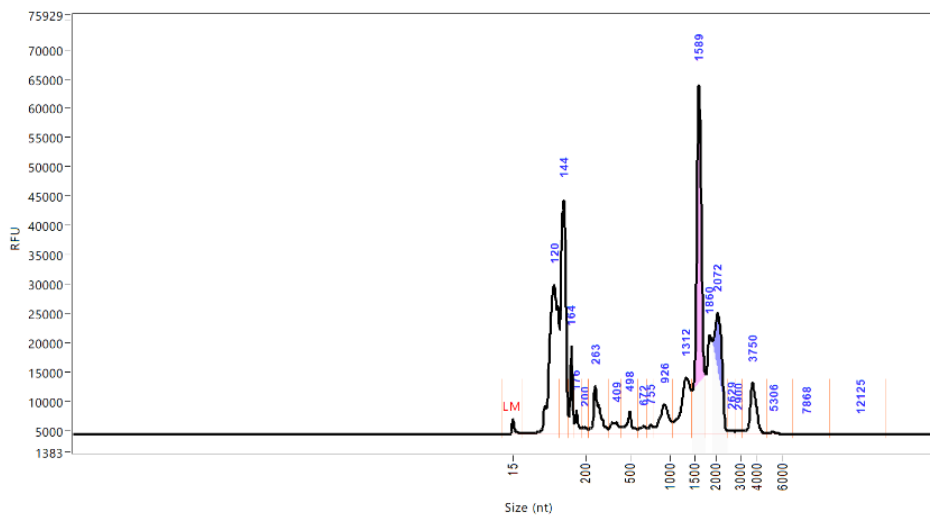
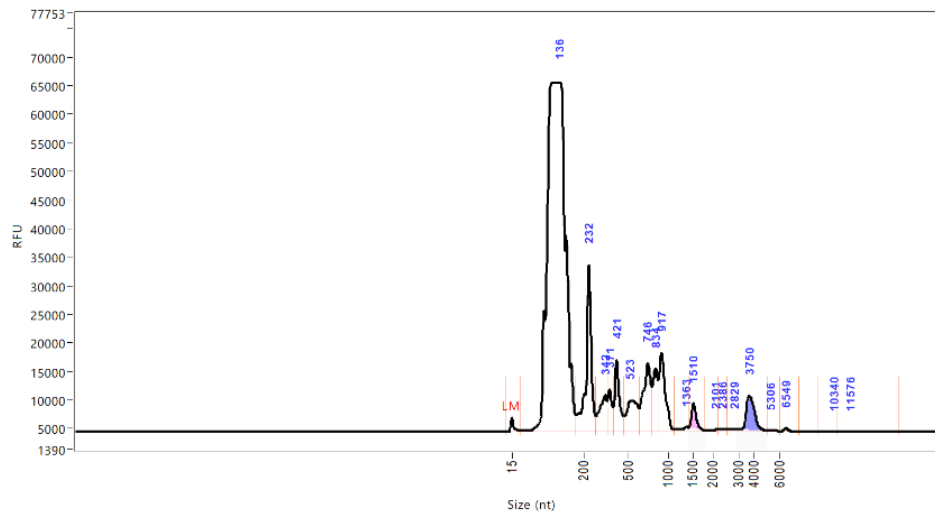
Annex C: Quality control of vesicular RNA performed at Genomescan.

The quality of the vesicular RNA samples, which were extracted using a phenol/chloroform-based method, was determined using the fragment analyzer Agilent DNF-472 HS RNA (15 nt) kit on a Fragment Analyzer (Agilent). The traces of the vesicular RNA isolated from KD cells (CD9KD, CD81KD, CHMP4CKD and SYNGR2KD) are shown. Light pink small rRNA subunit peak, purple large rRNA subunit, LM= loading marker, RFU= relative fluorescent units.

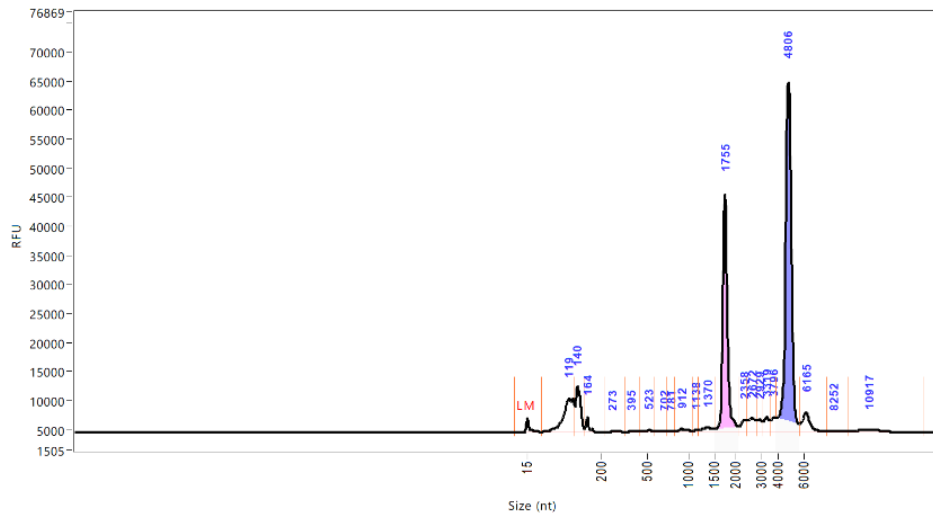
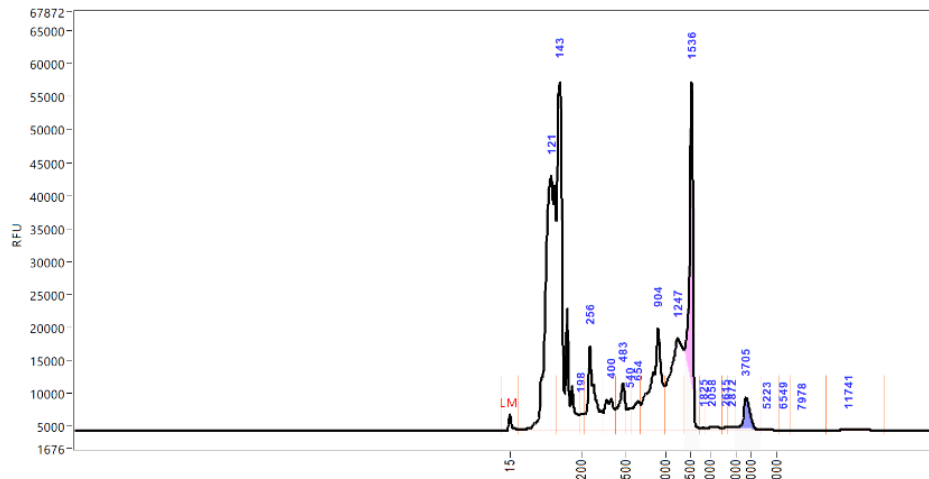
CD9KD



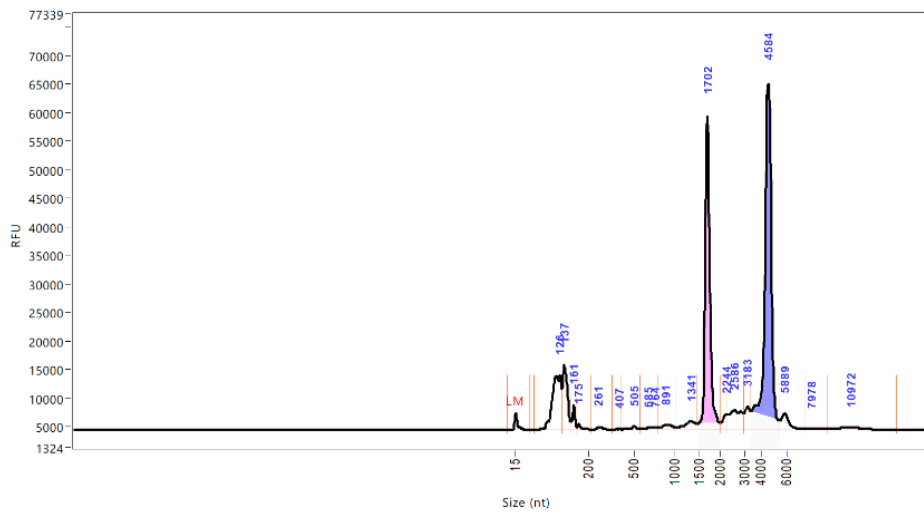
CD81KD

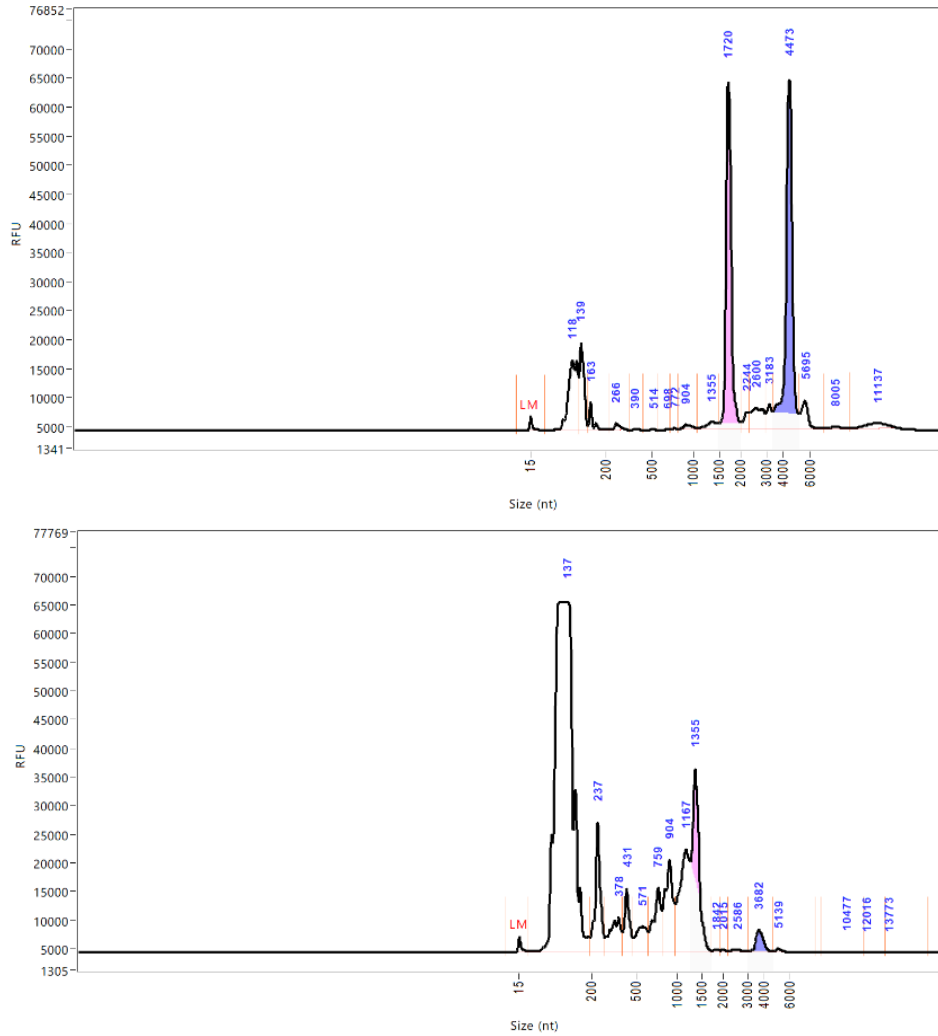


CHMP4CKD



SYNGR2KD





Annex D: Quality control of cellular RNA performed at Genomescan.

The quality of the cellular RNA samples, which were extracted using a phenol/chloroform-based method, was determined using the fragment analyzer Agilent DNF-472 HS RNA (15 nt) kit on a Fragment Analyzer (Agilent). The traces of the cellular RNA isolated from the KD cells (CD9KD, CD81KD, CHMP4CKD and SYNGR2KD) are shown. Light pink small rRNA subunit peak, purple large rRNA subunit, LM= loading marker, RFU= relative fluorescent units.

References

- ABDALLA, M., GOC, A., SEGAR, L. & SOMANATH, P. R. 2013. Akt1 mediates alpha-smooth muscle actin expression and myofibroblast differentiation via myocardin and serum response factor. *J Biol Chem*, 288, 33483-93.
- ABUSAMRA, A. J., ZHONG, Z., ZHENG, X., LI, M., ICHIM, T. E., CHIN, J. L. & MIN, W. P. 2005. Tumor exosomes expressing Fas ligand mediate CD8+ T-cell apoptosis. *Blood Cells Mol Dis*, 35, 169-73.
- ACKERMANN, F., SCHINK, K. O., BRUNS, C., IZSVAK, Z., HAMRA, F. K., ROSENMUND, C. & GARNER, C. C. 2019. Critical role for Piccolo in synaptic vesicle retrieval. *Elife*, 8.
- ALLAM, A., YAKOU, M., PANG, L., ERNST, M. & HUYNH, J. 2021. Exploiting the STAT3 Nexus in Cancer-Associated Fibroblasts to Improve Cancer Therapy. *Front Immunol*, 12, 767939.
- ALLEN, M. D. & EMBRY, B. 1991. Biopsy of the prostate guided by transrectal ultrasonography: early experience in a teaching community hospital. *South Med J*, 84, 579-86.
- ALMEIDA, A., GABRIEL, M., FIRLEJ, V., MARTIN-JAULAR, L., LEJARS, M., CIPOLLA, R., PETIT, F., VOGT, N., SAN-ROMAN, M., DINGLI, F., LOEW, D., DESTOUCHES, D., VACHEROT, F., DE LA TAILLE, A., THERY, C. & MORILLON, A. 2022. Urinary extracellular vesicles contain mature transcriptome enriched in circular and long noncoding RNAs with functional significance in prostate cancer. *J Extracell Vesicles*, 11, e12210.
- ALVAREZ-ERVITI, L., SEOW, Y., YIN, H., BETTS, C., LAKHAL, S. & WOOD, M. J. 2011. Delivery of siRNA to the mouse brain by systemic injection of targeted exosomes. *Nat Biotechnol*, 29, 341-5.
- ANNES, J. P., CHEN, Y., MUNGER, J. S. & RIFKIN, D. B. 2004. Integrin $\alpha\beta 6$ -mediated activation of latent TGF- β requires the latent TGF- β binding protein-1. *Journal of Cell Biology*, 165, 723-734.
- ARINA, A., IDEL, C., HYJEK, E. M., ALEGRE, M. L., WANG, Y., BINDOKAS, V. P., WEICHSELBAUM, R. R. & SCHREIBER, H. 2016. Tumor-associated fibroblasts predominantly come from local and not circulating precursors. *Proc Natl Acad Sci U S A*, 113, 7551-6.
- ARTIGAS, L., COMA, M., MATOS-FILIPPE, P., AGUIRRE-PLANS, J., FARRÉS, J., VALLS, R., FERNANDEZ-FUENTES, N., DE LA HABA-RODRIGUEZ, J., OLVERA, A., BARBERA, J., MORALES, R., OLIVA, B. & MAS, J. M. 2020. In-silico drug repurposing study predicts the combination of pirfenidone and melatonin as a promising candidate therapy to reduce SARS-CoV-2 infection progression and respiratory distress caused by cytokine storm. *PLoS One*, 15, e0240149.
- AYALA, G. E., MUEZZINOGLU, B., HAMMERICH, K. H., FROLOV, A., LIU, H., SCARDINO, P. T., LI, R., SAYEEDUDDIN, M., ITTMANN, M. M., KADMON, D., MILES, B. J., WHEELER, T. M. & ROWLEY, D. R. 2011. Determining prostate cancer-specific death through quantification of stromogenic carcinoma area in prostatectomy specimens. *Am J Pathol*, 178, 79-87.
- BAGHBAN, R., ROZHANGAR, L., JAHANBAN-ESFAHLAN, R., SEIDI, K., EBRAHIMI-KALAN, A., JAYMAND, M., KOLAHIAN, S., JAVAHERI, T. & ZARE, P. 2020. Tumor microenvironment complexity and therapeutic implications at a glance. *Cell Commun Signal*, 18, 59.
- BAIETTI, M. F., ZHANG, Z., MORTIER, E., MELCHIOR, A., DEGEEST, G., GEERAERTS, A., IVARSSON, Y., DEPOORTERE, F., COOMANS, C., VERMEIREN, E., ZIMMERMANN, P. & DAVID, G. 2012. Syndecan-syntenin-ALIX regulates the biogenesis of exosomes. *Nat Cell Biol*, 14, 677-85.
- BALL, S. G., WORTHINGTON, J. J., CANFIELD, A. E., MERRY, C. L. & KIELTY, C. M. 2014. Mesenchymal stromal cells: inhibiting PDGF receptors or depleting fibronectin induces mesodermal progenitors with endothelial potential. *Stem Cells*, 32, 694-705.
- BARMAN, B., SUNG, B. H., KRISTOFIAK, E., PING, J., RAMIREZ, M., MILLIS, B., ALLEN, R., PRASAD, N., CHETYRKIN, S., CALCUTT, M. W., VICKERS, K., PATTON, J. G., LIU, Q. & WEAVER, A. M. 2022. VAP-A and its binding partner CERT drive biogenesis of RNA-containing extracellular vesicles at ER membrane contact sites. *Dev Cell*, 57, 974-994.e8.
- BARONI, S., ROMERO-CORDOBA, S., PLANTAMURA, I., DUGO, M., D'IPPOLITO, E., CATALDO, A., COSENTINO, G., ANGELONI, V., ROSSINI, A., DAIDONE, M. G. & IORIO, M. V. 2016. Exosome-

- mediated delivery of miR-9 induces cancer-associated fibroblast-like properties in human breast fibroblasts. *Cell Death Dis*, 7, e2312.
- BEN-NISSAN, G., KATZIR, N., FÜZESI-LEVI, M. G. & SHARON, M. 2022. Biology of the Extracellular Proteasome. *Biomolecules*, 12.
- BENTLEY, D. R., BALASUBRAMANIAN, S., SWERDLOW, H. P., SMITH, G. P., MILTON, J., BROWN, C. G., HALL, K. P., EVERS, D. J., BARNES, C. L., BIGNELL, H. R., BOUTELL, J. M., BRYANT, J., CARTER, R. J., KEIRA CHEETHAM, R., COX, A. J., ELLIS, D. J., FLATBUSH, M. R., GORMLEY, N. A., HUMPHRAY, S. J., IRVING, L. J., KARBELASHVILI, M. S., KIRK, S. M., LI, H., LIU, X., MAISINGER, K. S., MURRAY, L. J., OBRADOVIC, B., OST, T., PARKINSON, M. L., PRATT, M. R., RASOLONJATOVO, I. M., REED, M. T., RIGATTI, R., RODIGHIERO, C., ROSS, M. T., SABOT, A., SANKAR, S. V., SCALLY, A., SCHROTH, G. P., SMITH, M. E., SMITH, V. P., SPIRIDOU, A., TORRANCE, P. E., TZONEV, S. S., VERMAAS, E. H., WALTER, K., WU, X., ZHANG, L., ALAM, M. D., ANASTASI, C., ANIEBO, I. C., BAILEY, D. M., BANCARZ, I. R., BANERJEE, S., BARBOUR, S. G., BAYBAYAN, P. A., BENOIT, V. A., BENSON, K. F., BEVIS, C., BLACK, P. J., BOODHUN, A., BRENNAN, J. S., BRIDGHAM, J. A., BROWN, R. C., BROWN, A. A., BUERMANN, D. H., BUNDU, A. A., BURROWS, J. C., CARTER, N. P., CASTILLO, N., CHIARA, E. C. M., CHANG, S., NEIL COOLEY, R., CRAKE, N. R., DADA, O. O., DIAKOUMAKOS, K. D., DOMINGUEZ-FERNANDEZ, B., EARNSHAW, D. J., EGBUJOR, U. C., ELMORE, D. W., ETCHIN, S. S., EWAN, M. R., FEDURCO, M., FRASER, L. J., FUENTES FAJARDO, K. V., SCOTT FUREY, W., GEORGE, D., GIETZEN, K. J., GODDARD, C. P., GOLDA, G. S., GRANIERI, P. A., GREEN, D. E., GUSTAFSON, D. L., HANSEN, N. F., HARNISH, K., HAUDENSCHILD, C. D., HEYER, N. I., HIMMS, M. M., HO, J. T., HORGAN, A. M., et al. 2008. Accurate whole human genome sequencing using reversible terminator chemistry. *Nature*, 456, 53-9.
- BIFFI, G., ONI, T. E., SPIELMAN, B., HAO, Y., ELYADA, E., PARK, Y., PREALL, J. & TUVESON, D. A. 2019. IL1-Induced JAK/STAT Signaling Is Antagonized by TGFbeta to Shape CAF Heterogeneity in Pancreatic Ductal Adenocarcinoma. *Cancer Discov*, 9, 282-301.
- BIFFI, G. & TUVESON, D. A. 2021. Diversity and Biology of Cancer-Associated Fibroblasts. *Physiol Rev*, 101, 147-176.
- BLIJDDORP, C. J., HARTJES, T. A., WEI, K. Y., VAN HEUGTEN, M. H., BOVÉE, D. M., BUDDÉ, R. P. J., VAN DE WETERING, J., HOENDEROP, J. G. J., VAN ROYEN, M. E., ZIETSE, R., SEVERS, D. & HOORN, E. J. 2022. Nephron mass determines the excretion rate of urinary extracellular vesicles. *J Extracell Vesicles*, 11, e12181.
- BLIJDDORP, C. J., TUTAKHEL, O. A. Z., HARTJES, T. A., VAN DEN BOSCH, T. P. P., VAN HEUGTEN, M. H., RIGALLI, J. P., WILLEMSSEN, R., MUSTERD-BHAGGOE, U. M., BARROS, E. R., CARLES-FONTANA, R., CARVAJAL, C. A., ARNTZ, O. J., VAN DE LOO, F. A. J., JENSTER, G., CLAHSSEN-VAN GRONINGEN, M. C., CUEVAS, C. A., SEVERS, D., FENTON, R. A., VAN ROYEN, M. E., HOENDEROP, J. G. J., BINDELS, R. J. M. & HOORN, E. J. 2021. Comparing Approaches to Normalize, Quantify, and Characterize Urinary Extracellular Vesicles. *J Am Soc Nephrol*, 32, 1210-1226.
- BOBRIE, A., KRUMEICH, S., REYAL, F., RECCHI, C., MOITA, L. F., SEABRA, M. C., OSTROWSKI, M. & THERY, C. 2012a. Rab27a supports exosome-dependent and -independent mechanisms that modify the tumor microenvironment and can promote tumor progression. *Cancer Res*, 72, 4920-30.
- BOBRIE, A., KRUMEICH, S., REYAL, F., RECCHI, C., MOITA, L. F., SEABRA, M. C., OSTROWSKI, M. & THÉRY, C. 2012b. Rab27a supports exosome-dependent and -independent mechanisms that modify the tumor microenvironment and can promote tumor progression. *Cancer Res*, 72, 4920-30.
- BOCK, J. B., KLUMPERMAN, J., DAVANGER, S. & SCHELLER, R. H. 1997. Syntaxin 6 functions in trans-Golgi network vesicle trafficking. *Mol Biol Cell*, 8, 1261-71.
- BOESZE-BATTAGLIA, K., WALKER, L. P., DHINGRA, A., KANDROR, K., TANG, H. Y. & SHENKER, B. J. 2017. Internalization of the Active Subunit of the Aggregatibacter actinomycetemcomitans Cytotolethal Distending Toxin Is Dependent upon Cellugyrin (Synaptogyrin 2), a Host Cell Non-

- Neuronal Paralog of the Synaptic Vesicle Protein, Synaptogyrin 1. *Front Cell Infect Microbiol*, 7, 469.
- BOHUSLAV, J., CHEN, L. F., KWON, H., MU, Y. & GREENE, W. C. 2004. p53 induces NF-kappaB activation by an IkappaB kinase-independent mechanism involving phosphorylation of p65 by ribosomal S6 kinase 1. *J Biol Chem*, 279, 26115-25.
- BOLIS, M., BOSSI, D., VALLERGA, A., CESERANI, V., CAVALLI, M., IMPELLIZZIERI, D., DI RITO, L., ZONI, E., MOSOLE, S., ELIA, A. R., RINALDI, A., PEREIRA MESTRE, R., D'ANTONIO, E., FERRARI, M., STOFFEL, F., JERMINI, F., GILLESSEN, S., BUBENDORF, L., SCHRAML, P., CALCINOTTO, A., COREY, E., MOCH, H., SPAHN, M., THALMANN, G., KRUIHOF-DE JULIO, M., RUBIN, M. A. & THEURILLAT, J. P. 2021. Dynamic prostate cancer transcriptome analysis delineates the trajectory to disease progression. *Nat Commun*, 12, 7033.
- BOYER, M. J., CARPENTER, D., GINGRICH, J. R., RAMAN, S., SIROHI, D., TABRIZ, A. A., ROMPRE-BRODEUR, A., LUNYERA, J., BASHER, F., BITTING, R. L., KOSINSKI, A., CANTRELL, S., GORDON, A. M., EAR, B., GIERISCH, J. M., JACOBS, M. & GOLDSTEIN, K. M. 2023. VA Evidence-based Synthesis Program Reports. *Prognostic Value of Genomic Classifier Testing for Prostate Cancer: A Systematic Review*. Washington (DC): Department of Veterans Affairs (US).
- BRYANT, R. J., PAWLOWSKI, T., CATTO, J. W., MARSDEN, G., VESSELLA, R. L., RHEES, B., KUSLICH, C., VISAKORPI, T. & HAMDY, F. C. 2012. Changes in circulating microRNA levels associated with prostate cancer. *Br J Cancer*, 106, 768-74.
- BRZOZOWSKI, J. S., BOND, D. R., JANKOWSKI, H., GOLDIE, B. J., BURCHELL, R., NAUDIN, C., SMITH, N. D., SCARLETT, C. J., LARSEN, M. R., DUN, M. D., SKELDING, K. A. & WEIDENHOFER, J. 2018. Extracellular vesicles with altered tetraspanin CD9 and CD151 levels confer increased prostate cell motility and invasion. *Sci Rep*, 8, 8822.
- BUSATTO, S., VILANILAM, G., TICER, T., LIN, W. L., DICKSON, D. W., SHAPIRO, S., BERGESE, P. & WOLFRAM, J. 2018. Tangential Flow Filtration for Highly Efficient Concentration of Extracellular Vesicles from Large Volumes of Fluid. *Cells*, 7.
- CAMPBELL, M. G., CORMIER, A., ITO, S., SEED, R. I., BONDESSON, A. J., LOU, J., MARKS, J. D., BARON, J. L., CHENG, Y. & NISHIMURA, S. L. 2020. Cryo-EM Reveals Integrin-Mediated TGF-beta Activation without Release from Latent TGF-beta. *Cell*, 180, 490-501 e16.
- CANCER GENOME ATLAS RESEARCH, N. 2015. The Molecular Taxonomy of Primary Prostate Cancer. *Cell*, 163, 1011-25.
- CANCER GENOME ATLAS RESEARCH, N., WEINSTEIN, J. N., COLLISSON, E. A., MILLS, G. B., SHAW, K. R., OZENBERGER, B. A., ELLROTT, K., SHMULEVICH, I., SANDER, C. & STUART, J. M. 2013. The Cancer Genome Atlas Pan-Cancer analysis project. *Nat Genet*, 45, 1113-20.
- <https://www.cancerresearchuk.org/about-cancer/prostate-cancer> [accessed 10.01.2024]
- Cancertool: <http://genomics.cicbiogune.es/CANCERTOOL/index.html> [accessed 04.03.2021]
- CAPALBO, L., BASSI, Z. I., GEYMONAT, M., TODESCA, S., COPOIU, L., ENRIGHT, A. J., CALLAINI, G., RIPARBELLI, M. G., YU, L., CHOUDHARY, J. S., FERRERO, E., WHEATLEY, S., DOUGLAS, M. E., MISHIMA, M. & D'AVINO, P. P. 2019. The midbody interactome reveals unexpected roles for PP1 phosphatases in cytokinesis. *Nat Commun*, 10, 4513.
- CARLTON, J. G., CABALLE, A., AGROMAYOR, M., KLOC, M. & MARTIN-SERRANO, J. 2012. ESCRT-III governs the Aurora B-mediated abscission checkpoint through CHMP4C. *Science*, 336, 220-5.
- CARTHY, J. M., SUNDQVIST, A., HELDIN, A., VAN DAM, H., KLETSAS, D., HELDIN, C. H. & MOUSTAKAS, A. 2015. Tamoxifen Inhibits TGF-beta-Mediated Activation of Myofibroblasts by Blocking Non-Smad Signaling Through ERK1/2. *J Cell Physiol*, 230, 3084-92.
- CATALONA, W. J., RICHIE, J. P., AHMANN, F. R., HUDSON, M. A., SCARDINO, P. T., FLANIGAN, R. C., DEKERNION, J. B., RATLIFF, T. L., KAVOUSSI, L. R., DALKIN, B. L., WATERS, W. B., MACFARLANE, M. T. & SOUTHWICK, P. C. 2017. Comparison of Digital Rectal Examination and Serum Prostate Specific Antigen in the Early Detection of Prostate Cancer: Results of a Multicenter Clinical Trial of 6,630 Men. *J Urol*, 197, S200-S207.

- CHA, D. J., FRANKLIN, J. L., DOU, Y., LIU, Q., HIGGINBOTHAM, J. N., DEMORY BECKLER, M., WEAVER, A. M., VICKERS, K., PRASAD, N., LEVY, S., ZHANG, B., COFFEY, R. J. & PATTON, J. G. 2015. KRAS-dependent sorting of miRNA to exosomes. *Elife*, 4, e07197.
- CHAIROUNGDU, A., SMITH, D. L., POCHARD, P., HULL, M. & CAPLAN, M. J. 2010. Exosome release of beta-catenin: a novel mechanism that antagonizes Wnt signaling. *J Cell Biol*, 190, 1079-91.
- CHAKRABORTY, D., SUMOVA, B., MALLANO, T., CHEN, C. W., DISTLER, A., BERGMANN, C., LUDOLPH, I., HORCH, R. E., GELSE, K., RAMMING, A., DISTLER, O., SCHEIT, G., SENOLT, L. & DISTLER, J. H. W. 2017. Activation of STAT3 integrates common profibrotic pathways to promote fibroblast activation and tissue fibrosis. *Nat Commun*, 8, 1130.
- CHAN, S. C. & DEHM, S. M. 2014. Constitutive activity of the androgen receptor. *Adv Pharmacol*, 70, 327-66.
- CHARRIN, S., MANIÉ, S., OUALID, M., BILLARD, M., BOUCHEIX, C. & RUBINSTEIN, E. 2002. Differential stability of tetraspanin/tetraspanin interactions: role of palmitoylation. *FEBS Lett*, 516, 139-44.
- CHEN, I. H., XUE, L., HSU, C. C., PAEZ, J. S., PAN, L., ANDALUZ, H., WENDT, M. K., ILIUK, A. B., ZHU, J. K. & TAO, W. A. 2017a. Phosphoproteins in extracellular vesicles as candidate markers for breast cancer. *Proc Natl Acad Sci U S A*, 114, 3175-3180.
- CHEN, J. Y., LIN, C. H. & CHEN, B. C. 2017b. Hypoxia-induced ADAM 17 expression is mediated by RSK1-dependent C/EBPbeta activation in human lung fibroblasts. *Mol Immunol*, 88, 155-163.
- CHEN, S., ZHU, G., YANG, Y., WANG, F., XIAO, Y.-T., ZHANG, N., BIAN, X., ZHU, Y., YU, Y., LIU, F., DONG, K., MARISCAL, J., LIU, Y., SOARES, F., LOO YAU, H., ZHANG, B., CHEN, W., WANG, C., CHEN, D., GUO, Q., YI, Z., LIU, M., FRASER, M., DE CARVALHO, D. D., BOUTROS, P. C., DI VIZIO, D., JIANG, Z., VAN DER KWAST, T., BERLIN, A., WU, S., WANG, J., HE, H. H. & REN, S. 2021a. Single-cell analysis reveals transcriptomic remodellings in distinct cell types that contribute to human prostate cancer progression. *Nature Cell Biology*, 23, 87-98.
- CHEN, Y., MCANDREWS, K. M. & KALLURI, R. 2021b. Clinical and therapeutic relevance of cancer-associated fibroblasts. *Nat Rev Clin Oncol*, 18, 792-804.
- CHEN, Y. T., CHANG, F. C., WU, C. F., CHOU, Y. H., HSU, H. L., CHIANG, W. C., SHEN, J., CHEN, Y. M., WU, K. D., TSAI, T. J., DUFFIELD, J. S. & LIN, S. L. 2011. Platelet-derived growth factor receptor signaling activates pericyte-myofibroblast transition in obstructive and post-ischemic kidney fibrosis. *Kidney Int*, 80, 1170-81.
- CHETEH, E. H., SARNE, V., CEDER, S., BIANCHI, J., AUGSTEN, M., RUNDQVIST, H., EGEVAD, L., OSTMAN, A. & WIMAN, K. G. 2020. Interleukin-6 derived from cancer-associated fibroblasts attenuates the p53 response to doxorubicin in prostate cancer cells. *Cell Death Discov*, 6, 42.
- CHIRIACO, M. S., BIANCO, M., NIGRO, A., PRIMICERI, E., FERRARA, F., ROMANO, A., QUATTRINI, A., FURLAN, R., ARIMA, V. & MARUCCIO, G. 2018. Lab-on-Chip for Exosomes and Microvesicles Detection and Characterization. *Sensors (Basel)*, 18.
- CHOWDHURY, R., WEBBER, J. P., GURNEY, M., MASON, M. D., TABI, Z. & CLAYTON, A. 2015. Cancer exosomes trigger mesenchymal stem cell differentiation into pro-angiogenic and pro-invasive myofibroblasts. *Oncotarget*, 6, 715-31.
- CHRZANOWSKA-WODNICKA, M. & BURRIDGE, K. 1996. Rho-stimulated contractility drives the formation of stress fibers and focal adhesions. *J Cell Biol*, 133, 1403-15.
- CIONI, B., NEVEDOMSKAYA, E., MELIS, M. H. M., VAN BURGSTEDEN, J., STELLOO, S., HODEL, E., SPINOZZI, D., DE JONG, J., VAN DER POEL, H., DE BOER, J. P., WESSELS, L. F. A., ZWART, W. & BERGMAN, A. M. 2018. Loss of androgen receptor signaling in prostate cancer-associated fibroblasts (CAFs) promotes CCL2- and CXCL8-mediated cancer cell migration. *Mol Oncol*, 12, 1308-1323.
- CLANCY, J. W., ZHANG, Y., SHEEHAN, C. & D'SOUZA-SCHOREY, C. 2019. An ARF6-Exportin-5 axis delivers pre-miRNA cargo to tumour microvesicles. *Nat Cell Biol*, 21, 856-866.
- CLAYTON, A., COURT, J., NAVABI, H., ADAMS, M., MASON, M. D., HOBOT, J. A., NEWMAN, G. R. & JASANI, B. 2001. Analysis of antigen presenting cell derived exosomes, based on immunomagnetic isolation and flow cytometry. *Journal of Immunological Methods*, 247, 163-174.

- COCUCCI, E., RACCHETTI, G. & MELDOLESI, J. 2009. Shedding microvesicles: artefacts no more. *Trends in Cell Biology*, 19, 43-51.
- COLOMBO, M., MOITA, C., VAN NIEL, G., KOWAL, J., VIGNERON, J., BENAROCH, P., MANEL, N., MOITA, L. F., THERY, C. & RAPOSO, G. 2013. Analysis of ESCRT functions in exosome biogenesis, composition and secretion highlights the heterogeneity of extracellular vesicles. *J Cell Sci*, 126, 5553-65.
- CONTINOLO, S., BARUZZI, A., MAJEED, M., CAVEGGION, E., FUMAGALLI, L., LOWELL, C. A. & BERTON, G. 2005. The proto-oncogene Fgr regulates cell migration and this requires its plasma membrane localization. *Exp Cell Res*, 302, 253-69.
- CORCORAN, C., RANI, S., O'BRIEN, K., O'NEILL, A., PRENCIPE, M., SHEIKH, R., WEBB, G., MCDERMOTT, R., WATSON, W., CROWN, J. & O'DRISCOLL, L. 2012. Docetaxel-resistance in prostate cancer: evaluating associated phenotypic changes and potential for resistance transfer via exosomes. *PLoS One*, 7, e50999.
- CORTAZAR, A. R., TORRANO, V., MARTIN-MARTIN, N., CARO-MALDONADO, A., CAMACHO, L., HERMANOVA, I., GURUCEAGA, E., LORENZO-MARTIN, L. F., CALOTO, R., GOMIS, R. R., APAOLAZA, I., QUESADA, V., TRKA, J., GOMEZ-MUNOZ, A., VINCENT, S., BUSTELO, X. R., PLANES, F. J., ARANSAY, A. M. & CARRACEDO, A. 2018. CANCERTOOL: A Visualization and Representation Interface to Exploit Cancer Datasets. *Cancer Res*, 78, 6320-6328.
- COSTA, A., KIEFFER, Y., SCHOLER-DAHIREL, A., PELON, F., BOURACHOT, B., CARDON, M., SIRVEN, P., MAGAGNA, I., FUHRMANN, L., BERNARD, C., BONNEAU, C., KONDRATOVA, M., KUPERSTEIN, I., ZINOVYEV, A., GIVEL, A. M., PARRINI, M. C., SOUMELIS, V., VINCENT-SALOMON, A. & MECHTA-GRIGORIOU, F. 2018. Fibroblast Heterogeneity and Immunosuppressive Environment in Human Breast Cancer. *Cancer Cell*, 33, 463-479 e10.
- CRONIN, R., BROOKE, G. N. & PRISCHI, F. 2021. The role of the p90 ribosomal S6 kinase family in prostate cancer progression and therapy resistance. *Oncogene*, 40, 3775-3785.
- crukcanerintelligence.shinyapps.io/CancerStatsDataHub/ [accessed 10.01.2024]
- CZERWINSKA, M., BILEWICZ, A., KRUSZEWSKI, M., WEGIEREK-CIUK, A. & LANKOFF, A. 2020. Targeted Radionuclide Therapy of Prostate Cancer-From Basic Research to Clinical Perspectives. *Molecules*, 25.
- D'SOUZA-SCHOREY, C. & SCHOREY, JEFFREY S. 2018. Regulation and mechanisms of extracellular vesicle biogenesis and secretion. *Essays in Biochemistry*, 62, 125-133.
- DAVIES, G., MASON, M. D., MARTIN, T. A., PARR, C., WATKINS, G., LANE, J., MATSUMOTO, K., NAKAMURA, T. & JIANG, W. G. 2003. The HGF/SF antagonist NK4 reverses fibroblast- and HGF-induced prostate tumor growth and angiogenesis in vivo. *Int J Cancer*, 106, 348-54.
- DE LA CUESTA, F., PASSALACQUA, I., RODOR, J., BHUSHAN, R., DENBY, L. & BAKER, A. H. 2019. Extracellular vesicle cross-talk between pulmonary artery smooth muscle cells and endothelium during excessive TGF-beta signalling: implications for PAH vascular remodelling. *Cell Commun Signal*, 17, 143.
- DEANS, R. M., MORGENS, D. W., OKESLI, A., PILLAY, S., HORLBECK, M. A., KAMPMANN, M., GILBERT, L. A., LI, A., MATEO, R., SMITH, M., GLENN, J. S., CARETTE, J. E., KHOSLA, C. & BASSIK, M. C. 2016. Parallel shRNA and CRISPR-Cas9 screens enable antiviral drug target identification. *Nat Chem Biol*, 12, 361-6.
- DEMORY BECKLER, M., HIGGINBOTHAM, J. N., FRANKLIN, J. L., HAM, A. J., HALVEY, P. J., IMASUEN, I. E., WHITWELL, C., LI, M., LIEBLER, D. C. & COFFEY, R. J. 2013. Proteomic analysis of exosomes from mutant KRAS colon cancer cells identifies intercellular transfer of mutant KRAS. *Mol Cell Proteomics*, 12, 343-55.
- DESAI, K., MCMANUS, J. M. & SHARIFI, N. 2021. Hormonal Therapy for Prostate Cancer. *Endocr Rev*, 42, 354-373.
- DESMOULIÈRE, A., GEINOZ, A., GABBIANI, F. & GABBIANI, G. 1993. Transforming growth factor-beta 1 induces alpha-smooth muscle actin expression in granulation tissue myofibroblasts and in quiescent and growing cultured fibroblasts. *J Cell Biol*, 122, 103-11.

- DEY, N., GHOSH-CHOUDHURY, N., KASINATH, B. S. & CHOUDHURY, G. G. 2012. TGFbeta-stimulated microRNA-21 utilizes PTEN to orchestrate AKT/mTORC1 signaling for mesangial cell hypertrophy and matrix expansion. *PLoS One*, 7, e42316.
- DIXSON, A. C., DAWSON, T. R., DI VIZIO, D. & WEAVER, A. M. 2023. Context-specific regulation of extracellular vesicle biogenesis and cargo selection. *Nat Rev Mol Cell Biol*, 24, 454-476.
- DONG, L., HUANG, C. Y., JOHNSON, E. J., YANG, L., ZIEREN, R. C., HORIE, K., KIM, C. J., WARREN, S., AMEND, S. R., XUE, W. & PIENTA, K. J. 2021. High-Throughput Simultaneous mRNA Profiling Using nCounter Technology Demonstrates That Extracellular Vesicles Contain Different mRNA Transcripts Than Their Parental Prostate Cancer Cells. *Anal Chem*, 93, 3717-3725.
- DONG, X., JIANG, D., WANG, L., ZHAO, J., YU, L., HUANG, Y., WU, X., ZHU, Y., ZHAO, Y., ZHAO, Q., ZHANG, G. & LI, X. 2022. VPS28 regulates brain vasculature by controlling neuronal VEGF trafficking through extracellular vesicle secretion. *iScience*, 25, 104042.
- DONG, X., ZHAO, B., IACOB, R. E., ZHU, J., KOKSAL, A. C., LU, C., ENGEN, J. R. & SPRINGER, T. A. 2017. Force interacts with macromolecular structure in activation of TGF-beta. *Nature*, 542, 55-59.
- DRAGOVIC, R. A., GARDINER, C., BROOKS, A. S., TANNETTA, D. S., FERGUSON, D. J., HOLE, P., CARR, B., REDMAN, C. W., HARRIS, A. L., DOBSON, P. J., HARRISON, P. & SARGENT, I. L. 2011. Sizing and phenotyping of cellular vesicles using Nanoparticle Tracking Analysis. *Nanomedicine*, 7, 780-8.
- DUIJVESZ, D., RODRIGUEZ-BLANCO, G., HOOGLAND, A. M., VERHOEF, E. I., DEKKER, L. J., ROOBOL, M. J., VAN LEENDERS, G., LUIDER, T. M. & JENSTER, G. 2019. Differential tissue expression of extracellular vesicle-derived proteins in prostate cancer. *Prostate*, 79, 1032-1042.
- DURMAZ, E., DRIBIKA, L., KUTNYANSZKY, M. & MEAD, B. 2024. Utilizing extracellular vesicles as a drug delivery system in glaucoma and RGC degeneration. *Journal of Controlled Release*, 372, 209-220.
- EAVES, L. A., GARDNER, A. J. & FRY, R. C. 2020. Tools for the assessment of epigenetic regulation. *Environmental Epigenetics in Toxicology and Public Health*.
- EDEN, E. R., HUANG, F., SORKIN, A. & FUTTER, C. E. 2012. The role of EGF receptor ubiquitination in regulating its intracellular traffic. *Traffic*, 13, 329-37.
- EDER, T., WEBER, A., NEUWIRT, H., GRUNBACHER, G., PLONER, C., KLOCKER, H., SAMPSON, N. & EDER, I. E. 2016. Cancer-Associated Fibroblasts Modify the Response of Prostate Cancer Cells to Androgen and Anti-Androgens in Three-Dimensional Spheroid Culture. *Int J Mol Sci*, 17.
- EGEVAD, L., DELAHUNT, B., FURUSATO, B., TSUZUKI, T., YAXLEY, J. & SAMARATUNGA, H. 2020. Benign mimics of prostate cancer. *Pathology*.
- EIKESDAL, H. P., BECKER, L. M., TENG, Y., KIZU, A., CARSTENS, J. L., KANASAKI, K., SUGIMOTO, H., LEBLEU, V. S. & KALLURI, R. 2018. BMP7 Signaling in TGFBR2-Deficient Stromal Cells Provokes Epithelial Carcinogenesis. *Mol Cancer Res*, 16, 1568-1578.
- EIRO, N., FERNANDEZ-GOMEZ, J., SACRISTAN, R., FERNANDEZ-GARCIA, B., LOBO, B., GONZALEZ-SUAREZ, J., QUINTAS, A., ESCAF, S. & VIZOSO, F. J. 2017. Stromal factors involved in human prostate cancer development, progression and castration resistance. *J Cancer Res Clin Oncol*, 143, 351-359.
- EIRO, N., FERNANDEZ-GOMEZ, J. M., GONZALEZ-RUIZ DE LEON, C., FRAILE, M., GONZALEZ-SUAREZ, J., LOBO-RODRIGUEZ, B., GARCIA-RODRIGUEZ, J., ESCAF, S. & VIZOSO, F. J. 2022. Gene Expression Profile of Stromal Factors in Cancer-Associated Fibroblasts from Prostate Cancer. *Diagnostics (Basel)*, 12.
- EL-SAYED, I. Y., DAHER, A., DESTOUCHES, D., FIRLEJ, V., KOSTALLARI, E., MAILLE, P., HUET, E., HAIDAR-AHMAD, N., JENSTER, G., DE LA TAILLE, A., ABOU MERHI, R., TERRY, S. & VACHEROT, F. 2017. Extracellular vesicles released by mesenchymal-like prostate carcinoma cells modulate EMT state of recipient epithelial-like carcinoma cells through regulation of AR signaling. *Cancer Lett*, 410, 100-111.
- ELSHARKASY, O. M., NORDIN, J. Z., HAGEY, D. W., DE JONG, O. G., SCHIFFELERS, R. M., ANDALOUSSI, S. E. & VADER, P. 2020. Extracellular vesicles as drug delivery systems: Why and how? *Adv Drug Deliv Rev*, 159, 332-343.

- ELYADA, E., BOLISETTY, M., LAISE, P., FLYNN, W. F., COURTOIS, E. T., BURKHART, R. A., TEINOR, J. A., BELLEAU, P., BIFFI, G., LUCITO, M. S., SIVAJOTHI, S., ARMSTRONG, T. D., ENGLE, D. D., YU, K. H., HAO, Y., WOLFGANG, C. L., PARK, Y., PREALL, J., JAFFEE, E. M., CALIFANO, A., ROBSON, P. & TUVESON, D. A. 2019. Cross-Species Single-Cell Analysis of Pancreatic Ductal Adenocarcinoma Reveals Antigen-Presenting Cancer-Associated Fibroblasts. *Cancer Discov*, 9, 1102-1123.
- EPSTEIN, J. I. 2018. Prostate cancer grading: a decade after the 2005 modified system. *Mod Pathol*, 31, S47-63.
- EPSTEIN, J. I., ZELEFSKY, M. J., SJOBERG, D. D., NELSON, J. B., EGEVAD, L., MAGI-GALLUZZI, C., VICKERS, A. J., PARWANI, A. V., REUTER, V. E., FINE, S. W., EASTHAM, J. A., WIKLUND, P., HAN, M., REDDY, C. A., CIEZKI, J. P., NYBERG, T. & KLEIN, E. A. 2016. A Contemporary Prostate Cancer Grading System: A Validated Alternative to the Gleason Score. *Eur Urol*, 69, 428-35.
- ERDOGAN, B., AO, M., WHITE, L. M., MEANS, A. L., BREWER, B. M., YANG, L., WASHINGTON, M. K., SHI, C., FRANCO, O. E., WEAVER, A. M., HAYWARD, S. W., LI, D. & WEBB, D. J. 2017. Cancer-associated fibroblasts promote directional cancer cell migration by aligning fibronectin. *J Cell Biol*, 216, 3799-3816.
- EREZ, N., TRUITT, M., OLSON, P., ARRON, S. T. & HANAHAN, D. 2010. Cancer-Associated Fibroblasts Are Activated in Incipient Neoplasia to Orchestrate Tumor-Promoting Inflammation in an NF-kappaB-Dependent Manner. *Cancer Cell*, 17, 135-47.
- EROZENCI, L. A., PHAM, T. V., PIERSMA, S. R., DITS, N. F. J., JENSTER, G. W., VAN ROYEN, M. E., MOORSELAAR, R. J. A., JIMENEZ, C. R. & BIJNSDORP, I. V. 2021. Simple urine storage protocol for extracellular vesicle proteomics compatible with at-home self-sampling. *Sci Rep*, 11, 20760.
- FALGUIERES, T., CASTLE, D. & GRUENBERG, J. 2012. Regulation of the MVB pathway by SCAMP3. *Traffic*, 13, 131-42.
- FAN, S. J., KROEGER, B., MARIE, P. P., BRIDGES, E. M., MASON, J. D., MCCORMICK, K., ZOIS, C. E., SHELDON, H., KHALID ALHAM, N., JOHNSON, E., ELLIS, M., STEFANA, M. I., MENDES, C. C., WAINWRIGHT, S. M., CUNNINGHAM, C., HAMDY, F. C., MORRIS, J. F., HARRIS, A. L., WILSON, C. & GOBERDHAN, D. C. 2020. Glutamine deprivation alters the origin and function of cancer cell exosomes. *Embo j*, 39, e103009.
- FAN, Y., PIONNEAU, C., COCOZZA, F., BOELLE, P. Y., CHARDONNET, S., CHARRIN, S., THERY, C., ZIMMERMANN, P. & RUBINSTEIN, E. 2023. Differential proteomics argues against a general role for CD9, CD81 or CD63 in the sorting of proteins into extracellular vesicles. *J Extracell Vesicles*, 12, e12352.
- FANKHAUSER, C. D., PARRY, M. G., ALI, A., COWLING, T. E., NOSSITER, J., SUJENTHIRAN, A., BERRY, B., MORRIS, M., AGGARWAL, A., PAYNE, H., VAN DER MEULEN, J. & CLARKE, N. W. 2023. A low prostate specific antigen predicts a worse outcome in high but not in low/intermediate-grade prostate cancer. *European Journal of Cancer*, 181, 70-78.
- FENG, L., HOLLSTEIN, M. & XU, Y. 2006. Ser46 phosphorylation regulates p53-dependent apoptosis and replicative senescence. *Cell Cycle*, 5, 2812-9.
- FENSTER, S. D., KESSELS, M. M., QUALMANN, B., CHUNG, W. J., NASH, J., GUNDELFINGER, E. D. & GARNER, C. C. 2003. Interactions between Piccolo and the actin/dynamin-binding protein Abp1 link vesicle endocytosis to presynaptic active zones. *J Biol Chem*, 278, 20268-77.
- FERREIRA, J. V., DA ROSA SOARES, A., RAMALHO, J., MÁXIMO CARVALHO, C., CARDOSO, M. H., PINTADO, P., CARVALHO, A. S., BECK, H. C., MATTHIESEN, R., ZUZARTE, M., GIRÃO, H., VAN NIEL, G. & PEREIRA, P. 2022. LAMP2A regulates the loading of proteins into exosomes. *Sci Adv*, 8, eabm1140.
- FIRKOWSKA, M., MACIAS, M. & JAWORSKI, J. 2019. ESCRT Proteins Control the Dendritic Morphology of Developing and Mature Hippocampal Neurons. *Mol Neurobiol*, 56, 4866-4879.
- FOJ, L., FERRER, F., SERRA, M., AREVALO, A., GAVAGNACH, M., GIMENEZ, N. & FILELLA, X. 2017. Exosomal and Non-Exosomal Urinary miRNAs in Prostate Cancer Detection and Prognosis. *Prostate*, 77, 573-583.

- FUJITA, K., KUME, H., MATSUZAKI, K., KAWASHIMA, A., UJIKE, T., NAGAHARA, A., UEMURA, M., MIYAGAWA, Y., TOMONAGA, T. & NONOMURA, N. 2017. Proteomic analysis of urinary extracellular vesicles from high Gleason score prostate cancer. *Sci Rep*, 7, 42961.
- FUJITA, K. & NONOMURA, N. 2018. Urinary biomarkers of prostate cancer. *Int J Urol*, 25, 770-779.
- FULLER, C. W., MIDDENDORF, L. R., BENNER, S. A., CHURCH, G. M., HARRIS, T., HUANG, X., JOVANOVIĆ, S. B., NELSON, J. R., SCHLOSS, J. A., SCHWARTZ, D. C. & VEZENOV, D. V. 2009. The challenges of sequencing by synthesis. *Nat Biotechnol*, 27, 1013-23.
- GAGGIOLI, C., HOOPER, S., HIDALGO-CARCEDO, C., GROSSE, R., MARSHALL, J. F., HARRINGTON, K. & SAHAI, E. 2007. Fibroblast-led collective invasion of carcinoma cells with differing roles for RhoGTPases in leading and following cells. *Nat Cell Biol*, 9, 1392-400.
- GALLEGO ROMERO, I., PAI, A. A., TUNG, J. & GILAD, Y. 2014. RNA-seq: impact of RNA degradation on transcript quantification. *BMC Biol*, 12, 42.
- GANESH, K., BASNET, H., KAYGUSUZ, Y., LAUGHNEY, A. M., HE, L., SHARMA, R., O'ROURKE, K. P., REUTER, V. P., HUANG, Y. H., TURKEKUL, M., ER, E. E., MASILIONIS, I., MANOVA-TODOROVA, K., WEISER, M. R., SALTZ, L. B., GARCIA-AGUILAR, J., KOCHER, R., LOWE, S. W., PE'ER, D., SHIA, J. & MASSAGUE, J. 2020. L1CAM defines the regenerative origin of metastasis-initiating cells in colorectal cancer. *Nat Cancer*, 1, 28-45.
- GARCIA-CAMPOS, M. A., ESPINAL-ENRIQUEZ, J. & HERNANDEZ-LEMUS, E. 2015. Pathway Analysis: State of the Art. *Front Physiol*, 6, 383.
- GARCIA-SILVA, S., BENITO-MARTIN, A., NOGUES, L., HERNANDEZ-BARRANCO, A., MAZARIEGOS, M. S., SANTOS, V., HERGUETA-REDONDO, M., XIMENEZ-EMBUN, P., KATARU, R. P., LOPEZ, A. A., MERINO, C., SANCHEZ-REDONDO, S., GRANA-CASTRO, O., MATEI, I., NICOLAS-AVILA, J. A., TORRES-RUIZ, R., RODRIGUEZ-PERALES, S., MARTINEZ, L., PEREZ-MARTINEZ, M., MATA, G., SZUMERA-CIECKIEWICZ, A., KALINOWSKA, I., SALTARI, A., MARTINEZ-GOMEZ, J. M., HOGAN, S. A., SARAGOVI, H. U., ORTEGA, S., GARCIA-MARTIN, C., BOSKOVIC, J., LEVESQUE, M. P., RUTKOWSKI, P., HIDALGO, A., MUNOZ, J., MEGIAS, D., MEHRARA, B. J., LYDEN, D. & PEINADO, H. 2021. Melanoma-derived small extracellular vesicles induce lymphangiogenesis and metastasis through an NGFR-dependent mechanism. *Nat Cancer*, 2, 1387-1405.
- GÉZSI, A., KOVÁCS, Á., VISNOVITZ, T. & BUZÁS, E. I. 2019. Systems biology approaches to investigating the roles of extracellular vesicles in human diseases. *Experimental & Molecular Medicine*, 51, 1-11.
- Ghoshal, B., Bertrand, E. and Bhattacharyya, S.N. 2021. Non-canonical argonaute loading of extracellular vesicle-derived exogenous single-stranded miRNA in recipient cells. *Journal of Cell Science*, 134(9). doi:<https://doi.org/10.1242/jcs.253914>.
- GILLESSEN, S., ATTARD, G., BEER, T. M., BELTRAN, H., BJARTELL, A., BOSSI, A., BRIGANTI, A., BRISTOW, R. G., CHI, K. N., CLARKE, N., DAVIS, I. D., DE BONO, J., DRAKE, C. G., DURAN, I., EELES, R., EFSTATHIOU, E., EVANS, C. P., FANTI, S., FENG, F. Y., FIZAZI, K., FRYDENBERG, M., GLEAVE, M., HALABI, S., HEIDENREICH, A., HEINRICH, D., HIGANO, C. T. S., HOFMAN, M. S., HUSSAIN, M., JAMES, N., KANESVARAN, R., KANTOFF, P., KHAULI, R. B., LEIBOWITZ, R., LOGOTHETIS, C., MALUF, F., MILLMAN, R., MORGANS, A. K., MORRIS, M. J., MOTTET, N., MRABTI, H., MURPHY, D. G., MURTHY, V., OH, W. K., OST, P., O'SULLIVAN, J. M., PADHANI, A. R., PARKER, C., POON, D. M. C., PRITCHARD, C. C., REITER, R. E., ROACH, M., RUBIN, M., RYAN, C. J., SAAD, F., SADE, J. P., SARTOR, O., SCHER, H. I., SHORE, N., SMALL, E., SMITH, M., SOULE, H., STERNBERG, C. N., STEUBER, T., SUZUKI, H., SWEENEY, C., SYDES, M. R., TAPLIN, M. E., TOMBAL, B., TURKERI, L., VAN OORT, I., ZAPATERO, A. & OMLIN, A. 2020. Management of Patients with Advanced Prostate Cancer: Report of the Advanced Prostate Cancer Consensus Conference 2019. *Eur Urol*, 77, 508-547.
- GNANAPRAGASAM, V. J., BRATT, O., MUIR, K., LEE, L. S., HUANG, H. H., STATIN, P. & LOPHATANANON, A. 2018. The Cambridge Prognostic Groups for improved prediction of disease mortality at diagnosis in primary non-metastatic prostate cancer: a validation study. *BMC Med*, 16, 31.

- GOC, A., SABBINENI, H., ABDALLA, M. & SOMANATH, P. R. 2015. p70 S6-kinase mediates the cooperation between Akt1 and Mek1 pathways in fibroblast-mediated extracellular matrix remodeling. *Biochim Biophys Acta*, 1853, 1626-35.
- <https://www.gov.uk/government/news/biggest-prostate-cancer-screening-trial-in-decades-to-start-in-uk> [accessed 02.01.2024]
- GOICHEVA, V., WANG, H. W., GADEA, B. B., SHREE, T., HUNTER, K. E., GARFALL, A. L., BERMAN, T. & JOYCE, J. A. 2010. IL-4 induces cathepsin protease activity in tumor-associated macrophages to promote cancer growth and invasion. *Genes Dev*, 24, 241-55.
- GONG, Y., SCOTT, E., LU, R., XU, Y., OH, W. K. & YU, Q. 2013. TIMP-1 promotes accumulation of cancer associated fibroblasts and cancer progression. *PLoS One*, 8, e77366.
- GORDETSKY, J. B., SCHAFFER, K. & HURLEY, P. J. 2022. Current conundrums with cribriform prostate cancer. *Histopathology*, 80, 1038-1040.
- GREER, M. D., SHIH, J. H., LAY, N., BARRETT, T., KAYAT BITTENCOURT, L., BOROFSKY, S., KABAKUS, I. M., LAW, Y. M., MARKO, J., SHEBEL, H., MERTAN, F. V., MERINO, M. J., WOOD, B. J., PINTO, P. A., SUMMERS, R. M., CHOYKE, P. L. & TURKBELY, B. 2017. Validation of the Dominant Sequence Paradigm and Role of Dynamic Contrast-enhanced Imaging in PI-RADS Version 2. *Radiology*, 285, 859-869.
- GRIFFITHS, D., CARNELL-MORRIS, P. & WRIGHT, M. 2020. Nanoparticle Tracking Analysis for Multiparameter Characterization and Counting of Nanoparticle Suspensions. *Methods Mol Biol*, 2118, 289-303.
- GRIGORIEV, I., SPLINTER, D., KEIJZER, N., WULF, P. S., DEMMERS, J., OHTSUKA, T., MODESTI, M., MALY, I. V., GROSVELD, F., HOOGENRAAD, C. C. & AKHMANOVA, A. 2007. Rab6 regulates transport and targeting of exocytotic carriers. *Dev Cell*, 13, 305-14.
- GRIGORIEV, I., YU, K. L., MARTINEZ-SANCHEZ, E., SERRA-MARQUES, A., SMAL, I., MEIJERING, E., DEMMERS, J., PERANEN, J., PASTERKAMP, R. J., VAN DER SLUIJS, P., HOOGENRAAD, C. C. & AKHMANOVA, A. 2011. Rab6, Rab8, and MICAL3 cooperate in controlling docking and fusion of exocytotic carriers. *Curr Biol*, 21, 967-74.
- GROSS, J. C., CHAUDHARY, V., BARTSCHERER, K. & BOUTROS, M. 2012. Active Wnt proteins are secreted on exosomes. *Nat Cell Biol*, 14, 1036-45.
- GUNGOR, M. Z., UYSAL, M. & SENTURK, S. 2022. The Bright and the Dark Side of TGF-beta Signaling in Hepatocellular Carcinoma: Mechanisms, Dysregulation, and Therapeutic Implications. *Cancers (Basel)*, 14.
- HAMDY, F. C., DONOVAN, J. L., LANE, J. A., MASON, M., METCALFE, C., HOLDING, P., DAVIS, M., PETERS, T. J., TURNER, E. L., MARTIN, R. M., OXLEY, J., ROBINSON, M., STAFFURTH, J., WALSH, E., BOLLINA, P., CATTO, J., DOBLE, A., DOHERTY, A., GILLATT, D., KOCKELBERGH, R., KYNASTON, H., PAUL, A., POWELL, P., PRESCOTT, S., ROSARIO, D. J., ROWE, E., NEAL, D. E. & PROTEC, T. S. G. 2016. 10-Year Outcomes after Monitoring, Surgery, or Radiotherapy for Localized Prostate Cancer. *N Engl J Med*, 375, 1415-1424.
- HANAHAH, D. & WEINBERG, R. A. 2011. Hallmarks of cancer: the next generation. *Cell*, 144, 646-74.
- HÄNZELMANN, S., CASTELO, R. & GUINNEY, J. 2013. GSVA: gene set variation analysis for microarray and RNA-Seq data. *BMC Bioinformatics*, 14, 7.
- HARTJES, T. A., SLOTMAN, J. A., VREDENBREGT, M. S., DITS, N., VAN DER MEEL, R., DUIJVESZ, D., KULKARNI, J. A., FRENCH, P. J., VAN CAPPELLEN, W. A., SCHIFFELERS, R. M., HOUTSMULLER, A. B., JENSTER, G. W. & VAN ROYEN, M. E. 2020. EVQuant; high-throughput quantification and characterization of extracellular vesicle (sub)populations. *bioRxiv*, 2020.10.21.348375.
- HENDRIX, A., LIPPENS, L., PINHEIRO, C., THÉRY, C., MARTIN-JAULAR, L., LÖTVALL, J., LÄSSER, C., HILL, A. F. & WITWER, K. W. 2023. Extracellular vesicle analysis. *Nature Reviews Methods Primers*, 3.

- HESSVIK, N. P., PHUYAL, S., BRECH, A., SANDVIG, K. & LLORENTE, A. 2012. Profiling of microRNAs in exosomes released from PC-3 prostate cancer cells. *Biochimica et Biophysica Acta (BBA) - Gene Regulatory Mechanisms*, 1819, 1154-1163.
- HESSVIK, N. P., SAGINI, K., ROMERO, S., RAMIREZ-GARRASTACHO, M., RODRIGUEZ, M., TUTTUREN, A. E. V., KVALVAAG, A., STANG, E., BRECH, A., SANDVIG, K. & LLORENTE, A. 2023. siRNA screening reveals that SNAP29 contributes to exosome release. *Cell Mol Life Sci*, 80, 177.
- HINZ, B., CELETTA, G., TOMASEK, J. J., GABBIANI, G. & CHAPONNIER, C. 2001. Alpha-smooth muscle actin expression upregulates fibroblast contractile activity. *Mol Biol Cell*, 12, 2730-41.
- HIRZ, T., MEI, S., SARKAR, H., KFOURY, Y., WU, S., VERHOEVEN, B. M., SUBTELNY, A. O., ZLATEV, D. V., WSZOLEK, M. W., SALARI, K., MURRAY, E., CHEN, F., MACOSKO, E. Z., WU, C. L., SCADDEN, D. T., DAHL, D. M., BARYAWNO, N., SAYLOR, P. J., KHARCHENKO, P. V. & SYKES, D. B. 2023. Dissecting the immune suppressive human prostate tumor microenvironment via integrated single-cell and spatial transcriptomic analyses. *Nat Commun*, 14, 663.
- HOSAKA, K., YANG, Y., SEKI, T., FISCHER, C., DUBEY, O., FREDLUND, E., HARTMAN, J., RELIGA, P., MORIKAWA, H., ISHII, Y., SASAHARA, M., LARSSON, O., COSSU, G., CAO, R., LIM, S. & CAO, Y. 2016. Pericyte-fibroblast transition promotes tumor growth and metastasis. *Proc Natl Acad Sci U S A*, 113, E5618-27.
- HOSHINO, A., COSTA-SILVA, B., SHEN, T. L., RODRIGUES, G., HASHIMOTO, A., TESIC MARK, M., MOLINA, H., KOHSAKA, S., DI GIANNATALE, A., CEDER, S., SINGH, S., WILLIAMS, C., SOPLOP, N., URYU, K., PHARMER, L., KING, T., BOJMAR, L., DAVIES, A. E., ARARSO, Y., ZHANG, T., ZHANG, H., HERNANDEZ, J., WEISS, J. M., DUMONT-COLE, V. D., KRAMER, K., WEXLER, L. H., NARENDRAN, A., SCHWARTZ, G. K., HEALEY, J. H., SANDSTROM, P., LABORI, K. J., KURE, E. H., GRANDGENETT, P. M., HOLLINGSWORTH, M. A., DE SOUSA, M., KAUR, S., JAIN, M., MALLYA, K., BATRA, S. K., JARNAGIN, W. R., BRADY, M. S., FODSTAD, O., MULLER, V., PANTEL, K., MINN, A. J., BISSELL, M. J., GARCIA, B. A., KANG, Y., RAJASEKHAR, V. K., GHAJAR, C. M., MATEI, I., PEINADO, H., BROMBERG, J. & LYDEN, D. 2015. Tumour exosome integrins determine organotropic metastasis. *Nature*, 527, 329-35.
- HOSSEINI-BEHESHTI, E., PHAM, S., ADOMAT, H., LI, N. & TOMLINSON GUNS, E. S. 2012. Exosomes as biomarker enriched microvesicles: characterization of exosomal proteins derived from a panel of prostate cell lines with distinct AR phenotypes. *Mol Cell Proteomics*, 11, 863-85.
- HSU, C., MOROHASHI, Y., YOSHIMURA, S., MANRIQUE-HOYOS, N., JUNG, S., LAUTERBACH, M. A., BAKHTI, M., GRØNBORG, M., MÖBIUS, W., RHEE, J., BARR, F. A. & SIMONS, M. 2010. Regulation of exosome secretion by Rab35 and its GTPase-activating proteins TBC1D10A-C. *J Cell Biol*, 189, 223-32.
- HSU, Y. L., HUANG, M. S., HUNG, J. Y., CHANG, W. A., TSAI, Y. M., PAN, Y. C., LIN, Y. S., TSAI, H. P. & KUO, P. L. 2020. Bone-marrow-derived cell-released extracellular vesicle miR-92a regulates hepatic pre-metastatic niche in lung cancer. *Oncogene*, 39, 739-753.
- [HTTPS://GCO.IARC.FR](https://GCO.IARC.FR). 2024. Available: <https://gco.iarc.fr> [Accessed 03.01.2024].
- HUANG, Q., HSUEH, C. Y., SHEN, Y. J., GUO, Y., HUANG, J. M., ZHANG, Y. F., LI, J. Y., GONG, H. L. & ZHOU, L. 2021. Small extracellular vesicle-packaged TGFbeta1 promotes the reprogramming of normal fibroblasts into cancer-associated fibroblasts by regulating fibronectin in head and neck squamous cell carcinoma. *Cancer Lett*, 517, 1-13.
- HUANG, S., OUYANG, N., LIN, L., CHEN, L., WU, W., SU, F., YAO, Y. & YAO, H. 2012. HGF-induced PKCzeta activation increases functional CXCR4 expression in human breast cancer cells. *PLoS One*, 7, e29124.
- HUANG, X., YUAN, T., LIANG, M., DU, M., XIA, S., DITTMAR, R., WANG, D., SEE, W., COSTELLO, B. A., QUEVEDO, F., TAN, W., NANDY, D., BEVAN, G. H., LONGENBACH, S., SUN, Z., LU, Y., WANG, T., THIBODEAU, S. N., BOARDMAN, L., KOHLI, M. & WANG, L. 2015. Exosomal miR-1290 and miR-375 as prognostic markers in castration-resistant prostate cancer. *Eur Urol*, 67, 33-41.
- HUANG, Y. H., HU, J., CHEN, F., LECOMTE, N., BASNET, H., DAVID, C. J., WITKIN, M. D., ALLEN, P. J., LEACH, S. D., HOLLMANN, T. J., IACOBUIZIO-DONAHUE, C. A. & MASSAGUE, J. 2020. ID1

- Mediates Escape from TGFbeta Tumor Suppression in Pancreatic Cancer. *Cancer Discov*, 10, 142-157.
- HUANG, Z., YANG, M., LI, Y., YANG, F. & FENG, Y. 2018. Exosomes Derived from Hypoxic Colorectal Cancer Cells Transfer Wnt4 to Normoxic Cells to Elicit a Prometastatic Phenotype. *Int J Biol Sci*, 14, 2094-2102.
- HUNG, M. E. & LEONARD, J. N. 2016. A platform for actively loading cargo RNA to elucidate limiting steps in EV-mediated delivery. *J Extracell Vesicles*, 5, 31027.
- HUNT, J. M. T., SAMSON, C. A., RAND, A. D. & SHEPPARD, H. M. 2023. Unintended CRISPR-Cas9 editing outcomes: a review of the detection and prevalence of structural variants generated by gene-editing in human cells. *Hum Genet*, 142, 705-720.
- HURWITZ, S. N., CONLON, M. M., RIDER, M. A., BROWNSTEIN, N. C. & MECKES, D. G. 2016a. Nanoparticle analysis sheds budding insights into genetic drivers of extracellular vesicle biogenesis. *Journal of Extracellular Vesicles*, 5, 31295.
- HURWITZ, S. N., NKOSI, D., CONLON, M. M., YORK, S. B., LIU, X., TREMBLAY, D. C. & MECKES, D. G. 2017. CD63 Regulates Epstein-Barr Virus LMP1 Exosomal Packaging, Enhancement of Vesicle Production, and Noncanonical NF- κ B Signaling. *Journal of Virology*, 91, JVI.02251-16.
- HURWITZ, S. N., RIDER, M. A., BUNDY, J. L., LIU, X., SINGH, R. K. & MECKES, D. G., JR. 2016b. Proteomic profiling of NCI-60 extracellular vesicles uncovers common protein cargo and cancer type-specific biomarkers. *Oncotarget*, 7, 86999-87015.
- IBORRA-EGEA, O., GÁLVEZ-MONTÓN, C., ROURA, S., PEREA-GIL, I., PRAT-VIDAL, C., SOLER-BOTIJA, C. & BAYES-GENIS, A. 2017. Mechanisms of action of sacubitril/valsartan on cardiac remodeling: a systems biology approach. *npj Systems Biology and Applications*, 3.
- ICZKOWSKI, K. A., VAN LEENDERS, G., TARIMA, S., WU, R., VAN DER KWAST, T., BERNEY, D. M., EVANS, A. J., WHEELER, T. M., RO, J. Y., SAMARATUNGA, H., DELAHUNT, B., SRIGLEY, J., VARMA, M., TSUZUKI, T. & EGEVAD, L. 2021. Cribriform prostate cancer: Morphologic criteria enabling a diagnosis, based on survey of experts. *Ann Diagn Pathol*, 52, 151733.
- IGUCHI, Y., EID, L., PARENT, M., SOUCY, G., BAREIL, C., RIKU, Y., KAWAI, K., TAKAGI, S., YOSHIDA, M., KATSUNO, M., SOBUE, G. & JULIEN, J. P. 2016. Exosome secretion is a key pathway for clearance of pathological TDP-43. *Brain*, 139, 3187-3201.
- IMJETI, N. S., MENCK, K., EGEA-JIMENEZ, A. L., LECOINTRE, C., LEMBO, F., BOUGUENINA, H., BADACHE, A., GHOSSOUB, R., DAVID, G., ROCHE, S. & ZIMMERMANN, P. 2017. Syntenin mediates SRC function in exosomal cell-to-cell communication. *Proc Natl Acad Sci U S A*, 114, 12495-12500.

informatics.jax.org/vocab/gene_ontology [accessed 08.08.2022]

- INNGJERDINGEN, M., TORGERSEN, K. M. & MAGHAZACHI, A. A. 2002. Lck is required for stromal cell-derived factor 1 alpha (CXCL12)-induced lymphoid cell chemotaxis. *Blood*, 99, 4318-25.
- ISHII, K., SASAKI, T., IGUCHI, K., KAJIWARA, S., KATO, M., KANDA, H., HIROKAWA, Y., ARIMA, K., MIZOKAMI, A. & SUGIMURA, Y. 2018. Interleukin-6 induces VEGF secretion from prostate cancer cells in a manner independent of androgen receptor activation. *Prostate*, 78, 849-856.
- ITTMANN, M. 2018. Anatomy and Histology of the Human and Murine Prostate. *Cold Spring Harb Perspect Med*, 8.
- JAE, N., MCEWAN, D. G., MANAVSKI, Y., BOON, R. A. & DIMMELER, S. 2015. Rab7a and Rab27b control secretion of endothelial microRNA through extracellular vesicles. *FEBS Lett*, 589, 3182-8.
- JAMES, N. D., SYDES, M. R., CLARKE, N. W., MASON, M. D., DEARNALEY, D. P., SPEARS, M. R., RITCHIE, A. W., PARKER, C. C., RUSSELL, J. M., ATTARD, G., DE BONO, J., CROSS, W., JONES, R. J., THALMANN, G., AMOS, C., MATHESON, D., MILLMAN, R., ALZOUEBI, M., BEESLEY, S., BIRTLE, A. J., BROCK, S., CATHOMAS, R., CHAKRABORTI, P., CHOWDHURY, S., COOK, A., ELLIOTT, T., GALE, J., GIBBS, S., GRAHAM, J. D., HETHERINGTON, J., HUGHES, R., LAING, R., MCKINNA, F., MCLAREN, D. B., O'SULLIVAN, J. M., PARIKH, O., PEEDELL, C., PROTHEROE, A., ROBINSON, A. J., SRIHARI, N., SRINIVASAN, R., STAFFURTH, J., SUNDAR, S., TOLAN, S., TSANG, D.,

- WAGSTAFF, J., PARMAR, M. K. & INVESTIGATORS, S. 2016. Addition of docetaxel, zoledronic acid, or both to first-line long-term hormone therapy in prostate cancer (STAMPEDE): survival results from an adaptive, multiarm, multistage, platform randomised controlled trial. *Lancet*, 387, 1163-77.
- JANAS, T., JANAS, M. M., SAPON, K. & JANAS, T. 2015. Mechanisms of RNA loading into exosomes. *FEBS Lett*, 589, 1391-8.
- JASSAL, B., MATTHEWS, L., VITERI, G., GONG, C., LORENTE, P., FABREGAT, A., SIDIROPOULOS, K., COOK, J., GILLESPIE, M., HAW, R., LONEY, F., MAY, B., MILACIC, M., ROTHFELS, K., SEVILLA, C., SHAMOVSKY, V., SHORSER, S., VARUSAI, T., WEISER, J., WU, G., STEIN, L., HERMJAKOB, H. & D'EUSTACHIO, P. 2020. The reactome pathway knowledgebase. *Nucleic Acids Res*, 48, D498-D503.
- JEPPESEN, D. K., FENIX, A. M., FRANKLIN, J. L., HIGGINBOTHAM, J. N., ZHANG, Q., ZIMMERMAN, L. J., LIEBLER, D. C., PING, J., LIU, Q., EVANS, R., FISSELL, W. H., PATTON, J. G., ROME, L. H., BURNETTE, D. T. & COFFEY, R. J. 2019. Reassessment of Exosome Composition. *Cell*, 177, 428-445 e18.
- JIAO, B., AN, C., DU, H., TRAN, M., WANG, P., ZHOU, D. & WANG, Y. 2021. STAT6 Deficiency Attenuates Myeloid Fibroblast Activation and Macrophage Polarization in Experimental Folic Acid Nephropathy. *Cells*, 10.
- JIN, X., WANG, J., WANG, Z., PANG, W., CHEN, Y. & YANG, L. 2024. Chromatin-modifying protein 4C (CHMP4C) affects breast cancer cell growth and doxorubicin resistance as a potential breast cancer therapeutic target. *J Antibiot (Tokyo)*, 77, 93-101.
- JOHNS, L. E. & HOULSTON, R. S. 2003. A systematic review and meta-analysis of familial prostate cancer risk. *BJU Int*, 91, 789-94.
- JOHNSTONE, R. M., MATHEW, A., MASON, A. B. & TENG, K. 1991. Exosome formation during maturation of mammalian and avian reticulocytes: evidence that exosome release is a major route for externalization of obsolete membrane proteins. *J Cell Physiol*, 147, 27-36.
- JOSHI, B. S., DE BEER, M. A., GIEPMANS, B. N. G. & ZUHORN, I. S. 2020. Endocytosis of Extracellular Vesicles and Release of Their Cargo from Endosomes. *ACS Nano*, 14, 4444-4455.
- JUAN, T. & FURTHAUER, M. 2018. Biogenesis and function of ESCRT-dependent extracellular vesicles. *Semin Cell Dev Biol*, 74, 66-77.
- KAJIMOTO, T., OKADA, T., MIYA, S., ZHANG, L. & NAKAMURA, S. 2013. Ongoing activation of sphingosine 1-phosphate receptors mediates maturation of exosomal multivesicular endosomes. *Nat Commun*, 4, 2712.
- KAMISASANUKI, T., TOKUSHIGE, S., TERASAKI, H., KHAI, N. C., WANG, Y., SAKAMOTO, T. & KOSAI, K. 2011. Targeting CD9 produces stimulus-independent antiangiogenic effects predominantly in activated endothelial cells during angiogenesis: a novel antiangiogenic therapy. *Biochem Biophys Res Commun*, 413, 128-35.
- KAMRAN, S. C. & ZIETMAN, A. L. 2021. Radiation treatment in prostate cancer: covering the waterfront. *BJU Int*, 128, 398-407.
- KARNOUB, A. E., DASH, A. B., VO, A. P., SULLIVAN, A., BROOKS, M. W., BELL, G. W., RICHARDSON, A. L., POLYAK, K., TUBO, R. & WEINBERG, R. A. 2007. Mesenchymal stem cells within tumour stroma promote breast cancer metastasis. *Nature*, 449, 557-63.
- KASIVISVANATHAN, V., RANNIKKO, A. S., BORGHI, M., PANEBIANCO, V., MYNDERSE, L. A., VAARALA, M. H., BRIGANTI, A., BUDAUS, L., HELLAWELL, G., HINDLEY, R. G., ROOBOL, M. J., EGGNER, S., GHEI, M., VILLERS, A., BLADOU, F., VILLEIRS, G. M., VIRDI, J., BOXLER, S., ROBERT, G., SINGH, P. B., VENDERINK, W., HADASCHIK, B. A., RUFFION, A., HU, J. C., MARGOLIS, D., CROUZET, S., KLOTZ, L., TANEJA, S. S., PINTO, P., GILL, I., ALLEN, C., GIGANTI, F., FREEMAN, A., MORRIS, S., PUNWANI, S., WILLIAMS, N. R., BREW-GRAVES, C., DEEKS, J., TAKWOINGI, Y., EMBERTON, M., MOORE, C. M. & COLLABORATORS, P. S. G. 2018. MRI-Targeted or Standard Biopsy for Prostate-Cancer Diagnosis. *N Engl J Med*, 378, 1767-1777.
- KATO, M., PLACENCIO-HICKOK, V. R., MADHAV, A., HALDAR, S., TRIPATHI, M., BILLET, S., MISHRA, R., SMITH, B., ROHENA-RIVERA, K., AGARWAL, P., DUONG, F., ANGARA, B., HICKOK, D., LIU, Z. &

- BHOWMICK, N. A. 2019. Heterogeneous cancer-associated fibroblast population potentiates neuroendocrine differentiation and castrate resistance in a CD105-dependent manner. *Oncogene*, 38, 716-730.
- KAUR, S., LIVAK, F., DAABOUL, G., ANDERSON, L. & ROBERTS, D. D. 2022. Single vesicle analysis of CD47 association with integrins and tetraspanins on extracellular vesicles released by T lymphoblast and prostate carcinoma cells. *Journal of Extracellular Vesicles*, 11.
- KENNEWEG, F., BANG, C., XIAO, K., BOULANGER, C. M., LOYER, X., MAZLAN, S., SCHROEN, B., HERMANS-BEIJNSBERGER, S., FOINQUINOS, A., HIRT, M. N., ESCHENHAGEN, T., FUNCKE, S., STOJANOVIC, S., GENSCHEL, C., SCHIMMEL, K., JUST, A., PFANNE, A., SCHERF, K., DEHMEL, S., RAEMON-BUETTNER, S. M., FIEDLER, J. & THUM, T. 2019. Long Noncoding RNA-Enriched Vesicles Secreted by Hypoxic Cardiomyocytes Drive Cardiac Fibrosis. *Mol Ther Nucleic Acids*, 18, 363-374.
- KILINC, S., PAISNER, R., CAMARDA, R., GUPTA, S., MOMCILOVIC, O., KOHNZ, R. A., AVSAROGLU, B., L'ETOILE, N. D., PERERA, R. M., NOMURA, D. K. & GOGA, A. 2021. Oncogene-regulated release of extracellular vesicles. *Dev Cell*, 56, 1989-2006 e6.
- KIM, H. I., PARK, J., ZHU, Y., WANG, X., HAN, Y. & ZHANG, D. 2024. Recent advances in extracellular vesicles for therapeutic cargo delivery. *Exp Mol Med*, 56, 836-849.
- KIM, J. Y., JEON, S., YOO, Y. J., JIN, H., WON, H. Y., YOON, K., HWANG, E. S., LEE, Y. J., NA, Y., CHO, J. & LEE, Y. S. 2019. The Hsp27-Mediated Ikbalpha-NFkappaB Signaling Axis Promotes Radiation-Induced Lung Fibrosis. *Clin Cancer Res*, 25, 5364-5375.
- KIOUMOURTZOGLU, D., PRYOR, P. R., GOULD, G. W. & BRYANT, N. J. 2015. Alternative routes to the cell surface underpin insulin-regulated membrane trafficking of GLUT4. *J Cell Sci*, 128, 2423-9.
- KOEPPEN, K., HAMPTON, T. H., BARNABY, R., ROCHE, C., GERBER, S. A., GOO, Y. A., CHO, B. K., VERMILYEA, D. M., HOGAN, D. A. & STANTON, B. A. 2023. An rRNA fragment in extracellular vesicles secreted by human airway epithelial cells increases the fluoroquinolone sensitivity of *P. aeruginosa*. *Am J Physiol Lung Cell Mol Physiol*, 325, L54-L65.
- KONERMANN, S., LOTFY, P., BRIDEAU, N. J., OKI, J., SHOKHIREV, M. N. & HSU, P. D. 2018. Transcriptome Engineering with RNA-Targeting Type VI-D CRISPR Effectors. *Cell*, 173, 665-676 e14.
- KOPONEN, A., KERKELÄ, E., ROJALIN, T., LÁZARO-IBÁÑEZ, E., SUUTARI, T., SAARI, H. O., SILJANDER, P., YLIPERTTULA, M., LAITINEN, S. & VIITALA, T. 2020. Label-free characterization and real-time monitoring of cell uptake of extracellular vesicles. *Biosensors and Bioelectronics*, 168, 112510.
- KRISHN, S. R., SALEM, I., QUAGLIA, F., NARANJO, N. M., AGARWAL, E., LIU, Q., SARKER, S., KOPENHAVER, J., MCCUE, P. A., WEINREB, P. H., VIOLETTE, S. M., ALTIERI, D. C. & LANGUINO, L. R. 2020. The alphavbeta6 integrin in cancer cell-derived small extracellular vesicles enhances angiogenesis. *J Extracell Vesicles*, 9, 1763594.
- KUGERATSKI, F. G., HODGE, K., LILLA, S., MCANDREWS, K. M., ZHOU, X., HWANG, R. F., ZANIVAN, S. & KALLURI, R. 2021. Quantitative proteomics identifies the core proteome of exosomes with syntenin-1 as the highest abundant protein and a putative universal biomarker. *Nat Cell Biol*, 23, 631-641.
- KULKARNI, A. A., THATCHER, T. H., OLSEN, K. C., MAGGIRWAR, S. B., PHIPPS, R. P. & SIME, P. J. 2011. PPAR-gamma ligands repress TGFbeta-induced myofibroblast differentiation by targeting the PI3K/Akt pathway: implications for therapy of fibrosis. *PLoS One*, 6, e15909.
- KUMAR, A., KUMAR, P., SHARMA, M., KIM, S., SINGH, S., KRIDEL, S. J. & DEEP, G. 2022. Role of extracellular vesicles secretion in paclitaxel resistance of prostate cancer cells. *Cancer Drug Resist*, 5, 612-624.
- KUMAR, D., NEW, J., VISHWAKARMA, V., JOSHI, R., ENDERS, J., LIN, F., DASARI, S., GUTIERREZ, W. R., LEEF, G., PONNURANGAM, S., CHAVAN, H., GANADEN, L., THORNTON, M. M., DAI, H., TAWFIK, O., STRAUB, J., SHNAYDER, Y., KAKARALA, K., TSUE, T. T., GIROD, D. A., VAN HOUTEN, B., ANANT, S., KRISHNAMURTHY, P. & THOMAS, S. M. 2018. Cancer-Associated

- Fibroblasts Drive Glycolysis in a Targetable Signaling Loop Implicated in Head and Neck Squamous Cell Carcinoma Progression. *Cancer Res*, 78, 3769-3782.
- KUMAR, R., TANG, Q., MULLER, S. A., GAO, P., MAHLSTEDT, D., ZAMPAGNI, S., TAN, Y., KLINGL, A., BOTZEL, K., LICHTENTHALER, S. F., HOGLINGER, G. U. & KOEGLSPERGER, T. 2020. Fibroblast Growth Factor 2-Mediated Regulation of Neuronal Exosome Release Depends on VAMP3/Cellubrevin in Hippocampal Neurons. *Adv Sci (Weinh)*, 7, 1902372.
- LAMPARSKI, H. G., METHA-DAMANI, A., YAO, J.-Y., PATEL, S., HSU, D.-H., RUEGG, C. & LE PECQ, J.-B. 2002. Production and characterization of clinical grade exosomes derived from dendritic cells. *Journal of Immunological Methods*, 270, 211-226.
- LANG, J., ZHAO, X., QI, Y., ZHANG, Y., HAN, X., DING, Y., GUAN, J., JI, T., ZHAO, Y. & NIE, G. 2019. Reshaping Prostate Tumor Microenvironment To Suppress Metastasis via Cancer-Associated Fibroblast Inactivation with Peptide-Assembly-Based Nanosystem. *ACS Nano*, 13, 12357-12371.
- LAUFMAN, O., HONG, W. & LEV, S. 2011. The COG complex interacts directly with Syntaxin 6 and positively regulates endosome-to-TGN retrograde transport. *J Cell Biol*, 194, 459-72.
- LAVIE, D., BEN-SHMUEL, A., EREZ, N. & SCHERZ-SHOVAL, R. 2022. Cancer-associated fibroblasts in the single-cell era. *Nat Cancer*, 3, 793-807.
- LAWSON, P., SHOLL, A. B., BROWN, J. Q., FASY, B. T. & WENK, C. 2019. Persistent Homology for the Quantitative Evaluation of Architectural Features in Prostate Cancer Histology. *Sci Rep*, 9, 1139.
- LAZARO-IBANEZ, E., LUNAVAT, T. R., JANG, S. C., ESCOBEDO-LUCEA, C., OLIVER-DE LA CRUZ, J., SILJANDER, P., LOTVALL, J. & YLIPERTTULA, M. 2017. Distinct prostate cancer-related mRNA cargo in extracellular vesicle subsets from prostate cell lines. *BMC Cancer*, 17, 92.
- LÁZARO-IBÁÑEZ, E., NEUVONEN, M., TAKATALO, M., THANIGAI ARASU, U., CAPASSO, C., CERULLO, V., RHIM, J. S., RILLA, K., YLIPERTTULA, M. & SILJANDER, P. R. M. 2017. Metastatic state of parent cells influences the uptake and functionality of prostate cancer cell-derived extracellular vesicles. *Journal of Extracellular Vesicles*, 6, 1354645.
- LEE, Y., JEONG, M., PARK, J., JUNG, H. & LEE, H. 2023. Immunogenicity of lipid nanoparticles and its impact on the efficacy of mRNA vaccines and therapeutics. *Experimental & Molecular Medicine*, 55, 2085-2096.
- LI, B., REN, M. Y., CHEN, Y. Z., MENG, Y. Q., SONG, T. N., SU, Z. P. & YANG, B. 2022a. SYNGR2 serves as a prognostic biomarker and correlates with immune infiltrates in esophageal squamous cell carcinoma. *J Gene Med*, 24, e3441.
- LI, C., INESS, A., YOON, J., GRIDER, J. R., MURTHY, K. S., KELLUM, J. M. & KUEMMERLE, J. F. 2015a. Noncanonical STAT3 activation regulates excess TGF-beta1 and collagen I expression in muscle of stricturing Crohn's disease. *J Immunol*, 194, 3422-31.
- LI, W., ZHU, H., ZHAO, X., BRANCHO, D., LIANG, Y., ZOU, Y., BENNETT, C. & CHOW, C. W. 2015b. Dysregulated Inflammatory Signaling upon Charcot-Marie-Tooth Type 1C Mutation of SIMPLE Protein. *Mol Cell Biol*, 35, 2464-78.
- LI, X. Q., ZHANG, R., LU, H., YUE, X. M. & HUANG, Y. F. 2022b. Extracellular Vesicle-Packaged CDH11 and ITGA5 Induce the Premetastatic Niche for Bone Colonization of Breast Cancer Cells. *Cancer Res*, 82, 1560-1574.
- LIBERZON, A., BIRGER, C., THORVALDSDOTTIR, H., GHANDI, M., MESIROV, J. P. & TAMAYO, P. 2015. The Molecular Signatures Database (MSigDB) hallmark gene set collection. *Cell Syst*, 1, 417-425.
- LIBERZON, A., SUBRAMANIAN, A., PINCHBACK, R., THORVALDSDOTTIR, H., TAMAYO, P. & MESIROV, J. P. 2011. Molecular signatures database (MSigDB) 3.0. *Bioinformatics*, 27, 1739-40.
- LIN, W., FANG, J., WEI, S., HE, G., LIU, J., LI, X., PENG, X., LI, D., YANG, S., LI, X., YANG, L. & LI, H. 2023. Extracellular vesicle-cell adhesion molecules in tumours: biofunctions and clinical applications. *Cell Commun Signal*, 21, 246.
- LING, C. C., BURMAN, C., CHUI, C. S., KUTCHER, G. J., LEIBEL, S. A., LOSASSO, T., MOHAN, R., BORTFELD, T., REINSTEIN, L., SPIROU, S., WANG, X. H., WU, Q., ZELEFSKY, M. & FUKS, Z. 1996.

- Conformal radiation treatment of prostate cancer using inversely-planned intensity-modulated photon beams produced with dynamic multileaf collimation. *Int J Radiat Oncol Biol Phys*, 35, 721-30.
- LIOW, E., HOWARD, N., JUNG, C. H., POPE, B., CAMPBELL, B. K., NGUYEN, A., KERGER, M., RUDDLE, J. B., ANTON, A., THOMAS, B., CHU, K., DUNDEE, P., PETERS, J. S., COSTELLO, A. J., RYAN, A. S., HOVENS, C. M., TRAN, B. & CORCORAN, N. M. 2022. Phase 2 Study of Neoadjuvant FGFR Inhibition and Androgen Deprivation Therapy Prior to Prostatectomy. *Clin Genitourin Cancer*, 20, 452-458.
- LIPPONEN, P., AALTOMAA, S., TAMMI, R., TAMMI, M., AGREN, U. & KOSMA, V. M. 2001. High stromal hyaluronan level is associated with poor differentiation and metastasis in prostate cancer. *Eur J Cancer*, 37, 849-56.
- LIU, C., YU, S., ZINN, K., WANG, J., ZHANG, L., JIA, Y., KAPPES, J. C., BARNES, S., KIMBERLY, R. P., GRIZZLE, W. E. & ZHANG, H. G. 2006. Murine mammary carcinoma exosomes promote tumor growth by suppression of NK cell function. *J Immunol*, 176, 1375-85.
- LIU, M., LI, Y., ZHANG, C. & ZHANG, Q. 2022. Role of aurora kinase B in regulating resistance to paclitaxel in breast cancer cells. *Hum Cell*, 35, 678-693.
- LOGING, W., RODRIGUEZ-ESTEBAN, R., HILL, J., FREEMAN, T. & MIGLIETTA, J. 2011. Cheminformatic/bioinformatic analysis of large corporate databases: Application to drug repurposing. *Drug Discovery Today: Therapeutic Strategies*, 8, 109-116.
- LÖTVALL, J., HILL, A. F., HOCHBERG, F., BUZÁS, E. I., DI VIZIO, D., GARDINER, C., GHO, Y. S., KUROCHKIN, I. V., MATHIVANAN, S., QUESENBERRY, P., SAHOO, S., TAHARA, H., WAUBEN, M. H., WITWER, K. W. & THÉRY, C. 2014. Minimal experimental requirements for definition of extracellular vesicles and their functions: a position statement from the International Society for Extracellular Vesicles. *J Extracell Vesicles*, 3, 26913.
- LOVE, M. I., HUBER, W. & ANDERS, S. 2014. Moderated estimation of fold change and dispersion for RNA-seq data with DESeq2. *Genome Biol*, 15, 550.
- LU, A., WAWRO, P., MORGENS, D. W., PORTELA, F., BASSIK, M. C. & PFEFFER, S. R. 2018. Genome-wide interrogation of extracellular vesicle biology using barcoded miRNAs. *eLife*, 7, e41460.
- LU, W., ZHANG, J., WU, Y., SUN, W., JIANG, Z. & LUO, X. 2023. Engineered NF- κ B siRNA-encapsulating exosomes as a modality for therapy of skin lesions. *Front Immunol*, 14, 1109381.
- LU, Y., ZHAO, X., LIU, Q., LI, C., GRAVES-DEAL, R., CAO, Z., SINGH, B., FRANKLIN, J. L., WANG, J., HU, H., WEI, T., YANG, M., YEATMAN, T. J., LEE, E., SAITO-DIAZ, K., HINGER, S., PATTON, J. G., CHUNG, C. H., EMMRICH, S., KLUSMANN, J. H., FAN, D. & COFFEY, R. J. 2017. lncRNA MIR100HG-derived miR-100 and miR-125b mediate cetuximab resistance via Wnt/ β -catenin signaling. *Nat Med*, 23, 1331-1341.
- LUGA, V., ZHANG, L., VILORIA-PETIT, A. M., OGUNJIMI, A. A., INANLOU, M. R., CHIU, E., BUCHANAN, M., HOSEIN, A. N., BASIK, M. & WRANA, J. L. 2012. Exosomes mediate stromal mobilization of autocrine Wnt-PCP signaling in breast cancer cell migration. *Cell*, 151, 1542-56.
- LV, C., LI, F., LI, X., TIAN, Y., ZHANG, Y., SHENG, X., SONG, Y., MENG, Q., YUAN, S., LUAN, L., ANDL, T., FENG, X., JIAO, B., XU, M., PLIKUS, M. V., DAI, X., LENGNER, C., CUI, W., REN, F., SHUAI, J., MILLAR, S. E. & YU, Z. 2017a. MiR-31 promotes mammary stem cell expansion and breast tumorigenesis by suppressing Wnt signaling antagonists. *Nat Commun*, 8, 1036.
- LV, D., GUO, L., ZHANG, T. & HUANG, L. 2017b. PRAS40 signaling in tumor. *Oncotarget*, 8, 69076-69085.
- MA, Q., LIANG, M., WU, Y., DOU, C., XU, J., DONG, S. & LUO, F. 2021. Small extracellular vesicles deliver osteolytic effectors and mediate cancer-induced osteolysis in bone metastatic niche. *J Extracell Vesicles*, 10, e12068.
- MA, X., CHEN, Z., CHEN, W., CHEN, Z., SHANG, Y., ZHAO, Y., LI, L., ZHOU, C., HE, J. & MENG, X. 2024. lncRNA AL139294.1 can be transported by extracellular vesicles to promote the oncogenic behaviour of recipient cells through activation of the Wnt and NF- κ B2 pathways in non-small-cell lung cancer. *J Exp Clin Cancer Res*, 43, 20.

- MARIE, P. P., FAN, S. J., MASON, J., WELLS, A., MENDES, C. C., WAINWRIGHT, S. M., SCOTT, S., FISCHER, R., HARRIS, A. L., WILSON, C. & GOBERDHAN, D. C. I. 2023. Accessory ESCRT-III proteins are conserved and selective regulators of Rab11a-exosome formation. *J Extracell Vesicles*, 12, e12311.
- MARTENS-UZUNOVA, E. S., KUSUMA, G. D., CRUCITTA, S., LIM, H. K., COOPER, C., RICHES, J. E., AZAD, A., OCHIYA, T., BOYLE, G. M., SOUTHEY, M. C., DEL RE, M., LIM, R., RAMM, G. A., JENSTER, G. W. & SOEKMADJI, C. 2021. Androgens alter the heterogeneity of small extracellular vesicles and the small RNA cargo in prostate cancer. *J Extracell Vesicles*, 10, e12136.
- MASSAGUE, J. & SHEPPARD, D. 2023. TGF-beta signaling in health and disease. *Cell*, 186, 4007-4037.
- MATEESCU, B., KOWAL, E. J., VAN BALKOM, B. W., BARTEL, S., BHATTACHARYYA, S. N., BUZAS, E. I., BUCK, A. H., DE CANDIA, P., CHOW, F. W., DAS, S., DRIEDONKS, T. A., FERNANDEZ-MESSINA, L., HADERK, F., HILL, A. F., JONES, J. C., VAN KEUREN-JENSEN, K. R., LAI, C. P., LASSER, C., LIEGRO, I. D., LUNAVAT, T. R., LORENOWICZ, M. J., MAAS, S. L., MAGER, I., MITTELBRUNN, M., MOMMA, S., MUKHERJEE, K., NAWAZ, M., PEGTEL, D. M., PFAFFL, M. W., SCHIFFELERS, R. M., TAHARA, H., THERY, C., TOSAR, J. P., WAUBEN, M. H., WITWER, K. W. & NOLTE-'T HOEN, E. N. 2017. Obstacles and opportunities in the functional analysis of extracellular vesicle RNA - an ISEV position paper. *J Extracell Vesicles*, 6, 1286095.
- MATHIEU, M., MARTIN-JAULAR, L., LAVIEU, G. & THERY, C. 2019. Specificities of secretion and uptake of exosomes and other extracellular vesicles for cell-to-cell communication. *Nat Cell Biol*, 21, 9-17.
- MATHIEU, M., NÉVO, N., JOUVE, M., VALENZUELA, J. I., MAURIN, M., VERWEIJ, F. J., PALMULLI, R., LANKAR, D., DINGLI, F., LOEW, D., RUBINSTEIN, E., BONCOMPAIN, G., PEREZ, F. & THÉRY, C. 2021. Specificities of exosome versus small ectosome secretion revealed by live intracellular tracking of CD63 and CD9. *Nature Communications*, 12.
- MATSUI, W. H. 2016. Cancer stem cell signaling pathways. *Medicine (Baltimore)*, 95, S8-S19.
- MATSUSHITA, T., LE HUU, D., KOBAYASHI, T., HAMAGUCHI, Y., HASEGAWA, M., NAKA, K., HIRAO, A., MURAMATSU, M., TAKEHARA, K. & FUJIMOTO, M. 2016. A novel splenic B1 regulatory cell subset suppresses allergic disease through phosphatidylinositol 3-kinase-Akt pathway activation. *J Allergy Clin Immunol*, 138, 1170-1182.e9.
- MAZUROV, D., BARBASHOVA, L. & FILATOV, A. 2013. Tetraspanin protein CD9 interacts with metalloprotease CD10 and enhances its release via exosomes. *Febs j*, 280, 1200-13.
- MCCULLOUGH, J., FISHER, R. D., WHITBY, F. G., SUNDQUIST, W. I. & HILL, C. P. 2008. ALIX-CHMP4 interactions in the human ESCRT pathway. *Proc Natl Acad Sci U S A*, 105, 7687-91.
- MCGOUGH, I. J. & VINCENT, J. P. 2016. Exosomes in developmental signalling. *Development*, 143, 2482-93.
- MCKENZIE, A. J., HOSHINO, D., HONG, N. H., CHA, D. J., FRANKLIN, J. L., COFFEY, R. J., PATTON, J. G. & WEAVER, A. M. 2016. KRAS-MEK Signaling Controls Ago2 Sorting into Exosomes. *Cell Rep*, 15, 978-987.
- MCKIERNAN, J., NOERHOLM, M., TADIGOTLA, V., KUMAR, S., TORKLER, P., SANT, G., ALTER, J., DONOVAN, M. J. & SKOG, J. 2020. A urine-based Exosomal gene expression test stratifies risk of high-grade prostate Cancer in men with prior negative prostate biopsy undergoing repeat biopsy. *BMC Urol*, 20, 138.
- MENCK, K., SÖNMEZER, C., WORST, T. S., SCHULZ, M., DIHAZI, G. H., STREIT, F., ERDMANN, G., KLING, S., BOUTROS, M., BINDER, C. & GROSS, J. C. 2017. Neutral sphingomyelinases control extracellular vesicles budding from the plasma membrane. *J Extracell Vesicles*, 6, 1378056.
- MERRIEL, S. W. D., FUNSTON, G. & HAMILTON, W. 2018. Prostate Cancer in Primary Care. *Adv Ther*, 35, 1285-1294.
- MIZUTANI, K., TERAZAWA, R., KAMEYAMA, K., KATO, T., HORIE, K., TSUCHIYA, T., SEIKE, K., EHARA, H., FUJITA, Y., KAWAKAMI, K., ITO, M. & DEGUCHI, T. 2014. Isolation of prostate cancer-related exosomes. *Anticancer Res*, 34, 3419-23.

- MODI, A., VAI, S., CARAMELLI, D. & LARI, M. 2021. The Illumina Sequencing Protocol and the NovaSeq 6000 System. *In: MENGONI, A., BACCI, G. & FONDI, M. (eds.) Bacterial Pangenomics: Methods and Protocols.* New York, NY: Springer US.
- MOHIDEEN, A., JOHANSEN, S. D. & BABIAK, I. 2020. High-Throughput Identification of Adapters in Single-Read Sequencing Data. *Biomolecules*, 10.
- MOSA, M. H., MICHELS, B. E., MENCHE, C., NICOLAS, A. M., DARVISHI, T., GRETEN, F. R. & FARIN, H. F. 2020. A Wnt-Induced Phenotypic Switch in Cancer-Associated Fibroblasts Inhibits EMT in Colorectal Cancer. *Cancer Res*, 80, 5569-5582.
- MOTRO, B., ITIN, A., SACHS, L. & KESHET, E. 1990. Pattern of interleukin 6 gene expression in vivo suggests a role for this cytokine in angiogenesis. *Proc Natl Acad Sci U S A*, 87, 3092-6.
- MOULIN, C., CRUPI, M. J. F., ILKOW, C. S., BELL, J. C. & BOULTON, S. 2023. Extracellular Vesicles and Viruses: Two Intertwined Entities. *Int J Mol Sci*, 24.
- MUCCI, L. A., HJELMBORG, J. B., HARRIS, J. R., CZENE, K., HAVELICK, D. J., SCHEIKE, T., GRAFF, R. E., HOLST, K., MOLLER, S., UNGER, R. H., MCINTOSH, C., NUTTALL, E., BRANDT, I., PENNEY, K. L., HARTMAN, M., KRAFT, P., PARMIGIANI, G., CHRISTENSEN, K., KOSKENVUO, M., HOLM, N. V., HEIKKILA, K., PUKKALA, E., SKYTTE, A., ADAMI, H. O., KAPRIO, J. & NORDIC TWIN STUDY OF CANCER, C. 2016. Familial Risk and Heritability of Cancer Among Twins in Nordic Countries. *JAMA*, 315, 68-76.
- MUKHERJEE, A., EPPERLY, M. W., FISHER, R., HOU, W., SHIELDS, D., SAIFUL HUQ, M., PIFER, P. M., MULHERKAR, R., WILHITE, T. J., WANG, H., WIPF, P. & GREENBERGER, J. S. 2023. Inhibition of tyrosine kinase Fgr prevents radiation-induced pulmonary fibrosis (RIPF). *Cell Death Discov*, 9, 252.
- MURALIDHARAN-CHARI, V., CLANCY, J., PLOU, C., ROMAO, M., CHAVRIER, P., RAPOSO, G. & D'SOUZA-SCHOREY, C. 2009. ARF6-regulated shedding of tumor cell-derived plasma membrane microvesicles. *Curr Biol*, 19, 1875-85.
- NAEEM, M., MAJEED, S., HOQUE, M. Z. & AHMAD, I. 2020. Latest Developed Strategies to Minimize the Off-Target Effects in CRISPR-Cas-Mediated Genome Editing. *Cells*, 9.
- NAITO, Y., YOSHIOKA, Y. & OCHIYA, T. 2022. Intercellular crosstalk between cancer cells and cancer-associated fibroblasts via extracellular vesicles. *Cancer Cell Int*, 22, 367.
- NAKAMURA, K., SAWADA, K., KINOSE, Y., YOSHIMURA, A., TODA, A., NAKATSUKA, E., HASHIMOTO, K., MABUCHI, S., MORISHIGE, K. I., KURACHI, H., LENGYEL, E. & KIMURA, T. 2017. Exosomes Promote Ovarian Cancer Cell Invasion through Transfer of CD44 to Peritoneal Mesothelial Cells. *Mol Cancer Res*, 15, 78-92.
- NAM, R. K., SASKIN, R., LEE, Y., LIU, Y., LAW, C., KLOTZ, L. H., LOBLAW, D. A., TRACHTENBERG, J., STANIMIROVIC, A., SIMOR, A. E., SETH, A., URBACH, D. R. & NAROD, S. A. 2010. Increasing hospital admission rates for urological complications after transrectal ultrasound guided prostate biopsy. *J Urol*, 183, 963-8.
- NGUYEN, E. V., PEREIRA, B. A., LAWRENCE, M. G., MA, X., REBELLO, R. J., CHAN, H., NIRANJAN, B., WU, Y., ELLEM, S., GUAN, X., WU, J., SKHINAS, J. N., COX, T. R., RISBRIDGER, G. P., TAYLOR, R. A., LISTER, N. L. & DALY, R. J. 2019. Proteomic Profiling of Human Prostate Cancer-associated Fibroblasts (CAF) Reveals LOXL2-dependent Regulation of the Tumor Microenvironment. *Mol Cell Proteomics*, 18, 1410-1427.
- NI, J., DONG, Z., HAN, W., KONDRIKOV, D. & SU, Y. 2013. The role of RhoA and cytoskeleton in myofibroblast transformation in hyperoxic lung fibrosis. *Free Radic Biol Med*, 61, 26-39.
- NICE. 2021. *Prostate cancer: diagnosis and management ng131* [Online]. Available: <https://www.nice.org.uk/guidance/ng131> [Accessed].
- NIELSEN, C. P., JERNIGAN, K. K., DIGGINS, N. L., WEBB, D. J. & MACGURN, J. A. 2019. USP9X Deubiquitylates DVL2 to Regulate WNT Pathway Specification. *Cell Rep*, 28, 1074-1089.e5.
- NISHIKAI-YAN SHEN, T., KANAZAWA, S., KADO, M., OKADA, K., LUO, L., HAYASHI, A., MIZUNO, H. & TANAKA, R. 2017. Interleukin-6 stimulates Akt and p38 MAPK phosphorylation and fibroblast migration in non-diabetic but not diabetic mice. *PLoS One*, 12, e0178232.

- NOLTE-'T HOEN, E., CREMER, T., GALLO, R. C. & MARGOLIS, L. B. 2016. Extracellular vesicles and viruses: Are they close relatives? *Proc Natl Acad Sci U S A*, 113, 9155-61.
- NUNEZ LOPEZ, Y. O., ILIUK, A., PETRILLI, A. M., GLASS, C., CASU, A. & PRATLEY, R. E. 2022. Proteomics and Phosphoproteomics of Circulating Extracellular Vesicles Provide New Insights into Diabetes Pathobiology. *Int J Mol Sci*, 23.
- O'BRIEN, K., BREYNE, K., UGHETTO, S., LAURENT, L. C. & BREAKFIELD, X. O. 2020. RNA delivery by extracellular vesicles in mammalian cells and its applications. *Nat Rev Mol Cell Biol*, 21, 585-606.
- O'BRIEN, K., UGHETTO, S., MAHJOU, S., NAIR, A. V. & BREAKFIELD, X. O. 2022. Uptake, functionality, and re-release of extracellular vesicle-encapsulated cargo. *Cell Rep*, 39, 110651.
- O'GRADY, T., NJOCK, M. S., LION, M., BRUYR, J., MARIAVELLE, E., GALVAN, B., BOECKX, A., STRUMAN, I. & DEQUIEDT, F. 2022. Sorting and packaging of RNA into extracellular vesicles shape intracellular transcript levels. *BMC Biol*, 20, 72.
- ÖHLUND, D., HANDLY-SANTANA, A., BIFFI, G., ELYADA, E., ALMEIDA, A. S., PONZ-SARVISE, M., CORBO, V., ONI, T. E., HEARN, S. A., LEE, E. J., CHIO, I. I. C., HWANG, C.-I., TIRIAC, H., BAKER, L. A., ENGLE, D. D., FEIG, C., KULTTI, A., EGBLAD, M., FEARON, D. T., CRAWFORD, J. M., CLEVERS, H., PARK, Y. & TUVESON, D. A. 2017. Distinct populations of inflammatory fibroblasts and myofibroblasts in pancreatic cancer. *Journal of Experimental Medicine*, 214, 579-596.
- OLEJNICZAK, M., GALKA, P. & KRZYZOSIAK, W. J. 2010. Sequence-non-specific effects of RNA interference triggers and microRNA regulators. *Nucleic Acids Res*, 38, 1-16.
- OLUMI, A. F., GROSSFELD, G. D., HAYWARD, S. W., CARROLL, P. R., TLSTY, T. D. & CUNHA, G. R. 1999. Carcinoma-associated fibroblasts direct tumor progression of initiated human prostatic epithelium. *Cancer Res*, 59, 5002-11.
- ONG, X. R. S., BAGGULEY, D., YAXLEY, J. W., AZAD, A. A., MURPHY, D. G. & LAWRENTSCHUK, N. 2020. Understanding the diagnosis of prostate cancer. *Med J Aust*, 213, 424-429.
- ORR, B., RIDDICK, A. C., STEWART, G. D., ANDERSON, R. A., FRANCO, O. E., HAYWARD, S. W. & THOMSON, A. A. 2012. Identification of stromally expressed molecules in the prostate by tag-profiling of cancer-associated fibroblasts, normal fibroblasts and fetal prostate. *Oncogene*, 31, 1130-42.
- OSTEIKOETXEA, X., SILVA, A., LAZARO-IBANEZ, E., SALMOND, N., SHATNYEVA, O., STEIN, J., SCHICK, J., WREN, S., LINDGREN, J., FIRTH, M., MADSEN, A., MAYR, L. M., OVERMAN, R., DAVIES, R. & DEKKER, N. 2022. Engineered Cas9 extracellular vesicles as a novel gene editing tool. *J Extracell Vesicles*, 11, e12225.
- OSTROWSKI, M., CARMO, N. B., KRUMEICH, S., FANGET, I., RAPOSO, G., SAVINA, A., MOITA, C. F., SCHAUER, K., HUME, A. N., FREITAS, R. P., GOUD, B., BENAROCHE, P., HACOEN, N., FUKUDA, M., DESNOS, C., SEABRA, M. C., DARCHEN, F., AMIGORENA, S., MOITA, L. F. & THERY, C. 2010. Rab27a and Rab27b control different steps of the exosome secretion pathway. *Nat Cell Biol*, 12, 19-30; sup pp 1-13.
- ØVERBYE, A., SKOTLAND, T., KOEHLER, C. J., THIEDE, B., SEIERSTAD, T., BERGE, V., SANDVIG, K. & LLORENTE, A. 2015. Identification of prostate cancer biomarkers in urinary exosomes. *Oncotarget*, 6, 30357-76.
- OZDEMIR, B. C., PENTCHEVA-HOANG, T., CARSTENS, J. L., ZHENG, X., WU, C. C., SIMPSON, T. R., LAKLAI, H., SUGIMOTO, H., KAHLERT, C., NOVITSKIY, S. V., DE JESUS-ACOSTA, A., SHARMA, P., HEIDARI, P., MAHMOOD, U., CHIN, L., MOSES, H. L., WEAVER, V. M., MAITRA, A., ALLISON, J. P., LEBLEU, V. S. & KALLURI, R. 2015. Depletion of Carcinoma-Associated Fibroblasts and Fibrosis Induces Immunosuppression and Accelerates Pancreas Cancer with Reduced Survival. *Cancer Cell*, 28, 831-833.
- PAKULA, H., OMAR, M., CARELLI, R., PEDERZOLI, F., FANELLI, G. N., PANNELLINI, T., SOCCIARELLI, F., VAN EMMENIS, L., RODRIGUES, S., FIDALGO-RIBEIRO, C., NUZZO, P. V., BRADY, N. J., DINALANKARA, W., JERE, M., VALENCIA, I., SALADINO, C., STONE, J., UNKENHOLZ, C., GARNER, R., ALEXANDERANI, M. K., KHANI, F., DE ALMEIDA, F. N., ABATE-SHEN, C., GREENBLATT, M. B., RICKMAN, D. S., BARBIERI, C. E., ROBINSON, B. D., MARCHIONNI, L. &

- LODA, M. 2024. Distinct mesenchymal cell states mediate prostate cancer progression. *Nat Commun*, 15, 363.
- PALAND, N., KAMER, I., KOGAN-SAKIN, I., MADAR, S., GOLDFINGER, N. & ROTTER, V. 2009. Differential influence of normal and cancer-associated fibroblasts on the growth of human epithelial cells in an in vitro cocultivation model of prostate cancer. *Mol Cancer Res*, 7, 1212-23.
- PALMULLI, R., COUTY, M., PIONTEK, M., PONNAIAH, M., DINGLI, F., VERWEIJ, F., CHARRIN, S., TANTUCCI, M., SASIDHARAN, S., RUBINSTEIN, E., KONTUSH, A., LOEW, D., LHOMME, M., ROOS, W., RAPOSO, G. & NIEL, G. V. 2022.
- PALOR, M., STEJSKAL, L., MANDAL, P., LENMAN, A., ALBERIONE, M. P., KIRUI, J., MOELLER, R., EBNER, S., MEISSNER, F., GEROLD, G., SHEPHERD, A. J. & GROVE, J. 2020. Cholesterol sensing by CD81 is important for hepatitis C virus entry. *J Biol Chem*, 295, 16931-16948.
- PALVIAINEN, M., SARASWAT, M., VARGA, Z., KITKA, D., NEUVONEN, M., PUHKA, M., JOENVAARA, S., RENKONEN, R., NIEUWLAND, R., TAKATALO, M. & SILJANDER, P. R. M. 2020. Extracellular vesicles from human plasma and serum are carriers of extravesicular cargo-Implications for biomarker discovery. *PLoS One*, 15, e0236439.
- PAN, J., MA, Z., LIU, B., QIAN, H., SHAO, X., LIU, J., WANG, Q. & XUE, W. 2023. Identification of cancer-associated fibroblasts subtypes in prostate cancer. *Front Immunol*, 14, 1133160.
- PAN, X., QU, K., YUAN, H., XIANG, X., ANTHON, C., PASHKOVA, L., LIANG, X., HAN, P., CORSI, G. I., XU, F., LIU, P., ZHONG, J., ZHOU, Y., MA, T., JIANG, H., LIU, J., WANG, J., JESSEN, N., BOLUND, L., YANG, H., XU, X., CHURCH, G. M., GORODKIN, J., LIN, L. & LUO, Y. 2022. Massively targeted evaluation of therapeutic CRISPR off-targets in cells. *Nat Commun*, 13, 4049.
- PANIGRAHI, G. K., PRAHARAJ, P. P., PEAK, T. C., LONG, J., SINGH, R., RHIM, J. S., ABD ELMAGEED, Z. Y. & DEEP, G. 2018. Hypoxia-induced exosome secretion promotes survival of African-American and Caucasian prostate cancer cells. *Sci Rep*, 8, 3853.
- PARK, J. E., TAN, H. S., DATTA, A., LAI, R. C., ZHANG, H., MENG, W., LIM, S. K. & SZE, S. K. 2010. Hypoxic tumor cell modulates its microenvironment to enhance angiogenic and metastatic potential by secretion of proteins and exosomes. *Mol Cell Proteomics*, 9, 1085-99.
- PARKHOMCHUK, D., BORODINA, T., AMSTISLAVSKIY, V., BANARU, M., HALLEN, L., KROBITSCH, S., LEHRACH, H. & SOLDATOV, A. 2009. Transcriptome analysis by strand-specific sequencing of complementary DNA. *Nucleic Acids Res*, 37, e123.
- PEAK, T. C., PANIGRAHI, G. K., PRAHARAJ, P. P., SU, Y., SHI, L., CHYR, J., RIVERA-CHAVEZ, J., FLORES-BOCANEGRA, L., SINGH, R., VANDER GRIEND, D. J., OBERLIES, N. H., KERR, B. A., HEMAL, A., BITTING, R. L. & DEEP, G. 2020. Syntaxin 6-mediated exosome secretion regulates enzalutamide resistance in prostate cancer. *Mol Carcinog*, 59, 62-72.
- PEINADO, H., ALECKOVIC, M., LAVOTSHKIN, S., MATEI, I., COSTA-SILVA, B., MORENO-BUENO, G., HERGUETA-REDONDO, M., WILLIAMS, C., GARCIA-SANTOS, G., GHAJAR, C., NITADORI-HOSHINO, A., HOFFMAN, C., BADAL, K., GARCIA, B. A., CALLAHAN, M. K., YUAN, J., MARTINS, V. R., SKOG, J., KAPLAN, R. N., BRADY, M. S., WOLCHOK, J. D., CHAPMAN, P. B., KANG, Y., BROMBERG, J. & LYDEN, D. 2012. Melanoma exosomes educate bone marrow progenitor cells toward a pro-metastatic phenotype through MET. *Nat Med*, 18, 883-91.
- PENG, Y., ZHAO, M., HU, Y., GUO, H., ZHANG, Y., HUANG, Y., ZHAO, L., CHAI, Y. & WANG, Z. 2022. Blockade of exosome generation by GW4869 inhibits the education of M2 macrophages in prostate cancer. *BMC Immunology*, 23, 37.
- PFRIEGER, F. W. & VITALE, N. 2018. Cholesterol and the journey of extracellular vesicles. *J Lipid Res*, 59, 2255-2261.
- PHAM, T. T., CHEN, H., NGUYEN, P. H. D., JAYASINGHE, M. K., LE, A. H. & LE, M. T. N. 2023. Endosomal escape of nucleic acids from extracellular vesicles mediates functional therapeutic delivery. *Pharmacological Research*, 188, 106665.
- PIENTA, K. J. 2001. Preclinical mechanisms of action of docetaxel and docetaxel combinations in prostate cancer. *Semin Oncol*, 28, 3-7.

- PIERORAZIO, P. M., WALSH, P. C., PARTIN, A. W. & EPSTEIN, J. I. 2013. Prognostic Gleason grade grouping: data based on the modified Gleason scoring system. *BJU Int*, 111, 753-60.
- PING, Q., YAN, R., CHENG, X., WANG, W., ZHONG, Y., HOU, Z., SHI, Y., WANG, C. & LI, R. 2021. Cancer-associated fibroblasts: overview, progress, challenges, and directions. *Cancer Gene Ther*, 28, 984-999.
- PLIKUS, M. V., WANG, X., SINHA, S., FORTE, E., THOMPSON, S. M., HERZOG, E. L., DRISKELL, R. R., ROSENTHAL, N., BIERNASKIE, J. & HORSLEY, V. 2021. Fibroblasts: Origins, definitions, and functions in health and disease. *Cell*, 184, 3852-3872.
- POGGIO, M., HU, T., PAI, C. C., CHU, B., BELAIR, C. D., CHANG, A., MONTABANA, E., LANG, U. E., FU, Q., FONG, L. & BLELLOCH, R. 2019. Suppression of Exosomal PD-L1 Induces Systemic Anti-tumor Immunity and Memory. *Cell*, 177, 414-427 e13.
- PROBERT, C., DOTTORINI, T., SPEAKMAN, A., HUNT, S., NAFEE, T., FAZELI, A., WOOD, S., BROWN, J. E. & JAMES, V. 2018. Communication of prostate cancer cells with bone cells via extracellular vesicle RNA; a potential mechanism of metastasis. *Oncogene*, 38, 1751-1763.
- QIN, H., YANG, Y., JIANG, B., PAN, C., CHEN, W., DIAO, W., DING, M., CAO, W., ZHANG, Z., CHEN, M., GAO, J., ZHAO, X., QIU, X. & GUO, H. 2021. SOX9 in prostate cancer is upregulated by cancer-associated fibroblasts to promote tumor progression through HGF/c-Met-FRA1 signaling. *Febs j*, 288, 5406-5429.
- RADISKY, D. C., KENNY, P. A. & BISSELL, M. J. 2007. Fibrosis and cancer: do myofibroblasts come also from epithelial cells via EMT? *J Cell Biochem*, 101, 830-9.
- RAJA, M. K., PREOBRASCHENSKI, J., DEL OLMO-CABRERA, S., MARTINEZ-TURRILLAS, R., JAHN, R., PEREZ-OTANO, I. & WESSELING, J. F. 2019. Elevated synaptic vesicle release probability in synaptophysin/gyrin family quadruple knockouts. *eLife*, 8.
- RAJAN, P., STOCKLEY, J., SUDBERY, I. M., FLEMING, J. T., HEDLEY, A., KALNA, G., SIMS, D., PONTING, C. P., HEGER, A., ROBSON, C. N., MCMENEMIN, R. M., PEDLEY, I. D. & LEUNG, H. Y. 2014. Identification of a candidate prognostic gene signature by transcriptome analysis of matched pre- and post-treatment prostatic biopsies from patients with advanced prostate cancer. *BMC Cancer*, 14, 977.
- RAPOSO, G., NIJMAN, H. W., STOORVOGEL, W., LIEJENDEKKER, R., HARDING, C. V., MELIEF, C. J. & GEUZE, H. J. 1996. B lymphocytes secrete antigen-presenting vesicles. *J Exp Med*, 183, 1161-72.
- RASKOVA, M., LACINA, L., KEJIK, Z., VENHAUEROVA, A., SKALICKOVA, M., KOLAR, M., JAKUBEK, M., ROSEL, D., SMETANA, K., JR. & BRABEK, J. 2022. The Role of IL-6 in Cancer Cell Invasiveness and Metastasis-Overview and Therapeutic Opportunities. *Cells*, 11.
- RAWLA, P. 2019. Epidemiology of Prostate Cancer. *World J Oncol*, 10, 63-89.
- REBELLO, R. J., OING, C., KNUDSEN, K. E., LOEB, S., JOHNSON, D. C., REITER, R. E., GILLESSEN, S., VAN DER KWAST, T. & BRISTOW, R. G. 2021. Prostate cancer. *Nat Rev Dis Primers*, 7, 9.
- REYES-GORDILLO, K., SHAH, R., POPRATILOFF, A., FU, S., HINDLE, A., BRODY, F. & ROJKIND, M. 2011. Thymosin-beta4 (Tbeta4) blunts PDGF-dependent phosphorylation and binding of AKT to actin in hepatic stellate cells. *Am J Pathol*, 178, 2100-8.
- RIDDER, K., KELLER, S., DAMS, M., RUPP, A. K., SCHLAUDRAFF, J., DEL TURCO, D., STARMANN, J., MACAS, J., KARPOVA, D., DEVRAJ, K., DEPBOYLU, C., LANDFRIED, B., ARNOLD, B., PLATE, K. H., HOGLINGER, G., SULTMANN, H., ALTEVOGT, P. & MOMMA, S. 2014. Extracellular vesicle-mediated transfer of genetic information between the hematopoietic system and the brain in response to inflammation. *PLoS Biol*, 12, e1001874.
- RINGUETTE GOULET, C., BERNARD, G., TREMBLAY, S., CHABAUD, S., BOLDUC, S. & POULIOT, F. 2018. Exosomes Induce Fibroblast Differentiation into Cancer-Associated Fibroblasts through TGFbeta Signaling. *Mol Cancer Res*, 16, 1196-1204.
- RODRIGUEZ, R. & KRISHNAN, Y. 2023. The chemistry of next-generation sequencing. *Nat Biotechnol*, 41, 1709-1715.
- ROUCOURT, B., MEEUSSEN, S., BAO, J., ZIMMERMANN, P. & DAVID, G. 2015. Heparanase activates the syndecan-syntenin-ALIX exosome pathway. *Cell Res*, 25, 412-28.

- RUAN, Z., TAKAMATSU-YUKAWA, K., WANG, Y., USHMAN, M. L., LABADORF, A. T., ERICSSON, M., IKEZU, S. & IKEZU, T. 2022. Functional genome-wide short hairpin RNA library screening identifies key molecules for extracellular vesicle secretion from microglia. *Cell Rep*, 39, 110791.
- SACKMANN, V., SINHA, M. S., SACKMANN, C., CIVITELLI, L., BERGSTRÖM, J., ANSELL-SCHULTZ, A. & HALLBECK, M. 2019. Inhibition of nSMase2 Reduces the Transfer of Oligomeric α -Synuclein Irrespective of Hypoxia. *Front Mol Neurosci*, 12, 200.
- SAHAI, E., ASTSATUROV, I., CUKIERMAN, E., DENARDO, D. G., EGEBLAD, M., EVANS, R. M., FEARON, D., GRETEN, F. R., HINGORANI, S. R., HUNTER, T., HYNES, R. O., JAIN, R. K., JANOWITZ, T., JORGENSEN, C., KIMMELMAN, A. C., KOLONIN, M. G., MAKI, R. G., POWERS, R. S., PURE, E., RAMIREZ, D. C., SCHERZ-SHOVAL, R., SHERMAN, M. H., STEWART, S., TLSTY, T. D., TUVESON, D. A., WATT, F. M., WEAVER, V., WEERARATNA, A. T. & WERB, Z. 2020. A framework for advancing our understanding of cancer-associated fibroblasts. *Nat Rev Cancer*, 20, 174-186.
- SALMON, H., FRANCISZKIEWICZ, K., DAMOTTE, D., DIEU-NOSJEAN, M. C., VALIDIRE, P., TRAUTMANN, A., MAMI-CHOUAIB, F. & DONNADIEU, E. 2012. Matrix architecture defines the preferential localization and migration of T cells into the stroma of human lung tumors. *J Clin Invest*, 122, 899-910.
- SANTANGELO, L., GIURATO, G., CICCHINI, C., MONTALDO, C., MANCONE, C., TARALLO, R., BATTISTELLI, C., ALONZI, T., WEISZ, A. & TRIPODI, M. 2016. The RNA-Binding Protein SYNCRIP Is a Component of the Hepatocyte Exosomal Machinery Controlling MicroRNA Sorting. *Cell Rep*, 17, 799-808.
- SANTOS, M. F., RAPPA, G., FONTANA, S., KARBANOVA, J., AALAM, F., TAI, D., LI, Z., PUCCI, M., ALESSANDRO, R., MORIMOTO, C., CORBEIL, D. & LORICO, A. 2022. Anti-Human CD9 Fab Fragment Antibody Blocks the Extracellular Vesicle-Mediated Increase in Malignancy of Colon Cancer Cells. *Cells*, 11.
- SAOUD, R., HEIDAR, N. A., CIMADAMORE, A. & PANER, G. P. 2020. Incorporating Prognostic Biomarkers into Risk Assessment Models and TNM Staging for Prostate Cancer. *Cells*, 9.
- SCHLIENGER, S., CAMPBELL, S. & CLAING, A. 2014. ARF1 regulates the Rho/MLC pathway to control EGF-dependent breast cancer cell invasion. *Mol Biol Cell*, 25, 17-29.
- SEGU-VERGES, C., CANO, S., CALDERON-GOMEZ, E., BARTRA, H., SARDON, T., KAVERI, S. & TERCENIO, J. 2022. Systems biology and artificial intelligence analysis highlights the pleiotropic effect of IVIg therapy in autoimmune diseases with a predominant role on B cells and complement system. *Front Immunol*, 13, 901872.
- SEKHOACHA, M., RIET, K., MOTLOUNG, P., GUMENKU, L., ADEGOKE, A. & MASHELE, S. 2022. Prostate Cancer Review: Genetics, Diagnosis, Treatment Options, and Alternative Approaches. *Molecules*, 27.
- SHAH, K., GAGLIANO, T., GARLAND, L., O'HANLON, T., BORTOLOTTI, D., GENTILI, V., RIZZO, R., GIAMAS, G. & DEAN, M. 2020. Androgen receptor signaling regulates the transcriptome of prostate cancer cells by modulating global alternative splicing. *Oncogene*, 39, 6172-6189.
- SHEARER, R. F. & SAUNDERS, D. N. 2015. Experimental design for stable genetic manipulation in mammalian cell lines: lentivirus and alternatives. *Genes Cells*, 20, 1-10.
- SHEPHARD, A. P., GILES, P., MBENGUE, M., ALRAIES, A., SPARY, L. K., KYNASTON, H., GURNEY, M. J., FALCON-PEREZ, J. M., ROYO, F., TABI, Z., PARTHIMOS, D., ERRINGTON, R. J., CLAYTON, A. & WEBBER, J. P. 2021. Stroma-derived extracellular vesicle mRNA signatures inform histological nature of prostate cancer. *J Extracell Vesicles*, 10, e12150.
- SHI, X., YOUNG, C. D., ZHOU, H. & WANG, X. 2020. Transforming Growth Factor-beta Signaling in Fibrotic Diseases and Cancer-Associated Fibroblasts. *Biomolecules*, 10.
- SHINTANI, Y., FUJIWARA, A., KIMURA, T., KAWAMURA, T., FUNAKI, S., MINAMI, M. & OKUMURA, M. 2016. IL-6 Secreted from Cancer-Associated Fibroblasts Mediates Chemoresistance in NSCLC by Increasing Epithelial-Mesenchymal Transition Signaling. *J Thorac Oncol*, 11, 1482-92.

- SHLOMOVITZ, I., ERLICH, Z., ARAD, G., EDRY-BOTZER, L., ZARGARIAN, S., COHEN, H., MANKO, T., OFIR-BIRIN, Y., COOKS, T., REGEV-RUDZKI, N. & GERLIC, M. 2021. Proteomic analysis of necroptotic extracellular vesicles. *Cell Death Dis*, 12, 1059.
- SKOG, J., WURDINGER, T., VAN RIJN, S., MEIJER, D. H., GAINCHE, L., SENA-ESTEVEZ, M., CURRY, W. T., JR., CARTER, B. S., KRICHEVSKY, A. M. & BREAKEYFIELD, X. O. 2008. Glioblastoma microvesicles transport RNA and proteins that promote tumour growth and provide diagnostic biomarkers. *Nat Cell Biol*, 10, 1470-6.
- SMEENK, L., VAN HEERINGEN, S. J., KOEPEL, M., GILBERT, B., JANSSEN-MEGENS, E., STUNNENBERG, H. G. & LOHRUM, M. 2011. Role of p53 serine 46 in p53 target gene regulation. *PLoS One*, 6, e17574.
- SMITH, R., LIU, M., LIBY, T., BAYANI, N., BUCHER, E., CHIOTTI, K., DERRICK, D., CHAUCHEREAU, A., HEISER, L., ALUMKAL, J., FEILER, H., CARROLL, P. & KORKOLA, J. E. 2020. Enzalutamide response in a panel of prostate cancer cell lines reveals a role for glucocorticoid receptor in enzalutamide resistant disease. *Sci Rep*, 10, 21750.
- SNEEGGEN, M., PEDERSEN, N. M., CAMPSTEIJN, C., HAUGSTEN, E. M., STENMARK, H. & SCHINK, K. O. 2019. WDFY2 restrains matrix metalloproteinase secretion and cell invasion by controlling VAMP3-dependent recycling. *Nat Commun*, 10, 2850.
- SOBO, K., LE BLANC, I., LUYET, P. P., FIVAZ, M., FERGUSON, C., PARTON, R. G., GRUENBERG, J. & VAN DER GOOT, F. G. 2007. Late endosomal cholesterol accumulation leads to impaired intra-endosomal trafficking. *PLoS One*, 2, e851.
- SOEKMADJI, C., RICHES, J. D., RUSSELL, P. J., RUELCKE, J. E., MCPHERSON, S., WANG, C., HOVENS, C. M., CORCORAN, N. M., HILL, M. M. & NELSON, C. C. 2017a. Modulation of paracrine signaling by CD9 positive small extracellular vesicles mediates cellular growth of androgen deprived prostate cancer. *Oncotarget*, 8, 52237-52255.
- SOEKMADJI, C., ROCKSTROH, A., RAMM, G. A., NELSON, C. C. & RUSSELL, P. J. 2017b. Extracellular Vesicles in the Adaptive Process of Prostate Cancer during Inhibition of Androgen Receptor Signaling by Enzalutamide. *Proteomics*, 17.
- SORK, H., CORSO, G., KRJUTSKOV, K., JOHANSSON, H. J., NORDIN, J. Z., WIKLANDER, O. P. B., LEE, Y. X. F., WESTHOLM, J. O., LEHTIO, J., WOOD, M. J. A., MAGER, I. & EL ANDALOUSSI, S. 2018. Heterogeneity and interplay of the extracellular vesicle small RNA transcriptome and proteome. *Sci Rep*, 8, 10813.
- SOUZA, A. G., IB, B. S., CAMPOS-FERNANDEZ, E., MARANGONI, K., VA, F. B., ALVES, P. T., GOULART, L. R. & ALONSO-GOULART, V. 2018. Extracellular vesicles as drivers of epithelial-mesenchymal transition and carcinogenic characteristics in normal prostate cells. *Mol Carcinog*, 57, 503-511.
- STACHOWIAK, J. C., SCHMID, E. M., RYAN, C. J., ANN, H. S., SASAKI, D. Y., SHERMAN, M. B., GEISLER, P. L., FLETCHER, D. A. & HAYDEN, C. C. 2012. Membrane bending by protein-protein crowding. *Nat Cell Biol*, 14, 944-9.
- STATELLO, L., GUO, C. J., CHEN, L. L. & HUARTE, M. 2021. Gene regulation by long non-coding RNAs and its biological functions. *Nat Rev Mol Cell Biol*, 22, 96-118.
- STAUFER, O., HERNANDEZ BUCHER, J. E., FICHTLER, J., SCHROTER, M., PLATZMAN, I. & SPATZ, J. P. 2022. Vesicle Induced Receptor Sequestration: Mechanisms behind Extracellular Vesicle-Based Protein Signaling. *Adv Sci (Weinh)*, 9, e2200201.
- STEVENS, R. J., AKBERGENOVA, Y., JORQUERA, R. A. & LITTLETON, J. T. 2012. Abnormal synaptic vesicle biogenesis in Drosophila synaptogyrin mutants. *J Neurosci*, 32, 18054-67, 18067a.
- STUFFERS, S., SEM WEGNER, C., STENMARK, H. & BRECH, A. 2009. Multivesicular endosome biogenesis in the absence of ESCRTs. *Traffic*, 10, 925-37.
- SU, H., LI, F., RANEK, M. J., WEI, N. & WANG, X. 2011. COP9 signalosome regulates autophagosome maturation. *Circulation*, 124, 2117-28.
- SUAREZ, H., ANDREU, Z., MAZZEO, C., TORIBIO, V., PEREZ-RIVERA, A. E., LOPEZ-MARTIN, S., GARCIA-SILVA, S., HURTADO, B., MORATO, E., PELAEZ, L., ARRIBAS, E. A., TOLENTINO-CORTEZ, T., BARREDA-GOMEZ, G., MARINA, A. I., PEINADO, H. & YANEZ-MO, M. 2021. CD9 inhibition

- reveals a functional connection of extracellular vesicle secretion with mitophagy in melanoma cells. *J Extracell Vesicles*, 10, e12082.
- SUBRAMANIAN, A., TAMAYO, P., MOOTHA, V. K., MUKHERJEE, S., EBERT, B. L., GILLETTE, M. A., PAULOVICH, A., POMEROY, S. L., GOLUB, T. R., LANDER, E. S. & MESIROV, J. P. 2005. Gene set enrichment analysis: a knowledge-based approach for interpreting genome-wide expression profiles. *Proc Natl Acad Sci U S A*, 102, 15545-50.
- SUN, Q., QI, X., ZHANG, Y., WU, X., LIANG, M., LI, C., LI, D., CARDONA, C. J. & XING, Z. 2016. Synaptogyrin-2 Promotes Replication of a Novel Tick-borne Bunyavirus through Interacting with Viral Nonstructural Protein NSs. *J Biol Chem*, 291, 16138-49.
- SUN, Y., TANG, L., WU, C., WANG, J. & WANG, C. 2023a. RSK inhibitors as potential anticancer agents: Discovery, optimization, and challenges. *Eur J Med Chem*, 251, 115229.
- SUN, Y., ZHAO, Y., NI, X., YANG, Y., FU, Z., LIU, R., ZHANG, C. Y. & CHEN, X. 2023b. In vivo self-assembled small RNA targets H19 lncRNA for the treatment of colorectal cancer. *J Control Release*, 358, 142-160.
- SWEENEY, C. J., CHEN, Y. H., CARDUCCI, M., LIU, G., JARRARD, D. F., EISENBERGER, M., WONG, Y. N., HAHN, N., KOHLI, M., COONEY, M. M., DREICER, R., VOGELZANG, N. J., PICUS, J., SHEVRIN, D., HUSSAIN, M., GARCIA, J. A. & DIPAOLA, R. S. 2015. Chemohormonal Therapy in Metastatic Hormone-Sensitive Prostate Cancer. *N Engl J Med*, 373, 737-46.
- TABOGA, S. R., SCORTEGAGNA, E., SIVIERO, M. P. & CARVALHO, H. F. 2008. Anatomy of smooth muscle cells in nonmalignant and malignant human prostate tissue. *Anat Rec (Hoboken)*, 291, 1115-23.
- TAKAHASHI, A., OKADA, R., NAGAO, K., KAWAMATA, Y., HANYU, A., YOSHIMOTO, S., TAKASUGI, M., WATANABE, S., KANEMAKI, M. T., OBUSE, C. & HARA, E. 2017. Exosomes maintain cellular homeostasis by excreting harmful DNA from cells. *Nat Commun*, 8, 15287.
- TAKAI, S., HANAI, Y., MATSUSHIMA-NISHIWAKI, R., MINAMITANI, C., OTSUKA, T., TOKUDA, H. & KOZAWA, O. 2008. P70 S6 kinase negatively regulates fibroblast growth factor 2-stimulated interleukin-6 synthesis in osteoblasts: function at a point downstream from protein kinase C. *J Endocrinol*, 197, 131-7.
- TAMAI, K., TANAKA, N., NAKANO, T., KAKAZU, E., KONDO, Y., INOUE, J., SHIINA, M., FUKUSHIMA, K., HOSHINO, T., SANO, K., UENO, Y., SHIMOSEGAWA, T. & SUGAMURA, K. 2010. Exosome secretion of dendritic cells is regulated by Hrs, an ESCRT-0 protein. *Biochemical and Biophysical Research Communications*, 399, 384-390.
- TANG, B. L. 2020. SNAREs and developmental disorders. *J Cell Physiol*.
- TANG, S., BUCHKOVICH, N. J., HENNE, W. M., BANJADE, S., KIM, Y. J. & EMR, S. D. 2016. ESCRT-III activation by parallel action of ESCRT-I/II and ESCRT-0/Bro1 during MVB biogenesis. *Elife*, 5.
- TANNOCK, I. F., DE WIT, R., BERRY, W. R., HORTI, J., PLUZANSKA, A., CHI, K. N., OUDARD, S., THÉODORE, C., JAMES, N. D., TURESSON, I., ROSENTHAL, M. A. & EISENBERGER, M. A. 2004. Docetaxel plus prednisone or mitoxantrone plus prednisone for advanced prostate cancer. *N Engl J Med*, 351, 1502-12.
- TAVAKOLI DARGANI, Z., SINGLA, R., JOHNSON, T., KUKREJA, R. & SINGLA, D. K. 2018. Exosomes derived from embryonic stem cells inhibit doxorubicin and inflammation-induced pyroptosis in muscle cells. *Can J Physiol Pharmacol*, 96, 304-307.
- TAVAZOIE, S., HUGHES, J. D., CAMPBELL, M. J., CHO, R. J. & CHURCH, G. M. 1999. Systematic determination of genetic network architecture. *Nat Genet*, 22, 281-5.
- TAYLOR, B. S., SCHULTZ, N., HIERONYMUS, H., GOPALAN, A., XIAO, Y., CARVER, B. S., ARORA, V. K., KAUSHIK, P., CERAMI, E., REVA, B., ANTIPIN, Y., MITSIADES, N., LANDERS, T., DOLGALEV, I., MAJOR, J. E., WILSON, M., SOCCI, N. D., LASH, A. E., HEGUY, A., EASTHAM, J. A., SCHER, H. I., REUTER, V. E., SCARDINO, P. T., SANDER, C., SAWYERS, C. L. & GERALD, W. L. 2010. Integrative genomic profiling of human prostate cancer. *Cancer Cell*, 18, 11-22.
- THÉRY, C., AMIGORENA, S., RAPOSO, G. & CLAYTON, A. 2006. Isolation and characterization of exosomes from cell culture supernatants and biological fluids. *Curr Protoc Cell Biol*, Chapter 3, Unit 3.22.

- THERY, C., WITWER, K. W., AIKAWA, E., ALCARAZ, M. J., ANDERSON, J. D., ANDRIANTSITOHAINA, R., ANTONIOU, A., ARAB, T., ARCHER, F., ATKIN-SMITH, G. K., AYRE, D. C., BACH, J. M., BACHURSKI, D., BAHARVAND, H., BALAJ, L., BALDACCHINO, S., BAUER, N. N., BAXTER, A. A., BEBAWY, M., BECKHAM, C., BEDINA ZAVEC, A., BENMOUSSA, A., BERARDI, A. C., BERGESE, P., BIELSKA, E., BLENKIRON, C., BOBIS-WOZOWICZ, S., BOILARD, E., BOIREAU, W., BONGIOVANNI, A., BORRAS, F. E., BOSCH, S., BOULANGER, C. M., BREAKFIELD, X., BREGGIO, A. M., BRENNAN, M. A., BRIGSTOCK, D. R., BRISSON, A., BROEKMAN, M. L., BROMBERG, J. F., BRYL-GORECKA, P., BUCH, S., BUCK, A. H., BURGER, D., BUSATTO, S., BUSCHMANN, D., BUSSOLATI, B., BUZAS, E. I., BYRD, J. B., CAMUSSI, G., CARTER, D. R., CARUSO, S., CHAMLEY, L. W., CHANG, Y. T., CHEN, C., CHEN, S., CHENG, L., CHIN, A. R., CLAYTON, A., CLERICI, S. P., COCKS, A., COCUCCI, E., COFFEY, R. J., CORDEIRO-DA-SILVA, A., COUCH, Y., COUMANS, F. A., COYLE, B., CRESCITELLI, R., CRIADO, M. F., D'SOUZA-SCHOREY, C., DAS, S., DATTA CHAUDHURI, A., DE CANDIA, P., DE SANTANA, E. F., DE WEVER, O., DEL PORTILLO, H. A., DEMARET, T., DEVILLE, S., DEVITT, A., DHONDT, B., DI VIZIO, D., DIETERICH, L. C., DOLO, V., DOMINGUEZ RUBIO, A. P., DOMINICI, M., DOURADO, M. R., DRIEDONKS, T. A., DUARTE, F. V., DUNCAN, H. M., EICHENBERGER, R. M., EKSTROM, K., EL ANDALOUSSI, S., ELIE-CAILLE, C., ERDRUGGER, U., FALCON-PEREZ, J. M., FATIMA, F., FISH, J. E., FLORES-BELLVER, M., FORSONITS, A., FRELET-BARRAND, A., et al. 2018. Minimal information for studies of extracellular vesicles 2018 (MISEV2018): a position statement of the International Society for Extracellular Vesicles and update of the MISEV2014 guidelines. *J Extracell Vesicles*, 7, 1535750.
- THOMPSON, I. M., PAULER, D. K., GOODMAN, P. J., TANGEN, C. M., LUCIA, M. S., PARNES, H. L., MINASIAN, L. M., FORD, L. G., LIPPMAN, S. M., CRAWFORD, E. D., CROWLEY, J. J. & COLTMAN, C. A. 2004. Prevalence of Prostate Cancer among Men with a Prostate-Specific Antigen Level ≤ 4.0 ng per Milliliter. *New England Journal of Medicine*, 350, 2239-2246.
- TOMAS, D., SPAJIC, B., MILOSEVIC, M., DEMIROVIC, A., MARUSIC, Z. & KRUSLIN, B. 2010. Intensity of stromal changes predicts biochemical recurrence-free survival in prostatic carcinoma. *Scand J Urol Nephrol*, 44, 284-90.
- TORIBIO, V. & YANEZ-MO, M. 2022. Tetraspanins interweave EV secretion, endosomal network dynamics and cellular metabolism. *Eur J Cell Biol*, 101, 151229.
- TOTH, E. A., TURIK, L., VISNOVITZ, T., CSEREP, C., MAZLO, A., SODAR, B. W., FORSONITS, A. I., PETOVARI, G., SEBESTYEN, A., KOMLOSI, Z., DRAHOS, L., KITTEL, A., NAGY, G., BACSI, A., DENES, A., GHO, Y. S., SZABO-TAYLOR, K. E. & BUZAS, E. I. 2021. Formation of a protein corona on the surface of extracellular vesicles in blood plasma. *J Extracell Vesicles*, 10, e12140.
- TRAJKOVIC, K., HSU, C., CHIANTIA, S., RAJENDRAN, L., WENZEL, D., WIELAND, F., SCHWILLE, P., BRÜGGER, B. & SIMONS, M. 2008. Ceramide Triggers Budding of Exosome Vesicles into Multivesicular Endosomes. *Science*, 319, 1244-1247.
- TRICARICO, C., CLANCY, J. & D'SOUZA-SCHOREY, C. 2017. Biology and biogenesis of shed microvesicles. *Small GTPases*, 8, 220-232.
- TSAI, C. H., CHENG, H. C., WANG, Y. S., LIN, P., JEN, J., KUO, I. Y., CHANG, Y. H., LIAO, P. C., CHEN, R. H., YUAN, W. C., HSU, H. S., YANG, M. H., HSU, M. T., WU, C. Y. & WANG, Y. C. 2014. Small GTPase Rab37 targets tissue inhibitor of metalloproteinase 1 for exocytosis and thus suppresses tumour metastasis. *Nat Commun*, 5, 4804.
- TURKBEY, B., ROSENKRANTZ, A. B., HAIDER, M. A., PADHANI, A. R., VILLEIRS, G., MACURA, K. J., TEMPANY, C. M., CHOYKE, P. L., CORNUD, F., MARGOLIS, D. J., THOENY, H. C., VERMA, S., BARENTSZ, J. & WEINREB, J. C. 2019. Prostate Imaging Reporting and Data System Version 2.1: 2019 Update of Prostate Imaging Reporting and Data System Version 2. *Eur Urol*, 76, 340-351.
- TUTRONE, R., DONOVAN, M. J., TORKLER, P., TADIGOTLA, V., MCLAIN, T., NOERHOLM, M., SKOG, J. & MCKIERNAN, J. 2020. Clinical utility of the exosome based ExoDx Prostate(IntelliScore) EPI

- test in men presenting for initial Biopsy with a PSA 2-10 ng/mL. *Prostate Cancer Prostatic Dis*, 23, 607-614.
- TUTRONE, R., LOWENTRITT, B., NEUMAN, B., DONOVAN, M. J., HALLMARK, E., COLE, T. J., YAO, Y., BIESECKER, C., KUMAR, S., VERMA, V., SANT, G. R., ALTER, J. & SKOG, J. 2023. ExoDx prostate test as a predictor of outcomes of high-grade prostate cancer - an interim analysis. *Prostate Cancer Prostatic Dis*, 26, 596-601.
- TUXHORN, J. A., AYALA, G. E., SMITH, M. J., SMITH, V. C., DANG, T. D. & ROWLEY, D. R. 2002. Reactive stroma in human prostate cancer: induction of myofibroblast phenotype and extracellular matrix remodeling. *Clin Cancer Res*, 8, 2912-23.
- UMEDA, R., SATOUH, Y., TAKEMOTO, M., NAKADA-NAKURA, Y., LIU, K., YOKOYAMA, T., SHIROUZU, M., IWATA, S., NOMURA, N., SATO, K., IKAWA, M., NISHIZAWA, T. & NUREKI, O. 2020. Structural insights into tetraspanin CD9 function. *Nat Commun*, 11, 1606.
- URABE, F., KOSAKA, N., SAWA, Y., YAMAMOTO, Y., ITO, K., YAMAMOTO, T., KIMURA, T., EGAWA, S. & OCHIYA, T. 2020. miR-26a regulates extracellular vesicle secretion from prostate cancer cells via targeting SHC4, PFDN4, and CHORDC1. *Sci Adv*, 6, eaay3051.
- UZAMERE, I., WANG, Y., ZHENG, T. & ZHU, Y. 2022. Genetic determinants for the racial disparities in the risk of prostate and testicular cancers. *Commun Med (Lond)*, 2, 138.
- VALADI, H., EKSTROM, K., BOSSIOS, A., SJOSTRAND, M., LEE, J. J. & LOTVALL, J. O. 2007. Exosome-mediated transfer of mRNAs and microRNAs is a novel mechanism of genetic exchange between cells. *Nat Cell Biol*, 9, 654-9.
- VALLE, L. F., LEHRER, E. J., MARKOVIC, D., ELASHOFF, D., LEVIN-EPSTEIN, R., KARNES, R. J., REITER, R. E., RETTIG, M., CALAIS, J., NICKOLS, N. G., DESS, R. T., SPRATT, D. E., STEINBERG, M. L., NGUYEN, P. L., DAVIS, B. J., ZAORSKY, N. G. & KISHAN, A. U. 2021. A Systematic Review and Meta-analysis of Local Salvage Therapies After Radiotherapy for Prostate Cancer (MASTER). *Eur Urol*, 80, 280-292.
- VAN NIEL, G., CHARRIN, S., SIMOES, S., ROMAO, M., ROCHIN, L., SAFTIG, P., MARKS, M. S., RUBINSTEIN, E. & RAPOSO, G. 2011. The tetraspanin CD63 regulates ESCRT-independent and -dependent endosomal sorting during melanogenesis. *Dev Cell*, 21, 708-21.
- VAN NIEL, G., D'ANGELO, G. & RAPOSO, G. 2018. Shedding light on the cell biology of extracellular vesicles. *Nat Rev Mol Cell Biol*, 19, 213-228.
- VAN SOLINGE, T. S., MAHJOUR, S., UGHETTO, S., SAMMARCO, A., BROEKMAN, M. L. D., BREAKEFIELD, X. O. & O'BRIEN, K. P. 2023. Illuminating cellular and extracellular vesicle-mediated communication via a split-Nanoluc reporter in vitro and in vivo. *Cell Rep Methods*, 3, 100412.
- VATS, S. & GALLI, T. 2022. Role of SNAREs in Unconventional Secretion-Focus on the VAMP7-Dependent Secretion. *Front Cell Dev Biol*, 10, 884020.
- VERWEIJ, F. J., BEBELMAN, M. P., GEORGE, A. E., COUTY, M., BÉCOT, A., PALMULLI, R., HEILIGENSTEIN, X., SIRÉS-CAMPOS, J., RAPOSO, G., PEGTEL, D. M. & VAN NIEL, G. 2022. ER membrane contact sites support endosomal small GTPase conversion for exosome secretion. *J Cell Biol*, 221.
- VERWEIJ, F. J., BEBELMAN, M. P., JIMENEZ, C. R., GARCIA-VALLEJO, J. J., JANSSEN, H., NEEFJES, J., KNOL, J. C., DE GOEIJ-DE HAAS, R., PIERSMA, S. R., BAGLIO, S. R., VERHAGE, M., MIDDELDORP, J. M., ZOMER, A., VAN RHEENEN, J., COPPOLINO, M. G., HURBAIN, I., RAPOSO, G., SMIT, M. J., TOONEN, R. F. G., VAN NIEL, G. & PEGTEL, D. M. 2018. Quantifying exosome secretion from single cells reveals a modulatory role for GPCR signaling. *J Cell Biol*, 217, 1129-1142.
- VICENT, S., SAYLES, L. C., VAKA, D., KHATRI, P., GEVAERT, O., CHEN, R., ZHENG, Y., GILLESPIE, A. K., CLARKE, N., XU, Y., SHRAGER, J., HOANG, C. D., PLEVITIS, S., BUTTE, A. J. & SWEET-CORDERO, E. A. 2012. Cross-species functional analysis of cancer-associated fibroblasts identifies a critical role for CLCF1 and IL-6 in non-small cell lung cancer in vivo. *Cancer Res*, 72, 5744-56.

- VICKMAN, R. E., BROMAN, M. M., LANMAN, N. A., FRANCO, O. E., SUDYANTI, P. A. G., NI, Y., JI, Y., HELFAND, B. T., PETKEWICZ, J., PATERAKOS, M. C., CRAWFORD, S. E., RATLIFF, T. L. & HAYWARD, S. W. 2020. Heterogeneity of human prostate carcinoma-associated fibroblasts implicates a role for subpopulations in myeloid cell recruitment. *Prostate*, 80, 173-185.
- VILLARROYA-BELTRI, C., GUTIERREZ-VAZQUEZ, C., SANCHEZ-CABO, F., PEREZ-HERNANDEZ, D., VAZQUEZ, J., MARTIN-COFRECES, N., MARTINEZ-HERRERA, D. J., PASCUAL-MONTANO, A., MITTELBRUNN, M. & SANCHEZ-MADRID, F. 2013. Sumoylated hnRNP A2B1 controls the sorting of miRNAs into exosomes through binding to specific motifs. *Nat Commun*, 4, 2980.
- WANG, B., XU, X., YANG, Z., ZHANG, L., LIU, Y., MA, A., XU, G., TANG, M., JING, T., WU, L. & LIU, Y. 2019. POH1 contributes to hyperactivation of TGF- β signaling and facilitates hepatocellular carcinoma metastasis through deubiquitinating TGF- β receptors and caveolin-1. *EBioMedicine*, 41, 320-332.
- WANG, H. X., SHARMA, C., KNOBLICH, K., GRANTER, S. R. & HEMLER, M. E. 2015. EWI-2 negatively regulates TGF-beta signaling leading to altered melanoma growth and metastasis. *Cell Res*, 25, 370-85.
- WANG, L., WANG, D., YE, Z. & XU, J. 2023. Engineering Extracellular Vesicles as Delivery Systems in Therapeutic Applications. *Adv Sci (Weinh)*, 10, e2300552.
- WANG, T., GILKES, D. M., TAKANO, N., XIANG, L., LUO, W., BISHOP, C. J., CHATURVEDI, P., GREEN, J. J. & SEMENZA, G. L. 2014. Hypoxia-inducible factors and RAB22A mediate formation of microvesicles that stimulate breast cancer invasion and metastasis. *Proc Natl Acad Sci U S A*, 111, E3234-42.
- WANG, Y. S., TZENG, H. T., TSAI, C. H., CHENG, H. C., LAI, W. W., LIU, H. S. & WANG, Y. C. 2018. VAMP8, a vesicle-SNARE required for RAB37-mediated exocytosis, possesses a tumor metastasis suppressor function. *Cancer Lett*, 437, 79-88.
- WEBBER, J., MERAN, S., STEADMAN, R. & PHILLIPS, A. 2009. Hyaluronan orchestrates transforming growth factor-beta1-dependent maintenance of myofibroblast phenotype. *J Biol Chem*, 284, 9083-92.
- WEBBER, J., STEADMAN, R., MASON, M. D., TABI, Z. & CLAYTON, A. 2010. Cancer exosomes trigger fibroblast to myofibroblast differentiation. *Cancer Res*, 70, 9621-30.
- WEBBER, J. P., SPARY, L. K., MASON, M. D., TABI, Z., BREWIS, I. A. & CLAYTON, A. 2016. Prostate stromal cell proteomics analysis discriminates normal from tumour reactive stromal phenotypes. *Oncotarget*, 7, 20124-39.
- WEBBER, J. P., SPARY, L. K., SANDERS, A. J., CHOWDHURY, R., JIANG, W. G., STEADMAN, R., WYMANT, J., JONES, A. T., KYNASTON, H., MASON, M. D., TABI, Z. & CLAYTON, A. 2015. Differentiation of tumour-promoting stromal myofibroblasts by cancer exosomes. *Oncogene*, 34, 290-302.
- WEGENKA, U. M., BUSCHMANN, J., LÜTTICKEN, C., HEINRICH, P. C. & HORN, F. 1993. Acute-phase response factor, a nuclear factor binding to acute-phase response elements, is rapidly activated by interleukin-6 at the posttranslational level. *Mol Cell Biol*, 13, 276-88.
- WEHMAN, A. M., POGGIOLI, C., SCHWEINSBERG, P., GRANT, B. D. & NANCE, J. 2011. The P4-ATPase TAT-5 inhibits the budding of extracellular vesicles in *C. elegans* embryos. *Curr Biol*, 21, 1951-9.
- WEI, Z., BATAGOV, A. O., SCHINELLI, S., WANG, J., WANG, Y., EL FATIMY, R., RABINOVSKY, R., BALAJ, L., CHEN, C. C., HOCHBERG, F., CARTER, B., BREAKFIELD, X. O. & KRICHEVSKY, A. M. 2017. Coding and noncoding landscape of extracellular RNA released by human glioma stem cells. *Nat Commun*, 8, 1145.
- WELCH, M. P., ODLAND, G. F. & CLARK, R. A. 1990. Temporal relationships of F-actin bundle formation, collagen and fibronectin matrix assembly, and fibronectin receptor expression to wound contraction. *J Cell Biol*, 110, 133-45.
- WELSH, J. A., GOBERDHAN, D. C. I., O'DRISCOLL, L., BUZAS, E. I., BLENKIRON, C., BUSSOLATI, B., CAI, H., DI VIZIO, D., DRIEDONKS, T. A. P., ERDRUGGER, U., FALCON-PEREZ, J. M., FU, Q. L., HILL, A. F., LENASSI, M., LIM, S. K., MAHONEY, M. G., MOHANTY, S., MOLLER, A., NIEUWLAND, R., OCHIYA, T., SAHOO, S., TORRECILHAS, A. C., ZHENG, L., ZIJLSTRA, A., ABUELREICH, S.,

- BAGABAS, R., BERGESE, P., BRIDGES, E. M., BRUCALE, M., BURGER, D., CARNEY, R. P., COCUCCI, E., COLOMBO, F., CRESCITELLI, R., HANSER, E., HARRIS, A. L., HAUGHEY, N. J., HENDRIX, A., IVANOV, A. R., JOVANOVIC-TALISMAN, T., KRUIH-GARCIA, N. A., KU'ULEI-LYN FAUSTINO, V., KYBURZ, D., LASSER, C., LENNON, K. M., LOTVALL, J., MADDOX, A. L., MARTENS-UZUNOVA, E. S., MIZENKO, R. R., NEWMAN, L. A., RIDOLFI, A., ROHDE, E., ROJALIN, T., ROWLAND, A., SAFTICS, A., SANDAU, U. S., SAUGSTAD, J. A., SHEKARI, F., SWIFT, S., TER-OVANESYAN, D., TOSAR, J. P., USECKAITE, Z., VALLE, F., VARGA, Z., VAN DER POL, E., VAN HERWIJNEN, M. J. C., WAUBEN, M. H. M., WEHMAN, A. M., WILLIAMS, S., ZENDRINI, A., ZIMMERMAN, A. J., MISEV, C., THERY, C. & WITWER, K. W. 2024. Minimal information for studies of extracellular vesicles (MISEV2023): From basic to advanced approaches. *J Extracell Vesicles*, 13, e12404.
- WELTON, J. L., BRENNAN, P., GURNEY, M., WEBBER, J. P., SPARY, L. K., CARTON, D. G., FALCON-PEREZ, J. M., WALTON, S. P., MASON, M. D., TABI, Z. & CLAYTON, A. 2016. Proteomics analysis of vesicles isolated from plasma and urine of prostate cancer patients using a multiplex, aptamer-based protein array. *J Extracell Vesicles*, 5, 31209.
- WILHELM, B. T. & LANDRY, J. R. 2009. RNA-Seq-quantitative measurement of expression through massively parallel RNA-sequencing. *Methods*, 48, 249-57.
- WILLS, C. A., LIU, X., CHEN, L., ZHAO, Y., DOWER, C. M., SUNDSTROM, J. & WANG, H. G. 2021. Chemotherapy-Induced Upregulation of Small Extracellular Vesicle-Associated PTX3 Accelerates Breast Cancer Metastasis. *Cancer Res*, 81, 452-463.
- WILSON, M. J., SELLERS, R. G., WIEHR, C., MELAMUD, O., PEI, D. & PEEHL, D. M. 2002. Expression of matrix metalloproteinase-2 and -9 and their inhibitors, tissue inhibitor of metalloproteinase-1 and -2, in primary cultures of human prostatic stromal and epithelial cells. *J Cell Physiol*, 191, 208-16.
- WISDOM, R., JOHNSON, R. S. & MOORE, C. 1999. c-Jun regulates cell cycle progression and apoptosis by distinct mechanisms. *Embo j*, 18, 188-97.
- WOOD, M., FUDGE, K., MOHLER, J. L., FROST, A. R., GARCIA, F., WANG, M. & STEARNS, M. E. 1997. In situ hybridization studies of metalloproteinases 2 and 9 and TIMP-1 and TIMP-2 expression in human prostate cancer. *Clin Exp Metastasis*, 15, 246-58.
- WU, X., GONG, S., ROY-BURMAN, P., LEE, P. & CULIG, Z. 2013. Current mouse and cell models in prostate cancer research. *Endocr Relat Cancer*, 20, R155-70.
- WYCKOFF, J. B., WANG, Y., LIN, E. Y., LI, J. F., GOSWAMI, S., STANLEY, E. R., SEGALL, J. E., POLLARD, J. W. & CONDEELIS, J. 2007. Direct visualization of macrophage-assisted tumor cell intravasation in mammary tumors. *Cancer Res*, 67, 2649-56.
- XIAO, G. Y., TAN, X., RODRIGUEZ, B. L., GIBBONS, D. L., WANG, S., WU, C., LIU, X., YU, J., VASQUEZ, M. E., TRAN, H. T., XU, J., RUSSELL, W. K., HAYMAKER, C., LEE, Y., ZHANG, J., SOLIS, L., WISTUBA, II & KURIE, J. M. 2023. EMT activates exocytotic Rabs to coordinate invasion and immunosuppression in lung cancer. *Proc Natl Acad Sci U S A*, 120, e2220276120.
- XU, B., TENG, L. H., SILVA, S. D. D., BIJIAN, K., AL BASHIR, S., JIE, S., DOLPH, M., ALAOUI-JAMALI, M. A. & BISMAR, T. A. 2014. The significance of dynamin 2 expression for prostate cancer progression, prognostication, and therapeutic targeting. *Cancer Medicine*, 3, 14-24.
- YAMANO, K., WANG, C., SARRAF, S. A., MÜNCH, C., KIKUCHI, R., NODA, N. N., HIZUKURI, Y., KANEMAKI, M. T., HARPER, W., TANAKA, K., MATSUDA, N. & YOULE, R. J. 2018. Endosomal Rab cycles regulate Parkin-mediated mitophagy. *Elife*, 7.
- YAN, J., ZHANG, Z., YANG, J., MITCH, W. E. & WANG, Y. 2015. JAK3/STAT6 Stimulates Bone Marrow-Derived Fibroblast Activation in Renal Fibrosis. *J Am Soc Nephrol*, 26, 3060-71.
- YANG, D., LIU, J., QIAN, H. & ZHUANG, Q. 2023. Cancer-associated fibroblasts: from basic science to anticancer therapy. *Exp Mol Med*, 55, 1322-1332.
- YANG, L., PENG, X., LI, Y., ZHANG, X., MA, Y., WU, C., FAN, Q., WEI, S., LI, H. & LIU, J. 2019. Long non-coding RNA HOTAIR promotes exosome secretion by regulating RAB35 and SNAP23 in hepatocellular carcinoma. *Mol Cancer*, 18, 78.

- YANG, X., LIN, Y., SHI, Y., LI, B., LIU, W., YIN, W., DANG, Y., CHU, Y., FAN, J. & HE, R. 2016. FAP Promotes Immunosuppression by Cancer-Associated Fibroblasts in the Tumor Microenvironment via STAT3-CCL2 Signaling. *Cancer Res*, 76, 4124-35.
- YANG, Z., PENG, Y. C., GOPALAN, A., GAO, D., CHEN, Y. & JOYNER, A. L. 2017. Stromal hedgehog signaling maintains smooth muscle and hampers micro-invasive prostate cancer. *Dis Model Mech*, 10, 39-52.
- YEUNG, V., WEBBER, J. P., DUNLOP, E. A., MORGAN, H., HUTTON, J., GURNEY, M., JONES, E., FALCON-PEREZ, J., TABI, Z., ERRINGTON, R. & CLAYTON, A. 2018. Rab35-dependent extracellular nanovesicles are required for induction of tumour supporting stroma. *Nanoscale*, 10, 8547-8559.
- YU, G., WANG, L. G., HAN, Y. & HE, Q. Y. 2012. clusterProfiler: an R package for comparing biological themes among gene clusters. *OMICS*, 16, 284-7.
- YU, S., LIU, C., SU, K., WANG, J., LIU, Y., ZHANG, L., LI, C., CONG, Y., KIMBERLY, R., GRIZZLE, W. E., FALKSON, C. & ZHANG, H. G. 2007. Tumor exosomes inhibit differentiation of bone marrow dendritic cells. *J Immunol*, 178, 6867-75.
- YUANA, Y., KONING, R. I., KUIL, M. E., RENSEN, P. C., KOSTER, A. J., BERTINA, R. M. & OSANTO, S. 2013. Cryo-electron microscopy of extracellular vesicles in fresh plasma. *J Extracell Vesicles*, 2.
- ZEISBERG, E. M., POTENTA, S., XIE, L., ZEISBERG, M. & KALLURI, R. 2007. Discovery of endothelial to mesenchymal transition as a source for carcinoma-associated fibroblasts. *Cancer Res*, 67, 10123-8.
- ZHANG, D. X., VU, L. T., ISMAIL, N. N., LE, M. T. N. & GRIMSON, A. 2021. Landscape of extracellular vesicles in the tumour microenvironment: Interactions with stromal cells and with non-cell components, and impacts on metabolic reprogramming, horizontal transfer of neoplastic traits, and the emergence of therapeutic resistance. *Semin Cancer Biol*, 74, 24-44.
- ZHANG, H., FREITAS, D., KIM, H. S., FABIJANIC, K., LI, Z., CHEN, H., MARK, M. T., MOLINA, H., MARTIN, A. B., BOJMAR, L., FANG, J., RAMPERSAUD, S., HOSHINO, A., MATEI, I., KENIFIC, C. M., NAKAJIMA, M., MUTVEI, A. P., SANSONE, P., BUEHRING, W., WANG, H., JIMENEZ, J. P., COHEN-GOULD, L., PAKNEJAD, N., BRENDDEL, M., MANOVA-TODOROVA, K., MAGALHAES, A., FERREIRA, J. A., OSORIO, H., SILVA, A. M., MASSEY, A., CUBILLOS-RUIZ, J. R., GALLETI, G., GIANNAKAKOU, P., CUERVO, A. M., BLENIS, J., SCHWARTZ, R., BRADY, M. S., PEINADO, H., BROMBERG, J., MATSUI, H., REIS, C. A. & LYDEN, D. 2018a. Identification of distinct nanoparticles and subsets of extracellular vesicles by asymmetric flow field-flow fractionation. *Nat Cell Biol*, 20, 332-343.
- ZHANG, H., LIU, D., QIN, Z., YI, B., ZHU, L., XU, S., WANG, K., YANG, S., LIU, R., YANG, K. & XU, Y. 2023. CHMP4C as a novel marker regulates prostate cancer progression through cycle pathways and contributes to immunotherapy. *Front Oncol*, 13, 1170397.
- ZHANG, H. & LYDEN, D. 2019. Asymmetric-flow field-flow fractionation technology for exomere and small extracellular vesicle separation and characterization. *Nat Protoc*, 14, 1027-1053.
- ZHANG, M., CHEN, Z., WANG, Y., ZHAO, H. & DU, Y. 2022. The Role of Cancer-Associated Fibroblasts in Ovarian Cancer. *Cancers (Basel)*, 14.
- ZHANG, P., SAMUEL, G., CROW, J., GODWIN, A. K. & ZENG, Y. 2018b. Molecular assessment of circulating exosomes toward liquid biopsy diagnosis of Ewing sarcoma family of tumors. *Transl Res*, 201, 136-153.
- ZHANG, Q., JEPPESEN, D. K., HIGGINBOTHAM, J. N., DEMORY BECKLER, M., POULIN, E. J., WALSH, A. J., SKALA, M. C., MCKINLEY, E. T., MANNING, H. C., HIGHT, M. R., SCHULTE, M. L., WATT, K. R., AYERS, G. D., WOLF, M. M., ANDREJEVA, G., RATHMELL, J. C., FRANKLIN, J. L. & COFFEY, R. J. 2018c. Mutant KRAS Exosomes Alter the Metabolic State of Recipient Colonic Epithelial Cells. *Cell Mol Gastroenterol Hepatol*, 5, 627-629 e6.
- ZHANG, Q., LIU, R. X., CHAN, K. W., HU, J., ZHANG, J., WEI, L., TAN, H., YANG, X. & LIU, H. 2019a. Exosomal transfer of p-STAT3 promotes acquired 5-FU resistance in colorectal cancer cells. *J Exp Clin Cancer Res*, 38, 320.

- ZHANG, W., HONG, R., XUE, L., OU, Y., LIU, X., ZHAO, Z., XIAO, W., DONG, D., DONG, L., FU, M., MA, L., LU, N., CHEN, H., SONG, Y. & ZHAN, Q. 2017. Piccolo mediates EGFR signaling and acts as a prognostic biomarker in esophageal squamous cell carcinoma. *Oncogene*, 36, 3890-3902.
- ZHANG, X., SAI, B., WANG, F., WANG, L., WANG, Y., ZHENG, L., LI, G., TANG, J. & XIANG, J. 2019b. Hypoxic BMSC-derived exosomal miRNAs promote metastasis of lung cancer cells via STAT3-induced EMT. *Mol Cancer*, 18, 40.
- ZHANG, Y. W., WANG, L. M., JOVE, R. & VANDE WOUDE, G. F. 2002. Requirement of Stat3 signaling for HGF/SF-Met mediated tumorigenesis. *Oncogene*, 21, 217-26.
- ZHAO, H. & PEEHL, D. M. 2009. Tumor-promoting phenotype of CD90hi prostate cancer-associated fibroblasts. *Prostate*, 69, 991-1000.
- ZHAO, H., YANG, L., BADDOUR, J., ACHREJA, A., BERNARD, V., MOSS, T., MARINI, J. C., TUDAWA, T., SEVIOUR, E. G., SAN LUCAS, F. A., ALVAREZ, H., GUPTA, S., MAITI, S. N., COOPER, L., PEEHL, D., RAM, P. T., MAITRA, A. & NAGRATH, D. 2016. Tumor microenvironment derived exosomes pleiotropically modulate cancer cell metabolism. *Elife*, 5, e10250.
- ZHU, H., GUARIGLIA, S., YU, R. Y., LI, W., BRANCHO, D., PEINADO, H., LYDEN, D., SALZER, J., BENNETT, C. & CHOW, C. W. 2013. Mutation of SIMPLE in Charcot-Marie-Tooth 1C alters production of exosomes. *Mol Biol Cell*, 24, 1619-37, S1-3.
- ZHU, Q., YAMAKUCHI, M. & LOWENSTEIN, C. J. 2015. SNAP23 Regulates Endothelial Exocytosis of von Willebrand Factor. *PLoS One*, 10, e0118737.
- ZILBER, M. T., SETTERBLAD, N., VASSELON, T., DOLIGER, C., CHARRON, D., MOONEY, N. & GELIN, C. 2005. MHC class II/CD38/CD9: a lipid-raft-dependent signaling complex in human monocytes. *Blood*, 106, 3074-81.
- ZOMER, A., MAYNARD, C., VERWEIJ, F. J., KAMERMANS, A., SCHAFFER, R., BEERLING, E., SCHIFFELERS, R. M., DE WIT, E., BERENQUER, J., ELLENBROEK, S. I. J., WURDINGER, T., PEGTEL, D. M. & VAN RHEENEN, J. 2015. In Vivo imaging reveals extracellular vesicle-mediated phenocopying of metastatic behavior. *Cell*, 161, 1046-1057.
- ZOU, Y., SHI, H., LIU, N., WANG, H., SONG, X. & LIU, B. 2023. Mechanistic insights into heat shock protein 27, a potential therapeutic target for cardiovascular diseases. *Front Cardiovasc Med*, 10, 1195464.